HAL
open science

Metastability exchange optical pumping in 3He gas up to 30 mT: Efficiency measurements and evidence of laser-induced nuclear relaxation

Marion Batz

To cite this version:

Marion Batz. Metastability exchange optical pumping in 3He gas up to 30 mT: Efficiency measurements and evidence of laser-induced nuclear relaxation. Atomic Physics [physics.atom-ph]. Université Pierre et Marie Curie - Paris VI, 2011. English. NNT : . tel-00665393

HAL Id: tel-00665393

https://theses.hal.science/tel-00665393v1

Submitted on 1 Feb 2012

HAL is a multi-disciplinary open access archive for the deposit and dissemination of scientific research documents, whether they are published or not. The documents may come from teaching and research institutions in France or abroad, or from public or private research centers.

L'archive ouverte pluridisciplinaire **HAL**, est destinée au dépôt et à la diffusion de documents scientifiques de niveau recherche, publiés ou non, émanant des établissements d'enseignement et de recherche français ou étrangers, des laboratoires publics ou privés.

Département de Physique
École Normale Supérieure

Laboratoire Kastler Brossel

THÈSE de DOCTORAT de l'UNIVERSITÉ PARIS VI

Spécialité : Physique Atomique

présentée par

Marion BATZ

pour obtenir le grade de DOCTEUR de l'UNIVERSITÉ PARIS VI

Metastability exchange optical pumping in ^{3}He gas up to 30 mT: Efficiency measurements and evidence of laser-induced nuclear relaxation

---

Soutenue le 08 Juillet 2011
devant le jury composé de :

M.	**Hans-Jürgen ARENDS**	Universität Mainz	Rapporteur
M.	**Denis BOIRON**	Institut d'Optique	Rapporteur
M.	**Tomasz DOHNALIK**	Uniwersytet Jagielloński Kraków	Examinateur
Mme	**Lydia TCHANG-BRILLET**	Université Pierre et Marie Curie	Examinatrice
M.	**Werner HEIL**	Universität Mainz	Directeur de thèse
M.	**Pierre-Jean NACHER**	Laboratoire Kastler Brossel	Directeur de thèse

Merci ... Danke ... Dziękuję ... Thanks ...

... Werner Heil für die Wiederaufnahme in die Arbeitsgruppe nach Beendigung meines Referendariats, die Möglichkeit, ein interessantes Thema in Zusammenarbeit mit der ENS Paris zu bearbeiten, und die langjährige Finanzierung

... de tout cœur à mon directeur de thèse Pierre-Jean Nacher de l'encadrement excellent, pour avoir partagé son immense savoir scientifique, à la fois expérimental et théorique, ainsi que son enthousiasme, de sa grande disponibilité, même les soirs, week-ends et jours feriés, de son soutien continu, aussi pendant des périodes difficiles et pour l'occasion d'apprendre de lui pour la vie, l'art de positiver par exemple

... du fond du cœur également à Geneviève Tastevin, chercheuse toute aussi brillante d'un dynamisme incroyable, de l'excellente formation scientifique, de son optimisme et soutien continu, pour être souvent restée au labo avec moi tard le soir et pour avoir toujours pris soin de mon bien-être à Paris

... allen Mitgliedern der Arbeitsgruppe in Mainz, besonders Claudia Gemmel, Manuela Güldner, Gertrud Konrad, Anna Nikiel, Maricel Repetto und Kathlynne Tullney für die tolle weibliche Unterstützung, außerdem Raquel Muñoz Horta und Michael Borg für die nette Bürogemeinschaft sowie Fidel Ayala Guardia, Stefan Hiebel, Sergei Karpuk, Wolfgang Ketter, Jan Klemmer, Jochen Krimmer, Christian Mrozik, Ernst Otten, Daniel Rudersdorf, Zahir Salhi, Jörg Schmiedeskamp, Wolfgang Stampp und Michael Wolf für das angenehme Arbeitsklima und vielfältige Hilfe

... à tous les membres de l'équipe au LKB pour m'avoir toujours bien intégrée dans toutes les constellations de personnages et de la richesse culturelle, en particulier à Marie Abboud, Emmanuel Baudin et Mathieu Melich de leur aide scientifique et non-scientifique. Thanks also to Bartosz Głowacz, Kajum Safiullin and Cavin Talbot, not only for funny French lessons during lunch

... den Sekretariaten und gemeinsamen Einrichtungen am Institut für Physik: Mechanische Werkstatt, Glasbläserei, EDV-Service, Etatverwaltung. Ein besonderer Dank an Lars Funke und Heiko Lott sowie Peter Becker, Siegbert Felzer, Markus Kaltenborn und Wolfgang Wann für ihr großes Engagement beim Bau des Solenoiden. Ebenso an Christine Best und Elvira Stuck-Kerth für den Sonnenschein im Alltag, und auch an Michael Schlüter, Anton Gläser und Wolfram Vogt für stets schnelle und unbürokratische Hilfe

... à tous ceux qui contribuent à l'environnement scientifique et humain exceptionnel ainsi qu'aux conditions de travail privilégiées au LKB. Merci à tous les services administratifs et techniques du LKB et du département de Physique de l'ENS: les secrétariats, les ateliers mécanique du LKB, général et de verrerie, ainsi que les services généraux, électronique et

informatique. Merci en particulier à Linda Krikorian, Thierry Tardieu, Christophe Bernard, Didier Courtiade, Jean-François Point et Lionel Pérennès de leur aide rapide

... to my Polish friends and colleagues from Kraków for their warm welcome at the Atomic Optics Department of the Jagiellonian University and to Zbigniew Olejniczak for his interest in my work and the opportunity to learn from him during the visit of his lab at the Institute for Nuclear Physics, Polish Academy of Sciences. Special thanks to my kindred spirits, Katarzyna Cieślar and Anna Nikiel, for their sympathy and support. Un grand merci aussi à Tomasz Dohnalik pour avoir partagé sa sagesse scientifique et humaine, aussi pendant des séjours communs au LKB, et pour m'avoir fait l'honneur d'être membre de mon jury de thèse

... sincèrement aux membres du jury de l'intérêt pour ma thèse, surtout aux rapporteurs Denis Boiron et Hans-Jürgen Arends pour le travail de l'examen du manuscrit. Special thanks to the non-local members of the board of examiners for having accepted inconveniences

... to Deutsche Forschungsgemeinschaft (DFG) and European Commission, Marie Curie Early Stage Training, for main funding

... Gerhard Huber für die kontinuierliche Frankreich-spezifische Beratung und Unterstützung

... Ferenc Glück, Karlsruher Institut für Technologie, für die Hilfe bei der Homogenitätsoptimierung des Solenoiden und das Zurverfügungstellen seiner entwickelten Programme

... Anselm Deninger, TOPTICA Photonics AG, für interessante gemeinsame Messungen in Paris und einen Einblick in die Arbeitswelt von Physikern in der Industrie

... to my non-scientific friends for their patience and "grounding"

... meinen Eltern Hedi und Gerhard Batz für ihre vielfältige Unterstützung

... meinem Bruder Ingo Batz für den guten Zusammenhalt

... meinem Freund Rolf Dauer dafür, dass er schon mein halbes Leben lang bedingungslos zu mir hält

... to all of you who travelled to Paris for my PhD defence. It was a great pleasure!

Contents

List of Figures V

List of Tables XIV

List of Symbols, Constants, He OP lines, Abbreviations XVI

1 Introduction 1

2 MEOP basics and OP model 4

2.1 Short introduction to MEOP . . . 6
2.2 He level structure at low magnetic field . . . 8
2.3 Optical transition rates . . . 13
2.3.1 Monochromatic excitation . . . 13
2.3.2 Broadband excitation . . . 17
2.4 Rate equations for OP and ME in pure ^{3}He gas . . . 17
2.4.1 Generic OP rate equations . . . 19
2.4.2 Generic ME rate equations . . . 20
2.5 The improved 2-class OP model . . . 23
2.5.1 Relaxation processes . . . 23
2.5.2 Velocity-dependent light excitation . . . 24
2.5.3 Inhomogeneous light excitation and atomic response: 1-D model 28
2.6 Comparison of all rates relevant for MEOP in ^{3}He gas . . . 29
2.7 Numerical computation of MEOP dynamics . . . 31
2.7.1 Equation solving strategy . . . 31
2.7.2 Full rate equations . . . 31
2.7.3 Numerical implementation . . . 33
2.7.4 Input data and input parameters . . . 34
2.8 MEOP dynamics . . . 36
2.8.1 ME-driven spin temperature distribution . . . 37
2.8.2 Dynamics of polarisation decay (no OP) . . . 38
2.8.3 OP-driven MEOP dynamics . . . 42
2.8.4 Angular momentum budget . . . 46

2.9 Photon efficiencies for low field MEOP . . . 51
2.10 Final discussions . . . 57
2.10.1 Comparison with previous OP models . . . 57
2.10.2 Robustness of our computed OP results . . . 58
2.10.3 Conclusion . . . 60

3 Experimental setup **61**
3.1 Magnetic field, cells and rf discharge . . . 61
3.2 Optical setup . . . 66
3.3 Measurement and acquisition system . . . 73

4 Optical measurement of nuclear polarisation **75**
4.1 Longitudinal probe absorption measurements . . . 79
4.2 Polarisation measurements in the absence of OP light (during polarisation decay) . . . 84
4.2.1 Determination of M by C_8 probe . . . 87
4.2.2 Determination of M by C_9 probe . . . 89
4.2.3 Influence of residual π-light on longitudinal probe absorption measurements . . . 107
4.3 Polarisation measurements with OP light (during polarisation build-up) 109
4.4 Measurements of metastable density $n_{\mathrm{m}}^{\mathrm{S}}$ . . . 112
4.4.1 Determination of $n_{\mathrm{m}}^{\mathrm{S}}$ for single-component and multi-component transitions: Examples of C_8 and C_9 probe . . . 112
4.4.2 Influence of collisional broadening and lifetime . . . 117

5 Methods of data processing and data reduction **122**
5.1 Introduction to data reduction . . . 122
5.2 Polarisation build-up and decay . . . 124
5.2.1 Transmitted probe signals . . . 127
5.2.2 Demodulated probe signals . . . 130
5.3 Dedicated experiments to account for perturbations of 2^3S- and 2^3P-populations in presence of the pump laser . . . 133
5.4 Inferring *actual* M-values during polarisation build-up in presence of the pump laser . . . 140
5.5 Analysis of polarisation build-up kinetics . . . 141
5.6 Pump output signals . . . 150
5.6.1 Transmitted pump signals . . . 150
5.6.2 Demodulated pump signals . . . 152
5.7 Laser-enhanced relaxation . . . 155
5.7.1 Deriving polarisation loss rates Γ_{R} using the MEOP model . . . 156

5.7.2 Deriving polarisation loss rates Γ_{R} from a detailed balance of angular momentum . . . 159

6 Results **164**

6.1 Characterisation of the plasma without OP light . . . 164

6.1.1 Key plasma parameters for MEOP: $n_{\mathrm{m}}(M=0)$ and Γ_D . . . 166

6.1.2 Transverse distribution of 2^3S atoms . . . 176

6.1.3 Variation of metastable density with nuclear polarisation . . . 191

6.2 Results of dedicated experiments to account for perturbations of 2^3S- and 2^3P-populations . . . 197

6.2.1 Influence of probe detuning on apparent polarisation at $M=0$. 197

6.2.2 Computed M^a at $M=0$ with probe laser in resonance as function of pump laser power . . . 203

6.2.3 Example of apparent polarisation as function of actual polarisation . . . 206

6.2.4 Reproducibility of apparent polarisation in fixed OP conditions 208

6.2.5 Examples of M^a measured by probe on the C_9-transition . . . 212

6.2.6 Perturbations of 2^3S and 2^3P populations in higher magnetic field: $B=30$ mT versus 1 mT . . . 214

6.2.7 Scaling of M^a with incident pump laser power and pressure . . . 216

6.2.8 Effect of pump beam diameter and probe parameter x_s on apparent polarisation . . . 221

6.2.9 Conclusion . . . 221

6.3 Optical Pumping results at 1 mT . . . 222

6.3.1 Results at $B=1$ mT and $M=0$: Relaxation-free data to test and validate the model for MEOP kinetics . . . 222

6.3.2 Empirical determination of the intrinsic relaxation rate in the 2^3P state . . . 246

6.3.3 Results at M_{eq} ($B=1$ mT) and evidence of laser-enhanced relaxation . . . 253

6.3.4 Results as function of M ($B=1$ mT) and further characterisation of laser-induced relaxation . . . 270

6.4 Effects of magnetic field on OP performances . . . 277

6.5 Discussion of laser-enhanced relaxation effects . . . 285

6.5.1 Comparison of Γ_{L} rates of different works . . . 286

6.5.2 Radiation trapping . . . 289

6.5.3 OP-induced plasma 'poisoning' (e.g., by metastable He molecules) 292

7 Conclusion and Outlook **296**

A Tables and matrices for low magnetic field ($B < 0.162$ T): Transition frequencies and intensities for ^{3}He and ^{4}He, Zeeman shifts, hyperfine mixing parameters, vector and matrix operators **302**

B MEOP rate equations and angular momentum budget in the improved OP model **310**
B.1 The improved OP model 310
B.2 Two-class partition and description of local OP rates 311
B.3 Local rate equations for 2^3S and 2^3P populations 314
B.4 Rate equation for M, MEOP dynamics, and global angular momentum budget 319

C Computation of the average pump light intensity inside the cell for the improved OP model **321**

D Computation of photon efficiencies of C_8 and C_9 lines at null polarisation and in zero magnetic field, for the limits of no and full collisional mixing in the 2^3P state (Kastler and Dehmelt OP regimes) **326**

E Numerical demodulation of signals **331**
E.1 Requirements and characteristic functionalities 331
E.2 Rician noise in the context of lock-in detection 346

F Validation of methodological approach in analysis of polarisation build-up kinetics using synthetic data **352**

G Influence of stimulated emission on scaling of M^a with incident pump laser power and pressure **375**

Bibliography **380**

Abstract **395**

List of Figures

2.1 Basic MEOP setup and fine- and hyperfine-structures of the involved atomic states for ^{4}He and ^{3}He . . . 8
2.2 Structure of the 2^3S and 2^3P states of ^{3}He and ^{4}He and components of the 1083 nm optical transition at low magnetic field . . . 10
2.3 Reduced Zeeman shifts and relative changes of transition intensities for C_8 and C_9 as a function of magnetic field up to $B = 30$ mT . . . 12
2.4 Computed ^{3}He spectra for $B = 30$ mT for σ^+ and σ^- light . . . 14
2.5 Two-class OP model: Maxwell velocity distribution of atoms and spectral density distribution of the pumping laser . . . 25
2.6 Variation of ^{3}He populations in 2^3S as a function of nuclear polarisation in the spin temperature limit . . . 39
2.7 Computed differences of a_i populations in absence of OP with respect to ST distribution and corresponding difference between M^{S} and M as a function of M . . . 40
2.8 Under-estimation of ground state polarisation using ST formulas for probe absorption measurements performed during decay . . . 41
2.9 Analytical function and numerical computation of decay rate factor f_Γ 43
2.10 Computed differences of a_i populations under influence of OP on C_8 with respect to ST distribution . . . 44
2.11 Computed differences of a_i populations under influence of OP on C_9 with respect to ST distribution . . . 45
2.12 Computed apparent polarisation M^a: pump C8, 1 W, probe C_8 on optical axis . . . 46
2.13 Computed difference between 2^3S polarisation M^S and ground state polarisation M under influence of OP on C_8 and C_9 . . . 47
2.14 Computed photon efficiencies as function of M for C_8 and C_9 . . . 52
2.15 Computed photon efficiencies for C_8 and C_9 for different polarisation values as function of τ_P . . . 54
2.16 Ratio of photon efficiencies C_9/C_8 for different polarisation values as function of τ_P . . . 55
2.17 Computed power dependence of the photon efficiency of the C_9 line at M=0 and M=0.5. . . . 57

2.18 Influence of width of strongly pumped velocity class on time derivative of polarisation . . . 59

3.1 Overview of the experimental setup . . . 62
3.2 Non-optimised electrode configuration on 2.45 mbar-cell . . . 64
3.3 Methods to evaluate electrode configurations . . . 65
3.4 Photo and schematic of the optical setup used for low-field MEOP studies 67
3.5 Spatial power distribution of the pump laser . . . 69
3.6 Additional optical setup: Injection of probe laser into optical fibre . . . 71
3.7 Geometrical parameters specifying the probe paths . . . 72
3.8 Schematic of the measurement and acquisition system . . . 73

4.1 Computed ratios of $2^3\mathrm{S}-2^3\mathrm{P}_0$ absorption signals in transverse and longitudinal probe configuration . . . 78
4.2 Computed absorption spectrum of ^{3}He at $B = 30$ mT including transitions at $B = 0$ . . . 80
4.3 Experimental absorption spectrum of ^{3}He at $B = 30$ mT, $p_3 = 1.07$ mbar and $M \neq 0$ . . . 81
4.4 Longitudinal probe scheme in double pass configuration . . . 82
4.5 Reduced probe absorption signals on C_8 and C_9 as a function of M in spin temperature limit . . . 86
4.6 Computed M_8 from reduced ratio R_8 or from ratio r_8 of absorption signals as a function of probe frequency at $B = 30$ mT. . . . 88
4.7 M_9 in pure ^{3}He from *reduced* ratio of (computed) probe absorption signal as function of probe frequency for different B . . . 92
4.8 M_9 in pure ^{3}He from ratio r of probe absorption signals as function of probe frequency for different B . . . 94
4.9 Ratios of given nuclear polarisation values divided by determined M_9 as function of probe frequency in pure ^{3}He at $B = 30$ mT . . . 96
4.10 Ratio of given polarisation M divided by determined M_9 at fixed probe frequency as function of M in pure ^{3}He at $B = 30$ mT . . . 98
4.11 Influence of ^{4}He on M_9 at $B = 1$ mT and $M = 0.7$ . . . 99
4.12 Influence of ^{4}He on M_9 at $B = 30$ mT and $M = 0.7$ . . . 101
4.13 Ratios of given nuclear polarisation values divided by determined M_9 as function of probe frequency in ^{3}He with residual ^{4}He ($x_4 = 0.4$ %) at $B = 1$ mT . . . 102
4.14 Ratios of given nuclear polarisation values divided by determined M_9 as function of probe frequency in ^{3}He with residual ^{4}He ($x_4 = 0.4$ %) at $B = 30$ mT . . . 103
4.15 Ratio of given polarisation M divided by determined M_9 at fixed probe frequency as function of M in ^{3}He with 0.4 % of ^{4}He at $B = 1$ mT . . . 104

4.16 Ratio of given polarisation M divided by determined M_9 at fixed probe frequency as function of M in ^{3}He with 0.4 % of ^{4}He at $B = 30$ mT . . 106
4.17 Influence of π-light on the determination of M by probe absorption measurements 108
4.18 Computed OP light-induced changes in 2^3S and 2^3P$_0$ populations . . . 110
4.19 Comparison of transition intensities of unbroadened Gaussian and pressure broadened Voigt profiles at 2.67 mbar as function of probe frequency 118
4.20 Ratio of transition intensities of Gaussian line shape divided by $S(\omega/2\pi)$ of pressure broadened Voigt profile as function of probe frequency 120

5.1 Example of raw transmitted probe powers and temporal evolution of averaged transmitted probe power signals in polarisation build-up and decay protocol 126
5.2 Temporal evolution of probe transmission coefficients in polarisation build-up and decay protocol 129
5.3 Temporal evolution of probe absorption signals and their reduced ratio in polarisation build-up and decay protocol 130
5.4 Temporal evolution of nuclear polarisation in polarisation build-up and decay protocol 132
5.5 Temporal evolution of nuclear polarisation in dedicated experiments to account for perturbations of 2^3S- and 2^3P-populations in presence of the pump laser 135
5.6 Transmitted pump signal and first-order derivative in dedicated experiments 136
5.7 ΔM / Δt values deduced from dedicated experiments 138
5.8 Actual polarisation as function of apparent polarisation in dedicated experiments 139
5.9 Correction of apparent polarisation values during build-up to obtain actual polarisation values 141
5.10 Example of polarisation build-up and decay at $p_3 = 0.63$ mbar 142
5.11 Semi-logarithmic plots of polarisation build-up and decay 143
5.12 M_{eq} minus $M(t)$ (logarithmic scale) as function of time 145
5.13 $\dot{M}$ of experimental example for different lengths of fit intervals in the dedicated programme 148
5.14 Build-up times of experimental example as function of M for different input-values of M_{eq} in the programme 149
5.15 Transmitted pump power signal as function of time 151
5.16 Pump transmission coefficient T_p and absorbance for the pump laser $-\ln T_p$ as function of M during polarisation build-up. 153

5.17 Experimental and computed steady-state polarisation and rates of change of polarisation as function of incident pump laser power 155
5.18 Experimental and computed $\dot{M}$ for C_9 OP in 2.45 mbar and determined laser-induced relaxation rates (inset) as a function of M 157
5.19 ME contributions to the evolution of M computed as a function of M for OP on C_9 and C_8 158
5.20 Example of total relaxation rates for C_8 pumping as function of polarisation and absorbed laser power 162
5.21 Additional laser-induced loss rate Γ_L for an example of C_8 OP as a function of absorbed pump laser power 163

6.1 Impact of magnetic field on rf plasmas in low pressure ^{3}He gas 165
6.2 Impact of gas pressure on rf plasmas at low magnetic field 166
6.3 Different probe configurations for determination of metastable densities 167
6.4 Γ_D as function of $n_m(M = 0)$ at low field and low pressure (overview) . 170
6.5 Γ_D as function of $n_m(M = 0)$ at low field and low pressure (this work only) 171
6.6 Γ_D as function of $n_m(M = 0)$ at low field and low pressure (different pressure ranges) 172
6.7 Effect of magnetic field ($B = 1$ versus 30 mT) on plasmas at low pressure 174
6.8 Effect of high magnetic field ($B = 1.5$ T versus 2 mT) on plasmas at higher pressure ($p_3 = 8$ and 32 mbar) [Abb05b] 175
6.9 Theoretical radial n_m-distributions for different values of α and Gaussian fit of spatial pump laser profile 178
6.10 Fits of radial n_m-distributions in $B = 1$ and 30 mT at $p_3 = 2.45$ mbar . 180
6.11 Compilation of α-values at $p_3 = 2.45$ mbar in $B = 1$ and 30 mT 181
6.12 Compilation of α-values at $p_3 = 0.63$ mbar in $B = 1$ and 30 mT 184
6.13 Radial n_m-mappings at $p_3 = 0.63$ mbar at different magnetic fields between 1 and 30 mT 185
6.14 Ratio of absorbance values in the centre of the radial n_m-distribution divided by the integral value over the radial laser profile 187
6.15 Influence of pump beam diameter at fixed α on apparent polarisation M_8^a at $M = 0$ 189
6.16 Influence of α on probe absorptance at fixed pump beam diameter . . . 190
6.17 Relative variation of n_m in $B = 1$ mT and $p_3 = 1.19$ mbar as function of M, during continuous polarisation decay and from dedicated experiments during periods where the OP beam is blocked 192
6.18 Relative variation of n_m at $p_3 = 1.19$ mbar, in $B = 1$ and 30 mT as function of M^2 193

6.19 Apparent polarisation at $M = 0$ as function of probe frequency in $p_3 = 2.45$ mbar: $W_{\text{inc}} = 1.66$ W, different combinations of pump and probe-transitions (C_6, C_8 and C_9) 198
6.20 Apparent polarisation at $M = 0$ as function of probe detuning in $p_3 = 2.45$ mbar for various W_{inc}: different combinations of pump and probe-transitions (C_8 and C_9) 200
6.21 Apparent polarisation values at $M = 0$ in $p_3 = 0.63$ mbar for single-frequency OP applied on the C_8-transition as function of probe detuning 202
6.22 Computations of apparent polarisation at $M = 0$ in $p_3 = 2.45$ mbar and $B = 1$ mT as function of incident pump laser power, in 'strongly pumped velocity class' and 'weakly pumped velocity class' 204
6.23 Apparent polarisation as function of actual polarisation during a dedicated experiment to account for perturbations of 2^3S- and 2^3P-populations and corresponding computations in $B = 1$ mT 207
6.24 Reproducibility of apparent polarisation values in fixed OP-conditions at $p_3 = 0.63$ mbar, $B = 1$ mT 209
6.25 Reproducibility of apparent polarisation values in fixed OP-conditions at $p_3 = 2.45$ mbar, $B = 1$ mT 210
6.26 Apparent polarisation values for probe C_8 and C_9 in fixed pumping conditions: $W_{\text{inc}} = 1.66$ W on C_8 in $p_3 = 0.63$ and 1.19 mbar, $B = 1$ mT 212
6.27 Apparent polarisation values in $p_3 = 2.45$ mbar, $B = 1$ and 30 mT. Pump: C_8 and C_9 $W_{\text{inc}} = 1.66$ W, probe fixed to C_8. 215
6.28 Apparent polarisation values for different incident pump laser powers on C_8 and C_9 at fixed probe transition C_8 in $p_3 = 0.63$ mbar, $B = 1$ mT 216
6.29 Apparent polarisation values for different incident pump laser powers on C_8 and C_9 at fixed probe transition C_8 in $p_3 = 2.45$ mbar, $B = 1$ mT 217
6.30 Apparent polarisation as function of actual polarisation at fixed OP conditions for three different values of ^{3}He pressure 218
6.31 Apparent polarisation as function of actual polarisation at fixed ratio W_{inc}/p_3 in $B = 1$ mT 220
6.32 Experimental and computed pump transmission coefficient at $M = 0$ in $B = 1$ mT and $p_3 = 0.63$ mbar as function of incident pump laser power 225
6.33 Experimental and computed pump transmission coefficient at $M = 0$ in $B = 1$ mT and $p_3 = 0.63$ mbar for different assumptions of $\gamma_{\text{r}}^{\text{P}}$ 226
6.34 Comparison of pump and probe transmission coefficients in presence of the pump laser in $B = 1$ mT and $p_3 = 0.63$ mbar, $M = 0$ 227
6.35 Experimental and computed pump transmission coefficient on C_9 at $M = 0$ in $B = 1$ mT and $p_3 = 2.45$ mbar as function of incident pump laser power 229

6.36 Comparison of pump and probe transmission coefficients in presence of the pump laser in $B = 1$ mT and $p_3 = 2.45$ mbar, $M = 0$ 231
6.37 Experimental time derivative of polarisation at $M = 0$ and $p_3 = 0.63$ mbar: fixed n_m (weak discharge), C_8 and C_9 transitions. Computations: Influence of $\gamma_\mathrm{r}^\mathrm{P}$ at fixed α. 234
6.38 Experimental time derivative of polarisation at $M = 0$ and $p_3 = 0.63$ mbar: fixed transition (C_8) and different n_m (two discharges). Computations: Influence of α on $\dot{M}(0)$ at fixed $\gamma_\mathrm{r}^\mathrm{P}$. 236
6.39 Experimental and computed time derivative of polarisation at $M = 0$ and $p_3 = 2.45$ mbar as function of incident pump laser power 237
6.40 Experimental and computed values of $\dot{M}(0)$ as function of absorbed laser power, both on the C_8-transition at $M = 0$ for three different pressure values 239
6.41 Photon efficiency of C_8 pump transition at $p_3 = 0.63$ mbar 242
6.42 Photon efficiency of C_8 pump transition at $p_3 = 1.19$ mbar 243
6.43 Photon efficiency of C_8 pump transition at $p_3 = 2.45$ mbar 244
6.44 Empirical determination of intrinsic relaxation rate in 2^3P by comparison of experimental and computed ratios of photon efficiencies η_{C9}/η_{C8} at $M = 0$ 248
6.45 Steady state polarisation at $p_3 = 0.63$ mbar, pump and probe C_8 and $B = 1$ mT as function of incident pump laser power 255
6.46 Steady state polarisation at $p_3 = 1.19$ mbar, pump and probe C_8 and $B = 1$ mT as function of incident pump laser power 256
6.47 Steady state polarisation at $p_3 = 2.45$ mbar, pump C_9, probe C_8 and $B = 1$ mT as function of incident pump laser power 258
6.48 Experimental steady-state polarisation values as function of ^{3}He-pressure 259
6.49 Total relaxation rate Γ_R at steady state polarisation M_eq at $p_3 = 0.63$ mbar, $B = 1$ mT and OP on C_8 as function of incident and absorbed laser power 263
6.50 Total relaxation rate Γ_R at steady state polarisation M_eq, $B = 1$ mT and OP on C_8 for three different pressure values as function of incident and absorbed laser power 265
6.51 Difference between total relaxation rate Γ_R and decay rate Γ_D at steady state polarisation M_eq at $p_3 = 0.63$ mbar, $B = 1$ mT and OP on C_8 as function of absorbed laser power 267
6.52 Difference between total relaxation rate Γ_R and decay rate Γ_D at steady state polarisation M_eq at $p_3 = 1.19$ mbar, $B = 1$ mT and OP on C_8 as function of absorbed laser power 268
6.53 Difference between total relaxation rate Γ_R and decay rate Γ_D at steady state polarisation M_eq at $p_3 = 2.45$ mbar, $B = 1$ mT and OP on C_8 as function of absorbed laser power 269

6.54 Comparison of Γ_L-values from polarisation build-up kinetics and in steady state conditions at $p_3 = 0.63$ mbar, $B = 1$ mT and OP on C_8 as function of absorbed laser power . . . 271
6.55 Examples of differences between experimental total polarisation loss rates Γ_R and decay rates Γ_D at three values of ^{3}He-pressure as function of absorbed OP power (C_8-pumping, $B = 1$ mT) . . . 273
6.56 Differences between experimental total polarisation loss rates Γ_R and decay rates Γ_D for C_8- and C_9-pumping at $p_3 = 2.45$ mbar and $B = 1$ mT as function of absorbed OP power . . . 275
6.57 Steady state polarisation obtained on C_8 and C_9 at 1 and 30 mT as a function of metastable density at fixed $W_{inc} = 1.66$ W for three values of ^{3}He pressure . . . 278
6.58 Time derivative of polarisation at $M = 0$ for C_8-pumping at 2.45 mbar as a function of absorbed pump laser power in $B = 1$ and 30 mT, weak discharge . . . 280
6.59 OP-induced relaxation rates Γ_L for C_8-pumping as a function of absorbed pump laser power, in $B = 1$ and 30 mT, 2.45 mbar, weak discharge . . . 281
6.60 Comparison of 1 and 30 mT data at 2.45 mbar: fraction of absorbed pump laser power, steady state polarisation and total relaxation rate at M_{eq} as function of absorbed pump laser power at M_{eq}: weak discharge, C_8 and C_9 pumping . . . 283
6.61 Comparison of 1 and 30 mT data at 2.45 mbar: fraction of absorbed pump laser power, steady state polarisation and total relaxation rate at M_{eq} as function of absorbed pump laser power at M_{eq}: strong discharge, C_9 pumping . . . 284
6.62 Comparison of OP-induced relaxation rates at steady state or during complete build-up kinetics of different works in different conditions of pressure and magnetic field as a function of absorbed pump laser power per cell volume . . . 287
6.63 Functions f_k and ratios f_k/M of [Eck92] . . . 291
6.64 Variation of the steady-state values of $\Gamma_L/(W_{abs}V_c)$ with 2^3S atom number density n_m^S . . . 293

C.1 Scheme illustrating the analytical derivation of the local pump light intensity $I(z)$ . . . 322
C.2 Evolution of local pump light intensity $I(z)$ under the influence of progressive resonant absorption by the gas . . . 324

D.1 Involved magnetic sublevels in C_9 σ^+ excitation . . . 328
D.2 C_8 OP cycle with no collisional redistribution in 2^3P . . . 328

E.1 Comparison of demodulated probe signals (magnitude) obtained in simplified and non-simplified approach of numerical demodulation 338
E.2 Averaged transmitted probe powers during polarisation build-up (simplified and non-simplified approach) 339
E.3 Comparison of probe absorption signals proportional to absorbances $-\ln(T_s^{\pm})$ using simplified and non-simplified approaches for the numerical demodulation of signals 340
E.4 Comparison of demodulated σ^+ probe signals (simplified approach) at different incident pump laser powers 342
E.5 Comparison of demodulated σ^- probe signals (simplified approach) processed with different time constants τ 343
E.6 Comparison of demodulated pump signals obtained by an analogue lock-in amplifier or numerically post-processed 345
E.7 Comparison of magnitude and in-phase component in noisy synthetic data (noise amplitude: 0.01) 347
E.8 Comparison of magnitude and in-phase component in noisy synthetic data (noise amplitude: 0.1) 349
E.9 Comparison of magnitude and in-phase difference signals: Subtraction of noiseless from noisy synthetic data (noise amplitude: 0.1) 350

F.1 $\dot{M}$ and T_b values for synthetic data generated by the MEOP-model . . 353
F.2 Extrapolation of $\dot{M}(M=0)$ on generated C_8-data 355
F.3 Different fitting polynomials on noisy data with additional relaxation . 356
F.4 Fitting polynomials on a different example of noisy data with additional relaxation 359
F.5 Extrapolation of $\dot{M}(M=0)$ on generated C_9-data 361
F.6 $\dot{M}$ of noisy synthetic data for different lengths of fit intervals in the dedicated programme 363
F.7 Ratios of extrapolated and theoretical $\dot{M}(0)$ values for different polynomial fits on three outputs of the dedicated programme using different lengths of fit intervals to determine build-up times 366
F.8 Influence of the choice of M_{eq} in build-up analysis on build-up time constants T_b 369
F.9 Determination of T_b by exponential fits on $M(t)$ versus linear fits on $\ln(M_{\mathrm{eq}} - M)$ 371
F.10 Behaviour of linear fits on noisy exponential decay in logarithmic representation 372

G.1 Theoretical verification of scaling of apparent polarisation values with W_{inc}/p_3 in Kastler- and Dehmelt-regimes 376

G.2 Populations and apparent polarisation at $M = 0$ (probe C_8) as function of reduced incident power (pump C_8) for *no* collisional redistribution in 2^3P 377
G.3 Populations and apparent polarisation at $M = 0$ (probe C_8) as function of reduced incident power (pump C_8) for *full* collisional redistribution in 2^3P 377

List of Tables

2.1 Computed photon efficiencies η_{C8} and η_{C9} at $M = 0$ for $B = 1$ mT . . . 53

3.1 Table of gas pressures and inner dimensions of quartz glass cells used in this work . . . 64

5.1 Typical timing of polarisation build-up and decay protocol . . . 125

6.1 Average normalised probe absorption rate as function of α in different probe configurations . . . 168

6.2 Apparent polarisation values at $M = 0$ in $p_3 = 2.45$ mbar for different values of incident pump laser powers and different combinations of pump- and probe-transitions in resonance . . . 201

6.3 Compilation of error-weighted mean values of η_{C8} and standard deviations for different ^{3}He-pressures . . . 245

A.1 Optical transition intensities T_{ij} and transition frequencies ϵ_{ij} of ^{3}He in $B = 0$ . . . 303

A.2 Optical transition intensities $T_{ij}^{(4)}$ and transition frequencies $\epsilon_{ij}^{(4)}$ of ^{4}He in $B = 0$ . . . 304

A.3 Coefficients of equations (2.2) and (2.3) for C_8, C_9 and D_0 . . . 305

A.4 Optical transition intensities T_{ij}, transition frequencies ϵ_{ij} and reduced Zeeman shifts of ^{3}He in $B = 0 - 30$ mT: C_8 line . . . 306

A.5 Optical transition intensities T_{ij}, transition frequencies ϵ_{ij} and reduced Zeeman shifts of ^{3}He in $B = 0 - 30$ mT: C_9 $\sigma+$ . . . 307

A.6 Optical transition intensities T_{ij}, transition frequencies ϵ_{ij} and reduced Zeeman shifts of ^{3}He in $B = 0 - 30$ mT: C_9 $\sigma-$ . . . 307

A.7 Matrix elements of operator L ($B < 0.162$ T) . . . 308

A.8 Matrix elements of $2E^3$ ($B < 0.162$ T) . . . 308

A.9 Matrix elements of $2F^3$ ($B < 0.162$ T) . . . 309

D.1 Photon efficiency values at $M = 0$ and $B = 0$ for C_8 and C_9 in 'Kastler' and 'Dehmelt' OP regimes . . . 330

F.1 Statistical parameters of fits on $\dot{M}$ values of noisy data 357
F.2 Statistical parameters of fits on $\dot{M}$ of noisy data (different example of Gaussian noise) 358
F.3 Extrapolation of $\dot{M}(0)$ by polynomial fits (no error weighting) on $\dot{M}$ values provided by the dedicated programme for different lengths of the fit intervals 364
F.4 Extrapolation of $\dot{M}(0)$ by polynomial fits (with error weighting) on $\dot{M}$ provided by the dedicated programme for different lengths of the fit intervals 365

List of Symbols

A	$\propto -\ln(T_s)$ probe absorption signal and amplitude prefactor of radial n_m-distribution
A_+	σ^+ probe absorption signal
A_-	σ^- probe absorption signal
A_i	labelling of magnetic 2^3S sublevels ($i = 1 - 6$)
A_s	$= 1 - T_s$: probe absorptance
A_p	$= \frac{P_p}{S_p} \propto -\ln(T_p)$ pump absorption signal
A_0	$= 1 - T_p(M = 0) = \frac{W_{\text{abs}}(M=0)}{W_{\text{inc}}}$: pump absorptance at $M = 0$ = fraction of absorbed pump power at zero nuclear polarisation
A_{eq}	$= 1 - T_p(M_{\text{eq}}) = \frac{W_{\text{abs}}(M\text{eq})}{W_{\text{inc}}}$: pump absorptance at M_{eq} = fraction of absorbed pump power at steady-state nuclear polarisation
a	$= \frac{\text{FWHM}}{2\sqrt{\ln 2}}$. $2a$: waist of pumping beam diameter
a_i	relative population of 2^3S sublevel A_i
a_i^*	population of 2^3S sublevel A_i in strongly pumped velocity class
a_i'	population of 2^3S sublevel A_i in weakly pumped velocity class
B	magnetic field
B_j	labelling of 2^3P sublevels ($j = 1 - 18$)
b_j	relative population of 2^3P sublevel B_j
b_j^*	population of 2^3P sublevel B_j in strongly pumped velocity class
b_j'	population of 2^3P sublevel B_j in weakly pumped velocity class
C	$= \left\langle \frac{\dot{M}(0)}{W_{\text{nom}}\, A_0} \right\rangle$: scaling factor in angular momentum budget, proportional to photon efficiency
C_1 to C_9	^{3}He lines for the 2^3S-2^3P transition
D	Doppler width
d_{cell}	inner diameter of glass cell, filled with ^{3}He and/or ^{4}He
dx_s	radial distance between ingoing and outcoming centres of probe beam in cell
E	optical transition energy of He atom
e^-	electron
F	total angular momentum of hyperfine level
f_Γ	function describing the change of ME contribution to polarisation decay in 1^1S_0 in absence of OP
f_Γ'	function describing the change of ME contribution to polarisation decay in 1^1S_0 during OP
He(1^1S_0)	ground state helium atom
He^+	helium ion
He^*	metastable helium atom

He_2^*	metastable helium molecule
I	nuclear spin angular momentum
I_z	z-component of nuclear spin angular momentum
$I(r,z)$	local light intensity [W/cm^2]
I_0	incident pump light intensity [W/cm^2]
I_{T}	transmitted pump light intensity [W/cm^2]
I_{abs}	absorbed pump intensity [W/cm^2]
I_{inc}	incident pump laser intensity [W/cm^2]
$I_{\mathrm{cell}}(r)$	average pump light intensity (uniform in z-direction) [W/cm^2]
J	total electronic angular momentum
$< J_z^* >$	mean z-component of total electronic angular momentum in 2^3S
k_a	local absorption rate
k_{I}	$= W_{\mathrm{inc}}/W_{\mathrm{nom}}$ experimentally determined loss factor of pump laser power due to losses on optical elements along optical path
L	$= \frac{\mathrm{FWHM}}{2\sqrt{\ln 2}}$ Gaussian linewidth of broadband laser
L_{cell}	inner length of glass cell, filled with ^{3}He and/or ^{4}He
L_{path}	optical path length of probe beam inside cell
M	$= < m_I >$: nuclear polarisation in ground state (1^1S)
$\dot{M}$	$= dM/dt$: time derivative of polarisation
M^a	apparent polarisation in presence of OP light (2^3S populations driven away from ST distribution, populations in 2^3P created)
M^{a*}	apparent polarisation in the 'strongly pumped velocity class'
$M^{a'}$	apparent polarisation in the 'weakly pumped velocity class'
M_{eq}	steady state polarisation
M_8	nuclear polarisation measured by C_8 probe laser in absence of OP light
M_9	nuclear polarisation measured by C_9 probe laser in absence of OP light
M_8^{a}	apparent nuclear polarisation in presence of the pump laser determined by probe laser tuned to C_8 transition
M_9^{a}	apparent nuclear polarisation in presence of the pump laser determined by probe laser tuned to C_9 transition
M_{av}	average polarisation value in each $\frac{\Delta M}{\Delta t}$ interval of dedicated experiments to account for perturbations of 2^3S- and 2^3P-populations in presence of the pump laser
M^{S}	2^3S nuclear polarisation in metastable state
m_F	total angular momentum quantum number
m_I	nuclear angular momentum quantum number
m_J	total electronic angular momentum quantum number
m_S	angular momentum quantum number associated to the spin of the electron
N	total number of He atoms in the cell
N_{g}	total number density ($N_g = N/V_c$) of ground state atoms (1^1S)

$N_{\mathrm{g}}^{\pm}$	number densities of the two nuclear spin states $m_I = \pm 1/2$
n_{m}	metastable density = total number density of atoms in 2^3S state [atoms/m^3]
$n_{\mathrm{m}}^{\mathrm{S}}$	mean value of n_{m} measured along the inclined probe beam path
$n_{\mathrm{m}}^{\mathrm{ax}}$	maximum value of n_{m} on axis
n_m^{8+}	metastable density deduced from absorption measurement on C_8 with σ^+ light polarisation
n_m^{8-}	metastable density deduced from absorption measurement on C_8 with σ^- light polarisation
n_{P}	2^3P state density
P_p	demodulated pump signal (in-phase component)
p_3	^{3}He gas pressure
p_4	^{4}He gas pressure
R	reduced ratio of probe absorption signals, normalised to $M = 0$: $R = \frac{A_+ A_-(0)}{A_- A_+(0)}$
R_{c}	inner radius of the cell
R^{exp}	experimentally measured reduced ratio of probe absorption signals
R^{th}	computed reduced ratio of probe absorption signals
R_{mir}	reflectivity of the back-reflecting mirror behind cell exit window
r	ratio of probe absorption signals $r = \frac{A_+}{A_-}$ and radial distance to cell axis
$S(\omega/2\pi)$	transition intensity as function of probe frequency $\omega/2\pi$ in pressure-broadened Voigt profile
S_p	transmitted pump power signal
T	transmission coefficient of laser light and $T = 1/\beta$ spin temperature and temperature
-ln(T)	cell absorbance for laser light
-$\frac{\ln(T)}{L_{\mathrm{path}}}$	absorption coefficient
-ln(T_s)	absorbance probe laser
-ln(T_p)	absorbance pump laser
T_b	build-up time constant (M-dependent)
T_{ij}	2^3S - 2^3P transition matrix element between A_i and B_j
T_{80}	C_8 transition intensity in $B = 0$, equal for σ^+ and σ^- light polarisations $T_{80} = T_{5,17} = T_{6,18}$
T_{8+}	transition intensity of C_8 σ^+ light (B-dependent)
T_{8-}	transition intensity of C_8 σ^- light (B-dependent)
T_{90}	C_9 transition intensity in $B = 0$
T_p	pump light transmission coefficient

T_s	probe light transmission coefficient
T_s^+	σ^+ probe transmission coefficient
T_s^-	σ^- probe transmission coefficient
V_c	cell volume
v	atomic velocity projection along the probe beam
$\bar{v}$	$= 2\pi c D \,/\, \omega_{ij}$: mean atomic velocity, related to the Doppler width
W_abs	total absorbed pump laser power [W]
W_inc	total incident pump laser power [W], integrated over the radial distribution of pump laser power
W_nom	total nominal output power of pump laser [W]
w_G	$= 2D\sqrt{\ln 2}$: Doppler FWHM
w_L	Lorentz FWHM (collisional line broadening)
x	$= \mathrm{e}^\beta = (1+M)/(1-M)$: spin temperature parameter
x_4	$= \frac{p_4}{p_3}$: isotopic ratio of ^{4}He to ^{3}He partial gas pressures
x_s	radial distance between the ingoing (or outcoming) probe beams and the cell axis
dx_s	offset of the V-shaped probe configuration with respect to the cell axis
y_s	vertical distance between the spatially separated σ^+ (or σ^-) probe components and the cell axis
Z_+	Zeeman shift of the C_8 σ^+ absorption line
Z_-	Zeeman shift of the C_8 σ^- absorption line
z_gap	longitudinal gap between the cell exit window and the back-reflecting mirror
z_in	longitudinal coordinate of the cell entrance window
z_out	longitudinal coordinate of the cell exit window
α	radial n_m-parameter: exponent of cosine fit function of radial metastable density profiles
$1/\beta$	spin temperature
Δ	width of velocity class of strongly pumped atoms
δ	uncertainty on measured PD voltage of transmitted pump light and detuning parameter in determination of n_m
δ^{ij}	$=(\omega - \omega_{ij})\,/2\pi$: frequency detuning of laser light with respect to optical transition
Γ_D	decay rate of ground state nuclear polarisation without pumping light in presence of a plasma
Γ_L	additional OP-induced (laser-induced) relaxation rate for ground state nuclear polarisation
Γ_R	total OP-enhanced (laser-enhanced) relaxation rate for ground state nuclear polarisation
Γ_RT	additional reabsorption-induced loss rate (radiation trapping)

Γ_Ξ	additional loss rate due to relaxing long-lived species Ξ created through the 2^3P state (plasma 'poisoning')
$\overline{\Gamma_e}$	average metastability exchange rate for 1^1S atoms
Γ_g	intrinsic ground state nuclear relaxation rate
$\Gamma'/2$	total damping rate of the optical coherence between the 2^3S and 2^3P states
γ	radiative decay rate of the 2^3P state
γ_e	metastability exchange rate for 2^3S atoms
γ_{ij}	optical transition rate from metastable sublevel A_i to excited sublevel B_j
$\gamma_\mathrm{r}^\mathrm{S}$	$= \tau_S^{-1}$: nuclear relaxation rate in the 2^3S state
$\gamma_\mathrm{r}^\mathrm{P}$	$= \tau_P^{-1}$: nuclear relaxation rate in the 2^3P state
γ_{ij}^*	computed OP rate in the strongly pumped velocity class
$\gamma(\nu_0)$	inferred OP rate in centre of the strongly pumped velocity class in resonance
γ_OP	characteristic pumping rate
η	photon efficiency
η^D	photon efficiency in Dehmelt OP regime
η^K	photon efficiency in Kastler OP regime
η_{C8}	photon efficiency on the C_8-transition
η_{C9}	photon efficiency on the C_9-transition
$\overline{\eta}$	error-weighted mean value of η
σ_η	standard deviation of $\overline{\eta}$
κ	slope in linear fit of Γ_R-data as function of W_abs
π	light polarisation perpendicular to magnetic field
θ	angle of probe beam with respect to cell axis
$\theta_\pm$	mixing parameters of electronic and nuclear angular momenta [Cou02]
Σ^*	fraction of incident pump laser power acting on 'strongly pumped velocity class'
Σ'	fraction of incident pump laser power acting on 'weakly pumped velocity class'
σ	cross section for collision induced transitions out of the $2^3\mathrm{P}_0$ level
σ^+	right-handed circular polarisation for light propagating along the magnetic field axis
σ^-	left-handed circular polarisation for light propagating along the magnetic field axis
$\widetilde{\sigma}$	$= \hbar\omega\frac{\sqrt{\pi}\alpha f}{m_e\omega D}$: optical cross section [m^2]
τ_LIA	time constant of numerical demodulation
τ_P	intrinsic relaxation time of 2^3P level
ω	angular frequency of laser light
ω_{80}	angular frequency of the C_8 transition in $B = 0$

$\omega_{ij}(B)$	angular transition frequency of each line component in $B \neq 0$
ω_{8+}	angular frequency of the C_8 σ^+ transition in $B \neq 0$
ω_{8-}	angular frequency of the C_8 σ^- transition in $B \neq 0$
$\Delta\omega$	± 0.38 GHz: estimate of realistic probe detuning range
$\varkappa_r$	input parameter in numerical implementation of OP model: fraction of decay rate in ground state induced by 2^3S relaxation through ME
$\varkappa_+$	input parameter in numerical implementation of OP model: fraction of incident power with σ^+ polarisation
$\varkappa_\pi$	input parameter in numerical implementation of OP model: fraction of incident power with π polarisation
Ξ	relaxing long-lived species created through the 2^3P state, e.g., metastable molecules He_2^*

Constants

$A_S = -4.493$ GHz	hyperfine coupling constant of 2^3S level of ^{3}He [Cou02]
$A_P = -4.283$ GHz	hyperfine coupling constant of 2^3P level of ^{3}He [Cou02]
$c = 2.99792458 \times 10^8$ m/s	speed of light in vacuum [COD10]
$D = 1.187473$ GHz	Doppler width of ^{3}He at room temperature ($T = 300$ K); FWHM $= 2D\sqrt{\ln 2} = 1.977272$ GHz
$f = 0.5391$	oscillator strength of the 2^3S-2^3P transition [Wie66, Dra96]
$h = 6.62606957(29) \times 10^{-34}$ J s	Planck constant [COD10]
$\hbar = 1.054571726(47) \times 10^{-34}$ J s	Planck constant $h/2\pi$ [COD10]
$k_B = 1.3806488(13) \times 10^{-23}$ J/K	Boltzmann constant [COD10]
$M_{\mathrm{at}} = M_3 = 3.024315$ u	atomic mass of ^{3}He ($M_4 = 4.032980$ u for ^{4}He) [COD10]
$m_e = 9.10938291(40) \times 10^{-31}$ kg	electron mass [COD10]
$N_A = 6.02214129(27) \times 10^{23}$ mol^{-1}	Avogadro constant [COD10]
$R_m = 8.3144621(75)$ J mol^{-1} K^{-1}	universal molar gas constant [COD10]
u $= 1.660538921(73) \times 10^{-27}$ kg	atomic mass unit [COD10]
$\alpha = 7.2973525698(24) \times 10^{-3}$	fine structure constant [COD10]
$\omega_8 = 1.739199 \times 10^{15}$ s^{-1}	angular frequency of C_8 transition in zero magnetic field: $\omega_8 = 2\pi c/\lambda(C_8)$

Wavelengths of helium OP lines (2^3S-2^3P transition)

Wavelengths of selected He lines in vacuum in nm:

isotope	line	[ASD11]	[Mar87]
^{4}He	D_0	1082.90911	1082.9081
^{4}He	D_1	1083.02501	1083.0250
^{4}He	D_2	1083.03398	1083.0341
^{3}He	C_9	1083.03081	
^{3}He	C_8	1083.05716	

^{3}He wavelengths are computed from D_2 in ^{4}He using $\Delta\lambda = -\lambda^2\Delta\nu/c$, with $\lambda^2/c = 0.39123\times10^{-20}$ m·s $= 3.9123\times10^{-3}$ nm/GHz and two different values of $\Delta\nu$ taken from [Cou02]: C_9-D_2 = 0.8106 GHz and C_9-C_8 = 6.7397 GHz.

Abbreviations

APC	angle polished connector
AR	anti reflex
FWHM	full width at half maximum $= 2a\sqrt{\ln 2}$
hf	hyperfine
ME	metastability exchange
MEOP	metastability exchange optical pumping
NMR	nuclear magnetic resonance
OP	optical pumping
PE	photon efficiency
rf	radio frequency
SE	stimulated emission and spin exchange
SEOP	spin exchange optical pumping
ST	spin temperature

Chapter 1

Introduction

In the last years, hyperpolarised noble gases, whose nuclear polarisations are enhanced relative to thermal equilibrium, have become more and more interesting for different branches of physics. In particular the stable isotopes ^{3}He and ^{129}Xe, both with nuclear spin 1/2, are well suited for several applications.

In order to create such hyperpolarisations, optical pumping techniques are used. In 1950, Alfred Kastler first proposed the main principle of optical pumping to change relative populations of Zeeman levels and of hyperfine levels of the ground state of atoms [Kas50]. In this seminal paper, he already mentions the potential applications for NMR of gas hyperpolarisation by optical pumping.
Metastability exchange optical pumping (MEOP), discovered in 1963 [Col63], exclusively applies to ^{3}He as demonstrated by various attempts for other gases [Sch69b, Lef77, Xia10], while spin-exchange optical pumping (SEOP), that involves an alkali vapour [Bou60, Hap72, Wal97, Ric02, Cha03, Bab06, Che07], can be used to efficiently polarise ^{129}Xe as well.

Polarised ^{3}He is a versatile tool in different fields of fundamental physics and in biomedical science. Applications include

- spin filters for polarising neutrons [Bat05, Gen05, Lel07, Par09],
- scattering targets on electron beams [Ber03, Kri09] or photon beams [Kri11] for investigations of the structure of nucleons,
- symmetry breaking tests in search of Lorentz and CPT violation [Gem10a, Gem10b, Bro10],
- investigations of nonlinear NMR dynamics in hyperpolarised liquid ^{3}He [Hay07, Bau08a, Bau08b] and
- magnetic resonance imaging of the lung in humans [Bee04, Sta09, Bee09], and in animals [Cie07a, Cie07b, McG08].

In MEOP, optical pumping is actually performed between two excited levels. The 2^3S level, which plays the role of a ground state for the OP process, is populated by electron collisions in a plasma discharge in a gas at moderate pressure (usually up to a few millibars). For the ^{3}He isotope, in this excited metastable state, an efficient coupling between the nucleus and the electrons (the hyperfine (hf) interaction) results in a strong entanglement of electronic and nuclear spin states. Therefore, the OP-enforced optical orientation of the electronic angular momentum simultaneously induces nuclear orientation as well. This nuclear orientation is transferred through metastability exchange (ME) collisions to the much more numerous atoms having remained in the true (1^1S_0) ground state.

When laser light with adequate spectral characteristics at 1083 nm is used, MEOP provides very high nuclear polarisation (> 0.7) with good photon efficiency ($\sim$1 polarised nucleus per absorbed photon) [Nac85]. During the last years, suitable high power fibre lasers [Mue01, Gen03, Tas04] have been developed as well as adequate polarising units comprising different mechanical compression schemes so as to obtain polarised gas samples in the order of atmospheric pressure required in most of the above mentioned applications. Two established techniques are peristaltic compressors [Nac99] for use in compact tabletop polarisers [Cho02, Cho03, Suc05] and piston compressors [Bee03, Sch04, Wol04, Bat05, Hus05, And05].

Although many conceptual and technical issues in MEOP of ^{3}He and its applications could have been solved as broached above, maximum experimentally obtainable polarisation values are still limited, and differences between theoretically expected and experimentally measured quantities are observed.
However, especially in fundamental physics applications, high nuclear polarisation is crucial since figures of merit vary non-linearly with M for instance.
Therefore, the goal of the present work was to understand current limitations of ^{3}He MEOP and to ultimately reduce and overcome them.

Motivated by the spectacular increase of steady state polarisation observed in high magnetic field (1.5 T [Abb04], 0.45 - 2 T [Nik07] and 4.7 T [Nik12]) which also extends the range of operating pressures to several tens or hundreds of mbar (which would make subsequent compression for application significantly easier to perform), systematic ^{3}He MEOP studies of performances and relaxation mechanisms were carried out in the present work in magnetic fields below 30 mT and at low pressure of 0.63-2.45 mbar. The investigations comprised experiments in a dedicated setup as well as comparisons to theoretical expectations.
The choice of examined pressure and field ranges was governed by practical aspects (close to standard conditions in polarising units) and by the following consideration: Above 10 mT [Pav70], hf-coupling and ME process in the 2^3S state are almost unaffected, whereas higher excited states in the radiative cascade in the plasma

are strongly *de*coupled. Angular momentum loss by emission of circularly polarised fluorescence light is thus reduced in the radiative cascade, which was expected to yield a potential increase of OP performances.
Polarisation decay rates in absence of OP were indeed reduced in magnetic fields up to 30 mT at fixed metastable density. Nevertheless, the obtained polarisation values were not improved at high laser power, and it could be shown that polarisation loss associated to hyperfine coupling in the highest excited states involved in the radiative cascade is not the dominant phenomenon setting limits to OP performances. We found clear evidence of additional OP-induced relaxation effects instead.

The manuscript is organised in the following way: In chapter 2, basic aspects of MEOP that are essential for this work are presented. In particular, the OP model used as tool to gain further insight into OP processes and for comparisons between theoretical expectations and experimental observations is introduced. Chapter 3 describes the constructed experimental setup. In chapter 4, an optical technique to accurately measure nuclear polarisation by monitoring absorption of a weak probe laser at 1083 nm is presented in detail. Chapter 5 deals with methodological aspects of data reduction and introduces all obtained experimental signals as well as all derived physical quantities. Chapter 6 is dedicated to the presentation of the main results of the present work: Characterisation of the plasma, systematic probe measurements to evaluate the robustness of the method and systematic measurements of OP kinetics as function of nuclear polarisation varying different parameters such as ^{3}He pressure, rf excitation level and thus metastable densities and decay rates, probe and pump transitions, and incident pump laser power. From the measured physical quantities, photon efficiencies were determined, and total relaxation rates during polarisation build-up could be inferred. The limiting case at null nuclear polarisation provided relaxation free data to evaluate the OP model. Furthermore, the intrinsic relaxation rate in the 2^3P state could be empirically determined.

Selected aspects that could not be treated in the main text corpus are presented in more detail in the appendices of this work.

Chapter 2

MEOP basics and OP model

This chapter provides an introduction to the physics of MEOP through a short presentation of the different processes involved in MEOP and of the rate equations used to describe the time evolution of the internal variables of ^{3}He atoms. Since a number of simplifications are needed for a detailed analysis of dynamics of the whole system, a substantial part of this chapter is devoted to the presentation of the OP model and of the computational approach that have been developed for quantitative analysis of OP kinetics. The remaining of the chapter deals with a discussion of MEOP dynamics where, in particular, the useful concept of photon efficiency is introduced. Illustrative examples of computed kinetic evolution are provided for the physical quantities most relevant for this work.

The basic introductory material can be found in a number of references because theoretical background and OP models have been both established and regularly refined since the discovery of ^{3}He MEOP in 1963 [Col63]. However, their exhaustive description is disseminated in several publications using different notations. We try to focus on the aspects that are essential for the present work, to provide a unified and synthetic presentation of the material needed in the following chapters, and to use consistent notations as close as possible to the original ones. Emphasis is thus put on MEOP features specifically relevant for low field operation, as well as on physical discussions of the various contributions to the time evolution of ^{3}He nuclear polarisation.

The first theoretical articles on MEOP were written in the 1970s [Col63, Gre64, Dan71a, Dan71b, Dup73]. At that time, OP on the 2^3S-2^3P transition was performed using the weak light from a helium lamp and rather low polarisations (of the order of 0.1) were obtained. Simple linearised models were sufficient to account for such pumping experiments. When laser sources at 1083 nm were developed in the 1980s, much higher nuclear polarisations were obtained. A detailed model for MEOP without restriction on the pump light intensity nor on the nuclear polarisation was then proposed [Nac85]. It is based on rate equations for the populations of the 2^3S, 2^3P, and

ground states that accurately take into account the effects of metastability exchange collisions and of absorption and emission of light at 1083 nm. Correlations between atomic orientations and velocities, created for instance by a spectrally narrow laser in a room temperature gas, are also considered in this model, but only in a crude phenomenological way. This model only describes low field MEOP and it has been established and used for parameters corresponding to low pressure situations (in the mbar range) where MEOP was known to have the highest efficiency. This model has been also used to discuss OP experiments with a broadband laser [Led00, Wol04]. In [Wol04], a different implementation of the model developed in [Nac85] was realised including two distinct aspects which are discussed in section 2.10.1. Extensions to the model of [Nac85] in specific situations have been proposed, but not fully developed, for OP in ^{3}He-^{4}He isotopic mixtures [Lar91] and for OP in high magnetic fields [Cou02, Nac02, Abb04].

Recently, a more comprehensive model has been developed for MEOP and implemented into a new Fortran program at LKB. This improved OP model is based on similar rate equations for the populations of all Zeeman sublevels but it is suitable for arbitrary magnetic field and for pure ^{3}He gas as well as for isotopic gas mixtures. It provides a unified frame that is also more adequate for a description of MEOP with modern, broadband fibre lasers. The improved OP model will be described in detail in a forthcoming publication [Nac12]. In the present work, it is simply used as a tool to compute populations in 2^3S and 2^3P at arbitrary nuclear polarisation M and to derive the time evolution of M under combined OP, ME and relaxation processes. Furthermore, theoretical predictions are compared to experimental data which contributes to a deeper understanding of the processes involved in MEOP of ^{3}He. Such quantitative comparisons have triggered, in particular, a detailed and substantiated investigation of relaxation mechanisms during polarisation build-up described in this manuscript.

This chapter is organised in the following way:

- A quick introduction to MEOP in pure ^{3}He gas and ^{3}He$-^4$He gas mixtures is provided in section 2.1. The structure of the ground state and the two lowest triplet states of ^{3}He and ^{4}He is described in the 0$-$30 mT range (section 2.2 and appendix A). A comprehensive description of the various 2^3S-2^3P optical transition rates involved in MEOP experiments (depending on the characteristics of the incident light) can be found in section 2.3.
- The rate equations needed to quantitatively describe the evolution of the system under the combined action of OP and ME are introduced in section 2.4. The generic equations derived and used in [Nac85] and [Cou02] are recalled. They are indeed oversimplified and are not appropriate to describe MEOP dynamics at high power with broadband light sources. The rate equations relevant for the improved OP model have been derived shortly before the start of this work. They are briefly described in sec-

tion 2.5 and the full set of valid rate equations and useful formulas are included in appendix B. Their derivation and the physical discussion of the underlying assumptions exceed the scope of this PhD manuscript and will be reported elsewhere [Nac12].
- The improved OP model, developed to suitably describe broadband excitation with high light power and to better take into account the inherent complexity associated with the (internal and external) dispersion of OP rates in the cell, relies on a number of pragmatic approximations and simplifications described in section 2.5. For the resolution of the whole set of coupled rate equations, as usual, advantage is taken of the strong hierarchy of evolution rates between the various physical processes involved in MEOP. This hierarchy is described in section 2.6. Then, the main features of the Fortran program implemented and used at LKB to compute the full OP kinetics are presented in section 2.7 where, in particular, the strategy used to solve the set of non linear rate equations, the self-consistent computation of local light intensities and absorption rates, and definitions of input parameters are detailed.
- Section 2.8 describes the main features of the time evolution of ^{3}He nuclear polarisation that results from the competing effects of ME, OP, and relaxation. It provides a physical insight on MEOP dynamics (section 2.8.3) and, in particular, on the transfer of angular momentum from the incident polarised light to the internal degrees of freedom of the ^{3}He atoms (section 2.8.4). Photon efficiencies have so far been pragmatically used to quantify MEOP performances [Cou01, Abb05b], in a way that is quite similar to that used for spin exchange optical pumping of noble gases [Wal97, Bar98a, Bab03]. A detailed analysis of the global angular momentum budget for MEOP is included here to clarify this concept and to establish an explicit link between the various contributions to the rate equations and the net amount of nuclear orientation created in the ground state. Photon efficiencies of the two OP transitions used for our work in pure ^{3}He gas are extensively discussed in a dedicated section (2.9). This presentation provides the grounds for the analysis of experimentally recorded polarisation dynamics and for quantitative assessment of the strong laser-enhanced relaxation that is one of the major outcomes of this work.
- Finally, the robustness of the improved OP model is discussed and comparison with previous models is made in section 2.10.

2.1 Short introduction to MEOP

MEOP can be described as a 3-step process, although in reality the corresponding physical processes are simultaneously involved:
- Since optical pumping is actually performed between two excited states of the helium atom (see figure 2.1) the first mandatory step consists in populating the 2^3S metastable state that plays the role of a ground state for the OP process. A weak rf discharge is sustained in the He gas at moderate pressure (usually up to a few millibars) to

populate higher excited states by electron collisions in the plasma, with a radiative cascade ending as the 2^3S state. This discharge is maintained at all times (it is usually slowly modulated in amplitude for more sensitive optical measurements), so that all MEOP processes described here occur in presence of the plasma created in the gas. In steady state the proportion of atoms sustained in the metastable state is typically of order of a few parts per million (average 2^3S atom number densities: $0.5-10\times10^{16}$ atoms/m^3).
- In a second step, OP (i.e., laser-driven cycles of absorption of circularly polarised pump light and radiative de-excitation) is performed on the closed $2^3\mathrm{S}-2^3\mathrm{P}$ dipolar electric transition at 1083 nm. For the ^{3}He isotope, in the excited 2^3S metastable state an efficient coupling between the nucleus and the electrons (the hyperfine interaction) results in a strong entanglement of electronic and nuclear spin states. Therefore the OP-enforced optical orientation of the electronic angular momentum simultaneously induces nuclear orientation as well.
- In a third step, this *nuclear* orientation of the 2^3S state is transferred through metastability exchange collisions to the much more numerous atoms having remained in the true ground state ($1^1\mathrm{S}_0$) that holds no electronic angular momentum ($J = 0$). The electronic angular momentum of the metastable atoms is not affected during ME collisions.[1]

OP can also be performed on the 2^3S state of ^{4}He atoms in an isotopic gas mixture, which is an efficient scheme providing high ^{3}He nuclear polarisations [Gen03, Sto96a] via ME collisions between atoms of both helium isotopes. It can be advantageously used when the presence of ^{4}He is desired or is not a nuisance, e.g, for low temperature studies of polarised mixtures or for neutron spin filters applications. In other situations, the presence of ^{4}He can be a disadvantage, e.g., for the precise determination of nuclear polarisation by measurements of probe absorption rates (see chapter 4). For these reasons, the level structure of ^{4}He is also presented in this section.

In summary, for pure ^{3}He gas the two key processes in MEOP are a net transfer of angular momentum in the metastable state from the absorbed light to the He atoms by OP and a transfer of nuclear angular momentum between metastable and ground state He atoms by ME collisions. As argued in [Cou02] and references therein, the description of both processes can be legitimately made in terms of the populations of the Zeeman sublevels of the three involved levels in order to analyse the time evolution of the ensemble of atoms contained in the OP cell at room temperature: For a gas confined in a cell, the quantum states of the atoms can be statistically described by density matrices that specify the internal state of the atoms and depend on their external states (position and kinetic momentum, hence velocity). These density matrices are usually fully characterised by their diagonal elements that correspond to the populations of the relevant eigenstates (the Zeeman sublevels), i.e., coherences are

[1] ME collisions are fast processes where the colliding 2^3S and $1^1\mathrm{S}_0$ atoms just exchange electronic excitations with no change of nuclear orientations. They induce no global loss of angular momentum.

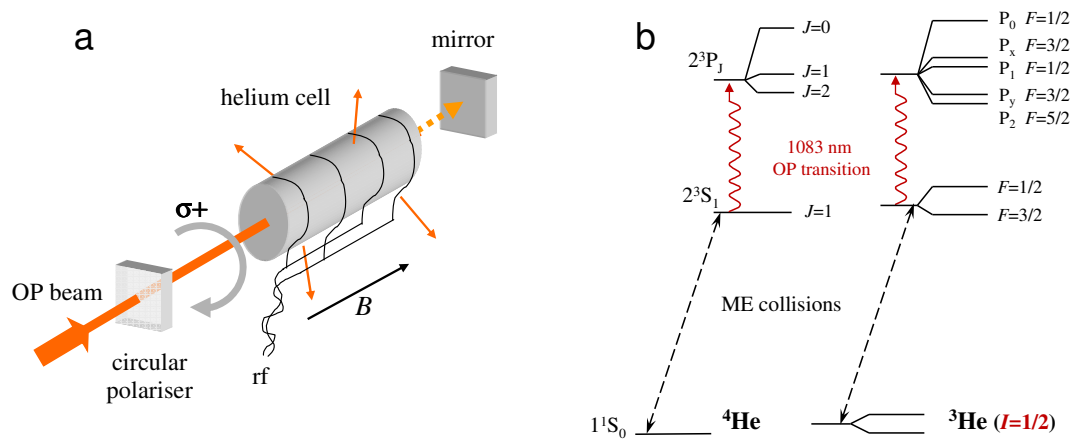

Figure 2.1: **a:** Schematic view of a basic MEOP setup. In a ^{3}He gas cell, a weak rf discharge promotes a small fraction of the atoms into the excited metastable state 2^3S, where resonant absorption of 1083 nm light occurs. This OP light is circularly polarised and propagates along the direction of the applied magnetic field B. For enhanced absorption, the light is usually back-reflected for a second pass through the cell. Nuclear polarisation is transferred to atoms in the ground state by metastability exchange collisions. **b:** Fine- and hyperfine-structures of the atomic states of He involved in the MEOP process for the ^{4}He (left) and ^{3}He (right) isotopes, in low magnetic field (below a few 10 mT), and the main physical processes involved in MEOP are shown. Notations for the 2^3P hyperfine sublevels of the ^{3}He atom are those of [Nac85, Cou02]. The Zeeman effect in the ground state of ^{3}He is grossly exaggerated to highlight the existence of two magnetic sublevels and the possibility of nuclear polarisation.

ignored. Off-diagonal elements are indeed created during metastability exchange collisions but they can be neglected for usual MEOP conditions (at low enough pressure or in high enough magnetic field [Cou02]). Off-diagonal elements can also be created when coherent light is used for pumping with a V-type or Λ-type scheme, with two optical transitions addressing at least one common sublevel in the lower state or the upper state, respectively. However, such excitation schemes are avoided in standard MEOP conditions, where light polarisation is carefully controlled and laser beams with well-defined helicity are used.

2.2 He level structure at low magnetic field

We use the notations of reference [Cou02] (in particular, for labelling of Zeeman sublevels of hyperfine levels subscripts increase with increasing energies; the difference

in notations with reference [Nac85] is specified in footnote 1 of [Cou02]) where the structure and energies of the sublevels of the 2^3S and 2^3P states are derived for both isotopes in arbitrary magnetic field. For simplicity we only discuss in this manuscript the limiting case relevant for the experiments performed in this work and describe below the He level structure in low magnetic field (as done also in reference [Bat11]).

The 2^3S state of ^{4}He ($J = S = 1$) has three magnetic sublevels ($m_S = -1$,0, and +1), linearly split at all values of the applied magnetic field B by the Zeeman energy. They are named Y_1 to Y_3 and their populations y_1 to y_3. The 2^3P state of ^{4}He ($L = 1,\ S = 1$) has three fine-structure levels with J =0, 1, and 2, hence nine Zeeman sublevels named Z_1 to Z_9 with populations z_1 to z_9 (see figure 2.2c and d).

There are twice as many Zeeman sublevels for ^{3}He due to its two nuclear spin states: six in the 2^3S state (A_1 to A_6, populations a_1 to a_6) and eighteen in the 2^3P state (B_1 to B_{18}, populations b_1 to b_{18}, see section 2.4) that has five fine- and hyperfine-structure levels (see figure 2.2a and b). In low magnetic field, the F=3/2 ($J = 1$) and F=1/2 ($J = 1$) hyperfine levels of the 2^3S state of ^{3}He are well resolved and split by 6.74 GHz, the F=5/2 ($J = 2$) and F=1/2 ($J = 0$) hyperfine levels of the 2^3P state of ^{3}He are split by 34.4 GHz (figure 2.2a).

The absorption spectra for ^{3}He and ^{4}He, computed for negligible collisional broadening (section 4.4.2) and for room-temperature Doppler widths (equation (2.11)) are represented in figures 2.2e and f. Optical transition energies ϵ are referenced to the energy of the C_1 component in zero field and they are expressed in frequency units (ϵ/h). The well-resolved C_8 and C_9 components exciting the 2^3P_0 state are the transitions most commonly used for MEOP of ^{3}He in low magnetic field, whereas the C_8 component and the D_0 component of the ^{4}He 1083 nm line (also exciting the 2^3P_0 state) are used for MEOP of isotopic gas mixtures [Lar91, Sto96a, Gen03]. Optical transition frequencies ϵ_{ij}/h for ^{3}He and ^{4}He in $B = 0$ are listed in tables A.1 and A.2 in appendix A.

The magnetic sublevels can be described using the product states of the decoupled basis $|m_S, m_I\rangle$. For the 2^3S state A_1 and A_4 are pure states of maximum $|m_F|$=3/2 but the other Zeeman sublevels involve large field-dependent hyperfine mixing parameters θ_- and θ_+ [Cou02] (recalled in appendix A). Up to $B = 0.162$ T, for which sublevels A_4 and A_5 cross, the sublevels can be written:

$$\begin{aligned}
A_1 &= |-1,-\rangle \\
A_2 &= \cos\theta_- \,|-1,+\rangle + \sin\theta_- \,|0,-\rangle \\
A_3 &= \cos\theta_+ \,|0,+\rangle + \sin\theta_+ \,|1,-\rangle \\
A_4 &= |1,+\rangle \\
A_5 &= \cos\theta_- \,|0,-\rangle - \sin\theta_- \,|-1,+\rangle \\
A_6 &= \cos\theta_+ \,|1,-\rangle - \sin\theta_+ \,|0,+\rangle \,.
\end{aligned} \tag{2.1}$$

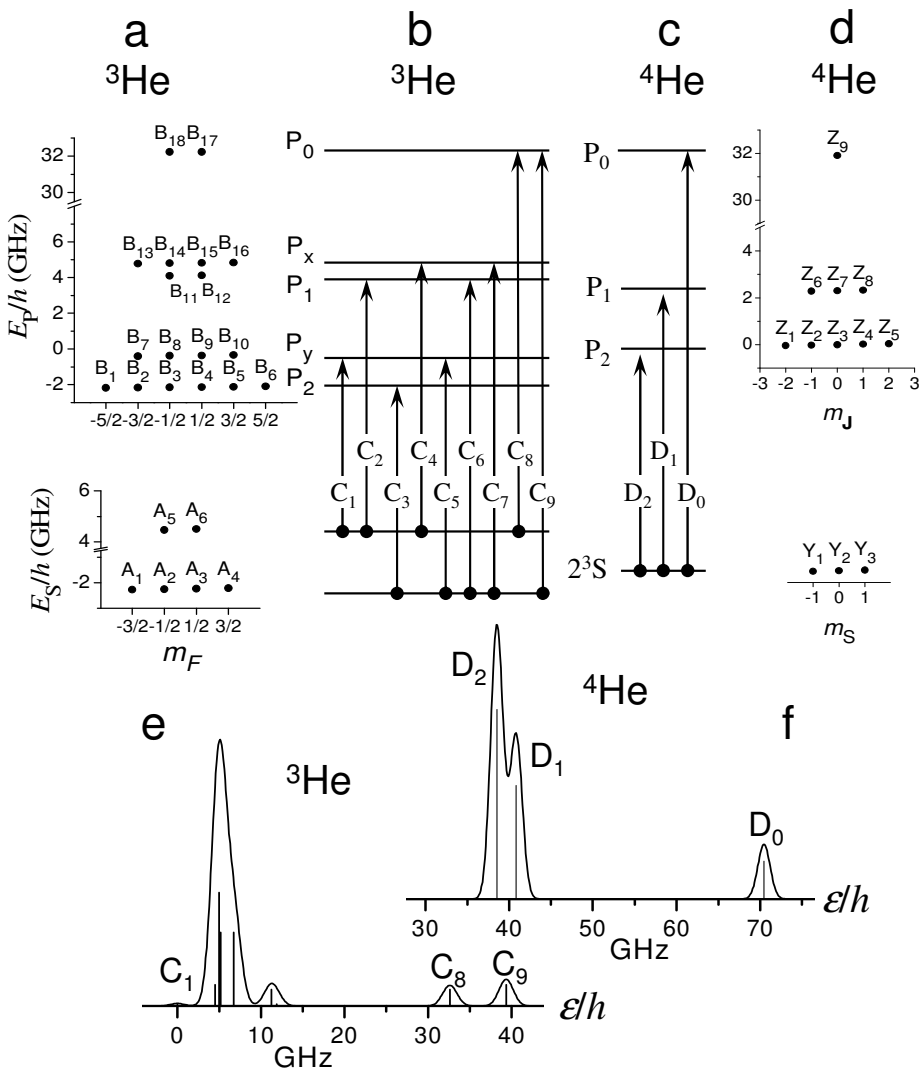

Figure 2.2: Structure of the 2^3S and 2^3P states of ^{3}He and ^{4}He and components of the 1083 nm optical transition at low magnetic field (for negligible Zeeman effect, e.g., $B \leq$10 mT). **a:** Plot of the energies of the six 2^3S sublevels and of the eighteen 2^3P sublevels of ^{3}He as a function of their total angular momentum projection m_F. **b**: Diagram and **e:** Spectrum of the 9 allowed components of the 1083 nm transition of ^{3}He. **c:** Diagram and **f:** Spectrum for ^{4}He (3 line components).
The spectra (e, f) are computed from the amplitudes of the transition matrix elements T_{ij} of the fine and hyperfine line components (vertical bars) assuming pure Doppler broadenings at room temperature (equation (2.11)). **d:** Plot of the energies of the three 2^3S sublevels and of the nine 2^3P sublevels of ^{4}He as a function of their electronic angular momentum projections m_J ($m_J = m_S$ in the 2^3S state where the orbital angular momentum equals zero).

Strong and maximal mixing of electronic and nuclear angular momenta occurs at B=0, with $\sin^2\theta_-$=2/3 and $\sin^2\theta_+$=1/3. At B = 30 mT, the highest field value used in this work, $\sin\theta_+$ is reduced by 8 % and $\sin\theta_-$ by 5 % only.

Over the whole range of field strengths that we have experimentally studied (B=0−30 mT), strong mixing of electronic and nuclear angular momenta thus occurs in the 2^3S state. Similarly, the 2^3P state levels are only weakly affected by fields up to 30 mT. The mixing parameters and the sublevel energies, in particular those of the 2^3P_0 sublevels addressed by the C_8 and C_9 transitions used for ^{3}He MEOP (see figure 2.2b), linearly depend on B for low fields.

Transition matrix elements T_{ij} for ^{3}He and $T_{ij}^{(4)}$ for ^{4}He in zero magnetic field are listed in tables A.1 and A.2 in appendix A. They have been computed for $\sigma^\pm$ and π light polarisation and for all 2^3S−2^3P transition components (C_1 to C_9 for ^{3}He, D_0 to D_2 for ^{4}He) using equations and data of [Cou02] in $B = 0$. The values given for ^{3}He are slightly different from those of [Nac85] due to the use of a more accurate Hamiltonian.

Transition matrix elements T_{ij} as well as transition frequencies ϵ_{ij}/h are moderately modified at low magnetic field strength and Taylor expansions can be used at finite B:

$$\varepsilon_{ij}(B)/h = \varepsilon_{ij}(0)/h + C_\epsilon^{(1)}B + C_\epsilon^{(2)}B^2 \tag{2.2}$$

$$T_{ij}(B) = T_{ij}(0) + C_T^{(1)}B + C_T^{(2)}B^2. \tag{2.3}$$

The coefficients of the 2nd-order Taylor expansions (equations (2.2) and (2.3)) are listed in table A.3 (appendix A) for all components involved by light excitation on the C_8 and C_9 lines of ^{3}He. For the D_0 line of ^{4}He a similar Taylor expansion to second order of $\varepsilon_{ij}^{(4)}/h$ and $T_{ij}^{(4)}$ is performed and its coefficients are also listed.

For convenience transition frequencies, reduced Zeeman shifts (i.e., Zeeman shift values divided by Doppler width), and transition matrix elements for C_8 and C_9, σ^+ and σ^- light polarisations, are listed for eight B values between 0 and 30 mT experimentally relevant for this work in tables A.4, A.5 and A.6 (appendix A).

Figure 2.3 displays the reduced Zeeman shifts (according to equations (4.25) and (4.26) for C_8 σ^+ and C_8 σ^-, respectively; according to equations (4.37) and (4.38) for the two line components of C_9 σ^+, and to corresponding equations for C_9 σ^-) and relative changes in transition matrix elements up to 30 mT.
For ^{3}He, absolute Zeeman line shifts of C_8 and C_9 do not exceed ± 30 MHz/mT and the relative changes in transition matrix elements do not exceed 0.6 %/mT. Hence, OP rates are almost field-independent up to several mT.

At B = 30 mT, the Zeeman shifts for the C_8 line amount to 0.46 and 0.42 times the Doppler width D for σ^- and σ^+ light respectively, and transition matrix elements change by ∓9 % for $\sigma^\pm$ light. For the C_9 line we have to distinguish between the two

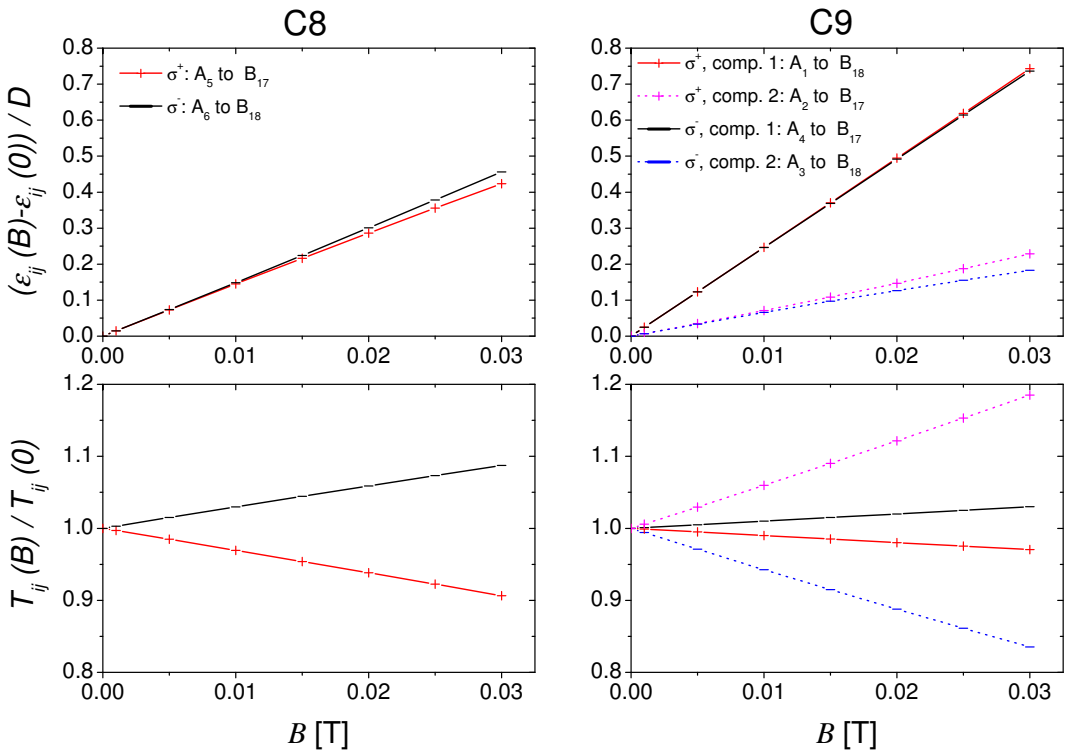

Figure 2.3: Top: Reduced Zeeman shifts at room temperature according to equations (4.25) and (4.26), listed in table A.4 for C_8 (left), and according to equations (4.37) and (4.38), listed in tables A.5 and A.6 for C_9 (right). Zeeman shifts are scaled to Doppler width using $D(300\text{ K})$=1.187473 GHz (eq. (2.11)). FWHM amounts to $2D\sqrt{\ln 2}$ =1.98 GHz for ^{3}He at 300 K.
Bottom: Relative transition intensities for C_8 (left) and C_9 (right) as a function of magnetic field up to $B = 30$ mT.
C_8 line: $\epsilon_{ij}(0)/h = 32.605$ GHz (from C_1 line, see figure 2.2e), $T_{ij}(0)$= 0.29185;
C_9 line: the two transitions components are individually considered (see text and legend); $\epsilon_{ij}(0)/h = 39.344$ GHz (from C_1 line, see figure 2.2e), $T_{ij}(0) = 0.28111$ (component 1) and 0.0937 (component 2).

types of line components: the one addressing the $m_F = \pm\ 3/2$ sublevels of the 2^3S, $F = 3/2$ state, named "component 1", that contributes to 3/4 of the total transition rate at $B = 0$; the other one, addressing $m_F = \pm\ 1/2$ sublevels of the same hyperfine state, called "component 2", that contributes to 1/4 of the total transition rate at $B = 0$. At $B = 30$ mT the Zeeman shift of component 1 (resp. 2) amounts to $0.74 \times D$ (resp. $0.2 \times D$) and the transition matrix elements vary by ± 3 % (resp. ± 18 %) for $\sigma^{\pm}$ light for component 1 (resp. 2). Component 2 thus exhibits a higher relative change of the transition matrix element but it only contributes 3 times less than component 1 to the total optical transition rate.

The absorption spectra of the C_8 and C_9 components of ^{3}He at 30 mT are represented in figure 2.4. They are computed for room-temperature Doppler line broadening and negligible collisional broadening (see chapter 4.4.2). Spectra computed for B =1 and 30 mT taking into account collisional line broadening for typically our maximum gas pressure are displayed in figure 4.19. Experimental absorption spectra at $B = 30$ mT, $M = 0$ and $M = 0.5$ can be found in figure 4.3.

2.3 Optical transition rates

This section deals with 2^3S-2^3P optical transition rates for monochromatic and for broadband light excitation. The first case is especially relevant for the determination of metastable densities based on the measurements of light absorption rates performed with a weak single-frequency probe laser (see chapter 4). The second case is relevant for the description of excitation of He atoms by our broadband pump laser and these transition rates will be involved in the general discussion of MEOP rate equations (section 2.4). They are especially important for the description of the improved OP model presented in section 2.5.

2.3.1 Monochromatic excitation

For an atom at rest the optical transition rate γ_{ij} for the transition component between the 2^3S sublevel A_i and the 2^3P sublevel B_j is given by (equation (8) of [Cou02] with $1/\tau_{ij} = \gamma_{ij}$):

$$\gamma_{ij}(\vec{r}) = \frac{4\pi\alpha f}{m_e \omega \Gamma'}\, I(\vec{r})\, \frac{(\Gamma'/2)^2}{(\Gamma'/2)^2 + (\omega - \omega_{ij})^2}\, T_{ij}, \tag{2.4}$$

where α is the fine-structure constant, $f = 0.5391$ the oscillator strength of the 2^3S-2^3P transition, m_e the electron mass, and I the light intensity at the position $\vec{r}$ of the atom inside the cell. Furthermore ω and ω_{ij} designate the angular frequencies of the light and of the atomic transition, respectively, and T_{ij} the matrix element of the transition between A_i and B_j. This optical transition rate γ_{ij} is experimentally relevant in all cases where a well resolved single-component line is used, either by polarisation

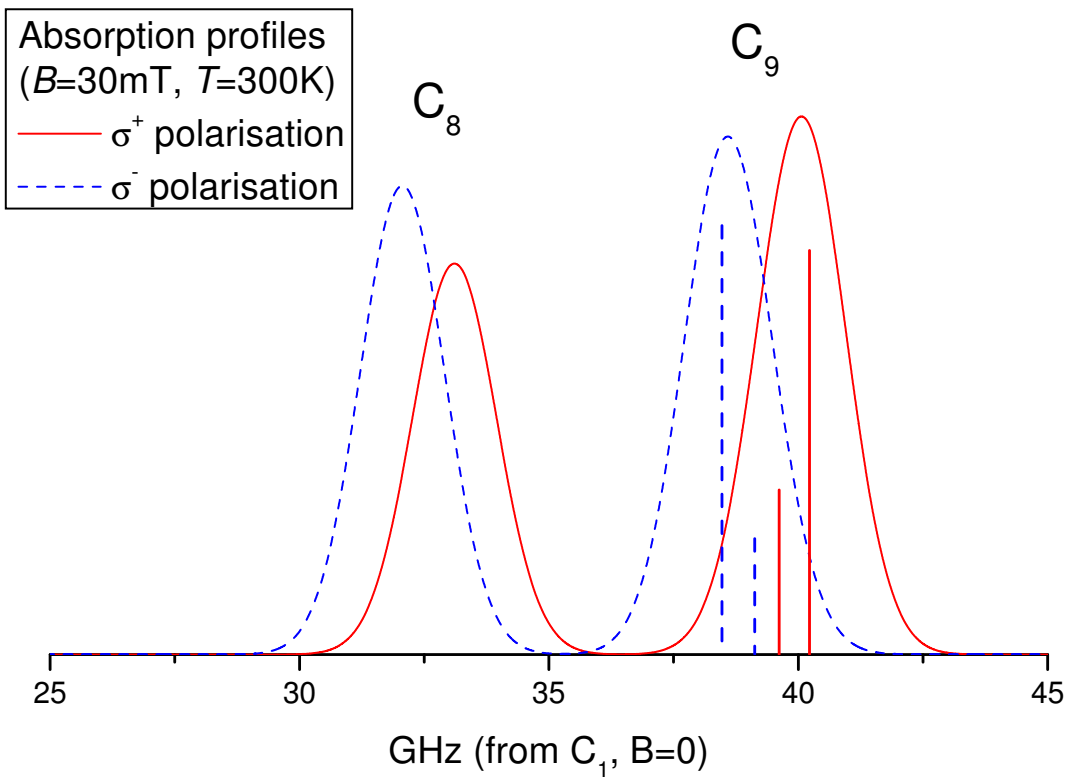

Figure 2.4: Computed ^{3}He C_8 and C_9 absorption spectra at null polarisation in B=30 mT for gas at room temperature with no collisional broadening. Solid (resp. dashed) lines correspond to σ^+ (resp. σ^-) polarisation. The vertical bars (same line styles) represent the positions and amplitudes (matrix elements T_{ij}) of the two unresolved components of the C_9 line (e.g., $A_1 \rightarrow B_{17}$ and $A_2 \rightarrow B_{18}$ for σ^+ polarisation). Transition frequencies are referenced to the frequency of the C_1 resonance at $B = 0$ (see text). The C_8−C_9 splitting is equal to 6.739 GHz at B=0 (see appendix A)

selection at low B (e.g., for the C_8-line probe at low gas pressure) or by frequency selection[2] when the Zeeman shifts are large enough to remove the degeneracy between line polarisation components (above $B = 0.1$ T). $\Gamma'/2$ is the total damping rate of the optical coherence of the transition between the 2^3S and 2^3P states:

$$\Gamma'/2 = \gamma + \pi w \tag{2.5}$$

resulting from the combined effects of the radiative decay rate γ (cf. section 2.6) and of atomic collisions. The contribution w to the linewidth arising from collisions can be neglected at low pressure.[3]

For a moving atom the optical transition rate γ_{ij} also depends on the projection v_z of the atom velocity along the light propagation axis, due to Doppler shift:

$$\gamma_{ij}(\vec{r}, v_z) = \frac{4\pi\alpha f}{m_e \omega \Gamma'}\, I(\vec{r})\, \frac{(\Gamma'/2)^2}{(\Gamma'/2)^2 + (\omega - \omega_{ij} - \omega_{ij}\, v_z/c)^2}\, T_{ij}. \tag{2.6}$$

where c is the speed of light.

The gas atoms contained in our room temperature cells are *not* at rest. For the Maxwell distribution of velocities at thermal equilibrium, an average local optical transition rate $\overline{\gamma_{ij}}$ can be obtained from equation (2.4) by statistical averaging over atomic velocity projections, which leads to (equation (45) of [Cou02]):

$$\overline{\gamma_{ij}}(\vec{r}) = \frac{4\pi\alpha f}{m_e \omega \Gamma'}\, \frac{T_{ij} I(\vec{r})}{\bar{v}\sqrt{\pi}} \int_{-\infty}^{\infty} \frac{(\Gamma'/2)^2\, \mathrm{e}^{-(v/\bar{v})^2} dv}{(\Gamma'/2)^2 + (\omega - \omega_{ij} - \omega_{ij}\, v/c)^2}, \tag{2.7}$$

where $\bar{v}$ is the most probable velocity:

$$\bar{v} = \sqrt{2k_B T/M_3} \tag{2.8}$$

that depends on the atomic mass M_3 of the ^{3}He atom and varies with the temperature T of the gas (k_B is the Boltzmann constant). For our purpose the Doppler width D_{ij} of the $A_i \rightarrow B_j$ transition component, that is given by:

$$D_{ij} = (\omega_{ij}/2\pi)\, \sqrt{2k_B T/M_3 c^2}. \tag{2.9}$$

and related to $\bar{v}$ through:

$$\bar{v} = 2\pi c D_{ij}/\omega_{ij}, \tag{2.10}$$

[2]Frequency selection may become an issue at higher pressure due to collisional line broadening, since transitions lying away from the targeted transition component can contribute to the excitation.

[3]For the ^{4}He isotope, this pressure-dependent FWHM collisional broadening (in frequency units) has been measured to be of order 20 MHz/mbar [Blo85, Tac05]. Computations from atomic potentials provide a value of 18.2 MHz/mbar for ^{4}He as well at T=300 K [Vri04], from which a value of w=21 MHz/mbar at T=300 K for the collisional broadening for the ^{3}He isotope is derived in [Nac12].

is considered to be identical to that of the other transition components. Neglecting the small differences in resonance frequencies in equation (2.9), we will indeed use in this manuscript a single Doppler width D for the $2^3\mathrm{S} \rightarrow 2^3\mathrm{P}$ transition defined by :

$$D = (\omega_8/2\pi)\sqrt{2k_BT/M_3c^2}, \tag{2.11}$$

where ω_8 is the angular frequency of the C_8 transition in zero magnetic field ($\omega_8 = 1.739199 \times 10^{15}$ s^{-1}, numerical values provided in list of symbols starting page XVI at the beginning of this manuscript).

For our low-pressure room temperature ^{3}He gas ($\Gamma'/2 \ll 2\pi D$) the integral in equation 2.7 can be easily computed (equation (46) of [Cou02]; see footnote 6 there for corresponding equation in [Nac85]) and leads to a Gaussian variation of the average optical transition rate $\overline{\gamma_{ij}}$ with the frequency detuning of the light $\delta^{ij} = (\omega - \omega_{ij})/2\pi$:

$$\overline{\gamma_{ij}}(\vec{r}) \simeq \frac{\sqrt{\pi}\alpha f}{m_e\omega D}\, T_{ij}\, I(\vec{r})\, \mathrm{e}^{-(\delta^{ij}/D)^2}. \tag{2.12}$$

The numerical value of the prefactor appearing in equation (2.12) is for ^{3}He:

$$\frac{\sqrt{\pi}\alpha f}{m_e\omega D} = 3.7064 \times \sqrt{300/T} \times 10^3\ \mathrm{s}^{-1}/(\mathrm{W/m}^2). \tag{2.13}$$

We have again approximated ω by ω_8 and used equation (2.11) where we have inserted the value of the Doppler width at 300 K (D(300 K)=1.187473 GHz for ^{3}He) in order to let the temperature dependence explicitly appear in equation (2.13).

In the present work (gas pressure: 0.63−2.45 mbar) the C_8 and C_9 transitions are well resolved and probe absorption rates are used for measurements of ^{3}He nuclear polarisation and metastable number density (cf. chapter 4). For probe light tuned to the single-component C_8 line, the local absorption rates involved in these measurements can be directly computed using the appropriate coefficient $\overline{\Gamma_{ij}}$ (depending on light polarisation in the beam), inferred from equation (2.12) and defined as:

$$\overline{\Gamma_{ij}}(\vec{r}) = \overline{\gamma_{ij}}(\vec{r})/I(\vec{r}) \tag{2.14}$$

(see section 4.1). For probe light tuned to the two-component C_9 line the local probe absorption rate involves a similar expression where the contributions of the two line components simultaneously excited must be added.

At higher pressure, collisional broadening has to be taken into account and the computation of the thermal average $\overline{\gamma_{ij}}$ of individual optical transition rates γ_{ij} yields Voigt profiles that significantly differ from the above-described Gaussian Doppler profile, due to the increased contribution of the individual (Lorentzian) atomic response in the convolution with the statistical (Gaussian) distribution of atomic velocities.

The coefficient $\overline{\Gamma}$ that would be relevant for probe absorption measurements thus involves additional contributions from all overlapping line components. Again, this is not an issue in the present work (for quantitative assessment see section 4.4.2.).

The only similar problem that may arise is encountered in our probe light absorption measurements when the laser source is tuned to the C_9 line. Residual ^{4}He atoms in the cell may indeed contribute to light absorption due to the coincidence of the strong D_1 and D_2 lines of ^{4}He with the C_9 line of ^{3}He introduced by the isotope shift (for line spectra see figure 2.2 and for transition matrix elements see tables A.1 and A.2 in appendix A). This issue is discussed in section 4.2.2.

2.3.2 Broadband excitation

For broadband excitation the individual transition rates from A_i to B_j must include a sum over the spectral distribution of light intensity. For a light source characterised by a Gaussian spectral profile with line width L and a detuning δ_{L}^{ij} from the resonance frequency $\omega_{ij}/2\pi$, the velocity-dependent optical transition rate for a moving atom is given by the following expression (similar to equation (15) of [Bat11], where null detuning was assumed):

$$\gamma_{ij}(\vec{r}, v_z) = \frac{\sqrt{\pi}\alpha f}{m_{\mathrm{e}}\omega L}\, T_{ij}\; I(\vec{r})\; e^{-\left(\delta_{\mathrm{L}}^{ij} - D v_z/\bar{v}\right)^2/L^2}. \tag{2.15}$$

For an ensemble of moving atoms at thermal equilibrium submitted to such a broadband excitation, the convolution with the Maxwellian velocity distribution yields the following average local optical transition rate $\overline{\gamma_{ij}}$:

$$\overline{\gamma_{ij}}(\vec{r}) = \frac{\sqrt{\pi}\alpha f}{m_{\mathrm{e}}\omega}\, T_{ij}\; I(\vec{r})\; \frac{D}{\sqrt{D^2 + L^2}}\; e^{-\delta_{\mathrm{L}}^{ij\,2}/(D^2+L^2)}. \tag{2.16}$$

2.4 Rate equations for OP and ME in pure ^{3}He gas

The main problem that is met when modelling OP arises from the *dispersion of local optical transition rates* γ_{ij} due to the *velocity dependence* of the atomic Doppler shifts. The atoms with a given velocity projection v_z along the OP light beam direction constitute a **velocity class** associated to a single optical transition rate. For this velocity class, the generic OP rate equations given below are *position-dependent* since the optical transition rates γ_{ij} are proportional to the inhomogeneous pump light intensity $I_{\mathrm{cell}}(\vec{r})$ present inside the cell.

In our experiments, the variation of the light intensity I_{cell} with position $\vec{r}$ inside the gas cell is both due to the radial intensity profile of the incident pumping beam and to the variation of the amount of light absorbed along the pump beam path, induced by the non uniform spatial distribution of the 2^3S atoms in the cell

(see section 2.5.3). Indeed, the 2^3S number density vanishes near the wall, where the metastable atoms deexcite, and everywhere else locally depends on the uncontrolled balance in the rf plasma between excitation, quenching, and diffusion processes (that may be influenced also by the pump light, due to optogalvanic effects).

Besides these two difficulties, strong non linearities appear at high pump powers since, as recalled below, the local light absorption rate involves the product of the optical transition rate γ_{ij} and of the difference $a_i - b_j$ of populations in the 2^3S and 2^3P states that both depend on pumping light intensity. All these intrinsic issues will be dealt with by the assumptions and simplifications introduced in the OP model described in section 2.5.

In this section, we recall the rate equations describing the processes of OP and ME introduced in previous work [Nac85, Cou02, Bat11]. They are not valid for a realistic physical description of the system since, even if the experimental variation with position can be assumed to be implicit in the 2^3S and 2^3P rate equations, the intrinsic variations of optical transition rates (hence of all populations of metastable and excited states) with atomic velocities are ignored. They should be considered as **generic rate equations** (for populations in a generic velocity class excited with an optical transition rate γ_{ij}) that are useful for a simple description of the general structure of the more appropriate rate equations and for a simpler physical discussion of the various contributions of key processes (ME, OP and relaxation) to MEOP dynamics. Actually these generic equations have to be replaced by similar ones for the various velocity classes involved and supplemented by the contributions of all processes that may couple these velocity classes (e.g., atom−atom collisions). This was done for instance in [Nac85] in the context of the over-simplified model mentioned in the introduction, where all 2^3S atoms addressed by the lasers where considered to belong to a single velocity class and to be excited with an identical optical transition rate and all other 2^3S atoms where considered not excited at all (this is discussed in more details in section 2.5). The full set of rate equations relevant for the present work is given in appendix B: they are derived from the generic ones in the context of the improved OP model introduced in section 2.5 (this derivation will be shortly published [Nac12]). They are local both in space and momentum in the metastable and excited states. The derivation and justification of the modifications that must be applied to the (more simple) generic mathematical expressions obtained from these generic rate equations used below also falls beyond the scope of the present work and only the results are given in this manuscript. The corresponding mathematical expressions, appropriate and valid within the improved 2-class OP model, are listed in appendix B.

For the excited ^{3}He states ME and OP processes are here described in terms of the generic populations a_i and b_j and number density of atoms in the metastable state n_m. The local number density of 2^3S atoms in sublevel A_i is $n_m a_i$ and the

a_is are populations satisfying $\sum_{i=1}^{6} a_i = 1$. For convenience, to avoid one additional parameter and an additional equation, the populations b_js in the 2^3P state are defined so that the number density of atoms in sublevel B_j of the 2^3P state is $n_m b_j$. Hence the b_js are not "true" populations ($\sum_{k=1}^{18} b_k < 1$) and their sum depends on the OP light intensity. In the following, for clarity, the variation with position of the *local* generic quantities listed above (a_i, b_j, n_m) and of the *local* optical transition rates γ_{ij} used below is generally omitted. It is explicitly specified only when average values over the cell volume are involved.

In contrast, in the ground state the ^{3}He nuclear polarisation M can be safely considered to be *uniform* and velocity-independent inside the whole gas cell, thanks to fast atomic diffusion (see section 2.6). The nuclear polarisation M is defined as the difference of populations of the two nuclear spin states $m_I = \pm 1/2$ and, hence, directly measures the longitudinal component of nuclear spin angular momentum in the ground state $\langle I_z \rangle_{1^1\mathrm{S}_0}$ since:

$$\langle I_z \rangle_{1^1\mathrm{S}_0} = \frac{\hbar}{2} M. \tag{2.17}$$

M can also be expressed as the relative difference of corresponding number densities $N_\mathrm{g}^\pm$:

$$M = \frac{N_\mathrm{g}^+ - N_\mathrm{g}^-}{N_\mathrm{g}^+ + N_\mathrm{g}^-} = \frac{N_\mathrm{g}^+ - N_\mathrm{g}^-}{N_\mathrm{g}} \tag{2.18}$$

where N_g is the number density of ground state ^{3}He atoms (almost equal to the constant gas number density in the sealed cell).

2.4.1 Generic OP rate equations

For the closed 2^3S - 2^3P optical transition the joint time evolution of the populations a_i and b_j under light excitation is described by (equations (13) and (14) in reference [Bat11])[4]:

$$\left.\frac{da_i}{dt}\right|_{\mathrm{OP}} = \gamma \sum_{j=1}^{18} T_{ij} b_j + \sum_{j=1}^{18} \gamma_{ij}(b_j - a_i) \tag{2.19}$$

$$\left.\frac{db_j}{dt}\right|_{\mathrm{OP}} = -\gamma b_j + \sum_{i=1}^{6} \gamma_{ij}(a_i - b_j), \tag{2.20}$$

[4]No full set of OP rate equations has been provided in reference [Cou02], where depopulation OP (see section 6.3.2) with monochromatic excitation could be described by a single and very simple equation (equation (42)).

using the radiative decay rate γ of the 2^3P state (cf. section 2.6), the matrix elements T_{ij}, and the optical transition rates γ_{ij} (cf. section 2.3).[5]

For the 2^3S atoms, the first part of equation (2.19) describes the contribution of spontaneous emission of light by all 2^3P atoms and the second part represents the net balance between absorption by 2^3S atoms and stimulated emission by 2^3P atoms. For the 2^3P atoms, the first part of equation (2.20) represents spontaneous radiative decay to the 2^3S state and the second part, driven by light excitation, corresponds to the net balance between growth through excitation of 2^3S atoms and decrease through stimulated emission.

2.4.2 Generic ME rate equations

The ME process leads to a joint time evolution of the populations a_i and of the ground state nuclear polarisation M described by:

$$\left.\frac{da_i}{dt}\right|_{\mathrm{ME}} = \gamma_{\mathrm{e}} \left(-a_i + \sum_{k=1}^{6} (E^3_{ik} + M F^3_{ik}) a_k \right) \tag{2.21}$$

$$\left.\frac{dM}{dt}\right|_{\mathrm{ME}} = \gamma_{\mathrm{e}} \int_{\mathrm{cell}} \frac{d^3\vec{r}}{V_{\mathrm{c}}} \frac{n_{\mathrm{m}}(\vec{r})}{N_{\mathrm{g}}} \left(\sum_{k=1}^{6} L_k a_k(\vec{r}) - M \right). \tag{2.22}$$

Equation (2.21) is equivalent to equation (35) of reference [Cou02] for pure ^{3}He gas. For equation (2.22), in contrast with equation (33) of reference [Cou02], we have explicitly taken into account the spatial inhomogeneity of the 2^3S number density. The ME collision rate γ_{e} is proportional to gas pressure (cf. section 2.6). The matrix operators E^3 and F^3 as well as the vector operator L have field dependent coefficients that are given in appendix A.

These ME operators are derived from a detailed analysis of the changes in internal variables for the colliding 2^3S and $1^1\mathrm{S}_0$ He atoms during metastability exchange [Cou02] and equations (2.21) and (2.22) duly conserve angular momentum. This can be shown as follows. On the one hand the components of the vector operator L are closely related to the values of the projection of the longitudinal component of the nuclear spin angular momentum in the 2^3S Zeeman sublevels:

$$L_k = \left\langle \mathrm{A}_k \left| \frac{2}{\hbar} I_z \right| \mathrm{A}_k \right\rangle \tag{2.23}$$

[5] In this work we systematically neglect all potential contributions of other radiative processes in the plasma associated to OP-induced changes of deexcitation from higher excited states, i.e., we assume $b_j = 0$ in the absence of OP light.

and equation (2.22) can actually be written as:

$$\left.\frac{dM}{dt}\right|_{\mathrm{ME}} = \gamma_{\mathrm{e}} \int_{\mathrm{cell}} \frac{d^3\vec{r}}{V_{\mathrm{c}}} \frac{n_{\mathrm{m}}(\vec{r})}{N_{\mathrm{g}}} \left(M^{\mathrm{S}}(\vec{r}) - M\right), \tag{2.24}$$

where we have introduced the *local* nuclear polarisation in the metastable state, M^{S}:

$$M^{\mathrm{S}}(\vec{r}) = \sum_{k=1}^{6} L_k a_k(\vec{r}), \tag{2.25}$$

that is, of course, related to the local value of the longitudinal component of nuclear spin angular momentum in the metastable state $\langle I_z \rangle_{2^3\mathrm{S}}$ by:[6]

$$\frac{\hbar}{2} M^{\mathrm{S}}(\vec{r}) = \langle I_z \rangle_{2^3\mathrm{S}} (\vec{r}). \tag{2.26}$$

On the other hand one can easily check that, for all $k = 1 - 6$, the matrix operators E^3 and F^3 satisfy:

$$\sum_i m_{\mathrm{F}}(i)(E^3 + MF^3)_{ik} = -\frac{1}{2}(L_k - M) + m_{\mathrm{F}}(k). \tag{2.27}$$

This built-in property of the ME operators then ensures, for this set of generic ME contributions to the rate equations, that:

$$\sum_i m_{\mathrm{F}}(i) \left.\frac{da_i(\vec{r})}{dt}\right|_{\mathrm{ME}} = -\gamma_{\mathrm{e}} \frac{M^{\mathrm{S}}(\vec{r}) - M}{2} \tag{2.28}$$

so that the condition for the global conservation of angular momentum projections:

$$\int_{\mathrm{cell}} \frac{d^3\vec{r}}{V_{\mathrm{c}}} n_{\mathrm{m}}(\vec{r}) \left.\frac{d \langle F_z \rangle_{2^3\mathrm{S}} (\vec{r})}{dt}\right|_{\mathrm{ME}} + N_{\mathrm{g}} \left.\frac{d \langle I_z \rangle_{1^1\mathrm{S}_0}}{dt}\right|_{\mathrm{ME}} = 0 \tag{2.29}$$

is automatically fulfilled since:

$$\langle F_z \rangle_{2^3\mathrm{S}} (\vec{r}) = \hbar \sum_i m_{\mathrm{F}}(i)\ a_i(\vec{r}) \tag{2.30}$$

is the local value of the longitudinal component of the total angular momentum in the metastable state (equations (2.24) and (2.28) just have to be combined).

The physical interpretation of equation (2.24) is straightforward: the time evolution of the ground state polarisation M is driven by its difference with the average nuclear polarisation $\overline{M^{\mathrm{S}}}$ in the 2^3S state, defined as:

$$\overline{M^{\mathrm{S}}} = \frac{\int_{\mathrm{cell}} d^3\vec{r}\, n_{\mathrm{m}}(\vec{r})\ M^{\mathrm{S}}(\vec{r})}{\int_{\mathrm{cell}} d^3\vec{r}\, n_{\mathrm{m}}(\vec{r})}, \tag{2.31}$$

[6] The 2^3S nuclear polarisation M^{S} was noted $\langle I \rangle_m$ in [Nac85].

if the ME contribution (2.24) is formally re-written as:

$$\left.\frac{dM}{dt}\right|_{\mathrm{ME}} = \overline{\Gamma}_{\mathrm{e}} \left(\overline{M^{\mathrm{S}}}(\vec{r}) - M \right), \tag{2.32}$$

and an average metastability exchange rate for the atoms in the ground state, $\overline{\Gamma_{\mathrm{e}}}$, is introduced and defined as:

$$\overline{\Gamma}_{\mathrm{e}} = \gamma_{\mathrm{e}} \int_{\mathrm{cell}} \frac{d^3\vec{r}}{V_{\mathrm{c}}} \frac{n_{\mathrm{m}}(\vec{r})}{N_{\mathrm{g}}}. \tag{2.33}$$

This spatially averaged ME rate is the analogue of the ME rate Γ_{e} appearing in equation (33) for the time evolution of M in reference [Cou02], here generalised to the case of non uniform number density of 2^3S atoms n_{m}.

The nuclear polarisation $M^{\mathrm{S}}(\vec{r})$ of the metastable atoms can simply be written as (valid up to $B = 0.162$ T):

$$M^{\mathrm{S}} = \sum_{k=1}^{6} L_k a_k = (a_4 - a_1) + L_-(a_2 - a_5) + L_+(a_3 - a_6), \tag{2.34}$$

making use of the field-dependent coefficients $L_{\pm}{=}c_{\pm} - s_{\pm}$ (given in appendix A) associated to the components of the operator L, where $c_{\pm} = \cos^2\theta_{\pm}$ and $s_{\pm} = \sin^2\theta_{\pm}$ explicitly vary with B through the mixing parameters $\theta_{\pm}$, and $L_{\pm}(B = 0) = \pm 1/3$.

ME and OP processes are both described in 2^3S by non linear rate equations. In equation (2.19) the prefactor γ_{ij} is proportional (see section 2.3) to the pump light intensity I_{cell} present inside the cell that, in turns, depends on the a_{i} populations due to absorption of the incident light by He atoms. Equation (2.21) explicitly includes M (as prefactor of the coefficients of the matrix operator F^3) whose time evolution results from a combination of all a_{i} populations (through $M^{\mathrm{S}} = \sum_k L_k a_k$ in equation (2.24)). We also recall that these non linear local equations are only generic ones where optical transition rates γ_{ij} and hence the quantities a_i, b_j, and n_{m} have some implicit velocity-dependence due to the dispersion of Doppler shifts. Moreover, due to the non linearity of OP contributions, one cannot simply use a statistical average $\overline{\gamma_{ij}}$ (equation (2.16)) of individual optical transition rates γ_{ij} (equation (2.15)) to accurately describe MEOP kinetics when powerful broadband pump lasers are used. Finally the contributions of relaxation (that tends to damp any imbalanced distribution of atoms between Zeeman sublevels in the ground, metastable, and excited states) and, in particular, of the collisional redistribution in the 2^3P state have not yet been taken into account. The simplifications and assumptions introduced to address these issues and to write a valid full set of equations are described in the following section.

2.5 The improved 2-class OP model

To suitably describe all relevant processes in MEOP with a limited number of parameters, two major simplifications and one approximation are introduced. They essentially deal with the problems raised by relaxation, the velocity-dependent character of OP contributions, and the computation of the local pump laser intensity. They are successively described in the following.

2.5.1 Relaxation processes

Relaxation refers here to the effect of additional processes that couple populations of the various Zeeman sublevels within each atomic state. Numerous processes are involved (especially in the rf plasma) and the corresponding relaxation rates may not be *a priori* known. Therefore the OP model that is used involves a phenomenological description of all such processes by simple rate equations that correspond to uniform redistribution between Zeeman sublevels with a single relaxation rate in each state. This pragmatical approach is identical to the one used in reference [Nac85] and the set of contributions of relaxation to the time evolution of the system have the **generic form** recalled below (equations (12), (11) and (18) in reference [Bat11]):

$$\left.\frac{db_j}{dt}\right|_{\mathrm{r}} = \gamma_r^{\mathrm{P}} \left[\left(\frac{1}{18} \sum\nolimits_{k=1}^{18} b_k \right) - b_j \right] \tag{2.35}$$

$$\left.\frac{da_i}{dt}\right|_{\mathrm{r}} = \gamma_r^{\mathrm{S}} \left(\frac{1}{6} - a_i \right) \tag{2.36}$$

$$\left.\frac{dM}{dt}\right|_{\mathrm{r}} = -\Gamma_{\mathrm{g}}\, M. \tag{2.37}$$

However, in the context of the improved model described here, equations (2.35) to (2.37) must be replaced by the appropriate full set of valid equations given in appendix B.

Orders of magnitude for parameters γ_r^{P}, γ_r^{S}, and Γ_{g} are discussed in the following section (2.6). This may be a far too coarse description, in particular for the 2^3P state. The main contribution to 2^3P relaxation comes from collisional redistribution and, due to the large fine structure splittings in helium, resorting to a single rate is questionable (see page 253). Still an approximate value of $\gamma_{\mathrm{r}}^{\mathrm{P}}$ can be inferred from experimental measurements of OP efficiencies (see section 6.3.2). Processes contributing to the 2^3S relaxation rate $\gamma_{\mathrm{r}}^{\mathrm{S}}$ are not known but non-radiative de-excitation processes definitely set its lower bound. The ground state relaxation rate Γ_{g} *a priori* describes all processes directly acting on the nuclear polarisation of the ^{3}He gas. As we shall see, we have no direct access to this quantity in the experiments but measurements of plasma decay rates yield lower bounds.

2.5.2 Velocity-dependent light excitation

Even if the continuous Boltzmann distribution of atomic velocities was binned in a finite number of velocity classes, solving the corresponding set of rate equations would be a difficult task since their populations are coupled by velocity-changing collisional processes (including ME) with ill-known collision rates. Instead, to account for the dispersion of atomic velocities with as few free parameters as possible, a coarse description with two broad velocity classes is used. This is similar to the partition of the velocity distribution originally introduced in reference [Nac85]. However in the improved model both velocity classes are associated to finite optical transition rates. The computation of the average optical transition rate assigned to each velocity class will be explained and discussed in detail in a forthcoming publication [Nac12]. Here we only give the final result and stick to a basics description of the underlying physical arguments with the help of figure 2.5.
The upper graph (figure 2.5a) represents the Maxwellian distribution of atomic velocities (statistical weight proportional to $\exp -v_z^2/\bar{v}^2$, where $\bar{v}$ is the most probable velocity associated to the Gaussian Doppler width D, equations (2.8) and (2.11)). The lower graph (figure 2.5b) represents the spectral distribution of pumping laser intensity as a function of the reduced frequency difference $(\omega - \omega_{ij})/2\pi D$, with a central laser frequency $\omega_{\mathrm{L}}/2\pi = \omega_{ij}/2\pi - \delta_{\mathrm{L}}^{ij}$ close to the atomic transition frequency. Atoms with different velocities, hence different Doppler shifts, experience different optical transition rates (maximal for atoms with velocity v_{L} corresponding to a Doppler shift equal to the laser frequency detuning δ_{L}^{ij}). The hatched part in the velocity distribution (figure 2.5a) constitutes the velocity class of **strongly pumped atoms**, in the centre of the velocity distribution with a velocity projection $|v_z| < v_z^*$. The other class of **weakly pumped atoms**, contains all other atoms in the wings of the velocity distribution. Figure 2.5b represents a detuned laser profile (by an amount δ_{L}^{ij} from the atomic transition). This detuning is kept as small as possible in the experiments. It cannot be strictly null when OP is performed on the C_9 line at finite magnetic field strength, due to the difference in resonance frequencies for the two components that are simultaneously excited (Zeeman splitting is about 21 MHz/mT). But all experiments have been performed in a double-pass configuration for the OP beam and atoms with positive and negative velocity projections experience almost equal pumping rates. For this reason, we consider the symmetric velocity interval of figure 2.5a to define the strongly pumped class.

The approach (partition in two broad velocity classes) and the notations used are similar to those of reference [Nac85] but the final rate equations are actually quite different. In reference [Nac85], the pump laser was assumed to be a narrow-band one, or to have a spectral profile composed of a small number of discrete narrow modes. As a result atoms not lying in the strongly pumped class could be considered as *not* pumped at all. In contrast, currently used fibre lasers have a broad emission

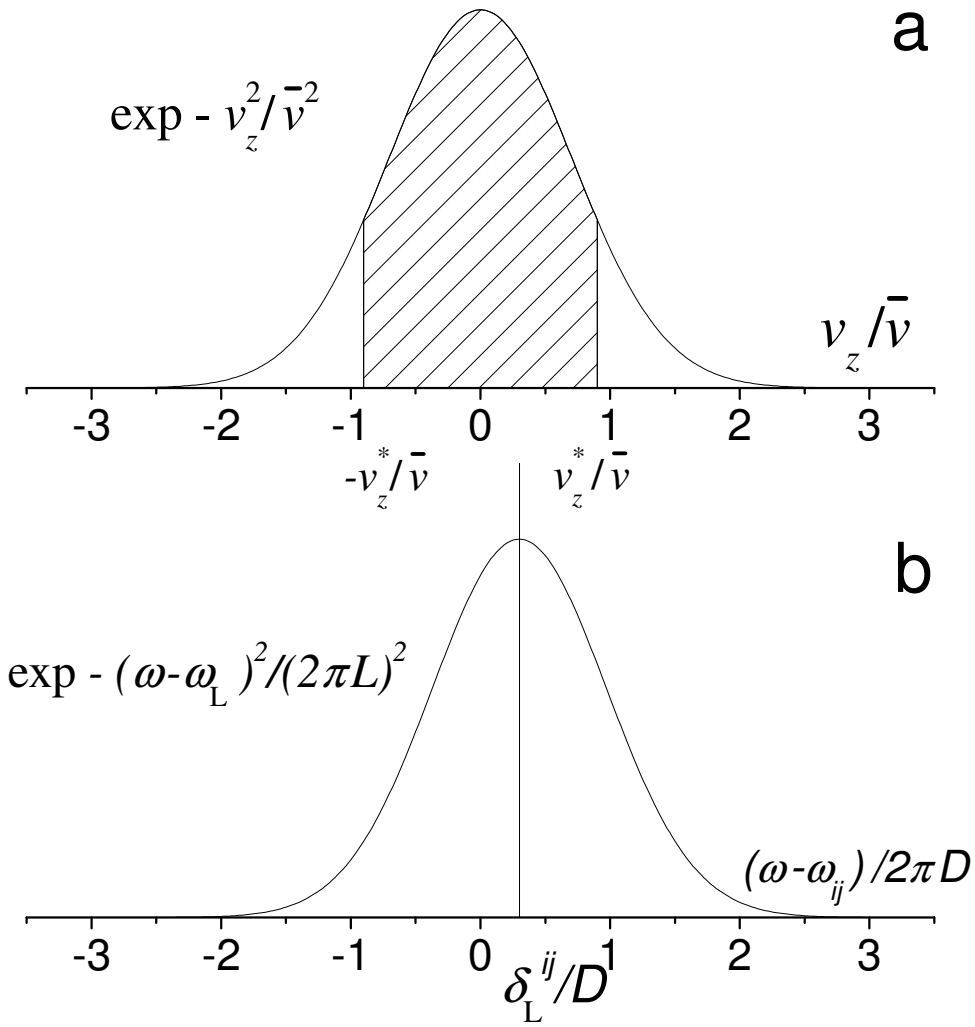

Figure 2.5: Two-class OP model. **a:** Maxwell velocity distribution of atoms characterised by its most probable velocity $\overline{v}$ and Gaussian width D (see section 2.3). It is split in two broad classes using the velocity boundary v_z^*. The atoms with $|v_z| < v_z^*$ belong to the "strongly pumped" class (hatched area); the atoms with $|v_z| > v_z^*$ belong to the "weakly pumped" class. **b:** spectral profile of the pump laser (Gaussian width: L, frequency detuning: $\delta_{\mathrm{L}}^{ij} = (\omega_{ij} - \omega_{\mathrm{L}})/2\pi$ with respect to the atomic transition frequency $\omega_{ij}/2\pi$).

spectrum, tailored to match the Doppler width of ^{3}He [Tas04]. For the laser used in this work, the spectral profile has been measured to be approximately Gaussian with a characteristic width $L \simeq 1.02$ GHz (FWHM $= 2L\sqrt{\ln 2} \simeq 1.7$ GHz), as displayed in figure 2.5b. Hence atoms in *both* classes experience significant OP intensity.

The two broad velocity classes are described by distinct sets of local quantities (a_i, b_j, $n_{\mathrm{m}}, \gamma_{ij}$). The metastable density is noted $n^*_{\mathrm{m}}(\vec{r})$ (respectively $n'_{\mathrm{m}}(\vec{r})$) for the strongly (weakly) pumped class and corresponds to an integral over the velocity projection interval $-v^*_z < v_z < v^*_z$ (resp. $v_z < -v^*_z$ and $v^*_z < v_z$). The 2^3S populations a^*_{i} (resp. a'_{i}) satisfy $\sum_i a^*_i = 1$ (resp. $\sum_i a'_i = 1$). They are resonantly coupled to the 2^3P populations b^*_j (resp. b'_j) and the corresponding local number density of excited atoms is equal to $n^*_{\mathrm{m}}(\vec{r})\sum_j b^*_j$ (resp. $n'_{\mathrm{m}}(\vec{r})\sum_j b'_j$). The local optical transition rate γ^*_{ij} (resp. γ'_{ij}) is *chosen* to be equal to the computed average of the individual velocity-dependent rates for broadband excitation $\gamma_{ij}(v_z, \vec{r})$ (equation (2.15)) over the corresponding velocity range using the Boltzmann statistical weight. This yields:

$$\gamma^*_{ij}(\vec{r}) = \bar{\gamma}_{ij}(\vec{r})\frac{n_{\mathrm{m}}(\vec{r})}{n^*_{\mathrm{m}}(\vec{r})}\Sigma^* = \frac{\bar{\gamma}_{ij}(\vec{r})\Sigma^*}{\mathrm{erf}(\Delta/D)} \tag{2.38}$$

$$\gamma'_{ij}(\vec{r}) = \bar{\gamma}_{ij}(\vec{r})\frac{n_{\mathrm{m}}(\vec{r})}{n'_{\mathrm{m}}(\vec{r})}\Sigma' = \frac{\bar{\gamma}_{ij}(\vec{r})\Sigma'}{1-\mathrm{erf}(\Delta/D)}, \tag{2.39}$$

where the average local optical transition rate $\bar{\gamma}_{ij}(\vec{r})$ is defined as:

$$\bar{\gamma}_{ij}(\vec{r}) = \frac{\sqrt{\pi}\alpha f}{m_{\mathrm{e}}\omega D}\, T_{ij}\;\; I_{\mathrm{cell}}(\vec{r}), \tag{2.40}$$

and (assuming negligible pump detuning) the two dimensionless factors Σ^* and Σ' are given by:

$$\Sigma^* = \frac{D}{\sqrt{L^2+D^2}}\;\; \mathrm{erf}\left(\frac{\sqrt{L^2+D^2}\Delta}{LD}\right) \tag{2.41}$$

$$\Sigma' = \frac{D}{\sqrt{L^2+D^2}} - \Sigma^* \tag{2.42}$$

(L and D are laser and Doppler widths, respectively; Δ is a characteristic frequency offset, defined by $\Delta/D = v^*_z/\bar{v}$, that corresponds to the maximum Doppler frequency shift in the strongly pumped velocity class; the error function, erf, in equation (2.41) arises from a Gaussian integral over the truncated range of velocities).

The width of the strongly pumped velocity class Δ is a free parameter in the OP model that we also choose to be equal to the laser width: Δ/L =1. In section 2.8, we show that this choice is reasonable as it has a limited influence on the computed OP results.

The rate equations for the whole system are different from the generic ones and from those of reference [Nac85]:

- There are two sets of OP rate equations, one for each velocity class.

- The ME rate equations in the 2^3S state are modified. They include, for each velocity class, contributions still related to the ground state nuclear polarisation but now originating from both velocity classes. The ME rate equation in the ground state is also modified. It includes the sum of two driving terms, one for each velocity class (associated to the respective local 2^3S nuclear polarisations).

- Both sets of 2^3P populations relax with an identical rate γ_r^{P}.

- An additional set of collisional rate equations is introduced to describe the transfer of 2^3S atoms from one velocity-class to the other. The corresponding term is neglected for atoms in the 2^3P atoms state, in which the collisions that are able to change the atom velocities are likely to also induce a change in internal variables (i.e., to contribute to relaxation of the Zeeman populations).

The frequent ME collisions play a key role in the MEOP process, and they modify the velocities as well as the internal variables of 2^3S atoms. It is usually assumed that ME collisions have small impact parameters (they require a significant overlap between electronic orbitals, and the centrifugal barrier of the potential must be overcome). In the ME process the velocity projection of the colliding 2^3S atom thus has a high probability to be strongly modified. For simplicity, we assume that the velocities before and after collision are uncorrelated and that the outgoing velocity projection is randomly distributed according to the Maxwell distribution of figure 2.5a. This leads in the 2-class OP model to ME rate equations coupling the populations a_{i}^* and a_{i}' with weights simply given by the densities n_{m}^* and n_{m}' (equation (B.12) in appendix B).

In contrast to the ME collisions, elastic velocity-changing collisions, that do not affect the internal spin variables of the 2^3S atoms, may occur with large impact parameters and thus lead only to small changes in velocities. In the 2-class model they are relevant only for atoms with velocities close to the class boundaries and thus induce a weak average coupling between the populations of the two classes. Large velocity changes, that would more efficiently couple these populations, involve collisions with small enough impact parameters that, consequently, are likely to also strongly affect internal atomic states and hence to be ME collisions already taken into account by the modified exchange rate equations. For this reason, velocity-changing collisions are taken into account by additional rate equations that describe a uniform redistribution between velocity classes characterised by a single and small rate: the collisional parameter $\gamma_{\mathrm{c}} \ll \gamma_{\mathrm{e}}$, that is typically set to 10^3 s^{-1}.

Attributing full velocity redistribution to ME collisions and a small contribution to elastic velocity-changing collisions presumably over-/under-estimates each effect if considered separately, but this is believed to provide a reasonable description of the global impact of collisions of 2^3S atoms.

2.5.3 Inhomogeneous light excitation and atomic response: 1-D model

A last simplification is made to allow quantitative but still manageable description of the system: the longitudinal variations of the 2^3S number density and of the local light intensity are both neglected inside the cell and only radial variations are considered.

For the 2^3S density, the de-excitation of the metastable atoms on the cell windows can be reasonably assumed to have a negligible overall impact in our fairly long cylindrical cells with aspect ratio 5 (length over diameter, see section 3.1). The inhomogeneity of the rf excitation pattern has been pragmatically assessed visually using the distribution of visible light emitted by the plasma and reduced by implementation of a large number of ring electrodes (cf. section 3.1). The variation of the 2^3S atom number density can be reasonably assumed to be weak, due to the strong damping provided by fast atomic diffusion, and no attempt has been made to quantify the residual fluctuations (in contrast with the radial distribution profiles that have been mapped). In the OP model the distribution of atoms is assumed to be perfectly symmetrical, to be independent of the longitudinal coordinate (z, distance from the entrance window), and to vary only with the radial coordinate (r, distance to the axis).

For the light intensity, a configuration with the pump beam aligned with the cell axis, propagating parallel to it and back-reflected by a high-quality mirror has been chosen in the experiment. The incident light intensity thus only depends on the radial coordinate r. The (uncontrollable) attenuation due to progressive resonant absorption by the gas leads to a significant gradual change of the local light intensity with the longitudinal coordinate z along the first pass (contribution $I_1(r, z)$) and with $(L_{\text{cell}} - z)$ along the second pass (contribution $I_2(r, z)$). As a first approximation, for weak absorption the combination of both changes leads to a fairly good compensation. Assuming a constant rate of absorption per unit length, the intensity $I(r, z) = I_1(r, z) + I_2(r, z)$ can be analytically and numerically checked to be almost uniform at fixed distance r to the cell axis. To a very good approximation the value at the middle of the cell can (and was) used for local intensity $I_{\text{cell}}(r) = I(r, L_{\text{cell}}/2)$.

However when absorption in the gas becomes more significant a better approximation must be used for more accurate results. This is the case for our systematic investigations of MEOP, where higher gas pressures and rf discharges well beyond their extinction threshold have been used. Therefore the uniform value that is assigned to the local intensity $I_{\text{cell}}(r)$ is now, in the improved OP model, replaced by the average light intensity that is computed from the distribution $I(r, z)$ obtained for a constant absorption rate (see appendix C).

In short, the improved OP model relies on an approximate but realistic 1D-description where all local quantities only depend on the radial coordinate r that measures the distance to the optical axis.

2.6 Comparison of all rates relevant for MEOP in ^{3}He gas

The easiest way to solve the system of coupled non linear equations described in the previous section is to take advantage of the great difference in the evolution rates of atomic internal states for the 2^3P, 2^3S and 1^1S_0 states. Numerical estimates of the relevant rates are provided below.

The ME- and OP-induced changes that occur in the two excited states (2^3S and 2^3P) of the helium atom are by far the fastest ones. A single and convenient scale is provided by the radiative decay rate of the 2^3S-2^3P transition by spontaneous emission (measured by [Lan68] and related to the oscillator strength of the 2^3S-2^3P transition $f = 0.5391$ [Wie66, Dra96]):

$$\gamma = 1.022 \times 10^7 \text{ s}^{-1}. \tag{2.43}$$

The resonant absorption and stimulated emission of light by the ^{3}He atoms involve one or more optical transition rate(s) γ_{ij}. For broadband optical pumping with a tuned light source, the improved 2-class model involves the average pumping rate $\overline{\gamma_{ij}}$ that can be written as $\overline{\gamma_{ij}} = T_{ij}\ \gamma_{\text{OP}}$ (equation (2.40)), where $\gamma_{\text{OP}} = \frac{\sqrt{\pi}\alpha f}{m_e \omega D}\ I_{\text{cell}}(\vec{r})$ is a characteristic pumping rate independent of the selected transition(s) $\text{A}_i \rightarrow \text{B}_j$ and proportional to the local light intensity $I_{\text{cell}}(\vec{r})$. The prefactor has been computed to be equal to 3.7064×10^3 s^{-1}/(W/m^2) for ^{3}He at room temperature (relation (2.13)). The order of magnitude of the pumping rates is then set by:

$$\gamma_{\text{OP}}/\gamma = 3.627\ I_{\text{cell}}[\text{W cm}^{-2}] \tag{2.44}$$

where $I_{\text{cell}}[\text{W cm}^{-2}]$ is the value of the local intensity expressed in W/cm^2 unit. The actual velocity-dependent pumping rates (equations (2.38) and (2.39)) involve an additional spectral prefactor that is of order unity ($D/\sqrt{L^2 + D^2} = 0.766$ for L =1.02 GHz (1.7 GHz FWHM) typical of dedicated 1083 nm fibre lasers) and dimensionless factors that are also of order 1 for $\Delta = L$: $\text{erf}(\Delta/D) = 0.775$, $\Sigma^* = 0.712$. In our experiments, the pump beam has a Gaussian transverse intensity profile with typical waist $2a = 1.6$ cm (FWHM: $2a\sqrt{\ln 2}$, see equation (3.2)) so that, if W_{inc} is the incident light power, the maximal light intensity value (reached on the cell axis average light intensity) is equal to $I_{\text{inc}}(r = 0) = W_{\text{inc}}/(\pi a^2) = W_{\text{inc}}/(2.0 \text{ cm}^2)$. Light absorption is weak in our experiments (light transmittances usually exceed 70 %) and is here neglected. As a result, taking into account back reflection of the pump light, the maximal pumping rate is such that $\gamma_{\text{OP}}/\gamma \sim 3.3\ W_{\text{inc}}[\text{W}]$.

The ME exchange with the ground state atoms occurs with a pressure-dependent

rate γ_e given by γ_e/p_3=3.75×10^6 s^{-1}/mbar [Dup71][7], so that:

$$\gamma_e/\gamma = 0.367\ p_3[\text{mbar}]. \tag{2.45}$$

The collisional redistribution between Zeeman sublevels in the 2^3P state results in a pressure-dependent relaxation rate γ_r^{P} for b_i populations that is observed in our experiments to be on the order of $\gamma_r^{\mathrm{P}}/p_3 \simeq 0.32\times10^7$ s^{-1}/mbar (this is inferred from measurements of OP performance, see chapter 6.3.2), so that:

$$\gamma_r^{\mathrm{P}}/\gamma \simeq 0.313\ p_3[\text{mbar}]. \tag{2.46}$$

In comparison, in standard conditions the redistribution between Zeeman sublevels in the 2^3S state is fortunately significantly slower. Quenching of metastable atoms by collisions with impurities, de-excitation, ionisation, or formation of metastable molecules may limit the 2^3S atoms lifetime. A typical value (actually, just a lower bound) of the relaxation rate γ_r^{S} for a_i populations is provided by de-excitation on the cell wall, mainly due to diffusion of metastable atoms in the gas. Using the diffusion coefficient given in [Fit68], this yields $\gamma_r^{\mathrm{S}} \simeq 10^3$ s^{-1} at mbar pressures (using the diffusion time associated to the lowest diffusion mode in our cylindrical cells), so that:

$$\gamma_r^{\mathrm{S}}/\gamma \simeq 10^{-4}. \tag{2.47}$$

ME drives the evolution of the nuclear polarisation in the ground state with a typical rate $\overline{\Gamma_e}$ (cf. equation (2.33)) that is 6 orders of magnitude smaller than that of the 2^3S state, due to the difference in number densities, so that:

$$\overline{\Gamma_{\mathrm{e}}}/\gamma \sim 0.4 \times 10^{-6}\ p_3[\text{mbar}]. \tag{2.48}$$

Other processes may contribute to the evolution of the nuclear ground state polarisation M, among which intrinsic nuclear relaxation (dipole-dipole relaxation [New93] in dilute gas is actually negligible), relaxation by magnetic field inhomogeneities [Sch65, Cat88a, Cat88b, Has90] (a potentially fast process at low pressure for poorly controlled field maps), wall relaxation, or relaxation by spin coupling interactions with co-existing species (e.g., paramagnetic impurities [Sch06a, Den06, Sch06b, Hut07]). The corresponding ground state relaxation rate can be measured in the absence of rf excitations (e.g., by NMR or by periodically turning the discharge back on to perform the optical measurements) but this does not correspond to our operating conditions for MEOP. In presence of the plasma the relaxation rate Γ_{g} may be different and there is no experimental way to measure its contribution independently of that of ME (cf. equation (2.71)).

[7] In [Nac85], the values for the metastability exchange time τ_e at 1 torr on page 2065 should be τ_e=2.0×10^{-7}s at 300K [Dup71], τ_e=2.2×10^{-6}s at 77K [Zhi76], and 2.8×10^{-4}s at 4.2K [Bar77].

The comparison of the above-compiled rates shows that the evolution of 2^3S populations occurs on a much faster time scale (typically microseconds) than that of the ground state nuclear polarisation M (typically seconds, or more). The response to laser excitation and competing physical processes can thus be considered to be almost instantaneous in the 2^3S states and the populations of the Zeeman sublevels to reach a quasi-stationary state that adiabatically follows the slow evolution of the nuclear polarisation of the ^{3}He gas.

2.7 Numerical computation of MEOP dynamics

2.7.1 Equation solving strategy

The method used to solve the entire set of coupled non-linear rate equations and to compute OP kinetics is heavily based on the conclusion of the previous section:
1/ *at fixed nuclear polarisation* M the steady-state solutions of the full rate equations for the 2^3S and 2^3P populations are computed, for instance as a function of the incident pump power at fixed other operating conditions.
2/ the M-dependent steady state 2^3S populations are used to compute the ME-induced source term in the full rate equation for the ground state polarisation.
The full rate equation for M can be time-integrated to obtain the polarisation $M(t)$ at all times t, starting from the initial condition $M(t = 0) = 0$.

The whole set of internal variables is then known at all times t and any other quantities relevant for characterisation of OP kinetics, for consistency checks, or for comparison with experimental findings, can be computed. Numerous examples can be found in this manuscript. Complementary results and systematic checks performed to validate the improved OP model will be shortly published. In this work we have been especially interested in the computation of quantities that can be experimentally investigated such as the value of 2^3S nuclear polarisation, of pump and probe light absorption, of photon efficiencies, of polarisation decay rates, of apparent ^{3}He nuclear polarisation as a measure of the OP-driven changes in the distribution of 2^3S populations, etc. Both the stationary values (i.e., at null[8] ($M = 0$) and steady-state ($M = M_{eq}$) polarisations) and the time variation, i.e. during polarisation growth and decay, have been studied for all these physical quantities.

2.7.2 Full rate equations

The full rate equations are obtained by addition of the contributions of OP, ME, relaxation, and for the 2^3S state of elastic collisions in the framework of the improved

[8]Stationary situations at $M = 0$ are experimentally obtained at low pressure using magnets near the cell to induce strong magnetic relaxation and prevent any significant nuclear polarisation to build up in the ground state.

model.
- The generic full rate equations can be written using the rate equations provided in section 2.4. The quasi-stationary solutions for the populations in 2^3S and 2^3P states satisfy:

$$\left.\frac{db_j(\vec{r})}{dt}\right|_{\mathrm{OP}} + \left.\frac{db_j(\vec{r})}{dt}\right|_{\mathrm{r}} = 0 \quad \text{for j=1,...,18} \tag{2.49}$$

$$\left.\frac{da_i(\vec{r})}{dt}\right|_{\mathrm{OP}} + \left.\frac{da_i(\vec{r})}{dt}\right|_{\mathrm{ME}} + \left.\frac{da_i(\vec{r})}{dt}\right|_{\mathrm{r}} = 0 \quad \text{for i=1,...,6} \tag{2.50}$$

where the spatial dependence has been made explicit. These quasi-stationary solutions correspond to local steady-state populations that are parametrised in terms of the slowly varying polarisation M, which can occasionally be made explicit using the convenient notation $a_i(\vec{r}, M)$ and $b_j(\vec{r}, M)$ for 2^3S and 2^3P states, respectively, in the following. The generic full rate equation for the slow variation of the uniform ^{3}He nuclear polarisation then reads:

$$\begin{aligned}\frac{dM}{dt} &= \left.\frac{dM}{dt}\right|_{\mathrm{ME}} + \left.\frac{dM}{dt}\right|_{\mathrm{r}} \\ &= \gamma_{\mathrm{e}} \int_{\mathrm{cell}} \frac{d^3\vec{r}}{V_{\mathrm{c}}} \frac{n_{\mathrm{m}}(\vec{r})}{N_{\mathrm{g}}} \left(M^{\mathrm{S}}(\vec{r}, M) - M\right) - \Gamma_{\mathrm{g}}\, M,\end{aligned} \tag{2.51}$$

where (equation (2.25)):

$$M^{\mathrm{S}}(\vec{r}, M) = \sum_{k=1}^{6} L_k a_k(\vec{r}, M).$$

We note here that the combination of equations (2.28) and (2.50) yields:

$$\left.\frac{dM}{dt}\right|_{\mathrm{ME}} = \int_{\mathrm{cell}} \frac{d^3\vec{r}}{V_{\mathrm{c}}} \frac{n_{\mathrm{m}}(\vec{r})}{N_{\mathrm{g}}} 2 \sum_i m_{\mathrm{F}}(i) \left(\left.\frac{da_i(\vec{r})}{dt}\right|_{\mathrm{OP}} + \left.\frac{da_i(\vec{r})}{dt}\right|_{\mathrm{r}} \right). \tag{2.52}$$

In the framework of the improved 2-class OP model the generic equations (2.49) and (2.50) for the populations in 2^3S and 2^3P states are replaced by a larger set of full rate equations given in appendix B The appropriate full rate equation for the ground state polarisation involves a weighted average of the contributions of the two sets of steady-state local 2^3S populations $a_i^*(\vec{r}, M)$ and $a_i'(\vec{r}, M)$. It may be written, using the appropriately modified definition of the local nuclear polarisation of the metastable

atoms $M^{\mathrm{S}}(\vec{r})$ (see appendix B), as[9]:

$$\begin{aligned}\frac{dM}{dt} &= \left.\frac{dM}{dt}\right|_{\mathrm{e}} + \left.\frac{dM}{dt}\right|_{\mathrm{r}} \\ &= \gamma_{\mathrm{e}} \int_{\mathrm{cell}} \frac{d^3\vec{r}}{V_{\mathrm{c}}} \frac{n_{\mathrm{m}}(\vec{r})}{N_{\mathrm{g}}} (M^{\mathrm{S}}(\vec{r}, M) - M) - \Gamma_{\mathrm{g}}\, M,\end{aligned} \tag{2.53}$$

where:

$$M^{\mathrm{S}}(\vec{r}, M) = \sum_{k=1}^{6} L_k \frac{n^*_{\mathrm{m}}(\vec{r}) a^*_k(\vec{r}, M) + n'_{\mathrm{m}}(\vec{r}) a'_k(\vec{r}, M)}{n_{\mathrm{m}}(\vec{r})} \tag{2.54}$$

is the appropriate expression of the local 2^3S nuclear angular momentum.

2.7.3 Numerical implementation

The improved OP model is numerically implemented in a series of dedicated computer Fortran programs developed at LKB by Pierre-Jean Nacher that are designed to compute for instance: 1/ at fixed M, the 2^3S and 2^3P populations in the two velocity classes and all relevant physical quantities as a function of the incident laser power; 2/ at fixed incident laser power, the 2^3S and 2^3P populations in the two velocity classes and all relevant physical quantities as a function of the ground state polarisation. As discussed in section 2.5.3, in the improved OP model the key local quantities such as the light intensity $I_{\mathrm{cell}}(r)$ or the 2^3S atom number densities n^*_{m} and n'_{m} depend only on one position variable, the radial coordinate r (distance to the optical axis). Computations are performed as a function of this radial position, for a finite number of discrete r values and spatial averages (required to compute, e.g., the time derivative of M or the transmitted probe light power along the tilted beam paths) and involve discrete sums over these radial positions.

The structure of the numerical implementation heavily relies on the method described in section 2.7.1 that was successfully used for the earlier work [Nac85]:

- In a first step, the b^*_j and b'_j populations are eliminated from the full rate equations for the 2^3S populations using the full rate equations for the 2^3P populations. This is possible because in the model all atoms that are in 2^3P have been radiatively transferred from 2^3S and, in steady state conditions, the matrices that describe these radiative transfers are real, symmetric, and can easily be inverted (because velocity-changing collisions have been neglected in the 2^3P state, as explained in section 2.5.2). The b^*_j and b'_j populations are thus obtained as functions of the a^*_i, a'_i, and I_{cell} variables.

[9]Note that the ME term (e) in the framework of the improved 2-class OP model describes the contribution of local exchanges with ground state atoms through collisions that strongly modify the velocities of colliding atoms in addition to modifying the internal variables.

- In a second step, the uniform value of the light intensity inside the cell $I_{\text{cell}}(r)$ is computed in a self-consistent iterative way, taking into account the absorption by the gas (with uniform absorption rate k_a, see appendix C for more details). This procedure is needed since the absorption rate depends on the 2^3S populations and, at fixed polarisation M, the 2^3S populations depend on $I_{\text{cell}}(r)$ due to the contribution of OP rate equations (B.15) & (B.16) and (B.37) & (B.38) given in appendix B (or see the generic equations (2.19) and (2.20)) to the full rate equations (B.35) & (B.36) and (B.13) & (B.14) (or see the generic ones (2.49) and (2.50)). For each radial position r, the iteration starts from twice the incident pump light intensity $I_{\text{inc}}(r)$, computed from input parameters W_{inc} (incident laser power) and waist $2a$ (specifying the Gaussian transverse profile of the pump beam intensity) as described in section 2.7.4. Then the corresponding steady-state 2^3S populations $a_i^*(r, M)$ and $a_i'(r, M)$ are computed, the absorption rate k_a is deduced and used to compute $I_{\text{cell}}(r)$ using equation (C.9) of appendix C. A new set of steady-state 2^3S populations a_i^* and a_i' is computed, etc. The iteration rapidly converges to a consistent set of I_{cell}, a_i^*, and a_i' values for each discrete radial position r.

- In a third step, all requested physical quantities are computed from the steady-state 2^3S populations $a_i^*(r, M)$ and $a_i'(r, M)$ and corresponding local intensity $I_{\text{cell}}(r)$: the 2^3P populations $b_j^*(r, M)$ and $b_j'(r, M)$, total absorbed power W_{abs} (from the local absorbed intensity $I_{\text{abs}}(r)$, easily obtained from the sums of b_j^* and b_j' populations, thanks to the energy conservation rule), the local 2^3S nuclear polarisation $M^{\text{S}}(r, M)$, the time derivative $\dot{M}(r, M)$, the integrated probe transmittances for various light paths, frequencies, and polarisations, etc.

Note: Here and from now on the conventional notation $\dot{M}$ is used as substitute for the explicit time derivative of polarisation: $\dot{M} = dM/dt$, for compactness in the text and clarity in the mathematical formulas.

The computations are performed for MEOP conditions that are specified by the collection of data and parameters provided as input values as well as some fixed parameters included in the Fortran code. They are all listed in the next section.

2.7.4 Input data and input parameters

The quantitative input values needed for the numerical computation of the OP kinetics can be described as follows:

1/ A set of input data files provides transition matrix elements T_{ij} and transition frequencies ϵ_{ij}/h for the allowed $\text{A}_i \rightarrow \text{B}_j$ components of the $2^3\text{S}-2^3\text{P}$ transition, including all light polarisations (σ^+, σ^- and π) and He isotopes (^{3}He and ^{4}He) for the selected field strength B.

2/ The most frequently modified MEOP conditions are provided through an input

parameter file that includes the following quantities.

- for plasma conditions: the ^{3}He pressure p_3, the proportion of metastable atoms present in the plasma (defined as $n_{\rm m}^{\rm S}/N_{\rm g}$ where $n_{\rm m}^{\rm S}$ is the average 2^3S number density along the V-shaped probe beam paths, see section 3.2 and below), and the exponent α that characterise the transverse profile of 2^3S atom density.

The ground state number density $N_{\rm g}$ is inferred from the input pressure p_3 and the fixed gas temperature T (see below) using the ideal gas law. The local 2^3S number density $n_{\rm m}(r)$ is inferred, for all radial positions r inside the cell, from α and $n_{\rm m}^{\rm S}$ using the known analytical variation of $n_{\rm m}$ with radial coordinate r (see section 6.1.2) as well as the geometry of the probe paths (see below).

- for relaxation processes: the relaxation time $\tau_{\rm P} = 1/\gamma_r^{\rm P}$ in the 2^3P state, the elastic velocity-changing collision time $\tau_{\rm c} = 1/\gamma_c$ in the 2^3S state, the polarisation decay rate Γ_D in the ground state (in the absence of OP) and the fraction $\varkappa_r$ of this decay rate that is induced by 2^3S state relaxation through ME.

The intrinsic ground state relaxation rate Γ_g in the absence of OP is inferred as $\Gamma_g = (1-\varkappa_r)\Gamma_D$ and the intrinsic 2^3S relaxation rate $\gamma_r^{\rm S}$ is inferred from $\varkappa_r\Gamma_D$ using equations (2.68) and (2.71) with $f_\Gamma = 1$.

- for light excitation: the incident power $W_{\rm inc}$, the tuning frequency $\omega_{\rm L}$, the fraction $\varkappa_\pi$ of incident power with light polarisation π, the σ^+-polarisation index $\varkappa_+$ for the incident power $(1-\varkappa_\pi)W_{\rm inc}$ with circular light polarisation, the laser spectral width L, the beam waist $2a$ (see chapter 3.2).

The fraction $\varkappa_\pi$ is always set to 0 for the pump beam (it propagates parallel to the field axis in the experiments). It is only used for quantitative evaluation of potential artefacts due to residual π-polarisation light due, e.g. to misalignment of B with the optical axis. The index $\varkappa_+$ is ± 1 for pure circular $\sigma^\pm$ light polarisation. The program combines power $W_{\rm inc}$ and waist $2a$ to compute the incident light intensity profile $I_{\rm inc}(r)$ needed as input for self-consistent computation of the distribution of local light intensity $I_{\rm cell}(r)$ inside the cell when there is absorption by the He gas (see section 2.5.3).

- for the OP model: the frequency width Δ of the strongly pumped velocity-class.

- for cell geometry: the internal diameter $2R_{\rm cell}$ and internal length $L_{\rm cell}$

3/ The other relevant MEOP conditions or geometrical dimensions are specified through fixed parameters included in the Fortran source code. This includes, for instance:

- the (fixed) gas temperature T. It is set equal to 300K since 1/ it has a moderate impact on OP kinetics and 2/ the rf power dissipated in the gas is limited (typically 1 W, ranging from 5 times less to 3 times more when systematic investigations of plasma conditions are performed).[10] T actually determines the (fixed) Doppler

[10] If large changes of gas temperature occurred in the cell T would actually impact the gas pressure, since the ^{3}He number density is fixed in the sealed cell. T implicitly determines also indirectly involved

width D.

- the geometrical parameters that describe the V-shaped probe beam paths (see section 3.2) that in our experiments consist of 2 coplanar straight paths, symmetrically tilted with respect to the optical axis, and included in a vertical ($0xz$) plane: the (potential) vertical offset $dx_{\rm s}$ of the symmetry axis of the V-shaped paths, the $x_{\rm s}$ and $y_{\rm s}$ parameters that specify the transverse coordinates ($x_{\rm s} \pm dx_{\rm s},\ y_{\rm s}$, cf. figure 3.7) of the point where the incident $\sigma^{\pm}$ probe beam component hits the cell entrance window; the distance $z_{\rm gap}$ along the optical axis ($0z$) between cell exit window and the back-reflecting mirror (see figure 3.7).

- the radiative decay rate γ of the excited 2^3P state.

4/ Finally, the executable file prompts for any missing variables such as M, for instance, when OP kinetics are computed for various values of $W_{\rm inc}$.

With these input parameters, the dedicated programs compute and return the values, e.g., of the maximum value of the 2^3S density on the cell axis ($n^0_{\rm m}$), dimensionless parameters Σ^* and Σ' for the pumping rates in strongly and weakly pump beams (respectively), the 2^3S relaxation rate $\gamma^{\rm S}_r$, etc. The programs provide a variety of complementary output data files with, e.g., the computed transmittances for the probe beams for all combinations of tuning (C_8 and C_9 lines) and polarisation (σ^+, σ^-, and π).

The input parameters can be arbitrarily set. The computations reported in this manuscript have mostly been performed with either realistic or measured values. Experimental values are available for p_3 (gas filling pressure), $n^{\rm S}_{\rm m}$ (from transmitted probe powers, see section 4.4), α (from 1083 nm absorption maps, see section 6.1.2), $\tau_{\rm P}$ (collisional mixing time inferred from photon efficiencies, see section 6.3.2), Γ_D, $W_{\rm inc}$, $\omega_{\rm L}$, L, $2a$, and of course B. As already mentioned, the model-dependent parameter Δ is set equal to L. The (limited) impact of this choice is discussed in section 2.8. The used input parameters are systematically specified in figure captions when computed results are plotted.

2.8 MEOP dynamics

In this section, the physical discussions and computations of relevant physical quantities make use of the MEOP rate equations. For clarity we stick here to the generic equations described in section 2.4. They are perfectly valid in the absence of light excitation and so are the results obtained when only ME is involved (spin temperature distribution, section 2.8.1), or when ME and relaxation only are involved (polarisation decay, section 2.8.2). In the presence of OP the main conclusions driven in section 2.8.3 hold of course within the framework of the improved OP model and the corresponding

quantities, such as the collisional cross sections.

valid mathematical expressions are provided in appendix B. The reported numerical results are correct since all computations have been performed using the improved OP model.

2.8.1 ME-driven spin temperature distribution

In the absence of OP and relaxation, equation (2.50) reduces to:

$$\left.\frac{da_i}{dt}\right|_{\mathrm{ME}} = 0 \tag{2.55}$$

At all magnetic field strengths a unique distribution satisfies equation (2.55). It is given by the following formulas, with the Zeeman sublevel labelling valid up to B=0.162 T:

$$a_1^{\mathrm{ST}} = \frac{(1-M)^3}{2M^2+6} \tag{2.56a}$$

$$a_2^{\mathrm{ST}} = a_5^{\mathrm{ST}} = \frac{(1-M)^2(1+M)}{2M^2+6} \tag{2.56b}$$

$$a_3^{\mathrm{ST}} = a_6^{\mathrm{ST}} = \frac{(1-M)(1+M)^2}{2M^2+6} \tag{2.56c}$$

$$a_4^{\mathrm{ST}} = \frac{(1+M)^3}{2M^2+6}. \tag{2.56d}$$

In isotopic mixtures, a unique distribution is similarly established for ^{4}He atoms by ME with ^{3}He atoms [Cou02]:

$$y_1^{\mathrm{ST}} = \frac{(1-M)^2}{M^2+3},\ y_2^{\mathrm{ST}} = \frac{1-M^2}{M^2+3},\ \text{ and }\ y_3^{\mathrm{ST}} = \frac{(1+M)^2}{M^2+3} \quad \text{for } m_J = -1,\ 0,\ \text{and } 1. \tag{2.57}$$

For the 2^3S sublevels of ^{3}He atoms, the distribution has the following remarkable property:

$$\frac{a_2^{\mathrm{ST}}}{a_1^{\mathrm{ST}}} = \frac{a_3^{\mathrm{ST}}}{a_2^{\mathrm{ST}}} = \frac{a_4^{\mathrm{ST}}}{a_3^{\mathrm{ST}}} = \frac{a_6^{\mathrm{ST}}}{a_5^{\mathrm{ST}}} = \mathrm{e}^{1/T} = \mathrm{e}^{\beta} = \frac{1+M}{1-M} \tag{2.58}$$

The ratios of populations of two adjacent 2^3S sublevels exhibit the same behaviour for ^{4}He in isotopic mixtures. The populations a_i^{ST} and y_i^{ST} of Zeeman sublevels are thus distributed according to [Cou02]:

$$a_i^{\mathrm{ST}} = e^{\beta m_{\mathrm{F}}(i)}/(e^{3\beta/2} + 2e^{\beta/2} + 2e^{-\beta/2} + e^{-3\beta/2}) \quad \text{for } ^3\text{He}, \tag{2.59}$$

$$y_i^{\mathrm{ST}} = e^{\beta m_{\mathrm{S}}(i)}/(e^{\beta} + 1 + e^{-\beta}) \quad \text{for } ^4\text{He}. \tag{2.60}$$

This corresponds to a Boltzmann distribution, associated to the hyperfine angular momentum projection m_{F} for ^{3}He (m_{S} for ^{4}He respectively), characterised by a spin temperature[11] $T = 1/\beta$ that is solely determined by the ground state nuclear polarisation M. The spin temperature T varies from 0 at $M = \pm 1$ ($\beta = \mp\infty$) to infinity at $M = 0$ ($\beta = 0$) where $a_i^{\mathrm{ST}} = 1/6$, with $T = \beta = 1$ for $M = 0.46$.

The method used to infer the ground state polarisation from measurements of $2^3\mathrm{S}-2^3\mathrm{P}$ absorption rates relies on the specificity of this purely ME-driven distribution [Cou02, Tal11]: as explained in chapter 4, measurements of transmitted powers for two different probe light polarisations can be combined so as to eliminate the external parameter $n_{\mathrm{m}}^{\mathrm{S}}$ and to infer M from the resulting combination of a_i^{ST} populations, provided that other processes do not significantly skew the 2^3S populations.

In figure 2.6, the evolution of the 2^3S populations computed in the spin temperature limit (only ME, no OP and no relaxation) is represented as a function of nuclear polarisation M. As expected, all a_i^{ST} are equal to 1/6 at $M = 0$. The sublevel populations with identical m_{F} (one for each hyperfine level F) remain equal at all M values (equations (2.56b) and (2.56c)).

With respect to the ground state, the spin temperature distribution yields:

$$\left.\frac{dM}{dt}\right|_{\mathrm{ME}} = 0. \tag{2.61}$$

This directly results from equation (2.55) and conservation of angular momentum (equation (2.28)). Alternatively, one can analytically check that the spin temperature populations (equations (2.56a) to (2.56d)) satisfy $\sum_{i=1}^{6} L_i a_i^{\mathrm{ST}} = M$. Metastability exchange leads to equal nuclear polarisations in the metastable and in the ground states

$$M^{\mathrm{S}} = M \quad \text{at spin temperature.} \tag{2.62}$$

2.8.2 Dynamics of polarisation decay (no OP)

In the absence of OP, the ^{3}He nuclear polarisation M irreversibly decays to zero (at room temperature, the equilibrium value of M in B=30 mT is on the order of 10^{-7}). In MEOP experiments all major sources of relaxation are carefully avoided. However, in the rf plasma the relaxation in the 2^3S state significantly contributes to the decay of ground state polarisation through ME collisions. When the $2^3\mathrm{S}-2^3\mathrm{P}$ optical transition is not excited, the steady-state 2^3S populations $a_i^{\text{no OP}}$ satisfy:

$$\left.\frac{da_i^{\text{no OP}}}{dt}\right|_{\mathrm{r}} + \left.\frac{da_i^{\text{no OP}}}{dt}\right|_{\mathrm{ME}} = 0, \tag{2.63}$$

[11] The concept of a spin temperature distribution was first introduced by [And59] who investigated spin-exchange collisions in alkalines.

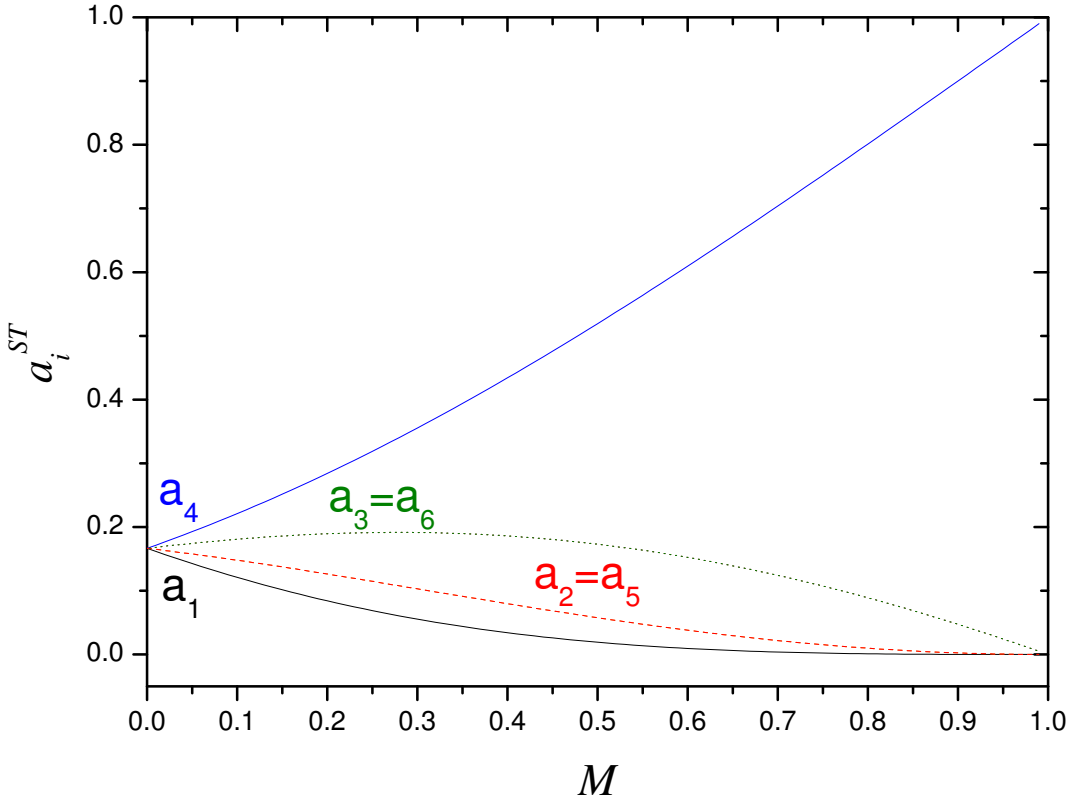

Figure 2.6: Computed variation of ^{3}He populations a_i^{ST} in 2^3S as a function of nuclear polarisation M in the spin temperature limit (ME, no OP, no relaxation).

and actually depart from the ST distribution:

$$a_i^{\text{no OP}} = a_i^{\text{ST}} + \delta a_i^{\text{r}} \tag{2.64}$$

The population difference δa_i^{r} (the superscript 'r' stands for relaxation) from the ST is *uniform* since: 1/ the ME rate equations contain no position-dependent source term, and 2/ any potential inhomogeneity (e.g., resulting from OP after the pump beam is stopped) would be quickly damped by atomic diffusion (millisecond time scale, see section 2.6). It can be analytically computed since the steady-state populations $a_i^{\text{no OP}}$ are the solutions of the following linear set of equations, obtained by combination of equations (2.21) and (2.36) with (2.63):

$$(\gamma_e + \gamma_r^{\text{S}})a_{\text{i}} - \gamma_e \sum_{k=1}^{6} (E_{ik}^3 + MF_{ik}^3)a_k = \frac{\gamma_r^{\text{S}}}{6}. \tag{2.65}$$

Results will be published elsewhere [Nac12]. The population difference δa_i^{r} can also be numerically computed by running the program based on the improved OP model for $W_{\text{inc}} \to 0$. The results are displayed in figure 2.7 (left graph). The departure from ST distribution induced by 2^3S relaxation is found to be very small for realistic input parameters, as expected since $\gamma_r^{\text{S}}/\gamma_e \ll 1$ (cf. section 2.6).

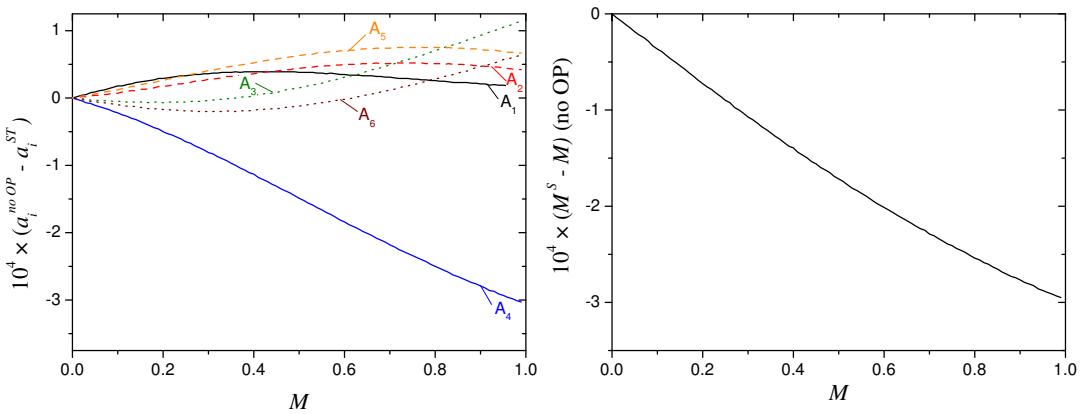

Figure 2.7: Left: Computed differences of populations of all six 2^3S sublevels A_i in absence of OP $a_i^{\text{no OP}}$ with respect to ST distribution as a function of M. Right: Corresponding difference between nuclear polarisation in 2^3S (M^{S}) and ground state (M) as a function of M. Parameters used in computations: $p_3 = 1.19$ mbar, $n_{\text{m}}(0) = 1.6\times10^{16}$ atoms/m^3, $\alpha = 0$, $\Gamma_{\text{D}} = (550\text{s})^{-1}$, $1/\gamma_{\text{r}}^{\text{P}} = 2.57\times10^{-7}$ s, $W_{\text{inc}} = 1\times10^{-20}$ W.

The $a_i^{\text{no OP}}$ values can thus be safely replaced by the a_i^{ST} ones for, e.g., the computation of absolute 2^3S number densities from the probe transmittances measured during polarisation decay (see section 4.2). The small relaxation-induced skewing of

the 2^3S populations has also a negligible impact on the ratios (C_8 probe) or combinations (C_9 probe) of the 2^3S populations used for experimental measurements of ^{3}He nuclear polarisation. Using the ST formulas thus yields $M^{(r)}$ values that negligibly under-estimate the ^{3}He nuclear polarisation M, as illustrated for C_8 probe light in figure 2.8.

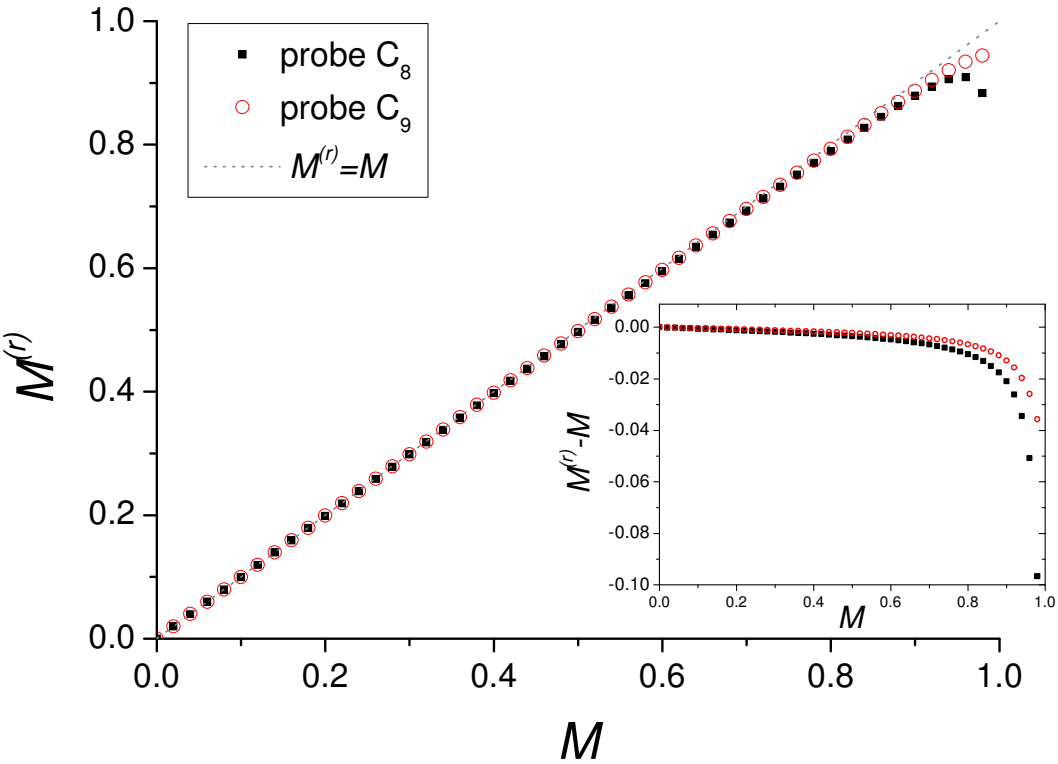

Figure 2.8: Quantitative assessment of the under-estimation of ground state polarisation obtained when ST formulas are used, for probe absorption measurements performed during decay (C_8 and C_9 lines, see legend). Polarisation values $M^{(r)}$ (main plot) and differences $M^{(r)} - M$ (inset) are computed from the numerical data displayed in figure 2.7, using eq. (2.58). For instance, $M^{(r)} = (1 - R_8)/(1 + R_8)$ with $R_8 = a_5^{\text{no OP}}/a_6^{\text{no OP}}$ for C_8 probe (see section 4.2.1 and ref. [Tal11])

The small relaxation-induced skewing of the 2^3S populations also contributes to ^{3}He polarisation decay through (2.24), and using equations (2.64) and (2.62) this contribution can be written as:

$$\left.\frac{dM}{dt}\right|_{\text{ME}}^{\text{no OP}} = -\overline{\Gamma_{\text{e}}}\left(\sum_{i=1}^{6} L_i a_i^{\text{no OP}} - M\right) = -\overline{\Gamma_{\text{e}}}\sum_{i=1}^{6} L_i \delta a_i^{\text{r}} \tag{2.66}$$

where $\overline{\Gamma_{\text{e}}}$ is the average ME rate for the atoms in the ground state given by equation

(2.33). This driving term involves the difference $M^{\mathrm{S}} - M = \sum_{i=1}^{6} L_i \delta a_i^{\mathrm{r}}$ displayed in figure 2.7 (right graph). It vanishes at $M = 0$ (where the nuclear polarisation in the 2^3S state, M^{S} is also equal to 0) and can be written at finite M as :

$$\left.\frac{dM}{dt}\right|_{\mathrm{ME}}^{\text{no OP}} = -f_\Gamma \Gamma^0_{\mathrm{ME}} M, \tag{2.67}$$

where Γ^0_{ME} is the (ME-induced) additional relaxation rate at small polarisations $M \ll 1$ [Dup73]:

$$\Gamma^0_{\mathrm{ME}} = \frac{11}{3} \int_{\mathrm{cell}} \frac{d^3\vec{r}}{V_{\mathrm{c}}} \frac{n_{\mathrm{m}}(\vec{r})}{N_{\mathrm{g}}} \gamma_{\mathrm{r}}^{\mathrm{S}} = \frac{11}{3} \frac{\Gamma_{\mathrm{e}}}{\gamma_e} \gamma_{\mathrm{r}}^{\mathrm{S}}, \tag{2.68}$$

and the function f_Γ describes the small decrease of the ME-induced contribution to polarisation decay at higher M. The analytical expression of f_Γ can be obtained from the comparison of equations (2.66) and (2.67) that gives:

$$\sum_{i=1}^{6} L_i \delta a_i^{\mathrm{r}} = f_\Gamma \frac{11}{3} \frac{\gamma_r^{\mathrm{S}}}{\gamma_e} M, \tag{2.69}$$

which, to first order in $\gamma_r^{\mathrm{S}}/\gamma_e$, yields:

$$f_\Gamma = \frac{1 + \frac{M^2}{11}}{1 + \frac{M^2}{3}}. \tag{2.70}$$

This can be compared to the numerical results, reported in figure 9 of reference [Bat11], obtained using the OP model for MEOP kinetics (again, with input parameter $W_{\mathrm{inc}} \to 0$). Figure 2.9 shows that both results nicely agree (to better than 10^{-4}).

Finally, using the full rate equation (2.51), the evolution of ground state nuclear polarisation is given during decay by:

$$\left.\frac{dM}{dt}\right|^{\text{no OP}} = -\Gamma_g M + \left.\frac{dM}{dt}\right|_{\mathrm{ME}}^{\text{no OP}} = -(\Gamma_g + f_\Gamma \Gamma^0_{\mathrm{ME}})\ M, \tag{2.71}$$

where $\Gamma_{\mathrm{D}} = \Gamma_g + f_\Gamma \Gamma^0_{\mathrm{ME}}$ is the decay rate of polarisation measured in the absence of OP. Polarisation decays have been systematically monitored in our experiments to characterise plasma conditions (see section 6.1.1) and equation (2.71) will be used for our analysis of results (section 5.7.1).

2.8.3 OP-driven MEOP dynamics

The pumping light competes with ME and 2^3S relaxation. It promotes some He atoms to the 2^3P state and redistributes 2^3S atoms between Zeeman sublevels. The a_i populations are then driven significantly away from spin temperature distribution and

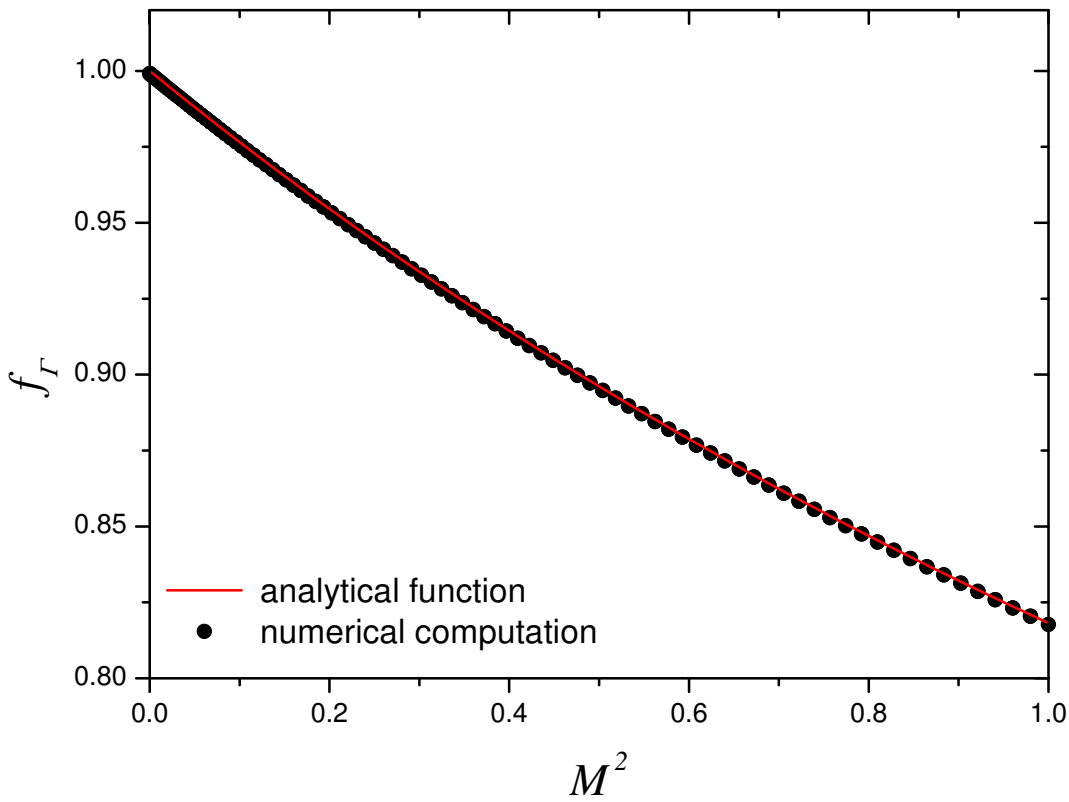

Figure 2.9: Analytic and numerical results obtained with the improved OP model (same data as in figure 9 of [Bat11]) for the decay rate factor f_Γ, plotted as a function of M^2. f_Γ characterises the deviation of ME-induced polarisation decay from the small M limit [Dup73] (see text).

become *position-dependent*:

$$a_i^{\mathrm{OP}}(\vec{r}, M) = a_i^{\mathrm{ST}}(M) + \delta a_i^{\mathrm{OP}}(\vec{r}, M). \tag{2.72}$$

This makes the absorption-based measurements of polarisation a lot less straightforward. We have explicated here the spatial variation of the M-dependent steady-state generic populations a_i that must be replaced by $a_i^*(\vec{r}, M)$ and $a_i'(\vec{r}, M)$ in the improved OP model.

Direct comparison of two independent 2^3S-2^3P absorption rates [Cou02] does no longer yield M and one must quantitatively determine the impact of the OP-induced skewing of the populations (see sections 4.3 and 5.3). Figures 2.10 and 2.11

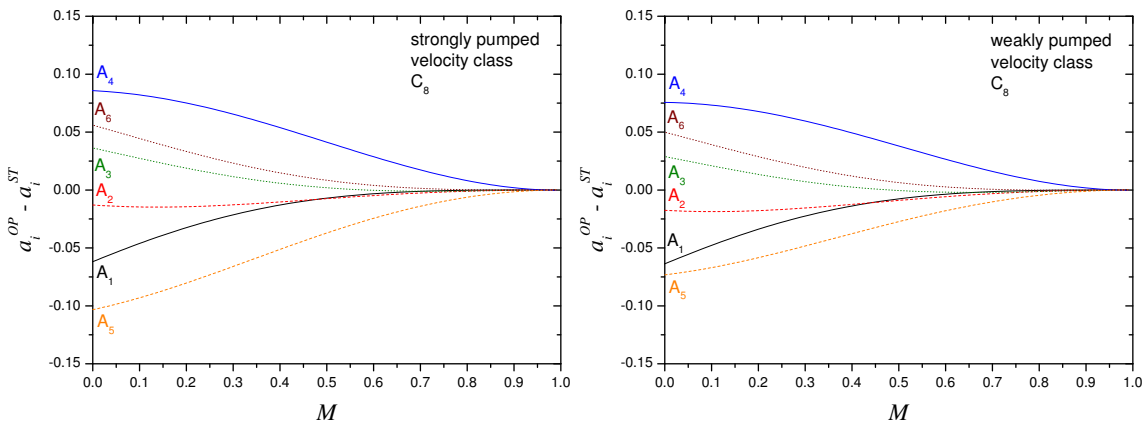

Figure 2.10: Computed OP-driven differences of populations of the 2^3S sublevels A_i with respect to ST distribution under influence of OP on the C_8 transition with: $W_{\mathrm{inc}} = 1$ W, σ^+ light ($A_5 \rightarrow B_{17}$), pumping beam diameter: $2a = 1.6$ cm, width of strongly pumped velocity class $\Delta = L = 1.02$ GHz, $\alpha = 0$. All other parameters used for computations: see caption of figure 2.7. The displayed data correspond to the values obtained for $r = 0$ (i.e., along the optical axis). Left: Strongly pumped velocity class, right: weakly pumped velocity class.

show examples of computed populations differences $a_i^{\mathrm{OP}} - a_i^{\mathrm{ST}}$ in the strongly and weakly pumped velocity classes for OP on C_8 and C_9 lines, respectively. The sublevels addressed by the pumping are the most depleted ones, as expected. Furthermore, populations differences with respect to ST are much higher during OP than during decay (note the difference in vertical scales between figures 2.10or 2.11 and 2.7).

The significant OP-induced changes in 2^3S distribution of populations have a large impact on the experimental measurements of ^{3}He nuclear polarisation. Using the ST formulas yields *apparent* values of M, noted M^a, that *substantially over-estimate* the ^{3}He nuclear polarisation. The difference between apparent (M^a) and actual (M) polarisation values is maximal at $M = 0$ and decreases towards large $|M|$. This is

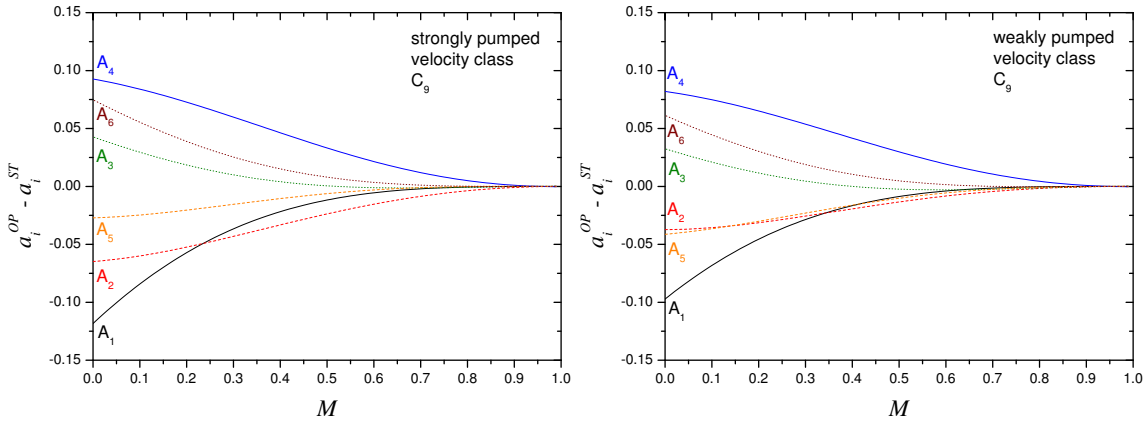

Figure 2.11: Computed OP-driven differences of populations of the 2^3S sublevels A_i with respect to ST distribution under influence of OP on the C_9 transition with $W_{\text{inc}} = 1$ W, σ^+ light ($A_1 \to B_{18}$ and $A_2 \to B_{17}$), pumping beam diameter: $2a = 1.6$ cm. All other parameters used for computations: see caption of figure 2.7. The displayed data correspond to the values obtained for $r = 0$ (i.e., along the optical axis). Left: Strongly pumped velocity class, right: weakly pumped velocity class.

illustrated for C_8 σ^+ pumping in figure 2.12 where M^a values at fixed M are much larger for a probe tuned to the C_8 line that addresses the pumped Zeeman sublevels. For comparison, the dashed line shows, for a C_8 probe, the values that would be obtained if the 2^3P populations were ignored. This shows that stimulated emission plays a significant role in probe absorption for usual MEOP conditions.

The skewing of the 2^3S populations, hence the discrepancy $(M^a - M)$, depends on the competition between OP and ME, therefore it decreases when gas pressure rises because γ_e scales with p_3 (equation (2.45)). The discrepancy $(M^a - M)$ also depends on the pressure-dependent collisional mixing rate in 2^3P state (equation (2.46)), as will be shown in appendix G.

Through ME, the OP-induced skewing of the He 2^3S distribution also provides the driving term for polarisation build-up. Figure 2.13 displays the computed difference between 2^3S and ground state nuclear polarisations $(M^{\text{S}} - M)$ for C_8 and C_9 pumping at the same incident light power. This difference varies from 0.11 at $M = 0$ to 0 at $M = 1$ for C_8 pumping and is about twice as large for C_9 pumping. The difference between the 2^3S nuclear polarisations in the strongly and weakly pumped velocity classes is also much larger for C_9 pumping. For C_8, it might appear astonishing that $M^{\text{S}} - M$ is larger for the weakly pumped class than for the strongly pumped one. This is due to the fact that in the 2^3S, $F = 1/2$ state electronic and nuclear angular momenta are anti-parallel (see equations (2.23) and (2.30)). At $B = 0$, for instance, for sublevel A_5, $m_{\text{F}}(5) = -1/2$ whereas $L_5 = +0.3$ and for sublevel A_6, $m_{\text{F}}(6) =$

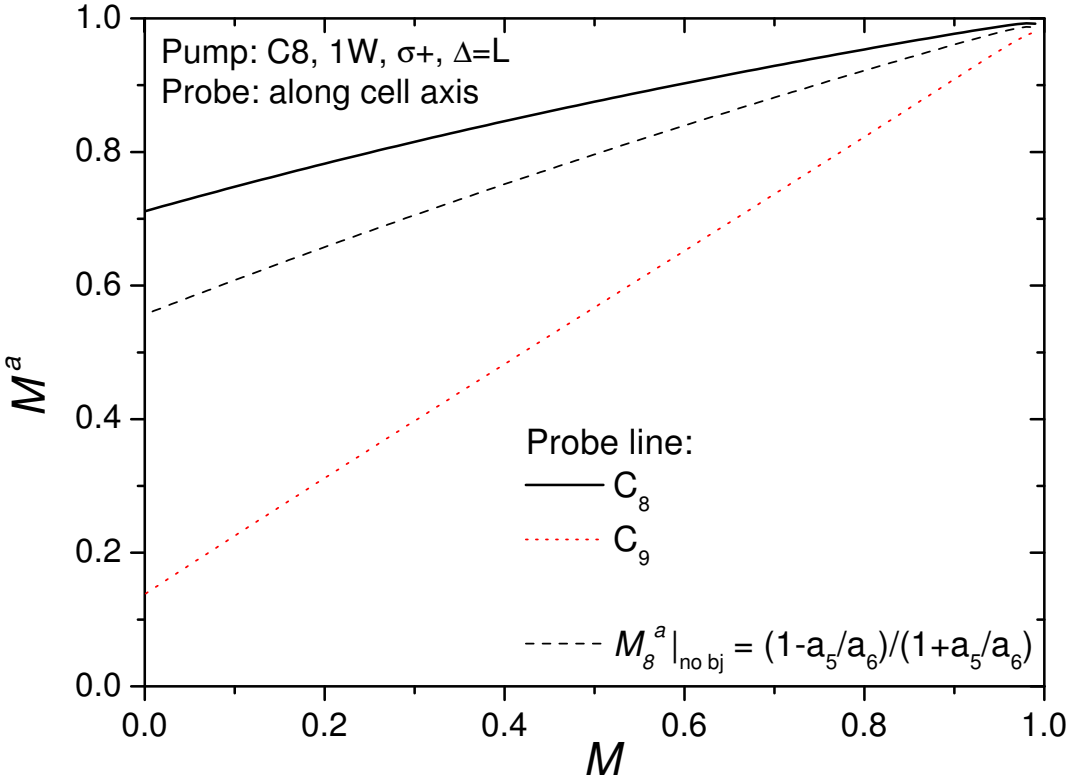

Figure 2.12: Solid line: Computed apparent polarisation M^a for the same realistic MEOP conditions as in figures 2.10, for a C_8 probe beam aligned with the optical axis. For comparison, the dashed line shows the values that would be obtained if the 2^3P populations were ignored (see text).

$+1/2$ whereas $L_6 = -0.3$, see appendix A. M^{S} arises from a complex combination of different processes (e.g., redistribution in 2^3P and re-emission into 2^3S, coupling of nuclear to electronic angular momenta) that depends among other parameters on the relaxation rate γ_r^{P} in the 2^3P state. The experimental value at $p_3 = 1.19$ mbar was used for the computations of figure 2.13 ($1/\gamma_r^{\mathrm{P}} = 2.57 \times 10^{-7}$ s). In the limiting case of no collisional mixing ('Kastler' OP regime (see section 2.9): $\gamma_r^{\mathrm{P}} \to \infty$) the difference $M^{\mathrm{S}} - M$ is actually larger for the strongly pumped velocity class (as observed for C_9 pumping for which, in contrast, nuclear and electronic angular momenta are parallel in all 2^3S, $F = 3/2$ hyperfine sublevels).

2.8.4 Angular momentum budget

Polarisation build-up results from the global balance (i.e., including spatial averaging) between the angular momentum locally deposited by the photons and that lost by

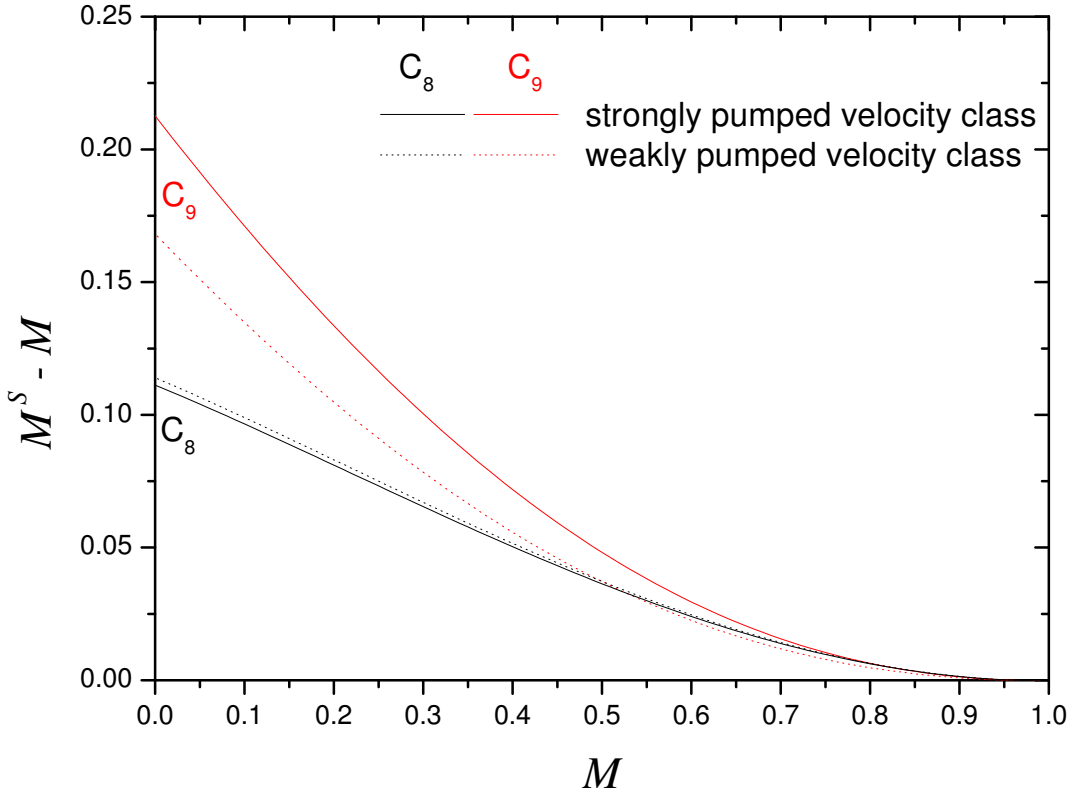

Figure 2.13: Computed difference between 2^3S polarisation M^S and ground state polarisation M under influence of OP on C_8 (black) and C_9 (red) transitions with $W_{\text{inc}} = 1$ W, σ^+ light, for the strongly (straight lines) and weakly pumped (dotted lines) velocity classes. All other parameters used for computations: see captions of figures 2.7 and 2.10.

relaxation. Using the generic rate equations of section 2.7.2 and equation (2.52), the global budget can be written as:

$$\frac{dM}{dt} = \int_{\text{cell}} \frac{d^3\vec{r}}{V_{\text{c}}} \frac{n_{\text{m}}(\vec{r})}{N_{\text{g}}} \, 2 \sum_i m_{\text{F}}(i) \left. \frac{da_i^{\text{OP}}(\vec{r})}{dt} \right|_{\text{OP}} - \int_{\text{cell}} \frac{d^3\vec{r}}{V_{\text{c}}} \frac{n_{\text{m}}(\vec{r})}{N_{\text{g}}} 2\gamma_r^{\text{S}} \sum_i m_{\text{F}}(i) \, a_i^{\text{OP}}(\vec{r}) + \left. \frac{dM}{dt} \right|_{\text{r}} . \tag{2.73}$$

The corresponding equation appropriate for the improved OP model is given in appendix B. The left hand side of equation (2.73) is the rate of increase of the net angular momentum accumulated in the ground state written in terms of ^{3}He atom nuclear polarisation. The first term in the right hand side is duly proportional to the rate of increase of the global projection of total angular momentum in the 2^3S state

induced by OP and the second one to the loss of total angular momentum in the 2^3S state due to relaxation. The last term corresponds to the loss of nuclear angular momentum in the ground state due to relaxation.

The computations made with the improved OP model yield:

$$\int_{\text{cell}} \frac{d^3\vec{r}}{V_\text{c}} \frac{n_\text{m}(\vec{r})}{N_\text{g}} 2\gamma_r^\text{S} \sum_i m_\text{F}(i)\ a_i^\text{OP}(\vec{r}) = f^0 + f'_\Gamma \Gamma^0_\text{ME} M \tag{2.74}$$

where the contribution of 2^3S relaxation to ground state polarisation loss induced by ME (left hand side of equation (2.74)) takes the value f^0 at $M = 0$ and where, for the remaining of its value at finite M, we have (for convenience and by analogy with equation (2.67)) introduced a coefficient f'_Γ that remains finite for $M \to 0$. The loss f^0 introduced by ME at $M = 0$ directly results from the OP-induced skewing of the 2^3S distribution of populations (see figure 2.13: $M^\text{S}(M = 0) \neq 0$). It can be shown, however, that the contribution f^0 to dM/dt is negligible, at most of order 10^{-3} of the first term in equation (2.73) for all our experimental conditions. The coefficient $f'_\Gamma \Gamma^0_\text{ME}$ is not a constant prefactor: it varies with M and slightly differs from $f_\Gamma \Gamma^0_\text{ME}$. The difference $f'_\Gamma - f_\Gamma$ is due to the further, OP-induced skewing of the 2^3S distribution as compared to the case of "pure" relaxation analysed in section 2.8.2. Detailed computations fall beyond the scope of this PhD work and will be reported elsewhere [Nac12]. Here, only the most important characteristics are broached: The difference $f'_\Gamma - f_\Gamma$ is found to scale linearly with the absorbed light power W_abs and with polarisation M, as confirmed by analytical calculations (in the simple case for C_8 pumping so far). It can usually be safely neglected. At moderate or high incident pump laser power for instance, where W_abs is of order 0.1 W and M of order 0.5, the relative difference $\frac{f'_\Gamma - f_\Gamma}{f_\Gamma}$ is of order 2.7 % for $p_3 = 1.33$ mbar, hence $(f'_\Gamma - f_\Gamma)\Gamma^0_\text{ME}$ is of order 1-2 % of the value of Γ_D, depending on the fraction of relaxation in the 2^3S state during decay (e.g. 1.35 % in case this fraction equals 0.5 exactly).

We thus can write (cf. equation (23) of [Bat11]):

$$\frac{dM}{dt} \simeq 2\eta \frac{W_\text{abs}}{N_\text{g} V_\text{c}\, \hbar\omega_8} - (\Gamma_\text{g} + f_\Gamma \Gamma^0_\text{ME}) M. \tag{2.75}$$

where η is the global **photon efficiency** for MEOP. We have again neglected here the small variation of the resonance angular frequency ω_{ij} from one component of the $2^3\text{S}-2^3\text{P}$ transition to the other at low field and used that of C_8 at $B = 0$ (see section 2.3.1). We emphasise that with this definition the photon efficiency η depends on all MEOP conditions (plasma conditions, pump beam characteristics, gas pressure, field, etc.) and is *a priori* not an intrinsic quantity. Its meaning is clear, though, since the quantity $R_{phot} = W_\text{abs}/\hbar\omega_8$ is the number of photons absorbed by unit time and $N_\text{g} V_\text{c}$ is the number of ^{3}He atoms contained in the cell. The number of polarised ^{3}He atoms

produced by unit time is thus equal to $R_{at} = N_{\mathrm{g}} V_{\mathrm{c}}\, dM/dt$ and the photon efficiency η is related to the ratio of these two numbers by:[12]

$$2\eta = R_{at}/R_{phot}. \tag{2.76}$$

The generic equation (2.73) or the equivalent one for the two-class model are obtained using the system of rate equations used to describe MEOP. Analytical calculations yield explicit expressions of the photon efficiency η and of the coefficient f_Γ that are significantly more simple for the single-component line C_8 than for the C_9 line (and/or for particular asymptotic limits such as $B = 0$, $M = 0, \gamma_r^{\mathrm{S}}/\gamma \ll 1$). The computer implementation of the improved OP model provides numerical values for arbitrary conditions and can be used for quantitative investigations of the behaviour, e.g., of η with any experimental parameter. The following section (2.9) is devoted to the discussion of the results obtained for the photon efficiencies relevant for our work: η_{C8} and η_{C9} for the C_8 and C_9 lines, respectively, at low field.

For the analysis of the experimental data, however, a more pragmatic approach is preferred so that the findings do not depend on any underlying model description. To this aim, we perform a similar angular momentum budget and, neglecting the contributions of the minority excited atoms, just write the rate of change of the ground state nuclear polarisation as the net balance between the inflow angular momentum actually transferred through OP cycles to the 2^3S atoms and an angular momentum loss directly associated to the majority ground state atoms:

$$\frac{dM}{dt} = 2\eta \frac{W_{\mathrm{abs}}}{N_{\mathrm{g}} V_{\mathrm{c}}\, \hbar\omega_8} - \Gamma_R M \tag{2.77}$$

The global polarisation loss rate Γ_R introduced here is not a constant, it may vary with M and MEOP conditions as does η. Equation (2.77) mainly involves known quantities (N_{g}, V_{c}, $\hbar\omega_8$) or experimentally measurable quantities (the ^{3}He nuclear polarisation M measured using the 1083 nm probe light absorption method, the time derivative of M obtained from the recorded time monitoring of the transmitted probe powers, and the absorbed power W_{abs}, monitored at all times and measured at steady state). We are left with two unknown quantities: the photon efficiency η and the polarisation loss rate Γ_R. Only one remains at null polarisation where:

$$\frac{dM}{dt}(M = 0) = 2\eta \frac{W_{\mathrm{abs}}(M = 0)}{N_{\mathrm{g}} V_{\mathrm{c}}\, \hbar\omega_8}, \tag{2.78}$$

[12] Abboud and coworkers have pragmatically characterised in [Abb05b] the performances of MEOP at high magnetic field by a photon efficiency just equal to R_{at}/R_{phot}. Since we have explicitly based our definition of the photon efficiency on an angular momentum approach, we end up with a photon efficiency twice smaller because I=1/2 (see equation (2.17)).

that can be equivalently written as:

$$\eta = \frac{1}{2}\frac{\dot{M}(0)}{W_{\text{abs}}(0)} N_{\text{g}} V_{\text{c}}\, \hbar\omega_8. \tag{2.79}$$

- For the C_8 line, as shown in the next section, the photon efficiency is constant at fixed gas pressure. It can be then experimentally measured at $M = 0$ using equation (2.78) so that the rate of change of polarisation can be written at all times as:

$$\frac{dM}{dt} = \frac{W_{\text{abs}}(M)}{W_{\text{abs}}(0)}\frac{dM}{dt}(0) - \Gamma_R M, \tag{2.80}$$

which provides a way to experimentally infer the polarisation loss rate Γ_R at finite M as:

$$\Gamma_R(M) = \frac{1}{M}\left(\frac{W_{\text{abs}}(M)}{W_{\text{abs}}(0)}\frac{dM}{dt}(0) - \frac{dM}{dt}\right). \tag{2.81}$$

At steady state, in particular, $dM/dt(M_{\text{eq}}) = 0$ and $M = M_{eq}$ yield:

$$\Gamma_R(M_{eq}) = \frac{1}{M_{eq}}\frac{W_{\text{abs}}(M_{eq})}{W_{\text{abs}}(0)}\frac{dM}{dt}(0). \tag{2.82}$$

Equations (2.77) to (2.82) will be extensively used in the analysis of experimental data (see chapter 6).

- For the C_9 line, as shown in the next section the photon efficiency η both depends on M and W_{abs} at fixed gas pressure. We must therefore rely on numerical computations to know the values of η and infer the effective relaxation rates Γ_R.

The numerical prefactor that appears in equations (2.77), (2.78) and (2.79) involves the following quantities:

- the number of ground state ^{3}He atoms; $N_{\text{g}}V_{\text{c}}$, is considered to be equal to the total number of atoms:

$$N_{\text{g}}V_{\text{c}} = \frac{p_3 V_{\text{c}}}{T}\frac{N_A}{R_m} = \frac{p_3[\text{mbar}]\ V_{\text{c}}[\text{cm}^3]}{T[\text{K}]}\ 7.243\times 10^{18}\ [\text{K mbar}^{-1}\ \text{cm}^{-3}] \tag{2.83}$$

where p_3 is the ^{3}He gas pressure, T the temperature, N_A Avogadro's number and R_m the molar gas constant.

- the energy of the $2^3\text{S}-2^3\text{P}$ transition:

$$\hbar\omega = 1.834\times 10^{-19}\ \text{Ws} \tag{2.84}$$

(numerical values provided in list of symbols starting page XVI at the beginning of this manuscript).

Hence:

$$\frac{N_{\text{g}}V_{\text{c}}\hbar\omega}{2} = \frac{p_3[\text{mbar}]\ V_{\text{c}}[\text{cm}^3]}{T[\text{K}]}\ 0.6642\ [\text{K mbar}^{-1}\ \text{cm}^{-3}\ \text{W s}]$$

2.9 Photon efficiencies for low field MEOP

The photon efficiencies η_{C8} and η_{C9} computed with the improved OP model are discussed in this section and selected results for B =1 mT are displayed in figures 2.14 to 2.17. Analytical calculations based on the MEOP rate equations can be performed for all field strengths to obtain explicit relations between η and the transition matrix elements T_{ij} as a function of the polarisation M and the map of light intensity $I_{\text{cell}}(\overrightarrow{r})$ inside the cell. In all manageable cases the analytical results have been checked to agree with the numerical ones and they will not be reported here. Appendix D describes the method used to directly compute at $B = 0$ the photon efficiency η in the simple case where all populations are equal in the 2^3S state and in the limit of either no or full collisional mixing in the 2^3P state ('Kastler' [Kas57] and 'Dehmelt' [Deh57] regimes, respectively), where it is obtained as the average net change in total angular momentum projection per absorbed photon ($\eta = \Delta m_F$, see first term in equation (2.73)). This derivation makes use of the transition matrix elements T_{ij} for computation of relative transition probabilities for $2^3\text{S} \rightarrow 2^3\text{P}$ radiative excitation and of the branching ratios for $2^3\text{P} \rightarrow 2^3\text{S}$ radiative de-excitation.

Photon efficiencies for C_8 and C_9 have been computed for spin-temperature 2^3S distributions to illustrate the variation of η with polarisation M at very low incident power, where η is independent of W_{inc}. The spin temperature limit determines the relative weights of the two components involved in the C_9 line. The values of the photon efficiencies η_{C8} and η_{C9} obtained for the two limiting cases of very short and very long relaxation times in 2^3P ('Dehmelt' or 'Kastler' OP regimes, respectively) are plotted in figure 2.14.

- For C_8 (single-component excitation) the photon efficiency only depends on the branching ratios from Zeeman sublevels of the 2^3P state, those from the excited component (see figure D.2 in appendix D) as well as those involved by collisional mixing in the 2^3P state (not shown in the figure for clarity). These branching ratios provide the intrinsic transition probabilities, independently of the actual populations in the corresponding sublevels. This explains why the photon efficiency η_{C8} is independent of M.

- For C_9 this holds for each of the two components *but* the weights of the components depend on the Zeeman populations, hence on M for the ST case considered here. In $B = 0$, the ratio of the weights of the m_F = -3/2 and m_F = -1/2 components is 3:1 at $M = 0$. At $M = 0.8$ this ratio amounts to 1:3. Both contributions vanish when $M \rightarrow 1$ but their ratio asymptotically reaches 1. The change in relative weights of the two components explains the decrease of η_{C9} observed at high M. The fact that the photon efficiency η_{C9} becomes equal to that of the C_8 line is due to the fact that the contribution of the C_9 component addressing the m_F = -3/2 level vanishes for $M \rightarrow 1$.

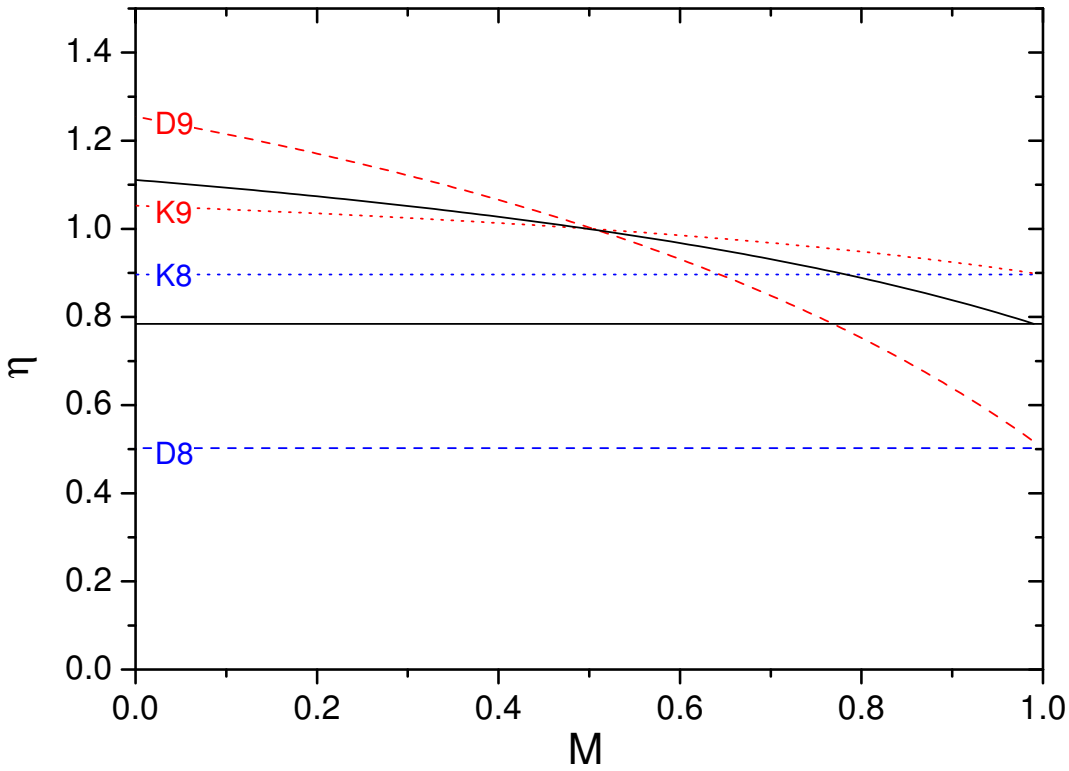

Figure 2.14: Computed photon efficiencies as function of M for C_8 and C_9 using the model for MEOP-kinetics for $W_{\rm inc} \to 0$ in the two limiting cases: 'Kastler' OP regime without collisional redistribution in the 2^3P state ($\gamma_{\rm r}^{\rm P} = 1$ s^{-1}: dotted lines, denoted K8 and K9 for C_8 and C_9 transitions respectively) and 'Dehmelt' OP regime with total collisional redistribution in the 2^3P state ($\gamma_{\rm r}^{\rm P} = 10^{20}$ s^{-1}: dashed lines, denoted D8 and D9 for C_8 and C_9 respectively). Solid lines without labels: 1.33 mbar, intermediate collisional regime ($1/\gamma_{\rm r}^{\rm P} = 2.3 \times 10^{-7}$ s) for C_9 (upper line) and C_8 (lower line). Other relevant parameters used for the computations: $B = 1$ mT; $W_{\rm inc}$ =1 μW with pure σ^+ light and no relaxation in ground and metastable states, i.e. $M = M^{\rm S}$ (spin temperature limit).

Table 2.1 provides the sets of extremal numerical values of η_{C8} and η_{C9} obtained at $M = 0$ and $M = 1$ for the Kastler and Dehmelt regimes for $B = 1$ mT in figure 2.14.

Table 2.1: Photon efficiencies η_{C8} and η_{C9} computed at $M = 0$ in the Kastler and or Dehmelt OP regimes (no and full collisional redistribution in 2^3P state, respectively) for $B = 1$ mT. At fixed collisional mixing rate, the photon efficiency η_{C8} does not vary with nuclear polarisation M and $\eta_{C9}(M = 1) = \eta_{C8}$.

$\eta(M = 0)$	C_8	C_9
Kastler	0.8962	1.0526
Dehmelt	0.5024	1.2547

The computations are performed at very low incident pump laser power (so that the populations in 2^3S are not perturbed) and without relaxation in the metastable state (to avoid any other contribution to the angular momentum budget except that of the photons). Also, pure σ^+ (or σ^-) pump light is used: any contribution from the other light polarisation would alter the budget and result in an effective photon efficiency that would decrease at high M due to the enhanced absorption of this other light polarisation.

Figure 2.15 shows computed values of η for different nuclear polarisation values as function of the relaxation time $\tau_P = 1/\gamma_r^{\mathrm{P}}$ in the excited 2^3P state. The curves from top to bottom show the variations of η_{C9} for increasing values of M. The photon efficiency η_{C9} is observed to be almost constant for $M = 0.5$, since the ratio of populations a_2/a_3=3 approximately compensates the ratio of transition matrix elements. The merging of η_{C8} and η_{C9} at very large M is observed to hold at all τ_P values (the bottom, dash-dot-dot curve for C_9 corresponds to $M = 0.995$, it almost coincides with the one for C_8 that is independent of M). The Dehmelt OP regime corresponds to the left-most data (short τ_P) in figure 2.15 and the Kastler OP regime to the right-most data (long τ_P). A sharp crossover is observed for $\tau_P \sim 1/\gamma$, as expected. The three empirically determined values of τ_P (see chapter 6.3.2) are indicated by arrows. They lie near the cross-over region and the inset of figure 2.15 shows that for our highest pressure p_3 =2.45 mbar η is not yet equal to the 'Dehmelt' regime value η^D corresponding to total collisional redistribution in 2^3P. The photon efficiencies for the lowest pressure p_3 =0.63 mbar are comparatively closer to the Kastler values.

In figure 2.16, the ratio of photon efficiencies η_{C9}/η_{C8} is presented for different values of nuclear polarisation as a function of the intrinsic relaxation time in 2^3P. This ratio is almost equal to 1 at $M = 0.995$ (bottom curve in figure 2.16) and increases up to 2.5 (resp. 1.18) at $M = 0$ (top curve) in the Dehmelt (resp. Kastler) regime.

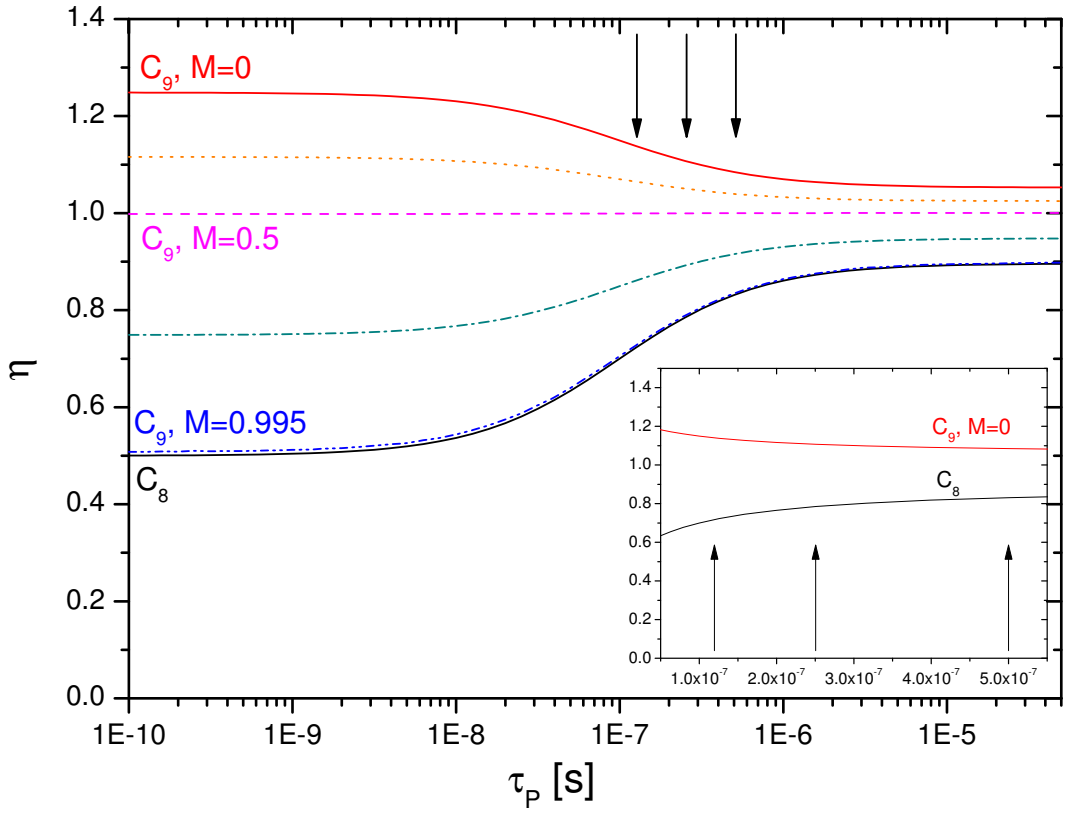

Figure 2.15: Computed photon efficiencies (parameters used for computations: see caption of figure 2.14) for C_8 and C_9 as function of the intrinsic relaxation time in the 2^3P state for different M values. Lines from top to bottom: solid: C_9, $M = 0$; dot: C_9, $M = 0.3$; dash: C_9, $M = 0.5$; dash-dot: C_9, $M = 0.8$; dash-dot-dot: C_9, $M = 0.995$; solid: C_8 (independent of M). Inset: η as function of τ_P in seconds (linear scale). Top: C_9, $M = 0$; bottom: C_8. The arrows in main plot and inset indicate the empirically determined values of τ_P (see chapter 6.3.2) for the different values of ^{3}He pressure. From left to right: 2.45 mbar, 1.19 mbar and 0.63 mbar. $B = 1$ mT.

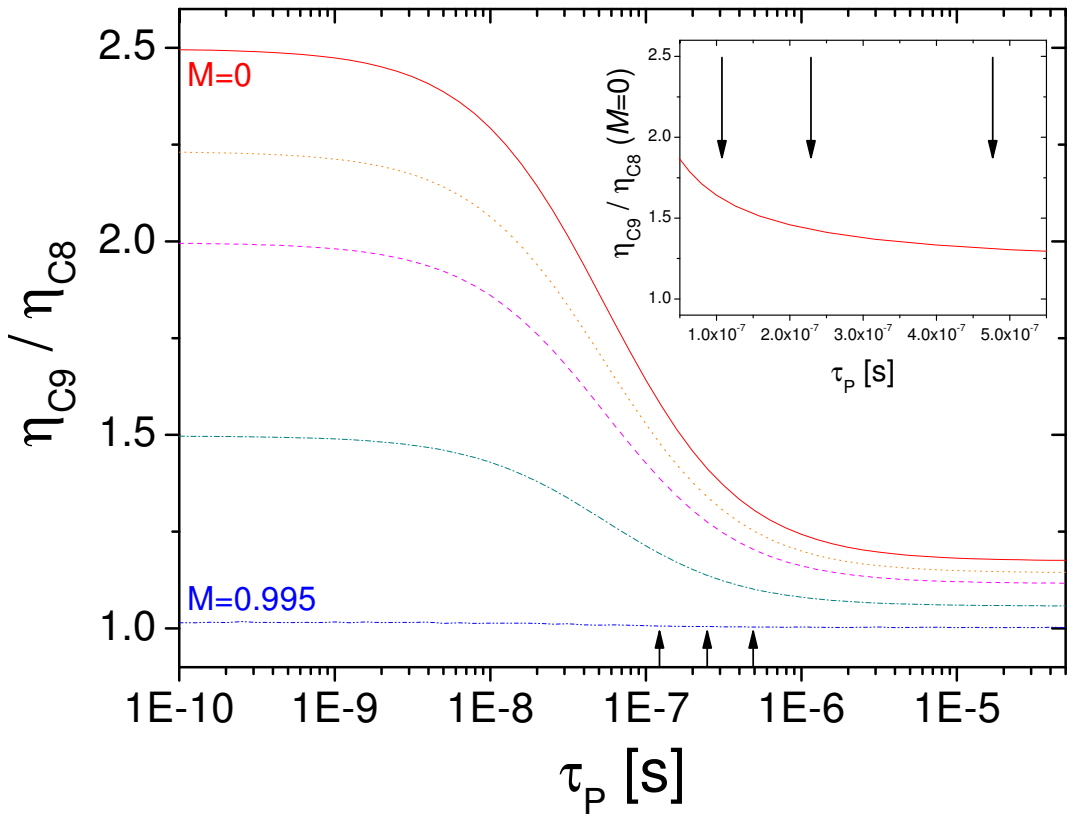

Figure 2.16: Ratio of computed photon efficiencies η for C_9 and C_8, same data as in figure 2.15 (parameters used for computations: see caption of figure 2.14) as function of the intrinsic relaxation time in the 2^3P state for different M values. Lines from top to bottom: solid: $M = 0$; dot: $M = 0.3$; dash: $M = 0.5$; dash-dot: $M = 0.8$; dash-dot-dot: $M = 0.995$. Inset: same data at $M = 0$ in linear scale. The arrows in main plot and inset indicate the empirically determined values of τ_P (see chapter 6.3.2) for the different values of ^{3}He pressure. From left to right: 2.45 mbar, 1.19 mbar and 0.63 mbar. $B = 1$ mT.

The ratio $\eta_{C9}/\eta_{C8}(M=0)$ ranges from approximately 1.6 to 1.3 for the three values of τ_P corresponding to our experimental gas pressures.

Throughout this work, for each cell, the empirically determined value of the intrinsic relaxation time in 2^3P (cf. chapter 6.3.2) has been used for numerical computations with the improved OP-model. Both η_{C8} and η_{C9} are *in*dependent of the radial distribution of metastable density, i.e., of the parameter α, in the very low power limit considered here. They significantly depend on collisional mixing in the 2^3P state, i.e., vary with the relaxation rate γ_r^P, shown in figures 2.15 and 2.16. Furthermore, they depend on the magnetic field strength through the involved ratios of transition matrix elements.

For single-component lines such as C_8 studied here, the photon efficiency does not depend on ^{3}He nuclear polarisation nor on OP light intensity. This is the case for the D_0 line of ^{4}He at low field as well, for instance, or for selected high-field transitions. At fixed low field strength, for ^{3}He, η_{C8} only depends on the relaxation rate in the 2^3P state whereas for ^{4}He, the photon efficiency of the D_0 line is a constant. The following expression can be directly inferred from rate equations (2.20) and (2.35):

$$\eta_{C8} = \frac{\gamma\eta_{C8}^K + \gamma_r^P\eta_{C8}^D}{\gamma + \gamma_r^P}, \tag{2.85}$$

where η_{C8}^K=0.896 (low-pressure OP limit $\gamma_r^P \ll \gamma$) and η_{C8}^D=0.5 (high pressure depopulation OP limit, $\gamma_r^P \gg \gamma$). Equation (2.85) results from the description of relaxation in 2^3P by redistribution with one single rate γ_r^P. However, the polarisation-independent character of η_{C8} will remain valid even if different collision rates for the various hyperfine levels in 2^3P are taken into account, as suggested by *ab initio* computations of J-changing cross-sections of reference [Vri04].

For C_9 the overall photon efficiency is a weighted average of contributions of the two line components. The relative weights are position-dependent through the 2^3S and 2^3P populations, that in turn depend on ^{3}He nuclear polarisation and on the local pump light intensity. Therefore η_{C9} depends in a non trivial way on M and on the incident pump power W_{inc}, as shown in figure 2.17.

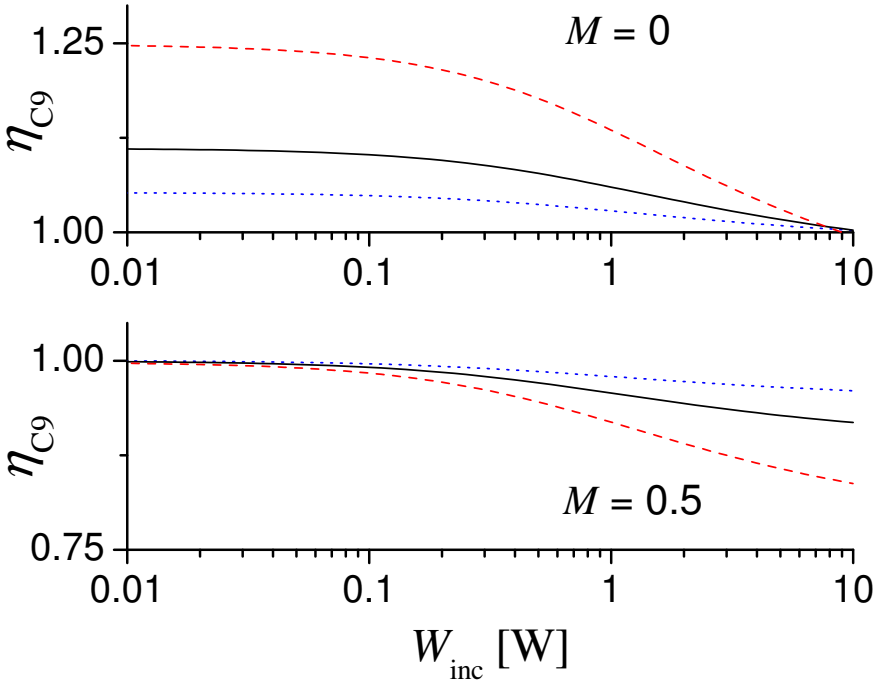

Figure 2.17: Computed power dependence of the photon efficiency of the C_9 line at M=0 (upper graph) and M=0.5 (lower graph) for the same three collisional regimes as in figure 2.14. η_{C9} is here the spatial average of the photon efficiency in the cell, computed for the following pump beam parameters: C_8 σ^+ pumping, 1.33 cm FWHM diameter, 1.7 GHz FWHM spectral width; uniform $n_m = 10^{-6} \times N_g = 3.2\times10^{16}$ at/m^3; L_{path} =2×30 cm.

2.10 Final discussions

2.10.1 Comparison with previous OP models

All OP models have to address the problem raised by the spectral response of He atoms to light excitation. The two-class model initially proposed by Nacher and Leduc [Nac85], where atoms are either jointly interacting with the laser beam or not pumped at all, breaks down at high power for broadband excitation: the centre of the velocity distribution is saturated and becomes "transparent" to pump light and the discarded contribution of the wings of the velocity distribution actually plays a significant role. This contribution is taken into account in the improved OP model where the atoms are now pumped (more weakly, though, than those of the central velocity class).

In reference [Wol04], Wolf and co-workers in Mainz have proposed a different modification of the original model developed in [Nac85]. The second velocity class

remains not pumped at all but the effect of radiative line broadening is taken into account by introducing a variation of the fraction of pumped atoms, n_{m}^{*} / n_{m}, with laser intensity. This accounts for stimulated emission and leads to an increase of the effective linewidth that scales with $\sqrt{I_{\mathrm{cell}}}$ for single-frequency or very narrow-band excitation.

A similar approach has been used for a short while at LKB where for narrow-band excitation, an adjustable fraction of pumped atoms has also been introduced in the model based on the measurements of saturated absorption spectra described in reference [Cou01].

In the improved OP model developed to reliably account for broadband excitation, the choice of width for the strongly pumped velocity class is found to be not critical (see the following section). Optical saturation is anyhow a less important issue when broadband laser sources are used, since the light intensity relevant for each velocity class is lower due to the frequency spread.

Another difference between the original model of [Nac85] and the improved OP model used in the present work lies in the way the transfer between velocity classes is treated. In the improved OP model, ME collisions contribute to a uniform redistribution over the two classes that was not considered in reference [Nac85]. In reference [Wol04] this randomisation of atomic velocities by ME is not included but the contribution of the elastic velocity-changing collisions occurs with a rate γ_C that is chosen equal to γ_e. This leads to a similar overall impact on MEOP dynamics as in our improved model.

2.10.2 Robustness of our computed OP results

All parameters except the width Δ of the strongly pumped velocity class are known, measured or fairly constrained by the experimental findings as will be shown in the following chapters. The order of magnitude of Δ is given by the laser spectral width L but its most suitable value is not known. However, the influence of this free parameter on results of computations is found to be very small for broadband OP.

This is illustrated for a $\pm$ 20 % relative change in class width around $\Delta = L$ in figure 2.18 that displays the rates of change of polarisation computed for C_8 and C_9 lines. The $\dot{M}$ curves obtained for the three different values of Δ at given transition appear superimposed and indistinguishable over the whole range of M (the differences are maximal at $M = 0$ and do not exceed $3{\times}10^{-4}$). When changing the width of the strongly pumped velocity class, the driving term $(M^{\mathrm{S}} - M)$ in the ground state rate equation (2.24) does change. However, the rate of change of polarisation $\dot{M}$, that results from a weighted average of the contributions of the a_i^* and a_i' populations and is spatially averaged over the cell volume, turns out to be extremely insensitive to the parameter Δ. The relative change in $\dot{M}$ is equal to $-$ 0.1 % and $+$ 0.5 % for $\Delta = 0.8\ L$ and 1.2 L, respectively.

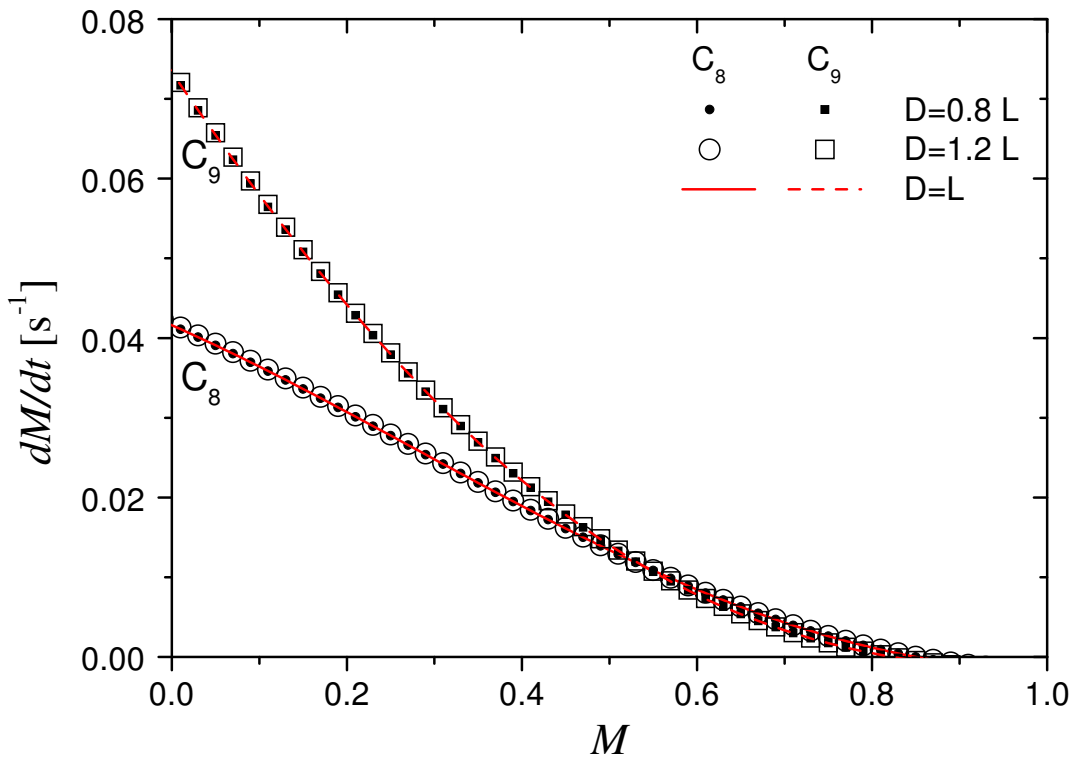

Figure 2.18: Influence of width Δ of strongly pumped velocity class on time derivative of polarisation on C_8 and C_9 as a function of M. Three different values of Δ are represented: $\Delta = L = 1.02$ GHz (laser spectral width), $\Delta = 0.8\ L$ and $\Delta = 1.2\ L$. Computations are performed with the same input parameters as data in figures 2.7 and 2.10 (see captions).

Comparison of pump absorptance values ($W_{\text{abs}}/W_{\text{inc}}$) for the same variations of Δ leads to the same conclusion, with results that are almost independent of M and exhibit a maximum relative difference of 0.8 %.

For C_8 OP, the relative change in apparent polarisation values measured with a C_8 probe laser aligned on the optical axis (where M^a-value is maximal, a worst-case upper bound in comparison with our experimental configuration) does not exceed $\pm$ 1.5 % at $M = 0$ and steadily decreases with M towards 0 at $M = 1$. Comparison with experimental results, as described in section 6.2 for various probe tunings (see figures 6.19 and 6.20), indicates that the improved OP model yields realistic computed values.

In conclusion, the dependence of characteristic MEOP quantities such as rates of change of polarisation, pump absorptances, and apparent polarisation values on the choice of the width Δ of the strongly pumped velocity class is negligible in standard operating conditions. The OP kinetics computed with the improved OP model appear extremely robust with respect to this free parameter.

2.10.3 Conclusion

The improved OP model still relies on a rather crude description of the velocity-dependent optical transition rates and this potentially limits the accuracy of its numerical predictions. A number of systematic studies have been made in this work to perform detailed comparisons of experimental and computed results. They are reported in the following chapters and show that this new model actually provides a realistic description of all features of low field MEOP as well as robust quantitative results.

Chapter 3

Experimental setup

This chapter deals with the dedicated experimental setup that has been built and used for the systematic measurements performed in this work to characterise MEOP kinetics and performances, over a wide range of conditions encompassing the usual operating parameters of ^{3}He polarisers: low magnetic field (few mT) and low pressures (few mbar).

The central part is the optical setup (section 3.2) that includes several optical elements as well as the ^{3}He-filled cell (section 3.1) through which pump and probe lasers (section 3.2) pass. The optical setup is located inside a home-made, end-compensated solenoid (also described in section 3.1) that produces a magnetic field of B up to 30 mT. A measurement and acquisition system is used to digitalise and record all optical and reference signals (section 3.3).

In the following, the various components of the experimental setup are presented. Figure 3.1 provides a global overview of the entire experimental setup.

3.1 Magnetic field, cells and rf discharge

Magnetic field

For the purpose of producing magnetic field strengths up to 30 mT, collinear with the cell and the optical axis, a 1.20 m long solenoid with end-correction coils providing high field homogeneity over the cell length (30 cm) has been designed and built. The solenoid has a 28 cm inner bore diameter and includes 3995 turns of 3.1 mm diameter enamelled aluminium wire wound in 10 layers on a single isolated Al cylinder. End-correction coils (length: 30.07 cm) include 97 turns each. The magnetic field in the centre of this resistive magnet is 3.9 mT/A, and the ohmic resistance amounts to 16.61 Ω (main coil: 15.67 Ω, correction coils: 0.47 Ω each). Two 6 cm thick hollow Al flanges have been attached at the ends of the magnet

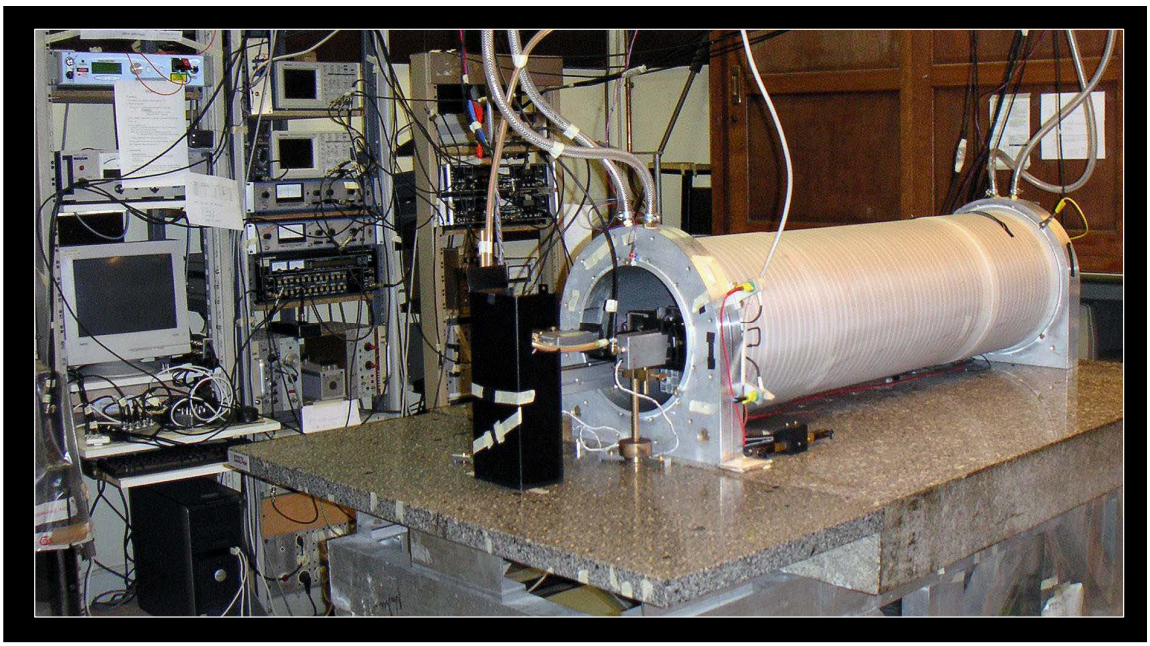

Figure 3.1: Overview of the experimental setup: In the front: End-compensated solenoid containing the optical setup (see figure 3.4). In the background: Left: Broadband 5 W fibre laser and data acquisition system. Centre: Monitoring equipment and lock-in amplifier for transmitted pump signal. Right: Control unit and current feed of probe laser, lock-in amplifiers for transmitted probe signals, discharge generator and amplifier.

for mechanical support and for cooling of the magnet bore. We routinely use water cooling of these Al flanges for continuous operation at $B \geq 10$ mT in controlled steady state conditions.
In the central field area, where the glass cell containing the ^{3}He-gas is located, a mean *longitudinal* relative field gradient of ΔB_z / B = 48 ppm/cm is achieved on axis over $l = 30$ cm (max. value: ΔB_z / B = 100 ppm/cm). The mean *radial* relative field gradient was measured to be ΔB_r / B = 33 ppm/cm over $r = 3$ cm, and not to exceed ΔB_r / B = 70 ppm/cm there.

Cells

For the systematic measurements in this work, cylindrical quartz glass cells with optically polished windows made of *Suprasil 1* glass were used. Prior to filling, a careful cleaning of the glass cells is essential. The cleaning procedure comprises rinsing with a tenside and phosphate based detergent and deionised water, bake out during several days under high vacuum (10^{-8} mbar range), and strong rf discharges using several batches of ^{4}He gas until only spectral lines of helium are observed in the plasma fluorescence by a hand spectroscope.
Our three ^{3}He cells have been prepared at Mainz University. The intended filling pressures were 0.65, 1.3 and 2.6 mbar to achieve a 1 : 2 : 4 pressure ratio. Due to technical problems, the pressure could only be measured with a poor accuracy during cell filling. Therefore, the exact ^{3}He contents (see table 3.1) were determined afterwards in the sealed cells, by means of NMR diffusion measurements at room temperature [Bar74, Lef82, Lef84].
By comparison of absorption measurements on the resolved C_8 and D_0 isotopic lines, the fractions of residual ^{4}He ($x_4 = \frac{p_4}{p_3}$) in the three cells could be determined: see table 3.1.
The outer dimensions of the cells are identical (length: 30 cm, diameter: 6 cm). The inner dimensions (see table 3.1) feature minor variations due to slightly different values of the wall thickness of the used quartz glass.

Rf discharge

A rf discharge is sustained in the cell using two external copper wire electrodes (of diameter 0.5 mm) connected to a voltage transformer tuned to the rf frequency (of order 2 MHz). Each electrode consists of a series of three (0.63 and 1.19 mbar-cells) or four (2.45 mbar-cell) rings, and the two sets of rings (used for capacitive coupling to the He gas) are interleaved to achieve homogeneous rf excitation. Partial amplitude modulation of the amplified rf power (around 70 Hz) and lock-in detection are used to improve the sensitivity of the absorption measurements.

Table 3.1: Table of gas pressures and inner dimensions of quartz glass cells used in this work

^{3}He gas pressure [mbar]	**0.63 ± 0.02**	**1.19 ± 0.03**	**2.45 ± 0.04**
inner length [cm]	29.4 ± 0.1		29.1 ± 0.1
inner diameter [cm]	5.6 ± 0.1		5.4 ± 0.1
inner volume [cm^3]	724.1 ± 26.0		666.5 ± 24.8
fraction of residual ^{4}He	(0.398 ± 0.011) %	(0.184 ± 0.006) %	$(6.84 \pm 0.2) \times 10^{-4}$

The electrode configuration has to be optimised in order to obtain uniform and stable plasmas over a wide range of rf excitation powers, also close to the extinction threshold. At higher ^{3}He pressure, simply interleaved copper wire rings in consecutive order do not yield best results according to our experiences. In the following, we briefly describe how the electrode configuration of the 2.45 mbar-cell has been optimised.

First of all, the number of rings of each electrode was increased to four (0.65 and 1.19 mbar: two pairs of three rings were sufficient for the same cell dimensions). Figure 3.2 is a photo of the obtained inhomogeneous plasma using just three rings per electrode on the 2.45 mbar-cell and shows the necessity for optimisation.

Second, while keeping an interleaved electrode configuration, the distance between

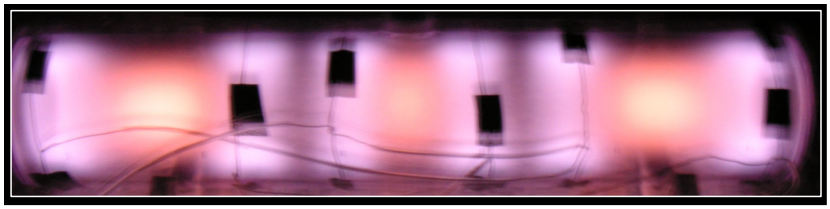

Figure 3.2: Inhomogeneous plasma in the 2.45 mbar-cell produced by a non-optimised electrode configuration using only three rings per electrode. The final optimised electrode configuration for this higher pressure cell uses four rings for each electrode and is sketched in figure 3.3. For comparison: The left photo of figure 6.2 shows the more homogeneously distributed plasma in the same cell with the optimised electrode configuration.

two adjacent rings and the wiring order of the rings of each electrode was modified, which changes the order of the voltage supply feed-in.

For evaluating different electrode configurations we rely on three complementary methods:

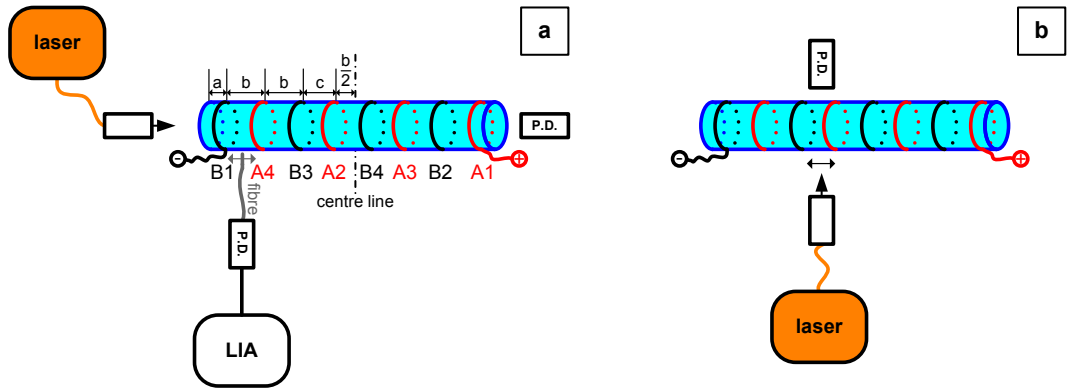

Figure 3.3: Methods to evaluate electrode configurations, especially needed at higher ^{3}He pressure.
a: Longitudinal absorption measurement (using the low power collimated monitor output of the pump laser in our case) and transverse luminosity measurements of the amplitude-modulated discharge at 15 different positions using a laterally adjustable plastic fibre connected to a photodiode (P.D.) and lock-in detection. The shown electrode configuration corresponds to the best solution for the 30 cm long 2.45 mbar-cell. Indicated distances: $a = 1.5$ cm, $b = 4$ cm, $c = 3.5$ cm. A and B designate the two different electrodes, and numbers indicate the order of wiring. Ring A1 (B1 resp.) is connected (only schematically drafted here) to the positive (negative resp.) pole of the voltage transformer. A2 is directly connected to A1, A3 to A2 and so forth, and in the same manner for electrode B. Connections between individual rings of a given electrode (A and B) are not sketched for simplicity.
b: Transverse measurements of local absorption with laterally adjustable laser and photodiode (15 measurement positions).

1. Global subjective assessment by investigating e.g., whether all sectors of the cell are illuminated and whether the visible fluorescence light is homogeneously distributed.

2. Longitudinal laser absorption measurement to measure the total absorption combined with transverse luminosity measurements of the fluorescence light (see figure 3.3a). The goal is to obtain maximum absorption at given rf excitation level with a transverse luminosity distribution as homogeneous as possible.

3. Transverse laser absorption measurements to quantify local absorption subsector by subsector (see figure 3.3b). These transverse measurements aim at obtaining maximum local absorption values at given rf level, distributed as homogeneously as possible.

The final optimised electrode configuration for the 2.45 mbar-cell is sketched in figure 3.3a, and the left photo of figure 6.2 shows the obtained plasma with these electrodes. The two extremal rings are close to the borders of the cylindrical cell (1.5 cm distance to cell windows), and the remaining six rings in-between are almost equally distributed (3.5-4 cm distance between two adjacent rings), and are thus symmetrical concerning positions with respect of the centre line of the cell. A non-symmetrical configuration concerning the wiring order of the rings of both electrodes yielded the best result.

3.2 Optical setup

The optical setup is shown and sketched in figure 3.4. Two laser sources are used: a broadband pump laser and a weak single-frequency probe laser. Both systems are described in the following.

Pump laser

For optical pumping a 5 Watt broadband (1.7 GHz fwhm) 1083 nm fibre laser is used (Keopsys, model YFL-1083-50-COL). The polarisation maintaining output fibre ends with an angle polished connector (APC) and is attached to an APC fibre mount placed at focal distance to the AR-coated $f = 7$ cm lens used for collimation. The collimated Gaussian output beam is circularly polarised and expanded to illuminate a large fraction of the transverse section of the cell for improved overlap with the broad distribution pattern of metastable atoms (see section 6.1.2). It propagates along the direction of the magnetic field and passes twice through the cell[1]. The whole

[1]The back-reflecting mirror is a metallic mirror (Amplivex, M.T.O.) that provides high reflectivity

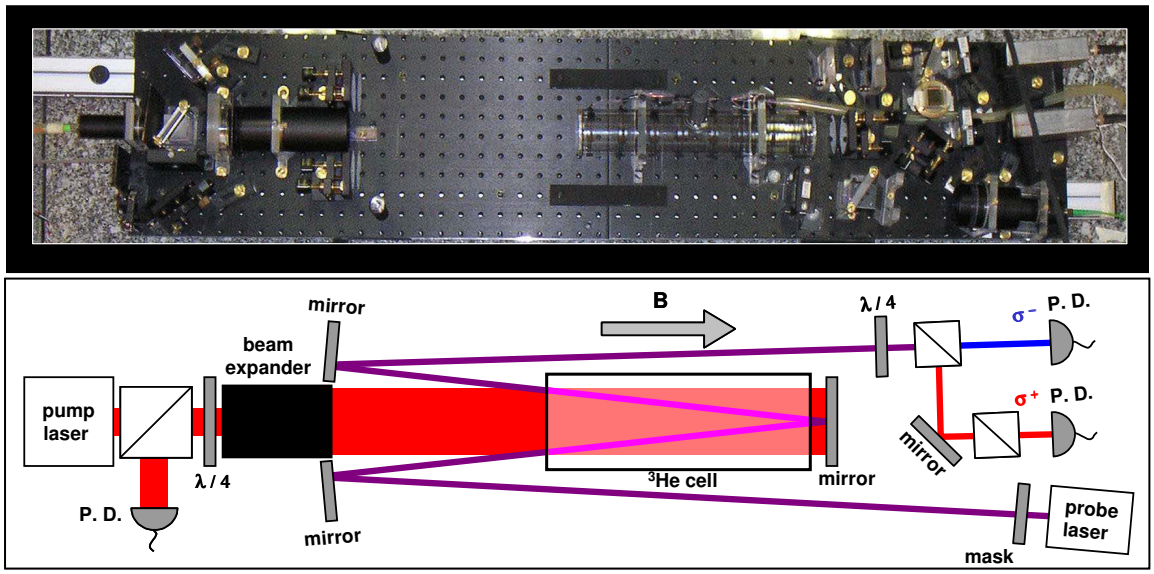

Figure 3.4: Photo and schematic of the optical setup used for low-field MEOP studies (top view). Pump and probe laser lights are delivered to the experiment by polarisation maintaining single-mode optical fibres. The Gaussian pump beam is collimated by a $f = 7$ cm lens, circularly polarised by an AR-coated polarising beam splitting cube (3 cm $\times$ 3 cm) and a quartz quarterwave plate ($\lambda/4$, diameter: 5 cm), and expanded to a beam diameter of 1.4 cm FWHM. The weak probe beam is split and polarised by a mask to obtain two vertically separated adjacent beams (this is not visible in this top view). The probe beams, with opposite circular polarisations, are separated after double pass through the cell by a circular analyser. Photodiodes (P.D.) are used to monitor the transmitted pump and probe beam powers.

transmitted pump beam, deflected by the circular polariser, is *entirely* collected by a lens, attenuated by neutral density filters and focussed on a monitoring photodiode for checks of laser tuning and measurements of the pump power absorption.

The Gaussian beam diameter is determined by transverse mapping (without discharge) using the dedicated experimental device for mappings of metastable densities briefly described in section 6.1.2. Transmitted pump power is scanned at 21 radial positions by a movable diaphragm (diameter: 3 mm) that can be precisely positioned every 3 millimetres.
The obtained experimental data points are fitted by a Gaussian distribution with exponential term $\exp[-2(r/w)^2]$, providing the width w. The input parameter needed by the program to model MEOP kinetics (cf. chapter 2.7) is the waist of the beam diameter $2a$, as defined in the Gaussian exponential term $\exp[-(r^2/a^2)]$. A comparison of both expressions yields:

$$a = \frac{w}{\sqrt{2}} \text{ and} \tag{3.1}$$

$$\text{FWHM} = w\sqrt{2\ln 2} = 2a\sqrt{\ln 2} \tag{3.2}$$

An example of a measured distribution of spatial power is provided in figure 3.5. At the beginning of this work, the beam diameter had been set to $2a = 2.23$ cm. The large series of systematic measurements reported in this manuscript have been performed with a slightly re-designed setup for which the beam diameter amounted to $2a = 1.6$ cm (FWHM = 1.4 cm, see Gaussian fit of width $w = 1.16$ cm in figure 3.5).

W_{inc} designates the total incident pump laser power in Watt i.e., the integrated light intensity over the radial beam profile. W_{inc} has been measured at the entrance-window of the cell, after pump beam collimator, polarising beam splitter cube, quarter wave plate and beam expander. Therefore, W_{inc} is determined by the laser output power and the losses introduced by the optical elements:

$$W_{\text{inc}} = (0.830 \pm 0.004)\, W_{\text{nom}}.$$

W_{nom} is the nominal output power of the pump laser, measured and displayed by the laser control unit that has been repeatedly checked to provide correct values. A measurement of pump laser power directly behind the pump beam collimator yielded: $W_{\text{inc}} = (0.902 \pm 0.002)\ W_{\text{nom}}$. The remaining loss arises from the contribution of optical elements (polarising beam splitter cube, quarter wave plate, beam expander).

In this manuscript, we will use different notations for the (total) pump laser power W (expressed in Watts) and for the pump laser intensity I (expressed in W/cm^2), i.e. the radial power density: $I(r) = \frac{W}{a^2}\, \mathrm{e}^{-r^2/a^2}$.

(measured losses amount to 0.2-0.3 % at an incident angle of 0° and to 0.1-0.2 % at 45°) with negligible alteration of the light polarisation. Good results are also obtained e.g., in gas polarisers with thick R_{max}-coated mirrors.

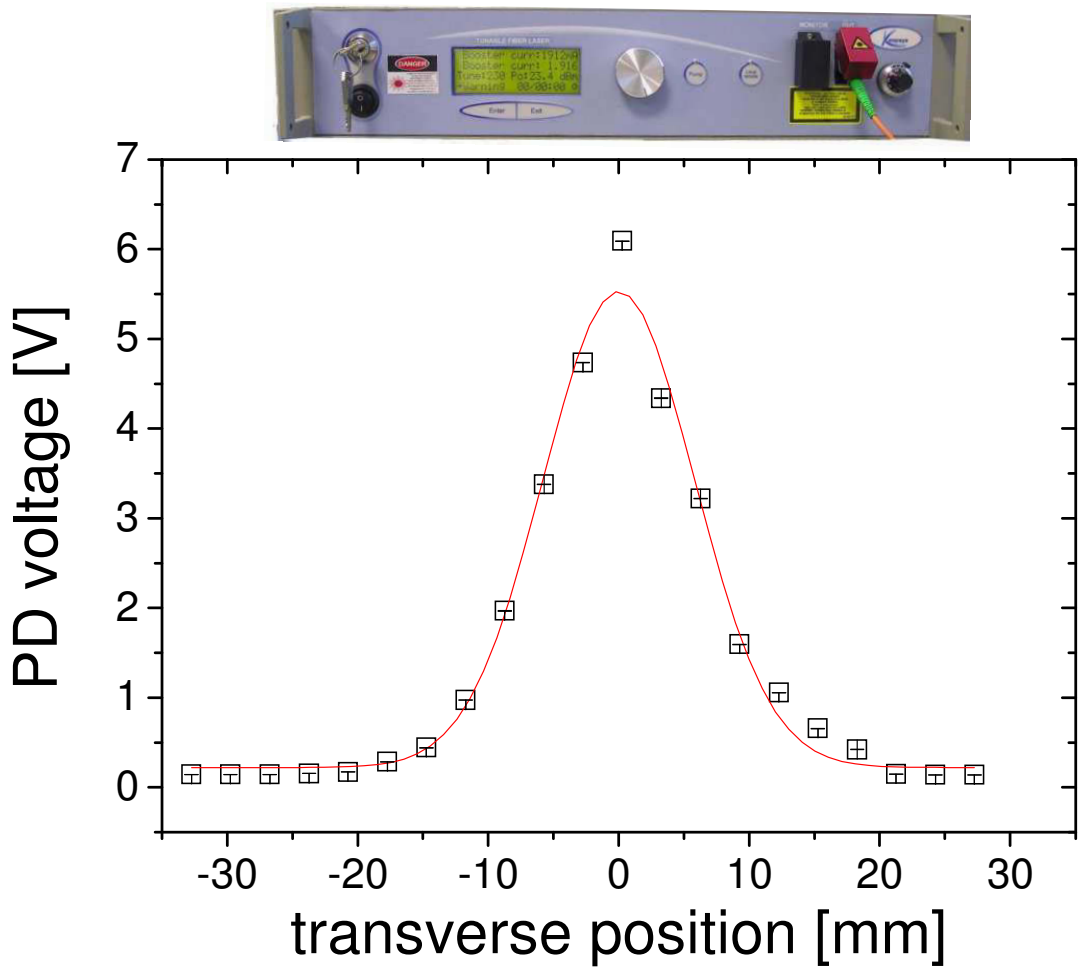

Figure 3.5: Spatial power distribution of the pump laser. Open squares: Experimental data points, line: Gaussian fit of width $w = 1.16$ cm ($2a = 1.6$ cm, FWHM: 1.4 cm). Photo on top: Control unit of 5 Watt broadband pump laser (Keopsys).

Probe laser

A longitudinal optical detection method is used to measure the nuclear polarisation in the gas during experiments (see chapter 4). The W-shaped design used for convenience (see figure 3.4) is such that the probe light experimental path inside the cell is actually slightly tilted with respect to the cell axis. The detection method is based on absorption measurements of two weak probe beams (15 μW/cm^2) with σ^+ and σ^- circular polarisations. The two beams are generated by the same single-frequency 1083 nm DBR laser diode (provider: Spectra Diode Labs (SDL), 50 mW output). The laser diode has an on-chip Peltier thermal controller, which allows precise and fast temperature control of the output frequency. The laser diode output beam is injected into an optical fibre that allows keeping this additional optical setup (see figure 3.6) in a separate place. The Gaussian beam is collimated at the fibre output, and a polarising beam splitter cube is used to achieve perfect linear polarisation. Plastic $\lambda/4$ sheets with crossed orientation ($\pm$ 45°) are inserted in the 2-hole mask.

The two probe beams with σ^+ and σ^- circular polarisations are separately monitored after double pass through the cell using two photodiodes. Photodiode signals are proportional to transmitted powers for polarisation components σ^+ and σ^- thanks to the use of an additional purifying polarising beam splitter cube on the deflected channel (crosstalk $\leq 10^{-3}$).
The measured probe signals after passage through the ^{3}He cell constitute averages of various pump conditions (transverse Gaussian profile of progressively absorbed pump beam, radial metastable density profile).

As described in [Tal11], the two probe components should ideally overlap exactly in order to measure absolute ratios of populations. However, in this situation, polarisation components that simultaneously address the same 2^3P Zeeman sublevel may interact, and the ratio of absorption signals has been observed to exhibit small frequency-dependent variations at finite nuclear polarisations (when the probe is tuned to the C_9 line in ^{3}He gas and when it is tuned to the D_0 line in isotopic gas mixtures). No such artefact has been noticed when the C_8 line is used. Systematic investigations have been made in a variety of experimental conditions and detailed results will be reported elsewhere. Using two spatially separated beams for the absorption measurements (σ^+ and σ^- in the longitudinal configuration of this work) has been checked to make the optical technique robust against probe detuning and accurate at all polarisations. These probe beams still remain very close so as to address nearly identical sets of atoms, and any small local differences (e.g., in the number density of metastable atoms) cancel out when reduced ratios of absorption signals are used (cf. equations (4.12) and (4.14)).
The discrepancies arising from slightly different geometrical probe paths followed by σ^+ or σ^- light respectively, range between 0.5 and 2 %, and this 'geometrical effect' is taken into account for the determination of metastable densities.

Figure 3.6: Additional optical setup: Injection of the probe laser (single-frequency DBR laser diode) into an optical fibre. The following optical elements are used (from top to bottom): Aluminium housing of the laser diode (with closed cover plate on the photo), inclined neutral density filter (to avoid feedback into the laser diode and reduce laser intensity), $\lambda/2$ halfwave plate (to rotate polarisation plane for laser intensity control), polarising beam splitting cube and $\lambda/4$ quarterwave plate (serve as optical isolator) and precisely adjustable fibre mount.

Figure 3.7 defines the geometrical parameters of the probe paths that have to be specified for computations using the model for MEOP kinetics among the input parameters (see section 2.7.4).
The longitudinal gap in the standard double-pass configuration between the cell exit

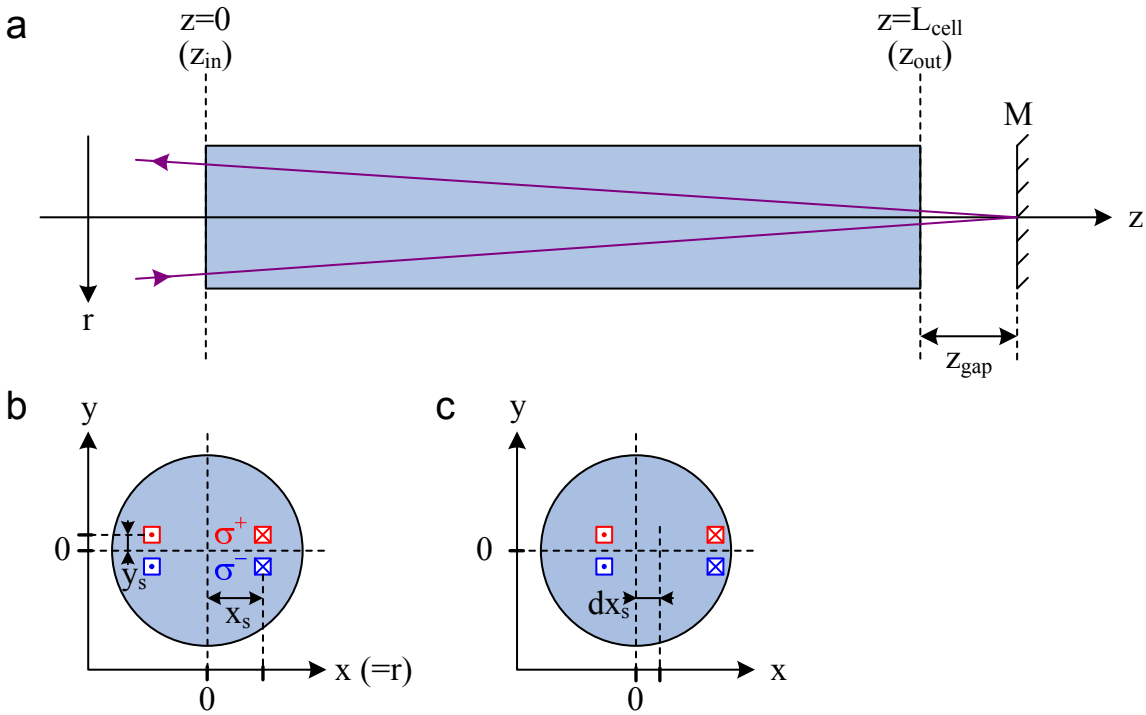

Figure 3.7: Geometrical parameters specifying the probe paths. **a:** Top view (the two vertically separated adjacent beams are not visible in this view). **b** and **c:** Side views onto the entrance window of the cell, in direction of the ingoing probe beams. **b:** Standard case with V-shaped probe paths symmetrically centred around $x = 0$ (cell axis). **c:** V-shaped probe paths with vertical offset dx_s from cell axis.

window and the back-reflecting mirror, z_{gap} (see figure 3.7a), typically amounts to 2.6 cm. The radial distance x_s between ingoing (or outcoming) probe beams and the cell axis ($x = 0$) is defined in figure 3.7b and a typical value is 1.9 cm. The distance in y-direction between the spatially separated σ^+ (or σ^-) probe components and the cell axis is designated by the parameter y_s and is fixed by the used mask to 0.8 cm. The mask also sets the surface area of each probe beam component to 0.65 cm^2. A possible offset dx_s of the V-shaped configuration with respect to the cell axis is specified in figure 3.7c, but has always been kept zero in this work.

For accurate absorption measurements, care must be taken in order to optimally separate weak probe and intense pump beams. Residual pump stray light as well as a contribution from the fluorescence light emitted by the plasma may be filtered out of the probe signals by a double modulation scheme as illustrated in the next section.

3.3 Measurement and acquisition system

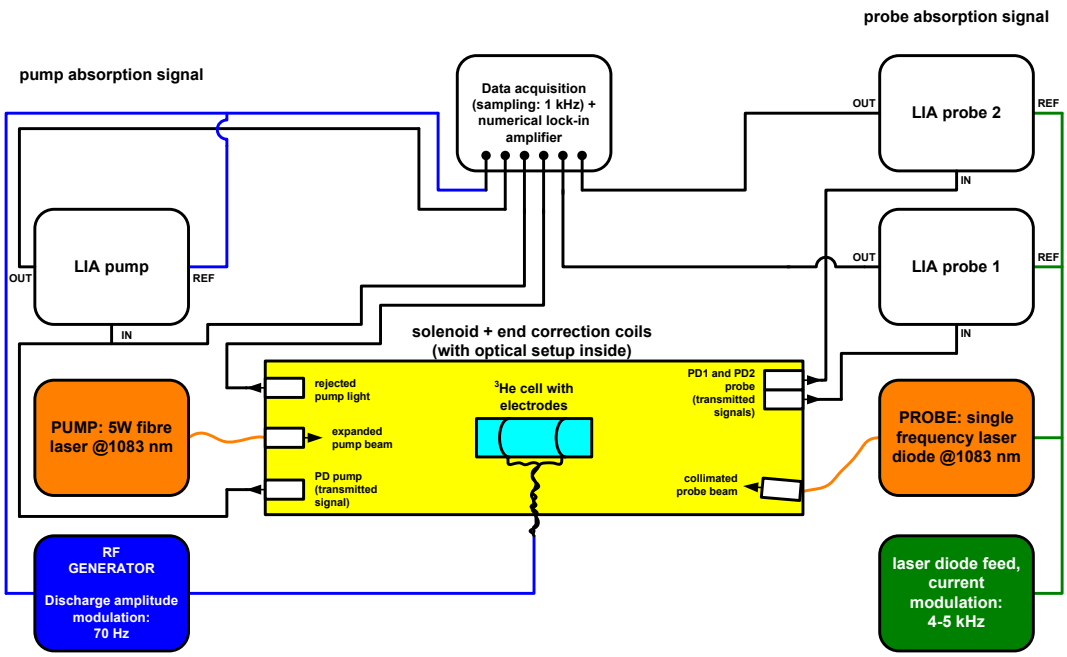

Figure 3.8: Schematic of the measurement and acquisition system. Details of the optical setup inside the solenoid: see figure 3.4.

Two different modulation schemes are used in the experiment:

1/ The probe laser current is modulated at 4-5 kHz to filter out remaining stray light from the pump laser by means of lock-in detection (alternatively a mechanical chopper can be used).

2/ The rf-discharge is usually modulated at 70 Hz, to allow distinction between atomic response (i.e. absorption of laser light at resonance) and power fluctuations of pump or probe lasers.

The fast demodulation at 4-5 kHz is carried out by two identical analogue lock-in amplifiers (EG&G model 5209), one for each probe light component σ^+ and σ^-.

These output-signals of the two lock-in amplifiers, the transmitted probe power signals for both light components, are recorded at a sampling rate of 1 kHz.

Furthermore, the following signals are recorded using simultaneous 16-bit A/D conversion at a sampling rate of 1 kHz (with a Data Translation USB module DT 9816): the transmitted power of the pump laser (output of photodiode), and three auxiliary signals, namely the TTL output synchronised to the frequency of the amplitude modulation of the discharge generator, the demodulated pump signal (output of a third lock-in amplifier (Ithaco model 3961 B): optional as the pump signal can be postprocessed by numerical demodulation just as applied to the probe signals, details are reported in chapter 5 and appendix E), and the rejected pump light component that does not pass the first beam splitter cube directly behind the pump beam collimator, but is deflected by 90° due to wrong light polarisation (not represented in figure 3.4). Recording the rejected pump light component allows to monitor polarisation changes of the pump light, and thus transmitted pump power towards the cell.

(Two-step) modulation of the discharge amplitude (and of the probe laser, when the pump laser is on, resp.) and lock-in amplification of the probe absorption signals typically improves SNR to 10000 (500-1000, resp.) e.g., statistical error on M: 0.02 %.

Chapter 4

Optical measurement of nuclear polarisation

In this chapter, an optical method to dynamically measure nuclear polarisation by monitoring absorption of a weak single-frequency probe laser at 1083 nm is described in detail. This accurate and highly sensitive method operates at arbitrary magnetic field and gas pressure and provides information about the total number density of atoms in the 2^3S state, i.e. the metastable density n_{m}, and about the relative populations of the probed 2^3S sublevels. As the distribution of populations in the 2^3S state is strongly coupled to that of the ground state by metastability exchange collisions, this optical method yields absolute values of the 1^1S nuclear polarisation M. It can be implemented into the optical setup either in a transverse configuration, perpendicular to the magnetic field as demonstrated and precisely characterised in [Big92], or in a longitudinal configuration with the probe beam being parallel to the magnetic field. In this work, a longitudinal probe scheme has been chosen. Independently of the chosen configuration, *no* calibration is needed to infer values of M, in contrast to other methods like discharge polarimetry.

In the following preliminary remarks, the basic ideas of absorption measurements at 1083 nm, including the transverse probe scheme, as well as two other methods to measure M, discharge polarimetry and NMR, that were *not* used in this work, are briefly introduced, and respective sensitivities are discussed in order to justify the choice of a longitudinal probe scheme in our work. The rest of the chapter covers a detailed description of all relevant aspects for this longitudinal probe scheme starting in section 4.1.

Discharge polarimetry

In standard helium OP experiments, polarimetry of discharge light is often used to assess nuclear polarisation in the ground state.

The main principle of discharge polarimetry is the analysis of circular polarisation of a chosen helium spectral line emitted by the discharge, that transfers atoms to various excited states preserving the nuclear spin state. Hyperfine coupling relates nuclear to electronic orientation in these excited states. Due to this hyperfine interaction, the visible light emitted by spontaneous emission in the radiative cascade is (partially) circularly polarised. The degree of circular polarisation is proportional to the nuclear orientation (in low magnetic field).

In [Lal68], this method is proposed to monitor the nuclear polarisation of the ground state. In [Pav70], an experimental implementation using a device with rotating quarter wave plate is described. Calibration of the circular polarisation of the emitted light is reported e.g., in [Pin74] using absorption measurements of a probe beam for calibration, in [Big92] with refined optical setup using a transverse probe beam configuration and in [Lor93] where a two-step calibration method is used: calibration of a ^{3}He NMR-system by comparison to water under identical conditions and in a second step, using the calibrated ^{3}He NMR-system to calibrate in turn the circular polarisation of the 668 nm-light emitted by the discharge. Most experimental realisations use this red line at 668 nm to monitor the nuclear ground state polarisation. In [Sto96b], the possibility of using another orange line at 588 nm is successfully implemented in a static polarimeter, and calibration and comparison measurements are performed making use of a second static polarimeter at 668 nm and pulsed NMR measurements.

Since hyperfine *de*coupling occurs with increasing magnetic field, discharge polarimetry looses its efficiency above approximately 10 mT [Pav70, Cou02]. Furthermore, it is restricted to limited ^{4}He isotropic ratios [Cou02] and low gas pressures ($\lesssim$ 5 mbar) [Cou02] because higher pressure increases the rate of depolarising collisions.

Nuclear magnetic resonance (NMR)

NMR techniques to infer nuclear polarisation are not well suited at low pressure gas due to its low sensitivity. Calibration is required to know the coil filling factors. Furthermore, the technique is difficult to implement in a MEOP setup where, in addition to geometrical constraints (1/ cell size and shape, 2/ limited bore size of the magnet), monitoring of OP dynamics in the plasma is especially challenging because of rf noise due to the discharge and because of short transverse relaxation time.

Absorption measurements at 1083 nm

The main idea to relate the magnitude of an optical absorption (or fluorescence) signal to nuclear polarisation of ^{3}He has been proposed in [Col63] and [Gre64], using a ^{4}He discharge lamp as probe (and pump) source. In [Dan71c], the method has been

refined by taking into account some imperfections of the pumping light (used as probe as well), namely the non-parallelism of the light with respect to the magnetic holding field and the imperfect circular polarisation. Furthermore, a narrow, weak collimated measuring beam, plane or circularly polarised is introduced. In [Tim71], this method is applied in OP experiments in order to examine the dependence of steady state polarisation and build-up times on ^{3}He pressure, pumping light intensity and metastable density, and to compare experimental results to theoretical predictions [Dan71b].

[Wal96] and [Mil98] are examples where optical absorption measurements were implemented in pure ^{4}He which allows to determine populations y_i and to infer absolute atom number densities.

The optical absorption method as implemented in our work requires to probe the populations in *two* (sets of) 2^3S sublevels (reasons are explained in subsection 4.2).
In low magnetic field, at $B \lesssim 50$ mT, as long as the Zeeman shift remains inferior to the Doppler width, it is possible to lock the probe laser frequency to the chosen transition at $B = 0$ and to dynamically measure the absorptions for two light polarisations simultaneously (e.g. σ and π in the transverse probe configuration or σ^+ and σ^- in the longitudinal configuration).
In higher magnetic field, when two sublevels are not degenerated anymore due to the larger Zeeman effect, and the Zeeman splittings are at least of the order of the Doppler line widths, two absorption measurements to probe two 2^3S sublevels must be performed using different probe laser frequencies. Experimental schemes to obtain such dual-frequency measurements (e.g., sweeping the probe laser frequency) are described in [Cou02] (0.0925 T) and [Suc07] (0.45-2 T, up to 67 mbar).

The longitudinal probe scheme is applicable to both resolved lines C_8 and C_9, to probe sublevels in $F = 1/2$ or $F = 3/2$, but is particularly straightforward for the single-component line C_8 as explained in subsection 4.2.1.
In a transverse probe configuration especially in long cells, the total absorption is smaller and additional optical windows are possibly required on the transverse probe path. This probe configuration is not applicable to C_8 as σ and π light address the same sublevels. The fact that the transverse configuration is only applicable to the multi-component line C_9 implies the intrinsic difficulties of probing the C_9 transition: at $B \neq 0$, measured absorption rates are sensitive to probe detuning, and transition intensities of both line-components depend on B, furthermore, traces of ^{4}He are susceptible to affect absorption rates on C_9. These (configuration-independent) issues of C_9 as probe transition are discussed in more detail in subsection 4.2.2.

For both probe schemes, figure 4.1 shows the variations of the relevant ratios of absorption signals (cf. section 4.2), A_π/A_σ for the transverse probe scheme, and $A_{\sigma^+}/A_{\sigma^-}$ for the longitudinal probe scheme, with nuclear polarisation M. For the transverse probe scheme, C_9 and D_0 lines provide a comparable sensitivity for polarisation measurements, quite high above $|M| \geq 0.2$. The sensitivity is reduced at small

M, with a quadratic departure of A_π/A_σ from 1 that results from the fact that each light component simultaneously addresses sublevels with opposite angular momenta. In contrast, the longitudinal probe scheme has a linear response at small M for all lines, with a higher sensitivity for the C_9 and D_0 lines. At high M, it has a reduced sensitivity for C_9 and D_0 with $A_{\sigma^+}/A_{\sigma^-} \simeq 1 - M^2$; the C_8 line retains a linear sensitivity, yet provides a limited precision since both absorption signals vanish at M=1.

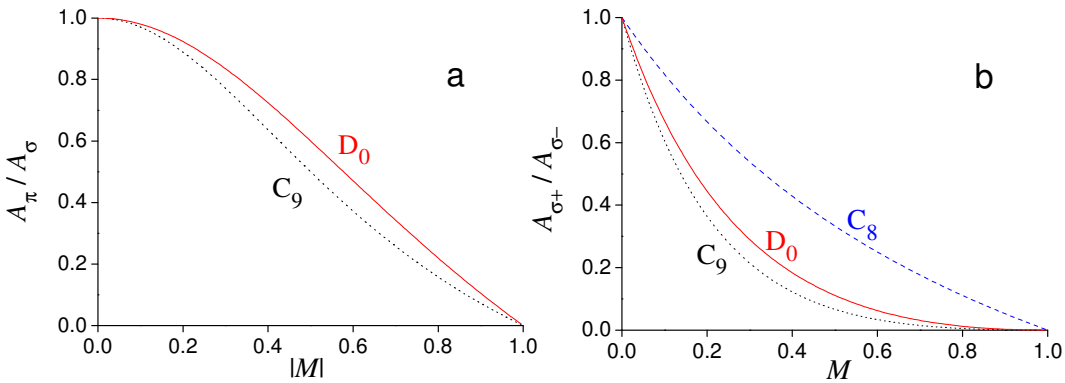

Figure 4.1: Ratios of $2^3S-2^3P_0$ absorption signals computed for transverse (a) and longitudinal (b) probe schemes as a function of ground state nuclear polarisation M, at zero magnetic field and at spin temperature equilibrium. **a:** Transverse probe scheme: D_0 (solid line) and C_9 (dotted line) provide comparable sensitivities at all M. Opposite polarisations M and $-M$ cannot be distinguished using A_π/A_σ. **b:** Longitudinal probe scheme: C_9 (dotted line) and D_0 (solid line) provide higher sensitivity than C_8 (dashed line) at small M, where accurate measurement can be performed in contrast to the transverse scheme. Identical curves would be obtained by plotting the inverted ratio $A_{\sigma-}/A_{\sigma+}$ for negative M values. (Figure taken from [Tal11]).

We perform absorption measurements of 1083 nm probe light using two *longitudinal* weak probe beams with σ^+ and σ^- polarisations (see section 3.2) in low magnetic field, and use the comparison of σ^+ and σ^- optical signals to measure the populations of two hf sublevels of the 2^3S state of ^3He atoms. The longitudinal configuration is chosen in this work for the good sensitivity (linear variation) at low M which allows precise monitoring of build-up dynamics. Furthermore, absorption is enhanced in our long cells, which yields high accuracy at very good SNR.
Section 4.1 presents the basic principles of longitudinal probe absorption measurements. Section 4.2 describes how the ground state nuclear polarisation M can be inferred from the ratio of light absorption rates, assuming that ME establishes a spin temperature (ST) equilibrium distribution of populations between the six 2^3S sublevels. Section 4.3 describes the effects of OP on the 2^3S and 2^3P populations,

and their impact on the determination of M. Knowing the ^{3}He polarisation, we can infer metastable atom densities from the absolute values of the light absorption rates. Section 4.4 focuses on the data reduction strategy used to reliably obtain the metastable density at all magnetic field strengths.

4.1 Longitudinal probe absorption measurements

In order to illustrate the conditions for the use of a longitudinal probe laser at fixed frequency in the present work, computed absorption spectra of ^{3}He for different light polarisations in $B = 0 - 30$ mT are presented in figure 4.2.

Energies and intensities of the optical transitions in ^{3}He at $B = 0$ are represented as well as computed absorption spectra at $B = 30$ mT for σ^-, π and σ^+ light polarisations. The shifts of the σ^- and σ^+ spectra at $B = 30$ mT compared to the transition frequencies at $B = 0$ are clearly visible. The Zeeman shifts up to 30 mT remain below Doppler width at room temperature, so that the low field approach mentioned in the preliminary remarks of this chapter, namely to fix the probe laser frequency to the transition frequency in $B = 0$ in order to monitor both light polarisations simultaneously is appropriate. Furthermore, the computed spectra show that only the two resolved lines C_8 and C_9 are appropriate to be used as probe transitions.

Figure 4.3 shows experimental absorption spectra for σ^+ and σ^- light polarisations at $B = 30$ mT for $M = 0$ and $M = 0.5$ (the corresponding computed spectrum at $M = 0$ is represented in figure 2.4). The difference between the σ^+ and σ^- peaks due to Zeeman splitting of energy levels amounts to approximately 1.05 GHz or 1.45 GHz at $B = 30$ mT in the C_8 or C_9 resonances respectively which is inferior to the Doppler width of ^{3}He gas at room temperature (cf. caption of figure 4.2). Hence, in most of the cases throughout this work (low and intermediate field 0-30 mT), the probe laser frequency has been locked to the transition frequency at $B = 0$ so that the evolution of σ^+ and σ^- peak intensities can be monitored as function of time which is equivalent to polarisation during build-up. Independently of the magnetic field, it is also possible just as well to sweep the probe laser frequency as demonstrated in figure 4.3 (more experimental examples of probe laser frequency sweeps, see section 6.2).

The probe beam components (with circular polarisations $\sigma^+$and σ^-) used in our experiments are obtained from a low power monochromatic laser beam that is substantially expanded and subsequently diaphragmed (see section 3.2). Therefore we legitimately consider here a probe beam with uniform light intensity I that is weak enough for the absorbed intensity to be proportional to the local intensity at any point along the beam path (linear regime). The variation of the probe beam intensity

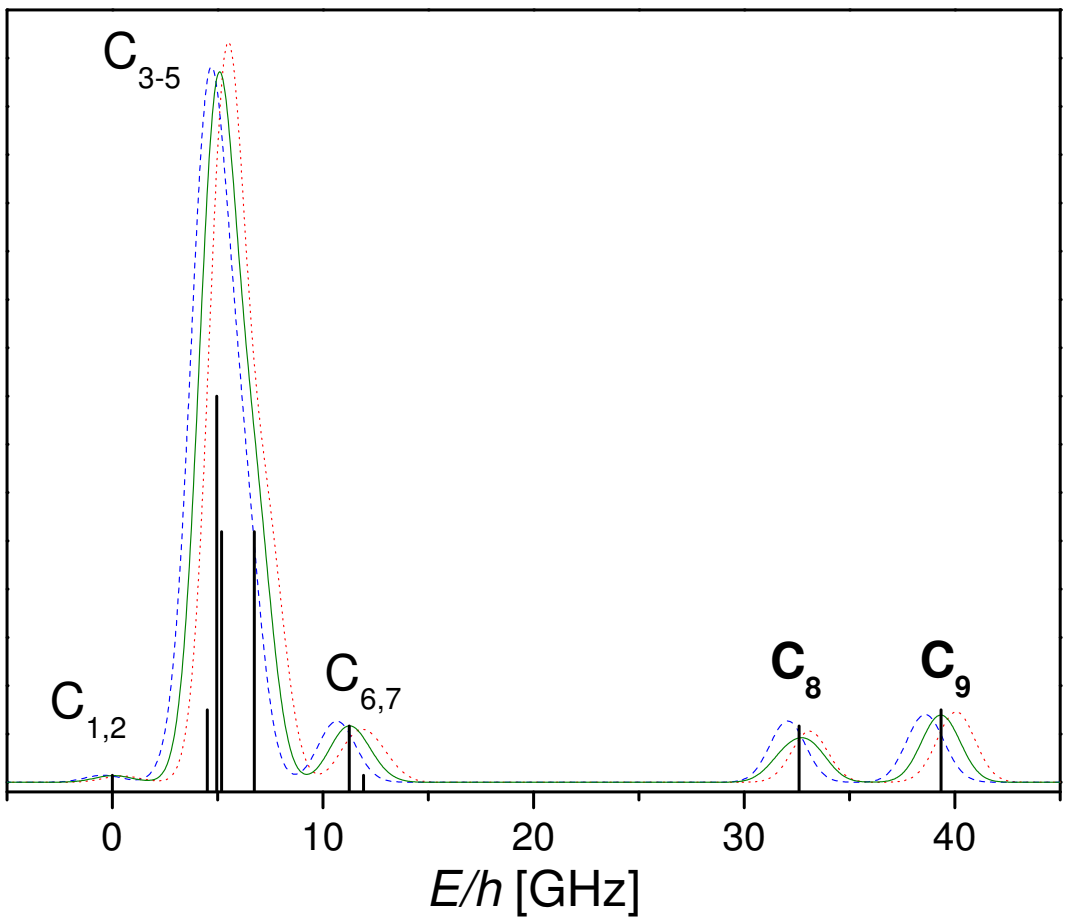

Figure 4.2: Frequencies and intensities of optical transitions in ^{3}He at $B = 0$ (vertical lines, from [Cou02]). Frequencies are referenced to the C_1 transition. The given intensities correspond to the partial sums of the transition matrix elements T_{ij} for each line.
In addition: Computed absorption spectrum of ^{3}He at $B = 30$ mT (by Fortran-programme developed in [Cou02] using a nominal Doppler width of 1.98 GHz (FWHM) which corresponds to the velocity distribution of ^{3}He at 300 K. Other sources susceptible to broaden the profiles of atomic lines, especially collisional broadening, are neglected.) Three light polarisations are represented: π (solid line), σ^+ (shifted towards higher frequencies at $B = 30$ mT: dotted line) and σ^- (shifted towards lower frequencies at $B = 30$ mT: dashed line).

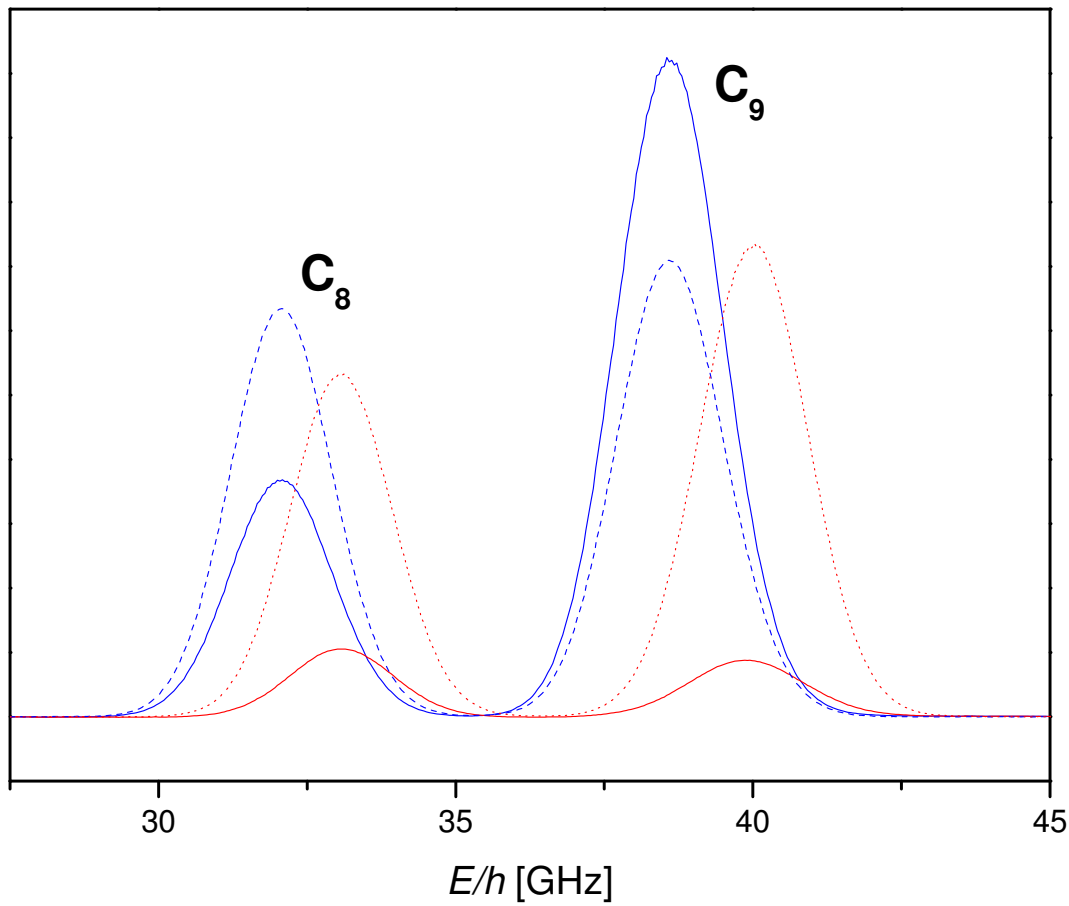

Figure 4.3: Experimental absorption spectrum of ^{3}He at $B = 30$ mT, $p_3 = 1.07$ mbar: Intensity (same convention as in figure 4.2) as function of probe laser frequency for $M = 0$ (dashed line: σ^-, dotted line: σ^+) and $M = 0.5$ (solid lines for both σ^- and σ^+, distinguishable by peak positions: same as at $M = 0$). This sweep of the probe laser frequency is recorded during a polarisation decay: the pump laser is turned off and the decay rate of $\Gamma_\mathrm{D} = (238\,\mathrm{s})^{-1}$ is sufficiently low so that $M =$ constant during a complete frequency sweep from approximately 27.5 GHz to 45 GHz within 10 to 20 s typically (frequency swept at 0.05-0.1 Hz approximately, leading to a sweeping rate of roughly 0.9-1.8 GHz/s).

at this point can thus be written as:

$$\frac{dI}{dl} = -k_a(l)\ I \tag{4.1}$$

where $k_a(l)$ is the local absorption rate and l the corresponding linear coordinate along the straight beam path. The probe transmission coefficient T_s, experimentally measured as the ratio of transmitted and incident beam powers, is therefore given by:

$$T_s = \frac{I_\mathrm{T}}{I_0} = \exp\left(-\int_0^{L_{path}} k_a(l)\ dl\right) \tag{4.2}$$

where I_T and I_0 are the incident and transmitted uniform probe intensities (see figure 4.4). Equation (4.2) is referred to as Lambert-Beer law.
In our experiments, both the number density of 2^3S atoms and the distributions of

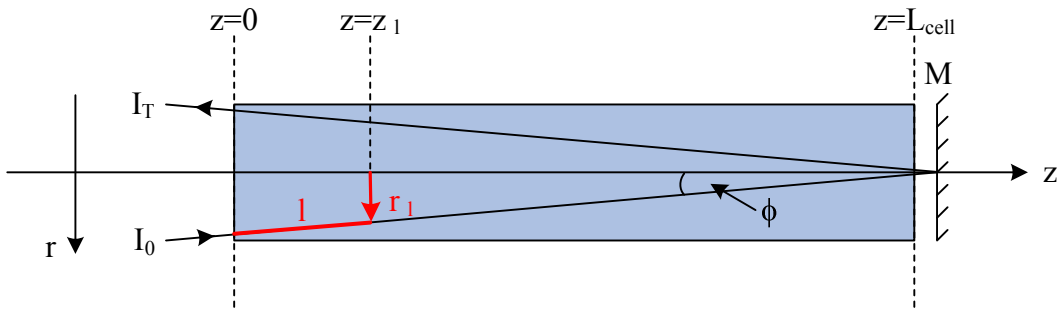

Figure 4.4: Longitudinal probe scheme in double pass configuration: the inclined probe beam (ϕ is the tilt angle) is back reflected by a mirror (M), all other parameters are explained in the text.

atoms between Zeeman sublevels of the upper and lower states inside the cell only depends on the radial distance r to the cell axis. Therefore, the probe transmission coefficient explicitly depends on the probe beam path geometry since, along the probe beam path, the local absorption rate $k_a(l)$ varies with the radial coordinate r_l that, in turn, varies with the longitudinal coordinate z_l (see figure 4.4).

The generic form of the local absorption rate is:

$$k_a(l) = \sum_{i,j} n_\mathrm{m}(r_l)\ \hbar\omega_{ij}\ \Gamma_{ij}\ (a_i(r_l) - b_j(r_l)), \tag{4.3}$$

where the coefficient Γ_{ij} is equal to $\Gamma_{ij} = \gamma_{ij}/I$ and γ_{ij} (resp., ω_{ij}) is the optical transition rate (resp., angular frequency) for the excited $\mathrm{A}_i \rightarrow \mathrm{B}_j$ line component of the $2^3\mathrm{S}-2^3\mathrm{P}$ atomic transition.

The single-frequency probe addresses atoms of a given velocity class, depending on its exact tuning. When OP introduces correlations between velocity and populations, absorption signals depend on probe frequency as illustrated in section 6.2.1. In the frame of the improved (2-class) OP model, populations of the strongly pumped class are the more relevant ones for a tuned probe, but they probably underestimate population skewing induced by the OP light in the centre of the velocity distribution.

For absorption measurements performed *in the absence of pump light* (i.e., during polarisation decay), as discussed in section 2.8.2, equation (4.3) is valid with $b_j = 0$ in the 2^3P state and $a_i \simeq a_i^{\mathrm{ST}}(M)$, where a_i^{ST} is the polarisation-dependent uniform spin-temperature distribution (equations (2.59) and (2.56)) established in the 2^3S state. It then reads:

$$k_a^{\ no\ OP}(l) = n_{\mathrm{m}}(r_l) \sum_{i,j} \hbar\omega_{ij}\ \overline{\Gamma_{ij}}\ a_i^{\mathrm{ST}}(M), \tag{4.4}$$

where $\overline{\Gamma_{ij}}$ is the coefficient associated to the Maxwell-averaged optical transition rate $\overline{\gamma_{ij}}$ for the $\mathrm{A}_i \rightarrow \mathrm{B}_j$ line component (equation (2.14)):

$$\overline{\Gamma_{ij}} = \frac{\sqrt{\pi}\alpha f}{m_e \omega D}\ T_{ij}\ \mathrm{e}^{-(\delta_{\mathrm{L}}^{ij}/D)^2}, \tag{4.5}$$

where the prefactor $\sqrt{\pi}\alpha f\ /\ (m_e\omega D)$ has the value given by equation (2.13). In equation (4.5), the transition matrix elements T_{ij} depend on magnetic field B, and δ_{L}^{ij} designates the probe detuning with respect to the atomic transition frequency (see section 2.3.1).

The probe absorbance in the absence of pump light is:

$$-\ln T_s^{\ \mathrm{no\ OP}} = \int_0^{L_{path}} k_a^{\ no\ OP}(l)\ dl = L_{\mathrm{path}}\ n_{\mathrm{m}}^{\mathrm{S}} \sum_{i,j} \hbar\omega_{ij}\ \overline{\Gamma_{ij}}\ a_i^{\mathrm{ST}}(M), \tag{4.6}$$

where

$$n_{\mathrm{m}}^{\mathrm{S}} = \frac{1}{L_{\mathrm{path}}} \int_0^{L_{\mathrm{path}}} n_{\mathrm{m}}(r_l)\ dl \tag{4.7}$$

is the average 2^3S number density along the probe beam path, and $T_s^{\ \mathrm{no\ OP}}$ the measured probe transmission coefficient in absence of pump laser light. In equation (4.6), $n_{\mathrm{m}}^{\mathrm{S}}$ depends on plasma conditions that vary with M, a_i^{ST} explicitly depends on nuclear polarisation, and $\overline{\Gamma_{ij}}$ depends on magnetic field and probe frequency.

We will explain in the following sections how the measurements of the light transmission coefficients for the σ^+ and σ^- probe beam components can be combined to infer the value of the ground state polarisation M (section 4.2) and of the metastable density $n_{\mathrm{m}}^{\mathrm{S}}$ (section 4.4). Actually the experimental data are combined to $\overline{n_{\mathrm{m}}^{\mathrm{S}}} = (\overline{n_{\mathrm{m}}^{\mathrm{S}+}} + \overline{n_{\mathrm{m}}^{\mathrm{S}-}})/2$ since we use a split probe beam (cf. section 3.2) and the two components σ^+ and σ^- do not exactly probe the rf plasma at the same locations inside the cell.

For absorption measurements performed *in the presence of pump light* (i.e., during polarisation build-up or at OP steady-state), the distributions of populations in 2^3S and 2^3P are expected to be strongly perturbed (see section 2.8.3 for quantitative description and illustrative computations) and we cannot exclude that the 2^3S number density is also altered by a resonant optogalvanic effect. For this reason no similar analysis of the measured transmission coefficients can be performed. In the absence of complementary measurements providing full knowledge of the distribution of atoms within Zeeman sublevels in the 2^3S and 2^3P states, no attempt is made to infer the 2^3S number density from our data in presence of pumping light. The polarisation measurements described in section 4.3 refer to measurements of the apparent nuclear polarisation M^a that is obtained from the measured probe transmission coefficients when equation (4.6) is used and the 2^3S number density is assumed to be unaltered (or, at least, to be similarly altered for the $\sigma^+$and σ^- probe beam components). The adequate form of equation (4.3), valid within the framework of the improved 2-class OP model and used, for instance, for the numerical computations of probe transmission coefficients is given in appendix B.

4.2 Polarisation measurements in the absence of OP light (during polarisation decay)

In section 2.8.2, it is discussed in detail, that during polarisation decay in absence of OP, the departure of the population distribution in 2^3S from a ST distribution induced by 2^3S relaxation is very small. Hence the populations $a_i^{\text{no OP}}$ can be safely replaced by the a_i^{ST} ones during polarisation decay.

The measured absorption signals, A_{σ^+} and A_{σ^-} in the longitudinal probe scheme, are the amplitudes of the modulation depth (i.e., the ratios of ac amplitudes to dc components) of the corresponding probe powers exiting the cell [Tal11]. Each ratio is robust against fluctuations of the incident power I_0 and directly proportional to the absorbance $-\ln T_s$, with a coefficient that only depends on the plasma response to the rf excitation [Cou02, Cou01]. Neglecting all constant prefactors, A is given by:

$$A(M) \propto n_{\text{m}}^{\text{S}}(M) \sum_{i,j} \hbar\omega_{ij}\, T_{ij}(B)\, \mathrm{e}^{-(\delta_{\text{L}}^{ij}/D)^2}\, a_i^{\text{ST}}(M). \tag{4.8}$$

By using the ratio r of the two measured absorption signals, A_{σ^+} and A_{σ^-}, which will be denoted A_+ and A_- for simplicity in the following

$$r(M) = \frac{A_+}{A_-}, \tag{4.9}$$

it is possible to eliminate $n_{\mathrm{m}}^{\mathrm{S}}(M)$. This elimination of $n_{\mathrm{m}}^{\mathrm{S}}$ in r is exact in case both probe light components have the same path or at uniform metastable density. In our configuration, σ^+ and σ^- components had to be spatially separated (cf. section 3.2), and the resulting small geometrical effect is taken into account for determinations of absolute values of metastable densities (cf. section 4.4). Furthermore, in the ratio r, the coefficient depending on plasma response to rf excitation, as well as L_{path} and the prefactor of equation (4.5) cancel out exactly. (In equation (4.8), they did not explicitly appear ("$\propto$" instead of "=") for clearness).
Thus, the ratio r of σ^+ and σ^- probe absorption signals only depends on nuclear polarisation M (and detuning and B).

The comparison with A-values measured at $M = 0$ yields the normalised, reduced ratio R of absorption signals:

$$R = \frac{r(M)}{r(M=0)} = \frac{A_+ A_-(0)}{A_- A_+(0)}. \tag{4.10}$$

As a matter of course, reduced ratios can be determined for absorption signals on C_8 and C_9 transitions, denoted R_8 and R_9. Details will be provided in sections 4.2.1 and 4.2.2; here, we will limit the discussion to some general remarks.
For the single-component transition C_8, no sum appears in equation (4.8), and therefore, the B-dependent transition intensities as well as the spectral factor exactly cancel out in each contribution of the reduced ratio R_8: in $\frac{A_+}{A_+(0)}$ and in $\frac{A_-}{A_-(0)}$.
For the two-component transition C_9, the reduced ratio R_9 depends on detuning due to the Zeeman shift: $\delta_{\mathrm{L}} = (\omega(B=0) - \omega_{ij}(B))/2\pi$. Detuning is different for each component at given light polarisation, and also different for σ^+ and σ^-. For the moderate magnetic fields used in this work up to 30 mT, the probe laser frequency ω_L was fixed to the transition in $B = 0$: $\omega_L = \omega(B = 0)$. In case $\omega_L \neq \omega(B = 0)$, an additional detuning has to be taken into account. The transition intensities $T_{ij}(B)$ also do not cancel out, since in A_+ and A_- as well as in $A_+(M = 0)$ $A_-(M = 0)$, a sum of both transition components has to be considered in each case. A small effect of dependencies on B and detuning remains in R_9, it is discussed in detail in section 4.2.2.

In practice, for all analyses throughout this work, the reduced ratios R_8 and R_9 are used to determine M_8 and M_9 respectively. Disadvantages of taking the simple ratio r for C_8 and C_9 as well as dependencies of the reduced ratio on magnetic field and detuning are illustrated by computed absorption signals in sections 4.2.1 and 4.2.2.

Figure 4.5 represents each contribution to the reduced ratio R separately: the reduced probe absorption signals $A_+ \,/\, A_+(0)$ and $A_- \,/\, A_-(0)$.
The variation of computed reduced probe absorption signals with nuclear polarisation M is shown in the spin temperature limit (cf. section 2.8.1), both for C_8 (left)

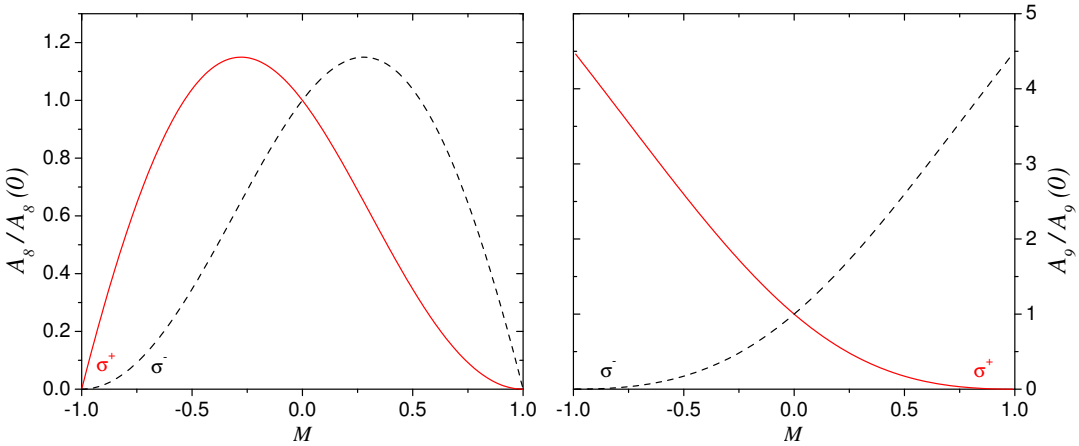

Figure 4.5: Reduced probe absorption signals ($A_\pm$ / $A_\pm(0)$) in spin temperature limit as a function of nuclear polarisation M. (Negative values of M can be obtained by σ^- pump light, positive M values by σ^+ pump light). Solid lines: σ^+ probe light, dashed lines: σ^- probe light. Left: C_8 transition, right: C_9 transition (note the different y-scales of C_8 and C_9 probe absorption signals). Computations are based on three simplifications: 1/ metastable density assumed to be independent of M: $n_\mathrm{m}^\mathrm{S}(M)$ / $n_\mathrm{m}^\mathrm{S}(0) = 1$; 2/ populations in 2^3P assumed to be negligible: $b_j = 0$ and 3/ $\gamma_\mathrm{r}^\mathrm{S} = 0$.

and C_9 (right), for the simple case where the metastable density is assumed to be independent of M: $n_\mathrm{m}^\mathrm{S}(M)$ / $n_\mathrm{m}^\mathrm{S}(0) = 1$. In the experiments, metastable density is observed to change with M (see section 6.1.3). However, as discussed above, the polarisation is inferred from reduced *ratios* of σ^+ and σ^- absorption signals for which the prefactor $n_\mathrm{m}^\mathrm{S}(M) / n_\mathrm{m}^\mathrm{S}(0)$ cancels out. This is one reason for the necessity to record *two* different absorption signals in order to provide the *ratio* of two absorption signals, that is *in*dependent of metastable density as function of polarisation.

Figure 4.5 thus merely provides a qualitative impression of the relation between calculated reduced probe absorption signals and nuclear polarisation, and hence is *not* intended to determine M quantitatively from measured probe absorption signals.

We now briefly sketch how the nuclear polarisation M can be determined from the ratio of probe absorption signals, and we infer a general formula.

In the spin temperature limit (introduced in section 2.8.1), the ratio of populations of *two* adjacent sublevels is known and can be expressed by equation (2.58) that we recall here for improved readability:

$$\frac{a_2^\mathrm{ST}}{a_1^\mathrm{ST}} = \frac{a_3^\mathrm{ST}}{a_2^\mathrm{ST}} = \frac{a_4^\mathrm{ST}}{a_3^\mathrm{ST}} = \frac{a_6^\mathrm{ST}}{a_5^\mathrm{ST}} = \mathrm{e}^\beta = \frac{1+M}{1-M}.$$

It is thus required to probe more than one relative population in 2^3S in order to

determine a *ratio* of adjacent populations, which constitutes the second reason for probing *two* different sublevels of the 2^3S state.

The nuclear ground state polarisation can then be deduced from a ratio of adjacent populations given by a measured ratio of two absorption signals using

$$M = \frac{e^{\beta} - 1}{e^{\beta} + 1}. \tag{4.11}$$

In the following two sections 4.2.1 and 4.2.2, this general formula will be refined for measurements with the probe laser tuned to C_8 and to C_9.

4.2.1 Determination of M by C_8 probe

For the single-component transition C_8, the determination of nuclear polarisation M_8 is a straight forward procedure. Knowing that C_8 σ^+ is a transition from the 2^3S sublevel A_5 to the 2^3P sublevel B_{17} and C_8 σ^- from A_6 to B_{18} respectively, and using equations (4.10), (4.8) and (2.58), the reduced ratio R_8 is given by:

$$R_8 = \left.\frac{A_+A_-(0)}{A_-A_+(0)}\right|_{C_8} = \frac{a_5(M)}{a_6(M)} = \frac{1}{e^{\beta}(C_8)} = \frac{1 - M_8}{1 + M_8}, \tag{4.12}$$

where M_8 designates the nuclear polarisation measured by a C_8 probe laser in absence of OP light. $a_i^{ST}(M = 0)$ equals 1/6, but cancels out in the reduced ratio anyway. For simplicity we write only a_i for a_i^{ST} here and in the following. Solving equation (4.12) for M_8 yields:

$$M_8 = \frac{1 - \frac{a_5}{a_6}}{1 + \frac{a_5}{a_6}} = \frac{1 - R_8}{1 + R_8}. \tag{4.13}$$

Equation (4.13) shows that M_8 determined from the reduced ratio R_8 is exact in all conditions, i.e. *completely* independent of probe detuning and of magnetic field ($T_{ij}(B)$-values cancel out).
Therefore, we do not distinguish the cases $B = 0$ and $B \neq 0$ for probe C_8.

Figure 4.6 represents computed M_8 values (more details on methodological aspects concerning these computations are given in the paragraph about C_9 probe at $B \neq 0$ in section 4.2.2) and illustrates the exactness of M_8 values inferred from the reduced ratio R_8 in $B = 30$ mT and the independence of probe detuning within reasonable limits (as long as other transitions play no role). For comparison M_8 inferred from r_8 is added as a function of probe detuning.
The advantage of taking the reduced ratio R_8 instead of the ratio r_8 for probe C_8 is clearly demonstrated in figure 4.6.

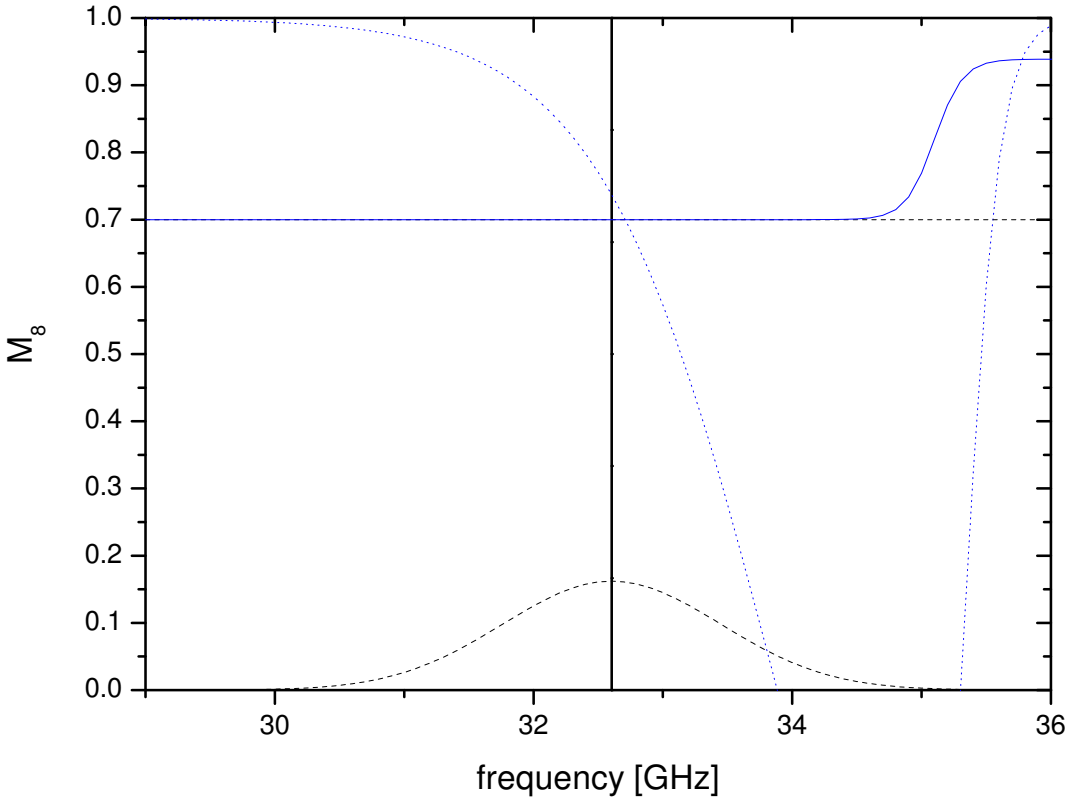

Figure 4.6: Computed nuclear polarisation M_8 for a probe laser tuned to the C_8 transition in spin temperature limit as a function of probe frequency at $B = 30$ mT and given $M = 0.7$ (dashed straight line). M_8 is either determined from the reduced ratio R_8 of absorption signals (solid line) or from the ratio r_8 of absorption signals (dotted line). The lowest dashed line is the absorption profile of the C_8 transition at $B = 0$.

4.2.2 Determination of M by C_9 probe

C_9 probe at $B = 0$

No simple analytical formula exists for the C_9 line for which each polarisation component addresses simultaneously two Zeeman sublevels. The reduced ratio R_9 of absorption signals can be expressed using equation (4.8) for $B = 0$, and equation (2.59) in order to express R_9 in terms of e^{β}:

$$R_9 = \frac{A_+A_-(0)}{A_-A_+(0)} = \frac{T_{1,18}\, a_1 + T_{2,17}\, a_2}{T_{4,17}\, a_4 + T_{3,18}\, a_3}$$
$$= \frac{T_{1,18}\, e^{-\frac{3}{2}\beta} + T_{2,17}\, e^{-\frac{1}{2}\beta}}{T_{4,17}\, e^{\frac{3}{2}\beta} + T_{3,18}\, e^{\frac{1}{2}\beta}} = \frac{3e^{-\frac{3}{2}\beta} + e^{-\frac{1}{2}\beta}}{3e^{\frac{3}{2}\beta} + e^{\frac{1}{2}\beta}}, \tag{4.14}$$

which takes into account the different transition intensities T_{ij} of the two components constituting C_9: $T_{1,18} = T_{4,17} = 0.28111$ and $T_{2,17} = T_{3,18} = 0.0937$ in zero magnetic field. The ratio of transition intensities of the two components of $3 : 1$ ($T_{1,18} : T_{2,17} = T_{4,17} : T_{3,18}$) is strictly valid at $B = 0$ only. (The effects of magnetic field on probe measurements on the C_9 transition are discussed in the following paragraph below.)

The reduced ratio R_9 can also be expressed as a function of M_9 (nuclear polarisation measured by a C_9 probe laser in absence of OP light). Using $e^{\beta} = (1+M)/(1-M)$ (cf. equation (2.58)) in equation (4.14) yields after simplification:

$$R_9 = \left(\frac{2 - M_9}{2 + M_9}\right)\left(\frac{1 - M_9}{1 + M_9}\right)^2. \tag{4.15}$$

This relation has to be solved (e.g., finding the root of a cubic polynomial, numerically, or using polynomial fits...) to infer M_9 from R_9.

We solved equation (4.14) for e^{β} :

$$e^{\beta}{}_{C9} = \frac{1}{9}\left(-1 + \frac{9 + R_9}{f(R_9)} + \frac{f(R_9)}{R_9}\right), \tag{4.16}$$

where $f(R_9)$ is given by:

$$f(R_9) = \left(351R_9^2 - R_9^3 + 9\sqrt{3}\, R_9 \sqrt{-R_9(3 - 506R_9 + 3R_9^2)}\right)^{1/3}. \tag{4.17}$$

Using equations (4.16) and (4.17) in equation (4.11) allows to determine the nuclear ground state polarisation M_9.

This analytic formula is applicable in the range of $R_9 > 0.006$, which in terms of nuclear polarisation corresponds to M-values < 0.79. At higher polarisation, i.e. lower values of R_9, the radicand of the second square root in equation (4.17) becomes negative.

Another possibility to infer M from the reduced ratio R_9 is to implement equation (4.15) in a dedicated programme in order to compute R_9 at given M_9 and to compare this computed R_9^{th} to the experimentally measured R_9^{exp}. Efficient numerical dichotomy with 20 steps rapidly provides 10^{-6} accuracy.

Furthermore, an approximation of M_9 as function of $-\ln\left(R_9^{-1}\right)$ can be used to infer M_9 from the inverse reduced ratio $R_9^{-1} = \frac{A_- A_+(0)}{A_+ A_-(0)}$:

$$M_9 = -0.2035\ \ln\left(R_9^{-1}\right) - 0.00439\left(\ln\left(R_9^{-1}\right)\right)^2 + 0.00105\left(\ln\left(R_9^{-1}\right)\right)^3. \tag{4.18}$$

For $M_9 \lesssim 0.75$, this cubic function constitutes a good approximation for practical use with residuals below 0.2 %.

Our standard procedure to infer M_9 consisted in using a dedicated programme into which the described dichotomic approach was implemented. Over the whole range of $-1 \leq M_9 \leq 1$, residuals are below 2×10^{-4}.

C_9 probe at $B \neq 0$

When C_9 is used as probe transition, each beam component σ^+ and σ^- simultaneously probes two 2^3S sublevels. In $B \neq 0$, this fact automatically entails a tuning issue, as it is impossible to keep detuning zero for *both* components at the same time. C_9 has a residual B dependency due to Zeeman shifts and due to the sum of the transition intensities of both components, different for σ^+ and σ^-, that do not cancel out in the reduced ratio.

The effects of B on C_9 probe measurements are presented here for pure ^{3}He first, before in the next paragraph the influence of residual ^{4}He at $B = 1$ mT and $B = 30$ mT is investigated.

In order to examine the influences of B on C_9 probe measurements, the model for MEOP-kinetics is used to compute absorption signals for the three light polarisations σ^+, σ^- and π as function of the probe frequency at given value of nuclear polarisation M defined by the user (π light is not required for our longitudinal probe scheme). The ratio of absorption signals r is computed for the given value of M and at $M = 0$, so that the reduced ratio R can be inferred as well. M_9 is then determined

either from the ratio r or from the reduced ratio R by dichotomy as described above, in the paragraph about C_9 probe at $B = 0$ on page 90, for two different assumptions:

1/ Either using a fixed ratio of transition intensities T_{ij} of the two components of $3:1$ (equation (4.14)) in order to evaluate whether the introduced error remains low enough in $B \neq 0$ to justify the use of this 'simplified approach', or

2/ taking into account the modified values of $T_{ij}(B)$ and the Zeeman shifts of σ^+ and σ^- components to determine M_9 more precisely ('exact approach'). In non-zero magnetic field, the transition intensities of the σ^+ and σ^- components of C_9 are no longer equal as in $B = 0$, and each $T_{ij}(B = 0)$ value in equation (4.14) has to be replaced by

$$T_{ij}(B)\ \exp\left[-\left(\frac{\omega_9(B=0)-\omega_{ij}(B)}{2\pi D}\right)^2\right], \tag{4.19}$$

with $\omega_9(B = 0) = 39.3442$ GHz: frequency of the C_9-transition in $B = 0$, $\omega_{ij}(B)$: transition frequency of each line component in $B \neq 0$ and D: Doppler width of ^{3}He, approximately 1.19 GHz at room temperature ($T = 300$ K). Furthermore, in order to normalise equation (4.14) at $B \neq 0$, it has to be divided by the ratio of sums of transition intensities of both C_9 components: $(T_{1,18}(B) + T_{2,17}(B))\ /\ (T_{4,17}(B) + T_{3,18}(B))$ (at $B = 0$, this ratio equals 1).
All figures in the following up to the end of this section 4.2 are based on computed probe absorption signals as explained above.

Figure 4.7 illustrates the influence of magnetic field on the determination of nuclear polarisation on the C_9 transition at given $M = 0.7$ in pure ^{3}He using (computed) reduced probe absorption ratios.
The solid lines representing M_9 as function of probe frequency for different values of B are determined using a fixed ratio of transition intensities T_{ij} of the two line components within C_9 of $3:1$ (see equation (4.14)) and neglecting Zeeman shifts of the σ^+ and σ^- polarisation components.
The relative errors introduced by this simplified approach lead to an underestimation of M and amount to 0.03 % at $B = 1$ mT (curve 1r), 0.1 % at $B = 3$ mT (curve 2r), 0.8 % at $B = 10$ mT (curve 3rb) and 6 % at $B = 30$ mT (curve 4rb), supposing in all cases the probe laser tuned to resonance in $B = 0$. For $B = 1$ and 3 mT, the errors are negligible and this simplified approach is justified. At higher B however, taking into account a possible detuning of the probe laser of up to $\pm$ 0.38 GHz, corresponding to a 10 % loss in absorption amplitude, the relative errors introduced by the simplified approach vary between 0.4 % and 1.2 % at $B = 10$ mT and between 5.4 % and 7 % at $B = 30$ mT, and are thus non-negligible for $B > 10$ mT, as they increase non-linearily with increasing B.
Taking into account the exact $T_{ij}(B)$ values and the Zeeman shifts of the σ^+ and σ^- components to determine M_9 from the reduced absorption ratio in $B \neq 0$ - this

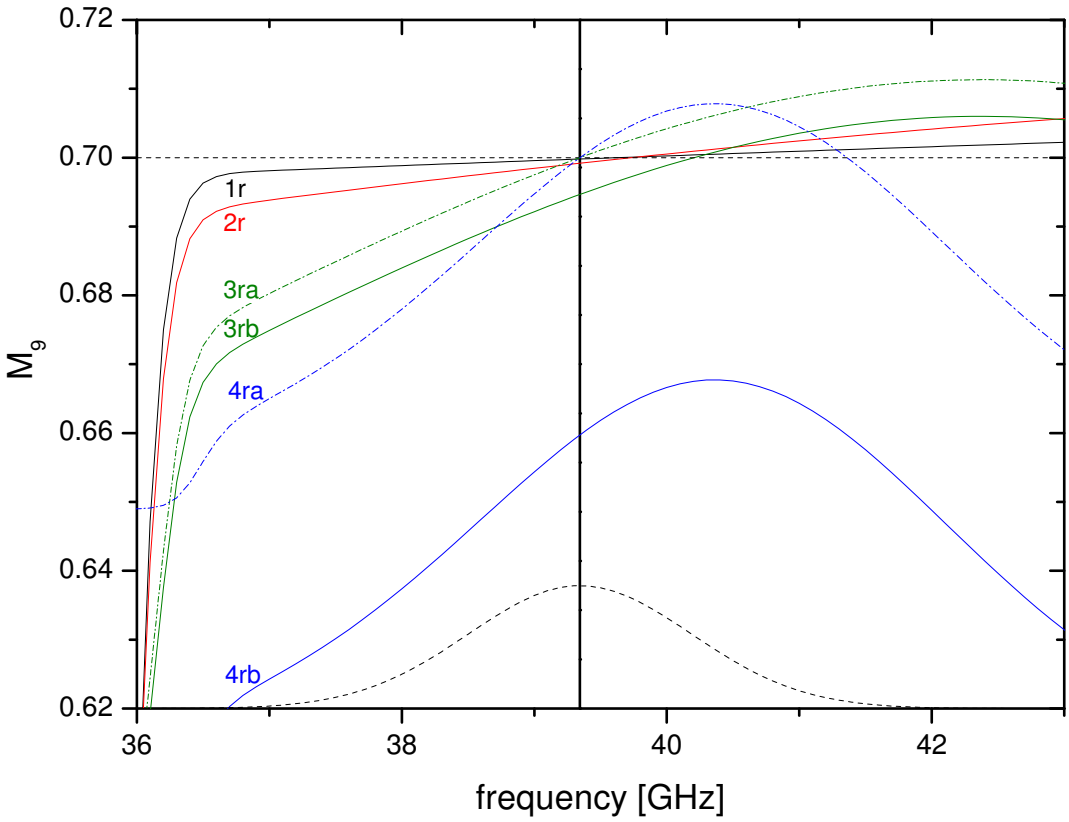

Figure 4.7: Nuclear polarisation M_9 in pure ^{3}He for a probe laser tuned to the C_9 transition in spin temperature limit as function of probe frequency for different magnetic field values B. M_9 is determined from computed probe absorption signals at given $M = 0.7$ (straight dashed line) by the model for MEOP-kinetics. The determination of M_9 is based on the *reduced* ratio R of probe absorption signals here (see text, indicator "r" on each curve). Curved dashed line (bottom): Absorption profile of C_9 transition as function of frequency (not to scale) at $M = 0$ and $B = 50\,\mu$T.
Solid lines: Fixed ratio of transition intensities of the two line-components within C_9 used and Zeeman shifts neglected: 1r: $B = 1$ mT, 2r: $B = 3$ mT, 3rb: $B = 10$ mT, 4rb: $B = 30$ mT; vertical solid line: $\omega_9(B = 0) = 39.3442$ GHz, frequency of the C_9-transition in $B = 0$.
Dash-dotted lines: $T_{ij}(B)$ and Zeeman shifts of σ^+ and σ^- components taken into account: 3ra: $B = 10$ mT, 4ra: $B = 30$ mT. Note the zoom on the y-axis with respect to figure 4.8.

is a less straight forward but more precise analysing procedure - solves the problem of residual errors on M_9 at $B = 10$ mT (curve 3ra) and $B = 30$ mT (curve 4ra), but only exactly in resonance of $B = 0$. Within a possible probe detuning of $\pm$ 0.38 GHz, these systematic relative errors amount to $\pm$ 0.4 % at $B = 10$ mT and $\pm$ 0.8 % at $B = 30$ mT. These relative errors of less than 1 % are acceptable, but care has to be taken in tuning the probe laser, so as to *not* exceed the above mentioned detuning limit, especially as detuning towards higher frequencies than $\omega_9(B = 0)$ can lead to an overestimation of M_9 compared to the given M of 0.7 in this case.

Figure 4.8 presents M_9 values determined from the ratio r of probe absorption signals (dotted lines) for different B values, either assuming a fixed ratio of $T_{ij}(B = 0)$ values and neglecting Zeeman shifts, or taking explicitly into account $T_{ij}(B)$ values and Zeeman shifts of σ^+ and σ^- components. For comparison, four curves at different values of B from figure 4.7 (determination of M_9 based on reduced ratio R, for fixed ratio of $T_{ij}(B = 0)$ and Zeeman shifts neglected) are added.
Obviously, even at lower B (curves 1 and 2 for $B = 1$ and 3 mT respectively), it is better to base the determination of M_9 on the *reduced* ratio R of probe absorption signals to limit systematic errors, especially in case of possible probe detuning. At higher B (curves 3b and 4b for $B = 10$ and 30 mT respectively), even in resonance, the nuclear polarisation is underestimated by 1 % at 10 mT and by more than 7 % at 30 mT. Taking into account the exact $T_{ij}(B)$ values and the Zeeman shifts of the σ^+ and σ^- components in the considered magnetic field, solves this issue in resonance, but within a realistic possible probe detuning of $\pm$ 0.38 GHz, M_9 varies by $\mp$ 4 % at $B = 10$ mT and by $\mp$ 14 % at $B = 30$ mT.

These results clearly show that it is preferable to always use the reduced ratio R_9 (see equation (4.14)) in order to determine nuclear polarisation values with the help of probe absorption measurements on the C_9 transition.

However, the previous graphs for probe C_9 also show that even the best possible analysing method (based on the reduced absorption ratio and taking into account exact transition intensities and Zeeman shifts of σ^+ and σ^- polarisation components in $B \neq 0$) does *not* eliminate the effect of a possible uncontrolled probe detuning in B. This constitutes one intrinsic difficulty of using C_9 as probe transition.

All previous graphs and corresponding observations concerning a probe laser tuned to the C_9 transition in pure ^{3}He, are valid for a given value of nuclear polarisation of $M = 0.7$. To conclude the discussion of effects of magnetic field on C_9 probe measurements, the ratios of *different* values of given M divided by the corresponding M_9 as function of the probe frequency are presented in figure 4.9 at $B = 30$ mT.

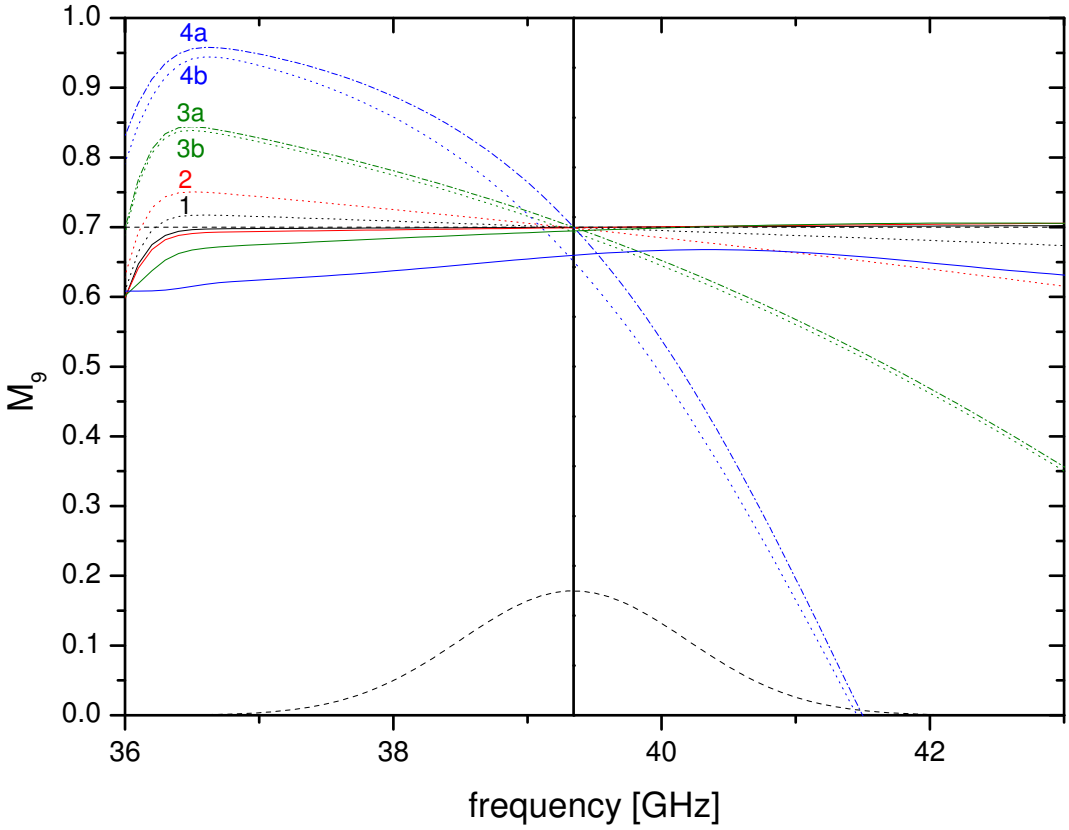

Figure 4.8: Dotted lines: M_9 of pure ^{3}He in spin temperature limit determined from ratio r of probe absorption signals at given $M = 0.7$ as function of probe frequency for different values of B. 1: $B = 1$ mT, 2: $B = 3$ mT, 3b: $B = 10$ mT, 4b: $B = 30$ mT. At all B: fixed ratio of transition intensities of the two line-components within C_9 used and Zeeman shifts neglected.
Dash-dotted lines: $T_{ij}(B)$ and Zeeman shifts of σ^+ and σ^- components taken into account: 3a: $B = 10$ mT, 4a: $B = 30$ mT (M_9 determined from ratio r in both cases as well).
Solid lines: Curves 1r, 2r, 3rb and 4rb (top down) from figure 4.7 for comparison (determination of M_9 based on reduced ratio R, for fixed ratio of $T_{ij}(B = 0)$ and Zeeman shifts neglected); vertical solid line: $\omega_9(B = 0)$
Dashed lines: $M = 0.7$ constant and absorption profile (not to scale) of C_9 ($M = 0$, $B = 50\,\mu$T).
Note that the vertical scale is different from figure 4.7.

$B = 1$ mT is not represented here since the M-dependence in very low field is negligibly small (for pure ^{3}He).
All values of M_9 in this paragraph are based on the reduced ratio R of probe absorption signals.
Two cases are shown for four different values of nuclear polarisation each: either using exact transition intensities and Zeeman shifts of σ^+ and σ^- polarisation components at $B = 30$ mT (dash-dotted lines: 'exact approach') or using a fixed ratio of T_{ij} values of the two line-components of $3:1$ and neglecting Zeeman shifts (solid lines: 'simplified approach') for the transformation from the reduced ratio R of probe absorption signals (in both cases) into M_9 values. The chosen values of nuclear polarisation are from top to bottom: $M = 0.01$ (a/A), $M = 0.3$ (b/B), $M = 0.7$ (c/C) and $M = 0.99$ (d/D).
The main observed features in figure 4.9 at $B = 30$ mT of the ratio of given polarisation divided by the determined M_9 values are the following: In both cases, either using exact T_{ij} values and corresponding Zeeman shifts or a fixed ratio of transition intensities of $3:1$, the highest discrepancies between M and M_9 appear generally at low nuclear polarisation values and increase with increasing probe detuning. Using exact transition intensities and Zeeman shifts for the given magnetic field value eliminates the dependency of M in resonance of $B = 0$.
Within a possible realistic detuning range of $\Delta\omega = \pm\ 0.38$ GHz, the exact approach qualitatively underestimates nuclear polarisation (ratio of $M/M_9 > 1$) below resonance and overestimates M above resonance (ratio of $M/M_9 < 1$, except for $M = 0.01$, the ratio passes to slightly higher values than 1 at + 0.186 GHz above resonance). Using the simplified approach of fixed $T_{ij}(0)$ values, the determined M_9 generally underestimates M. The ratios of M/M_9 are always above 1, for detuning towards lower and higher frequencies, and also $\neq 1$ in resonance.
For the exact approach, the quantitative discrepancy between M and M_9 amounts to 0.04 % (for $M = 0.99$) up to 0.9 % (for $M = 0.3$) at $\Delta\omega$ below resonance, and ranges between - 0.65 % and + 0.17 % (for $M = 0.7$ and $M = 0.01$ respectively) at $\Delta\omega$ above resonance, the dependency of nuclear polarisation is thus weak and not exceeding 1 % anyway.
For the simplified approach, the qualitative discrepancies are overall higher, and also the dependency of M is more pronounced (see figure 4.9).

In conclusion it is preferable to use the exact transition intensities and Zeeman shifts to transform the reduced ratio of absorption signals of a probe laser tuned to the C_9 transition to nuclear polarisation values M_9 at given B. However, an intrinsic advantage of using C_8 as probe transition instead of C_9 consists in the possibility to completely eliminate the effect of detuning in magnetic field.

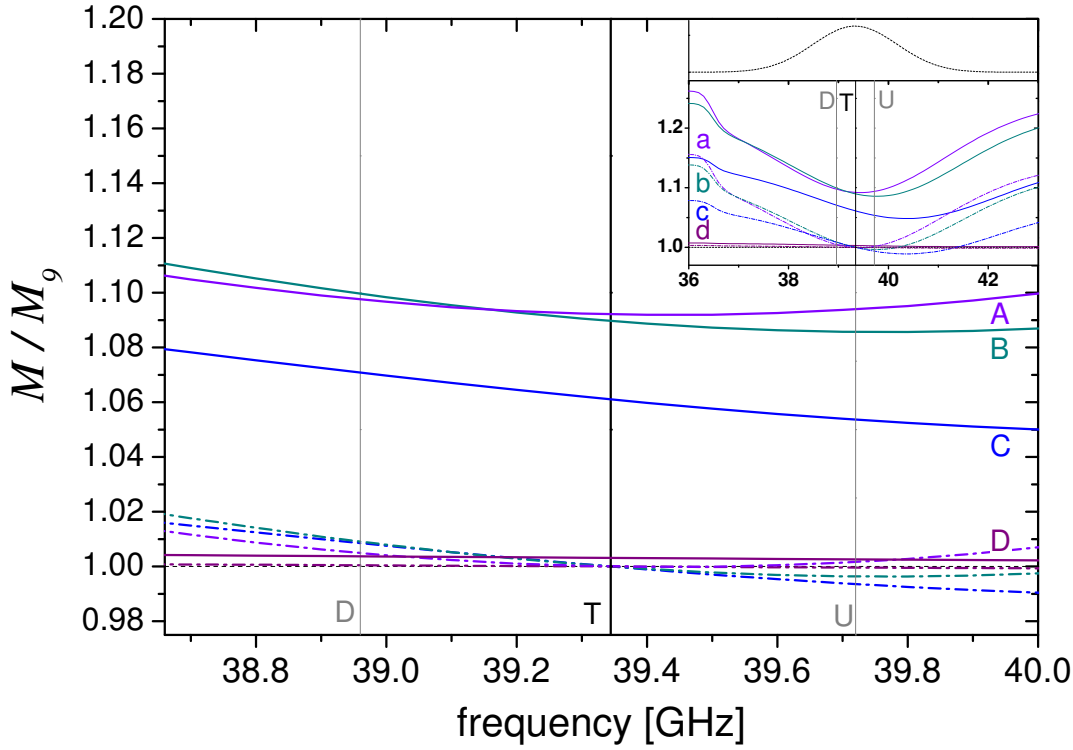

Figure 4.9: Ratios of different given nuclear polarisation values divided by the determined M_9 (based on the reduced ratio R of probe absorption signals) as function of probe frequency in pure ^{3}He at $B = 30$ mT: $M = 0.01$ (a/A), $M = 0.3$ (b/B), $M = 0.7$ (c/C) and $M = 0.99$ (d/D).
Dash-dotted lines (legend in *lower case letters* in the inset): Determination of M_9 using exact $T_{ij}(B)$ values and Zeeman shifts.
Solid lines (legend in *capital letters* in the main graph): Determination of M_9 using a fixed ratio of transition intensities of 3:1 and neglecting Zeeman shifts.
Central vertical line ('T' for '*t*uned' at $B = 0$): $\omega_9(B = 0)$, two lighter vertical lines (D ('*d*own'): $\Delta\omega$ below resonance and U ('*u*p'): $\Delta\omega$ above resonance): $\Delta\omega = \pm\, 0.38$ GHz (possible realistic probe detuning up to 10 % loss in the absorption amplitude).
Inset lower part: Global view over a larger frequency range of the same quantities as plotted in the main graph.
Inset upper part: Dashed line: C_9 absorption profile (not to scale) at $M = 0$, $B = 50\,\mu$T.

In the last part of this paragraph concerning intrinsic issues of using C_9 as probe transition in pure ^{3}He, the ratio of given M divided by the determined M_9 is discussed at fixed probe frequency as function of nuclear polarisation M. As in the paragraphs above, M_9 is inferred from computed probe absorption signals by the model for MEOP-kinetics, and its determination is **only based on reduced ratios** R of absorption signals **in the following**.

Figure 4.10 represents M/M_9 at $B = 30$ mT as function of M at three different fixed probe frequencies: at $\omega_9(B = 0)$ (curves 't' for exact approach and 'T' for simplified approach, explanations of approaches see page 91), at $\omega_9(B = 0) + \Delta\omega$ (curves 'u' and 'U'), and at $\omega_9(B = 0) - \Delta\omega$ (curves 'd' and 'D'). With respect to figure 4.9, the presented curves in figure 4.10 correspond to vertical cuts along the three vertical lines representing the resonance frequency and the borders of a realistic maximum possible detuning range to higher and lower frequencies.

Concerning the dependence of M/M_9 on nuclear polarisation M, figure 4.10 clearly shows that for the simplified approach (solid lines), the highest relative error is obtained at small absolute values of M, and it is decreasing with increasing absolute value of M. The maximum relative error of approximately 10 % is consistent with the value determined in figure 4.9. For the exact approach (dash-dotted lines), the relative error vanishes in resonance for all possible nuclear polarisation values between -1 and 1, and remains small (up to 1 %) within the possible assumed detuning range. As already observed in figure 4.9, for positive polarisation values, the relative error of M_9 with respect to the given M is higher when detuned below resonance (curve 'D') and lower when detuned above resonance (curve 'U') compared to the probe frequency exactly in resonance at $\omega_9(B = 0)$. This tendency is confirmed by the different representation in figure 4.10.

Effect of ^{4}He on C_9 probe at $B = 0$ and $B \neq 0$

The second intrinsic issue when using the two-component line C_9 as probe transition is the influence of possible residual traces of ^{4}He (remaining from the cell cleaning process prior to filling, see section 3.1) on the absorption measurements. Since the D_1 and D_2 resonances of ^{4}He are very close to the C_9 resonance of ^{3}He (about 1.5 GHz above and 0.8 GHz below, see tables A.1 and A.2), possible absorption of probe laser light by ^{4}He atoms thus leads to an error in the inferred nuclear ^{3}He polarisation. This error varies with the fraction x_4 of ^{4}He to ^{3}He partial pressures.

In the following, the influence of residual ^{4}He is discussed at given $M = 0.7$, for $B = 1$ mT and $B = 30$ mT. Like in the previous paragraphs, the model for MEOP-kinetics is used to compute σ^+ and σ^-absorption signals as a function of probe frequency at given value of nuclear polarisation M and given ratio x_4 (M and

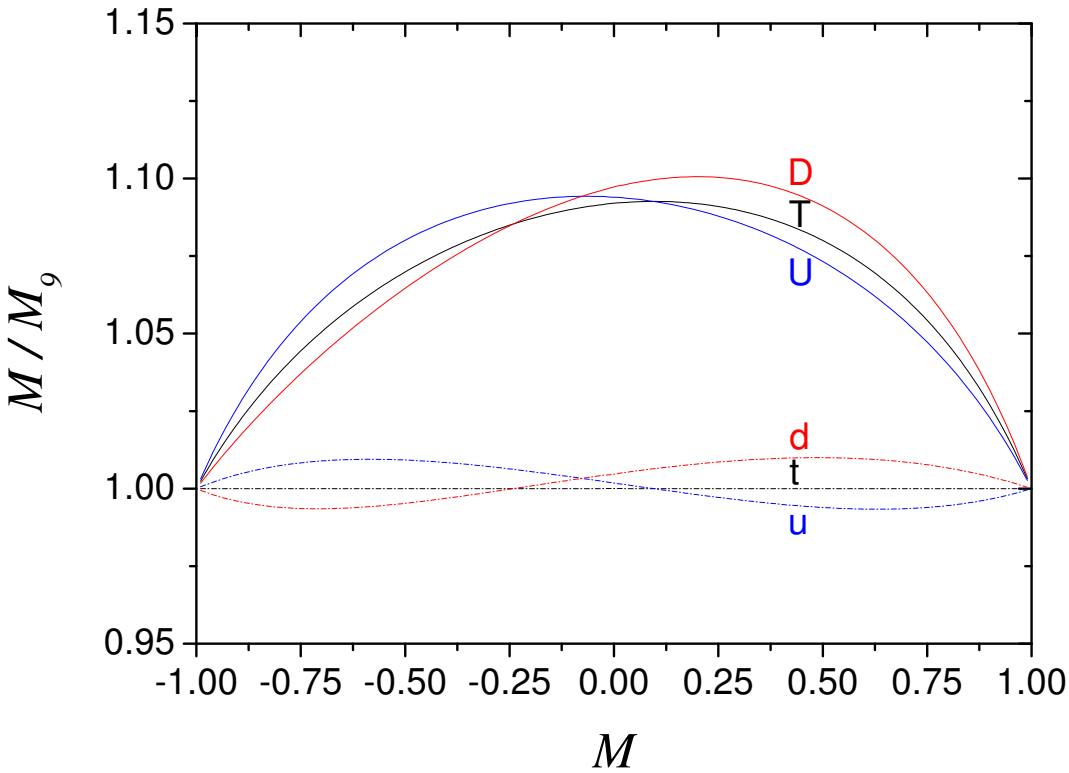

Figure 4.10: Ratio of given polarisation M divided by determined M_9 (based on the reduced ratio R of probe absorption signals) at fixed probe frequency as function of M in pure ^{3}He at $B = 30$ mT: t/T: 39.34422 GHz $= \omega_9(B = 0)$ ('*t*uned'), u/U: 39.72 GHz $= \omega_9(B = 0) + \Delta\omega$ ('*u*p'), d/D: 38.96 GHz $= \omega_9(B = 0) - \Delta\omega$ ('*d*own'). Dash-dotted lines (legend in lower case letters): Determination of M_9 using exact $T_{ij}(B)$ values and Zeeman shifts.
Solid lines (legend in capital letters): Determination of M_9 using a fixed ratio of transition intensities of 3 : 1 and neglecting Zeeman shifts.

x_4 are defined by the user).

Figure 4.11 represents computed nuclear polarisation values for probe on C_9 for different fractions of ^{4}He at given $M = 0.7$ and $B = 1$ mT. The determination of M_9 is based on the reduced ratio R of probe absorption signals.
Obviously, the discrepancies between the given value of M and the measured value

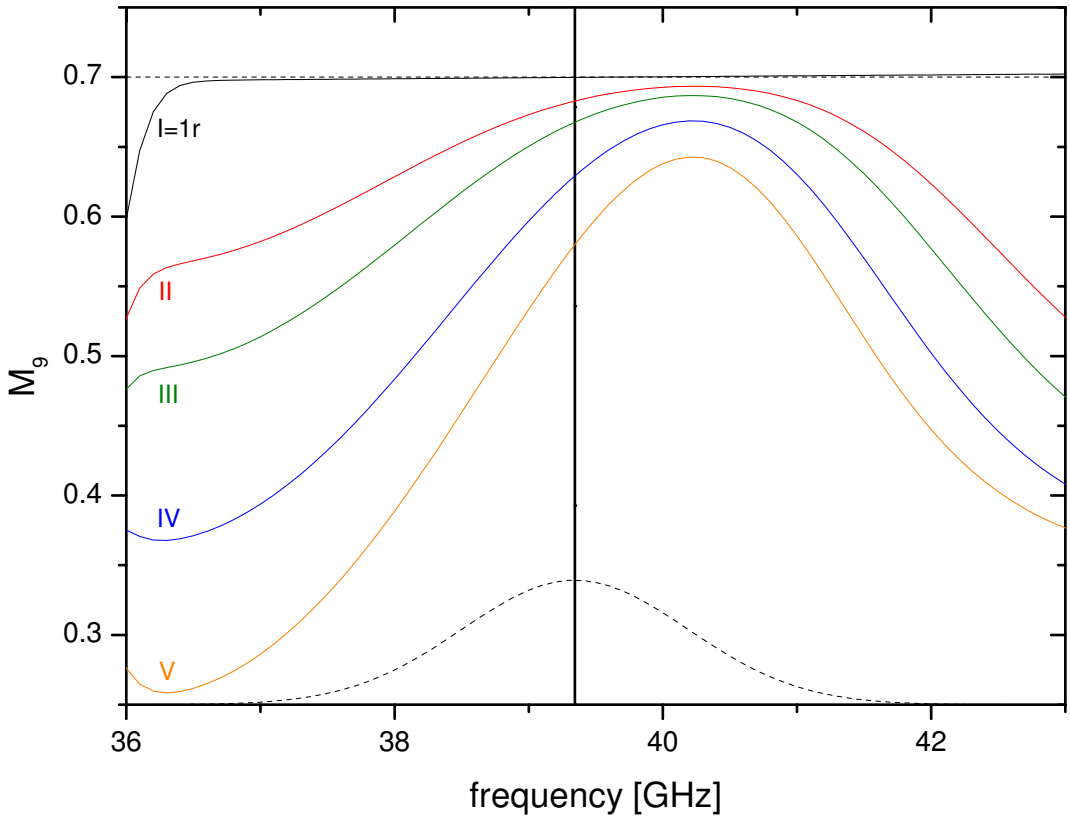

Figure 4.11: Influence of residual ^{4}He traces on measurement of nuclear polarisation by probe C_9 at $B = 1$ mT and $M = 0.7$ as function of probe frequency. M_9 is inferred using *reduced ratios* R of computed absorption signals for all different fractions x_4 of ^{4}He: curve I (corresponds to curve 1r of figure 4.7): pure ^{3}He, curve II: $x_4 = 0.1$ %, curve III: $x_4 = 0.2$ %, curve IV: $x_4 = 0.5$ %, curve V: $x_4 = 1$ %. Dashed lines: Top: Fixed $M = 0.7$; Bottom: C_9 absorption profile (not to scale) at $M = 0$, $B = 50\,\mu$T. Vertical solid line: $\omega_9(B = 0)$.

of M_9 increase with increasing fraction of ^{4}He: M_9 underestimates the given nuclear polarisation in all cases, and the relative errors in resonance range from 2.5 % for $x_4 = 0.1$ % to almost 21 % for $x_4 = 1$ % of ^{4}He. These discrepancies are even higher in case the probe is detuned to lower frequencies, and lower up to approxi-

mately 40.2 GHz, where a local minimum of relative errors is found. At this probe frequency the discrepancies vary between 1 % (for $x_4 = 0.1$ %) and 9 % (for $x_4 = 1$ %).

At higher magnetic field, residual traces of ^{4}He have an even stronger impact on probe absorption measurements of M on the C_9 transition. In figure 4.12, the influence of ^{4}He on M_9 at given $M = 0.7$ and $B = 30$ mT is shown. For different fractions of ^{4}He, M_9 is plotted as function of probe frequency. In all cases, the determination of M_9 is based on the reduced ratio R of computed probe absorption signals.
Furthermore, for $x_4 = 0$ and $x_4 = 1$ %, the simplified approach (using a fixed ratio of transition intensities of both C_9 line components of $B = 0$ and neglecting Zeeman shifts when transforming the reduced ratio of probe absorption signals into values of M_9) is compared to the exact approach (using the exact T_{ij} values and Zeeman shifts at $B = 30$ mT).

Under the influence of residual ^{4}He traces, even the exact approach is unable to yield exact M_9 values in resonance. However, it is capable of reducing the discrepancy between given M and M_9 from 45 % using the simplified approach to 34 % using the exact approach for a fraction of $x_4 = 1$ % of ^{4}He in resonance. For less important fractions of ^{4}He, the relative errors of M_9 with respect to the given M of 0.7 in this example decrease to 27 % for $x_4 = 0.5$ %, almost 13 % for $x_4 = 0.2$ % and more than 7 % for $x_4 = 0.1$ % (in $B = 30$ mT using the exact approach), but do not vanish for $x_4 > 0.1$ %. For $x_4 = 0.1$ %, it is possible that M_9 matches the given value of M in case the probe is detuned to higher frequencies. A local minimum of relative errors is observed at approximately 40.7 GHz, but the discrepancy of M_9 compared to M for $x_4 = 1$ % still amounts to almost 10 % there.

The experimentally determined fractions of residual ^{4}He in the three cells used throughout this work vary between $x_4 = 0.07$ % and 0.4 % (cf. chapter 3.1).

In the following paragraph, still for the case of residual traces of ^{4}He, the polarisation dependence of the ratio of a given value of M divided by the determined M_9 from computed probe absorption signals on C_9 is discussed. As fraction of ^{4}He, $x_4 = 0.4$ % - the highest measured value in one of the cells used in this work - is chosen to give a realistic upper bound of the effect.
Figure 4.13 represents the ratio of M/M_9 as function of probe detuning in $B = 1$ mT. It clearly shows that the relative error introduced by using the probe laser on the C_9 transition is higher than in pure ^{3}He (at $B = 1$ mT, this effect does not play any role yet in pure ^{3}He), and the general tendency with traces of ^{4}He is different from the behaviour in pure ^{3}He. In the frequency range between 38.96 GHz and 39.72 GHz, corresponding to a realistic maximum possible detuning, the relative error now increases with *in*creasing M (in contrast to pure ^{3}He, see figure 4.7). Below resonance (at 38.96 GHz), the relative error is higher than above resonance

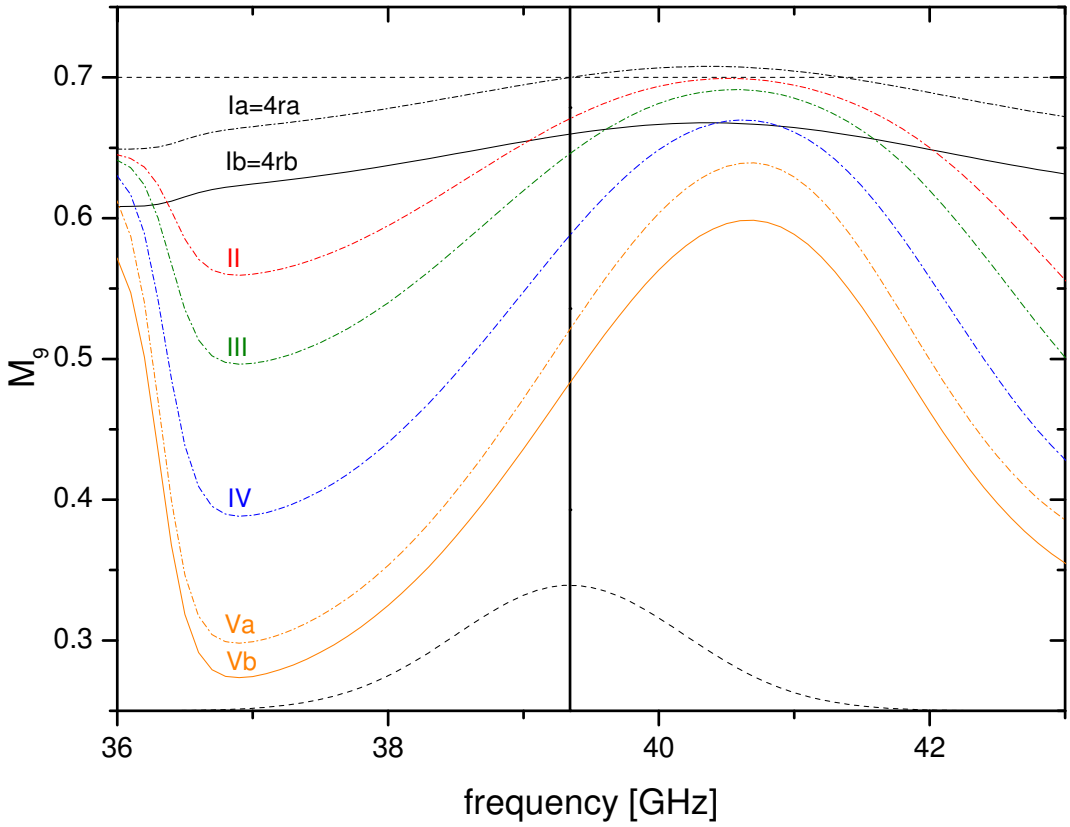

Figure 4.12: Influence of residual ^{4}He traces on measurement of nuclear polarisation by probe C_9 at $B = 30$ mT and $M = 0.7$ as function of probe frequency. M_9 is inferred using reduced ratios R of computed absorption signals for all different fractions x_4 of ^{4}He.
Dash-dotted lines: Exact approach using $T_{ij}(B)$ values and Zeeman shifts of $B = 30$ mT: Ia (corresponds to curve 4ra of figure 4.7): pure ^{3}He, II: $x_4 = 0.1$ %, III: $x_4 = 0.2$ %, IV: $x_4 = 0.5$ %, Va: $x_4 = 1$ %.
Solid lines: Simplified approach using a fixed ratio of transition intensities of 3 : 1 and neglecting Zeeman shifts: Ib (corresponds to curve 4rb of figure 4.7): pure ^{3}He, Vb: $x_4 = 1$ %.
Dashed lines: see caption of figure 4.11.

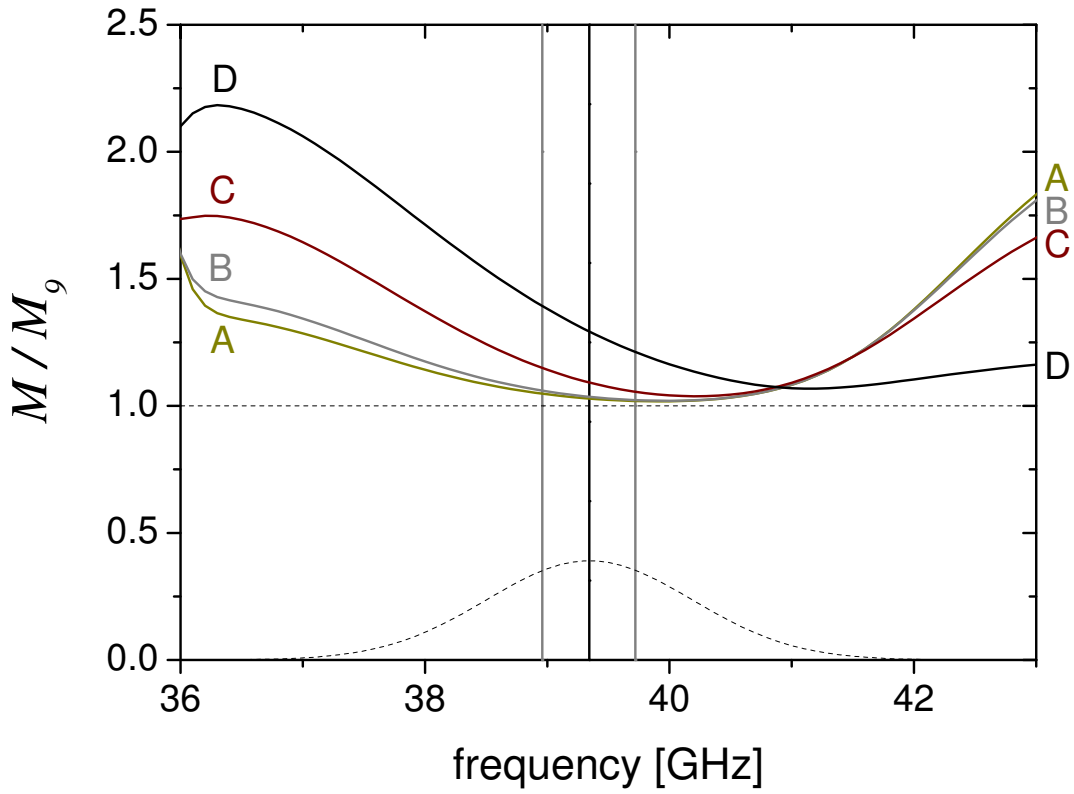

Figure 4.13: Ratios of given nuclear polarisation values divided by the determined M_9 as function of probe frequency in ^{3}He with residual ^{4}He ($x_4 = 0.4$ %) at $B = 1$ mT: $M = 0.01$ (A), $M = 0.3$ (B), $M = 0.7$ (C) and $M = 0.99$ (D). The exact approach yields no difference from the simplified approach (definitions see page 91) in this case, since the transition intensities are not much different from $B = 0$ and Zeeman shifts remain very small (see appendix A) in low magnetic field.
Vertical lines and dashed line: see caption of figure 4.9, note the different vertical scale.

and ranges between almost 5 % (at $M = 0.01$) and almost 40 % (at $M = 0.99$). At 39.72 GHz, the relative error amounts to almost 2 % at very small M and increases up to approximately 21 % at very high M.

At $B = 30$ mT (figure 4.14), the qualitative behaviour with residual ^{4}He of $x_4 = 0.4$ % is the same as in low field, but relative errors quantitatively increase with increasing magnetic field, at least in the examined range up to 30 mT.
Figure 4.14 shows ratios of given polarisation divided by M_9 as function of probe frequency at $B = 30$ mT.
Just as in low field, with residual traces of ^{4}He, it is impossible to obtain agreement

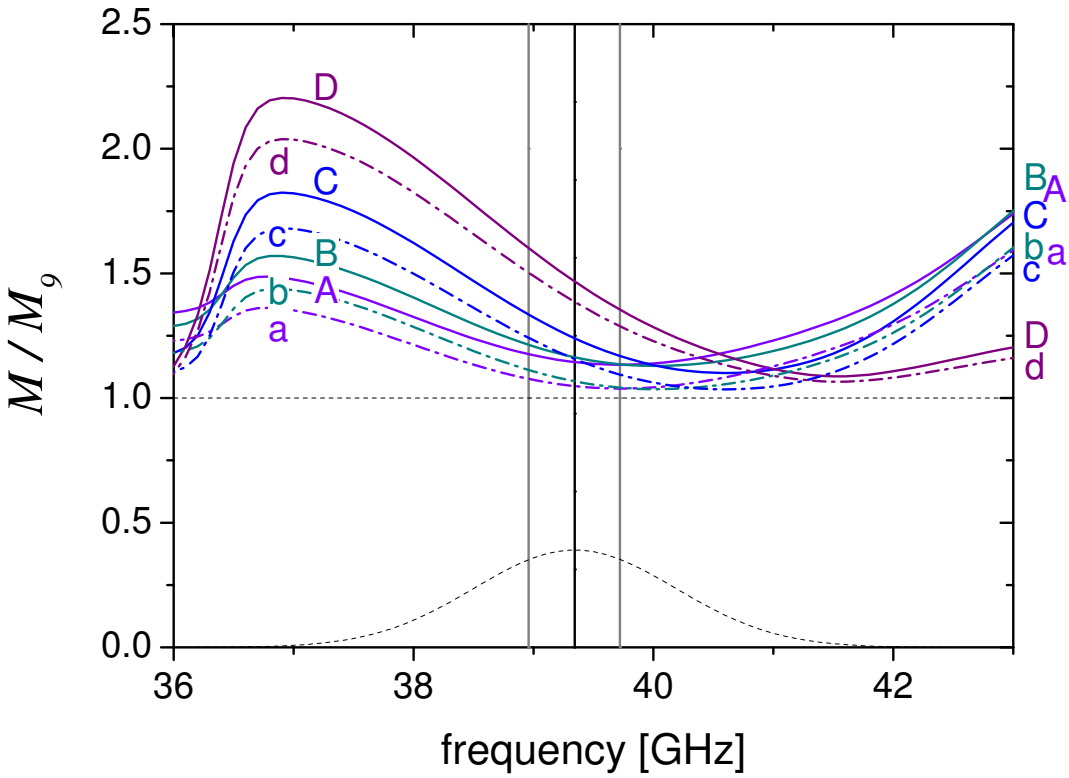

Figure 4.14: Ratios of given nuclear polarisation divided by the determined M_9 as function of probe frequency in ^{3}He with residual ^{4}He ($x_4 = 0.4$ %) at $B = 30$ mT: $M = 0.01$ (a/A), $M = 0.3$ (b/B), $M = 0.7$ (c/C) and $M = 0.99$ (d/D).
Dash-dotted lines (legend in lower case letters): exact approach.
Solid lines (legend in capital letters): simplified approach (descriptions of both approaches: see page 91).
Vertical lines and dashed line: see caption of figure 4.9, note the different vertical scale.

between M and M_9, i.e. ratio = 1, in resonance, even not by the exact approach using accurate $T_{ij}(B)$ values and taking Zeeman-shifts into account. The exact approach yields smaller relative errors though (see figure 4.14).

In the last part of this subsection concerning intrinsic issues of using C_9 as probe transition with residual traces of ^{4}He, the ratio M/M_9 is discussed at fixed probe frequency as function of nuclear polarisation M.

Figure 4.15 shows the ratio of M/M_9 for ^{3}He with $x_4 = 0.4$ % of residual ^{4}He traces at $B = 1$ mT. In low field, there is no observable difference between the exact approach and the simplified one.

It confirms the tendency observed in figure 4.13: The ratio of M/M_9 never equals 1,

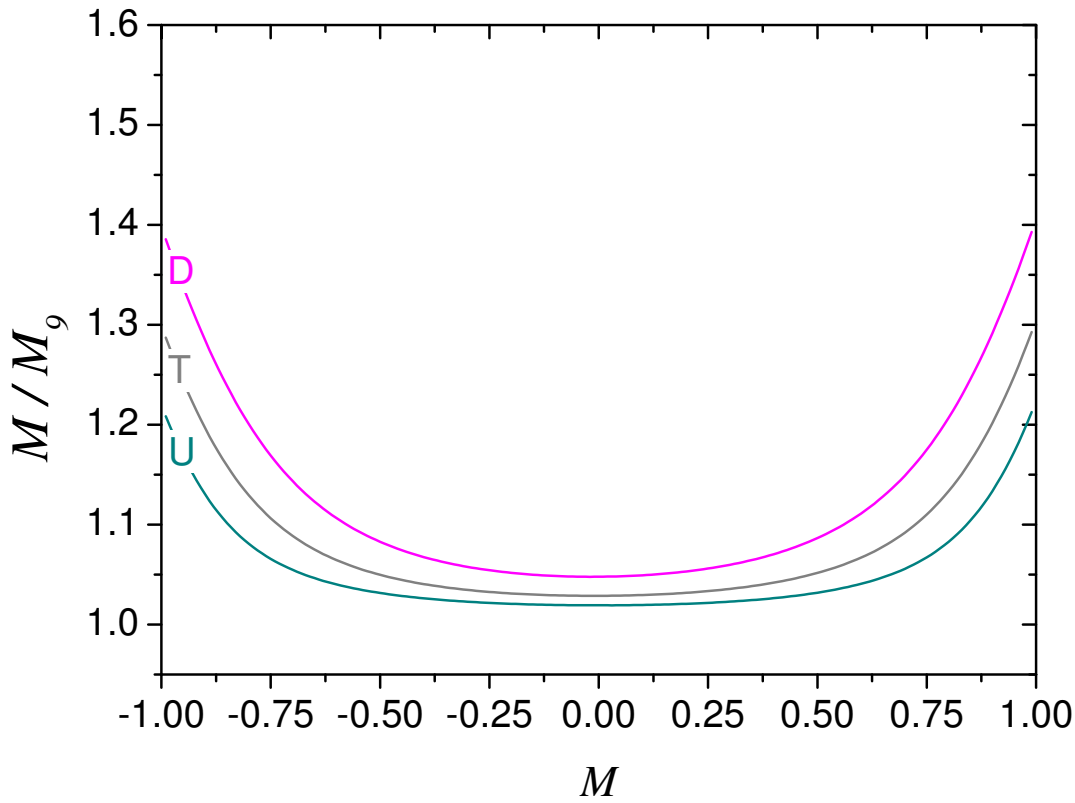

Figure 4.15: Ratio of given polarisation M divided by determined M_9 at fixed probe frequency as function of M in ^{3}He with 0.4 % of ^{4}He at $B = 1$ mT: T ('tuned'): 39.34422 GHz, U ('up'): 39.72 GHz, D ('down'): 38.96 GHz. No observable difference between exact and simplified approach in this case.

meaning that in presence of residual ^{4}He, the actual polarisation is never exactly measured by a probe on the C_9 line. Furthermore, with traces of ^{4}He, the polarisation dependence of the ratio M/M_9 is different than in pure ^{3}He. With residual ^{4}He,

it increases with increasing absolute polarisation value (curves facing upwards at high M), whereas in pure ^{3}He, the M dependence is the opposite: small relative errors at high M as illustrated in figures 4.10 (curves facing downwards at high M) and 4.9. Besides, the relative error of M_9 is higher when detuned to lower frequencies ($\omega < \omega_9(B = 0)$: curve 'D') than above resonance ($\omega > \omega_9(B = 0)$: curve 'U') in accordance with figure 4.13. Furthermore, the maximum relative error at high M and $\Delta\omega$ below resonance in the latter figure is quantitatively confirmed in figure 4.15.

In figure 4.16, M/M_9 is plotted for $x_4 = 0.4$ % of residual ^{4}He at $B = 30$ mT as function of M.
The behaviour of M/M_9 is qualitatively the same as at 1 mT (see figure 4.15): the relative errors of M_9 compared to the given value of M increase with increasing M, and the highest errors are observed when the probe laser is detuned to frequencies below resonance (curves 'D' or 'd' for simplified or exact approaches respectively). As expected, the exact approach is better suited to minimise discrepancies between M_9 and M, but the fact that it is impossible to reduce the relative error to zero with residual traces of ^{4}He in $B = 30$ mT is confirmed.

Two general observations should be retained:
Independently of the magnetic field, shown here for the two extreme cases of $B = 1$ mT and 30 mT relevant for our work, for ^{3}He *with* residual traces of ^{4}He, the ratio of M/M_9 is always > 1 i.e., in all cases with residual ^{4}He, M_9 underestimates M. That is also the case for pure ^{3}He at $B = 30$ mT, but only using the simplified approach. The exact approach in pure ^{3}He is capable to reduce relative errors of M_9 with respect to M to zero at $B \neq 0$ in resonance. But as soon as residual ^{4}He plays a role, a ratio of M/M_9 of exactly 1 can never be obtained.

In summary, the use of C_9 as probe transition raises two main intrinsic issues: First, the influence of magnetic field: In pure ^{3}He and in resonance only, this influence can be eliminated using the reduced ratio R of probe absorption signals and exact $T_{ij}(B)$ values and Zeeman shifts to transform this reduced ratio into values of nuclear polarisation. It is impossible though to purge the influence of magnetic field on probe measurements on C_9 when the probe is detuned by an unknown amount.

Second the influence of residual traces of ^{4}He: In resonance, it is impossible to eliminate this influence, not even in low magnetic field. In higher magnetic field, the impact of residual ^{4}He is actually more important.

Throughout this work, almost all of the experimental recordings were performed with the probe laser tuned to the C_8 line since probe measurements on C_8 are exempt of these limitations. M_8 is *in*dependent of magnetic field and possible

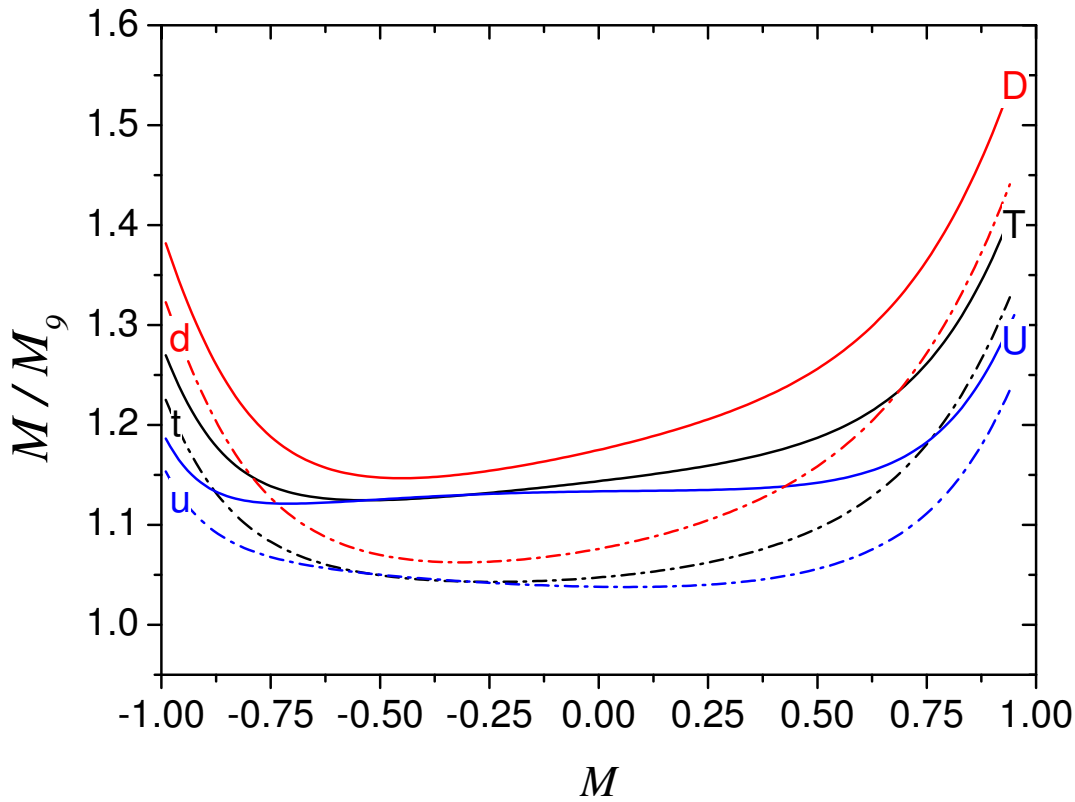

Figure 4.16: Ratio of given polarisation M divided by determined M_9 at fixed probe frequency as function of M in ^{3}He with 0.4 % of ^{4}He at $B = 30$ mT: t/T ('tuned'): 39.34422 GHz, u/U ('up'): 39.72 GHz, d/D ('down'): 38.96 GHz. Dash-dotted lines (legend in lower case letters): Determination of M_9 based on the reduced ratio of probe absorptions using exact $T_{ij}(B)$ values and Zeeman shifts. Solid lines (legend in capital letters): Determination of M_9 based on the reduced ratio of probe absorptions using a fixed ratio of transition intensities of 3 : 1 and neglecting Zeeman shifts.

probe detuning when its determination is based on the reduced ratio R of probe absorption signals.

However, despite these intrinsic difficulties of C_9 as probe transition, it should not be completely discarded since in some experimental situations, it can constitute an advantageous compromise e.g., for monitoring OP dynamics with intense pump laser on C_8 in low field. In this case, probe measurements on C_9 are less perturbed by processes affecting the 2^3S and 2^3P populations. These processes are presented in section 4.3.

4.2.3 Influence of residual π-light on longitudinal probe absorption measurements

The considerations in this subsection are generally relevant for probe absorption signals, independently of the chosen transition C_8 or C_9: The influence of a small fraction of π-polarisation within the probe light, originating on the one hand from the non-parallel probe beam incidence compared to the magnetic holding field axis (inclined probe configuration, see chapter 3.2), and emerging on the other hand from field components of the terrestrial magnetic field non-parallel to the holding field. This influence of the earth field results in a slight change of the overall magnetic field axis compared to the pump and probe laser beams. Here, only the impact on the determination of M by the probe beam is presented.

A 'contamination' of the measured σ^+- and σ^--probe absorption signals by a small fraction of π-light signifies that *not only one* 2^3S sublevel (or one set of sublevels for probe C_9) is monitored, but also a second one (or a second, different set of sublevels for probe C_9).

In order to quantify the error arising from this effect, computed absorption signals for the three light polarisations σ^+, σ^- and π by the model for MEOP-kinetics at given probe frequency and magnetic field as function of polarisation are used to create 'contaminated' σ^+- and σ^--probe absorption rates by different fractions of π-light, keeping the overall beam intensity constant. Using these 'contaminated' probe absorption rates to infer M_8 and M_9 in the habitual way (see sections 4.2.1 and 4.2.2) yields the following relative errors in the determined nuclear polarisation presented in figure 4.17 for probe C_8 and C_9 in resonance ($B = 0$) as function of M, at $B = 1$ mT and 30 mT.

Independently of the fraction of π-light, its presence generally leads to an underestimation of the determined nuclear polarisation by probe absorption measurements on C_8 or C_9 (ratios M/M_8 and M/M_9 always > 1). For the (unrealistic) high fraction

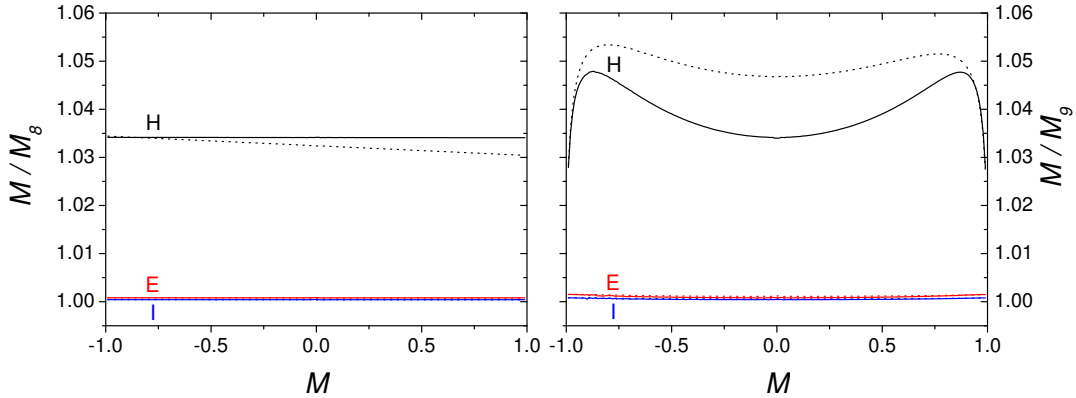

Figure 4.17: Influence of π-light on the determination of M by probe absorption measurements on C_8 (left) and C_9 (right) using computed probe absorption signals by the model for MEOP-kinetics as function of M. The ratio of given M divided by the determined M_8 or M_9 is represented as function of M at $B = 1$ mT (solid lines) and at $B = 30$ mT (dotted lines) for different fractions of π-light. H: high fraction of π-light: 3.3 % (which corresponds to the influence of the terrestrial field in a very low holding field of $B = 0.15$ mT), E: realistic fraction of π-light due to earth magnetic field in $B = 1$ mT (minimum B in this work): 8.05 $\times 10^{-4}$, I: realistic fraction of π-light due to inclined probe configuration: 4.2 $\times 10^{-4}$.

of π-light, the relative error ranges between 3 and 5 % depending on the transition and the applied magnetic field. For the C_8 probe transition, the relative error at $B = 1$ mT is higher than at $B = 30$ mT, whereas for C_9, the relative error is higher at 30 mT compared to 1 mT. For the realistic fractions of π-light, 8.05 $\times 10^{-4}$ (due to the earth magnetic field in a holding field of $B = 1$ mT) and 4.2 $\times 10^{-4}$ (due to the probe inclination) there is almost no difference observable between 1 and 30 mT: on C_8, mean relative errors amount to 0.08 % due to terrestrial field influences ('E' in figure 4.17) and to 0.04 % due to probe inclination respectively ('I' in figure 4.17), both at 1 and 30 mT. On C_9, mean relative errors at 1 mT are slightly smaller than at 30 mT. They amount to 0.1 % ('E') and 0.05 % ('I') at 1 mT, and range between 0.12 % ('E') and 0.07 % ('I') at 30 mT.

Under typical conditions of this work, the influence of additional π-light components on the determination of nuclear polarisation by probe absorption measurements is thus negligible.

4.3 Polarisation measurements with OP light (during polarisation build-up)

As discussed in section 2.8.3, the distribution of metastable atoms between 2^3S sublevels is deeply modified when a pump laser drives 2^3S-2^3P transitions. Moreover, a significant fraction of He atoms are promoted to the 2^3P level.
These two effects simultaneously occur and both contribute to change the probe light absorption signals:

1/ The populations a_{i} are no longer distributed according to the spin temperature distribution associated to the current nuclear polarisation M.

2/ The absorption rate for the $A_{\mathrm{i}} \rightarrow B_{\mathrm{j}}$ component varies, since it is proportional to $(a_{\mathrm{i}} - b_{\mathrm{j}})$ and $b_{\mathrm{j}} \neq 0$.
We introduce the *apparent* polarisations M_8^{a} and M_9^{a} as defined by the values inferred from the reduced ratios R_8 and R_9 using the spin-temperature formulas (equations (4.13) for probe C_8 and (4.15) for probe C_9). Due to the two above-mentioned effects, these apparent polarisations can significantly differ from the *actual* nuclear polarisation M of the ground state. They depend on various experimental conditions (pump laser tuning, polarisation, power, transverse profile; probe line; gas pressure).

In figure 4.18, the effect of OP-light on 2^3S and 2^3P populations of the strongly pumped velocity class is illustrated for 5 W of incident laser power for C_8 σ^+ pumping at a pressure of p_3=1.33 mbar (further parameters, see caption).
With the help of the model for MEOP-kinetics, all a_i and b_j populations are explicitly computed in the spin temperature limit (no perturbations of populations), and under the influence of OP light for a fictitious probe exactly on the cell axis to show the maximum possible impact and for an inclined longitudinal probe path corresponding to the experimental situation. The impact on the tilted longitudinal probe path is smaller due to the radial Gaussian intensity distribution of the pump laser.

At $M = 0$ (left part of figure 4.18), in the spin temperature limit, the 2^3S populations are uniformly distributed and the 2^3P populations are exactly zero (b_j=0). Under the influence of pump light, significant populations are created in 2^3P, and a strong 'overpolarisation' in 2^3S is induced. 'Overpolarisation' in the case of σ^+ pump light implies smaller a_i^* for negative m_F Zeeman levels and higher a_i^* for positive m_F Zeeman levels respectively, compared to the spin temperature limit. Determining the 2^3S polarisation averaged over the whole cell volume according to equation (2.31) taking into account all a_i^* and a_i' sublevels influenced by the pump laser (cf. equation (B.45)) yields $\overline{M^{\mathrm{S}}} = 0.039$. This result shows that under the influence of intense OP light, $M = \overline{M^{\mathrm{S}}}$ is no longer valid.

Determining M either by a probe tuned to C_8 or C_9 - by the formulas presented in sections 4.2.1 and 4.2.2 valid for the spin temperature assumption - reveals that

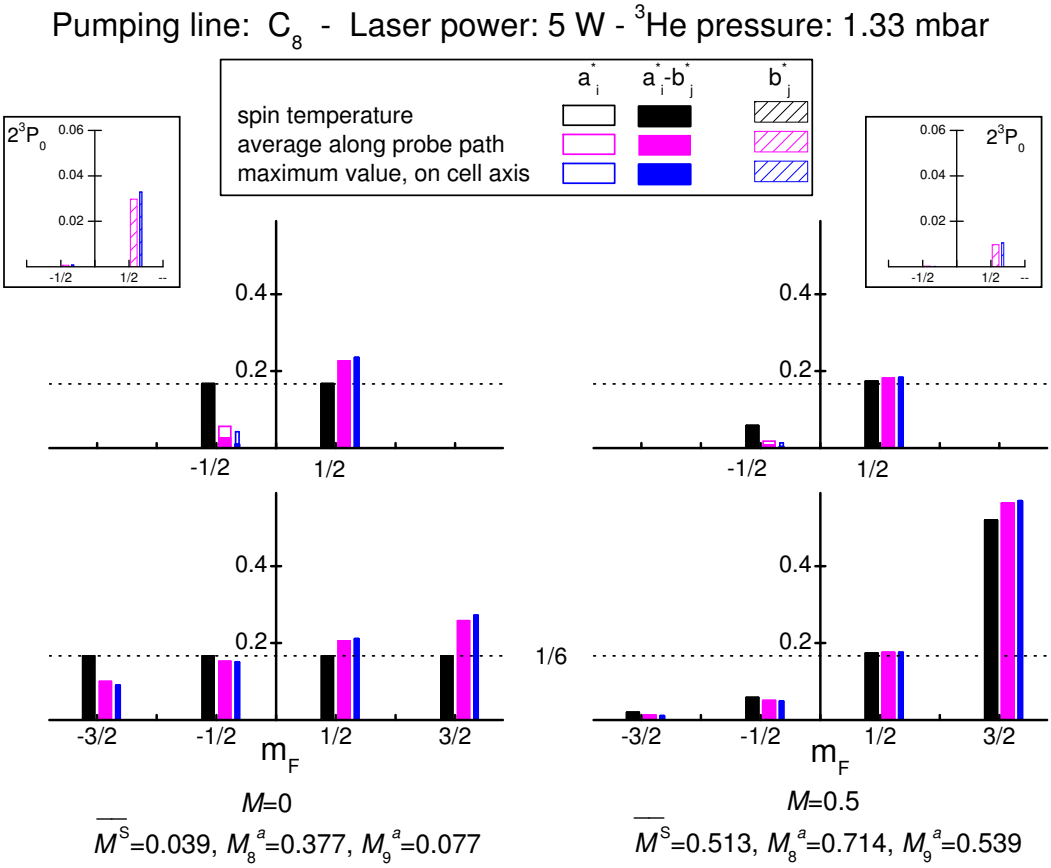

Figure 4.18: Computed OP light-induced changes in 2^3S and 2^3P$_0$ populations of the strongly pumped velocity class at $p_3 = 1.33$ mbar and $B = 50\ \mu$T, for two values of M: On the left: $M = 0$, on the right: $M = 0.5$. Lower plots: 2^3S populations a_1^* to a_4^* ($F = 3/2$), upper plots: 2^3S populations a_5^* and a_6^* ($F = 1/2$). Insets: 2^3P$_0$ populations b_{18}^* and b_{17}^*. Black (left) bars: ST populations in the absence of OP. Blue (right) bars: Example of modified populations on the axis of the Gaussian pump beam (C$_8$ σ^+ pumping, $W_{\rm inc} = 5$ W, 1.33 cm FWHM diameter, 1.7 GHz FWHM spectral width; uniform $n_{\rm m} = 3.2 \times 10^{16}$ at/m^3, $L_{\rm path} = 2 \times 30$ cm). Magenta (central) bars: Modified populations along the inclined probe path at otherwise identical conditions. For the two examples of modified populations in 2^3S (on axis and along the inclined probe path), $a_{\rm i}^*$ (open bars) and differences $a_{\rm i}^* - b_{\rm j}^*$ (filled bars) are represented. Differences are most visible for A_5, the sublevel addressed by the σ^+ pump.

the changed probe absorption signals due to intense pump light yield higher apparent polarisation values compared to the actual polarisation. At $M = 0$, the following apparent polarisation values along the inclined probe path are obtained from populations $a_i^* - b_j^*$ in the strongly pumped velocity class for the probe transitions C_8 and C_9: $M_8^a = 0.377$ and $M_9^a = 0.077$.

At $M = 0.5$ (right part of figure 4.18), the OP light-induced populations in 2^3P are less significant than at $M = 0$, and the difference between 2^3S populations under the influence of OP light compared to the spin temperature limit is less important which is reflected in the determined polarisation values: $\overline{M^S} = 0.513$, $M_8^a = 0.714$ and $M_9^a = 0.539$.

To sum up, the perturbations of intense OP light are less important at higher M, and a C_8 probe is more affected than a C_9 probe, when the C_8 line is used for OP, since the same sublevels are pumped and probed. In the same way, for OP on C_9, the influence of pump light on the C_9 probe is more important than on the C_8 probe. Apparent polarisation M^a and 2^3S polarisation $\overline{M^S}$ are two quantities that are both affected by OP light, but the impact is different due to the different linear combinations of affected a_i sublevels that are used to determine either $\overline{M^S}$ or M^a (for probe C_8 or C_9). In order to infer M_8^a for example, only the populations of magnetic sublevels of the hyperfine state $F = 1/2$ for the strongly pumped atoms, a_5^* and a_6^*, are needed, whereas $\overline{M^S}$ constitutes a linear combination of *all* a_i^* and a_i' sublevels. Moreover, apparent polarisations M^a involve spatial integration along the probe beam path, whereas $\overline{M^S}$ involves an average over the whole cell volume.

The variation of M^a with M was illustrated for C_8 and C_9 probe in figure 2.12, where M^a has been computed for typical MEOP conditions at $p_3 = 1.19$ mbar, using the model for OP kinetics. It was shown that the major contribution arises from the skewing of the 2^3S distribution, and that already at pumping power $W_{inc} = 1$ W, the contribution of populations in the 2^3P state was noticeable. The effects are higher at lower pressure and/or higher pump laser power.

Given the intrinsic limitations of this OP model, for accurate measurements of nuclear polarisation, we rely on experimental results rather than on computed results to have the one-to-one correspondence between the inferred apparent polarisation M^a and actual polarisation M. To this aim, dedicated experiments were performed to compare, during polarisation build-up, the absorption-based values with and without OP light. The method is described in section 5.3. The results and their analysis are presented in section 6.2.
Such dedicated experiments have been performed in each gas cell, for the various investigated plasma conditions and pumping conditions.

We note here that, for improved accuracy, the values of the steady state nuclear

polarisation M_{eq} can be obtained from the analysis of polarisation decay (i.e., the unperturbed M_8 or M_9 value - measured just after the OP beam is stopped - is used).

4.4 Measurements of metastable density $n_{\mathrm{m}}^{\mathrm{S}}$

In the previous sections of this chapter, the main focus was on information that this optical method provides about *relative* populations of the probed 2^3S sublevels. In the present section, we discuss how probe absorption measurements yield information about the *total number density* of atoms in the 2^3S state, i.e. the metastable density n_{m}.

4.4.1 Determination of $n_{\mathrm{m}}^{\mathrm{S}}$ for single-component and multi-component transitions: Examples of C_8 and C_9 probe

Solving equation (4.6) (that uses optical transition rates $\overline{\gamma_{ij}}$ from A_i to B_j given in section 2.3) for $n_{\mathrm{m}}^{\mathrm{S}}$ directly yields the following expression for single-component transitions:

$$n_{\mathrm{m}}^{\mathrm{S}}(M) = \widetilde{\sigma}^{-1}\,\frac{(-\ln T_s)}{L_{\mathrm{path}}}\,\frac{1}{a_i(M)\,T_{ij}\,\mathrm{e}^{-(\delta_{\mathrm{L}}^{ij}/D)^2}}, \tag{4.20}$$

$$\text{with} \qquad \widetilde{\sigma} = \hbar\omega\frac{\sqrt{\pi}\alpha f}{m_e\omega D}, \tag{4.21}$$

$$\text{where } \widetilde{\sigma}^{-1} = 1.47105 \times \sqrt{T/300} \times 10^{15}\ \mathrm{m}^{-2}. \tag{4.22}$$

The parameter $\widetilde{\sigma}$ is an optical cross section that can be used to express absorption as a product of this cross section with length and density of the optical medium (as used for instance by [Wal96] and [Mil98]).

For the more general case of multi-component transitions, the contributions of all components have to be taken into account, and $n_{\mathrm{m}}^{\mathrm{S}}$ is given by:

$$n_{\mathrm{m}}^{\mathrm{S}}(M) = \widetilde{\sigma}^{-1}\,\frac{(-\ln T_s)}{L_{\mathrm{path}}}\,\frac{1}{\sum\limits_{i,j} a_i(M)\,T_{ij}\,\mathrm{e}^{-(\delta_{\mathrm{L}}^{ij}/D)^2}}. \tag{4.23}$$

Equations (4.20) and (4.23) are exclusively used during polarisation decay in absence of OP light in this work, where 2^3S populations can be safely described by the spin temperature populations a_i^{ST} (cf. section 4.2). Furthermore, 2^3P populations b_{j} are strictly zero. During polarisation decay, it is not only possible to determine $n_{\mathrm{m}}^{\mathrm{S}}$ at $M = 0$ from transmitted probe signals, but also to monitor the variation of $n_{\mathrm{m}}^{\mathrm{S}}$

with nuclear polarisation M. Details are specified in the example of probe C_8 below. During polarisation build-up in presence of the pump laser, 2^3S and 2^3P populations are strongly perturbed with respect to ST ($a_i \neq a_i^{ST}$ and $b_j \neq 0$), and an experimentally reliable determination of metastable densities is therefore not possible.

n_m^S inferred from measured probe transmission coefficients on C_8

We use equation (4.20) here to illustrate in detail, how the metastable density n_m^S along the inclined probe path can be determined using probe C_8 in longitudinal configuration with σ^+ and σ^- light polarisations. We also use this example to discuss the issue of small geometrical differences due to spatially separated σ^+ and σ^- beams, and the difficulties introduced in $B \neq 0$ by Zeeman shifts.

For improved readability, we introduce the following notations:
The transition frequency in $B = 0$ is denoted ω_{80}; in $B \neq 0$, the notations ω_{8+} and ω_{8-} are used for the angular frequencies of σ^+ and σ^- transitions respectively. With these notations, reduced (dimensionless) frequency shifts are defined:

$$\delta = (\omega - \omega_{80}) / 2\pi D \tag{4.24}$$

$$Z_+ = (\omega_{8+} - \omega_{80}) / 2\pi D \tag{4.25}$$

$$Z_- = (\omega_{80} - \omega_{8-}) / 2\pi D, \tag{4.26}$$

where δ characterises the detuning of the probe laser compared to the C_8 line in zero magnetic field and $Z_\pm$ designate the Zeeman shifts of the σ^+ and σ^- absorption lines in $B \neq 0$. For simplicity, the transition intensities as function of B are denoted T_{8+} for σ^+ light and T_{8-} for σ^+ light. In $B = 0$, the transition intensities are equal for both light polarisations and are therefore named by a single term: $T_{80} = 0.29185 = T_{5,17} = T_{6,18}$ in conventional terminology.
Z_+, Z_-, T_{8+} and T_{8-} are B-dependent, their numerical values in the applied range of B in this work are compiled in table A.4.
With these notations, the metastable densities deduced from absorption measurements on C_8 along the inclined probe path with σ^+ or σ^- light polarisations are given by re-written expressions of equation (4.20):

$$n_m^{8+} = \widetilde{\sigma}^{-1} \frac{(-\ln T_s^+)}{L_{\text{path}}} \frac{1}{a_5 T_{8+}} \exp\left(Z_+ - \delta\right)^2 \tag{4.27}$$

$$n_m^{8-} = \widetilde{\sigma}^{-1} \frac{(-\ln T_s^-)}{L_{\text{path}}} \frac{1}{a_6 T_{8-}} \exp\left(Z_- + \delta\right)^2 . \tag{4.28}$$

Since radial metastable density distributions are non uniform, and as spatially separated σ^+ and σ^- components do not probe exactly the same paths, measured probe

absorbances $-\ln T_s^+$ and $-\ln T_s^-$ in equations (4.27) and (4.28) are not necessarily exactly identical. This geometrical effect is observed to yield relative differences between 0.5 and 2 % in the experimental conditions of our work.

In the following, we describe the chosen strategies to determine n_{m}^8 and distinguish between $B = 1$ mT, where the detuning parameter δ in equations (4.27) and (4.28) has little impact, and higher values of magnetic field where δ has to be explicitly determined.

Determination of n_{m}^8 in $B = 1$ mT

The exponential terms of equations (4.27) and (4.28) can be rewritten as follows:

$$\exp\left(Z_\pm \mp \delta\right)^2 = \exp(Z_\pm^2)\exp\left(\mp 2Z_\pm\delta\right)\exp(\delta^2) = \exp(Z_\pm^2)\left\{1 \mp 2Z_\pm \pm \delta + ...\right\}, \tag{4.29}$$

where the term $\exp\left(\mp 2Z_\pm\delta\right)$ is replaced by the corresponding Taylor expansion neglecting higher orders, and δ is assumed to be small so that $\exp(\delta^2) \approx 1$. (This assumption is realistic, since the mean value of δ observed in our experiments at $B = 1$ mT for the 2.45 mbar-cell for instance amounts to 0.125 and thus $1 < \exp(\delta^2) \leq 1.016$.) Taking the mean value $(n_m^{8+} + n_m^{8-})/2$ using equation (4.29) for the exponential terms in equations (4.27) and (4.28) then yields:

$$\begin{aligned}\overline{n_{\mathrm{m}}^8} = \frac{\widetilde{\sigma}^{-1}}{2L_{\mathrm{path}}}\Bigg\{&\frac{-\ln T_s^- \exp Z_-^2}{a_6 T_{8-}} + \frac{-\ln T_s^+ \exp Z_+^2}{a_5 T_{8+}} \\ &+ 2\delta\left(\frac{-\ln T_s^- Z_- \exp Z_-^2}{a_6 T_{8-}} - \frac{-\ln T_s^+ Z_+ \exp Z_+^2}{a_5 T_{8+}}\right) + ...\Bigg\}.\end{aligned} \tag{4.30}$$

For the routine analysis in this work at $B = 1$ mT, only the first line of equation (4.30) was used to infer $\overline{n_{\mathrm{m}}^8}$ which does not require to determine δ.
The error introduced by this approximation has been evaluated by comparing the exact value of $\overline{n_{\mathrm{m}}^8}$ (line 1 + line 2 of equation (4.30)) to its approximation (only line 1 of equation (4.30)) as function of δ for different values of B. At 1 mT, there is no detectable difference between the exact value and its approximation. At higher B, the detuning δ has to be explicitly determined as described in the following.

Determination of n_{m}^8 in $1 < B \leq 30$ mT

In order to determine the detuning parameter δ that we consider essential for the determination of n_{m}^8 in $B > 1$ mT, the ratio n_m^{8-} / n_m^{8+} is expressed using equations (4.27), (4.28) and (2.58), and set to 1:

$$\frac{1-M}{1+M}\,\frac{\ln T_s^-}{\ln T_s^+}\,\frac{T_{8+}}{T_{8-}}\exp\left[2\delta\left(Z_+ + Z_-\right)\right]\exp\left(Z_-^2 - Z_+^2\right) = 1, \tag{4.31}$$

which provides δ when the nuclear polarisation M is known (e.g., at $M = 0$):

$$\delta = \frac{1}{2\,(Z_+ + Z_-)} \ln \left[\frac{1+M}{1-M} \, \frac{\ln T_s^+}{\ln T_s^-} \, \frac{T_{8-}}{T_{8+}} \right] - \frac{Z_- - Z_+}{2}. \tag{4.32}$$

(The last term of equation (4.32) arises from the slight asymmetry of the Zeeman shifts for σ^+ or σ^- light (cf. table A.4) and can in most cases be neglected. In $B = 30$ mT for example, $(Z_- - Z_+)$ / 2 equals 0.016 (and less in lower field), corresponding to 19.2 MHz with respect to the Doppler width of 1.19 GHz.)

Due to the geometrical effect of spatially separated probe beam components, the assumption used in equation (4.31) to set the ratio n_m^{8-} / $n_m^{8+} = 1$ is not exactly fulfilled. At higher B, we consider the ratio of probe absorbances to be a product of this geometrical effect and an additional effect of magnetic field. For this reason, one of the probe absorbances is multiplied by the ratio of signals in $B = 0$ in order to account for the geometrical effect, and the detuning parameter δ is then in turn explicitly determined using equation (4.32).

The determined value of δ is then used in equation (4.27) or (4.28) to determine the exact value of n_{m}^{8} accordingly. (Both equations, based on σ^+- or σ^--probe absorption signals, yield exactly the same value of metastable density when the geometrical effect is taken into account.)

In practice, the above described procedures were applied at $M = 0$, where $a_5 = a_6 = 1/6$ in ST distribution, to directly determine metastable densities along the inclined probe path from measured probe transmission coefficients. Results are presented in section 6.1.1.

The variation of metastable densities with nuclear polarisation (during decay) was then assessed by investigating relative variations of $n_{\mathrm{m}}^{\mathrm{S}}$ using equation (53) of [Cou02] that (corrected by its typographic errors, cf. equation (2.59)) reads as follows:

$$\frac{n_{\mathrm{m}}^{\mathrm{S}}(M)}{n_{\mathrm{m}}^{\mathrm{S}}(0)} = \frac{A}{A(0)} \, \frac{\mathrm{e}^{3\beta/2} + 2\mathrm{e}^{\beta/2} + 2\mathrm{e}^{-\beta/2} + \mathrm{e}^{-3\beta/2}}{6\mathrm{e}^{\beta m_{\mathrm{F}}}}. \tag{4.33}$$

This formula can be applied to σ^+ probe absorption signals as function of M with $m_{\mathrm{F}} = -1/2$ for a_5 or to σ^- probe absorption signals using $m_{\mathrm{F}} = +1/2$ for a_6. We routinely used both possibilities and determined the mean values of relative variations of $n_{\mathrm{m}}^{\mathrm{S}}$ with M. Results are presented in section 6.1.3.

$n_{\mathrm{m}}^{\mathrm{S}}$ inferred from measured probe transmission coefficients on C_9

The C_9 transition was only used in some rare cases (up to $B = 2$ mT) to determine metastable densities. For completeness, we provide here the used formulas based on equation (4.23), that reads for σ^+ probe absorption signals on C_9:

$$n_m^{9+} = \widetilde{\sigma}^{-1} \frac{\left(-\ln T_s^+\right)}{L_{\mathrm{path}}} \frac{1}{a_1\, T_{1,18}(B) \exp\left[-\left(\frac{\omega_{1,18}(B)-\omega}{2\pi D}\right)^2\right] + a_2\, T_{2,17}(B) \exp\left[-\left(\frac{\omega_{2,17}(B)-\omega}{2\pi D}\right)^2\right]}. \tag{4.34}$$

In analogy to C_8, the reduced Zeeman shifts in $B \neq 0$ and the detuning of the probe laser with respect to the C_9 components in zero magnetic field can be defined for the C_9 σ^+ components:

$$\delta_{1,18} = \left(\omega - \omega_{1,18}(0)\right)/2\pi D \tag{4.35}$$
$$\delta_{2,17} = \left(\omega - \omega_{2,17}(0)\right)/2\pi D \tag{4.36}$$
$$Z_{1,18}^+ = \left(\omega_{1,18}(B) - \omega_{1,18}(0)\right)/2\pi D \tag{4.37}$$
$$Z_{2,17}^+ = \left(\omega_{2,17}(B) - \omega_{2,17}(0)\right)/2\pi D. \tag{4.38}$$

Using these definitions, the arguments of the exponential functions in equation (4.34) can be simplified:

$$\frac{\omega_{1,18}(B) - \omega}{2\pi D} = \frac{\omega_{1,18}(B) - \omega_{1,18}(0) - (\omega - \omega_{1,18}(0))}{2\pi D} = Z_{1,18}^+ - \delta_{1,18} \tag{4.39}$$
$$\frac{\omega_{2,17}(B) - \omega}{2\pi D} = \frac{\omega_{2,17}(B) - \omega_{2,17}(0) - (\omega - \omega_{2,17}(0))}{2\pi D} = Z_{2,17}^+ - \delta_{2,17}, \tag{4.40}$$

so that equation (4.34) is reduced to:

$$n_m^{9+} = \widetilde{\sigma}^{-1} \frac{\left(-\ln T_s^+\right)}{L_{\mathrm{path}}} \frac{1}{a_1\, T_{1,18}(B) \exp\left[-\left(Z_{1,18}^+ - \delta_{1,18}\right)^2\right] + a_2\, T_{2,17}(B) \exp\left[-\left(Z_{2,17}^+ - \delta_{2,17}\right)^2\right]}. \tag{4.41}$$

Neglecting the detuning of the probe laser with respect to the C_9 components in zero magnetic field, equation (4.41) further simplifies to the final form used in this work:

$$n_m^{9+} = \widetilde{\sigma}^{-1} \frac{\left(-\ln T_s^+\right)}{L_{\mathrm{path}}} \frac{1}{a_1\, T_{1,18}(B) \exp\left[-\left(Z_{1,18}^+\right)^2\right] + a_2\, T_{2,17}(B) \exp\left[-\left(Z_{2,17}^+\right)^2\right]}. \tag{4.42}$$

In exact analogy to the formulas derived for C_9 σ^+ above, we provide just the final form used for determinations of $n_{\mathrm{m}}^{\mathrm{S}}$ by using the C_9 σ^- component:

$$n_m^{9-} = \widetilde{\sigma}^{-1} \frac{\left(-\ln T_s^-\right)}{L_{\mathrm{path}}} \frac{1}{a_4\, T_{4,17}(B) \exp\left[-\left(Z_{4,17}^-\right)^2\right] + a_3\, T_{3,18}(B) \exp\left[-\left(Z_{3,18}^-\right)^2\right]}. \tag{4.43}$$

(The B-dependent values of $Z^{\pm}$ and T_{ij} for all components of C_9 σ^+ and σ^- are listed up to $B = 30$ mT in tables A.5 and A.6).

In order to infer n^9_{m}, equations (4.42) and (4.43) were used to determine n^{9+}_m and n^{9-}_m that in turn served to calculate the mean value $\overline{n^9_{\mathrm{m}}}$.

4.4.2 Influence of collisional broadening and lifetime

Formulas (4.20) for single-component transitions and (4.23) for multi-component transitions are only valid in a low pressure limit. The precondition of a small damping rate of the optical transition coherence for equation (2.12) is only valid at low pressure where Γ' mainly comprises the radiative decay rate γ of the 2^3P state ($\gamma = 1.022 \times 10^7$ s^{-1} [Cou02]); at higher pressure, atomic collisions contribute to Γ' by a pressure-dependent amount of order 10^8 s^{-1}/mbar [Blo85]. Hence equation (2.12) constitutes a low pressure approximation.
Due to Lorentzian shaped collisional line broadening at higher pressure, the line shapes can no longer be approximated by Gaussian profiles as for pure Doppler broadening, but can be characterised by Voigt profiles (emerging from a convolution of Gaussian and Lorentzian profiles).
For the conditions of the present work ($p_3 = 0.63$-2.45 mbar, $B = 1$-30 mT), the effect of pressure broadened line profiles on the determination of n_{m} is quantified in the following. This quantification is based on methods and dedicated programmes developed in the context of high pressure OP in high magnetic field [Nik10, Nik12], where exact formulas for high pressure use are given, and consequences on the determination of metastable densities are discussed in detail.
An empirical dependence of the Lorentz width w_{L} from pressure is established in [Nik10] and [Nik12] by comparison of experimental profiles of a given probe transition with computed Voigt profiles at given magnetic field, polarisation, pressure and temperature. The FWHM of the Doppler width w_{G} is independent of pressure and computed by the programme according to the entered temperature by the user ($w_{\mathrm{G}} = 1.978$ GHz at $T = 300$ K). The input parameter w_{L} is varied until the experimentally recorded profile is matched best. This procedure is repeated for several pressures and the dependence of w_{L} from pressure is found to be linear. The estimation whether pressure broadened line profiles are already relevant for the determination of n_{m} in the present work is based on computations of Voigt profiles at 2.67 mbar (slightly higher than the highest pressure in the systematic investigations of this work), the Lorentz width w_{L} at 2.67 mbar amounts to 36 MHz (FWHM).

The dedicated programme that computes Voigt profiles provides transition intensities $S(\omega/2\pi)$ as function of probe frequency $\omega/2\pi$. In figure 4.19, $S(\omega/2\pi)$ is represented as function of probe frequency in the range of C_8 and C_9 for $B = 1$ mT

(central profiles), for $B = 30$ mT, σ^- light (profiles on the left) and for $B = 30$ mT, σ^+ light (profiles on the right). Two cases are shown over the complete frequency range: the low pressure limit of unbroadened Gaussian profiles ($w_\mathrm{L} = 1$ MHz) and the slightly broader Voigt profiles with lower amplitude in resonance for $p_3 = 2.67$ mbar ($w_\mathrm{L} = 36$ MHz).

Figure 4.19 illustrates qualitatively how pressure broadening influences the determi-

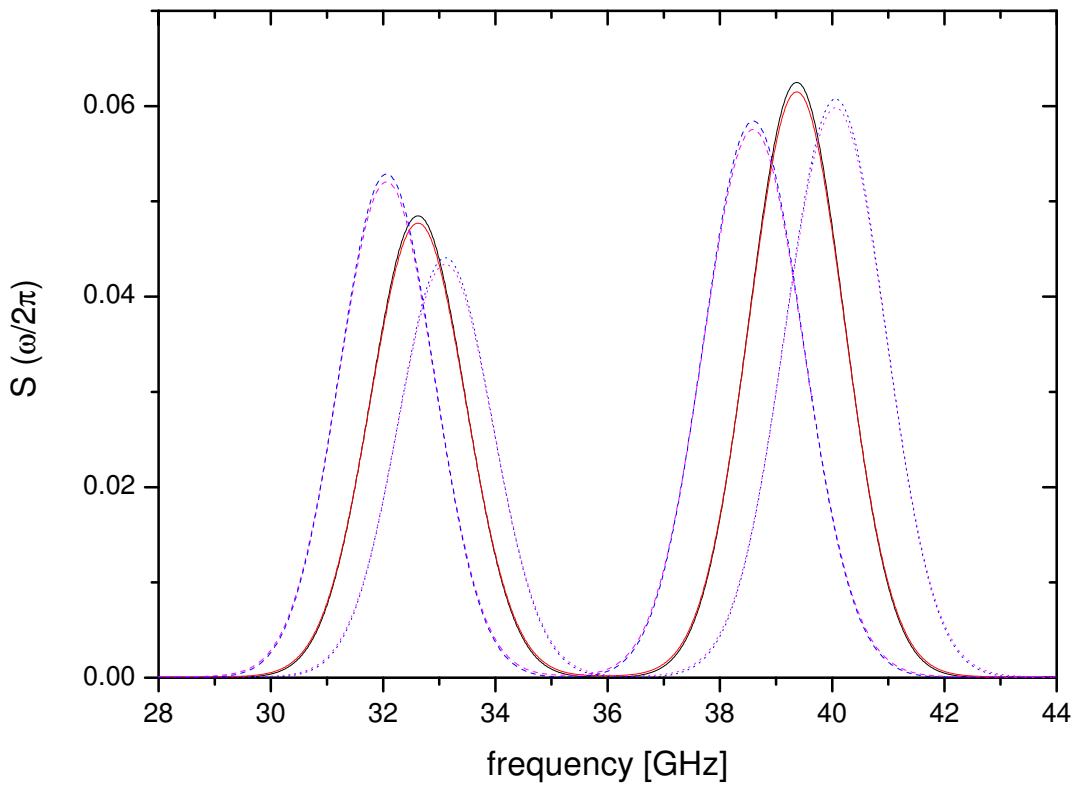

Figure 4.19: Transition intensities $S(\omega/2\pi)$ as function of probe frequency. The peaks between approximately 32 and 34 GHz correspond to the C_8 resonance, the peaks in the range of roughly 38 to 41 GHz to the C_9 resonance respectively. Solid lines: $B = 1$ mT, dashed lines: $B = 30$ mT, σ^-, dotted lines: $B = 30$ mT, σ^+. Two cases are represented over the complete frequency range: low pressure limit of unbroadened Gaussian profiles ($w_\mathrm{L} = 1$ MHz, slightly higher amplitudes in resonance peaks) and slightly broader Voigt profiles with lower amplitudes in resonance for $p_3 = 2.67$ mbar ($w_\mathrm{L} = 36$ MHz).

nation of the metastable density: The term $\sum_{i,j} a_i(M)\, T_{ij}\, \mathrm{e}^{-(\delta_\mathrm{L}^{ij}/D)^2}$ in the denominator of equation (4.23), which is valid in the low pressure limit only, has to be replaced by the corresponding transition intensity $S(\omega/2\pi)$ of the pressure broadened Voigt profile

($S(\omega/2\pi)$ contains appropriate normalisation constants). Since $S(\omega/2\pi)$ is lower in resonance than the transition intensity of the Gaussian Doppler profile, the resulting metastable density using correct transition intensities $S(\omega/2\pi)$ is higher than if the determination was based on a pure Gaussian profile (see equation (4.23)). This means that values of n_{m} neglecting effects of pressure broadening are *under*estimated.
Figure 4.20 quantifies relative systematic errors of n_{m} when neglecting effects of pressure broadening. For the same frequency range as chosen in figure 4.19, the ratio of pure Gaussian transition intensities $S(\omega/2\pi)$ with $w_{\mathrm{L}} = 1$ MHz divided by Voigt transition intensities is represented for $B = 30$ mT, σ^+ and σ^- at a pressure of 2.67 mbar and for $B = 1$ mT at $p_3 = 1.33$ mbar ($w_{\mathrm{L}} = 18$ MHz) and 2.67 mbar ($w_{\mathrm{L}} = 36$ MHz).
At $B = 1$ mT, figure 4.20 shows that the relative error on the metastable density n_{m} arising from pressure broadened Voigt profiles is linear with pressure, implying the highest relative errors in this work for the 2.45 mbar cell. Furthermore, the ratio of Gaussian divided by Voigt transition intensities at $B = 1$ mT is higher or equal to the ratio at $B = 30$ mT. On the C_8 resonance, the relative error of n_{m} at $B = 1$ mT amounts to 0.78 % at $p_3 = 1.33$ mbar and 1.6 % at $p_3 = 2.67$ mbar. There is no significant difference for $B = 30$ mT, σ^- and σ^+ at 2.67 mbar on C_8. On the C_9 resonance, the highest relative error is observed at $B = 1$ mT: 1.63 % at 2.67 mbar. Here, the relative errors at $B = 30$ mT are smaller and slightly different for the two light polarisations, ranging between 1.54 % for σ^+ and 1.55 % for σ^- light. For both resonances and independently of the magnetic field, the relative error decreases when detuned. It decreases by up to approximately 0.2 % when the probe is detuned by $\Delta\omega = \pm\ 0.38$ GHz, which is estimated to be a realistic possible probe detuning in section 4.2.

To conclude, the relative error on metastable densities arising from pressure broadening does not exceed 1.63 % in the conditions of the present work. This effect decreases with decreasing pressure, for the 1.19 mbar cell, it amounts to approximately half of the above mentioned value (0.79 %), and for the 0.63 mbar cell, it is almost negligible. The values of n_{m} are slightly underestimated when collisional broadening is not taken into account.

A comparison of the effect of pressure broadening on n_{m} with the relative geometric difference between n_{m} derived from σ^+ or σ^- probe absorption rates (both light polarisation components are spatially separated, see chapter 3.2), indicates that the effect of pressure broadening is smaller than the relative geometric difference, of the same order of magnitude however.
At $B = 1$ mT, where differences between values of n_{m} derived from one or the other

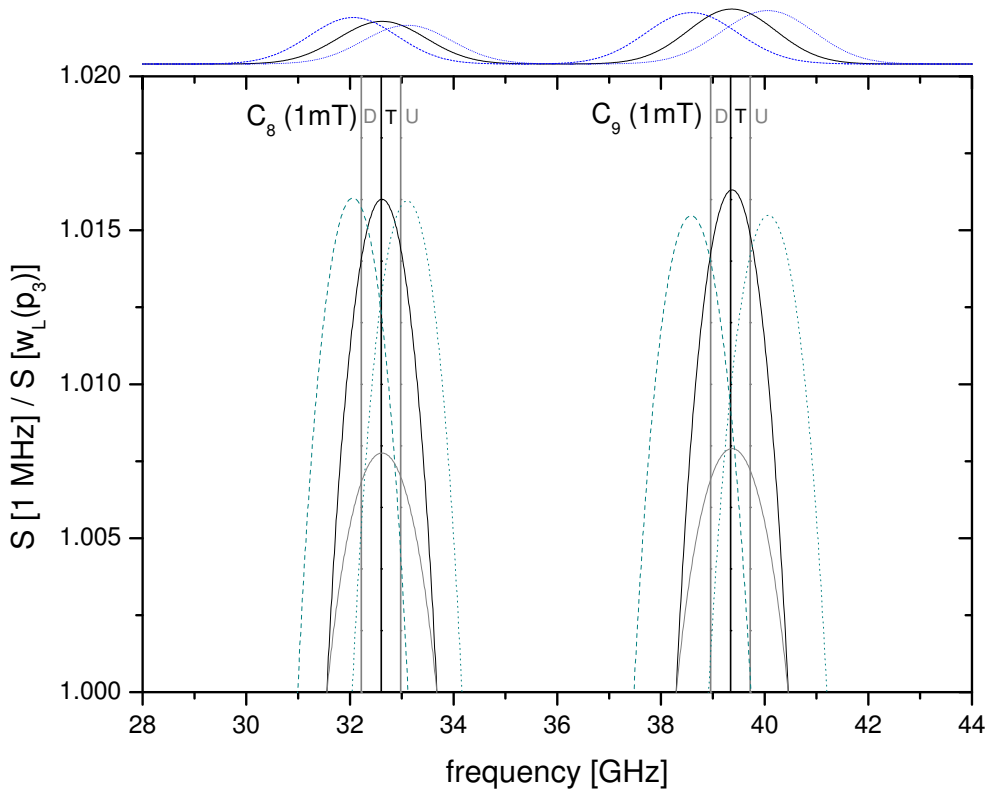

Figure 4.20: Ratio of transition intensities of Gaussian line shape divided by $S(\omega/2\pi)$ of pressure broadened Voigt profile as function of probe frequency. Solid lines: $B = 1$ mT, $p_3 = 1.33$ mbar ($w_\mathrm{L} = 18$ MHz) and 2.67 mbar ($w_\mathrm{L} = 36$ MHz). Dashed lines: $B = 30$ mT, σ^-, $p_3 = 2.67$ mbar, dotted lines: $B = 30$ mT, σ^+, $p_3 = 2.67$ mbar. T ('tuned'): The two dark vertical lines designate the resonance frequencies C_8 (left) and C_9 (right); D ('down') and U ('up'): the two lighter lines below and above each resonance frequency mark a possible realistic detuning range of $\pm$ 0.38 GHz. In addition, Gaussian profiles at $B = 1$ mT, $B = 30$ mT, σ^- and $B = 30$ mT, σ^+ from figure 4.19 are plotted above the main graph.

probe absorption rate are mainly geometric since Zeeman shifts remain small (see appendix A), the relative discrepancy between n_m^+ and n_m^- ranges between 0.5 % and 2 % for the different utilised cells.
Summing up, the relative error due to the neglected effect of pressure broadening leading to Voigt profiles instead of pure Gaussian Doppler profiles attains up to approximately 50 % of the relative geometric difference between n_m^+ and n_m^-. Whereas the geometric difference is an intrinsic property of the optical setup, the relative error due to pressure broadening can be eliminated by taking into account the transition intensities of the Voigt profile in all cases where the metastable density has to be known very precisely. For the routine analysis throughout this work it has not been taken into account by default.

Chapter 5

Methods of data processing and data reduction

In this chapter, we describe in detail which physical quantities can be deduced from the experimentally measured signals, and how the data is processed and analysed. One objective of this data reduction process is to directly compare experimental and computed OP results, as for example polarisation M, the time derivative of polarisation $\dot{M}$ during build-up, or pump and probe absorption signals.
The chapter is subdivided into several parts: After a short introduction (section 5.1), the mainly used experimental protocol in this work including data processing of all probe output signals is addressed in section 5.2. Then, all principles needed to analyse dedicated experiments to account for perturbations of 2^3S- and 2^3P-populations in presence of the pump laser are described in section 5.3. A short follow-up section (5.4) explains how the results of these dedicated experiments are used to infer actual polarisation values during polarisation build-up in presence of the pump laser. Afterwards, section 5.5 describes methods used to analyse polarisation build-up kinetics. In section 5.6, pump output signals are presented and uncertainties are discussed. The last part of the chapter covers developed strategies in the context of OP-enhanced relaxation in section 5.7.

5.1 Introduction to data reduction

All *transmitted* laser signals (having passed the cell with the gas discharge) recorded by the data acquisition system described in chapter 3.3 are still modulated at ~ 70 Hz. These pump and probe signals are post-processed *after* data acquisition. The signals are demodulated numerically using a specially designed programme described in appendix E. It provides three demodulated output signals: two demodulated probe signals divided by the averaged transmitted signals for σ^+- and σ^--probe light com-

ponents and the demodulated pump signal divided by the averaged transmitted pump signal[1], and five additional output signals, averaged with the same time-constant as the one chosen for the demodulated channels: transmitted light powers of both probe components and of the pump laser, smoothed demodulated pump signal of the analogue lock-in amplifier and the rejected pump light component.
Acquiring the rejected pump light signal allows to control light polarisation and power of the pump laser at all times.
Recording the demodulated pump signal by the analogue lock-in amplifier is not required in fact, as the transmitted pump signal is also demodulated numerically. However, for the the purpose of checking and comparing the outputs of the numerical demodulation and the analogue lock-in amplifier directly, the acquisition of this auxiliary channel is useful. An example of a direct comparison is presented in appendix E.

This first step of data processing, the numerical demodulation of signals, is common to all experimental protocols. Basically, three different kinds of experimental protocols are performed in order to acquire data from which all relevant information can be extracted.

The mostly used protocol in this work consists of a complete polarisation build-up in presence of the pump laser and a period of polarisation decay without pump laser. This protocol is described in more detail in subsection 5.2. It is performed with recording of two light polarisations of the probe laser (see sections 3.2 and 4.1) at fixed frequency tuned to resonance (C_8 in most cases, see conclusion of section 4.2.2). The pump laser is also tuned to resonance (mostly C_8 or C_9, in some cases C_6). The choice of the pump transition yielding best OP performances depends on experimental conditions like gas pressure.

As described in section 4.3, the intense pump laser affects the polarisation measurement performed by the probe laser. Therefore, dedicated experiments to account for these perturbations of the 2^3S- and 2^3P-populations by the pump laser have to be performed. This auxiliary protocol permits to reliably relate actual polarisations M to apparent polarisations M^a during polarisation build-up and is explained in subsection 5.3. Results from this auxiliary protocol are used in the polarisation build-up protocol to correct apparent polarisation values when the pump laser is switched on.

The third protocol consists in sweeping the probe laser frequency at a given polarisation value. It can be realised for example during a polarisation decay if the frequency sweep is fast enough compared to the nuclear relaxation time in the discharge. This way, the measurement can be carried out at temporally stationary M, and in addition, for different polarisation values during the decay. Furthermore, performing the sweep-protocol without pump laser during the acquisition has the

[1] As described in [Cou01] and in section 4.2, taking the ratio of the demodulated signal divided by the averaged power to infer probe and pump absorbances strongly reduces effects of laser intensity fluctuations and of optical thickness of the gas on the measured absorptions.

advantage of avoiding perturbations of 2^3S- and 2^3P-populations. However, it can also be performed on purpose in the presence of the pump laser to study systematic effects (at zero nuclear polarisation for example).
The probe laser frequency is typically swept over a range covering C_8 and C_9. It is sufficient to record one probe light polarisation only. In this case, the nuclear polarisation can be deduced from the ratio of the peak heights of C_8 and C_9 in the recorded absorption spectrum (either σ^+- or σ^-). Having recorded two light polarisations in the sweep-protocol, the nuclear polarisation can be deduced from the peak heights of σ^+- and σ^--components, either on the C_8-resonance or on the C_9-resonance.

5.2 Polarisation build-up and decay

This experimental protocol - including a complete polarisation build-up in presence of the pump laser as well as (parts of) the polarisation decay in presence of the rf discharge without pump laser - is the most commonly used protocol for the systematic studies of 2^3S-2^3P pumping below 30 mT. As described in detail in the following, this protocol allows to determine many important characteristic parameters for the OP process depending on the chosen settings, and thus contributes to gain deeper insight into the complex relaxation mechanisms in ^{3}He plasmas and to ultimately understand current limitations of ^{3}He MEOP.

In table 5.1, an example of a typical timing for the polarisation build-up and decay protocol is given. Before starting the data acquisition system, discharge and probe laser are switched on, whereas the pump laser is still blocked.
The given OP timing in table 5.1 is suitable for intermediate laser powers of order 1-2 Watts.

For weak discharges with *decay times* in the plasma of several hundred seconds, the recorded decay time given in table 5.1 corresponds to only a part of the complete decay. If the discharge parameters have not been changed during a given experimental run, this recorded part of the decay is long enough to check whether the plasma relaxation time has not changed from one experiment to the other (with lower accuracy on the exponential fit of the plasma relaxation time than if the acquired decay time is longer).
During routine data acquisition at given discharge parameters, a longer fraction of the complete decay has only been acquired once or twice per day. For acquiring a longer fraction of the decay, as a rule of thumb, the recorded decay time without pump laser in presence of the discharge was chosen to be of the order of the expected decay time Γ_D^{-1}, so that approximately one Γ_D^{-1} was acquired in order to have a high accuracy on the exponential fit of the decay time Γ_D^{-1}.

For stronger discharges with decay times in the plasma below 100 s, the

Table 5.1: Typical timing for the protocol of polarisation build-up and decay (given here for typical values of laser power and discharge intensity, cf. text). Beginning and end of the different acquisition periods are indicated in the following time format: e.g. 1'30" is equivalent to 1 minute and 30 seconds after the beginning of the data acquisition. Experimental changes at the beginning of each acquisition period are written in capital letters.

start	stop	probe	pump	discharge	remarks
0	0'30"	on	off	on	recording of zero-level
0'30"	1'00"	on	off	OFF	discharge off at M=0
1'00"	1'30"	on	off	ON	stabilisation of discharge at M=0
1'30"	4'00"	on	ON	on	polarisation build-up
4'00"	4'30"	on	on	OFF	discharge off at M_{eq}
4'30"	6'00"	on	on	ON	polarisation build-up continued
6'00"	10'00"	on	OFF	on	decay of nuclear polarisation
10'00"	10'30"	on	off	on	MAGNET is moved around close to cell
10'30"	11'00"	on	off	on	recording of zero-level WITHOUT magnet
11'00"	11'30"	OFF	off	on	probe offsets without pump at M=0
11'30"	12'00"	off	ON	on	probe offsets with pump + magnet (M=0)

recorded decay time given in table 5.1 corresponds to a long fraction of the decay as more than one Γ_{D}^{-1} is recorded, leading to a good accuracy of the exponential fit.

If the incident laser power is higher ($\gtrsim$ 2 W), the recorded *OP time* can be reduced as polarisation build-up is faster. The same applies for low gas pressure where polarisation build-up is also usually faster (see figure 6.40 for instance).
If the incident laser power is lower ($\lesssim$ 0.25 W), the recorded OP time has to be increased up to approximately 30 minutes at very low incident pump powers of less than 10 mW. In these cases, two short additional acquisition periods (15 seconds each) are added before the discharge is turned off at steady state polarisation M_{eq}: while the discharge is still switched on, the pump is switched off and on again in order to have the actual steady state polarisation without pump laser and the apparent one with pump laser on. Afterwards, the acquisition period with the discharge switched off at M_{eq} remains unchanged with respect to the typical protocol given in table 5.1, but the following second part of the polarisation build-up is restrained to 30 seconds only, because the incident laser power is too low to reach M_{eq} again in due time. Hence, the exponential fit of the polarisation decay does not start at M_{eq}, but this has no consequence on the extracted decay time Γ_{D}^{-1}.
These two additional acquisition periods are not necessary at higher incident pump

laser power, because the steady state polarisation is reached again at the end of the second polarisation build-up period (4'30" - 6'00"), so that the apparent steady state polarisation (with pump on, at the end of polarisation build-up) can be directly compared to the actual steady state polarisation (with pump off, at the beginning of polarisation decay).

In order to illustrate the typical timing of the polarisation build-up and decay protocol given in table 5.1, the right graph of figure 5.1 shows an example of averaged transmitted probe power signals. The example has been acquired at $p_3 = 0.63$ mbar (^{3}He-pressure), using a strong discharge and 0.42 W of incident pump laser power on the C_8-transition. The left graph of figure 5.1 presents the recorded TTL reference signal and shows two small sections of the raw transmitted probe powers in which the modulation of the absorption is clearly seen.

Initially (left section in left graph of figure 5.1) the gas is not polarised ($M = 0$)

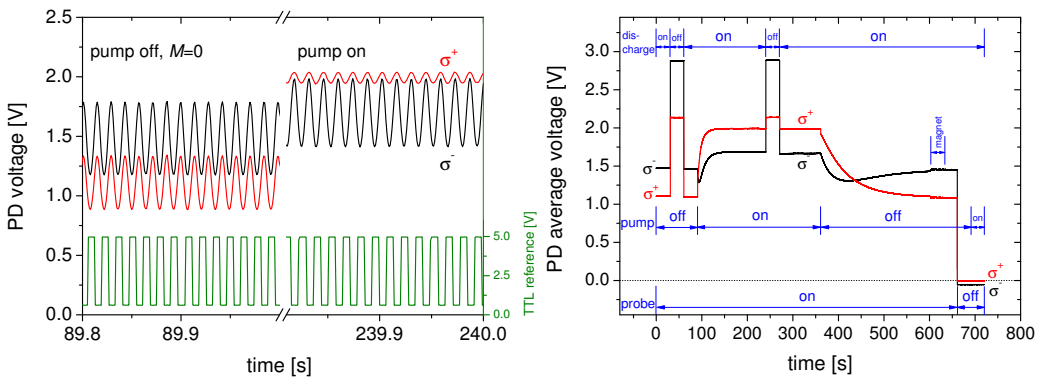

Figure 5.1: Example of raw and averaged transmitted probe power signals as function of time in the experimental protocol of polarisation build-up and decay.
$p_3 = 0.63$ mbar, pump: C_8, $W_{\rm inc} = 0.42$ W, probe: C_8, $B = 1$ mT, $\Gamma_{\rm D} = (69\ {\rm s})^{-1}$, $n_{\rm m}^{\rm S}(M = 0) = 3.34 \times 10^{16}$ atoms/m^3, data acquisition frequency: 1 kHz.
Left: Two subsections of raw PD voltage recordings (upper traces, modulated at $\sim$ 70 Hz) and TTL reference signal (lower trace). In the left section of the graph, discharge is on, pump is blocked, and transmitted probe powers are recorded at $M = 0$, showing nearly equal modulation depths. In the right section of the graph, after 150 seconds of MEOP, the ratio of the modulated absorptions is significantly modified.
Right: Time averaged transmitted probe power signals as function of time. Timing details: see table 5.1; signals are averaged by the time constant of the numerical demodulation: $\tau_{LIA} = 30$ ms. Upper line at $t = 0$: σ^--component of the probe laser; Lower line at $t = 0$: σ^+-component of the probe laser.

and the modulation depths of the σ^+ and σ^- components are nearly equal, of order

~ 40 %, which is higher than in most other experiements where the modulation depth usually did not exceed 30 %; later (right section in left graph) the gas is polarised ($M_{\mathrm{eq}} = 0.682$ as will be seen later, cf. right graph of figure 5.9) and both, absorption rates and modulation depths are different for the two components. The right graph of figure 5.1 shows the time evolution of the averaged absorption signals in the experimental protocol of polarisation build-up and decay. In the following, we explain for which purpose and in order to extract which experimental parameters the different acquisition periods shown in table 5.1 and figure 5.1 are needed.

The tool to numerically demodulate signals provides six types of output signals (cf. introduction in section 5.1). Within the present chapter, it is described in detail for every output signal which physical parameters can be deduced from it and how. The probe output signals of the numerical demodulation are discussed in subsections 5.2.1 and 5.2.2. The pump output signals are presented later, in subsections 5.6.1 and 5.6.2. One output signal, the demodulated pump signal of the analogue lock-in amplifier (Ithaco model 3961 B) is only averaged by the numerical demodulation and is subject to further investigations summarised in appendix E. The time constant used for the numerical demodulation is $\tau_{LIA} = 30$ ms in all examples of output signals shown in sections 5.2 - 5.4 and 5.6.
Like for the transmitted probe power signals shown in figure 5.1, all further explanations concerning the analysis of the polarisation build-up and decay protocol are given for an acquisition with the probe laser tuned to C_8. For acquisitions with the probe laser tuned to C_9, all steps of the analysis can be processed in a similar manner, the equations to determine nuclear polarisation and metastable density are given in chapter 4 (equations (4.13) and (4.30) for probe C_8, and equations (4.15), (4.42) and (4.43) for probe C_9).

5.2.1 Transmitted probe signals

The averaged transmitted probe power signals (right graph of figure 5.1) are first of all used to determine the electrical offsets of both probe components when the probe laser is switched off (acquisition period: 11' to 12'), and it is checked whether these offsets change when the pump laser is switched on, the probe laser remaining switched off (11'30" to 12'). In the investigated cases, the offsets of the probe signals did not change in presence of the pump laser, at high incident laser powers the noise level of the probe component with the same circular light polarisation as the pump laser is increased though. These offsets have to be considered for all steps of the analysis directly based on the transmitted probe power signals, and also when determining the polarisation with the help of the demodulated signals divided by the average transmitted probe power signals.

Probe transmission

In a second step, the transmitted probe power signals are used to determine the σ^+ and σ^- probe transmission coefficients T_s^+ and T_s^-, which equal 1 at maximum transmission (e.g. when the discharge is switched off) and 0 when the probe laser is turned off. In order to obtain T_s^+ and T_s^-, the average transmitted probe signal with offset subtracted as function of time of each probe component is divided by its value when the discharge is turned off (t = 0'30"-1'00" and 4'00"-4'30"). In general, the value of the first discharge off-period (pump off, $M = 0$) was used to determine the probe transmission coefficients. In practice, imperfect rejection of pump stray light is found to slightly affect transmission measurements on the σ^+ channel at high pump powers. This can influence the determination of the nuclear polarisation as function of time in case it is based on probe absorbances -ln(T_s^+) and -ln(T_s^-). It has no influence on the determination of the nuclear polarisation when it is based on the demodulated probe signals as done throughout this work and as described in section 5.2.2.

In figure 5.2, the probe transmission coefficients T_s^+ and T_s^- are represented as function of time for the chosen experimental example. In this case, the values of transmitted probe power signals were identical during both periods with discharge switched off, at $M = 0$ and M_{eq} respectively.

Metastable density at $M = 0$

In a third step, the probe absorbances -ln(T_s^+) and -ln(T_s^-) at $M = 0$ (see indicated period ($M = 0$, discharge ON) from $t = 30$ s to 60 s in figure 5.2) are used to determine the integrated metastable densities at $M = 0$ along the inclined probe paths, $n_{\mathrm{m}}^{\mathrm{S}\pm}(M = 0)$, using equations (4.30), or (4.27) and (4.28) for probe C_8. Details are described in section 4.4, where formulas to infer $n_{\mathrm{m}}^{\mathrm{S}}(M = 0)$ for probe C_9 are provided as well (equations (4.42) and (4.43)).

Three contributions have to be taken into account to quantify the error of $n_{\mathrm{m}}^{\mathrm{S}}$ at $M = 0$: the geometric difference of the two probe paths, the errors of the transmitted probe power signals (cf. figure 5.1), discharge off, and the errors of probe transmission coefficients T_s^+ and T_s^- at $M = 0$ (cf. figure 5.2), discharge on. Typical relative errors of $n_{\mathrm{m}}^{\mathrm{S}}(M = 0)$ range between 0.4 % and 4 %.

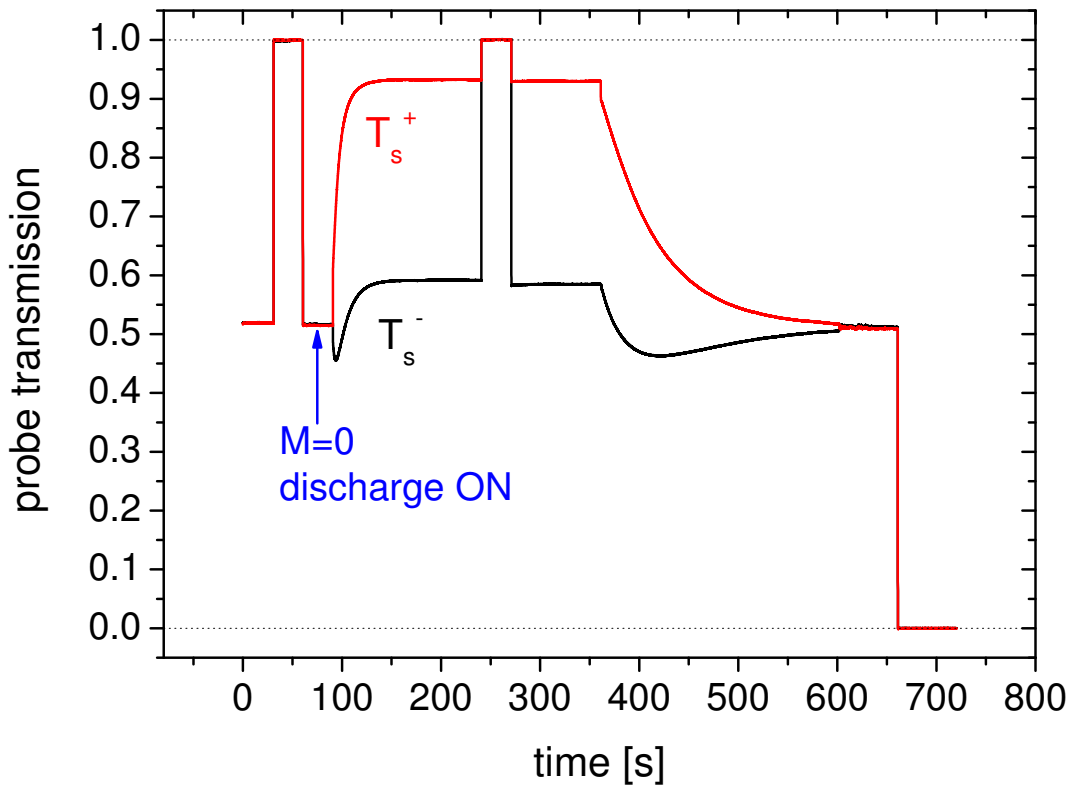

Figure 5.2: Probe transmission coefficients T_s^+ and T_s^- as function of time in the experimental protocol of polarisation build-up and decay. Timing and experimental details: see caption of figure 5.1. T_s^+ increases from $t = 90$ s on (pump laser released) up to a maximum value of 0.93, whereas T_s^- first decreases down to 0.46 and then increases up to a maximum value of 0.59. The two periods with $T_s^+ = T_s^- = 1$ ($t = 30$-60 s and $t = 240$-270 s) correspond to the periods during which the discharge is switched off (at $M = 0$ and at M_{eq} respectively); during the period with $T_s^+ = T_s^- = 0$ from $t = 660$ s up to 720 s the probe laser was switched off. T_s^+ and T_s^- values of the indicated period ($M = 0$, discharge ON) from $t = 30$ s to 60 s are used to determine the metastable density at $M = 0$ (see next paragraph).

5.2.2 Demodulated probe signals

Probe absorption signals

The second type of output signals of the numerical demodulation are determined by using the demodulated probe signals (i.e., raw signals shown in the left graph of figure 5.1 that are demodulated) and dividing them by the average transmitted powers (shown in the right graph of figure 5.1) for each probe component, so that the σ^+ and σ^- probe absorption signals, A_+ and A_- (see sections 4.1 and 4.2), are obtained. Whenever necessary, electrical offsets in the probe signals are corrected after numerical demodulation, automatically or manually depending on situations.

On the left of figure 5.3, the measured probe absorption signals A_+ and A_- are represented as function of time for the same example as in figure 5.1.
Subsequently, the reduced ratio of probe absorption signals is built $R = \frac{A_+A_-(0)}{A_-A_+(0)}$ (cf. equation (4.10)). As described in detail in section 4.2, when using C_8 as probe transition, the reduced ratio R_8 is independent of probe detuning and of magnetic field.
On the right of figure 5.3, the reduced ratio R_8 is shown as function of time for the chosen example.

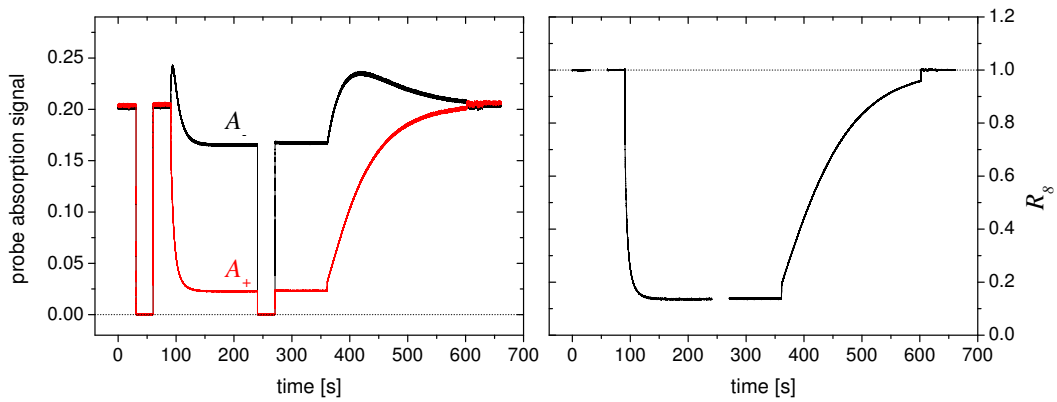

Figure 5.3: Left: Probe absorption signals A_+ and A_- as function of time; experimental settings: see caption of figure 5.1, timing details: see table 5.1. Right: Reduced ratio $R_8 = \frac{A_+A_-(0)}{A_-A_+(0)}$ as function of time. The two breaks in the curve (between $t = 30$ and 60 s and $t = 240$ and 270 s) correspond to the acquisition periods with discharge off. Building the ratio of both probe absorptions during these discharge off-periods leads to a division by a very small value close to zero. The obtained values have no physical sense and are thus not represented in the right graph during these periods.

Nuclear ground state polarisation

The deduction of the nuclear ground state polarisation M in the case of a C_8-probe is then a straight forward procedure (see equation (4.13)):

$$M_8 = \frac{1 - R_8}{1 + R_8}.$$

(Formulas to infer nuclear polarisation from measured probe absorption signals on C_9 are provided in section 4.2.2).

An example of M_8 as function of time is given in figure 5.4. Note that equation (4.13) yields *apparent* polarisation values for periods when the pump laser is on (t = 90 s to 360 s), and the *actual* polarisation for all other periods when the pump laser is off.

During the period when the pump laser is off (t = 361-600 s), the polarisation decay is fitted by a an exponential decay: $M = M_{\mathrm{eq}} \cdot \exp(-(t - t_0)\,\Gamma_{\mathrm{D}})$. With given t_0, this exponential fit yields the decay rate Γ_{D} and the steady state polarisation M_{eq} in the case of intermediate and high laser powers for which the timing of the experimental protocol is compliant to table 5.1, i.e. for which the steady state polarisation is reached again in the second part of the polarisation build-up (t = 270 - 360 s in the given example). In the case of low incident laser power, when two additional acquisition periods are introduced before switching off the pump laser (see page 125), the polarisation decay does not start at M_{eq}, and therefore cannot be determined by the exponential fit, but directly on the polarisation curve. The fact that the exponential fit in these cases does not start at M_{eq} does not affect the determination of the decay rate Γ_{D}.

Relative errors of extracted M_{eq} values amount to approximately 0.5 %, relative errors of extracted Γ_{D}-values are up to a factor of 5-10 smaller (depending on the signal-to-noise-ratio of the demodulated probe signals from which nuclear polarisation is inferred and on the length of the recorded decay period with respect to Γ_{D}) and are therefore negligible in this work.

In stationary conditions at zero nuclear polarisation and steady state polarisation, at the instants when the pump laser is switched on and off again, the shown build-up curve in figure 5.4 provides three important polarisation values: apparent polarisation at zero nuclear polarisation ($M = 0$), M_0^a (see left inset of figure 5.4), as well as actual and apparent polarisation at steady state polarisation, M_{eq} and M_{eq}^a (see right inset of figure 5.4). In the chosen example, they have the following values: $M_0^a = 0.158$, $M_{eq} = 0.682$ and $M_{eq}^a = 0.758$.

In order to reliably relate actual polarisations M to apparent polarisations M^a during polarisation build-up in presence of the pump laser, results of an auxiliary measurement protocol, which is explained in detail in the following section 5.3, are required.

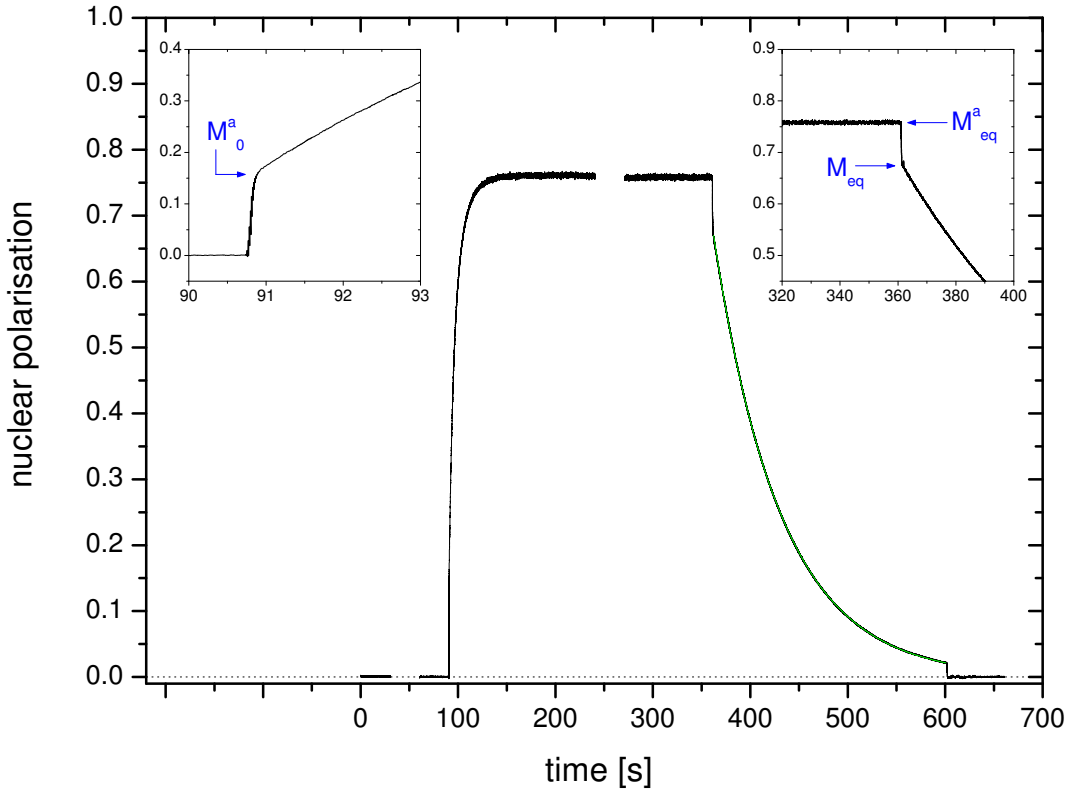

Figure 5.4: Build-up and decay of nuclear polarisation as function of time; experimental settings: see caption of figure 5.1, timing details: see table 5.1; time constant of the numerical demodulation: $\tau_{\mathrm{LIA}} = 30$ ms; $t = 90.8$-360.8 s: pump laser on: apparent polarisation, $t = 0$-90.8 s and 360.8-660 s: pump laser off: actual polarisation. The two breaks in the curve correspond to discharge off-periods, see caption of figure 5.3. Exponential fit of polarisation decay ($t = 361$-600 s): $M = M_{\mathrm{eq}} \cdot \exp(-(t - t_0)\,\Gamma_{\mathrm{D}})$ with $t_0 = 361$ s yields a steady state polarisation M_{eq} of 0.682 at the beginning of the decay and a decay rate Γ_{D} of $(69\mathrm{s})^{-1}$. Left inset: Detail at $M = 0$ to determine the apparent polarisation (pump on) at zero nuclear polarisation: $M_0^a = 0.158$; Right inset: Detail at $M = M_{\mathrm{eq}}$ to determine the apparent polarisation (pump on) at steady state polarisation: $M_{eq}^a = 0.758$. The vertical scale is the same in both insets ($\Delta M = 0.45$, but different starting and end points), whereas the horizontal scale is *not* the same in both insets (left: $\Delta t = 3$ s, right: $\Delta t = 80$ s).

5.3 Dedicated experiments to account for perturbations of 2^3S- and 2^3P-populations in presence of the pump laser

OP light from the pump laser depletes selected 2^3S sublevels so that populations are driven significantly away from the spin temperature distribution. Furthermore, it creates significant populations in the 2^3P state. Physical background information is given in section 2.8.3, consequences on the measurement of polarisation during polarisation build-up are described in section 4.3, and results of these dedicated experiments over the whole range of experimental conditions in comparison to computations by the model of MEOP-kinetics are presented in section 6.2. Here, the focus is on the description of how a reliable one-to-one correspondence between the inferred apparent polarisation M^{a} and actual polarisation M is established.

Hence, the main objective of this experimental protocol is to compare probe absorption signals *without* pump laser and *in presence of* the pump laser at different nuclear polarisation values during a build-up process. Therefore, the pump laser is periodically turned on and off (by blocking the pump beam between collimator and polarising beam splitter cube) during the polarisation build-up; the probe laser as well as the discharge have to remain switched on during the complete experiment.

Before starting the experiment, pump and probe lasers are tuned to the required transition, the pump laser power is chosen, and the discharge is set to the desired rf level. As it is possible that the gas is still polarised from earlier experiments, it also has to be made sure prior to starting the experiment that the nuclear polarisation M is zero. In the given magnetic field range of 0-30 mT, this can be conveniently achieved by moving around a small permanent magnet close to the cell and removing it before starting the experiment.

Timing details of this experimental protocol are given in the following as guiding values for typical pump laser power values of a few Watts and a weak discharge (decay time in the plasma of several hundred seconds); when the pump laser power is smaller ($\lesssim 0.5$ W), the pumping intervals are extended.

The data acquisition system is started and the pump beam remains typically blocked during the first 30 seconds of the experiment while probe laser and discharge are already switched on. This acquisition of the $M = 0$ level is necessary to obtain the ratio of both probe absorptions at zero nuclear polarisation (required in the determination of M, see equation (4.12) for probe C_8, or chapter 4 for a general description of the principle of measuring nuclear polarisations in this work).
After 30 seconds of zero-level recording, the pump laser is opened for five times 1 second approximately at the beginning of the pumping process, when nuclear polarisation builds up very fast, then five times 2 to 3 seconds approximately, after that, five times 5 to 6 seconds and finally, once 15 seconds to get close to the steady

state polarisation value at the end of the build-up process. The time intervals when the pump laser is blocked - in between these 16 pumping intervals - are always about 4 to 5 seconds long. This sequence of intervals with and without pump laser leads to a total acquisition time of about 3 minutes for one pump transition at fixed probe transition. If two different pump transitions are recorded at fixed probe transition, the acquisition time is doubled.

Concerning the analysis of this experimental protocol, the first step consists in extracting the nuclear polarisation from the ratio of measured probe absorption signals in the same way as described in detail for the polarisation build-up protocol (section 5.2). Therefore, the output signals of the numerical lock-in amplifier, namely the demodulated signal divided by the average power for both probe components, are used. As specified in chapter 4, this procedure can be performed either with the probe laser on C_8 or on C_9, using equations (4.13) or (4.15) respectively.

In figure 5.5, a typical temporal evolution of the nuclear polarisation (complete evolution on the left, selected detail on the right) is shown for this experimental protocol. The represented example is recorded at $p_3 = 1.19$ mbar, $B = 1$ mT, with pump and probe lasers on the C_8 transition, incident pump laser power of 1.66 W, decay rate $\Gamma_D = (617\,\mathrm{s})^{-1}$ and metastable density $n_m^S(M = 0) = 1.35 \times 10^{16}$ atoms/m^3. (This is not the corresponding dedicated experiment to the example presented in section 5.2, but for *all* different experimental conditions, such dedicated experiments to account for perturbations of 2^3S- and 2^3P-populations in presence of the pump laser were performed.)
In this chosen example, the perturbations of the 2^3S- and 2^3P-populations in presence of the pump laser are of intermediate extent: the perturbations are more important at lower pressure and/or higher pump laser power, and less important at higher pressure and/or lower pump laser power. Moreover, the perturbations are also generally less important when the probe laser is used on a *different* transition than the one that is pumped. These dependencies are presented in detail in chapter 6, section 6.2.
This polarisation build-up shows parts - during which the pump laser was switched off - where using the formulas valid in the spin temperature limit to infer the nuclear polarisation (cf. chapter 4) leads to correct actual polarisation values (examples in the plot named M_1 to M_4). Whenever the pump laser is switched on, using the formulas valid in the spin temperature limit leads to higher apparent values of the nuclear polarisation (examples in the plot named M_2^a and M_4^a). This discrepancy between actual and apparent polarisation values results from perturbations of the 2^3S- and 2^3P-populations due to the intense pump laser, its extent depends on the chosen transitions for pump and probe lasers, on the incident laser power and on the gas pressure.

The goal of these dedicated auxiliary experiments is to find a correction function for the given experimental conditions (pump and probe transitions, incident pump

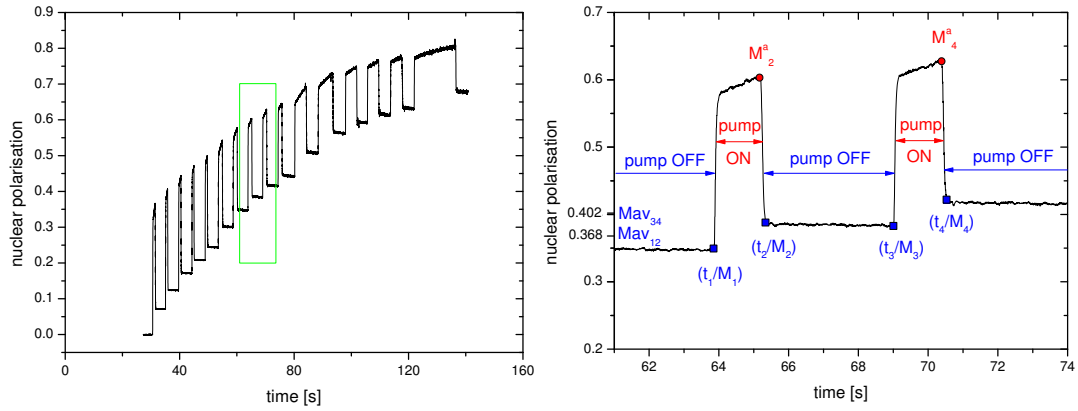

Figure 5.5: Temporal evolution of the nuclear polarisation in a dedicated experiment to account for perturbations of 2^3S- and 2^3P-populations due to the pump laser: the pump laser is switched on and off periodically (timing details: see text); $p_3 = 1.19$ mbar, pump: C_8, $W_{\text{inc}} = 1.66$ W, probe: C_8, $B = 1$ mT, $\Gamma_{\text{D}} = (617\,\text{s})^{-1}$, $n_{\text{m}}^{\text{S}}(M = 0) = 1.35 \times 10^{16}$ atoms/m^3. Left: Complete evolution, Right: Detail of selection (t = 61-74 s).

power, gas pressure and discharge intensity) that can be used for the main experimental protocol described in subsection 5.2 in order to reliably relate actual polarisation values to apparent ones at any instant of the polarisation build-up. This is very important for studying *dynamics* of OP-processes. Furthermore, these dedicated experiments provide information about the time derivative of polarisation ($\dot{M}$), that can be compared to corresponding $\dot{M}$-values extracted from the main experimental protocol. Selected comparisons of data derived from different experimental protocols in given experimental conditions are discussed in section 6.3.1.

In the following, it is described how the correction function, that relates M^a to M, is extracted from the experimental data, and how $\dot{M}$ is deduced.
In order to determine the time instants when the pump laser is turned off and on, the average transmitted pump signal is differentiated with respect to time t, and the x-positions of the peaks are determined on this first-order derivative (see figure 5.6). Positive peaks correspond to the instants when the pump has been turned on and negative peaks to the instants when the pump has been turned off respectively.
These positive and negative peak positions and the complete polarisation curve as function of time shown in figure 5.5 are used as input by a Fortran-programme[2]. This programme reads in the values for time and polarisation during the periods when the pump laser is turned off (e.g. between M_2 and M_3 in figure 5.5). During these periods, the nuclear polarisation starts to decay exponentially. In order to determine

[2]All programmes used for data reduction were developed at LKB by P.-J. Nacher.

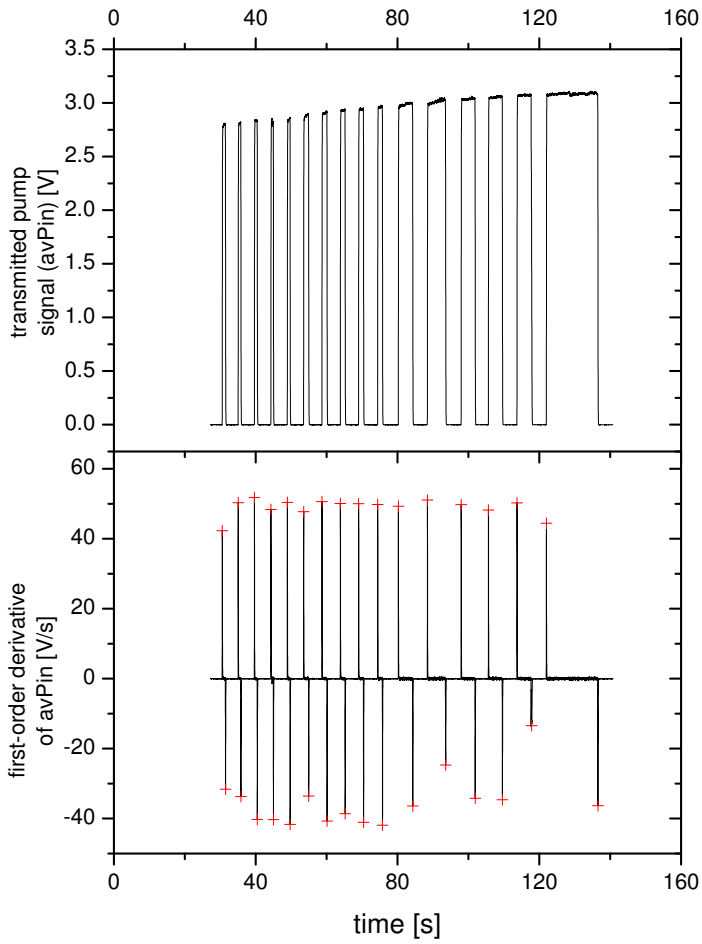

Figure 5.6: Top: Transmitted pump signal in a dedicated experiment to account for perturbations of 2^3S- and 2^3P-populations due to the pump laser (settings: see figure 5.5); Bottom: First-order time derivative of the transmitted pump signal, crosses mark the x-positions of the peaks which correspond to the instants when the pump laser has been switched on (positive peaks) and off respectively (negative peaks).

time- and polarisation-values at the end of each pumping period (e.g. M_2 and M_4) and at the beginning of each pumping period (e.g. M_1 and M_3), the programme performs linear fits on $\log(M)$ during these short periods of polarisation decay.
The *apparent* polarisation values at the end of each pumping period (e.g. M_2^a and M_4^a) are determined manually (this was found to be more reliable).
By this procedure, a table with pairs of time instants and actual polarisation values M (without pump laser) at the end of each pumping period is obtained, as well as the corresponding apparent polarisation values M^a (with pump laser switched on).
Furthermore, the programme determines the time derivative of polarisation: for example $\frac{\Delta M}{\Delta t} = \frac{M_2 - M_1}{t_2 - t_1}$ for two of the specified actual polarisation values in figure 5.5.
In the same way, the programme determines $\frac{\Delta M}{\Delta t}$ for all recorded pumping intervals.
As it is convenient to plot the determined values of $\frac{\Delta M}{\Delta t}$ as function of M so as to possibly compare them to other experiments, the programme also determines the average polarisation value M_{av} in each $\frac{\Delta M}{\Delta t}$ interval: $M_{av\,12} = (M_1 + M_2)/2$ for example.
Figure 5.7 shows the obtained values of $\frac{\Delta M}{\Delta t}$ as function of M_{av} for the chosen example.
In order to obtain the desired correction function for use in the main experimental protocol described in subsection 5.2, the inferred actual polarisation values M are plotted versus the apparent polarisation values M^a. For the purpose of relating the apparent polarisation values to the actual ones during the entire build-up, the experimental curve is fitted by a second-order polynomial, which empirically turned out to best fit experimental data.
For the chosen example (settings: see figure 5.5), this is represented in figure 5.8. In addition to the data points from the dedicated experiment, two experimental points from the corresponding polarisation build-up protocol are shown in the graph. In this standard protocol, pairs of apparent and actual polarisation values are directly obtained when the OP laser is released ($M = 0$) and blocked ($M = M_{\text{eq}}$: unperturbed value, measured during polarisation decay, just after the OP beam is stopped, cf. section 5.2). These two data points taken from the polarisation build-up protocol are in very good agreement with the experimental points and the correction function of the dedicated experiment. From this fact, it follows that the correction function determined in the dedicated experiment is well suitable to infer the actual polarisation value M for each apparent polarisation value M^a in this example. Dedicated experiments are acquired for all different experimental conditions (e.g., different incident pump powers, pump and probe transitions, rf excitation levels, gas pressures) used in the polarisation build-up protocol, and it is checked for each of these settings that data points at $M = 0$ and M_{eq} from this main protocol are in good agreement with experimental points obtained in the dedicated experiments.

In cases where the agreement is not as good as shown in the example of

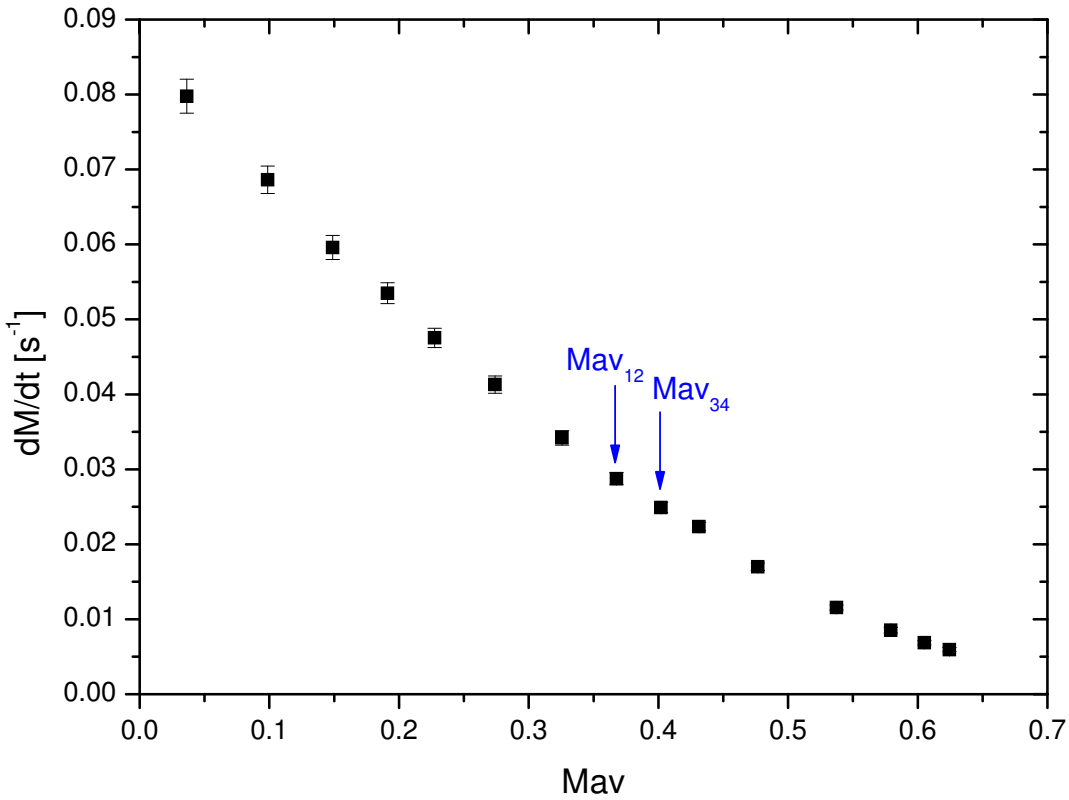

Figure 5.7: ΔM / Δt values as function of the average actual polarisation value M_{av} within a pumping interval, deduced from a dedicated experiment to account for perturbations of 2^3S- and 2^3P-populations due to the pump laser (settings: see figure 5.5). The two examples of M_{av}-values correspond to the ones of figure 5.5 (detail).

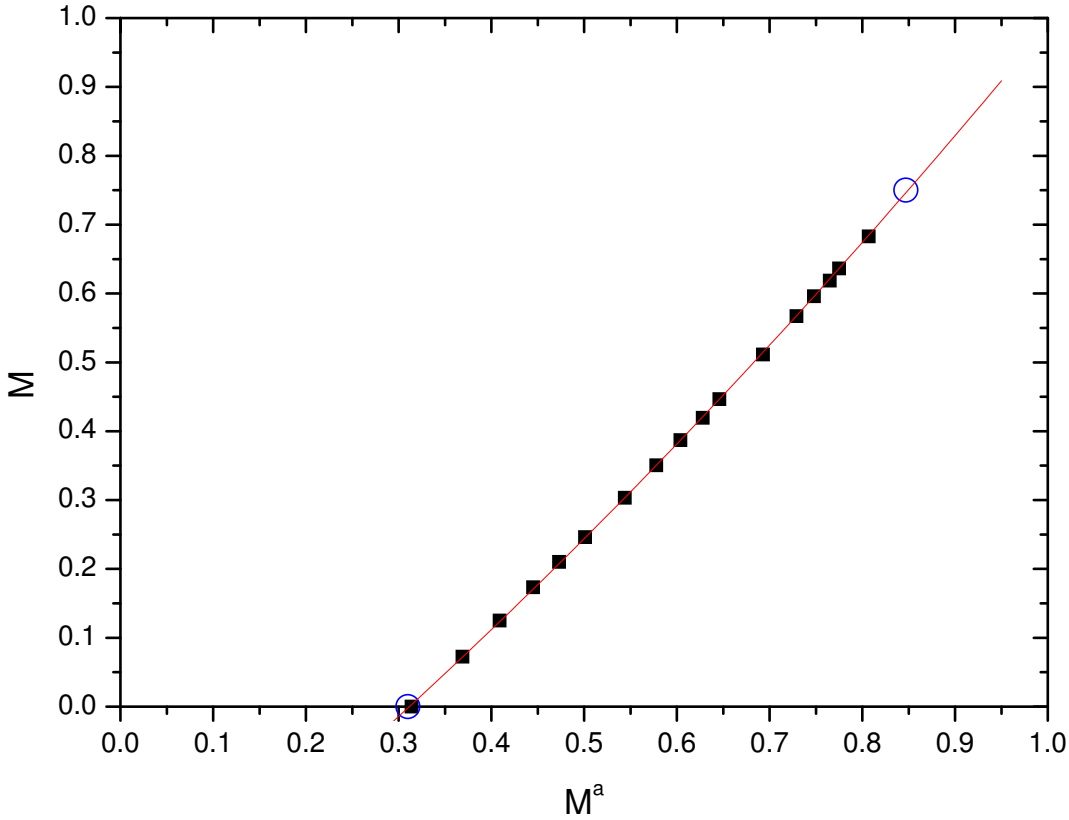

Figure 5.8: Filled squares: Actual polarisation M as function of apparent polarisation M^a in a dedicated experiment to account for perturbations of 2^3S- and 2^3P-populations due to the pump laser (settings: see figure 5.5). Open circles: Apparent polarisation values at beginning and end of OP period of corresponding OP experiment (same settings, but different experimental protocol, see subsection 5.2). Line: Polynomial fit on the data points of the dedicated experiment to determine the correction function for use in the protocol of polarisation build-up and decay: $M = -0.358 + 1.059 \cdot M^a + 0.289 \cdot (M^a)^2$.

figure 5.8, it is possible to proceed in the following way: A second-order polynomial, which empirically turned out to best fit experimental data has 3 free parameters: curvature, slope and axis intercept. Actually the curvature is constrained as it can be expressed as a function of absorbed pump laser power. Thus, the fit is reduced to 2 free parameters, and given the 2 measurements at $M = 0$ and M_{eq} from the standard protocol, a reliable transformation function that relates actual polarisation to apparent polarisation can be inferred.

To conclude, the possibility of accurately relating M to M^a during the entire polarisation build-up and for different experimental parameters and settings allows to reliably study OP dynamics over the whole range of experimental conditions.

5.4 Inferring *actual* M-values during polarisation build-up in presence of the pump laser

Using the results of this auxiliary measurement protocol described in section 5.3 allows to infer actual polarisation values M during polarisation build-up in presence of the pump laser in the most commonly used protocol for our systematic studies of 2^3S-2^3P$_0$ pumping below 30 mT. For *all* different experimental conditions, such dedicated experiments to account for perturbations of 2^3S- and 2^3P-populations in presence of the pump laser were performed.

In the following, we resume the discussion of the example of apparent polarisation as function of time represented in figure 5.4. The determined important polarisation values in stationary conditions (M_0^a, M_{eq} and M_{eq}^a, see caption of figure 5.4) are now used in the following way: The actual polarisation values at zero and steady state polarisation for the polarisation build-up and decay experiment are plotted as function of the apparent polarisation values (open circles in the left part of figure 5.9). Afterwards, the correction function extracted from the corresponding dedicated experiment (used methodology see section 5.3) is applied to the apparent polarisation values during the complete build-up and also included into the plot that represents the actual polarisation as function of the apparent one (line in left part of figure 5.9). The correction function meets the requirements[3] if it passes by the upper and lower borders marked by the pairs of actual and apparent polarisation values extracted from the polarisation build-up and decay protocol in stationary conditions.

The right part of figure 5.9 represents the entire polarisation curve as function of time for the chosen example. During the period of the polarisation build-up (t = 90.8 - 360.8 s), the temporal evolution of the *apparent* polarisation (upper curve) as well as of the *actual* polarisation (obtained by applying the adapted correction

[3]If that is not the case, see last paragraph of section 5.3, page 140, for an alternative strategy to infer a reliable transformation function that relates actual polarisation to apparent polarisation.

function to the apparent polarisation values, lower curve) are plotted. The actual polarisation as function of time (lower curve) exhibits no signs of overpolarisation effects at the beginning of the polarisation build-up (as shown in the left inset of figure 5.4 and explained in detail in section 4.3) and, what is more clearly observable without zooming into the plot, shows no difference in the transition region around $t = 360$ s between the corrected actual polarisation at M_{eq} in presence of the pump laser and the steady state polarisation value at the beginning of the decay without pump laser.

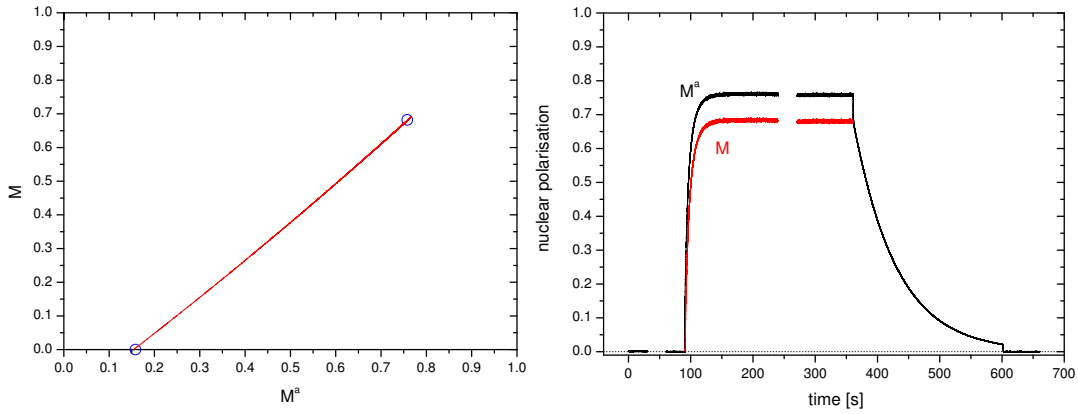

Figure 5.9: Correction of *apparent* polarisation values during polarisation build-up to obtain *actual* polarisation values; experimental settings: see caption of figure 5.1. Left: Actual polarisation M as function of apparent polarisation M^a; open circles: values from polarisation build-up and decay protocol obtained in stationary conditions (M_0 and M_{eq}), line: correction function from corresponding dedicated experiment applied to apparent polarisation values (used correction polynomial: $M = -0.157 + 0.999 \cdot M^a + 0.139 \cdot (M^a)^2$); Right: Complete polarisation curve as function of time; during polarisation build-up ($t = 90.8$ - 360.8 s): apparent polarisation M^a (upper curve) and actual polarisation M (lower curve). Obtained steady-state polarisation: $M_{\mathrm{eq}} = 0.682$.

5.5 Analysis of polarisation build-up kinetics

In the next paragraphs, the analysis of the polarisation build-up kinetics will be discussed and described. A general introduction explains the chosen strategy due to highly non-linear characteristics of the build-up process. A validation of the chosen method to process and analyse the build-up process using synthetic data generated

by the model of MEOP-kinetics (see chapter 2) is presented in appendix F.

The highly non-linear character of the MEOP-process can be well illustrated by examples of experimental data. Figure 5.10 shows an example of a polarisation build-up (27-176 s) towards the steady state polarisation $M_{\mathrm{eq}} = 0.682$ (dotted line) and a decay (176-416 s) at a ^{3}He-pressure of 0.63 mbar.

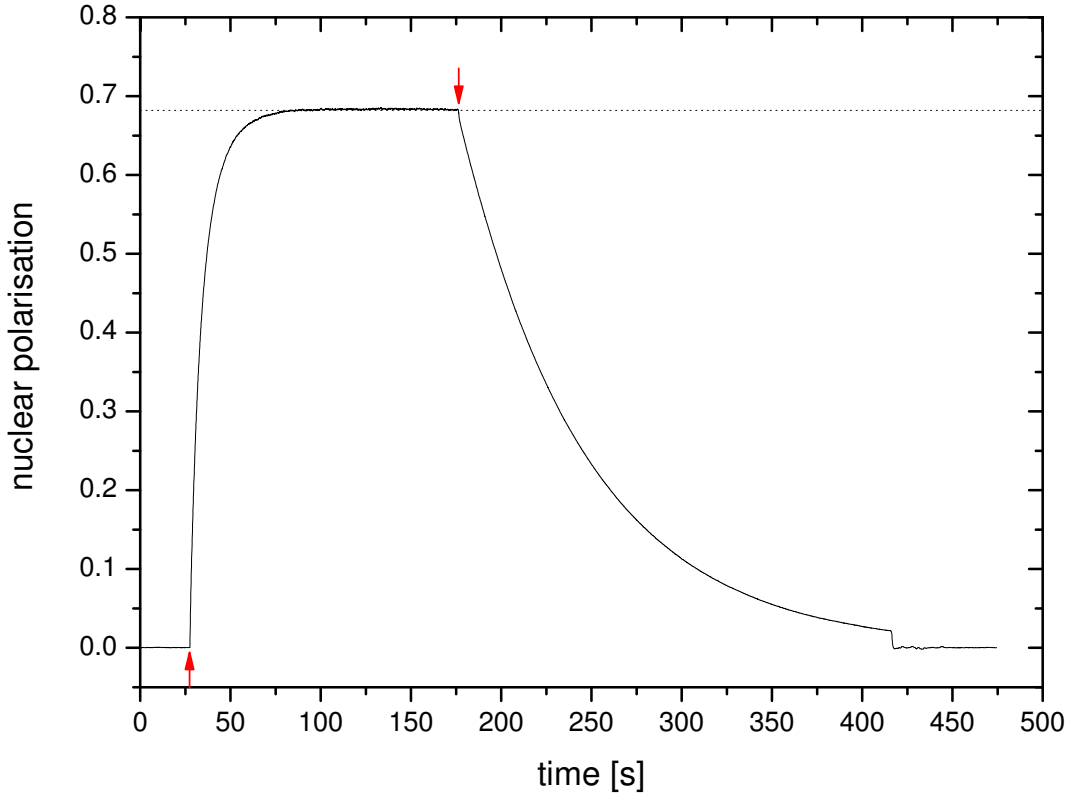

Figure 5.10: Polarisation build-up and decay at $p_3 = 0.63$ mbar, pump: C_8, $W_{\mathrm{inc}} = 0.42$ W, probe: C_8, $B = 1$ mT, $\Gamma_{\mathrm{D}} = (69\,\mathrm{s})^{-1}$, $n_{\mathrm{m}}^{\mathrm{S}}(0) = 3.34 \times 10^{16}$ atoms/m^3, data acquisition frequency: 1 kHz, signals averaged by the time constant of the numerical demodulation: $\tau_{\mathrm{LIA}} = 300$ ms; no periods with discharge switched off during this acquisition; arrow at $t = 27$ s: pump switched on, arrow at $t = 176$ s: pump switched off, dotted line: $M_{eq} = 0.682$, nuclear polarisation during build-up = actual polarisation (i.e., corrections to account for perturbations of 2^3S- and 2^3P-populations due to the pump laser are already applied, cf. subsection 5.3). At $t = 417$ s (up to $t = 447$ s), a magnet has been positioned close to the cell in order to record the final $M = 0$ level.

In figure 5.11, details of build-up and decay are represented separately and in the following way: On the left, the difference $M_{\mathrm{eq}} - M$ is plotted in semi-logarithmic

scale as function of time during build-up, on the right, the nuclear polarisation M is also plotted in semi-logarithmic scale as function of time during decay. It is clearly observable, that the *build-up* is *non*-exponential. In contrast to the build-up, the polarisation *decay* is always *mono*-exponential as indicated by the straight line over the whole range of polarisation values.

The time constant characterising the exponential decay, namely the decay rate Γ_{D}

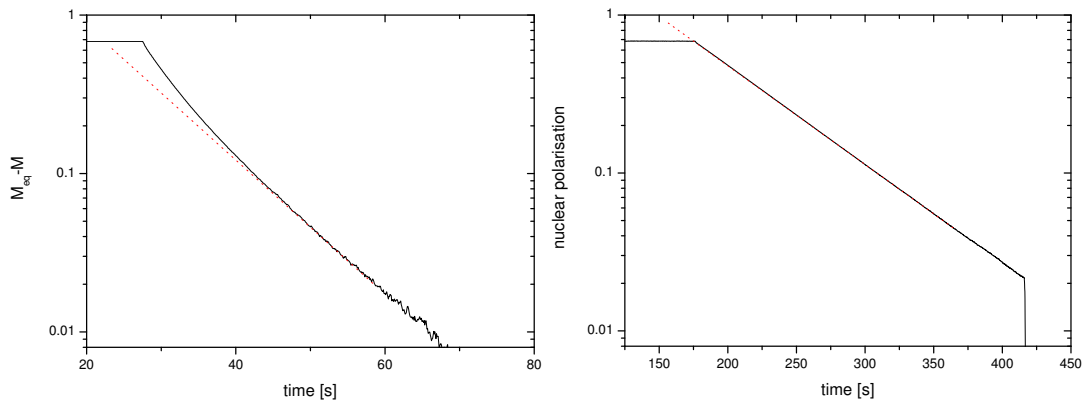

Figure 5.11: Left: Polarisation build-up: $M_{eq} - M$ is plotted as function of time (i.e., high ordinate-values correspond to small M-values); Right: M as function of time (i.e., high ordinate-values correspond to high M-values); dotted straight lines in both semi-logarithmic graphs: mono exponential guides for the eye. The build-up is *non*-exponential for $M_{eq} - M > 0.06$, i.e. for $M < 0.622$, the decay is always mono exponential. Experimental parameters: see caption of figure 5.10.

in presence of the discharge, can thus be determined by an exponential fit (in linear representation of the ordinate) of all polarisation values recorded after the pump laser has been switched off as function of time, as it is constant during the entire decay.
For the polarisation build-up, however, the fact that it is clearly *non*-exponential as shown in figure 5.11 and therefore cannot be characterised by one single time constant, has consequences on the strategy used to determine the characteristic parameters. Several exponential fits during polarisation build-up are performed on suitable time intervals in order to characterise polarisation growth, details are given in the next paragraphs.

A series of M-dependent build-up time constants $T_b(M_k)$ is thus obtained, with the corresponding time derivatives

$$\dot{M}(M_k) = \frac{M_{\mathrm{eq}} - M_k}{T_b(M_k)}. \tag{5.1}$$

Characterising OP build-up by $\dot{M} = \frac{dM}{dt}$ instead of T_b is more appropriate as it is a stand-alone significant parameter. This is in contrast to T_b, that is meaningful

only when M_{eq} is known and specified as well. Basing discussions of OP-dynamics only on $T_b(M = 0)$ can be misleading: the same $T_b(0)$ in two different experiments for example is *no* indication that OP dynamics are identical. One experiment could possibly have a high initial $\dot{M}(M = 0)$ (steep slope in the beginning of the build-up process) and a high M_{eq}, whereas the other one has a lower $\dot{M}(M = 0)$ (flat slope in the beginning of the build-up process) and a lower M_{eq}, both with the same ratio of $\frac{M_{eq}}{\dot{M}(0)}$, i.e. the same $T_b(0)$. In low field and low pressure MEOP, this can be the case for C_8-pumping at high laser power and C_9-pumping at lower laser power.

Time derivatives $\dot{M}$ as function of M

In order to determine $\dot{M}$ and T_b as function of nuclear ground state polarisation M, a dedicated Fortran-programme is used to process the data. As input, the programme reads in all actual values of M as function of t during build-up, and furthermore prompts for the steady-state polarisation value M_{eq}. When processing experimental data, the polarisation build-up starts at approximately $t = 90$ s due to the experimental protocol (see table 5.1). The exact value is determined in each data-file and subtracted as offset, so that for further data processing of the build-up process, t equals 0 s at the initial moment of the polarisation build-up process.
The programme then executes linear regressions on short sliding intervals of the natural logarithm of the difference between the entered asymptotic value M_{eq} and the current polarisation value $M(t)$ and thus determines in each interval the characteristic time constant T_b. This procedure of linear fits on $\ln(M_{eq} - M)$ is in most conditions completely equivalent to exponential fits on $M(t)$. This aspect is discussed in detail in appendix F.
An experimental example of the quantity $\ln(M_{eq} - M)$ is shown figure 5.12, which serves in the following to illustrate several details of data processing by the dedicated programme.
In a first step, the programme determines the total variation span of polarisation during build-up by building the difference between M_{eq} and the value of M in the first row of the input file. Based on this total variation span of polarisation, the length of the fit intervals and the number of fit intervals can be defined. The number of fit intervals is indirectly defined: after finishing the fit procedure on one interval, the initial M-value of the next fit interval is obtained by adding a certain fraction of the whole variation span to the initial M-value of the previous interval. For most of the investigated cases in this work, viable values were the following: $\frac{1}{10}$ of the total variation span to define the length of a fit interval and $\frac{1}{50}$ of the total variation span to be added to the initial M-value of the previous interval. In the example of figure 5.12, the total variation span of polarisation amounts to 0.68, the length of each fit interval is 0.068 (expressed in units of the ordinate), and the difference between the starting

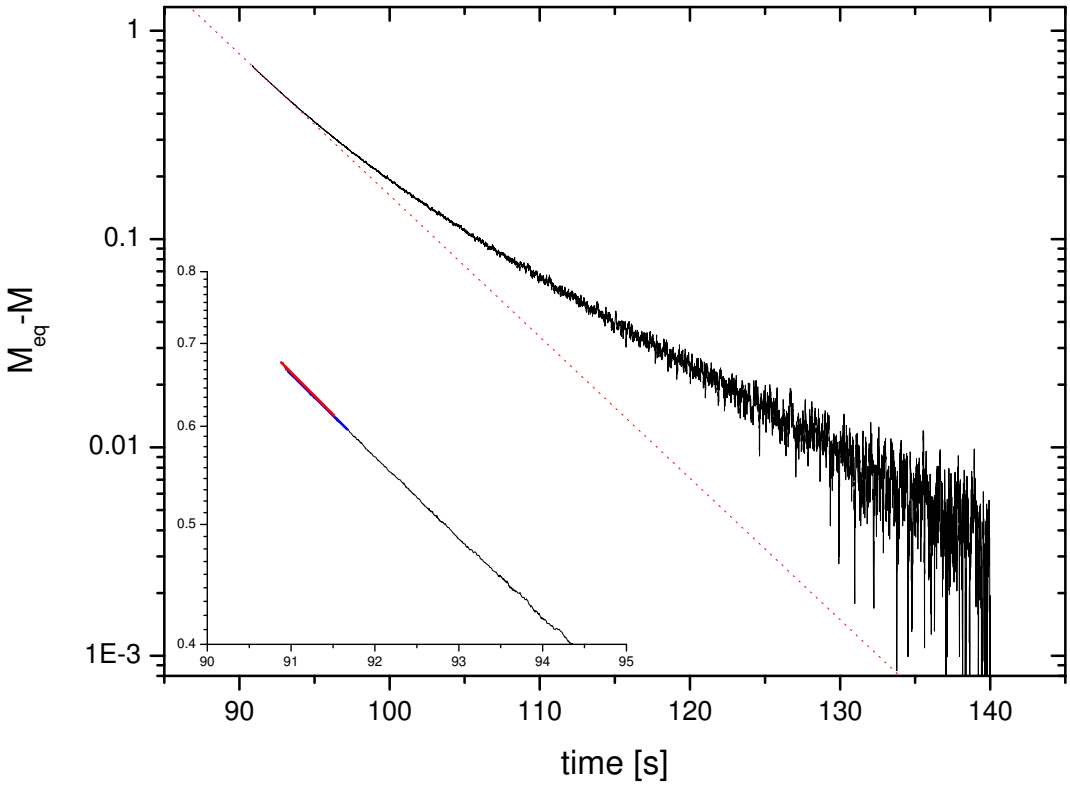

Figure 5.12: Difference between the asymptotic steady state polarisation M_{eq} and the current polarisation value $M(t)$ (logarithmic scale) as function of time to determine T_b and $\dot{M}$ (details see text, experimental settings: see caption of figure 5.1). Only the main part of the polarisation build-up is shown (up to t=140 s). It is characterised by fast changes in polarisation, and 99% of M_{eq} is reached. The long dotted straight line represents an exponential adjustement in the zone around $M = 0$ with M_{eq}=0.682. This adjustment yields $T_b = (6.39 \pm 0.04)$ s. Inset: Illustration of first two fit intervals used by the dedicated programme (details how length and starting points of the fit intervals are determined: see text). The linear regression in the second interval yields $T_b = (6.54 \pm 0.02)$ s.

points (ordinate-values) of two adjacent fit intervals equals approximately 0.014.
The consequences on $\frac{dM}{dt}$ when varying the length of the fit interval are discussed in appendix F.
In each of these short fit intervals, the polarisation build-up is modelled by an exponential function:

$$M(t) = M_{eq} - C\ \exp(-\frac{t}{T_b}). \tag{5.2}$$

As the programme takes $\ln(M_{eq} - M(t))$ as Y-parameter of the fit, the problem is simplified to a linear fit:

$$Y = P_1 + P_2\, X \tag{5.3}$$

$$\ln(M_{eq} - M(t)) = P_1 + P_2\, t \tag{5.4}$$

with $\ln(M_{eq} - M(t))$ as dependent parameter, time t as independent parameter and coefficients P_1, P_2 and C ($P_1 = \ln(C)$, which follows from rearranging equation (5.2), building the natural logarithm on both sides of the equation and comparing it to equation (5.4)).
In each short fit interval, the characteristic parameters of the polarisation build-up can be determined from each linear fit. The build-up time T_b results as well from the described comparison of equations (5.2) and (5.4):

$$T_b = -\frac{1}{P_2}. \tag{5.5}$$

The inset of figure 5.12 clearly shows that two adjacent fit intervals do have slightly different T_b and this fact underlines the necessity to carefully limit the length of each fit interval, in order to determine the build-up time variation precisely.
$\frac{dM}{dt}$ can be expressed using parameters of the linear fit as follows:

$$\frac{dM}{dt} = -P_2\,(M_{eq} - M_c) = \frac{M_{eq} - M_c}{T_b}, \tag{5.6}$$

with M_c: the polarisation value in the centre of the current fit interval defined by:

$$M_c = M_{eq} - \exp(a), \tag{5.7}$$

with $a = \ln(M_{eq} - M_c)$. As M_c is the searched quantity, a has to be determined by the programme in the following procedure: In each fit interval, the central time instant is determined by adding lower and upper borders and dividing the sum by 2. This central time instant is then subtracted from each time-value. The time-values are thus moved in a way that the shifted time variable in each fit interval is centred around zero and varies from a negative value to the same positive value. This shifted time variable serves as x-variable, $\ln(M_{eq} - M)$ is used as y-variable in the linear regression

yielding the slope P_2 in each fit interval. The auxiliary variable a is then obtained as follows:

$$a = \frac{s_y - s_x \cdot P_2}{n}, \tag{5.8}$$

with s_y: sum of all y-values, s_x: sum of all x-values in the fit interval consisting of n data pairs.
The number n of data points per fit interval is not the same for all intervals within the complete polarisation build-up, as the length of the intervals is fixed in units of the ordinate ($\ln(M_{eq} - M)$) and *not* in units of the abscissa (shifted time): In the beginning of the build-up process, the intervals are short and then become longer as the pumping process slows down with increasing nuclear polarisation M.
The sum s_x is a very small positive or negative number close to zero and characterises to what extent the data points are shifted from the centre of the fit interval. Hence the second term in the numerator of equation (5.8) is a sort of "correction" term to precisely determine the centre of the fit interval in units of the ordinate and thus M_c with the help of equations (5.7) and (5.8).

To summarize, the dedicated programme yields values of the time derivative of polarisation $\dot{M}$ and of the build-up time constant T_b, both as a function of nuclear polarisation M. These results are then used to extrapolate the value of $\dot{M}$ at zero polarisation ($M = 0$) by applying an empirical 2nd or 3rd order polynomial fit. $\dot{M}(M = 0)$ is given by the intercept with the $\frac{dM}{dt}$-axis, i.e. by the constant parameter of the polynomial fit function (details see appendix F).
The reason why we prefer to extrapolate $\dot{M}(M = 0)$ instead of $T_b(M = 0)$ is explained on page 143 and briefly recalled here: $\dot{M}(0)$ is independent of the steady state polarisation value M_{eq} and therefore a significant physical parameter in contrast to $T_b(0)$, which is only meaningful when M_{eq} is known as well, since $T_b(0)$ can be expressed using equation (5.6) by:

$$T_b(0) = \frac{M_{\text{eq}}}{\dot{M}(0)}. \tag{5.9}$$

Example of experimental polarisation growth

In order to complete the description of the polarisation build-up analysis, the developed methods are applied to the same experimental example as used in section 5.2. The results are presented and reviewed in the following. In appendix F, the chosen methodological approach is discussed and validated on synthetic data.

First of all, the acquired data (experimental parameters and settings, see caption of figure 5.1) were processed using the dedicated programme with standard intervals (spanning $\frac{1}{10}$ of the total variation of M during build-up) to determine T_b and $\dot{M}$,

and additionally with short intervals ($\frac{1}{20}$ of the total variation of M) and with long intervals ($\frac{1}{5}$ of the total variation of M). In figure 5.13, $\dot{M}$ values as function of M are represented for each used length of fit intervals in the programme.

Data illustrate that the influence of the length of fit intervals in the programme to

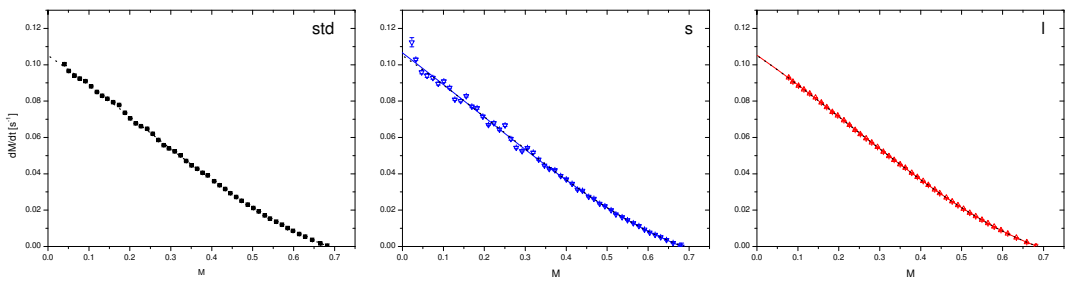

Figure 5.13: $\dot{M}$ as function of M of experimental example (settings and parameters, see caption of figure 5.1) for different lengths of fit intervals used in the dedicated programme. Left (filled squares): Standard intervals, dotted line: 3rd order polynomial fit to extrapolate $\dot{M}(0)$ from $\dot{M}$-values stemming from the Fortran programme using standard intervals. This fit function is plotted in the two other graphs as well as guide for the eye. Centre (open downward triangles): Short intervals, solid line: 3rd order polynomial fit on $\dot{M}$-values obtained by using short intervals in the dedicated programme. Right (open triangles): Long intervals, solid line: 3rd order polynomial fit on $\dot{M}$-values stemming from the dedicated programme using long intervals.

determine T_b and $\dot{M}$ on this experimental example is not as important as on synthetic data with a higher noise level shown in appendix F. As expected, the shorter the used fit intervals in the programme, the higher the vertical scatter of $\frac{dM}{dt}$-values, and the more values close to $M = 0$ the programme yields. Performing a 3rd order polynomial fit on the whole range of $\frac{dM}{dt}$-values obtained using standard intervals in the programme yields $\dot{M}(0) = 0.1052(2)$ s^{-1}. The extrapolated $\frac{dM}{dt}(0)$-value on long intervals by a 3rd order polynomial fit as well is less than 0.1 % higher and included within the error of the extracted $\frac{dM}{dt}(0)$-value from standard intervals. The ratio of $\frac{dM}{dt}(0)$ from short intervals divided by $\frac{dM}{dt}(0)$ from standard intervals amounts to 1.013 which shows that the discrepancy is higher than compared to long intervals, but still quite moderate on this experimental example with good SNR. The observed tendency is in accordance with conclusions from appendix F (example of synthetic data): too short fit intervals in the programme should be avoided, especially on data with low SNR.

In the following, for the same selected example of experimental data, the input-parameter of M_{eq} in the programme is varied and the influence on build-up time constants is examined. Figure 5.14 represents T_b as function of M for different

M_{eq}-values.

Just like for synthetic data (cf. appendix F), figure 5.14 - based on an experimental

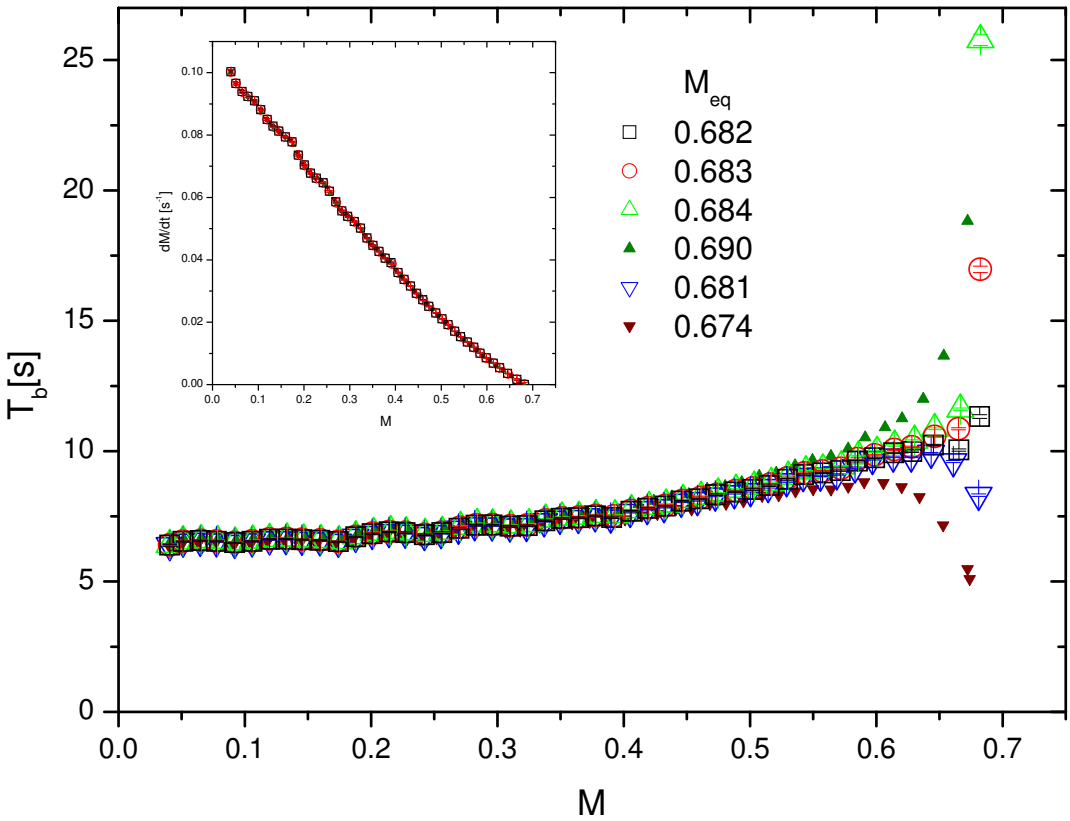

Figure 5.14: T_b as function of M of experimental data set (parameters and settings, see caption of figure 5.1) for different input-values of M_{eq} (see legend) in the dedicated programme. The actual M_{eq} is 0.682, the error bars for $M_{\text{eq}} = 0.690$ and 0.674 (not exceeding the errors for other M_{eq}-values) are not represented in the graph for a better legibility. Inset: $\dot{M}$ as function of M for $M_{\text{eq}} = 0.682$, 0.683, 0.690 and 0.674 (last two values: plotted without errors).

data set - illustrates that the choice of M_{eq} in the dedicated programme has an influence on build-up time constants mainly at high M. The actual M_{eq} is 0.682 and was determined in two different ways: first, by exponential fit during polarisation decay (pump laser off) which yields the initial M-value at the beginning of the decay and second, by determining the asymptotic value of actual polarisation obtained at the end of the build-up curve. The determined M_{eq}-values of both methods should of course be identical, if not, this can be an indication of a possible problem concerning the correction of M during build-up, cf. subsection 5.3. The agreement of both determined M_{eq}-values can still be delusive though, e.g. at low incident laser

power, when the OP time was not long enough to reach M_{eq}. In cases like this, it is easy to check whether the determined M_{eq} is reasonable by using different values of M_{eq} as input-parameter in the dedicated programme and verifying whether the resulting build-up times especially at high M vary regularly, without inflexion and in a monotone way when passing $M = M_{eq}$ as the MEOP-model predicts. Figure 5.14 shows that in this case, the determined M_{eq} of 0.682 is correct as it meets best the predictions of the MEOP-model concerning the behaviour of T_b when passing $M = M_{eq}$.
The relative error of T_b with respect to T_b of the correct M_{eq} when choosing a less appropriate input-value of M_{eq} in the programme amounts to 3 % at 0.9 M_{eq} and 62 % close to M_{eq} when varying M_{eq} by ± 0.3 %. When varying M_{eq} by ± 1.2 %, the relative error of T_b increases to 12 % at 0.9 M_{eq} and 81 % close to M_{eq}. On synthetic data (see appendix F), varying M_{eq} by ± 0.6 % led to $\frac{\Delta T_b}{T_b}$ of 8 % at 0.9 M_{eq} and 30 % close to M_{eq}. At 0.9 M_{eq}, the relative error of T_b of the experimental dataset is in good agreement with synthetic data; close to M_{eq}, $\frac{\Delta T_b}{T_b}$ of the chosen experimental example is higher than on synthetic data. However, not too much importance should be attached to this observation since build-up time constants at the *beginning* of the polarisation build-up are interesting and more pertinent values than towards the end of the polarisation build-up where T_b is tainted with higher uncertainties than at lower M, mainly due to the choice of M_{eq} in the dedicated programme.
The inset of figure 5.14 demonstrates that the consequences of the choice of M_{eq} on $\frac{dM}{dt}$ in the programme is negligible as expected, as $\dot{M}$ values are *in*dependent of M_{eq} in contrast to build-up times (cf. page 143).

With this experimental example which turns out to be concordant with the conclusions drawn from the example of synthetic data presented in detail in appendix F, the discussion of analysing procedures of the polarisation build-up process which is of great importance to characterise OP dynamics is concluded.

5.6 Pump output signals

5.6.1 Transmitted pump signals

An *absolute* value of the pump light transmission coefficient T_p is measured at steady state polarisation M_{eq}, from the ratio of the directly transmitted pump power signal in presence of the discharge divided by the corresponding signal without discharge (offsets (pump laser blocked) subtracted in both cases).
We designate by $A_{\mathrm{eq}} = 1 - T_p(M_{\mathrm{eq}})$ the fraction of absorbed pump power at steady-state nuclear polarisation.
An experimental example of a directly transmitted pump power signal S_p is provided in

figure 5.15 for the same experimental example as already shown earlier in section 5.2. The period during which the discharge is switched off ($t = 240 - 270$ s) is clearly distinguishable. Laser intensity fluctuations are also visible.

Using the transmitted pump power signals at steady state polarisation ($S_p(M_{\mathrm{eq}})$)

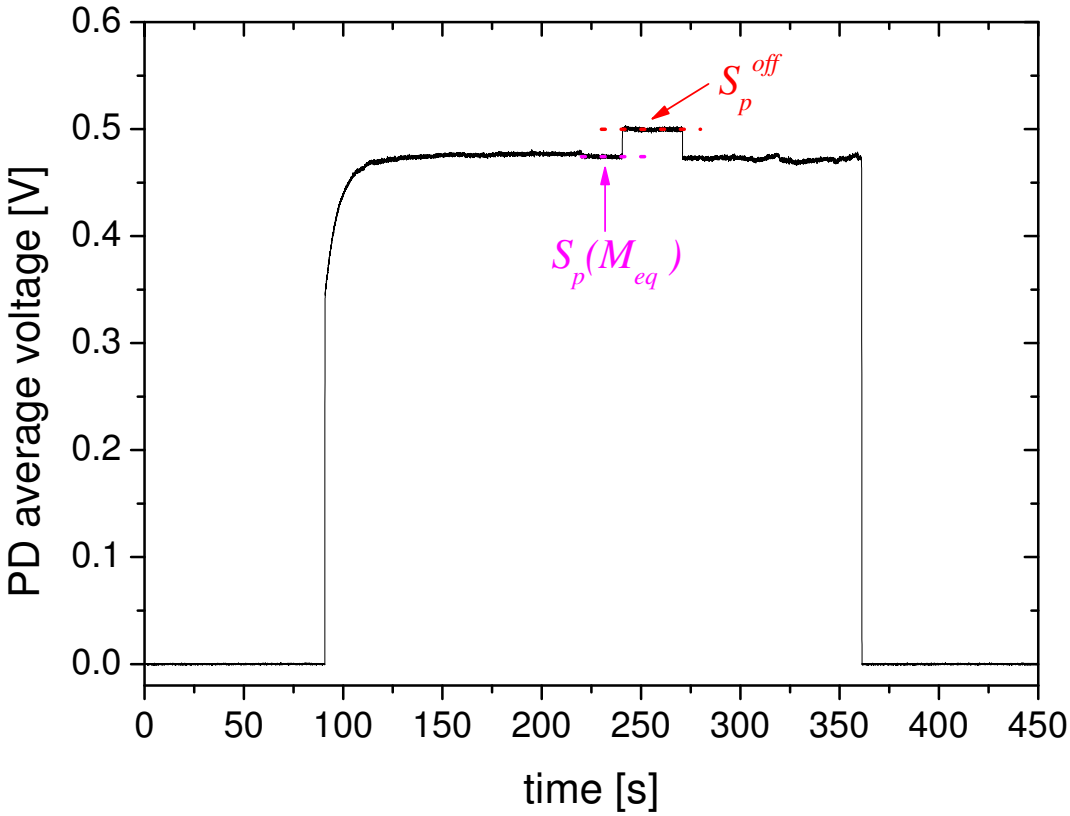

Figure 5.15: Transmitted pump power signal S_p as function of time. Same experimental example as represented for instance in figures 5.1 and 5.4. Signals are averaged by the time constant of the numerical demodulation: $\tau_{LIA} = 30$ ms; $p_3 = 0.63$ mbar, pump: C_8, $W_{\mathrm{inc}} = 0.42$ W, $B = 1$ mT, $n_{\mathrm{m}}^{\mathrm{S}}(M = 0) = 3.34 \times 10^{16}$ atoms/m^3. $t = 240 - 270$ s: discharge switched off.

and when the discharge is switched off (S_p^{off}), the fraction of absorbed pump power at steady-state nuclear polarisation is determined as follows:

$$A_{\mathrm{eq}} = 1 - \frac{S_p(M_{\mathrm{eq}})}{S_p^{\mathrm{off}}} = \frac{S_p^{\mathrm{off}} - S_p(M_{\mathrm{eq}})}{S_p^{\mathrm{off}}}. \tag{5.10}$$

The uncertainty dA_{eq} is obtained according to error propagation principles by quadratically adding up the non-correlated error contributions:

$$dA_{\mathrm{eq}} = \delta \sqrt{\left|\frac{\partial A_{\mathrm{eq}}}{\partial S_p^{\mathrm{off}}}\right|^2 + \left|\frac{\partial A_{\mathrm{eq}}}{\partial S_p(M_{\mathrm{eq}})}\right|^2}, \tag{5.11}$$

where δ is the uncertainty on the measured PD voltage of the transmitted pump light. Building the partial derivatives and simplification leads to:

$$dA_{\mathrm{eq}} = \delta \frac{\sqrt{1 + \left(\frac{S_p(M_{\mathrm{eq}})}{S_p^{\mathrm{off}}}\right)^2}}{S_p^{\mathrm{off}}}. \tag{5.12}$$

The relative uncertainty $\frac{dA_{\mathrm{eq}}}{A_{\mathrm{eq}}}$ is observed to range between 0.5 % and 4.4 %, (1.9 ± 0.4) % on average, in our analysed data.

5.6.2 Demodulated pump signals

Pump transmission values for all M during polarisation build-up are obtained by monitoring the demodulated pump signal P_p in a similar way as for the probe. The extrapolated value at M_{eq} is used for normalisation in the following way:

$$\frac{-\ln T_p(M)}{-\ln T_p(M_{\mathrm{eq}})} = \frac{(P_p/S_p)(M)}{(P_p/S_p)(M_{\mathrm{eq}})}, \tag{5.13}$$

where $-\ln T_p$ is the absorbance for the pump laser, P_p is the demodulated pump signal (in-phase component, which is the safest option instead of basing the data analysis on the magnitude, since Rician noise (cf. appendix E) can be an issue for pump absorption signals) and S_p is the average transmitted pump signal, as function of M and at M_{eq} respectively. Taking the ratio of P_p/S_p reduces effects of laser intensity fluctuations and of optical thickness of the gas on absorption [Cou01] as described in the introductory section 5.1 of this chapter. We designate this ratio of P_p/S_p by A_p (pump absorption signal) in the following. Pump transmission coefficients can then be expressed as a function of M:

$$T_p(M) = \exp\left[\ln T_p(M_{\mathrm{eq}}) \frac{A_p(M)}{A_p(M_{\mathrm{eq}})}\right]. \tag{5.14}$$

The pump transmission coefficient constitutes a very important quantity for determining $W_{\mathrm{abs}} = (1 - T_p)W_{\mathrm{inc}}$, the absorbed pump laser power that is essential for data analysis: along with $\dot{M}$, W_{abs} is needed to obtain photon efficiencies, that in

turn are required to quantitatively investigate total relaxation rates Γ_R (cf. sections 6.3.3, 6.3.4, 6.4 and 6.5).
The left graph in figure 5.16 represents an experimental example of the pump transmission coefficient T_p as function of M during polarisation build-up for the same experimental example as in figure 5.15. The strong discharge in this example is the reason for the relatively high variation of $T_p(M)$ between roughly 0.7 and 1.
The absorbed fraction of pump power at $M = 0$, denoted A_0, is determined with

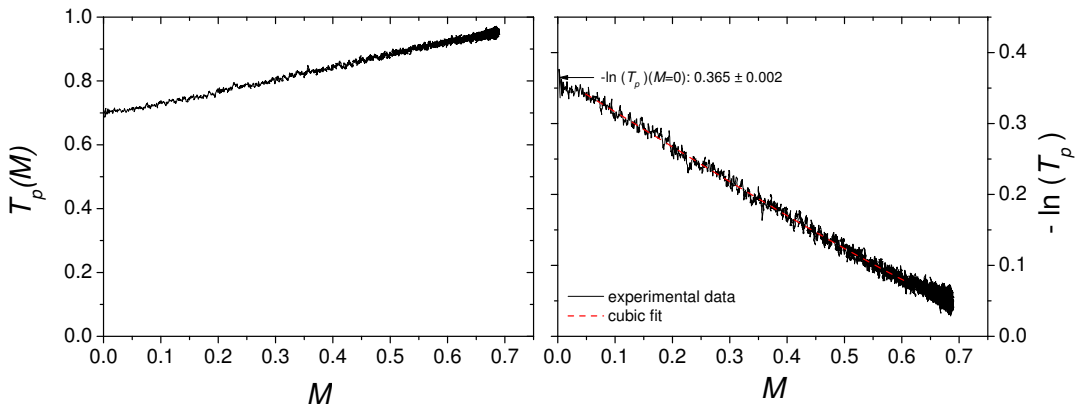

Figure 5.16: Left: Pump transmission coefficient T_p obtained from the pump absorption signal (time constant of numerical demodulation: $\tau_{\mathrm{LIA}} = 30$ ms) as function of M during polarisation build-up. Experimental settings: see caption of figure 5.15. Right: Absorbance for the pump laser $-\ln T_p$ as function of M during polarisation build-up of the same experiment. An empirical fit (3rd order polynomial here) is applied to extrapolate $-\ln T_p(M = 0) =: X_0 \pm \Delta X_0$. Using this value to determine the absorbed fraction of pump power at $M = 0$ (see text) yields: $A_0 = 0.306 \pm 0.006$ in this example (including error contributions from M_{eq}, see text).

the help of equation (5.13), written in a different way here (X being just a compact notation needed later in equation (5.17)):

$$X(M) := -\ln T_p(M) = -\frac{\ln T_p(M_{\mathrm{eq}})}{A_p(M_{\mathrm{eq}})}\, A_p(M). \tag{5.15}$$

In practice, the quantity $-\ln T_p$ is plotted as a function of M (see right graph of figure 5.16). An empirical second or third order polynomial fit is applied and the axis intercept at $M = 0$ yields $-\ln T_p(M = 0)$. Using this extrapolated value of $-\ln T_p(M = 0) =: X_0$, the pump absorptance at $M = 0$, A_0, is given by:

$$A_0 = 1 - \exp\left[\ln T_p(M = 0)\right]. \tag{5.16}$$

This procedure simplifies the error discussion since on the right hand side of equation (5.15), it is possible to separate individual errors on determined values at M_{eq}

and on the pump absorption signal (here at $M = 0$).
The uncertainty dX_0 is obtained by quadratically adding up the different error contributions, using compact notations ($T_p^{\mathrm{E}} := T_p(M_{\mathrm{eq}})$, $A_p^{\mathrm{E}} := A_p(M_{\mathrm{eq}})$, $A_p^0 := A_p(M = 0)$):

$$\begin{aligned} dX_0 &= \sqrt{\left(\left|\frac{\partial X|_{M=0}}{\partial T_p^{\mathrm{E}}}\right| \Delta T_p^{\mathrm{E}}\right)^2 + \left(\left|\frac{\partial X|_{M=0}}{\partial A_p^{\mathrm{E}}}\right| \Delta A_p^{\mathrm{E}}\right)^2 + \left(\left|\frac{\partial X|_{M=0}}{\partial A_p^0}\right| \Delta A_p^0\right)^2} \\ &= \sqrt{\left(\frac{A_p^0}{A_p^{\mathrm{E}}\, T_p^{\mathrm{E}}}\, \Delta T_p^{\mathrm{E}}\right)^2 + \left(\frac{\ln T_p^{\mathrm{E}}\, A_p^0}{(A_p^{\mathrm{E}})^2}\, \Delta A_p^{\mathrm{E}}\right)^2 + \left(\frac{\ln T_p^{\mathrm{E}}}{A_p^{\mathrm{E}}}\, \Delta A_p^0\right)^2} \\ &= \sqrt{\left(\frac{A_p^0}{A_p^{\mathrm{E}}}\right)^2 \left\{\left(\frac{\Delta T_p^{\mathrm{E}}}{T_p^{\mathrm{E}}}\right)^2 + \left(\ln T_p^{\mathrm{E}}\, \frac{\Delta A_p^{\mathrm{E}}}{A_p^{\mathrm{E}}}\right)^2\right\} + \left(\frac{\ln T_p^{\mathrm{E}}}{A_p^{\mathrm{E}}}\, \Delta A_p^0\right)^2}. \end{aligned} \tag{5.17}$$

The last error contribution in equation (5.17) corresponds to the error ΔX_0 of the extrapolated fit parameter $X_0 = -\ln T_p(M = 0)$. The other terms constitute error contributions from the pump transmission coefficient and the pump absorption signal, both at M_{eq}. In most cases, the sum of error contributions from M_{eq} in our data exceeds the error of the extrapolated fit parameter by a factor of 5 to 15 approximately.
Assuming equality of *relative* errors $\frac{dX_0}{X_0} = \frac{dA_0}{A_0}$, the absolute uncertainty dA_0 of the pump absorptance at $M = 0$ is given by:

$$dA_0 = \frac{dX_0}{X_0}\, A_0. \tag{5.18}$$

The relative uncertainty $\frac{dA_0}{A_0}$ is observed to range between 1.2 % and 5.2 %, (2.6 ± 0.4) % on average, in our analysed data.

5.7 Laser-enhanced relaxation

Relaxation phenomena play a key role with regard to OP performances. Being able to quantify polarisation losses during build-up is an important precondition for a better understanding of relaxation mechanisms and can contribute to ultimately overcome current limitations. Comparing experimental steady-state polarisations or rates of change of polarisation $\dot{M}$ (obtained as described in subsection 5.2) with the corresponding values computed using the MEOP-model can be used to derive relaxation rates.

Figure 5.17a displays an example of steady state polarisation values measured for various incident pump laser powers as well as the corresponding expected values computed for the same MEOP conditions using the improved OP model (cf. section 2.5). The measured steady state polarisation values are observed to be systematically lower

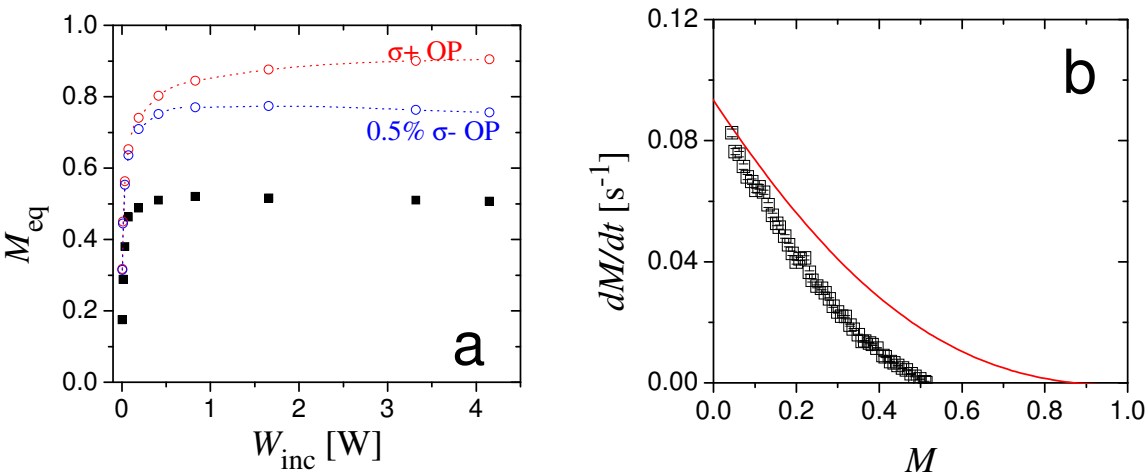

Figure 5.17: **a** - Experimental (filled squares) and computed (open circles) steady state polarisation values for a series of incident pump laser powers W_{inc}. Computations are made for a pure $\sigma+$ polarised pump (upper data) and for imperfect circular polarisation (lower data). Dotted lines through computed values are guides for the eye. **b** - Experimental (symbols) and computed (line) $\dot{M}$ are plotted as functions of M for W_{inc}=1.66 W. (MEOP conditions for all data: $p_3 = 2.45$ mbar, pump: C_9, probe: C_8, $B = 1$ mT, weak discharge: $\Gamma_{\mathrm{D}} = (835\ \mathrm{s})^{-1}$, $n_{\mathrm{m}}^{\mathrm{S}}(M = 0) = 1.73 \times 10^{16}$ atoms/m^3, α=1.5). For the computations, $\Gamma_{\mathrm{g}} = \Gamma_{\mathrm{ME}}^{0} = \Gamma_{\mathrm{D}}/2$, see equation (2.71).

than predicted when the experimental value of the decay rate Γ_D is used to constrain the input relaxation parameters for the computations (see caption). Even a rather poor polarisation of the OP light cannot account for the observed polarisations.

Figure 5.17b shows the comparison of experimental and computed $\dot{M}$ as function of M in the same cell and discharge conditions. They are in good agreement at $M = 0$, but experimental values decrease faster than predicted using Γ_{D} as relaxation parameter. The intercepts with the M-axis in figure 5.17b are the steady-state values plotted in figure 5.17a for this value of the laser power. The systematic discrepancies indicate that polarisation losses are underestimated during polarisation build-ups (except at $M = 0$) when only taking into account the relaxation rates measured during decays (i.e., without pump laser).

The next parts of this section describe two methods used to infer polarisation losses during build-ups. The first one makes explicit use of the MEOP model, while the second relies on angular momentum budget considerations.

5.7.1 Deriving polarisation loss rates Γ_{R} using the MEOP model

In the examples of figure 5.17 the improved OP model is used to compute $\dot{M}$ according to equation (2.51) as the balance of the volume-averaged ME-driven growth and of the loss term $-\Gamma_{\mathrm{g}}M$. In these examples, the rates $\gamma_{\mathrm{r}}^{\mathrm{S}}$ (for relaxation in the 2^3S state) and Γ_{g} (for direct relaxation of atoms in the ground state) are chosen to be consistent with the observed decay rate Γ_{D} as described in section 2.8.2. The global polarisation loss rate Γ_{R} introduced in equation (2.77) pragmatically combines losses resulting from relaxation in the 2^3S state and in the ground state. It is simply equal to the decay rate Γ_{D} measured in the absence of pumping. The difference between computed and measured $\dot{M}$ data is attributed to an additional, laser-induced loss rate Γ_{L} such that:

$$\dot{M}^{\mathrm{exp}}(M) = \dot{M}^{\mathrm{model}}(M) - \Gamma_{\mathrm{L}}M. \tag{5.19}$$

In that frame, relaxation is enhanced during MEOP and the global loss rate is increased with respect to the decay rate:

$$\Gamma_{\mathrm{R}} = \Gamma_{\mathrm{D}} + \Gamma_{\mathrm{L}}. \tag{5.20}$$

This is illustrated in the following for the example of C_9 pumping already displayed in figure 5.17b. Figure 5.18 shows two different computed $\dot{M}$ values for identical input parameters except the value of the radial n_{m} parameter α. Both values are reasonably close to those measured by mapping of the radial metastable distributions, reported in section 6.1.2. The resulting $\dot{M}$-curves differ primarily at small values of M, and tend to collapse at high M (the relative difference is of order 7-10 % for $M < 0.6$). The small differences between experiments and computations observed at $M = 0$ may result from various experimental uncertainties and from the coarse description of two velocity classes in the MEOP model. Similar behaviour of computed $\dot{M}$-curves is observed when slightly changing other parameters, e.g. the beam diameter.

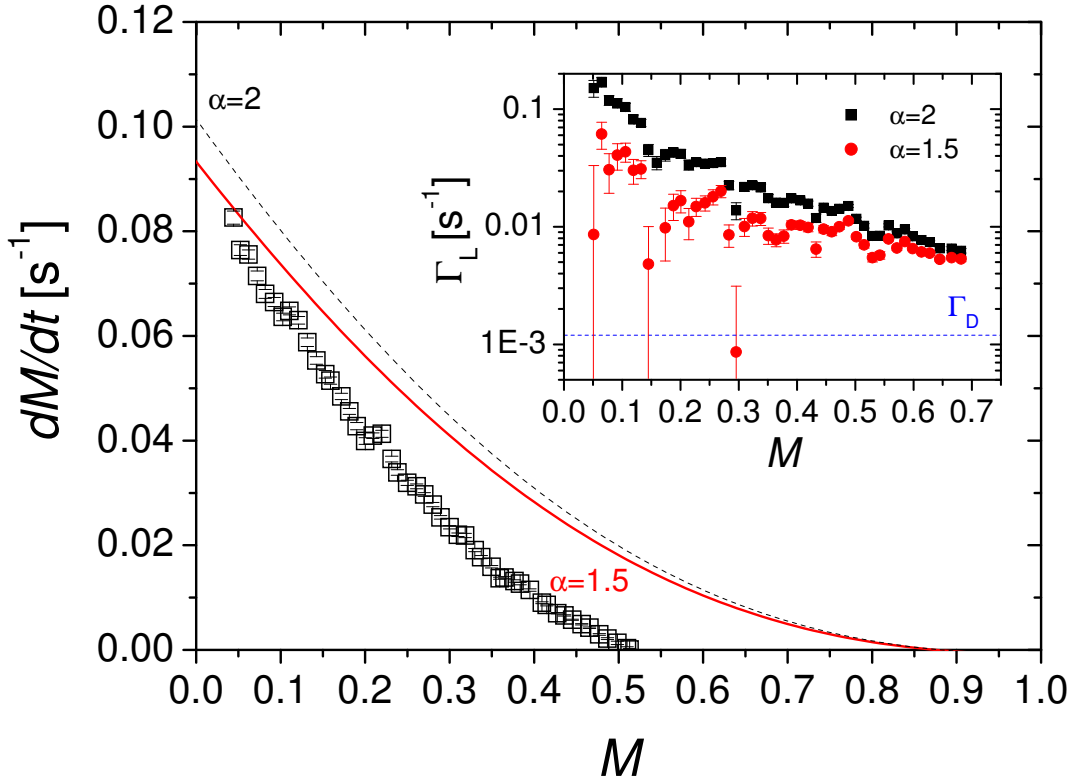

Figure 5.18: Experimental (open squares) and computed (lines) $\dot{M}$ are plotted as functions of M. Computed results are displayed for α=1.5 (solid line) and α=2 (dotted line). Inset: Additional relaxation rates Γ_L derived from equation (5.19) for the two values of α. (Same MEOP conditions as in figure 5.17b, with $W_{\text{inc}} = 1.66$ W).

When using the difference between $\dot{M}^{\text{model}}(M)$ and $\dot{M}^{\text{exp}}(M)$ point by point to infer Γ_{L} values (inset), the influence of the choice of parameters on the obtained results can be estimated. At small M, the effect $\Delta\Gamma_{\text{L}} = \Delta\dot{M}^{\text{model}}/M$ of a change of model parameters is artificially high (due to division by small M), and one is led to select parameters to avoid unphysical divergences. Nevertheless, reduced errors are observed at higher M, and the extracted Γ_{L} values become quite insensitive to this choice at M_{eq} (here $\Delta\Gamma_{\text{L}}/\Gamma_{\text{L}} = 16$ %). We thus believe that this approach based on the OP model produces robust results at or near M_{eq}. For the results of our work presented in chapter 6.3.4, it is only used at M_{eq}, mainly for the C_9 transition (where this method is the only possibility to infer laser-induced relaxation rates).

A slightly different (graphical) way to use computed results to infer Γ_{L} values from measured steady-state polarisations M_{eq} has been described in [Bat11]. In experimental steady-state, equation (5.19) simply reads $\Gamma_{\text{L}}M_{\text{eq}}=\dot{M}^{\text{model}}(M_{\text{eq}})$. This corresponds to the intersection of the curves plotted in figure 5.19, that displays computed values

of $\dot{M}^{\text{model}}$ for C_8 and C_9 OP. For these calculations, 2^3S and ground state relaxations

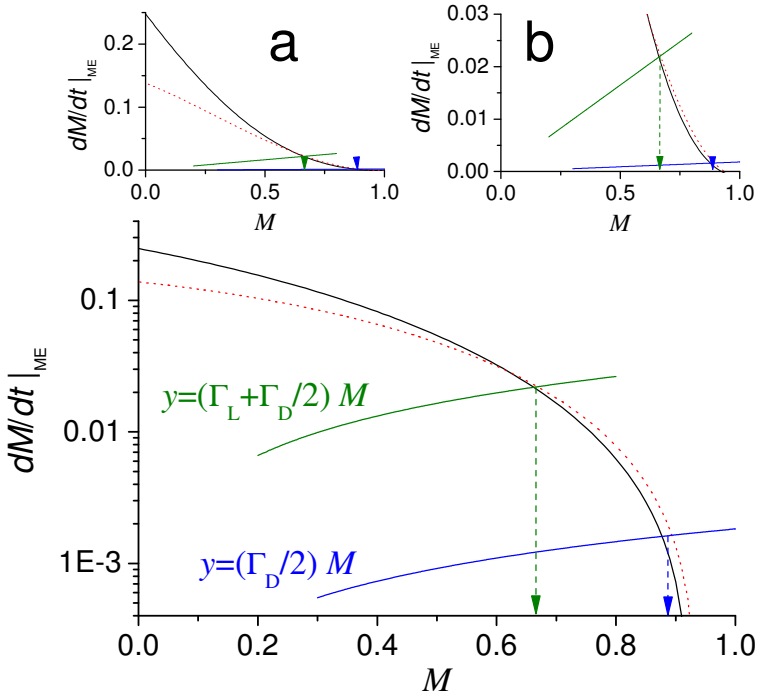

Figure 5.19: ME contributions to the evolution of M (equation (2.24)) are computed as a function of M for OP on C_9 (solid black line) and C_8 (dotted red line) lines. The semi-log scale in the bottom graph is used for convenient comparison of small values at large M (see linear plots **a** and **b**). In this representation, the linear functions are not straight lines (upper curve: $\Gamma_L + \Gamma_D/2$=0.033 s^{-1}; lower curve: $\Gamma_D/2$=1.83×10^{-3} s^{-1}). The vertical arrows point at the corresponding steady-state values ($\dot{M}$=0) on the M-axis. (MEOP conditions: W_{inc} = 1.66 W, p_3 = 1.19 mbar, probe transmittance T = 0.48 at M = 0, Γ_D = 3.667×10^{-3} s^{-1}).

are assumed to equally contribute to the measured polarisation decay in presence of a plasma: Γ^0_{ME}= Γ_g=Γ_D/2. If one assumes that nuclear relaxation of ground state atoms is not affected by the presence of the OP light, M_{eq} is graphically found to be of order 0.9 in figure 5.19 (at the crossing of $\dot{M}^{\text{model}}$ with the lower of the two curves y=$\Gamma_g M$). This value is found to be almost independent (±0.03 at most) of the chosen 2^3S relaxation rate, provided that Γ^0_{ME}+Γ_g=Γ_D. It is much higher than the steady-state polarisation measured in the 1.19 mbar cell, M_{eq}=0.67. This experimental value can be obtained at steady-state using the MEOP model only by assuming that Γ_g is much larger (here, 0.033 s^{-1}, corresponding to the upper of the two curves y=$\Gamma_g M$) with the OP beam than without it, which corresponds to an additional loss rate Γ_L=0.031 s^{-1}. Figure 5.19 clearly illustrates the high OP-enhanced relaxation

rate that is required to significantly reduce the computed steady state polarisation and make it equal to its experimental value M_{eq}. However an M-independent loss rate is assumed for simplicity, whereas our experimental findings reveal a more complex situation (see section 6.3.4).

5.7.2 Deriving polarisation loss rates Γ_{R} from a detailed balance of angular momentum

One may use the global angular momentum budget introduced in section 2.8.4 to directly relate the rates of change of polarisation $\dot{M}$ to the absorbed polarised light power W_{abs} by equations that do not depend on specific features of the 2-class MEOP model, and are thus expected to be more robust than the approach of the previous section. We recall for instance equation (2.77) that only involves two parameters, the photon efficiency η and the global polarisation loss rate Γ_{R}:

$$\dot{M} = 2\eta \frac{W_{\mathrm{abs}}}{N_{\mathrm{g}} V_{\mathrm{c}} \hbar\omega} - \Gamma_{\mathrm{R}} M.$$

For C_8 pumping (the photon efficiency is insensitive to M and to pumping intensity at fixed gas pressure), a simple method can be used to infer Γ_{R} from experimentally measured quantities only, based on equations (2.81) (during buildup) and (2.82) (at steady-state) recalled here for convenience:

$$\Gamma_{\mathrm{R}}(M) = \frac{1}{M}\left(\frac{W_{\mathrm{abs}}(M)}{W_{\mathrm{abs}}(0)}\dot{M}(0) - \dot{M}\right) \tag{5.21}$$

$$\Gamma_{\mathrm{R}}(M_{\mathrm{eq}}) = \frac{1}{M_{\mathrm{eq}}}\frac{W_{\mathrm{abs}}(M_{\mathrm{eq}})}{W_{\mathrm{abs}}(0)}\dot{M}(0). \tag{5.22}$$

These equations, extensively used in the next chapter 6, are here used for a brief discussion of the uncertainties and errors on Γ_{R} values produced by data processing. The right hand side of equation (5.22) can be rearranged in the following way:

$$\Gamma_R(M_{\mathrm{eq}}) = \frac{\dot{M}(0)}{W_{\mathrm{nom}} A_0} \times \frac{W_{\mathrm{nom}} A_{\mathrm{eq}}}{M_{\mathrm{eq}}}, \tag{5.23}$$

where A_0=1-$T_{\mathrm{p}}(0)$ is the pump absorptance at M=0 and A_{eq}=1-$T_{\mathrm{p}}(M_{\mathrm{eq}})$ the absorptance at M_{eq}. The nominal pump laser power W_{nom} is used instead of the less-precisely known W_{inc}, which is legitimate since the power loss factor k_{I} of optical elements cancels out. The first term on the right hand side corresponds to a scaling factor, with different values for each pressure, that is proportional to the photon efficiency: $\dot{M}(0)/(W_{\mathrm{nom}} A_0) = 2\eta k_{\mathrm{I}}/(N_{\mathrm{g}} V_{\mathrm{c}}\ \hbar\omega)$. Since the photon efficiency for C_8 is constant,

we take the *mean value* C of this first term for several experiments at given pressure instead of the individual values in order to decrease the corresponding statistical error:

$$\Gamma_R(M_{\mathrm{eq}}) = C\,\frac{W_{\mathrm{nom}}A_{\mathrm{eq}}}{M_{\mathrm{eq}}},\ \text{where}\ \ C = \left\langle \frac{\dot{M}(0)}{W_{\mathrm{nom}}A_0} \right\rangle \tag{5.24}$$

For this global pressure-dependent scaling factor, the total error ΔC on the mean value C is given by:

$$\Delta C = \sqrt{\left(\frac{\Delta\dot{M}(0)}{W_{\mathrm{nom}}A_0}\right)^2 + \left(\frac{\dot{M}(0)\Delta W_{\mathrm{nom}}}{W_{\mathrm{nom}}^2 A_0}\right)^2 + \left(\frac{\dot{M}(0)\Delta A_0}{W_{\mathrm{nom}}A_0^2}\right)^2}. \tag{5.25}$$

The third term on the right hand side of equation (5.25) yields the largest contribution to the total error ΔC and the second term the smallest one.

For the remaining individual data involved in the determination of the value of

$$\Gamma'_{\mathrm{R}}(M_{\mathrm{eq}}) = \frac{\Gamma_{\mathrm{R}}(M_{\mathrm{eq}})}{C} = \frac{W_{\mathrm{nom}}A_{\mathrm{eq}}}{M_{\mathrm{eq}}}, \tag{5.26}$$

assuming uncorrelated errors on the various measurements, the statistical error $\Delta\Gamma'_{\mathrm{R}}$ can be estimated using

$$\Delta\Gamma'_{\mathrm{R}} = \sqrt{\left(\frac{A_{\mathrm{eq}}\Delta W_{\mathrm{nom}}}{M_{\mathrm{eq}}}\right)^2 + \left(\frac{W_{\mathrm{nom}}\Delta A_{\mathrm{eq}}}{M_{\mathrm{eq}}}\right)^2 + \left(\frac{W_{\mathrm{nom}}A_{\mathrm{eq}}\Delta M_{\mathrm{eq}}}{M_{\mathrm{eq}}^2}\right)^2} \tag{5.27}$$

This individual error $\Delta\Gamma'_{\mathrm{R}}$ is dominated by the second term. More generally we observed that errors on pump absorptances at $M = 0$ and M_{eq} give the most important contributions, followed by errors on $\dot{M}$ values. Errors on nominal laser power and steady state polarisation are smaller. Global and individual errors are approximately of the same order of magnitude, typically ranging between 1 % and 5 %.

Extensive error considerations were made for the above presented case of total relaxation rates for C_8 at M_{eq}. These considerations fully validate the presented results in sections 6.3, 6.4 and 6.5. Similar considerations have to be done for obtained relaxation rates as a function of nuclear polarisation during complete build-up kinetics. They will be provided in the final published version of data.

In the derivation of laser-induced relaxation rates at arbitrary M values (equation (5.19)), the error on each value of Γ_{L} only arises from the statistical error due to SNR of $\dot{M}$. In this case it is not possible to take advantage of the same averaging of

a part of the involved quantities that is valid for the case of C_8 pumping at M_{eq} as described above. As a consequence, the individual error is higher. Another potential systematic bias that is not taken into account in the reported error bars is due to the fact that the model for MEOP kinetics - comprising necessarily simplifications and approximations discussed in chapter 2 - is used here to infer Γ_{L}. The direct approach based on global angular momentum conservation appears more robust, in particular at M_{eq} where pertinent averaging is susceptible to reduce errors.

One last important aspect has to be mentioned in this discussion of experimental errors: for the analysis of data, the potential correlation between errors on the involved quantities must be carefully taken into account. For instance, in the graphs where polarisation loss rates Γ_{R} are plotted against absorbed pump laser powers, the errors on the axes of abscissae and of ordinates are not statistically independent. Overlooking this point would lead to erroneous linear fits while weighting data points by statistical error bars, since the same error on W_{abs} appears in equations (5.25) and (5.27) in the determination of Γ_{R}. In contrast, this is not the case for the derivation of Γ_{L} rates based on the OP model: W_{abs} is not involved in the computation of $\dot{M}$ values and thus W_{abs} and Γ_{L} are statistically independent.

Figure 5.20 shows global polarisation loss rates Γ_R determined using equation (2.81) for $p_3 = 0.63$ mbar during polarisation build-up at fixed incident pump laser power of 0.415 W and in strong discharge conditions (see caption). Γ_R is represented as function of polarisation (on the left) and as function of absorbed laser power (on the right) that decreases during polarisation build-up while M increases.
The determination of the necessary experimental parameters for equation (2.81) is described in detail in subsection 5.2, some essential aspects are quickly recalled: The determination of M is based on absorption measurements of a weak probe laser and $\dot{M}$ is obtained by a dedicated programme executing sliding linear fits on $\ln(M_{\mathrm{eq}} - M)$. The absorbed laser power W_{abs} as function of M is obtained using pump transmission coefficients T_p, a polynomial fit serves to extrapolate the value of W_{abs} at $M = 0$. For M and $\dot{M}$, exact values are taken for the determination of Γ_{R} whereas for W_{abs}, the values of the polynomial fit enter into equation (2.81). This choice is based on the lower SNR of the intense pump laser compared to the weak probe laser (typical signal-to-noise-ratios of pump and probe signals: see for example page 344 in appendix E).
In the left graph of figure 5.20, the extracted total relaxation rate Γ_{R} is represented as a function of increasing nuclear polarisation M during build-up. The global dependency of Γ_{R} is linear with M apart from scatter at low polarisation values. This scatter can be imputed to the initial values of $\dot{M}$ during the fast pumping process at the beginning of the polarisation build-up, the values of W_{abs} in equation (2.81) being taken from a polynomial fit. Less scatter of Γ_R in the beginning of the build-up

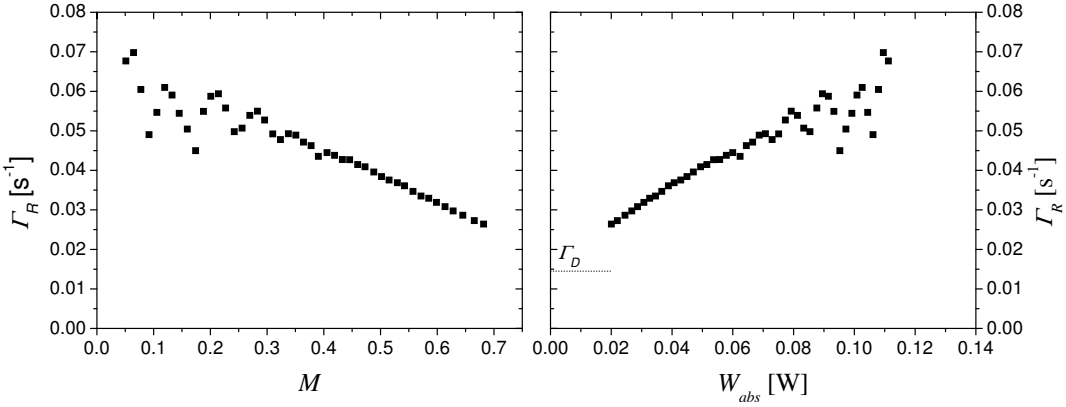

Figure 5.20: Total relaxation rates Γ_R during polarisation build-up for C_8 pumping as function of polarisation (left) and as function of absorbed laser power (right). Γ_R is determined using only experimentally measured parameters from the balance of angular momentum (equation (2.81)). The dotted horizontal line indicates the decay rate Γ_D measured in absence of the pump laser. Experimental parameters: $p_3 = 0.63$ mbar, pump: C_8, $W_\mathrm{inc} = 0.42$ W, probe: C_8, $B = 1$ mT, strong discharge: $\Gamma_\mathrm{D} = (69\,\mathrm{s})^{-1}$, $n_\mathrm{m}^\mathrm{S}(M = 0) = 3.34 \times 10^{16}$ atoms/m^3, $\alpha = 1.7$.

process is observed at lower values of incident pump laser power, and systematically in the second half of the polarisation build-up approximately, when the pumping process slows down.

In the right graph of figure 5.20, the total relaxation rate is plotted as a function of absorbed laser power during polarisation build-up. At the highest value of absorbed power corresponding to the beginning of the polarisation build-up, the total relaxation rate amounts to approximately 5 times the measured decay rate Γ_D in this example of a strong discharge.

In figure 5.21, Γ_D is subtracted from Γ_R, and resulting additional laser-induced loss rates Γ_L (cf. equation (5.20)) are represented as a function of absorbed pump laser power. We observe a linear increase of OP-induced relaxation rates with absorbed laser power.

In such examples of laser-induced loss rates Γ_L (or total loss rates Γ_R) as a function of absorbed pump laser power, the case of M_eq is comprised as limiting point at the smallest value of W_abs within each build-up.

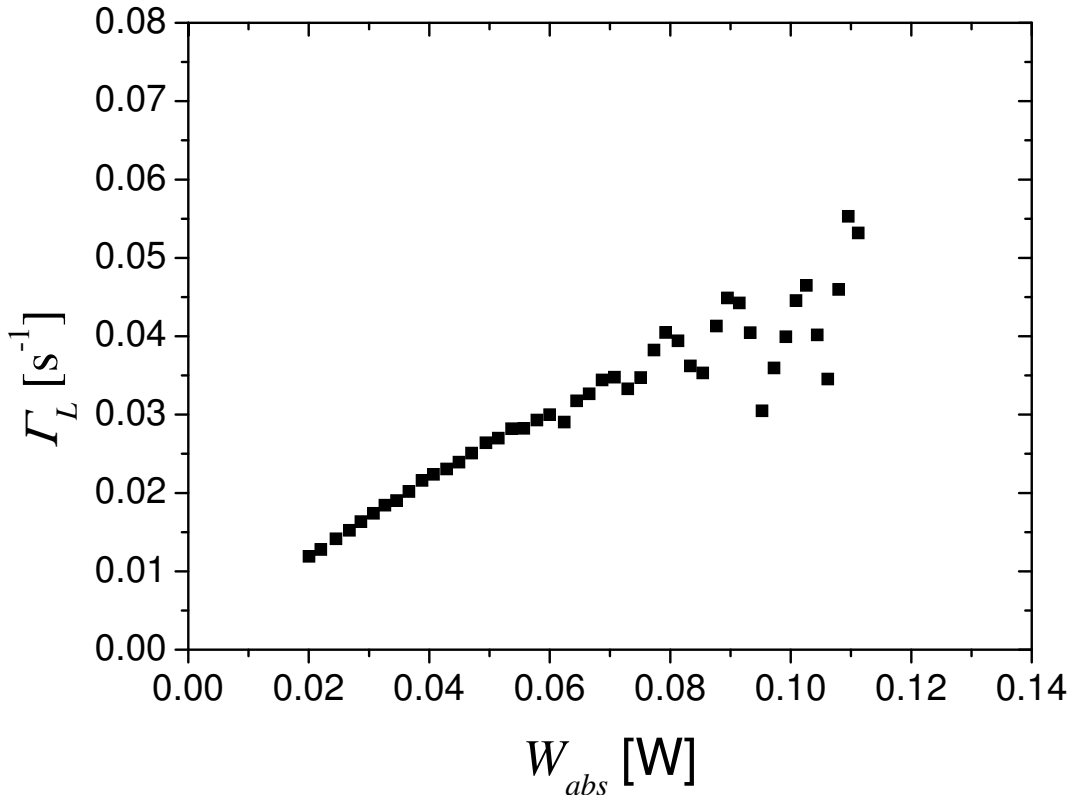

Figure 5.21: Additional laser-induced loss rates Γ_L (inferred using global angular momentum conservation, equation (2.81)) for the same example of C_8 OP as represented in figure 5.20 as a function of absorbed pump laser power.

Chapter 6

Results

This chapter presents the main achievements of the present work and is organised in five sections: In section 6.1, relevant plasma characteristics (metastable density n_{m} and polarisation decay rates Γ_{D}) in absence of OP light are described. OP light promotes a significant fraction of 2^3S atoms to the 2^3P state and redistributes 2^3S atoms between Zeeman sublevels. These perturbations introduced by OP light have been measured in dedicated experiments. Method and results are presented in section 6.2. Section 6.3, the main section in this chapter, presents OP results at 1 mT. Effects of magnetic field on OP performances are discussed in section 6.4. The chapter ends with section 6.5, where laser-enhanced relaxation effects are discussed.

6.1 Characterisation of the plasma without OP light

All data presented in this section have been collected to characterise plasmas in the *absence* of OP light. The section includes results as function of nuclear polarisation M and for different magnetic fields B. The first two subsections describe results obtained at *zero* nuclear polarisation: average number densities n_{m} are reported in subsection 6.1.1, and examples of radial distributions are presented in subsection 6.1.2. Subsection 6.1.3 focuses on changes in n_{m} observed during polarisation decays.
Plasma characteristics at low magnetic field ($B = 1$ mT) are completed by corresponding results at higher B.

Impact of magnetic field on rf plasmas in low pressure ^{3}He gas

The impact of magnetic field on ^{3}He plasmas at low pressure is qualitatively illustrated in figure 6.1.
Pictures show the same ^{3}He cell twice (5 cm $\times$ 5 cm cylinder, $p_3 = 1.33$ mbar) with

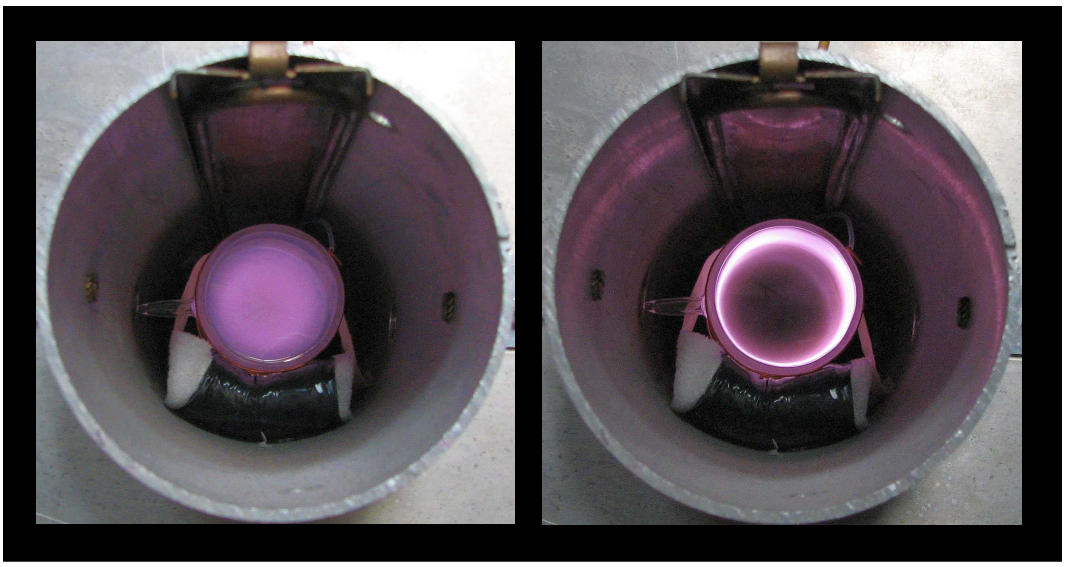

Figure 6.1: Impact of magnetic field on rf plasmas in low pressure ^{3}He gas. Left: Low magnetic field: $B = 1$ mT. Right: High magnetic field: $B = 0.1$ T. Cylindrical cell with outer dimensions: 5 cm $\times$ 5 cm, $p_3 = 1.33$ mbar (photos by G. Tastevin, LKB).

a pair of external wire electrodes (cf. section 3.1) lying in the bore of a resistive water cooled magnet, for identical rf excitation. A spectacular change in the spatial distribution of plasma brightness is observed when B is varied from 1 mT (left) to 0.1 T (right).

Impact of gas pressure on rf plasmas at low magnetic field

Figure 6.2 shows photos of ^{3}He plasmas taken in earth magnetic field at higher gas pressures (left: 2.45 mbar, right: 66.7 mbar).
A similar trend is observed: at high gas pressure, the fluorescence light is much more intense in the close vicinity of the outer electrodes whereas at low pressure (and low magnetic field: cf. left part of figure 6.1), it is quite homogeneously distributed over the whole cell volume.

Bright regions in the plasma indicate locations where radiative cascades contribute (most) to the creation of the 2^3S metastable state. Actual metastable

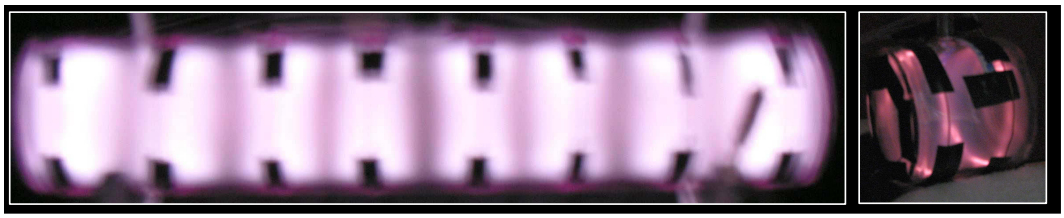

Figure 6.2: Impact of gas pressure on rf plasmas at low magnetic field. Left: $p_3 = 2.45$ mbar, cylindrical cell with outer dimensions: 30 cm $\times$ 6 cm. Right: $p_3 = 66.7$ mbar, cylindrical cell with outer dimensions: 5 cm $\times$ 5 cm. Both photos are taken in earth magnetic field (photo on the right: G. Tastevin, LKB).

density $n_{\mathrm{m}}(\vec{r})$ results from the balance of creation, diffusion and destruction by various processes, hence the map of $n_{\mathrm{m}}(\vec{r})$ does not directly reflect plasma brightness. However, mapping of $n_{\mathrm{m}}(\vec{r})$ in high-pressure cells reveals an inverted distribution (with a minimum on cell axis) correlated to plasma localisation near the cell wall.

The photos of figure 6.1 and 6.2 are shown to give a qualitative impression of gaseous helium plasmas. In the following subsections, a quantitative characterisation of average metastable atom densities and of radial distributions is provided for experimental conditions met in the present work: 0.63-2.45 mbar ^{3}He pressure and 1-30 mT magnetic field. Comparisons to other published work in different conditions are made.

6.1.1 Key plasma parameters for MEOP: $n_{\mathrm{m}}(M = 0)$ and Γ_D

Metastable densities at $M = 0$

One important parameter to characterise the plasma for OP applications is the value and spatial distribution $n_{\mathrm{m}}(\vec{r})$ of the 2^3S metastable atom number density. For simplicity, given the axial symmetry of our OP experiments in long longitudinal cells, we will neglect the longitudinal dependence of the density, and write the spatial distribution as $n_{\mathrm{m}}(r)$, where r is the radial distance to the cell axis.

Throughout this work, metastable density values have been determined from absorption measurements, usually along an inclined probe path. The averaged metastable density along the probe path, $n_{\mathrm{m}}^{\mathrm{S}}$, differs from the density on cell axis, $n_{\mathrm{m}}^{\mathrm{ax}} = n_{\mathrm{m}}(r = 0)$, whenever the density is non-uniform (see section 6.1.2).

When comparing metastable densities of different works to each other, different probe configurations and possibly different definitions of n_{m} should be taken into

account for a precise comparison of absolute n_{m}-values. Figure 6.3 illustrates three common probe configurations used in the different works of which metastable densities are presented later in this subsection.

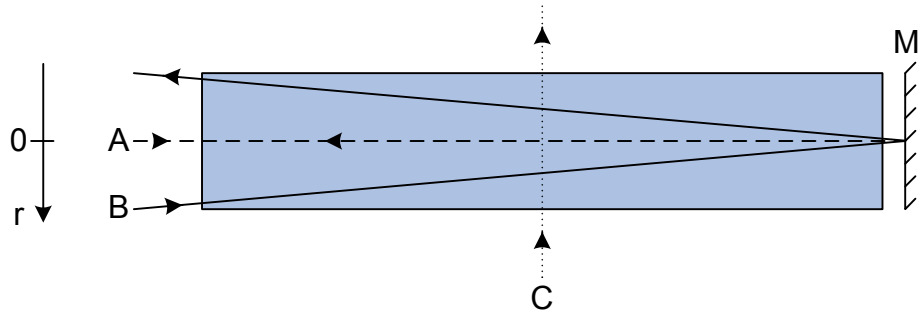

Figure 6.3: Different probe configurations for determination of metastable densities, the gas-filled cell and a mirror (M) are represented. Path A (dashed line): longitudinal on axis configuration (also possible in single-pass-configuration without mirror), path B (solid line): inclined, longitudinal configuration (used for example when pump and probe have to be implemented on the same optical setup for simultaneous measurements), path C (dotted line): transverse configuration (allows simultaneous probe and pump measurements as well, and is also possible in double-pass-configuration with additional mirror). The indicated r-direction is used in subsection 6.1.2 to represent radial n_{m}-distributions.

All presented probe configurations yield identical values of n_{m} in case of a uniform radial distribution of metastable atoms. Moreover, in low pressure, path A provides the maximum value of n_{m} on the optical axis, independently of the actual radial distribution. In the usual case of *non*-uniform radial repartition of n_{m}, the average absorption signal along the probe path is smaller than the maximum value in the centre of the distribution (in low pressure; in high pressure cells, the situation is different as $n_{\mathrm{m}}(r)$ distributions are inverted, with a minimum on cell axis). In case of low absorption, paths B and C yield identical values if the angle of path B is chosen as wide as possible so that incoming and outgoing beam are located directly at the edge of the cell wall.
Normalising the maximum value for a uniform distribution to 1, the average absorption rates on probe paths B and C are quantified in table 6.1 for different assumptions of the radial n_{m}-parameter α. Complete radial n_{m}-distributions of type $\cos^{\alpha}$, experimentally measured and theoretical ones, are presented and discussed in subsection 6.1.2.

The experimentally measured values of α in $p_3 = 0.63 - 2.45$ mbar and $B = 1 - 30$ mT range between 0.75 and 2.35 (details, see subsection 6.1.2). In this range of α, the relative discrepancy between values of absorption rates on probe paths 'B' and 'C' listed in table 6.1 amounts to 15 % maximum at low α down to 0.5. At

Table 6.1: Average normalised probe absorption rate A along the probe path in configurations 'B' and 'C' of figure 6.3, for different values of the radial n_{m}-parameter α.

α	$A(\mathrm{B})/A(\mathrm{A})$	$A(\mathrm{C})/A(\mathrm{A})$
0	1	1
0.5	0.83	0.71
1	0.69	0.59
1.5	0.59	0.52
2	0.50	0.47
2.5	0.44	0.43

higher $\alpha = 2.5$, this relative discrepancy diminishes to 2 % only.
As expected, the relative difference of path 'B' (or 'C' respectively) with respect to path 'A' increases with rising α as the radial n_{m}-distribution departs from a uniform shape.

The probe configurations used in different works to infer absolute values of n_{m} are the following: [Abb05b]: inclined, longitudinal probe ('B') in low B and transverse probe ('C') in high B; [Wol04]: longitudinal probe ('A') in single-pass-configuration; [Cou01]: inclined, longitudinal probe ('B'); this work: inclined, longitudinal probe ('B'). These works are used later in this subsection to give an overview of all investigated ranges of metastable densities and corresponding decay rates Γ_{D}. As no information about radial n_{m} distributions is provided in the mentioned other works, it is impossible to further take into account the different probe configurations, but this aspect is essential in case comparisons with high precision are required.

All the above discussed values of probe absorption rates refer to single-frequency lasers (as used in all cited works). If a less appropriate, spectrally broad laser is used instead to infer metastable densities, an additional spectral matching coefficient has to be taken into account by using the appropriate optical transition rate for broadband laser light (see equation (2.16)).

Decay rate Γ_{D} in the absence of OP

The decay rate Γ_{D} that characterises the mono-exponential decay of M in the absence of OP can be precisely determined on recorded polarisation decays in absence of the pump laser by exponential fit. In this manuscript, we use the expression *decay rate* to designate Γ_{D}, that depends on plasma characteristics like rf excitation level and metastable densities as will be illustrated in the following. The relative error of extracted Γ_{D}-values is almost negligible in this work (cf. section 5.2.2) and therefore not represented in the graphs of the following paragraphs.

As we shall see here, Γ_{D} is actually strongly correlated to n_{m} with a clear monotonic trend at fixed gas pressure: higher Γ_{D} rates are systematically measured at higher n_{m}. Γ_{D} is a pertinent quantity in absence of OP (cf. section 2.8.2), and at low incident pump laser powers. It has long been the key parameter that determined M_{eq} when powerful laser sources were not available [Col63, Gre64, Dan71a, Dan71b, Dup73, Nac85]. In the present work, as will be shown in sections 6.3.3 and 6.3.4, the relaxing processes at play in the plasma in the absence of OP light that induce a decay with the rate Γ_{D} are not the dominant phenomena limiting M_{eq} in strong OP conditions.

Plasmas at low magnetic field and low pressure

Figure 6.4 represents an overview of compiled measured polarisation decay rates in discharges as function of metastable density at $M = 0$ from different works in low magnetic field ($B = 1 - 2$ mT) and low pressure (most data between $p_3 = 0.5$ and 2.5 mbar, one dataset at 8 mbar).
It is intended as visualisation of a wide range of possible discharges at low field and low pressure and therefore, a logarithmic presentation is chosen. Data of this work, where $n_{\mathrm{m}}^{\mathrm{S}}(M = 0)$ is plotted on the axis of abscissae, are represented by filled symbols and are well embedded within the experimental range of former works. Two different regimes of discharges can be distinguished: The regime at low and intermediate metastable densities up to approximately 5.5×10^{16} atoms/m^3 and small decay rates up to approximately 0.02 s^{-1} is particularly suitable for optical pumping. All relevant data of this regime are discussed in more detail based on figures 6.5 (low field data of this work only) and 6.6 (pressure selective comparison to other works), and enhanced by moderate and high field data in figures 6.7 and 6.8.
In the special regime of very intense discharges, mainly explored at $p_3 = 2.45$ mbar in the present work, it is impossible to further increase $n_{\mathrm{m}}(0)$, only decay rates Γ_D continue rising. In [Cou01] and [Wol04], a change of regimes is less pronounced.

Later in this chapter, we use the terms "weak" and "strong discharges". "Weak" and "strong" refers to the level of rf power. When it is increased, higher metastable densities can be obtained, but decay rates increase at the same time. "Weak discharges" are close to the threshold of ignition and thus characterised by low Γ_{D} rates and low n_{m} values around 1×10^{16} atoms/m^3 and below (towards the left side of figure 6.4), "strong discharges" constitute the opposite limiting case with high Γ_{D} and n_{m} values around 5×10^{16} atoms/m^3.

In figure 6.5, low field data at $B = 1$ mT of the present work are presented for the three investigated pressure-values, 0.63, 1.19 and 2.45 mbar. Data from different experimental runs are discerned (phase I: 2005-2006, phase II: 2007-2008: electrode

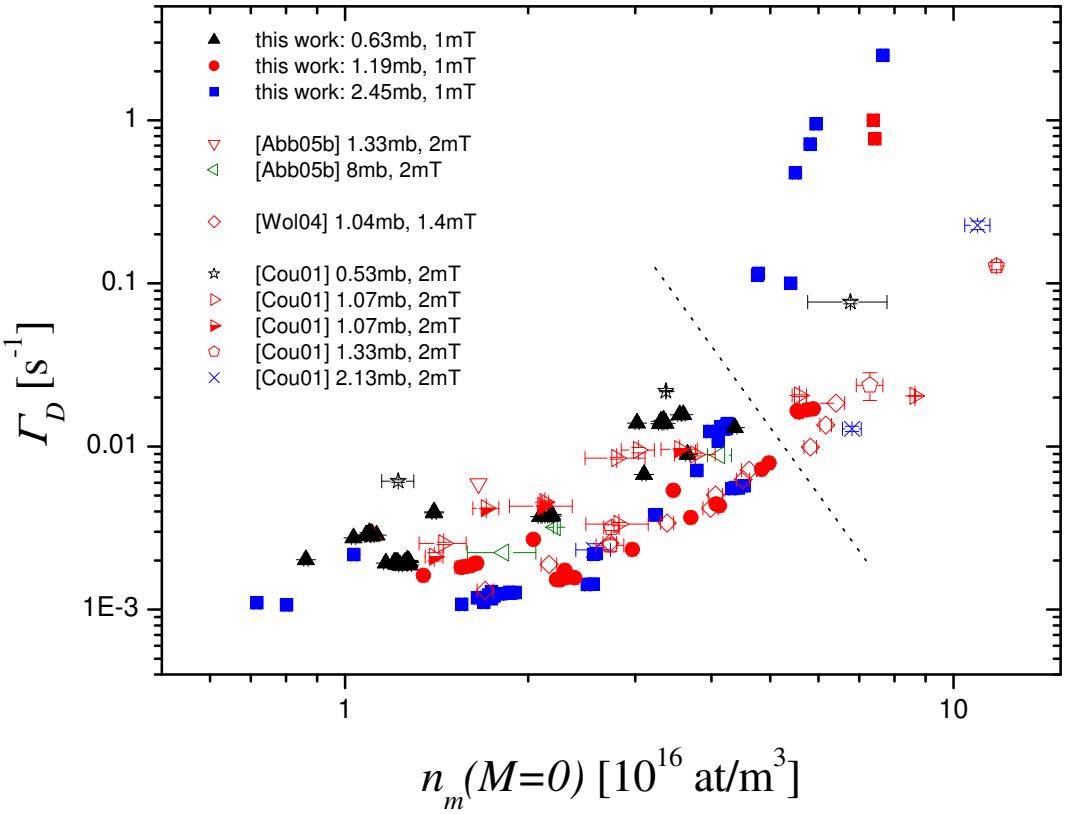

Figure 6.4: Compiled decay rates in a discharge as function of metastable density at $M = 0$ at low magnetic field and low pressure. Source, p_3, L_{path} and B: see legend. Two regimes of discharges (see text) are separated by the dotted line. Experimental error bars of this work (filled symbols) are smaller than the size of the symbol in most cases. All metastable densities of [Wol04] have been corrected based on original single-frequency absorption measurements in agreement with the author: correct n_{m}-values are higher than presented in [Wol04] by a factor of 1.67.

configurations of 0.63 and 1.19 mbar cells changed compared to phase I, electrode configuration of 2.45 mbar cell: unchanged).

On the left hand, only data of measurement phase I are represented. A general

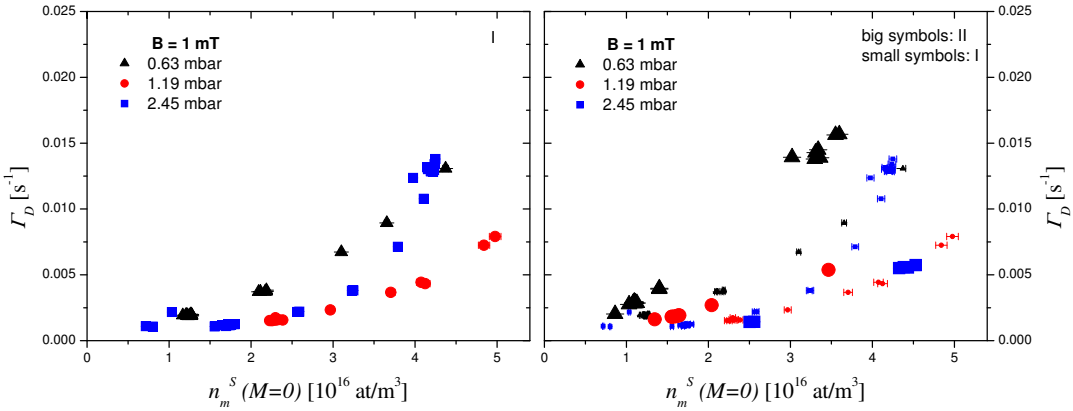

Figure 6.5: Decay rates in a plasma as function of metastable density from the present work, at $M = 0$, $B = 1$ mT and $p_3 = 0.63$ mbar (triangles), 1.19 mbar (circles) and 2.45 mbar (squares). Left: Results from data-acquisition phase I only. Right: Results from data-acquisition phases II (big symbols) and I (small symbols). Experimental error bars are only visible on small symbols, in all other cases, their size is of the same order as the symbol size.

tendency observed at all pressures separately is an increasing decay rate Γ_D with increasing metastable density n_m at $M = 0$. The highest absolute decay rates are usually found at lowest ^{3}He-pressure. Comparing 0.63 mbar- to 1.19 mbar- or 2.45 mbar data, this trend is confirmed. At higher metastable densities, above approximately 3×10^{16} atoms/m^3, Γ_D of 2.45 mbar departs from this expected trend however, and yields higher decay rates in comparison to 1.19 mbar. At least partly, this behaviour might be imputed to beginning difficulties to produce perfectly homogeneous discharges above 2 mbar (see photo of optimum electrode configuration on 2.45 mbar-cell on left part of figure 6.2).

Comparing metastable densities of different pressures with each other, it appears that the highest pressure does *not* yield the highest n_m-values. [Ich80] for example also measured a decrease of the $2^3\mathrm{S}_1$ density in helium as gas pressure increases.

Actual metastable densities arise from a complex balance of creation, diffusion (with a diffusion rate inversely proportional to pressure [Fit68]) and destruction by e.g., Penning collisions (described in section 6.1.3) or formation of a metastable molecule He_2^* [Emm88, Zha93] in a 3-body process involving two ground state atoms and one metastable helium atom: $\mathrm{He}^* + 2\ \mathrm{He}(1^1\mathrm{S}_0) \rightarrow \mathrm{He}_2^* + \mathrm{He}$.

On the right hand side of figure 6.5, data of measurement phase II are added for all three investigated pressure-values. For comparison, data of measurement phase

I are kept as well at smaller symbol size. At all pressures, two groups of discharges can be distinguished. At 0.63 and 1.19 mbar, this change of Γ_D at given n_m is associated to a change in the electrode configurations leading to higher decay rates at comparable metastable densities.

In the following four graphs of figure 6.6, already presented low field and low pressure data of different works in figure 6.4 are compared to our work ($n_\mathrm{m}^\mathrm{S}(M=0)$ values on x-axis) within different pressure ranges separately.
Graph 1 in figure 6.6 compares low pressure data of this work to metastable densities

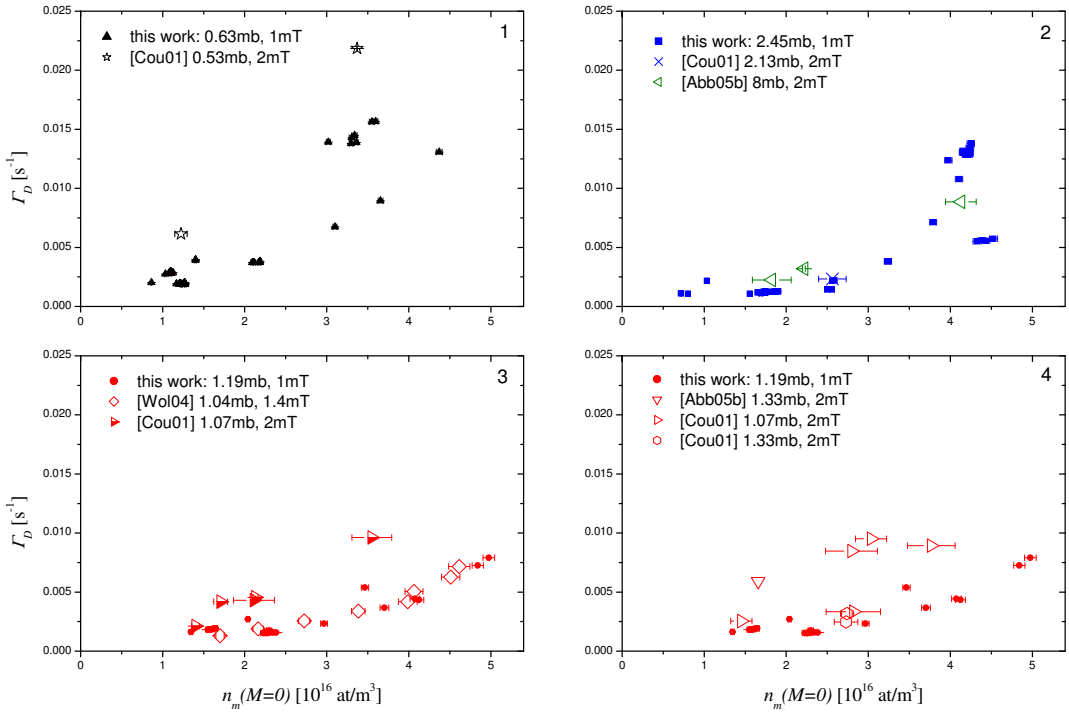

Figure 6.6: Decay rates in presence of a discharge as function of metastable density at $M = 0$, compiled from different works (open symbols, see legends) compared to this work (filled symbols), in low magnetic field (1-2 mT) and different pressure ranges. 1: $p_3 = 0.53 - 0.63$ mbar, 2: $p_3 = 2.13$ - 2.45 mbar and comparison to one higher pressure value: 8 mbar, 3 and 4: $p_3 = 1.04$ - 1.33 mbar. Concerning data of [Wol04]: see comment in caption of figure 6.4.

and corresponding decay rates from [Cou01]. Each represented data point of [Cou01] represents an average of up to eight individual measurements of n_m and Γ_D at fixed plasma conditions, the error bars indicate the standard deviation obtained from averaging in this case. In [Cou01], the covered range of metastable densities is comparable to that of our work. However, at given n_m, plasmas of [Cou01] are more

relaxing, i.e., higher Γ_D-rates are observed.
In graph 2 of figure 6.6, low-field-data at 2.13 mbar [Cou01] and 8 mbar [Abb05b] agree well within observed experimental variations of Γ_D at given n_m in the 2.45 mbar-cell used in our work.
Graphs 3 and 4 both represent decay rates in the plasma as function of metastable density between 1.04 and 1.33 mbar: For the sake of clearness, in order to avoid too many datasets in each graph, graph 3 compiles data obtained in longer cells (L_{cell} ranging from 0.3 to 1 m), whereas graph 4 compares data from short cells only ($L_{cell} = 0.05$ m) to data obtained in the 30 cm long 1.19 mbar-cell used in our work.
The distinction of different cell lengths constitutes an attempt to examine whether L_{cell} influences polarisation decay rates in the context of different contributions of radial and longitudinal diffusion modes in cylindrical cells of different dimensions [Tas87]. The ratio of diameter/length appears important, in the case of length $\gg$ diameter, only the diameter is a pertinent parameter in terms of diffusion.
The results in graph 3 show very good agreement in n_m and Γ_D between [Wol04] and our work. Decay rates measured in [Cou01] are higher at given metastable density compared to the other two works.
Most of the data represented in graph 4 exhibit higher Γ_D rates than measured in this work. In both datasets of [Cou01] however, there are also examples of less relaxing plasmas. It is difficult to reconstruct whether different decay rates in the same cell also correspond to different electrode configurations as observed in our work.
Altogether, cell length does not seem to be a pertinent parameter influencing polarisation decay rates in the plasma at given metastable density.

Effects of magnetic field on plasmas at several pressures

In this paragraph, changes of plasma characteristics in increased magnetic field are first investigated at low pressure (0.63-2.45 mbar) in $B = 30$ mT compared to 1 mT. In the second part, effects of high magnetic field (1.5 T) on plasmas are discussed at higher pressure of $p_3 = 8$ and 32 mbar [Abb05b].
Figure 6.7 displays decay rates Γ_D as a function of n_m at low pressure in moderate magnetic field of 30 mT. The observed changes mainly in relaxation rates do not give a uniform picture for all three investigated pressure-values.
At $p_3 = 0.63$ mbar, the measured Γ_D-rates at comparable metastable densities *in*crease by up to 35 % in $B = 30$ mT compared to low field (1 mT).
At $p_3 = 1.19$ mbar, no significant differences are found between relaxation rates at $B = 1$ and 30 mT.
At $p_3 = 2.45$ mbar, it is possible to obtain less relaxing discharges in increased magnetic field at given n_m. Γ_D in $B = 30$ mT is *de*creased by a factor of 2 on average compared to low field plasmas, and up to a factor of 4 at high n_m around

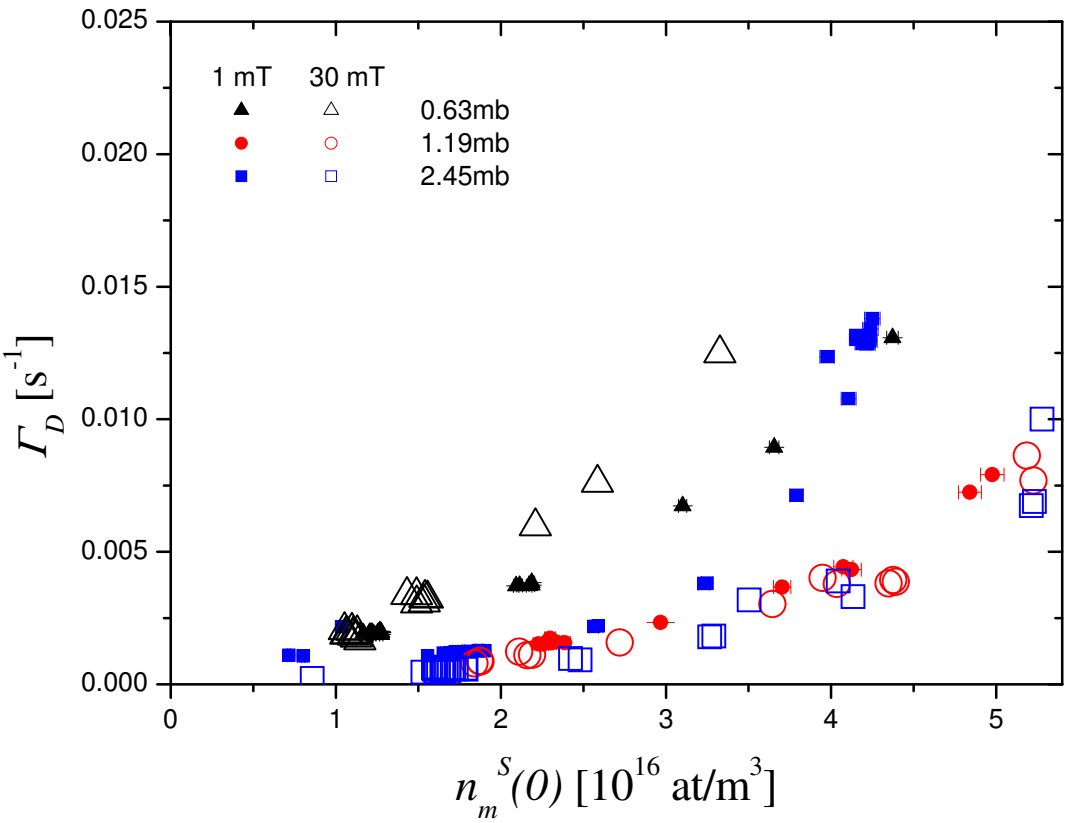

Figure 6.7: Effect of magnetic field on plasmas at low pressure. Discharge relaxation rates as function of metastable density at $M = 0$: triangles: $p_3 = 0.63$ mbar, circles: $p_3 = 1.19$ mbar, squares: $p_3 = 2.45$ mbar; (small) filled symbols: $B = 1$ mT, (big) open symbols: $B = 30$ mT (all data from this work). Error bars in $B = 30$ mT are of the same order as in 1 mT. For each pressure, data at 1 and 30 mT stem from the same data acquisition phase with given electrode configuration.

4×10^{16} atoms/m^3.

Similar measurements as in this work to characterise ^{3}He-plasmas in different mag-

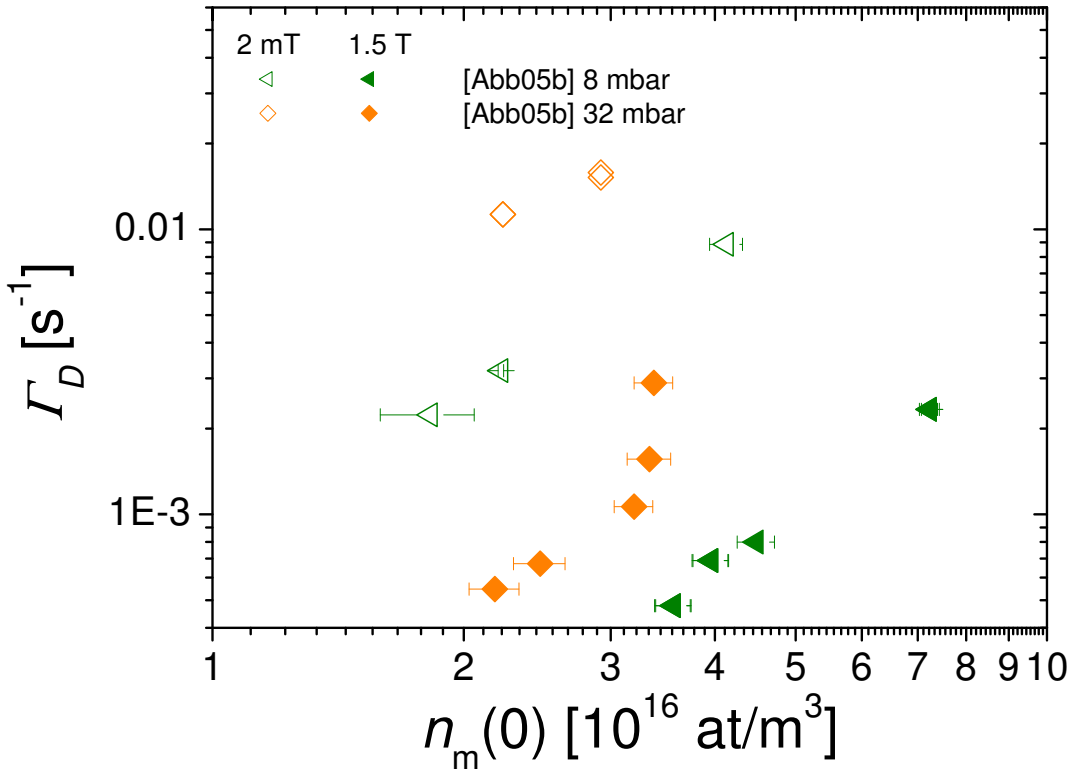

Figure 6.8: Effect of high magnetic field on plasmas at higher pressure. Discharge relaxation rates as function of metastable density at $M = 0$: triangles pointing to the left: $p_3 = 8$ mbar, diamonds: $p_3 = 32$ mbar; open symbols: $B = 2$ mT, filled symbols: $B = 1.5$ T (all data from [Abb05b]). Logarithmic scales are chosen to better represent the whole range of investigated n_m and Γ_D. Measurements in low and high B were performed in different setups, *not* using the same probe configurations (cf. page 168): Inclined longitudinal configuration in low B (path 'B' in figure 6.3 and table 6.1), transverse configuration (path 'C') in high B. This fact has consequences on direct quantitative comparisons of metastable densities.

netic fields have been performed before in [Abb05b] in a completely different pressure range and much higher magnetic field. Figure 6.8 shows discharge relaxation rates as function of metastable density at $M = 0$, in higher pressure of $p_3 = 8$ and 32 mbar and high magnetic field of $B = 1.5$ T (cf. figure 5.6 in [Abb05b]). We completed the graph by unpublished data from [Abb05b] in $B = 2$ mT for the pressure values for which these low field data existed. Comparing low to high field relaxation rates in these two higher pressure cells at given metastable density, a spectacular effect can

be observed: At 8 mbar and 32 mbar, it is possible to *de*crease the relaxation rate Γ_D in 1.5 T by approximately one order in magnitude compared to low field (2 mT). Due to the different probe configurations used at low and high B, more precise quantitative comparisons cannot be performed. Especially the condition "at given metastable density" in low and high field is not accurately fulfilled (cf. comments concerning figure 6.3 and table 6.1). In these higher pressure cells (8 and 32 mbar), even in low magnetic field, the inclined longitudinal probe configuration "misses" metastable atoms that are located near the cell walls.
It is unknown at which field value this spectacular effect occurs. Measurements of n_m and Γ_D in low pressure and high field as well as in high pressure at intermediate field values would be needed. (Plasma characterisations at intermediate field values have been performed for example in [Nik07], but in a different cell configuration that is more adapted to high field optical pumping. In this different cell configuration, [Nik10] indicates that at $p_3 = 32$ mbar, the relation between the product of n_m and decay rates Γ_D does not depend on magnetic field in the high B-range between 0.45 and 4.7 T). In order to allow a direct comparison to data of this work, measurements of cylindrical high pressure cells in low field would be required as well. Both mentioned cases, high pressure in low field and low pressure in high field, are not of particular interest for optical pumping, and have therefore not been investigated systematically until now.
Some existing measurements of [Abb05b] in 1.33 mbar indicate *no* significant decrease of relaxation rates in 1.5 T compared to 2 mT at low pressure (see figure 5.5 in [Abb05b] for high field data at 1.33 mbar).

6.1.2 Transverse distribution of 2^3S atoms

In contrast to the previous subsection where integral values of metastable densities along the inclined, longitudinal probe path, n_m^S, are considered, in the present subsection, radial distributions of $n_m(r)$ (r-direction defined in figure 6.3) of the cylindrical cells used in this work with inner diameter 5.4 or 5.6 cm (cf. chapter 3.1) are presented and discussed.
The knowledge of radial metastable distributions is essential when local absorption rates of probe or pump lasers are sought after for example.

First, model distributions are shown to give an overview of possible n_m-distributions in our experimental range of pressure and magnetic field, also in comparison to the spatial pump laser profile.
Second, experimental radial distributions of metastable densities are presented for the highest investigated pressure, 2.45 mbar, and the lowest one, 0.63 mbar, using two different experimental methods, yielding equivalent results. The experimental

results comprise radial n_{m}-distributions at different magnetic field values, $B = 1$ and 30 mT at 2.45 mbar, and four additional intermediate B-values between these two limiting cases at 0.63 mbar.
Third, after this detailed discussion of results concerning radial n_{m}-mappings from the present work, we shortly summarise findings on this topic from other works.

Chronologically, the results were actually obtained in reverse order. Experimentally recorded radial n_{m} data all featured bell-shaped distributions (as illustrated e.g. in figure 6.13) in the conditions of the present work. This common observation led us to describe such radial metastable distributions by a function of one free parameter, namely a cosine-function to the power of the radial n_{m}-parameter α:

$$y = A \ \cos^{\alpha}\left(\frac{\pi}{2}\,\frac{r}{R_c}\right), \tag{6.1}$$

where A is an amplitude-prefactor, and R_c is the inner radius of the cell. This is just a simple model function that automatically ensures $n_{\mathrm{m}} = 0$ at $r = R_c$ and has a maximum in the centre of the distribution. Its use is thus limited to the conditions of the present work. This model function is *not* suitable to describe radial metastable distributions in high pressure and/or high field.
In figure 6.9, model cosine-distributions, centred and normalised to $A = 1$, with values of α ranging between 0 (uniform distribution) and 2.5 are presented to give an impression of the influence of α on the shape of the radial distribution of metastable densities. Furthermore, a normalised Gaussian fit of the experimental, spatial pump laser profile is added for comparison.
Figure 6.9 clearly shows the influence of the radial n_{m}-parameter α on the shape of the radial distribution of metastable densities. Already at a low value of the exponent α in equation (6.1), e.g. $\alpha = 0.5$, the shape clearly departs from a uniform radial distribution at $\alpha = 0$ with normalised amplitude of 1 over the whole considered width in x-direction of 60 mm. When further increasing α, the width of the radial n_{m}-distribution decreases.
The radial pump laser profile which is represented by a Gaussian fit of experimental amplitudes is less broad however than the radial n_{m}-distributions for α ranging between 0 and 2.5. The spatial width of the pump laser profile amounts to 13.6 mm FWHM which corresponds to a waist of $2a = 16.3$ mm.

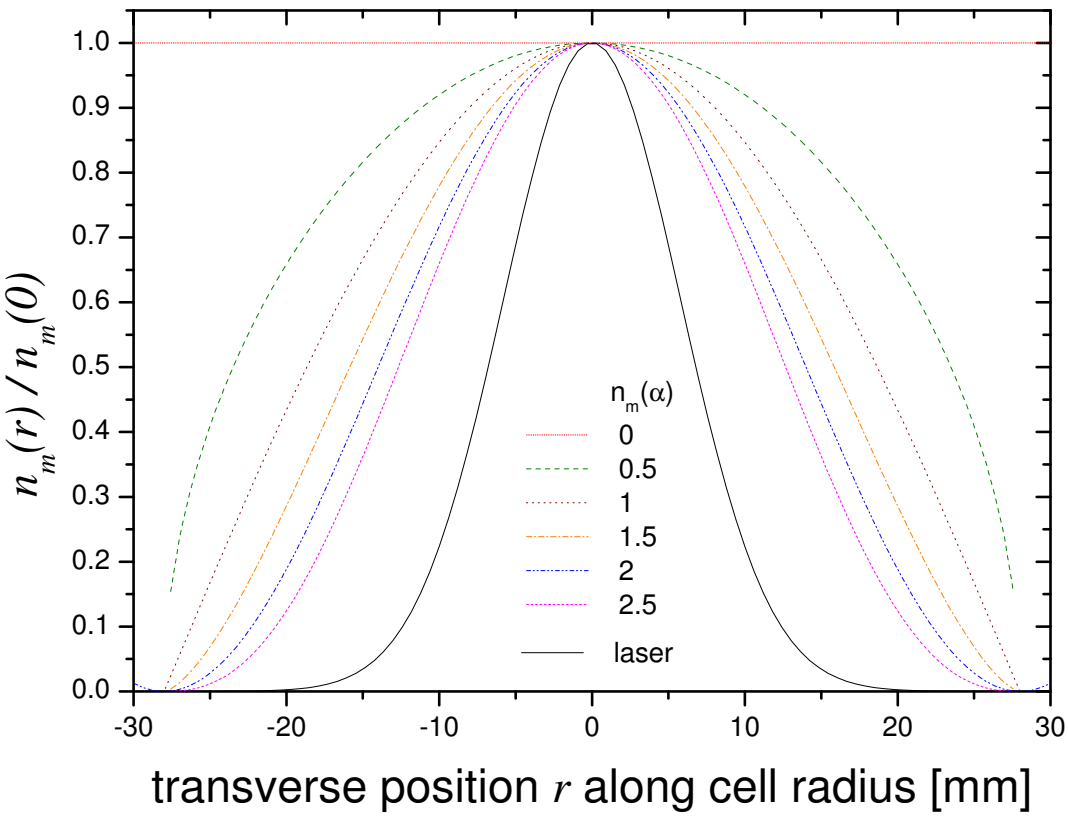

Figure 6.9: Normalised theoretical radial n_{m}-distributions (see equation (6.1)) for different values of α between 0 and 2.5 (see legend) and normalised Gaussian fit of experimental, spatial pump laser profile (solid line).

Radial distributions of metastable atoms at 2.45 mbar

At $p_3 = 2.45$ mbar, radial mappings of n_m-distributions have been recorded using a dedicated experimental device that mainly consists of a radially movable diaphragm of diameter 3 mm that can be precisely positioned. In the low power regime of linear absorption, the laser transmission coefficient T for each of the 21 radial positions (with 3 mm distance to the adjacent one) is measured, and the absorbance -ln(T) of the attenuated pump laser on the C_9-transition is represented as amplitude on the y-axis in all presented distributions.
The first example of radial n_m-distributions at $p_3 = 2.45$ mbar in figure 6.10 represents cosine-like fits as defined in equation (6.1) of experimental data at $B = 1$ and 30 mT, in weak and strong discharges at both magnetic field values. The actual experimental data points are added to give an impression of their non-negligible error bars and thus of the restrained pertinence of the extracted fit functions.
At given magnetic field B, figure 6.10 confirms the evident anticipation of higher -ln(T)-values in the centre of radial n_m-distributions in stronger discharges. For both cases of weak and strong discharges, the absorbance diminishes when increasing the magnetic field from 1 to 30 mT at comparable rf powers. Furthermore, the radial distribution becomes broader (= lower value of α) at higher B. This observation is clearly visible in the strong discharge even though amplitudes in the centre of the radial distribution are not renormalised to directly compare α-values at different magnetic field values.
A direct comparison of radial distributions with normalised amplitudes and different α-values is possible in figure 6.9 on model $\cos^\alpha$-distributions.

In the described way, using the radially movable diaphragm for the 2.45 mbar-cell, four discharges of different strengths were mapped at $B = 1$ mT and three discharges at $B = 30$ mT in total. A compilation of all determined α-values is represented in figure 6.11. In the left inset, α-values are plotted as a function of the negative natural logarithm of the integral probe-transmission coefficient T_s on the inclined path of the single-frequency probe. This parameter -ln(T_s) is not to be mistaken for -ln(T) of the broad attenuated pump laser used on the axis of ordinates in figure 6.10. This representation in the left inset of figure 6.11 is completed by the numerical ratios of α(1mT) / α(30mT) for discharges of comparable rf excitation levels in both magnetic fields. From a practical point of view, it is more advantageous to relate α-values to the average metastable densities measured along the inclined probe beam path at $M = 0$ ($n_\mathrm{m}^\mathrm{S}(M = 0)$, right inset) and to the ratio of $n_\mathrm{m}^\mathrm{S}(M = 0)$ and N_g, the total number density of ground state atoms (main graph), in order to allow comparison of α-values at different pressures.
The experimental values of the radial n_m-parameter α at $p_3 = 2.45$ mbar compiled in figure 6.11 range between 0.7 and 1.7. This general result signifies that no uniform

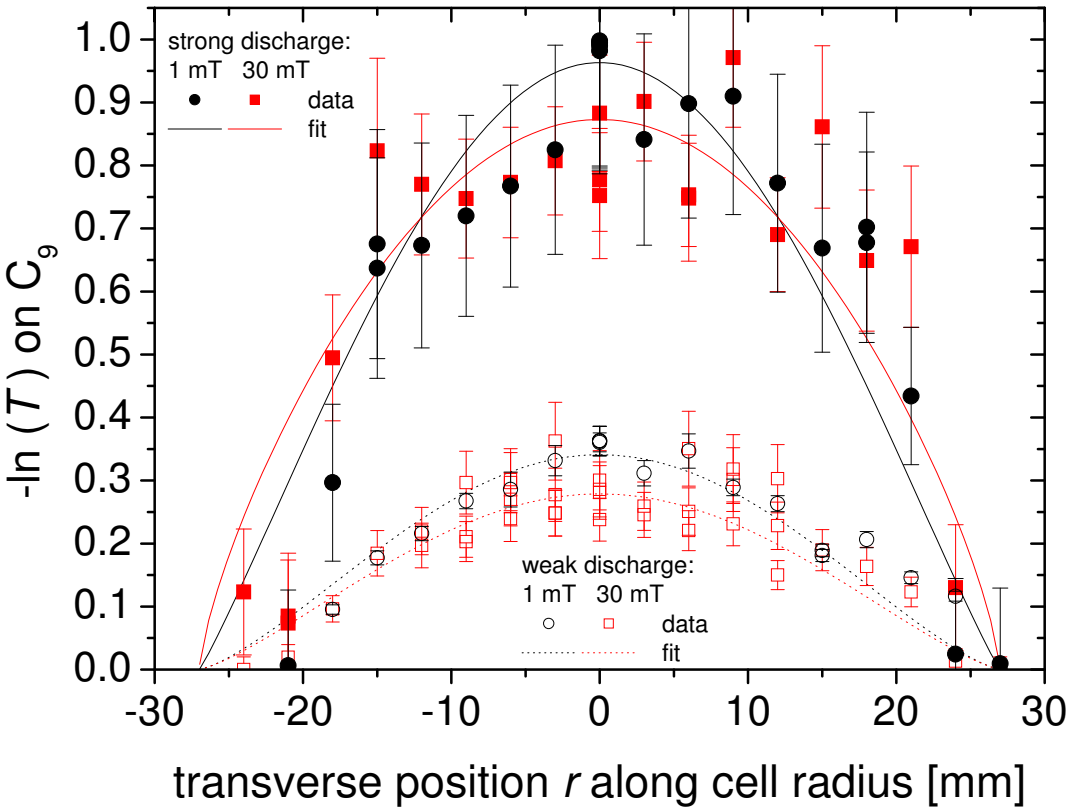

Figure 6.10: Cosine-like fits of $n_{\mathrm{m}}(r)$ data in $B = 1$ and 30 mT at $p_3 = 2.45$ mbar, in weak (data: open symbols, fits: dotted lines) and strong discharges (data: filled symbols, fits: solid lines). Plotted as amplitude on the y-axis is the absorbance -ln(T) of the attenuated pump laser on C_9 along the pump path as a function of different transverse r-positions of the 3 mm wide diaphragm. The inferred values of α are the following: strong discharge, 1 mT: $\alpha = 1.10 \pm 0.13$, 30 mT: $\alpha = 0.73 \pm 0.16$; weak discharge, 1 mT: $\alpha = 1.33 \pm 0.05$, 30 mT: $\alpha = 1.27 \pm 0.13$. These values of α are also reported in the next figure 6.11 at the following values of abscissae in the left inset ($-\ln$ of integral probe transmission coefficient on inclined probe path on C_9 transition): weak discharge: ≈ 0.35, strong discharge: ≈ 1.5.

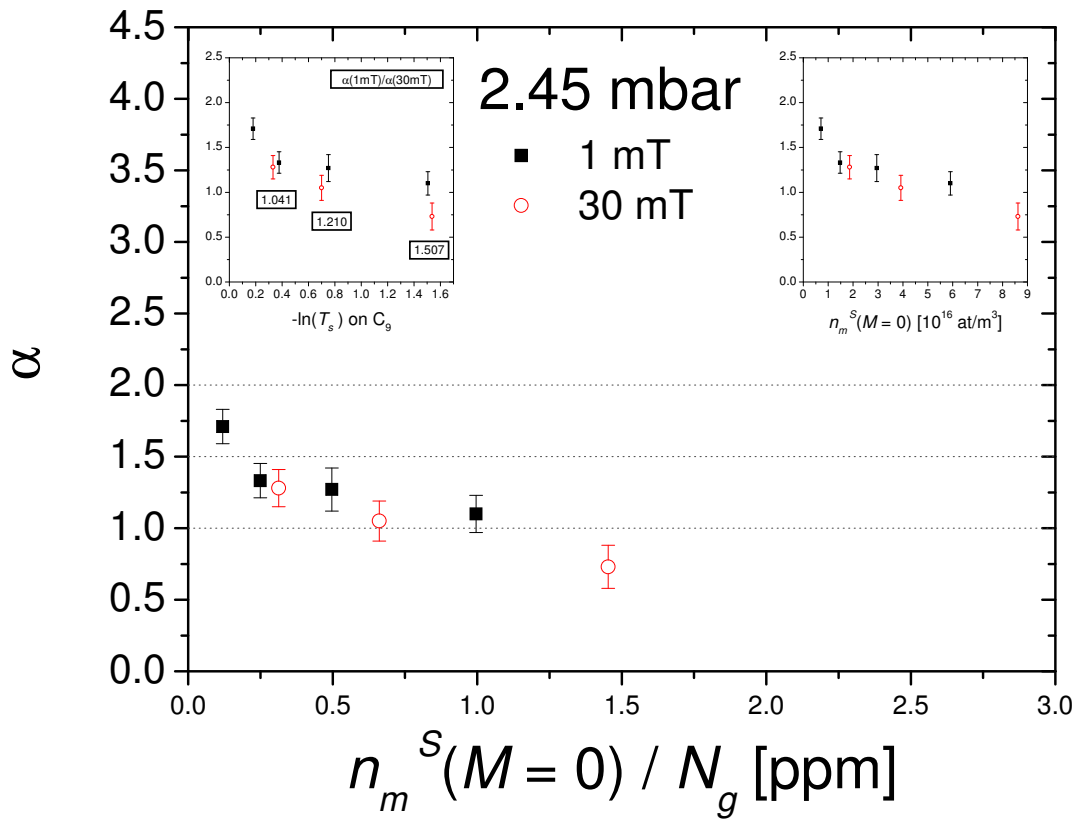

Figure 6.11: Compilation of α-values at $p_3 = 2.45$ mbar, in $B = 1$ mT (filled squares) and 30 mT (open circles). Left inset: The extracted radial n_{m}-parameter α is represented as function of $-\ln(T_s)$ where T_s is the integral transmission coefficient of the single-frequency probe laser on the inclined probe path, on the C_9-transition in these compiled examples. The numbers in boxes are numerical ratios of $\alpha(1\mathrm{mT}) / \alpha(30\mathrm{mT})$ for comparable discharge strengths in both B-fields. Right inset: Same data represented as a function of the average metastable density measured along the inclined probe beam path at $M = 0$: $n_{\mathrm{m}}^{\mathrm{S}}(M = 0)$. Main graph: Same data as function of the ratio of $n_{\mathrm{m}}^{\mathrm{S}}(M = 0)$ and N_{g}, the total number density of ground state atoms, in ppm. Dotted horizontal lines are guides for the eye.

($\alpha = 0$) radial distributions of metastable atoms are experimentally found at this ^{3}He-pressure.
When considering both investigated values of magnetic field separately, we observe that α decreases (distributions broaden) with increasing discharge strength, represented by the probe absorbance -ln(T_s) on C_9 here. At $B = 1$ mT, α decreases by up to 35 % at the strongest investigated discharge (corresponding to highest n_m) compared to the weakest one (lowest n_m).
In all examined regimes of discharge strengths, $\alpha(B = 30\ \mathrm{mT})$ appears lower than the corresponding radial n_m-parameter at $B = 1$ mT. This means that radial distributions at higher magnetic field are broader than at low B. The relative difference between α-values at low and higher B is less pronounced at weaker discharges than at stronger ones: at -ln(T_s) ≈ 0.35 and ≈ 0.7, the α-values of both investigated magnetic fields differ between 4 and 21 % but are compatible within experimental error bars. At the strongest examined discharge strength, at -ln(T_s) ≈ 1.5, the difference exceeds 50 %, and $\alpha(B = 30\ \mathrm{mT})$ is clearly below $\alpha(B = 1\ \mathrm{mT})$. However, at this pressure, increasing the magnetic field at given rf excitation level changes the plasma in a way that higher n_m-values can be obtained in most cases. Therefore, right inset and main graph of figure 6.11 appear better suitable for drawing conclusions and indicate that the radial n_m-parameter α decreases with increasing metastable density at $p_3 = 2.45$ mbar.

Radial n_m-mappings at 0.63 mbar

At $p_3 = 0.63$ mbar, radial mappings of n_m-distributions have been recorded using a different experimental method, mainly for a faster acquisition process and a more precise determination of the radial n_m-parameter α. A commercial beam profiler camera is used to record background-corrected images of the transmitted laser beam with rf discharge on and off. The light source is a single-frequency laser diode as used for the probe beam measurements: the output fibre is connected to the entrance port of the same collimator as used for the pump laser. A different collecting lens is used to focus the transmitted beam onto the CCD camera, after back reflection by the mirror behind the cell and deflection by the cube and quarterwave plate (cf. figure 3.4). For improved accuracy, the camera exposure time is set to maximum (1 second) and each of the two processed images (discharge off and on) is obtained by automatic averaging of 25 individual raw images, so that the total acquisition time is about $2 \times 25 \times 1 = 50$ seconds.
A 2-D absorbance map is achieved from the pixel-to-pixel ratio of the 'discharge on' and 'discharge off' images using the free *ImageJ* software[1]. 1-D profiles are then obtained by statistical averaging of several adjacent parallel lines (with arbitrary

[1] http://rsbweb.nih.gov/ij/

orientation) on both sides of the cell axis. Calibration of the magnifying factor of the whole imaging system is done using a home made calibration pattern of small holes attached to the back-reflecting mirror. Absorbance-values (-ln(T)) can thus be plotted as function of the transverse position r as defined in figure 6.3. These radial distributions are used to determine the radial n_{m}-parameter α by $\cos^{\alpha}$-fits as defined in equation (6.1).
In addition to the radially resolved single-frequency absorbance-values along the pump path, the integral absorption of the single-frequency probe laser along the inclined probe path is also measured for each discharge strength and magnetic field value B.

With this technique, 1-D profiles in the $p_3 = 0.63$ mbar cell have been obtained using the C_8-line for four discharges at $B = 1$ mT and three discharges at $B = 30$ mT. In addition, at fixed rf-level, 1-D profiles have been recorded for six values of the magnetic field intensity B.
Figure 6.12 shows a compilation of the results obtained at $B = 1$ mT and 30 mT.
Exponents α typically range between 1.1 and 1.3 at 30 mT and 2.1 and 2.2 at 1 mT, where α hardly varies with metastable density (a 5 % scatter is observed). At $B = 30$ mT, α steadily decreases with metastable density and changes by less than 20 %.
The relative error of determined α-values at $p_3 = 0.63$ mbar using the beam profiler mainly arises from the uncertainty in $r = 0$, the position of the cell axis in the image, and amounts to a maximum of 1.5 % (smaller than the one obtained at $p_3 = 2.45$ mbar with the movable diaphragm).
These data confirm the general trend observed at 2.45 mbar (broader n_{m}-distributions are found at 30 mT) but the impact of B strength is higher at lower pressure. Ratios of $\alpha(1\mathrm{mT})/\alpha(30\mathrm{mT})$ range from 1.6 to 2 at $p_3 = 0.63$ mbar (1.0 to 1.5 at $p_3 = 2.45$ mbar).

Figure 6.13 displays radial distributions obtained at $p_3 = 0.63$ mbar with the beam profiler at six different magnetic field strengths and given rf excitation level.
The -ln(T) amplitudes in the centre of the radial n_{m}-distributions for different magnetic field-values clearly diminish with increasing B. However, amplitudes are not normalised in figure 6.13, therefore the effect of radial broadening (experimentally realised by increasing magnetic field) is better visualised in figure 6.9, where theoretical $\cos^{\alpha}$-curves are renormalised to the maximum amplitude in the centre of the radial distribution of metastable atoms.
In the inset of figure 6.13, exponents α (extracted from the experimental distributions shown in the main graph) are compiled as function of B. This compilation confirms the clear influence of magnetic field on radial n_{m}-distributions. At low magnetic field, α-values at $B = 1$ and 2 mT are compatible within experimental error bars. At higher B, α-values decrease, meaning that radial distributions become broader. As

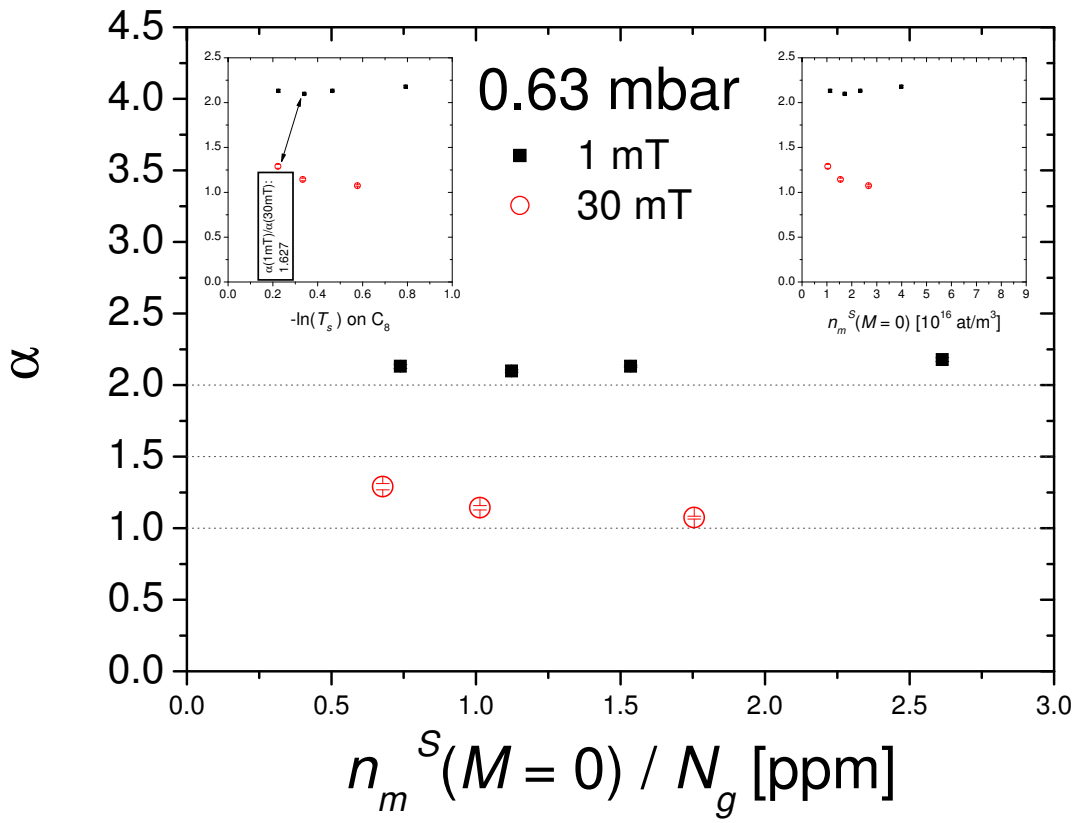

Figure 6.12: Compilation of α-values at $p_3 = 0.63$ mbar, in $B = 1$ mT (filled squares) and 30 mT (open circles). Left inset: The exponent α is represented as function of $-\ln(T_s)$ (measurements performed with C_8-line). The number in the box is the numerical ratio of $\alpha(1\text{mT}) \,/\, \alpha(30\text{mT})$ for the discharge which was mapped in several B-fields (complete compilation of α-values of this discharge as function of magnetic field: see inset of figure 6.13). Right inset: Same data represented as a function of the average metastable density measured along the inclined probe beam path at $M = 0$: $n_\text{m}^\text{S}(M = 0)$. Main graph: Same data as function of the ratio of $n_\text{m}^\text{S}(M = 0)$ and N_g, the total number density of ground state atoms, in ppm. Dotted horizontal lines are guides for the eye.

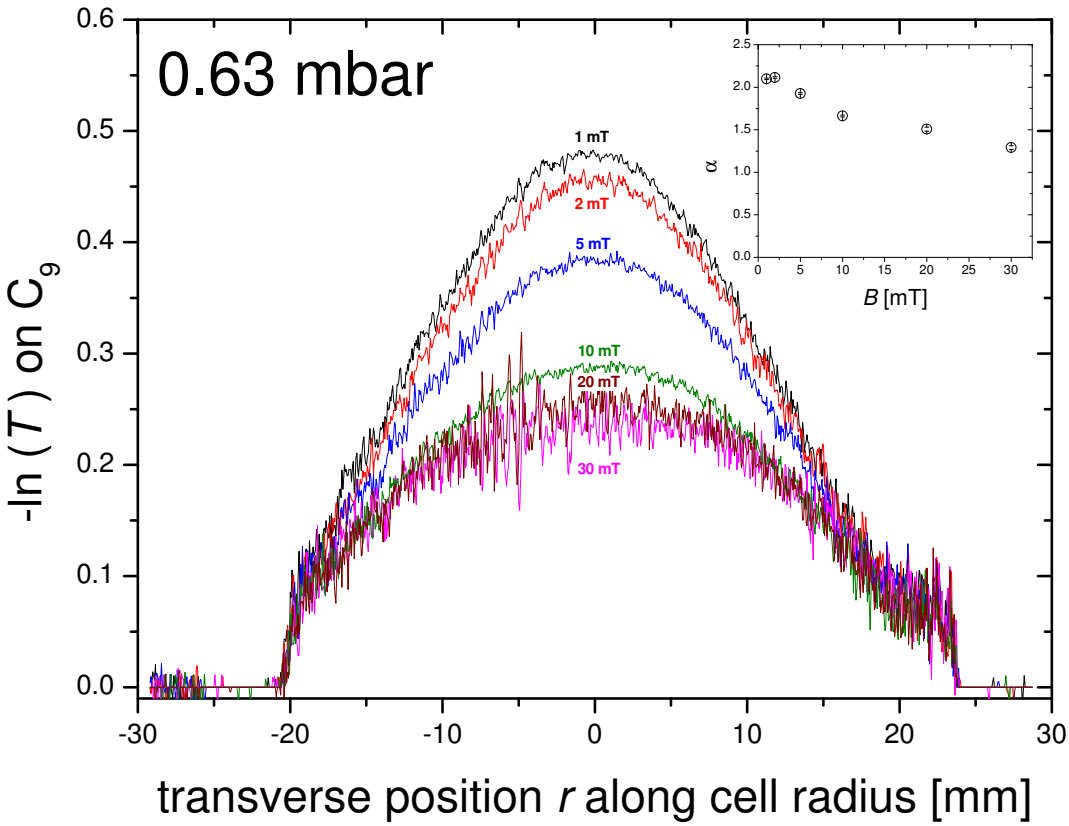

Figure 6.13: Radial n_{m}-mappings at $p_3 = 0.63$ mbar at given rf excitation level and different magnetic fields between 1 and 30 mT obtained with the beam profiler (see text). The graph shows the absorbance -ln(T) measured for monochromatic light tuned to the C_8-line and double-pass propagation along the cell axis, as a function of the transverse coordinate r as defined in figure 6.3. Inset: Extracted exponents α from these radial mappings as function of B.

already represented in the inset of figure 6.12, the decrease of α compared to 1 mT amounts to almost 63 % maximum at $B = 30$ mT for the chosen rf excitation level. Intermediate B-values confirm the qualitative behaviour of *de*creasing exponents α with *in*creasing magnetic field.

Radial n_{m}-distributions reported in other works

Comparing our results concerning radial distributions of metastable atoms in low-pressure-plasmas to other works in similar pressure-regimes reveals a qualitative agreement: [Mil98] presents a transverse metastable density profile of ^{4}He at 2.67 mbar with maximum n_{m} in the centre of the distribution and decreasing n_{m} towards the walls of the discharge tube. Experimental data points in [Mil98] are fitted by a second order polynomial.
[Ich80] also contains radial distributions of metastable atom densities for helium (and neon). Helium-profiles at 1.33 and 13.3 mbar yield similar qualitative behaviours as described above. It is clearly noted that the assumption of a uniform plasma becomes invalid, above 4 mbar for He. Our results indicate that this is the case already at lower pressure (see e.g., figures 6.12 and 6.11).
In [Som92], a radial metastable density profile for helium is computed at a pressure of 0.67 mbar. The qualitative shape of the n_{m}-distribution is similar to the experimental examples reported before. In these conditions, the spatial n_{m}-profile is diffusion dominated, whereas Penning ionisations and metastable relaxation are minor loss processes.

All cited works above are for zero magnetic field $B = 0$ and a helium pressure of 13.3 mbar maximum. In high magnetic field and/or at high helium pressure, radial distributions of metastable atoms qualitatively change. The maximum value of n_{m} is no longer found in the centre of the distribution, but located close to the cell walls with decreasing metastable densities towards the centre.
Quantitative measurements of radial n_{m}-profiles for four different pressure values in the range of 32 to 128 mbar at $B = 2$ T are presented in [Nik10] and [Doh11]. The experimental method is similar to the one used in this work for the 2.45 mbar cell, based on longitudinal absorption measurements using a single-frequency laser diode on various transverse r-positions.

Integral absorbance versus maximum in centre of radial distribution

This paragraph presents some additional results from radial n_{m}-measurements at 0.63 mbar. The results concern comparisons of measured laser absorbances -ln(T), either in the centre of the radial n_{m}-distribution or the integral value over the whole radial laser profile.

Figure 6.14 shows the ratio of both absorbance-values at $B = 1$ and 30 mT.
Data were obtained using the light path which in standard OP measurements is

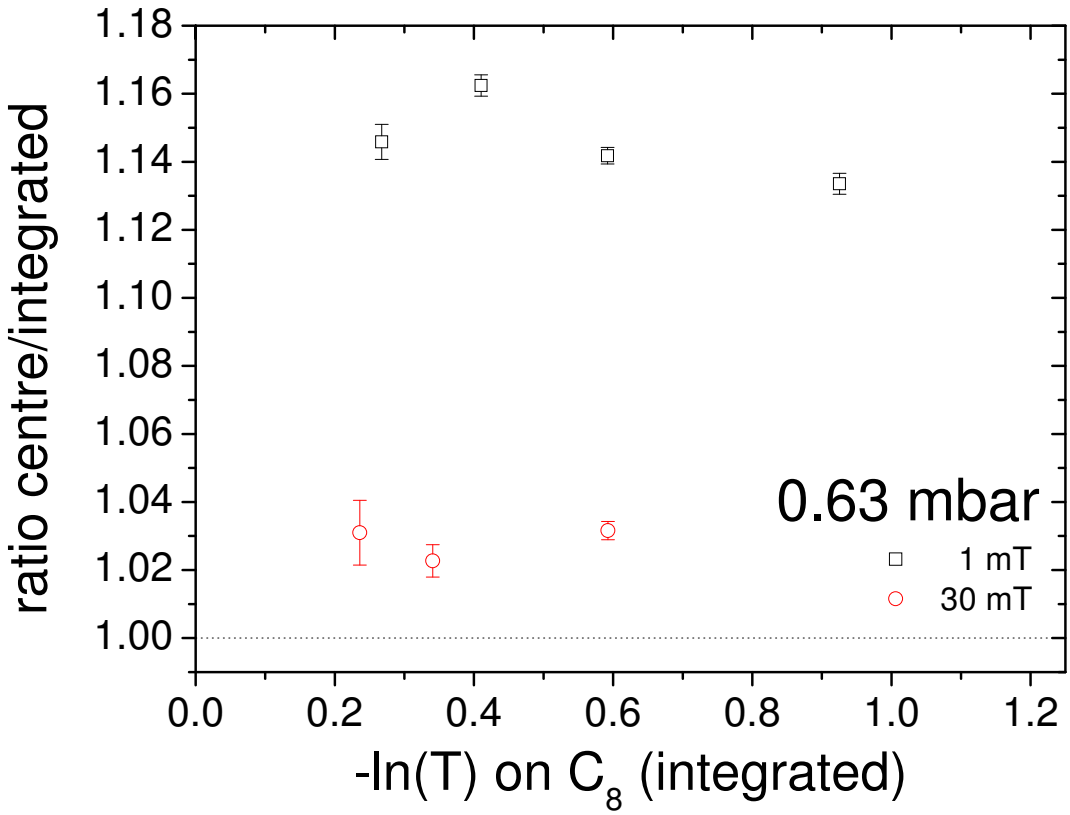

Figure 6.14: Ratio of absorbance values -ln(T) in the centre of the radial n_{m}-distribution divided by the integral value over the radial laser profile, at $B = 1$ mT (squares) and $B = 30$ mT (circles). Further conditions: $p_3 = 0.63$ mbar, weak single-frequency laser on the C_8-transition on the pump path. Dotted line visualises equality: ratio = 1.

habitually used for the pump laser, here using a weak single-frequency laser on the C_8-transition. A general observation is that the ratio of absorbance-values in the centre of the profile of metastable atoms divided by integral absorbance-values over the radial laser profile is roughly constant over the whole investigated -ln(T)-range when considering results of both magnetic field-values separately. A comparison of ratios in low and high B-fields reveals that at 30 mT, results are closer to equality (ratio = 1): -ln(T) (centre) is approximately 3 % above -ln(T) (integral over radial laser profile). At $B = 1$ mT, we find the same quantitative behaviour, but the relative difference between centre and integral amounts to approximately 15 %.
With the help of the OP model, we are able to compute -ln(T) values (centre and

integral over radial laser profile) to predict the expected behaviour. The ratios in figure 6.14 depend on α and the spatial beam diameter, that for this case amounts to $2a = 1.3$ cm (the difference compared to the usual 1.6 cm is arising from the use of a different (spatially) monomode fibre for the single-frequency laser). Comparing these computed ratios to experimentally observed ones constitutes a possibility to infer values of α. From these comparisons of computations and measurements at 0.63 mbar presented here, reasonable values of α are found.

Similar data also exist for 2.45 mbar, using the broadband pump laser, attenuated to low incident power, on the C_9-transition (data not presented here). Comparable qualitative results to the ones at 0.63 mbar are obtained at higher pressure. The use of two spectrally different lasers on two different transitions is no issue in this context, as the ratio of -ln(T) (centre) divided by -ln(T) (integral) is actually independent of the chosen transition and of the laser frequency spectrum. However, it is sensitive to the spatial Gaussian diameter of the laser and to the transverse distribution of metastable densities, i.e. to the parameter α.
Thus, comparisons of measurements and computations of -ln(T) values can also be used at 2.45 mbar to infer values of α, but the results are less satisfying. A possible reason might be correlated to the lower precision on the radial n_{m}-distribution and thus on the extrapolated value of -ln(T) in the centre of the fit obtained when using the dedicated device for n_{m}-mappings (2.45 mbar) compared to the use of the beam profiler as experimental device (0.65 mbar) to infer profiles of metastable densities.
Although at 0.63 mbar, reasonable values of α are found, direct mappings to infer α are considered more reliable with respect to comparisons of measurements and computations of -ln(T) values due to the sensitivity to both α and the spatial beam diameter.

Influence of α on OP model results

In order to examine the impact of the radial n_{m}-parameter α on OP model results like apparent polarisation in presence of the pump laser or probe absorptance, the model for MEOP kinetics is used to compute these OP quantities, first at fixed α for two different pump laser diameters, and second at fixed waist of the pump laser for two extreme cases of α.
All computations are performed at $B = 1$ mT, pump and probe C_8, zero nuclear polarisation $M = 0$, $p_3 = 0.63$ and 2.45 mbar. The qualitative behaviour is the same at both pressure values. The higher value of ^{3}He-pressure is chosen for the presentation of results of this investigation since at 2.45 mbar (and given magnetic field), α depends on discharge strength, and thus metastable density (see figure 6.11). In case the impact of α on OP quantities is high, the knowledge of α would therefore be more important than at low pressure, where no dependence of α on metastable

density is observed (see figure 6.12).

In figure 6.15, the influence of the pump beam diameter on apparent polarisation values M_8^{a}, at fixed radial n_{m}-parameter α of 1.5, is investigated.
M_8^{a} indicates to which extent populations in 2^3S are perturbed by the presence of the

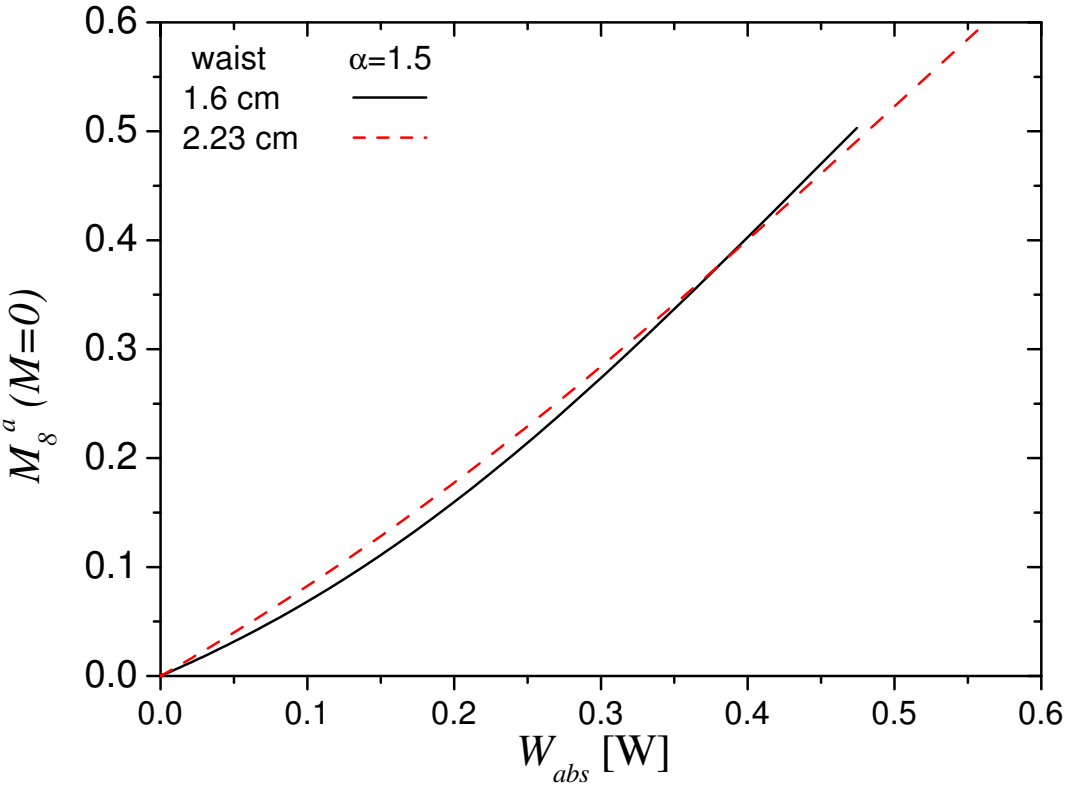

Figure 6.15: Influence of pump beam diameter at fixed $\alpha = 1.5$ on apparent polarisation M_8^{a} at $M = 0$, plotted as a function of absorbed pump laser power W_{abs}. Solid line: Waist of pump beam diameter: $2a = 1.6$ cm. Dashed line: Waist of pump beam diameter: $2a = 2.23$ cm. Input parameters for OP model: $p_3 = 2.45$ mbar, $B = 1$ mT, pump and probe transitions: C_8, weak discharge: $n_{\mathrm{m}} = 1.2 \times 10^{16}$ at/m^3, $\Gamma_{\mathrm{D}} = (850\,\mathrm{s})^{-1}$.

intense pump laser at null polarisation. The difference between M_8^{a}-values obtained at pump beam diameters 1.6 and 2.23 cm is zero at $W_{\mathrm{abs}} = 0$ (where $M_8^{\mathrm{a}} = M = 0$) and at $W_{\mathrm{abs}} = 0.38$ W. In between, M_8^{a} at $2a = 2.23$ cm is higher than at $2a = 1.6$ cm as expected due to a higher spatial overlap between pump profile and radial n_{m}-distribution. The maximum difference (0.0173) seen in this range of absorbed pump laser powers corresponds to a relative change of 10 % at $W_{\mathrm{abs}} = 0.20$ W. The maximum relative change (ratio of $M_8^{\mathrm{a}}(2.23\ \mathrm{cm})/M_8^{\mathrm{a}}(1.6\ \mathrm{cm})$) is actually, over the whole W_{abs}

scale, reached at $W_{\mathrm{abs}} = 9$ mW and is equal to + 32 %.

In figure 6.16, the pump beam diameter is fixed to $2a = 1.6$ cm, corresponding to the experimental value during most of the measurements performed for this work. Keeping all other parameters fixed (see figure 6.15 and corresponding comments), the radial n_{m}-parameter α is set to either 0.5 or 2.5, which largely covers the experimentally observed range of α-values (see figures 6.11 and 6.12). Relative values with respect to $\alpha = 0$ at constant $n_{\mathrm{m}}^{\mathrm{S}}$ are represented.

Relative probe absorptances yield qualitative different behaviour with increasing ab-

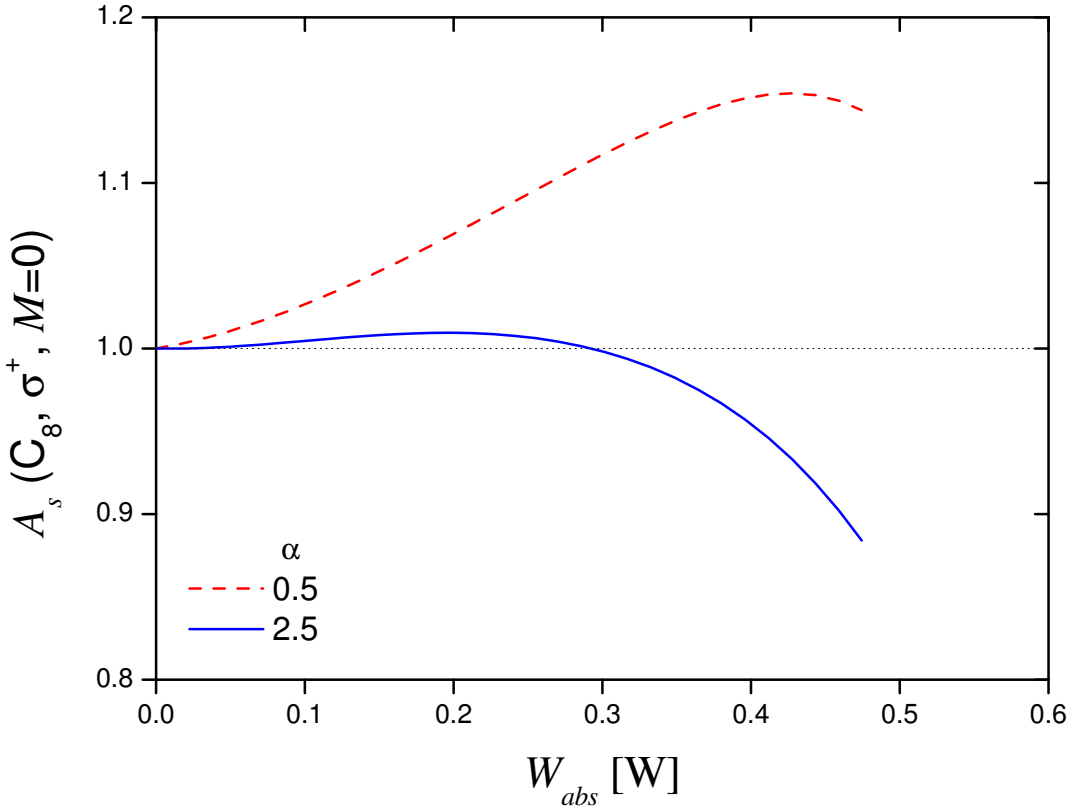

Figure 6.16: Influence of α on probe absorptance $A_s = 1 - T_s$ on C_8, σ^+, at $M = 0$. Relative values (at constant $n_{\mathrm{m}}^{\mathrm{S}}$) with respect to $\alpha = 0$ are represented for $\alpha = 0.5$ (dotted line) and $\alpha = 2.5$ (solid line) at fixed pump beam diameter of $2a = 1.6$ cm and plotted as function of absorbed pump laser power W_{abs}. Input parameters for OP model: see caption of figure 6.15.

sorbed pump laser power: At high α corresponding to a narrow distribution, relative $A_s(M = 0)$ values vary only slightly up to $W_{\mathrm{abs}} = 0.3$ W and keep decreasing down to 0.88 at 0.47 W. The corresponding relative $A_s(M = 0)$ values at low α exceed 1 over the whole range of absorbed pump laser powers attaining a local maximum of 1.15

at $W_{\mathrm{abs}} = 0.43$ W. In the case of higher α, metastable atoms start becoming 'transparent' (i.e., decreasing relative probe absorptance) at lower W_{abs} due to the more narrow n_{m} profile.

In summary, the computations presented in the last paragraphs reveal a moderate but sizeable influence of the radial n_{m}-parameter α on OP model results.

6.1.3 Variation of metastable density with nuclear polarisation

Experimentally observed variation of n_{m}

Relative variations of metastable densities with M are investigated during decays of nuclear polarisation in absence of the pump laser. Thus, populations in the 2^3S sublevels are not perturbed by the intense pump laser in all presented experimental examples, and the spin temperature formula for $n_{\mathrm{m}}^{\mathrm{S}}(M)$ / $n_{\mathrm{m}}^{\mathrm{S}}(0)$ given by equation (4.33) is valid.

Figure 6.17 shows relative variations of metastable densities $\left(n_{\mathrm{m}}^{\mathrm{S}}(M) \,/\, n_{\mathrm{m}}^{\mathrm{S}}(0)\right)$ as function of nuclear polarisation M at intermediate ^{3}He-pressure of 1.19 mbar. Short periods of polarisation decays from experiments with the OP beam alternatively applied and blocked (cf. chapters 5.3 and 6.2) are in good agreement with continuous data from recordings of polarisation decay.
Both experimental examples illustrate significant change in n_{m} (e.g., - 21 % when M decays from 0.74 to 0). At other ^{3}He-pressures, the observed behaviour is qualitatively the same, and quantitatively depending on the obtainable steady state-polarisation M_{eq}. At higher pressure, 2.45 mbar for instance, M_{eq}-values are lower than at low pressure (both in low magnetic field). Hence, the maximum relative variation of n_{m} is lower than observed at lower pressure.
The indicated allometric fit of form $y = 1 + a \cdot x^b$ in figure 6.17 yields a value of the exponent b of 2.113, thus close to 2 which points at a dependence of $n_{\mathrm{m}}^{\mathrm{S}}(M)$ / $n_{\mathrm{m}}^{\mathrm{S}}(0)$ with M^2. In the following, this M^2-dependence of the relative n_{m}-variation is verified.

In figure 6.18, the relative variation of metastable densities is represented as function of M^2 in two different magnetic fields: $B = 1$ and 30 mT.
When plotted as function of M^2, the relative variation of n_{m} yields a good quadratic dependence of M, i.e. almost linear with M^2, in both investigated magnetic fields. The observed behaviour in $B = 30$ mT is qualitatively the same as in low magnetic field. The relative increase of $n_{\mathrm{m}}^{\mathrm{S}}$ with M^2 (i.e., the slope, see figure 6.18) is 19 % higher at 30 mT compared to 1 mT.
When either inverting the polarity of the magnetic field or using the other circular

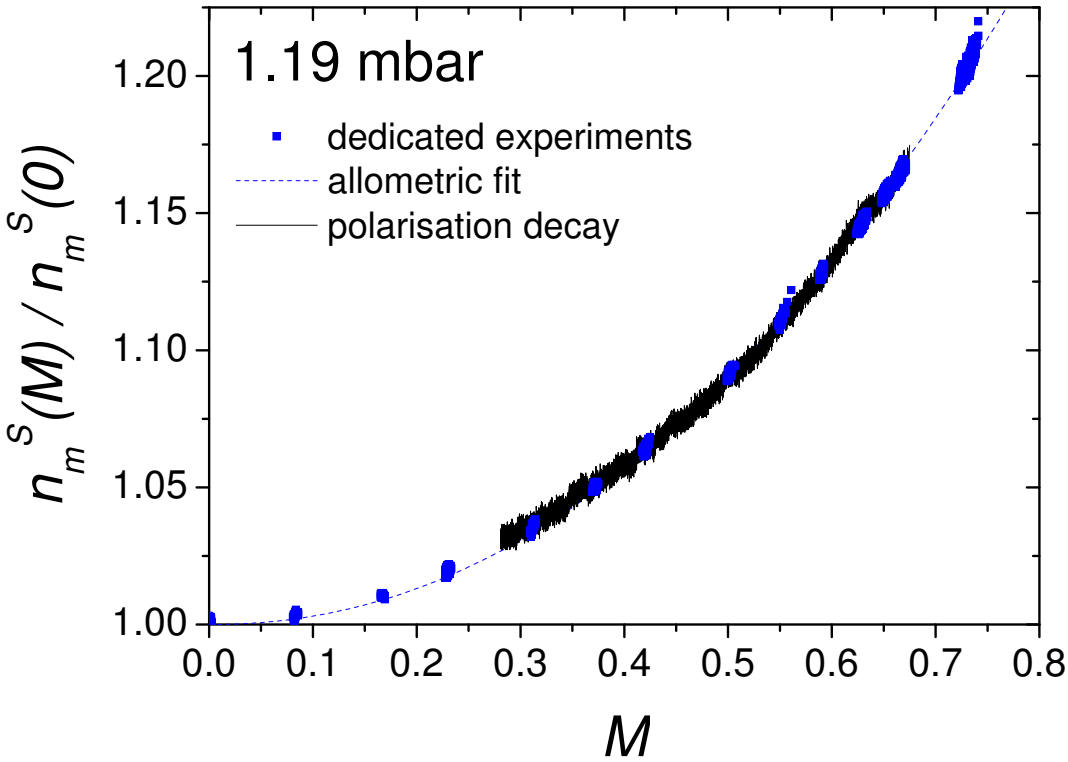

Figure 6.17: Relative variation $n_{\mathrm{m}}^{\mathrm{S}}(M)\ /\ n_{\mathrm{m}}^{\mathrm{S}}(0)$ in $B = 1$ mT and $p_3 = 1.19$ mbar as function of M, during continuous polarisation decay (in absence of the pump laser, black solid line) and from dedicated experiments to account for perturbations of 2^3S- and 2^3P-populations (see chapters 5.3 and 6.2) during periods where the OP beam is blocked (blue filled squares). Blue dashed line: allometric fit (empirically best suited on relative variation of n_{m}) of form $y = 1 + a \cdot x^b$ ($a = 0.392, b = 2.113$).

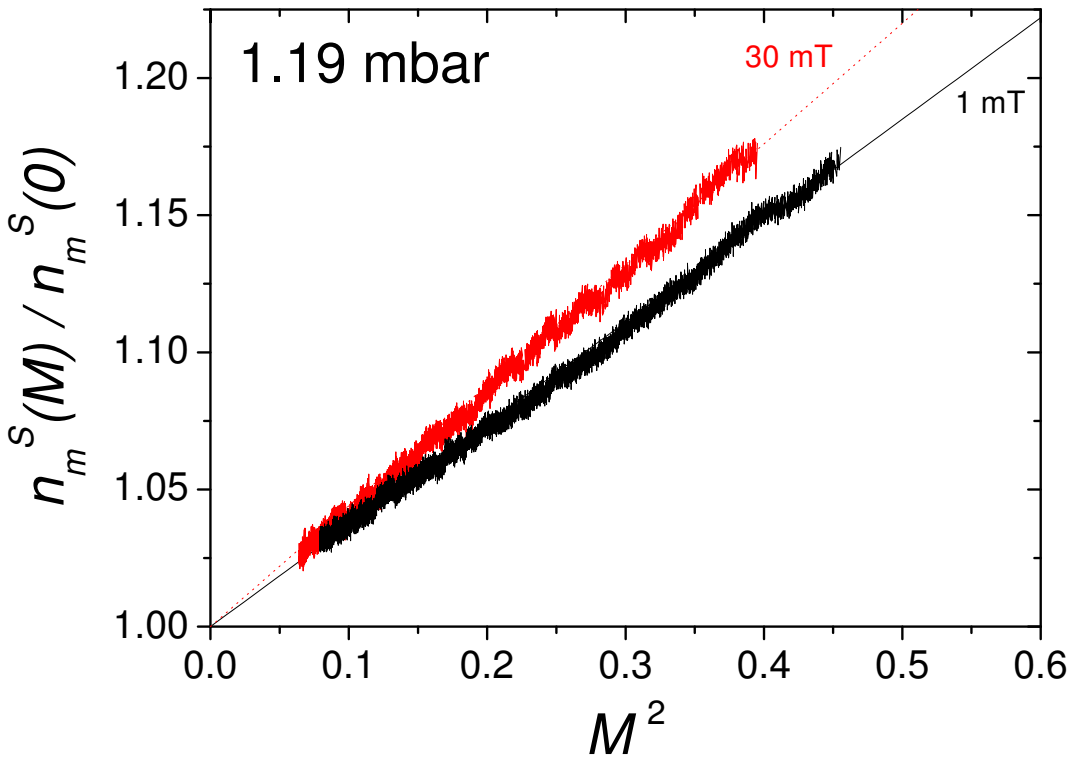

Figure 6.18: Example of relative variation $n_{\mathrm{m}}^{\mathrm{S}}(M) \,/\, n_{\mathrm{m}}^{\mathrm{S}}(0)$ as function of M^2, at $p_3 =$ 1.19 mbar, in $B = 1$ mT: black data and solid line as guide for the eye (slope: 0.37) and $B = 30$ mT: red data and dotted guide for the eye (slope: 0.44).

component of pump laser light for optical pumping, σ^- instead of the usually chosen σ^+-component, nuclear orientation builds up in the opposite sense, $-M$ instead of M. The observed relative change in n_m is the same however, independently of the sense of nuclear orientation, and plotting $n_\mathrm{m}^\mathrm{S}(M)$ / $n_\mathrm{m}^\mathrm{S}(0)$ as function of M^2 yields identical results.
The described behaviour, especially the quadratic dependence of the relative variation of metastable densities on nuclear polarisation, is very generally observed in various different experimental conditions like different pressures of ^{3}He or different discharge strengths. The observed significant change in n_m with increasing M^2 may for instance be attributed to the inhibiting effect of polarisation on Penning ionising collisions, a two-body process between two metastable helium atoms discussed in more detail in the next paragraph.
Some rare exceptions, where the relative variation of n_m departs from a M^2-dependence (and where a stronger increase with up to M^7 is observed, actually decrease has never been observed within this work), concern special conditions as for example a very weak discharge in the lowest pressure cell. Reasons that might contribute to this departure from the generally observed tendency are possibly diffusion to the cell walls which may be more important than Penning collisions at very low pressure, and a different discharge regime in which the proximity of the extinction threshold potentially effects the discharge, so that it may be more susceptible to components of the plasma.

Role of electronic orientation $< J_z^* >$

The electronic orientation $< J_z^* >$ in the 2^3S-state has an influence on the cross-section of ionising Penning collisions in the plasma:

$$\mathrm{He}(2^3\mathrm{S}_1) + \mathrm{He}(2^3\mathrm{S}_1) \rightarrow \mathrm{He}(1^1\mathrm{S}_0) + \mathrm{He}^+ + e^-. \tag{6.2}$$

As the total electronic spin should be conserved in Penning collisions according to the Wigner spin conservation rule (1927), they would be ultimately forbidden in a fully polarised system [Sch70] as the total electronic spin of the outgoing particles in the final state does not exceed 1, whereas in the initial state, it equals 2:

$$\begin{aligned} (\uparrow\uparrow) + (\uparrow\uparrow) &\quad \nrightarrow \quad (\uparrow\downarrow) + (\uparrow) + (\uparrow) \\ (\downarrow\downarrow) + (\downarrow\downarrow) &\quad \nrightarrow \quad (\uparrow\downarrow) + (\downarrow) + (\downarrow), \end{aligned} \tag{6.3}$$

denoting the spatial quantisation of the electronic spin symbolically: $(\uparrow)$ stands for 'spin up', $(\downarrow)$ for 'spin down', the absolute value amounting to 1/2.

In [Sch70] and [Hil72], spin conservation in ionising collisions between metastable ^{4}He atoms (or ^{3}He respectively) has been demonstrated experimentally, using OP to

optically orient the metastable helium atoms and detecting changes in the number density of electrons produced by this reaction. A decrease of electron density is observed with decreasing 1083 nm absorption, as electronic polarisation (and nuclear in ^{3}He) in 2^3S builds up: the cross-section of Penning collisions decreases because electronic spin conservation holds.
Spin conservation is also fulfilled in collisions between metastable He atoms and other species. In [Dmi76], a dependence of the cross section for Penning ionisation on the spin orientation of the colliding 2^3S He and Rb atoms has been experimentally observed. In [Sch69a], the same mechanism is used to transfer spin polarisation from optically pumped metastable He atoms to ions of Cd, Sr and Zn.

In the context of feasibility studies concerning Bose-Einstein condensation of spin-polarised metastable helium atoms at ultralow temperatures, theoretical analyses of decay kinetics and calculations of elastic and inelastic collision rates [Shl94, Fed96] showed that full spin polarisation of the gas should lead to suppression of the Penning ionisation rate by five orders of magnitude.
[Her00] measured the suppression of Penning ionisation in an ultracold metastable ^{4}He atomic cloud after spin-polarising the atoms by OP and thus deduced an experimental upper bound for the ionisation rate constant in the spin-polarised case, which emerged to be at least a factor of 20 lower than measured in an unpolarised gas.
BEC of spin-polarised metastable ^{4}He could actually be achieved in two groups almost simultaneously in 2001 [Rob01, Per01], which is - among other aspects - a striking evidence of the inhibiting effect of polarisation on ionising Penning collisions. In a profound experimental study [Léo05] of the mechanism of Penning ionisation in ultracold photoassociated ^{4}He dimers, it was confirmed that a common spin orientation of the trapped sample in the metastable state imposes a strict spin conservation rule that permits collisional Penning ionisation only through spin-dipole coupling that is relatively weak [Shl94]. However, it has been observed that weak couplings induced by molecular rotation can lead to ionisation of photoassociated molecules.

If the observed significant change in n_m with increasing M^2 is caused by advancing inhibition of Penning collisions at increasing nuclear ground state polarisation, transferred by ME collisions from the metastable state with strong hyperfine coupling between electronic and nuclear angular momenta, then the mean z-component of electronic angular momentum in 2^3S, $< J_z^* >$, is a meaningful parameter concerning the characterisation of dependencies for changes of the metastable density.
Based on the expressions of the magnetic eigenstates A_i of 2^3S in the decoupled basis $|m_S, m_I\rangle$ (see section 2.2 and appendix of [Cou02]), $< J_z^* >$ can be expressed in the

following way as function of the populations a_i in 2^3S:

$$< J_z^* >= (a_4 - a_1) + a_3 \sin^2\theta_+ - a_2 \cos^2\theta_- + a_6 \cos^2\theta_+ - a_5 \sin^2\theta_-, \tag{6.4}$$

with B-dependent mixing parameters θ_+ and θ_- of electronic and nuclear angular momenta (cf. appendix A). Equation (6.4) is valid for $B < 0.162$ T, at higher magnetic fields, level crossings and corresponding permutations of indices have to be taken into account [Cou02].
In spin temperature distribution, $a_2 = a_5$ and $a_3 = a_6$, so that equation (6.4) simplifies to

$$< J_z^* >= (a_4 - a_1) + (a_3 - a_2). \tag{6.5}$$

Using the expressions of populations a_i in the spin temperature limit as function of nuclear polarisation (equation (2.56)), $< J_z^* >$ can be written as function of M:

$$< J_z^* >= \frac{(1+M)^3 - (1-M)^3 + (1-M)(1+M)^2 - (1-M)^2(1+M)}{2M^2+6} = \frac{4M}{3+M^2}. \tag{6.6}$$

The relation between $n_\mathrm{m}(M)\,/\,n_\mathrm{m}(0)$ and the electronic angular momentum in 2^3S has been checked for different pressures and discharge conditions. A dependence of the relative change of n_m on $< J_z^* >^2$ is generally observed at small and intermediate $< J_z^* >$-values corresponding to M-values below 0.55 approximately.
Especially at small M, equation (6.6) can be approximated by $4M/3$ without introducing a significant error. Thus $< J_z^* >$ is approximately proportional to M which explains why experimentally, a dependence of $n_\mathrm{m}(M)\,/\,n_\mathrm{m}(0)$ on $< J_z^* >^2$ is observed at low and intermediate values of nuclear polarisation. Below $M = 0.55$, the relative error introduced by this approximation (neglecting the addend M^2 in the denominator of equation (6.6)) remains below 10 %. At $M = 1$, this relative error amounts to 33 %.

Discussion

The presented observations of increasing metastable densities with nuclear polarisation are in qualitative agreement with similar investigations at higher magnetic field of $B = 0.0925$ T ($p_3 = 1.07$ mbar) [Cou02] and of $B = 1.5$ T ($p_3 = 8 - 67$ mbar) [Abb05b].

The observed significant change in n_m induces an identical change of Γ^0_ME (equation (2.68)) that is not compensated by the variation of the factor f_Γ in equation (2.71) (see figure 2.9). The change in n_m also indicates that the plasma conditions are modified and suggests that Γ_g may vary with polarisation. Altogether, since $\Gamma_\mathrm{D} = \Gamma_g + f_\Gamma \Gamma^0_\mathrm{ME}$, the precisely exponential character of all observed decays (being a sign of a *constant* decay rate Γ_D) recorded in very different experimental situations is puzzling and can certainly not be attributed to an accidental compensation for these independently varying quantities.

6.2 Results of dedicated experiments to account for perturbations of 2^3S- and 2^3P-populations

In the following section, the main focus is on *results* of the dedicated experiments over the whole range of experimental conditions to account for perturbations of 2^3S- and 2^3P-populations mainly due to the influence of the intense pump laser. Physical background information on the mechanisms leading to over- or underpolarisation in 2^3S and a non-negligible population in 2^3P are given in sections 2.8.2, 2.8.3 and 4.3. Methodological aspects and ways to analyse data of these dedicated experiments are discussed in chapter 5.3.
In addition to experimental results, the present section is enriched by computations using the model of MEOP-kinetics to obtain a better understanding of the complex processes in 2^3S and 2^3P.

6.2.1 Influence of probe detuning on apparent polarisation at $M = 0$

In this paragraph, measurements of apparent polarisation at $M = 0$ as a function of atomic velocity v_z are presented and discussed. Such measurements can be realised in experiments by sweeping the single-frequency probe laser over different resonances in the presence of the broadband pump laser (1.7 GHz FWHM) tuned to a fixed transition. Scanning the probe frequency implies exploring the different velocity classes of the Doppler-broadened velocity distribution of the gas atoms. Due to the experimental configuration that laser beams are back-reflected by a mirror behind the ^{3}He-cell, at given detuning, atoms of the velocity class $+v_z$ are probed on the first pass through the cell towards the mirror, whereas on the return pass, atoms of the velocity class $-v_z$ are probed.
The nuclear polarisation M was maintained at zero with the help of magnets positioned on the cell during the entire sweeps of the probe laser frequency. These measurements were performed at $p_3 = 2.45$ mbar and repeated for several pump transitions and different values of incident laser power.
This procedure yields different combinations of probe and pump transitions, among them cases where the same 2^3S sublevels are probed and pumped and cases where probe and pump address different 2^3S sublevels. Figure 6.19 represents apparent polarisation values at $M = 0$ as function of probe detuning for different probe and pump combinations at fixed incident pump laser power of 1.66 W.
The right part of figure 6.19 shows three frequency sweeps of the probe laser within a frequency range containing the C_8 and C_9 resonances, each sweep in presence of a 1.66 W pump laser tuned to different transitions: C_6, C_8 and C_9. The left part

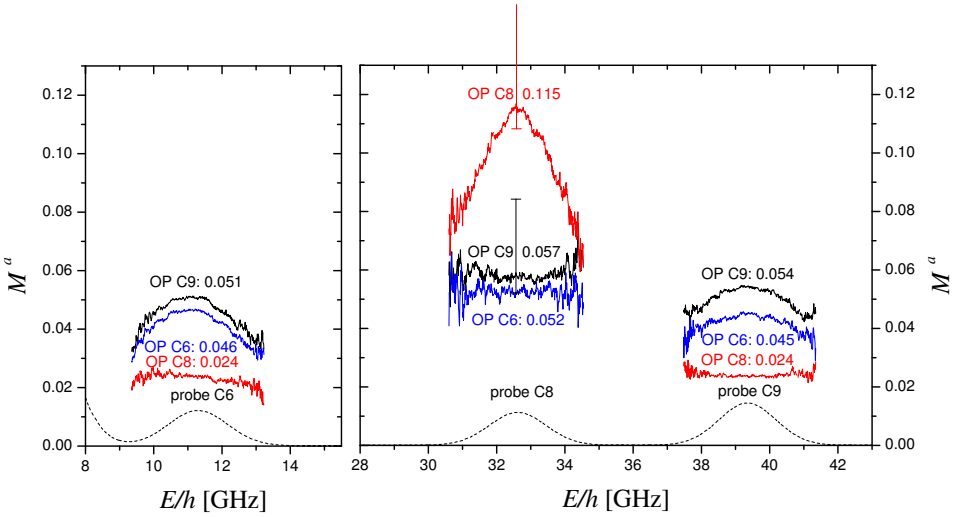

Figure 6.19: Apparent polarisation at $M = 0$ (magnets on cell) at 1.66 W of incident pump laser power as function of probe frequency in $p_3 = 2.45$ mbar and $B = 1$ mT. Left: Three frequency sweeps of the probe laser over C_6, either with pump on C_6, C_8 or C_9 (see labels in graph). Right: Idem with sweeps of the probe laser over the C_9- and C_8-resonances. The numbers included in the labels indicate the maximum value of M^a with probe laser in resonance for the different pump/probe-combinations. The two ranges of apparent polarisations indicated for probe C_8 designate the ranges of observed M^a-values at $M = 0$ in dynamic measurements (presented starting on page 206) in similar OP conditions. Dashed lines are recorded σ^- probe absorption signals at $M = 0$ and indicate the line-positions and -widths of probe C_6-, C_8- and C_9-resonances.

of the same figure corresponds to experiments in identical conditions, only the frequency range of the probe sweeps is different, covering the C_6 resonance. For a better understanding, we recall briefly the involved sublevels of the investigated transitions (details cf. section 2.2): C_6: from 2^3S_1, F=3/2 to 2^3P_1, F=1/2 (for absorption, or reversed direction for emission), C_8: 2^3S_1, F=1/2 to 2^3P_0, F=1/2 and C_9: 2^3S_1, F=3/2 to 2^3P_0, F=1/2. C_6 and C_9 address the same initial F-level in 2^3S_1, whereas C_8 and C_9 both attain 2^3P_0 (in case of absorption).
A general observation in both parts of figure 6.19 is that there are two different types of qualitative behaviour of the apparent polarisation as function of probe detuning: either approximately constant over the whole width of the probe transition, or strongly dependent on the probe frequency with a maximum of apparent polarisation in resonance. The cases with constant (non-zero) apparent polarisation at $M = 0$, independent of the probe detuning turn out to be the ones where *different* hyperfine-levels are probed and pumped: pump C_8 (addresses F=1/2 in 2^3S_1) for probe C_6 and C_9 (both address F=3/2 in 2^3S_1), and vice versa: pump C_6 and C_9 for probe C_8.
Whenever the same sublevels are probed and pumped, the apparent polarisation, inferred from the corresponding probe absorption rates, strongly depends on the probe detuning. Furthermore, the mean apparent polarisation value averaged over the whole width of the probe transition is of course inferior to the value measured by a centred probe in resonance (M^a-values indicated in labels of graphs).
For probe and pump, both tuned to C_8, the apparent polarisation values in the wings are about 40 % smaller than in the centre of the transition (all quantitative values are given here for 1.66 W of incident power provided by the broadband multimode pump laser characterised in section 3.2). This implies that the mean apparent polarisation (as computed by the model for MEOP-kinetics in the 'strongly pumped velocity class', see page 204) is about 20 % smaller than the value measured by a centred probe in resonance. For the probe laser tuned to C_9 and the pump laser on the C_6 or C_9 transitions, the decrease of apparent polarisation towards the borders of the transition amounts to slightly less or slightly more than 20 % respectively compared to resonance. For probe C_6 and pump C_6 or C_9, the apparent polarisation towards the borders of the transition decreases by 35 to 40 % with respect to the centre of the probe transition. The higher the decrease of apparent polarisation as function of detuning, the higher the difference between mean and maximum value (in resonance) of apparent polarisation.
When detuning the probe laser up to $\pm\Delta\omega$ corresponding to 10 % decrease in light absorption (possible realistic probe detuning, cf. section 4.2), the value of apparent polarisation only changes up to approximately 3-4 % for all probe transitions.

For a quantitative comparison, some more apparent polarisation values at $M = 0$ coming from dedicated (dynamic) experiments (as function of M as presented starting on page 206) at fixed probe laser are given here (corresponding to the ranges indicated on the right graph of figure 6.19 in the probe C_8-resonance): for

probe C_8 and pump C_8 with 1.66 W, the apparent polarisation at $M = 0$ covers a range between 0.108 and 0.169 in different experimental runs at fixed pressure ($p_3 = 2.45$ mbar, see figure 6.25). For probe C_8 and pump C_9 in the same conditions, M^a-values between 0.052 and 0.084 are observed.
The corresponding values from the static experiments with respect to polarisation, remaining at $M = 0$ during the complete frequency sweep of the probe laser (right graph of figure 6.19), fall in the observed range at $M = 0$ in dynamic experiments, where the probe laser frequency is fixed throughout the measurement, but M increases dynamically (no magnets on the cell).

Up to this point, the discussion of the variation of apparent polarisation with atomic velocity projection was based on measurements at a single value of incident pump laser power ($W_{\text{inc}} = 1.66$ W). In the next figure 6.20, probe frequency sweeps at $M = 0$ covering C_8 and C_9 are presented for *different* values of incident power of the broadband pump laser. Left and rights parts exhibit results with the pump laser tuned to the C_8- and the C_9-transition respectively.
The same qualitative behaviour is observed at all values of incident pump laser

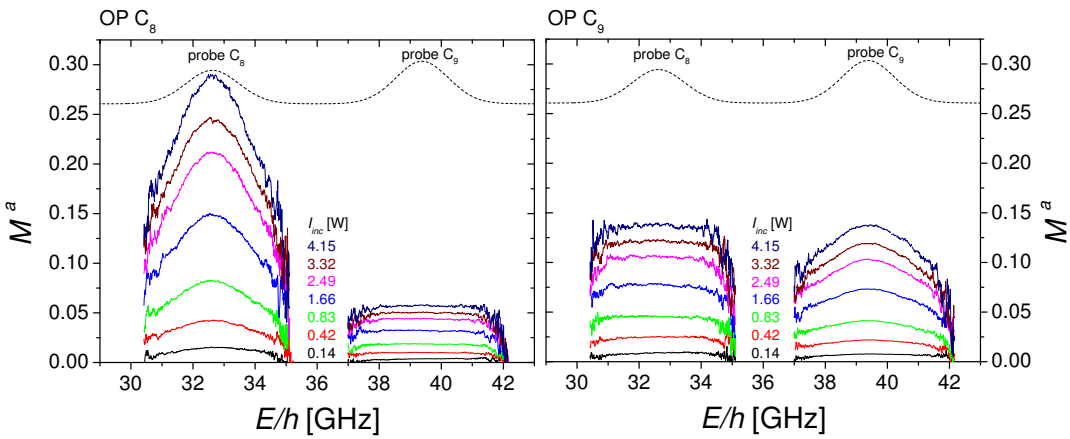

Figure 6.20: Apparent polarisation at $M = 0$ as function of probe detuning in $p_3 = 2.45$ mbar and $B = 1$ mT, for various W_{inc} from 0.14 W up to 4.15 W (from bottom to top, see legend) in $B = 1$ mT. Left: pump transition: C_8, right: pump transition: C_9. Dashed lines are recorded σ^- probe absorption signals at $M = 0$ and indicate the line-positions and -widths of probe C_8- and C_9-resonances.

power in figure 6.20: when probing the same transition as pumped, a strong dependence of apparent polarisation from probe detuning is observed, indicating large velocity-dependent changes in M^a when the probe scans the pumped transition. When different transitions are probed and pumped, the apparent polarisation is approximately constant over the whole width of the probe transition, i.e. independent

from probe detuning.
For a discussion of the quantitative behaviour of apparent polarisation values as function of W_{inc} on different pump transitions, the observed M^a-values in the centre of the probe resonances of figure 6.20 are compiled in table 6.2.
It shows that for each chosen pump-/probe-combination, the quantitative level

Table 6.2: Apparent polarisation values at $M = 0$ in $p_3 = 2.45$ mbar and $B = 1$ mT for different values of incident pump laser powers for different combinations of pump- and probe-transitions in resonance (from figure 6.20)

W_{inc}[W]	pump C_8		pump C_9	
	probe C_8	probe C_9	probe C_8	probe C_9
0.14	0.015	0.004	0.009	0.008
0.42	0.043	0.010	0.025	0.022
0.83	0.083	0.019	0.045	0.041
1.66	0.149	0.032	0.078	0.073
2.49	0.211	0.044	0.106	0.103
3.32	0.245	0.051	0.122	0.119
4.15	0.289	0.057	0.138	0.137

of apparent polarisation increases with incident pump laser power (M^a is roughly proportional to W_{inc}) until optical saturation of the 2^3S-2^3P_0 transition occurs (typically above 1W/cm^2).
The highest apparent polarisation values are observed when pump and probe are both on the C_8-transition, the combination pump on C_8 and probe on C_9 yields the lowest values of M^a. When the C_9-line is used for pumping, the pump-induced apparent polarisation values are about twice as large as these minimum values and similar for the two probe lines.
At 1.66 W in resonance of probe C_8, M^a-values measured in these probe frequency sweeps fall in the observed range at $M = 0$ in dynamic experiments (indicated ranges in figure 6.19 and mentioned on page 200), for both pump transitions C_8 and C_9.

To provide further insight into correlations introduced by OP between velocity and populations, figure 6.21 presents results of velocity-selective OP experiments in which the probe laser frequency is also swept over a range of 12 GHz, comprising the C_8 and C_9 resonances, but - in contrast to all other results of this section - using a *single*-frequency laser here as OP source on the C_8-transition, maintaining the system at null nuclear polarisation as well. On the first pass through the cell towards the back-reflecting mirror, atoms of the velocity class $+v_z$ are pumped by the single-frequency pump laser, and on the return pass, atoms of the velocity

class $-v_z$ are pumped (or vice versa depending on the sign of the detuning). Atoms that are not in one of these two velocity classes cannot be addressed at all by the single-frequency pump laser.

In the left half of the frequency range represented in figure 6.21, on top of a broad

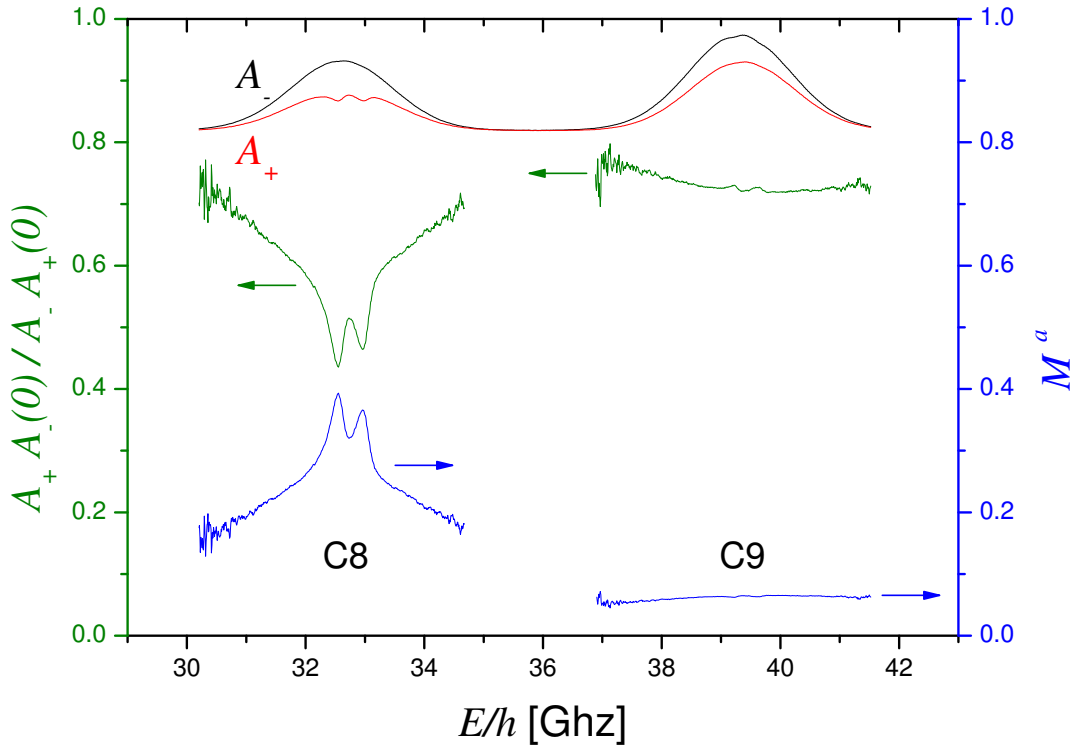

Figure 6.21: Apparent polarisation values at $M = 0$ (enforced by a strong magnet piece near the cell), $B = 1$ mT and $p_3 = 0.63$ mbar for single-frequency OP applied on the C_8-transition (slightly detuned from resonance), $W_{\text{inc}} = 1.72$ W as function of probe frequency. Represented signals from top to bottom: black: A_- (σ^- probe absorption signal); red: A_+ (σ^+ probe absorption signal); green: reduced ratio of absorption signals (corresponding axis of ordinates on the left); blue: apparent polarisation (corresponding y-axis on the right) inferred from this reduced ratio using spin-temperature formulas (see section 4.2).

pedestal (from velocity changing collisions), a strong velocity-selective effect is observed when the probe scans the pumped transition C_8. The *two* peaks in apparent polarisation (corresponding to two dips in the reduced ratio of absorption signals) arise from the fact that both pump and probe are back-reflected in the cell.

The right half of the frequency range (where the probe scans over C_9) shows non-zero apparent polarisation resulting from partial transfer by ME collisions. The fact that this non-zero apparent polarisation is very uniform hints at full velocity redistribution

by these collisions. Two small dips in apparent polarisation (corresponding to two small peaks in the reduced ratio of absorption signals) are observable. They can be attributed to significant OP light-induced populations created in 2^3P ($b_j \neq 0$).
In conclusion, the apparent polarisation (probe C_8 and C_9) reflects the velocity-dependent skewing of populations induced by the OP light: 'overpolarisation' in 2^3S and significant populations created in 2^3P (illustrated in figure 4.18).
The width of the velocity-selective peaks is broader at higher laser intensity due to radiative line broadening (see section 2.10.1).

The above presented result using a single-frequency laser source[2] (DFB diode) constitutes a 'by-product' of a detailed study of saturation of atomic absorption as a function of laser intensity performed for different types of modulation schemes applied on the current of the DFB diode. Thus, the suitability of this laser source with *variable* linewidth for OP of metastable ^{3}He could be tested and characterised using measurement protocols developed and validated in [Tas04] to investigate properties of a broadband ytterbium-doped tunable fibre laser.
Various fast frequency modulation schemes applied to single-mode lasers have been proposed and evaluated in [Elb90, Tre92, Che97, Mue01, Gen03] and [Adh06].
Besides the application of such spectrally shaped laser sources for OP of metastable ^{3}He, they are also used e.g. for transverse laser cooling of a metastable helium beam [Ras99].
The outcome of our study - including performances of a non-periodic modulation scheme based on the use of broadband white noise compared to sine wave modulation and to theoretical expectations - exceeds the scope of the present work and is reported in [Bat12].

6.2.2 Computed M^a at $M = 0$ with probe laser in resonance as function of pump laser power

In the following, we present computations at zero nuclear polarisation ($M = 0$) as well, but at fixed probe frequencies tuned to the C_8 and C_9 transitions as a function of incident pump laser power. All results presented in the rest of this section are obtained using the standard broadband pump laser source (characterised in section 3.2).
As described in detail in section 2.5.2, for simplification, the model for MEOP-kinetics distinguishes a 'strongly pumped velocity class' around the centre of the atomic transition, and a 'weakly pumped velocity class' situated in the wings of the Gaussian spectral distribution of pump laser.
In figure 6.22, the computed influence of the pump laser on 2^3S- and 2^3P-populations

[2]Performances of single-frequency OP, as for example steady state polarisation values, are com-

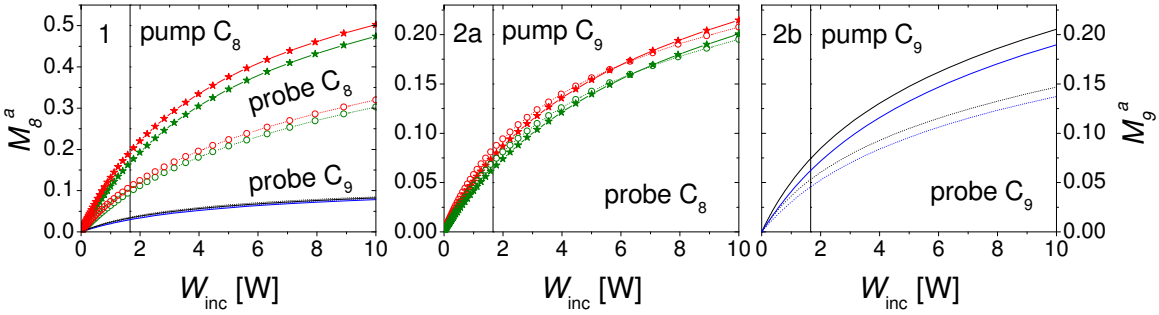

Figure 6.22: Computations of apparent polarisation at $M = 0$ in $p_3 = 2.45$ mbar and $B = 1$ mT as function of incident pump laser power, in 'strongly pumped velocity class' (solid lines + filled stars for probe C_8) and in 'weakly pumped velocity class' (dotted lines + open circles for probe C_8). Graph 1: pump C_8, probe C_8 (lines + symbols) and probe C_9 (lines only). Graph 2a: pump C_9, probe C_8 (lines + symbols), graph 2b: pump C_9, probe C_9 (lines only). Note the different vertical scales of graph 1 and graphs 2a/2b. In all graphs, computations for two typical discharges are represented: weak discharge: $n_{\mathrm{m}} = 1.75 \times 10^{16}$ atoms/m^3, $\alpha = 1.45$ (yields higher M^a, red lines for probe C_8, black lines for probe C_9) and stronger discharge: $n_{\mathrm{m}} = 4.2 \times 10^{16}$ atoms/m^3, $\alpha = 1.2$ (yields lower M^a, green lines for probe C_8, blue lines for probe C_9). Vertical lines in all 3 parts mark a value of $W_{\mathrm{inc}} = 1.66$ W.

at $p_3 = 2.45$ mbar using different pump transitions (C_8: graph on the left, C_9: graphs in centre and on the right) at $M = 0$ is presented as function of incident laser power. More precisely, the apparent polarisation inferred from computed probe absorption signals on C_8 or C_9 is plotted both for the 'strongly pumped velocity class' and the 'weakly pumped velocity class' and for both pump transitions. The width of the 'strongly pumped velocity class' is chosen to be of the same width as the broadband pump laser: $\Delta = L = 1.02$ GHz (the robustness of this choice is discussed in detail in subsection 2.10.2).

When the pump addresses the same 2^3S-sublevels that are probed, the overall influence is higher, and quantitatively different on each velocity class, as expected due to the Gaussian spectral distribution of the pump laser. When different sublevels in 2^3S are pumped and probed, the overall influence on measured apparent polarisation values is smaller and almost equivalent in both considered velocity classes by the OP model.

Concerning a quantitative comparison between computations of the model for MEOP kinetics and measured apparent polarisation values by the probe laser in resonance, the following aspect has to be taken into account when the same 2^3S sublevels are pumped and probed: Only the fraction Σ^* of the total incident pump laser power

parable to standard broadband OP in otherwise identical conditions, and therefore not shown here.

acts on the 'strongly pumped velocity class', leading to a computed OP rate γ^* in this considered velocity class, that is smaller than the OP rate $\gamma(\nu_0)$ in the centre of the transition where the probe laser monitors polarisation. Therefore, the computed apparent polarisation value in the 'strongly pumped class' constitutes a mean value across the whole width of this 'artificial' velocity class, that is of course smaller than the apparent polarisation measured by a probe laser centred in resonance of the transition where in reality, the whole incident power of the pump laser takes effect. Using equations from appendix B and [Nac12], the ratio of $\gamma(\nu_0)$ / γ^* is given by:

$$\frac{\gamma(\nu_0)}{\gamma^*} = \frac{D}{L}\,\frac{n_{\mathrm{m}}^*}{n_{\mathrm{m}}}\,\frac{1}{\Sigma^*} \tag{6.7}$$

An estimation assuming the same widths for pump laser and strongly pumped class (n_{m}^* / n_{m} = 0.77456 [Nac12] and Σ^* = 0.71179 [Nac12] for $\Delta = L = 1.02$ GHz; $D = 1.19$ GHz) yields an OP rate at resonance $\gamma(\nu_0)$ of approximately 1.27 γ^*.

For a more quantitative comparison of experimental apparent polarisation values (represented in figures 6.19 and 6.20) with computations, two different typical discharges, weak and strong, are taken into account for the computations in figure 6.22 in order show possible ranges of M^a at different values of n_{m}.
In the following, the four possible pump and probe combinations represented in figure 6.22 are discussed in more detail, all quantitative comparisons refer to $W_{\mathrm{inc}} = 1.66$ W.
First, for pump and probe, both on C_8 (cf. graph 1), M^a of the 'strongly pumped velocity class' (denoted by M^{a*}) remains about 35-40 % above M^a of the 'weakly pumped velocity class' (denoted by $M^{a'}$) for all values of incident pump laser power. The two examples of experiments investigating apparent polarisation at $M = 0$ (figures 6.19 and 6.20) yield M^a-values of 0.115 and 0.149 measured by probe C_8 in resonance, computations yield M^{a*} between 0.161 and 0.185, depending on high or low n_{m}, and $M^{a'}$ between 0.094 and 0.106. When the same sublevels are probed and pumped, we expect to find a higher experimental value than M^{a*}. In the considered case, this expectation is not confirmed, which means that the experimental n_{m} was probably higher than assumed in the computations and/or the radial distribution of metastable atoms differed.
Second, for pump C_8 and probe C_9 (cf. graph 1), $M^{a'}$ remains approximately 3-7 % above M^{a*} over the whole range of incident pump laser power. Computations predict apparent polarisation values between 0.028 (M^{a*} using high n_{m} in the MEOP-model) and 0.035 ($M^{a'}$ using low n_{m}) in this case, the two experimental values are 0.024 and 0.032 (see figures 6.19 and 6.20).
Third, for pump C_9 and probe C_8 (cf. graph 2a), $M^{a'}$ is up to 10 % higher than M^{a*} at lower values of incident pump laser power. Between 6.0 and 6.5 W, depending on n_{m}, the behaviour is reversed and M^{a*} is above $M^{a'}$ at higher W_{inc}. Computed values

of apparent polarisation at $W_{\text{inc}} = 1.66$ W vary between $M^{a*}(\text{high } n_{\text{m}}) = 0.060$ and $M^{a'}(\text{low } n_{\text{m}}) = 0.079$. The two M^a-values of the presented probe frequency sweeps (see figures 6.19 and 6.20) amount to 0.057 and 0.078 in resonance.
Fourth, for pump C_9 and probe C_9 (cf. graph 2b), M^{a*} is roughly 30 % higher than $M^{a'}$ over the investigated range up to $W_{\text{inc}} = 10$ W. Computations estimate M^a in the 'weakly pumped velocity class' between 0.043 and 0.050, for high or low n_{m}, respectively, and between 0.059 and 0.071 in the 'strongly pumped velocity class'. As expected (and explained on page 204), the experimental values of apparent polarisation with probe in resonance and at $W_{\text{inc}} = 1.66$ W of incident pump laser power, 0.054 and 0.073 (see figures 6.19 and 6.20), are above this computed range.
Furthermore, for pump C_9, the computations for the 'strongly pumped velocity class' predict that up to W_{inc} between 1 and 2 W, M^{a*} measured by probe C_8 is identical with the value measured by probe C_9. This prediction is confirmed experimentally within errors in both selected examples.
To conclude this quantitative comparison between experimental examples and computations for typical weak and strong discharges at $p_3 = 2.45$ mbar, it should be emphasised that given the experimental variability (e.g. comparison of figures 6.19 and 6.20 with probe in resonance and at $W_{\text{inc}} = 1.66$ W or using experimental data at $M = 0$ of figure 6.25), the computations agree reasonably well with experimental results and are able to fully explain the observed behaviour.

6.2.3 Example of apparent polarisation as function of actual polarisation

In a typical dedicated experiment to account for perturbations of the 2^3S- and 2^3P-populations in presence of the pump laser (experimental protocol, see section 5.3), the probe transition is fixed in resonance, and the apparent polarisation M^a is monitored while actual polarisation M builds up dynamically. In figure 6.23, M^a as function of M is presented at fixed probe transition C_8 and fixed incident pump laser power of 1.66 W, either on the C_8 or the C_9 transition. Computed apparent polarisation values are also shown for both broad velocity classes (probe C_8, pump C_8 and C_9).
From a qualitative perspective, the experiments show the expected behaviour, for instance that the influence of perturbations in 2^3S and 2^3P due to the intense pump laser is higher when probe and pump address the same sublevels (pump C_8, filled squares) than when different sublevels are probed and pumped (pump C_9, filled circles). The model for MEOP kinetics provides similar results.
However, a quantitative agreement between experiment and computations is not obtained when pump and probe are tuned to the same transition. As already explained on page 204, the model with its two velocity classes computes a mean value of apparent polarisation in the 'strongly pumped velocity class' that is lower than the

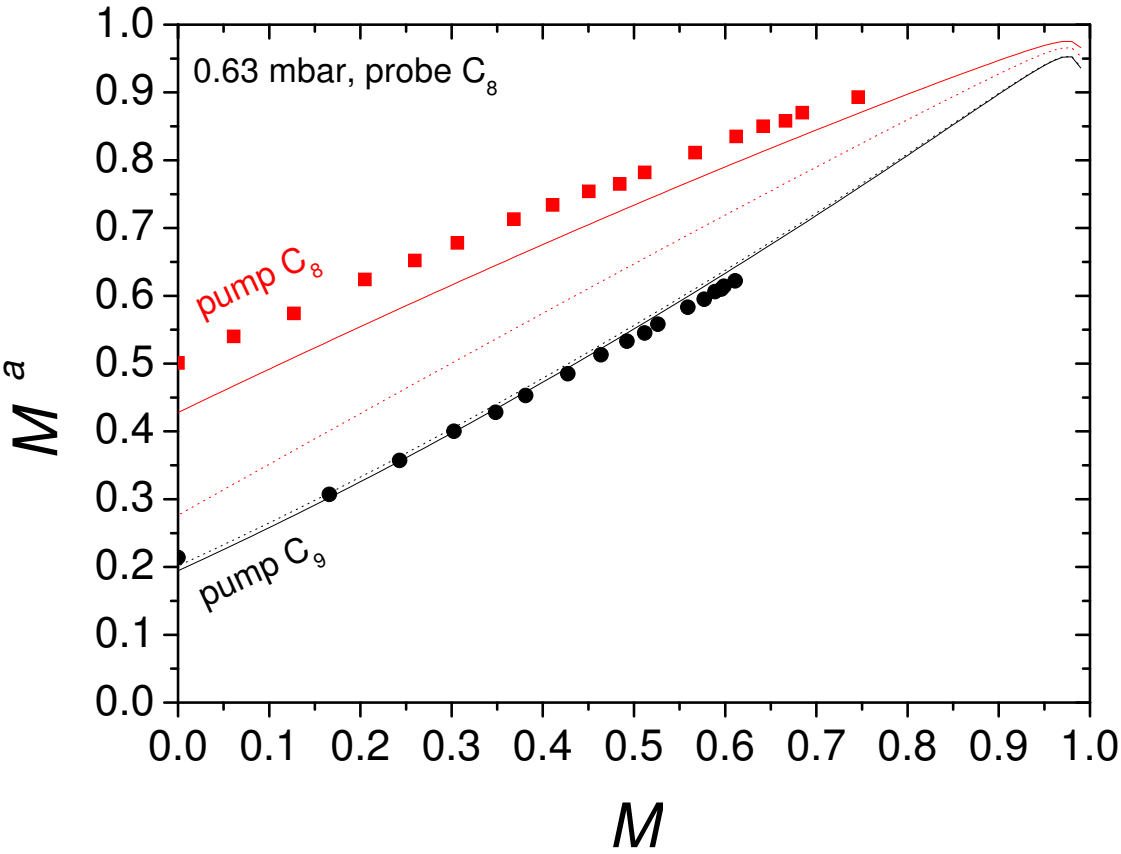

Figure 6.23: Apparent polarisation M^a as function of actual polarisation during a dedicated experiment (symbols) to account for perturbations of 2^3S- and 2^3P-populations and corresponding computations (lines) in $B = 1$ mT. Parameters: $p_3 = 0.63$ mbar, $n_{\mathrm{m}} = 1.08 \times 10^{16}$ atoms/m^3, $\alpha = 2.1$, fixed probe on C_8, pump on C_8 (filled squares) or pump on C_9 (filled circles) at $W_{\mathrm{inc}} = 1.66$ W. Computations are given for the 'strongly pumped velocity class' (solid lines) and the 'weakly pumped velocity class' (dotted lines).

actually measured one by the centred probe laser in resonance. This aspect remains valid as function of polarisation as well. Figure 6.23 shows that the computed values of apparent polarisation in both velocity classes (in principle corresponding to two different values of probe detuning) are below the experimental values for pump C_8: In the 'strongly pumped class', computed M^{a*}-values for different M are approximately 5-15 % below the experimental values.
In the case of different pump and probe transitions, represented here by pump C_9 and probe C_8, the differences between computed results in both velocity classes are much smaller (as expected), and the agreement between experiment and computations is satisfactory.

In the following, a compilation of selected experimental results at fixed pump beam diameter (waist $2a = 1.6$ cm) is presented in order to discuss different aspects that are relevant for the measurement of nuclear polarisation by probe absorption techniques.

6.2.4 Reproducibility of apparent polarisation in fixed OP conditions

In this subsection, the experimental reproducibility of apparent polarisation values measured at fixed OP conditions in $B = 1$ mT is investigated for two different pressure values, $p_3 = 0.63$ mbar and 2.45 mbar: Figures 6.24 and 6.25 represent data for both probe and pump on C_8 at $W_{\mathrm{inc}} = 1.66$ W. The only parameter that is not constant for all shown experiments is the metastable density. Computations for the 'strongly pumped class' at higher and lower n_{m} are added for both pressures.
In figure 6.24 illustrating the variability between different experiments at 0.63 mbar, two groups of experiments that differ up to approximately 20 % are observed: one featuring higher apparent polarisation values at given M corresponding to weak discharges (open triangles) and a second one with lower apparent polarisation values at given M corresponding to stronger discharges (filled triangles). The metastable density in the latter experiments is about a factor of three higher than in the first group. All shown data have been recorded during the same experimental run over a period of approximately four months.
The computations taking into account all relevant parameters for both, weak and strong discharges, differ about 5-15 % from the experimental data due to the reason described on page 204, as the same 2^3S sublevels are pumped and probed. The qualitative evolution of apparent polarisation values as function of actual polarisation is well described by the model for MEOP-kinetics and therefore well understood.

Concerning the variability of experimental data at 2.45 mbar (figure 6.25),

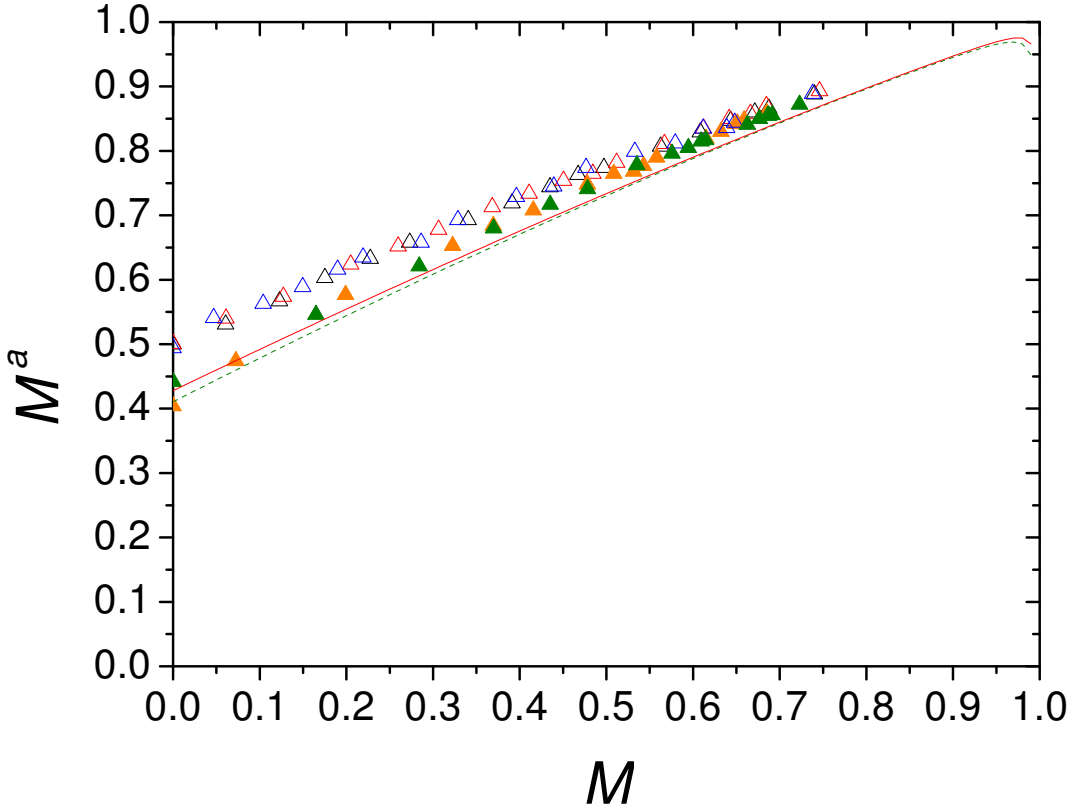

Figure 6.24: Reproducibility of apparent polarisation values in fixed OP-conditions at $p_3 = 0.63$ mbar, $B = 1$ mT: Pump and probe transitions: both C_8, $W_{\mathrm{inc}} = 1.66$ W. Open triangles and solid line: experimental data and corresponding computation (for 'strongly pumped velocity class') in weak discharges, $n_{\mathrm{m}}^{\mathrm{S}}(M = 0)$: between 8.6×10^{15} and 1.1×10^{16} atoms/m^3, $\alpha = 2.1$. Filled triangles and dashed line: experimental data and corresponding computation (for 'strongly pumped velocity class') in strong discharges, $n_{\mathrm{m}}^{\mathrm{S}}(M = 0)$: between 3.3 and 3.6×10^{16} atoms/m^3, $\alpha = 2.1$. (As observed in figure 6.12, the radial distribution of metastable atoms is largely independent of n_{m} at this pressure).

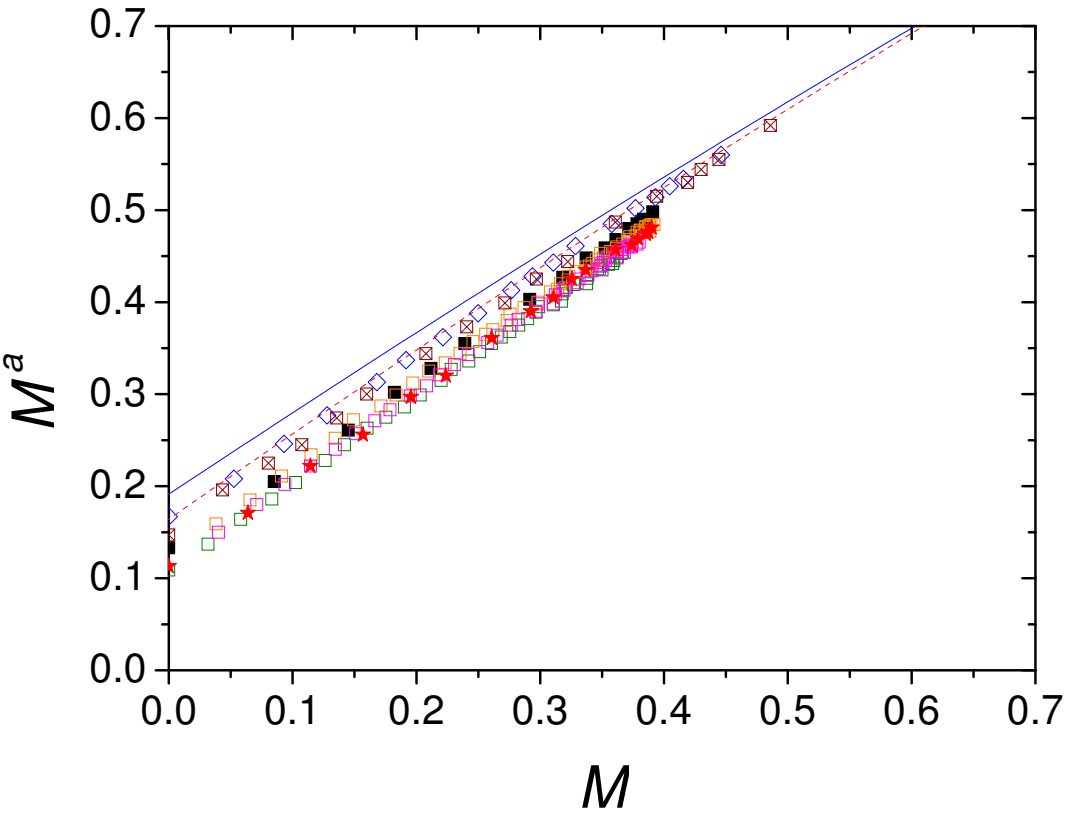

Figure 6.25: Reproducibility of apparent polarisation values in fixed OP-conditions at $p_3 = 2.45$ mbar, $B = 1$ mT: Pump and probe transitions: both C_8, $W_{\mathrm{inc}} = 1.66$ W. Open diamonds and solid line: experimental data and corresponding computation in very weak discharge, $n_{\mathrm{m}}^{\mathrm{S}}(M = 0)$: 1.75×10^{16} atoms/m^3, $\alpha = 1.45$. Open squares: experimental data in weak discharges (crossed: see text), $n_{\mathrm{m}}^{\mathrm{S}}(M = 0)$: between 2.55 and 2.6×10^{16} atoms/m^3. Filled squares: experimental data in intermediate discharge, $n_{\mathrm{m}}^{\mathrm{S}}(M = 0)$: 3.2×10^{16} atoms/m^3. Filled stars and dashed line: experimental data and corresponding computation in strong discharge, $n_{\mathrm{m}}^{\mathrm{S}}(M = 0)$: 4.5×10^{16} atoms/m^3, $\alpha = 1.2$.

a relative discrepancy of up to 40 % is observed between measured M^a-values at given M of different experiments, partially stemming from different experimental runs. The general tendency from 0.63 mbar experiments (figure 6.24) is confirmed to some extent: the highest values of apparent polarisation are obtained at very weak discharge (open diamonds).
The lowest values of M^a however, are obtained in a moderate discharge (open squares) with approximately 30 % higher metastable density than the very weak discharge (open diamonds). Both sets of data have been obtained during the same experimental run with about 2 months difference. Almost equivalent low values of apparent polarisation are also measured for the strongest discharge (filled stars). These data have been recorded about 2 years after the above mentioned ones in otherwise identical circumstances.
The presented data yield a good qualitative reproducibility, quantitatively limited however: data represented by 3 different colours of open squares are 3 direct, consecutive repetitions of the same experiment, whereas crossed open squares constitute data of approximately the same discharge in terms of metastable densities and decay rates, but recorded about 2 years later than the 3 consecutive experiments under identical conditions.
When comparing experimental M^a-values in figure 6.25 obtained in a discharge of intermediate rf excitation level (filled squares) with corresponding values of a weak discharge (open squares; both datasets recorded during the same experimental run with 4 days difference), apparent polarisation values of the stronger discharge are found above M^a-values of the weaker discharge, although observations at lower pressure (0.63 mbar) suggest the reversed case. In order to clarify this observation, the correlation between metastable densities and measured pump transmission coefficients at $M = 0$ was examined. The stronger the discharge, the smaller the observed $T_p(0)$-values as expected for almost all data represented in figure 6.25, except for the dataset of filled squares. These unusual pump transmission coefficients might be a reason for a different slope of apparent polarisation values as function of M and higher M^a-values than expected in this specific data set.
The computations of apparent polarisation values at 2.45 mbar shown in figure 6.25 exceed experimental values by approximately the same amount as the observed range of experimental reproducibility (up to about 40 % of relative discrepancy, 25 % at fixed rf excitation level). This quantitative behaviour is observed in a consistent way at this pressure value throughout this work (see also figure 6.27 for example). However, the qualitative behaviour of pump induced perturbations of 2^3S- and 2^3P-populations is well understood in the complete range of investigated pressures.

6.2.5 Examples of M^a measured by probe on the C_9-transition

In all examples of dynamic measurements of apparent polarisation as function of actual polarisation presented up to now in this section, the chosen probe transition was C_8, either with pump on C_8 as well, or pump on C_9 (see figure 6.23). Here, measurements and corresponding computations at *fixed* pumping transition C_8 and probe either in C_8- or C_9-resonances at two different pressures, 0.63 and 1.19 mbar, are presented in figure 6.26.

Comparisons between experimental data and computations are best discussed using

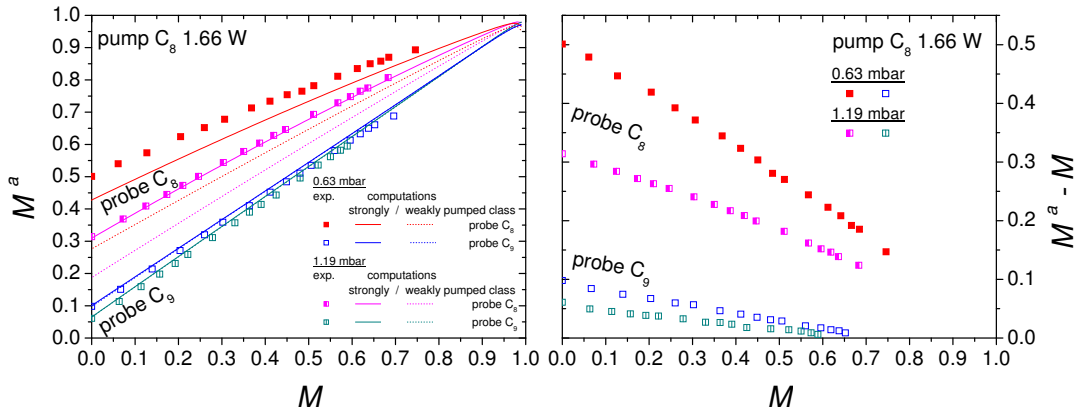

Figure 6.26: Left: Apparent polarisation values for different probe transitions in *fixed* pumping conditions: $W_{\text{inc}} = 1.66$ W on C_8, $B = 1$ mT. Probe C_9: open squares and open squares with vertical lines: experimental data in $p_3 = 0.63$ mbar and 1.19 mbar, respectively, with corresponding computations: solid line = 'strongly pumped velocity class', dotted line = 'weakly pumped velocity class'. Probe C_8: filled squares and half-filled squares: experimental data in $p_3 = 0.63$ mbar and 1.19 mbar, respectively, and corresponding computations of two different velocity classes, same line convention as for probe C_9. Further parameters used for computations: $p_3 = 0.63$ mbar: $n_{\text{m}}^{\text{S}}(M = 0) = 1.1 \times 10^{16}$ atoms/m^3, $\alpha = 2.1$; $p_3 = 1.19$ mbar: $n_{\text{m}}^{\text{S}}(M = 0) = 1.5 \times 10^{16}$ atoms/m^3, $\alpha = 2$. Right: Difference of apparent and actual polarisation as function of M (same experimental data as in graph on the left); from top to bottom (pump C_8, 1.66 W in all cases): filled squares: 0.63 mbar, probe C_8; half-filled squares: 1.19 mbar, probe C_8; open squares: 0.63 mbar, probe C_9; open squares with vertical line: 1.19 mbar, probe C_9.

the left graph of figure 6.26: When different 2^3S sublevels are pumped and probed (open squares with/without vertical lines), computed M^a-values in both velocity classes considered by the MEOP-model are almost identical (two lower solid lines are almost superimposed with the corresponding dotted lines), and agree reasonably

well with experimental M^a-values at both pressures: At $p_3 = 0.63$ or 1.19 mbar, discrepancies up to 5 % or 10 %, respectively, are observed.
When the same 2^3S sublevels are pumped and probed (filled and half-filled squares), computations of apparent polarisation values in both considered velocity-classes in the MEOP-model differ as expected: M^a of the weakly pumped velocity class is smaller than M^a of the strongly pumped velocity class at given actual polarisation value M. Furthermore, experimental M^a-values are above the computed ones in the strongly pumped class. Reasons for this observation are discussed on page 204. Quantitatively, experimental M^a-values in low pressure (0.63 mbar) are approximately 17 % above computed ones in the strongly pumped velocity class close to $M = 0$. This discrepancy decreases down to 3 % at around $M = 0.75$. In higher pressure (1.19 mbar), computed M^a-values of the strongly pumped velocity class are also above the corresponding ones of the weakly pumped velocity class as expected, and the quantitative agreement between experiment and computations in the strongly pumped class is very good in these conditions: The relative discrepancies range between 2 % at small M and 1 % at higher actual polarisation of order 0.7.

Dependencies of experimental apparent polarisation values on pressure and the choice of probe-transitions at given pump-transition are best discussed using the right graph of figure 6.26, where differences of apparent and actual polarisations $M^a - M$ are represented as function of M. For each choice of a probe line, the pump-induced differences between M^a and M systematically decrease with pressure and polarisation, and they increase by a factor of five when the C_8 line is used instead of the C_9 line for the probe. When the C_9 line is used for pumping (see figure 6.23 for 0.63 mbar), the pump-induced differences for each pressure are similar for the two probe lines (see probe resonances in figures 6.19 and 6.20 (right graph) for $p_3 = 2.45$ mbar) and about twice as large as those represented by the open symbols (= probe C_9, pump C_8) in figure 6.26 for $p_3 = 0.63$ and 1.19 mbar.
The above compiled observations concerning pump induced perturbations of populations and thus on measured apparent polarisation values as well as concerning comparisons between experiments and computations are similar to those derived from figure 6.23, where the *probe*-transition was fixed using two different pump-transitions.

Comparisons of measured pump-induced differences $M^a - M$ in the longitudinal probe scheme used throughout this work and a possible transverse probe configuration show that the transverse probe scheme is less prone to the impact of pump light than the longitudinal probe scheme (5 to 10 times less [Tal11], depending on the chosen OP transition). This is due to partial compensation of the effects on the transverse absorption signals of the pump-driven depopulation and overpopulation for pairs of 2^3S sublevels with opposite angular momenta [Tal11]. However, the longitudinal probe scheme has other advantages that led us to choose this configuration: It has a linear response at small M for all lines (C_8, C_9 and D_0), with a higher sensitivity

for the C_9 and D_0 lines. This high sensitivity at small M is particularly well suited for investigations of polarisation build-up kinetics. At high M, the longitudinal probe scheme retains a linear sensitivity on the C_8 line (reduced for C_9 and D_0) [Tal11]. Furthermore, in our long cells, L_{path} is longer in the longitudinal probe configuration compared to the transverse one, leading to higher SNR.

6.2.6 Perturbations of 2^3S and 2^3P populations in higher magnetic field: $B = 30$ mT versus 1 mT

Another aspect to be considered in the context of pump influences on probed populations is the question whether there is a correlation between magnetic field strength and overpolarisation in 2^3S.
Figure 6.27 presents experimental and computed apparent polarisation values in $p_3 = 2.45$ mbar as function of actual polarisation for probe C_8 and both pump transitions in $B = 1$ and 30 mT.
All experimental data shown in figure 6.27 were recorded within five consecutive days to assure stable conditions. From a global point of view, apparent polarisation values for the pump laser on the C_8 transition (with fixed probe on C_8 as well) are above M^a-values with pump on C_9 as expected.
Besides the discharges for which we provide experimental data *and* computations (see legend), experimental data of two additional discharges with the following metastable densities and characteristic decay rates are added in figure 6.27: red symbols: $n_{\text{m}}^{\text{S}}(M = 0) = 2.6 \times 10^{16}$ atoms/m^3, $\Gamma_{\text{D}} = (456\ \text{s})^{-1}$, $B = 1$ mT (filled symbols) only; blue symbols: $n_{\text{m}}^{\text{S}}(M = 0) = 1.57 \times 10^{16}$ atoms/m^3, $\Gamma_{\text{D}} = (2117\ \text{s})^{-1}$, $B = 30$ mT (open symbols) only.
For the pump laser fixed to the C_9-transition (circles), measured data cannot be distinguished by magnetic field neither by discharge strength. Computations confirm that practically no effect of B on apparent polarisation is expected. A good agreement between experiments and computations can be observed: discrepancies are ranging between 2.5 % around $M = 0.55$ and 12 % close to $M = 0$.
For the pump laser fixed to the C_8-transition (squares), computations predict slightly higher M^a-values at 1 mT compared to 30 mT. This prediction is confirmed by data of the corresponding discharge (black symbols). For other investigated discharges, measured results are qualitatively not very different yielding comparable slopes of M^a as function of M.
In conclusion, no correlation between increasing magnetic field and apparent polarisation values can be established. The differences observed between 1 and 30 mT are of the same order of magnitude as the dispersion of data in reproducibility tests (see figure 6.25).

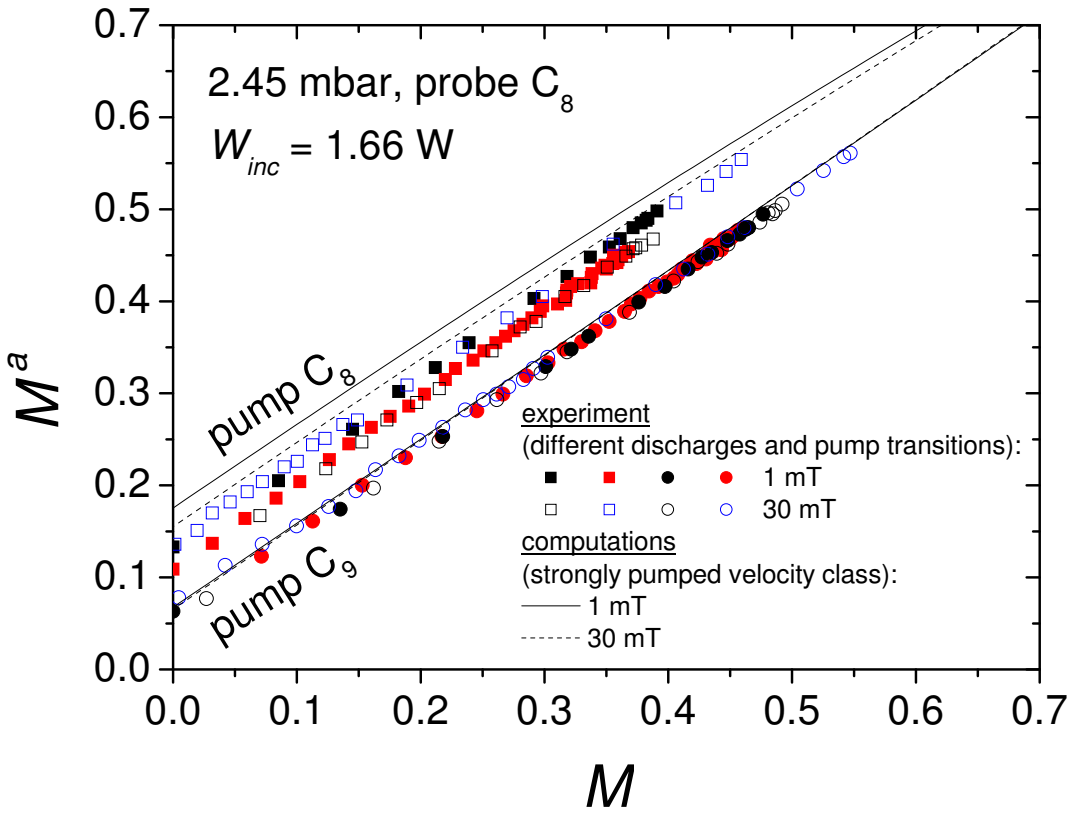

Figure 6.27: Comparison of apparent polarisation values at $B = 1$ mT (filled symbols for experimental data) and 30 mT (open symbols for experimental data) in $p_3 = 2.45$ mbar, probe fixed to C_8. Pumping conditions: $W_{\rm inc} = 1.66$ W, either on C_8 (squares) or C_9 (circles). Corresponding computations (strongly pumped velocity class only) with pump C_8 and pump C_9 for one discharge: $B = 1$ mT (solid lines): $n_{\rm m}^{\rm S}(M = 0)$: 3.2×10^{16} atoms/m^3, $\alpha = 1.27$, $\Gamma_{\rm D} = (263\ {\rm s})^{-1}$; $B = 30$ mT (dashed lines): $n_{\rm m}^{\rm S}(M = 0)$: 3.3×10^{16} atoms/m^3, $\alpha = 1.05$, $\Gamma_{\rm D} = (554\ {\rm s})^{-1}$ (experimental data of this discharge are given by black symbols. Red and blue symbols: different discharges: see text).

6.2.7 Scaling of M^a with incident pump laser power and pressure

1. Fixed pressure, variable incident pump laser power

In the following, the magnetic field is fixed to $B = 1$ mT, and dependencies of pump induced perturbations of 2^3S- and 2^3P-populations, manifested in apparent polarisation values M^a, on incident pump laser power and pressure are investigated. The first investigated aspect concerns examples at two fixed pressures, 0.63 and 2.45 mbar, and different values of incident pump laser power.
Figure 6.28 shows apparent polarisation values as function of actual nuclear polarisation for $p_3 = 0.63$ mbar at fixed probe transition C_8 and two pump transitions (C_8 and C_9) for different values of incident pump laser power.
Figure 6.29 represents results of similar measurements for the highest investigated

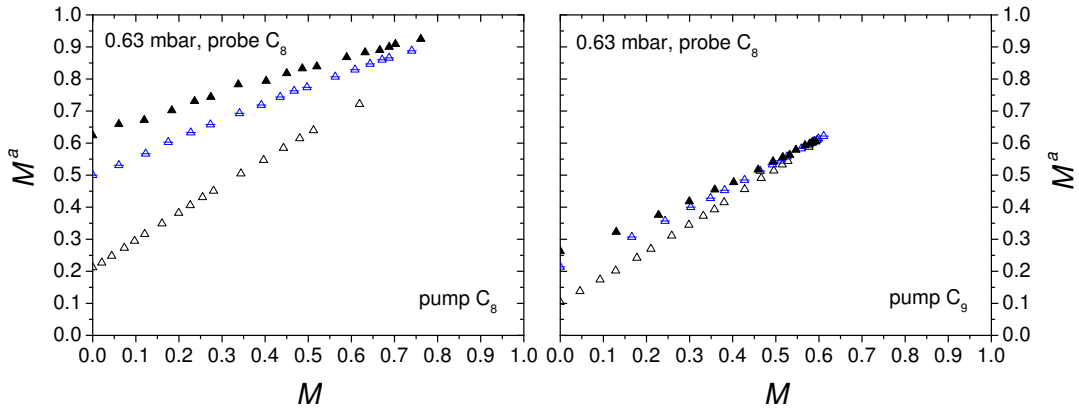

Figure 6.28: Apparent polarisation values for different incident pump laser powers and pump transitions at fixed probe transition C_8 in $p_3 = 0.63$ mbar, $B = 1$ mT. Left: Pump transition: C_8. Right: Pump transition: C_9. Different values of incident pump laser power $W_{\rm inc}$, from bottom to top: 0.42 W (open triangles), 1.66 W (open triangles with horizontal lines), 3.32 W (filled triangles). All data recorded at fixed, weak discharge: $n_{\rm m}^{\rm S}(M = 0) = 1.1 \times 10^{16}$ atoms/m^3, $\Gamma_{\rm D} = (350\,{\rm s})^{-1}$.

pressure of 2.45 mbar.
First, a general remark concerning figures 6.28 and 6.29: At each pressure, all represented data are from one single experimental run at fixed discharge (data recorded within 3 or 5 consecutive days at 0.63 or 2.45 mbar respectively). In all cases where several repeated recordings at the same OP conditions exist, the one yielding the highest M^a-values is always chosen for representation and comparison here.
Values of $\dot{M}(0)$ and pump transmission coefficients $T_p(M = 0)$ have been checked for

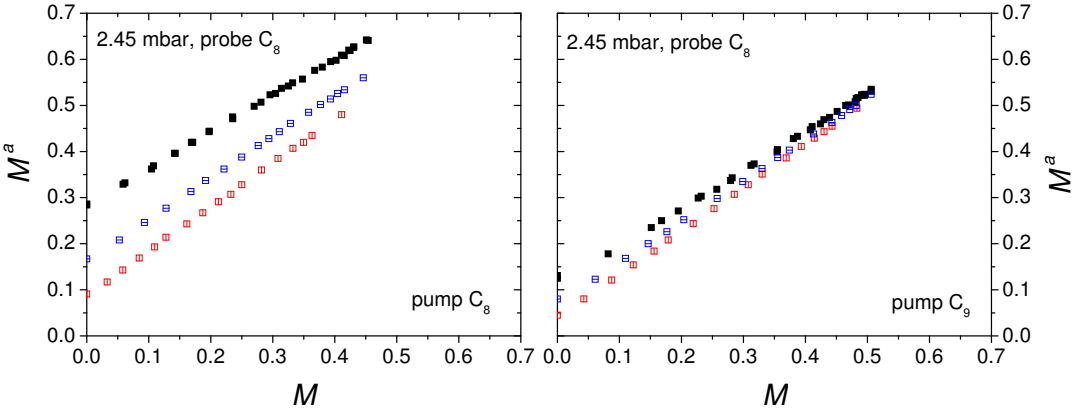

Figure 6.29: Apparent polarisation values for different incident pump laser powers and pump transitions at fixed probe transition C_8 in $p_3 = 2.45$ mbar, $B = 1$ mT. Left: Pump transition: C_8. Right: Pump transition: C_9. Different values of incident pump laser power W_{inc}, from bottom to top: 0.83 W (open squares with vertical line), 1.66 W (open squares with horizontal lines), 3.32 W (filled squares). All data recorded at fixed, weak discharge: $n_{\text{m}}^{\text{S}}(M = 0) = 1.75 \times 10^{16}$ atoms/m^3, $\Gamma_{\text{D}} = (835\,\text{s})^{-1}$. (Note that the y-axis scale here is different than in figure 6.28).

all chosen experiments at different values of incident pump laser power, they do not reveal any unexpected features and roughly scale with W_{inc}.

When considering each pressure individually (a comparison between different pressure-values at fixed W_{inc} is performed in the next paragraph), apparent polarisation at given actual polarisation is higher for pump on C_8 (left parts of figures 6.28 and 6.29) than for pump on C_9 (right parts of indicated figures) as expected, as the chosen probe transition is C_8 in all cases.

At given pump transition and pressure, apparent polarisation is qualitatively increasing with incident pump laser power due to increasing perturbations of 2^3S- and 2^3P-populations.

A non-linear scaling of $M^a(M = 0)$ with W_{inc} is expected given the computations of figure 6.22. Plotting $M^a(M = 0)$ as function of W_{abs} in a similar way as in figure 6.22 using the same parameters (graph not shown here) reveals that for pump C_8 and probe either on C_8 or C_9, apparent polarisation at $M = 0$ scales with absorbed laser power, but also not linearly (which is plausible as M^a varies between 0 and 1 while W_{abs} could reach ∞ apart from technical limitations). In the limit of very small W_{abs}, linear scaling of $M^a(M = 0)$ is observed up to approximately 0.1 W for probe C_8 and 0.15 W for probe C_9.

Using figures 6.28 and 6.29 to qualitatively compare M^a-values at $M = 0$ at the same incident pump laser power in given OP-conditions indicates that the lower the

pressure the higher apparent polarisation. This aspect is investigated in more detail in the next paragraph on scaling of M^a.

2. Fixed incident pump laser power, variable pressure

In order to examine a dependency of apparent polarisation on ^{3}He-pressure, figure 6.30 compiles measured M^a-values as function of actual polarisation for three different values of ^{3}He-pressure: 0.63, 1.19 and 2.45 mbar (2 datasets from figures 6.28 and 6.29 and one additional at 1.19 mbar), all OP conditions being constant: $W_{\text{inc}} = 1.66$ W, pump and probe on the C_8-transition.

Figure 6.30 shows that overpolarisation effects in 2^3S caused by intense OP-light

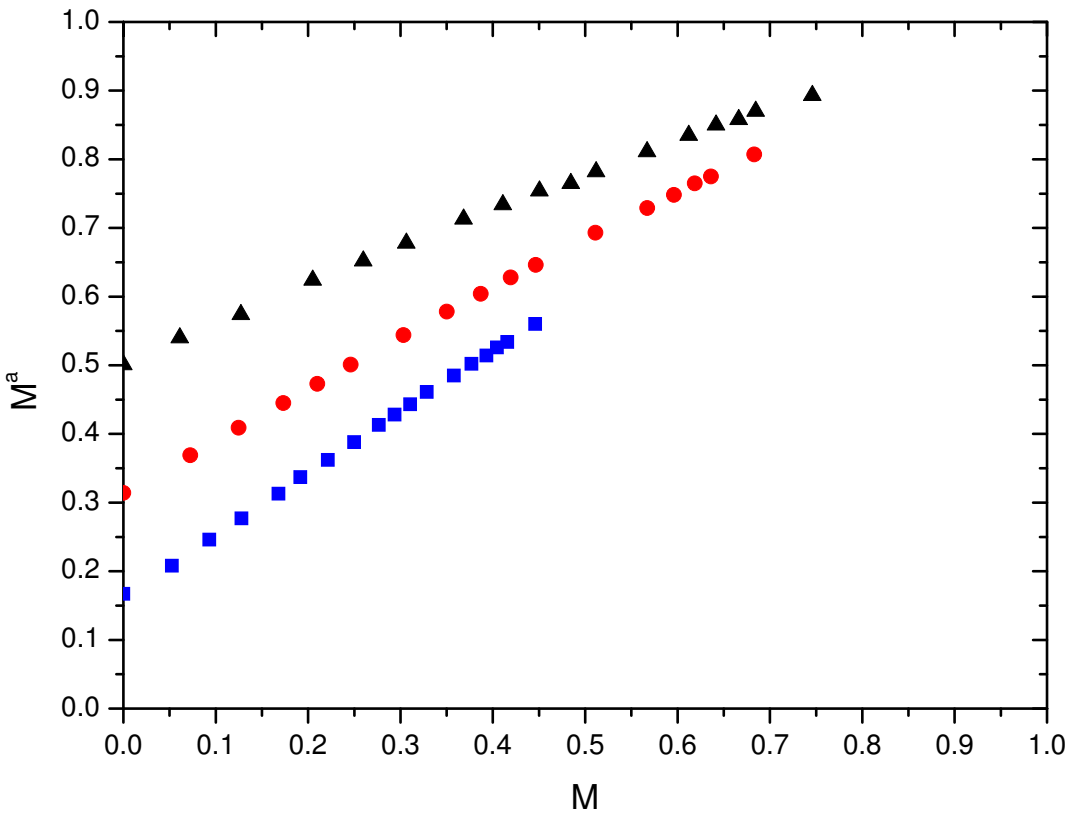

Figure 6.30: Apparent polarisation as function of actual polarisation at fixed OP conditions for three different values of ^{3}He pressure: Filled triangles: $p_3 = 0.63$ mbar, filled circles: $p_3 = 1.19$ mbar, filled squares: $p_3 = 2.45$ mbar. Incident pump laser power: 1.66 W, pump transition: C_8, probe transition: C_8.

decrease with increasing pressure: Low pressure (0.63 mbar) yields the highest values

of apparent polarisation at $M = 0$, high pressure (2.45 mbar) yields the lowest $M^a(0)$-value, and $M^a(0)$ of the intermediate pressure (1.19 mbar) is in-between both limiting cases.
For the same reasons as stated in the previous paragraph on qualitative scaling of M^a with W_{inc}, quantitative ratios of $M^a(0)$-values of different pressure-values at given W_{inc} are not investigated here. The slopes of the M^a versus M-curves in figure 6.30 are different for each displayed dataset due to obvious constraints: $M^{\mathrm{a}}(0) < M^{\mathrm{a}}(M) < 1$, involving smaller slopes in cases where the initial apparent polarisation value $M^{\mathrm{a}}(0)$ is high.

3. Fixed ratio W_{inc}/p_3

In this paragraph on scaling of apparent polarisation with the ratio of incident pump laser power and pressure as the model for MEOP-kinetics suggests, figure 6.31 represents apparent polarisation values as function of actual polarisation at approximately constant reduced power, which is the ratio of W_{inc} divided by pressure, for all recorded data. The maximum relative difference between reduced power values of different cells amounts to 4 %. In general, the higher this ratio, the higher the expected apparent polarisation.
Although reduced power values are similar for all data presented in figure 6.31, it was experimentally difficult to keep the absolute metastable densities constant in all three cells with different pressure-values, which would correspond to ideal conditions to compare resulting apparent polarisation values.
When comparing apparent polarisation values at given actual polarisation for the three weak discharges in figure 6.31 (open triangles at 0.63 mbar, filled circles (1.19 mbar) and filled squares (2.45 mbar)), a perfect superposition of data cannot be observed. At $M = 0$ for example, the relative difference of M^a-values amounts to 25 % between the lowest and highest pressures cells and to 10 % between the cells with $p_3 = 1.19$ and 2.45 mbar.
Absolute values of n_{m} have an influence on experimental apparent polarisation values since absorption depends on n_{m} and thus local laser power ($< W_{\mathrm{inc}}$) is potentially different. This effect can be illustrated by the example of two different discharges at low pressure: At $M = 0$ and exactly constant ratio W_{inc}/p_3 the relative difference between M^a-values of these two datasets equals 40 %, decreasing to a few percent at higher actual polarisation M. This relative discrepancy of apparent polarisation values at $M = 0$ is higher than the difference of approximately 20 % observed between discharges (differing by roughly the same factor in n_{m} as in the present example) in reproducibility tests at 0.63 mbar (cf. figure 6.24).

However, most of the dependency with pressure and power can be reproduced

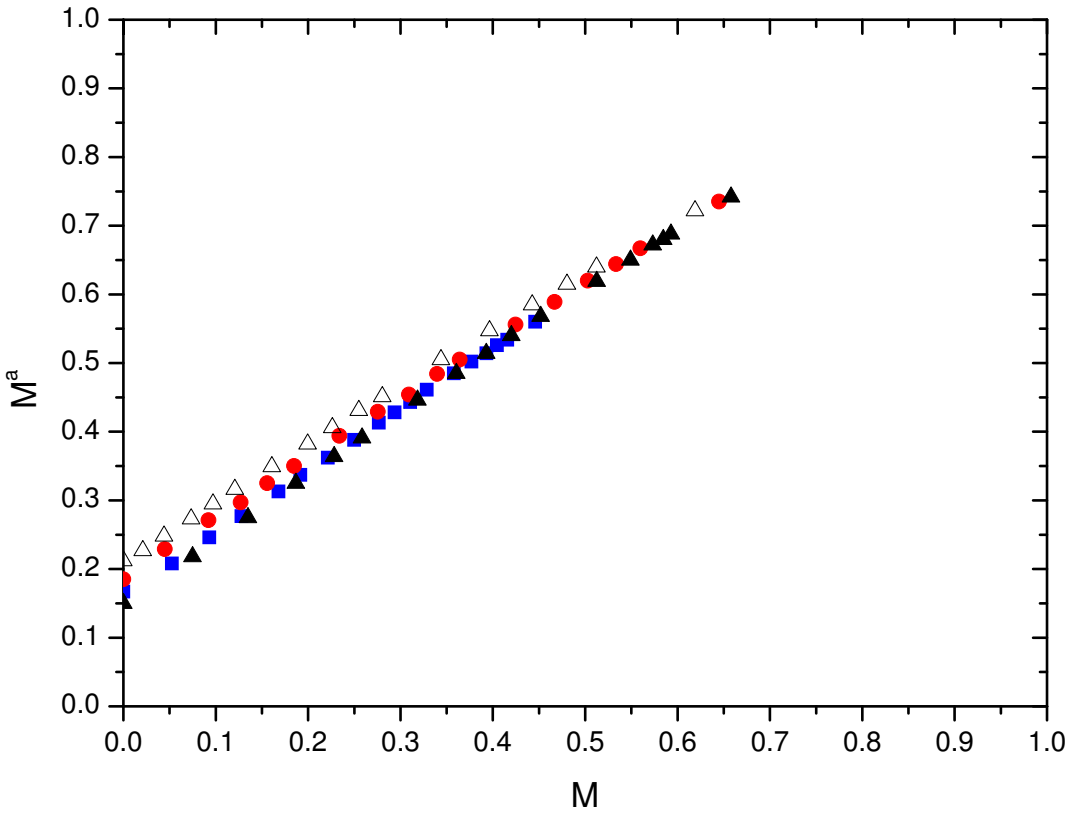

Figure 6.31: Experimental apparent polarisation M^a as function of actual polarisation M in $B = 1$ mT, at approximately constant reduced power (= ratio of $W_{\rm inc}/p_3$). Triangles: $p_3 = 0.63$ mbar, $W_{\rm inc} = 0.42$ W, $W_{\rm inc}/p_3 = 0.67$ W/mbar, $n_{\rm m}^{\rm S}(M = 0)$: 1.1 (open triangles) or 3.3 (filled triangles) $\times 10^{16}$ atoms/m^3; filled circles: $p_3 = 1.19$ mbar, $W_{\rm inc} = 0.83$ W, $W_{\rm inc}/p_3 = 0.70$ W/mbar, $n_{\rm m}^{\rm S}(M = 0)$: 1.35×10^{16} atoms/m^3; filled squares: $p_3 = 2.45$ mbar, $W_{\rm inc} = 1.66$ W, $W_{\rm inc}/p_3 = 0.68$ W/mbar, $n_{\rm m}^{\rm S}(M = 0)$: 1.75×10^{16} atoms/m^3.

only considering the combined parameter W_{inc}/p_3, and data collapse reasonably well in figure 6.31.
The most important aspect is that population differences $a_i - b_j$ are probed, whereas "scaling" considers the ratio of the optical pumping rate γ_{OP} divided by the metastability exchange rate γ_e and neglects stimulated emission effects for both pump and probe. This is discussed in more detail in appendix G.

6.2.8 Effect of pump beam diameter and probe parameter x_s on apparent polarisation

The measured averaged value of apparent polarisation along the longitudinally inclined probe path depends on the overlap of the pump beam that is Gaussian in its radial intensity distribution with the probe beam.
Two parameters influence this overlap of pump and probe beams: The diameter (waist) of the pump beam and the radial distance (on the entrance window of the gas-cell) between ingoing and outcoming centres of the probe beam ($2x_s$, see figure 3.7), depending on the opening angle of the V-shaped probe beam.
At fixed pump beam diameter (e.g. waist $2a = 1.6$ cm), M^a at given M increases with *de*creasing x_s. At smaller x_s, the opening angle between incoming and outgoing probe beam is smaller and thus the probe beam also passes through zones of higher radial pump laser intensity.
Furthermore, it has been verified with the help of the model for MEOP kinetics (computations not shown here), that at fixed radial probe parameter x_s, apparent polarisation at given actual polarisation (e.g. $M = 0$) increases with increasing pump beam diameter as the probe beam then passes through radial zones of the pump beam with higher intensity entailing higher overpolarisation effects in 2^3S.

6.2.9 Conclusion

The dedicated experiments to account for perturbations of 2^3S- and 2^3P-populations, from which a selection of results and corresponding computations is presented and discussed in the current section 6.2, are required for technical reasons in order to correlate apparent polarisation in presence of the pump laser to actual polarisation.
We showed that this correlation is reliably possible. The physical origin of the difference between M^a and M as well as its qualitative behaviour is well understood with the help of the model for MEOP-kinetics.

Moreover, such dedicated experiments are also of more fundamental interest in order to fully understand and describe all processes in 2^3S in detail, which exceeds the scope of this work. One could think of more sophisticated experiments where

all a_i sublevels are probed to infer the 2^3S-polarisation M^{S}, being a different linear combination of 2^3S-sublevels than M^a.

The main conclusion is to emphasise that the experimental correction of apparent polarisation values in order to obtain reliable actual polarisation values is adjusted for each new experimental condition and thus robust. Therefore, measuring nuclear polarisation by monitoring absorption of a weak probe laser is an experimental method, in which we have confidence. Hence the established evidence of laser-enhanced relaxation in section 6.3.3, based on a balance of angular momentum involving experimentally measured nuclear polarisation, pump transmission coefficients and values of $\dot{M}$ (see chapter 5.7), as well as its further characterisation as function of M in section 6.3.4 are reliable.

6.3 Optical Pumping results at 1 mT

In this section, the main results of optical pumping kinetics at $B = 1$ mT obtained from polarisation build-up and decay measurements (see chapter 5.2) are presented. The first subsection deals with relaxation-*free* data at zero polarisation which is very well appropriate for comparisons with computations of the model for MEOP kinetics. In the second subsection, the intrinsic relaxation time in the 2^3P level is empirically determined from comparisons of experimental with computed ratios of photon efficiencies on the C_8- and C_9-transitions. In the third subsection, we discuss results at steady state polarisation M_{eq} showing evidence of laser-induced relaxation exceeding measured polarisation decay rates in absence of OP. In the fourth subsection, results as function of polarisation are discussed, including a more detailed characterisation of laser-enhanced relaxation.

6.3.1 Results at $B = 1$ mT and $M = 0$: Relaxation-free data to test and validate the model for MEOP kinetics

Relaxation-free data at zero nuclear polarisation $M = 0$ are obtained from recorded polarisation dynamics during the build-up process. Light transmission coefficients of pump and probe lasers are monitored with sufficiently short time constants during acquisition so that their values and those of polarisation build-up rates at $M = 0$ can be reliably extrapolated (experimental protocol and methodological aspects, see sections 5.2, 5.4, 5.5 and 5.6).
Experimental data at zero nuclear polarisation are especially suitable for comparisons

with computed predictions by the model for MEOP kinetics since relaxation terms, included in the model by a phenomenological approach, are completely eliminated at $M = 0$.
In the following paragraphs, relevant experimental results and computations are presented and discussed for low field MEOP conditions.

Light transmission at $M = 0$

Zero polarisation $M = 0$ provides well-defined conditions, where light transmission coefficients of the spectrally wide pump laser and the inclined single-frequency probe laser depend on the density of metastable atoms and their radial distribution[3].
All (experimental and computed) pump transmission coefficients T_p presented in this work are total transmission values meaning that the entire transmitted pump light intensity (collected by a lens, attenuated by neutral density filters and focussed on a monitoring photodiode, see section 3.2) has been monitored and not just the central part of the Gaussian beam distribution in case a diaphragm was placed on the pump path. Computations yield both, central and total values of pump transmission, the latter are used for comparisons to the corresponding experimental values.
When comparing experimental with computed values of T_p, three input-parameters for the OP model remain difficult to be precisely specified:
First, the absolute value of the metastable density n_m that is inferred from absorption measurements of the inclined probe laser in absence of the pump laser. In presence of the pump, even at nuclear ground state polarisation $M = 0$, n_m is susceptible to changes due to intense pump light which creates electronic orientation in $2^3\mathrm{S}$ ($M^\mathrm{S} \neq 0$). A reason for changes in n_m is auto-ionising Penning collisions (see subsection 6.1.3) that are inhibited with increasing electronic polarisation favouring an increase of metastable density. The influence of the intense pump light on n_m is believed to be small and is difficult to assess. It has been neglected in all computations.
Second, the radial distribution of metastable atoms perpendicular to the optical axis is an important input parameter of the OP model that has been experimentally determined in the following OP conditions: For the 2.45 mbar-cell, the radial distribution has been mapped with a dedicated experimental device (described in section 3.2) for different discharges at $B = 1$ and 30 mT in order to obtain a (roughly linear) dependency of the parameter α of $n_\mathrm{m}/N_\mathrm{g}$ (see subsection 6.1.2). For the 0.63 mbar-cell, measurements in presence of the discharge and without discharge

[3]The observed changes in plasma localisation in higher magnetic field and/or higher pressure (cf. section 6.1) possibly require changes in the optical pumping setup. In order to increase absorption of pump light for example, it might be advantageous to adapt the pump laser profile to the toroidal plasma localisation. In [Nik10] and [Doh11], specially shaped pump laser profiles using axicons for use in high B and for high p_3 are presented, and the impact on OP performances is discussed.

have been recently performed using a beam profiler in order to infer the parameter α (results are presented in subsection 6.1.2). In other experimental situations (e.g., for the 1.19 mbar cell), the parameter α is not precisely known. In these cases, different hypotheses concerning the radial n_{m} distribution are tested in the computations of pump transmission coefficients and $\dot{M}$ values, and are discussed with respect to experimental results.
Third, the intrinsic relaxation rate in the 2^3P level, $\gamma_{\mathrm{r}}^{\mathrm{P}}$, is not directly measurable and therefore, the computations are based on different assumptions. At fixed α, the two limiting cases of the 'Kastler'- and 'Dehmelt'-regimes are investigated and furthermore, computations are performed using the empirically determined (pressure-dependent) value of $\gamma_{\mathrm{r}}^{\mathrm{P}}$ (see subsection 6.3.2). (If not otherwise specified, for each pressure value the corresponding empirically determined value of $\gamma_{\mathrm{r}}^{\mathrm{P}}$ is used as input parameter for the computations.)

In figure 6.32, computed pump transmission coefficients on C_8 and C_9 transitions at fixed empirically determined $\gamma_{\mathrm{r}}^{\mathrm{P}}$ are compared to experimental values for two different discharges in the 0.63 mbar cell as function of incident pump laser power.
Figure 6.32 and other graphs in this subsection are semi-logarithmic plots in order to expand the graphs in x-direction and thus to improve the representation of T_p at low W_{inc}.
The value of $\alpha = 2$, that is observed to be independent of the discharge strength and thus from n_{m} in this low pressure cell ($p_3 = 0.63$ mbar), stems from radial n_{m} measurements using a beam profiler. For the weak discharge, experimental and computed values of T_p at zero nuclear polarisation are shown for both transitions C_8 and C_9, for the strong discharge only for pump C_8. For both discharges and pump transitions, a good quantitative agreement between experiment and computations is obtained at higher W_{inc}. Above $W_{\mathrm{inc}} \gtrsim 0.4$ W, the discrepancies between experimental and computed pump transmission coefficients remain below 0.5 % (2 %) for the weak (strong) discharge, and there are experimental points at higher W_{inc} that agree with the computations within experimental errors. At lower W_{inc}, the observed relative discrepancy amounts to 5.5 % (12 %) for the weak (strong) discharge (experiment > computations).

In the next graph (figure 6.33), the influence of the choice of $\gamma_{\mathrm{r}}^{\mathrm{P}}$, the intrinsic relaxation rate in 2^3P, on computed T_p-values at $M = 0$ at fixed parameter α, is investigated in $p_3 = 0.63$ mbar.
The computations of T_p in figure 6.33 using the empirically determined value of $\gamma_{\mathrm{r}}^{\mathrm{P}}$ for $p_3 = 0.63$ mbar are closer to the values of T_p in the 'Kastler'(K)- than the 'Dehmelt'(D)-regime as expected. At low incident pump laser power, computed values of T_p(D) are marginally above T_p(K), then towards higher W_{inc}, starting above 0.01 W for pump on C_8 and slightly below 0.1 W for pump on C_9, computed

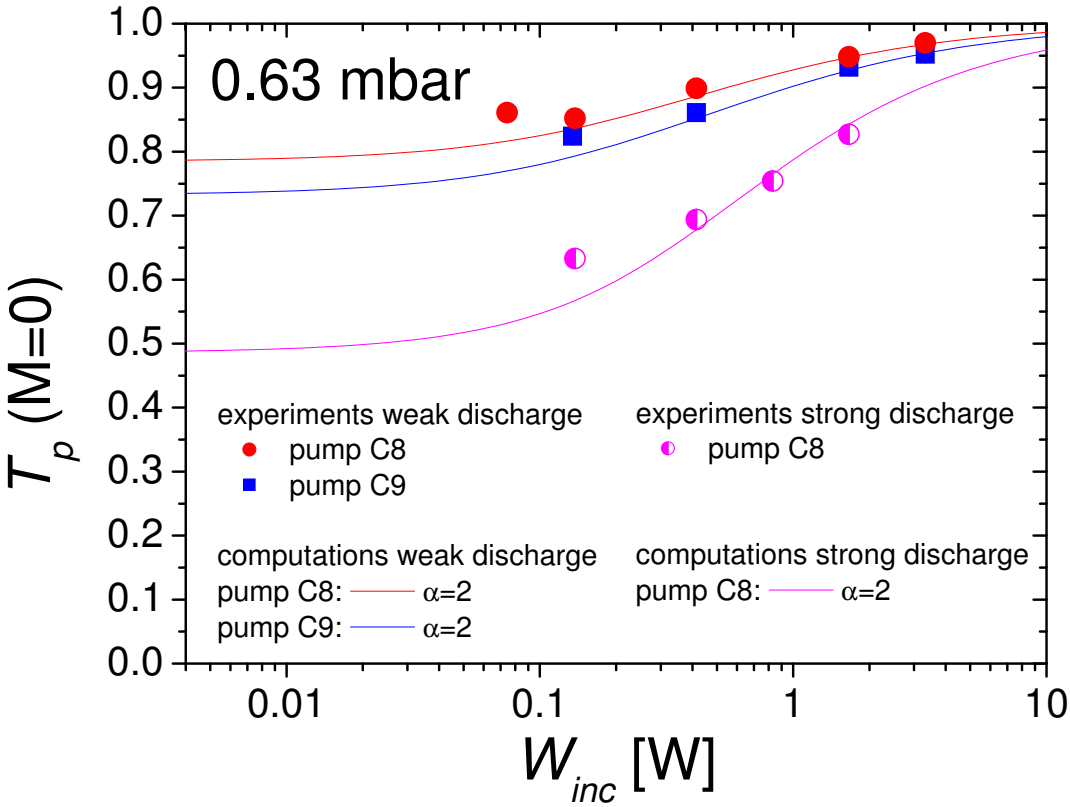

Figure 6.32: Pump transmission coefficient at $M = 0$ in $p_3 = 0.63$ mbar as function of incident pump laser power. Symbols: experimental data (error bars are of the same size as symbols), lines: computations. Weak discharge: filled circles: pump C_8, filled squares: pump C_9; strong discharge: half-filled circles: pump C_8. Solid lines: computations for $\alpha = 2$. Weak discharge: $n_{\mathrm{m}}^{\mathrm{S}}(M = 0) = 1.1 \times 10^{16}$ atoms/m^3; strong discharge: $n_{\mathrm{m}}^{\mathrm{S}}(M = 0) = 3.3 \times 10^{16}$ atoms/m^3. $1/\gamma_{\mathrm{r}}^{\mathrm{P}}$ (0.63 mbar): 5×10^{-7} s.

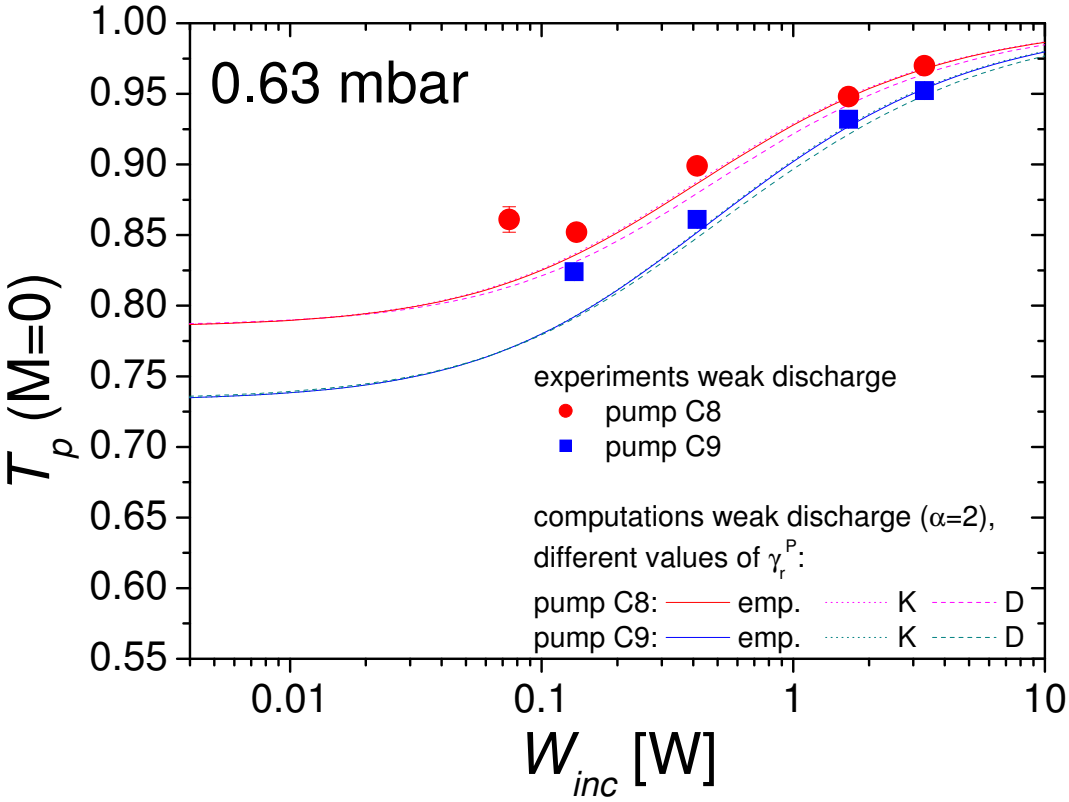

Figure 6.33: Experimental and computed pump transmission coefficient at $M = 0$ in $B = 1$ mT and $p_3 = 0.63$ mbar for different assumptions of γ_r^P, at fixed value of $\alpha = 2$: Same experimental data of weak discharge as in figure 6.32; computations with stated parameters in caption of figure 6.32 and three values of $1/\gamma_r^P$: solid lines: 4.86×10^{-7} s, dotted lines: 'Kastler' OP regime (no redistribution in 2^3P, $1/\gamma_r^P = 1$ s), dashed lines: 'Dehmelt' OP regime (complete redistribution in 2^3P, $1/\gamma_r^P = 1 \times 10^{-20}$ s).

values of T_p(D) remain below T_p values computed for $1/\gamma_r^P = 4.86 \times 10^{-7}$ s, the relative difference between both does not exceed 1 %.
The experimental errors of T_p are in most cases higher than this relative difference between computations using different values of γ_r^P. From these observations it can be concluded that the intrinsic relaxation time in 2^3P is not an extremely critical parameter in computations of the pump transmission coefficient at $M = 0$ and low pressure of 0.63 mbar, because it has no effect at small incident pump laser power and only a limited influence at higher W_{inc}.

In figure 6.34, transmission coefficients of the spectrally broadband pump laser (T_p) are compared to corresponding transmission coefficients of the single-frequency probe laser (T_s) in presence of the pump laser at $M = 0$ in $p_3 = 0.63$ mbar. Pump and probe are both on the C_8-transition, and the investigated probe component is the one with the same circular light-polarisation as the pump, σ^+. For this reason, the transmitted σ^+-probe signal is perturbed by parasitic stray light of the pump which is power dependent (cf. chapter 3.3). Computations of T_s take the influence of the pump light into account. Such computed values of T_s as well as of T_p using different assumptions for the radial n_m-parameter α are compared to experimental transmission coefficients.
A comparison of experimental pump and probe transmission coefficients in presence

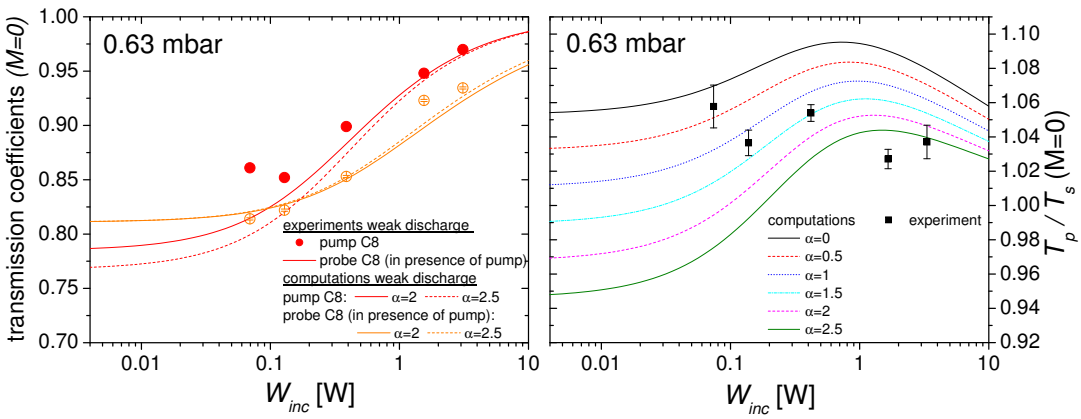

Figure 6.34: Comparison of pump (T_p) and probe (T_s) transmission coefficients in presence of the pump laser, both on C_8, σ^+, in $B = 1$ mT and $p_3 = 0.63$ mbar, $M = 0$. Left: Experimental T_p (filled circles) and T_s (open circles) for a weak discharge (parameters cf. caption of figure 6.32) with corresponding computations using $1/\gamma_r^P = 5 \times 10^{-7}$ s and two different values of α: 2 (solid lines) and 2.5 (dashed lines). Right: Ratio of T_p/T_s. Filled squares: experimental data (from left graph), lines: computations for different values of α between 0 and 2.5 (see legend).

of the pump laser at $M = 0$ (left graph of figure 6.34) shows $T_p > T_s$. This behaviour meets the expectations as the single-frequency probe laser is more efficiently absorbed than the spectrally broad multimode pump laser, and thus the total measured transmission of the less absorbed pump light is higher than of the probe light. Computed T_s-values are almost identical for different values of α up to approximately 0.1 W of incident pump laser power and experimental values are less than 1 % below the computations. At higher W_{inc}, experimental T_s-values are above computed ones, and computations using a higher value of α are closer to the experiment than computations with low α: at $W_{\text{inc}} > 1$ W, for $\alpha = 2$, the relative difference between experiment and computations ranges between 1.5 % and 3 % approximately. (The relative discrepancy between experiment and computations of pump transmission coefficients at $M = 0$ is already discussed in the comments concerning figure 6.32 above).
The experimental ratios of T_p/T_s in the right graph of figure 6.34 are all between 1.03 and 1.06, and thus almost constant within experimental errors. The value of the ratio at $W_{\text{inc}} = 0.074$ W is probably slightly too high as the determination of T_p at very low W_{inc} is problematic due to a poor SNR. Furthermore, the ratio of T_p/T_s at $W_{\text{inc}} = 1.66$ W is probably slightly too low because $T_s(1.66\ \text{W})$ appears too high compared to other T_s-values. In summary, T_s overall varies like T_p, that controls the populations, in spite of spectral and geometrical differences.
Comparisons of these experimental ratios to corresponding computed ratios show that values of α between 1.5 and 2.5 provide a reasonable overall agreement. More precisely, $\alpha \simeq 1.5$ is consistent with observations at moderate pump powers ($W_{\text{inc}} < 1$ W), but results at higher powers indicate a more narrow density profile (e.g., alpha = 2.5), possibly linked to an increase of the metastable density at high pumping intensity. This remains to be confirmed, for instance by direct measurements of probe transmission along the cell axis direction for various radial positions.

The next graphs represent the same kind of experimental and computed parameters, now for the highest pressure-value investigated systematically throughout this work, $p_3 = 2.45$ mbar.
In figure 6.35, experimental and computed pump transmission coefficients at zero nuclear polarisation for two different discharges as function of incident pump laser power are shown. For the sake of clarity, only the C_9 pump transition is plotted for both examined discharges. (Transmission coefficients for pump C_8 are represented in the left graph of figure 6.36 for the weak discharge.)
For the weak discharge in figure 6.35, experimental pump transmission coefficients at low incident pump laser power yield higher experimental errors than T_p-values at higher W_{inc}. Furthermore, the tendency that experimental T_p-values at W_{inc} between approximately 0.006 W and 0.035 W are too high by up to 18 % seems to be a sign of a systematic uncertainty due to low SNR or an unknown bias. The pump transmis-

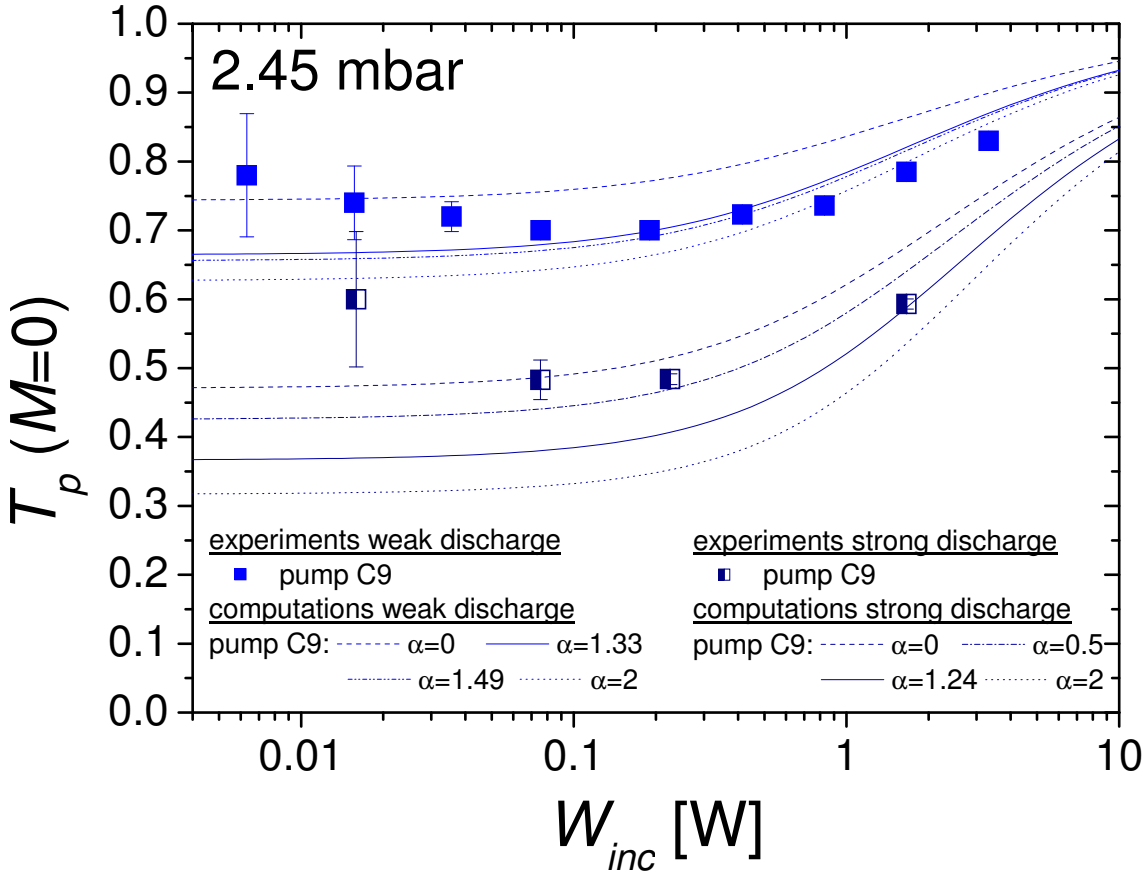

Figure 6.35: Pump transmission coefficient on C_9 at $M = 0$ in $p_3 = 2.45$ mbar as function of incident pump laser power. Symbols: experimental data (when error bars are invisible, they are of the same size as symbols), lines: computations. Weak discharge: filled squares: pump C_9; strong discharge: half-filled squares: pump C_9. Dashed lines: computations for $\alpha = 0$, dash-dotted line: $\alpha = 0.5$ (strong discharge only), solid lines: $\alpha = 1.24$ (strong discharge) or $\alpha = 1.33$ (weak discharge), dash-dot-dot line: $\alpha = 1.49$ (weak discharge only), dotted lines: computations for $\alpha = 2$. Weak discharge: $n_{\mathrm{m}}^{\mathrm{S}}(M = 0) = 1.7 \times 10^{16}$ atoms/m^3; strong discharge: $n_{\mathrm{m}}^{\mathrm{S}}(M = 0) = 4.2 \times 10^{16}$ atoms/m^3. $1/\gamma_{\mathrm{r}}^{\mathrm{P}}$ (2.45 mbar): 1.25×10^{-7} s.

sion coefficient at low incident pump laser power is expected to be roughly constant and then to increase with W_{inc}. This increase is observed in experimental data above approximatley 0.1 W.
Computations use different radial n_{m}-parameters α between 0 and 2 to obtain T_p-values in figure 6.35. For the weak discharge, two intermediate values are used: $\alpha = 1.33$ is extracted from an experimental radial mapping of a similar discharge with 1.5 % higher $n_{\mathrm{m}}/N_{\mathrm{g}}$-ratio, whereas $\alpha = 1.49$ stems from a linear fit of extracted α-values from four different radial discharge mappings over the whole range of $n_{\mathrm{m}}/N_{\mathrm{g}}$, from 0.135 to 1.04 (see figure 6.11). Both values provide near-identical results.
The agreement between experiment and computations is very good for intermediate values of incident pump laser power (0.1 W - 1 W).

For the strong discharge in figure 6.35, the experimental T_p-values at low W_{inc} up to approximately 0.1 W show the same behaviour as observed for the weak discharge: too high values with high experimental error. Computations using $\alpha = 0$ fit best in this range of incident pump laser powers, an excellent agreement is observed at $W_{\mathrm{inc}} = 0.075$ W for example, and the discrepancy increases towards lower values of W_{inc} up to approximately 12 %.
The radial n_{m}-parameter $\alpha = 1.24$ is extracted from the linear fit of different α-values as function of $n_{\mathrm{m}}/N_{\mathrm{g}}$ (see figure 6.11), as no experimental radial mapping has been recorded for a similar discharge, only for weaker and stronger discharges.
Over the whole range of incident pump laser power, computations using $\alpha = 2$ clearly yield too low values of $T_p(M = 0)$ for the chosen strong discharge with the pump laser tuned to the C_9 transition.

For both values of pressure that are investigated in detail in this section, the pump light absorption on a given transition scales with the metastable density as expected. In figure 6.32, at higher n_{m}, lower values of pump transmission coefficients are observed on C_8 in $p_3 = 0.63$ mbar, and this tendency is confirmed in figure 6.35 on C_9 in $p_3 = 2.45$ mbar.

In the following, experimental and computed transmission coefficients of the spectrally broad multimode pump laser are compared to the ones of the inclined single-frequency probe laser in presence of the pump, both on C_8 in 2.45 mbar and $B = 1$ mT. The left graph of figure 6.36 represents pump and probe transmission coefficients separately (denoted by T_p and T_s respectively), in the right graph, the ratio of $T_p/T_s(M = 0)$ is plotted as function of incident pump laser power.
In the left graph of figure 6.36, the pump transmission coefficients on C_8 exhibit the same qualitative behaviour as observed on C_9 (figure 6.35, weak discharge): The best agreement between experiment and computations is obtained in the intermediate range of incident pump laser power (roughly between 0.1 and 1 W), using $\alpha = 1.33$ or 1.49 from the experimental mappings. See the comments concerning figure 6.35

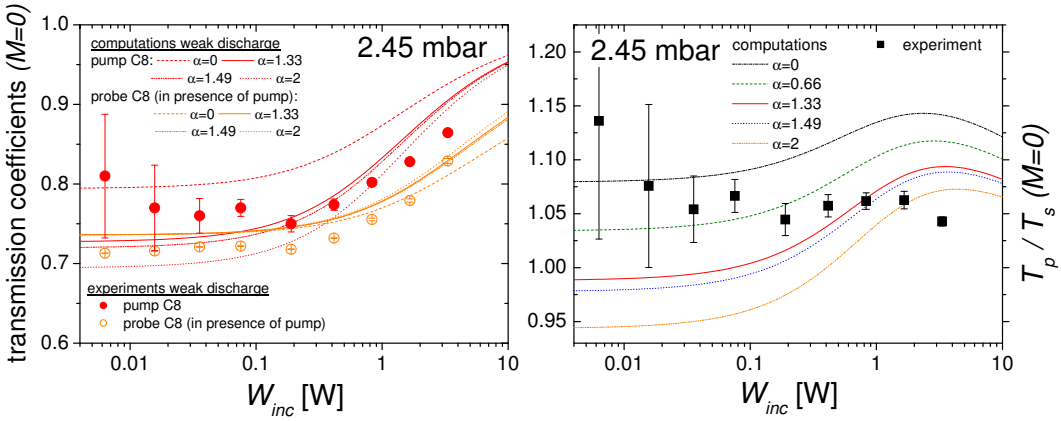

Figure 6.36: Comparison of pump (T_p) and probe (T_s) transmission coefficients in presence of the pump laser, both on C_8, σ^+, in $B = 1$ mT and $p_3 = 2.45$ mbar, $M = 0$. Left: Experimental T_p (filled circles) and T_s (open circles) for a weak discharge (parameters cf. caption of figure 6.35) with corresponding computations using $1/\gamma_r^P = 1.25 \times 10^{-7}$ s and different values of α: 0 (dashed lines), 1.33 (solid lines), 1.49 (dash-dot-dot lines) and 2 (dotted lines). Right: Ratio of T_p/T_s. Filled squares: experimental data (from left graph), lines: computations for five different values of α (see legend).

for a detailed discussion.

The single-frequency probe transmission coefficients on C_8 are below the broadband pump transmission coefficients as expected because the single-frequency probe laser is more efficiently absorbed. Up to $W_{\text{inc}} = 0.2$ W approximately, the relative difference between experiment and computations is almost constant and independent of α: computations are about 3 to 4 % above experimental points in this range of incident pump laser power.

With increasing W_{inc}, the agreement between computations and experimental points improves. Up to $W_{\text{inc}} = 1.66$ W, using small values of α in the computations fits best experimental T_s-values (e.g. for $\alpha = 0$, the experimental value of T_s is less than 1 % below the computed one at this value of W_{inc}). Towards higher values of incident pump laser power, using higher values of α leads to a better agreement: At $W_{\text{inc}} = 3.32$ W for example, the experimental value of $T_s(M = 0)$ is less than 1 % above the computed one, using the extracted value of α from the radial n_{m}-mappings. However, it is impossible to decide whether $\alpha = 1.33$ or 1.49 is better suited for the computations, the relative difference being less than 0.5 % between both computed T_s-values.

When comparing experimental and computed probe transmission coefficients over the whole range of incident pump laser power, a higher value of α in the computations seems to be more appropriate because the experimental curvature (increase of

T_s-values starting around $W_{\text{inc}} = 0.4$ W) is better reproduced. For an optimum agreement of each individual experimental and computed T_s-value at given W_{inc}, the complete computed curve would have to be shifted towards lower T_s-values by approximately 3 % though.

In the right graph of figure 6.36, the experimental ratios of pump divided by probe transmission coefficients in presence of the pump laser, both on C_8 at $M = 0$ (experimental data of the left graph), are approximately constant within experimental errors. A value of $T_p/T_s = 1.06$ would comply with the ratios at all values of W_{inc} except the highest one at 3.32 W.
The computed ratios are clearly not constant, only below 0.1 W approximately, then increase up to a local maximum situated between 2 W (for $\alpha = 0$) and 4 W (for $\alpha = 2$), followed by a slight decrease towards $W_{\text{inc}} = 10$ W.
Due to different general tendencies of experimental and computed T_s-values with increasing W_{inc}, no meaningful information - concerning the question which radial n_{m}-parameter α is appropriate in the computations to best fit experimental probe transmission coefficients at $M = 0$ over the whole range of W_{inc} - can be extracted from this plot. In the range up to 0.4 W, α between 0 and 1 is convenient, at $W_{\text{inc}} = 0.82$ W, an good agreement between experiment and computation can be observed for α between 1.33 and 1.49, and towards higher W_{inc}, higher values of α are better suitable.

To finish this section about pump transmission coefficients at $M = 0$, we would like to point out, that the conditions in the present work correspond to a regime of weak absorption where $-\ln T = (1 - T)$ (absorbance = absorptance) is fulfilled. Typical values of absorbed pump laser power $W_{\text{abs}} = (1 - T_p)\ W_{\text{inc}}$ range between 1×10^{-3} and 1 W.
Despite some quantitative discrepancies that can partly be attributed to the mentioned uncertainties concerning the choice of parameters, the theoretically predicted behaviour of the pump transmission coefficient at $M = 0$ as function of incident pump laser power is experimentally confirmed.

Initial polarisation growth (at $M = 0$)

In this paragraph, we present experimental $\dot{M}$ values at zero nuclear polarisation at $p_3 = 0.63$ and 2.45 mbar as function of incident pump laser power, in order to compare (at fixed pressure) either $\dot{M}(M = 0)$ of different transitions at given metastable density or to compare $\dot{M}(M = 0)$ at fixed transition for different n_{m}. Computations are presented based on different assumptions either of radial n_{m}-distribution at fixed intrinsic relaxation time in 2^3P, or of $\gamma_{\text{r}}^{\text{P}}$-values at fixed radial n_{m}-parameter α.

First, results at low pressure (0.63 mbar) are discussed before corresponding results at higher pressure (2.45 mbar) are presented. The low pressure part is organised in the following way: Based on figure 6.37, $\dot{M}(0)$ of C_8 and C_9 is compared at fixed n_m; computations in this figure show the influence of the parameter γ_r^P at fixed α on computed $\dot{M}(0)$-values.
In figure 6.38, $\dot{M}(0)$ at fixed transition C_8 is compared for two values of n_m; computations in this figure investigate the influence of α on $\dot{M}(0)$ at fixed γ_r^P.
In the second part (2.45 mbar), similar results are presented in figure 6.39 where both aspects of interest are combined in one graph: At fixed transition (C_9 here), $\dot{M}(0)$ obtained in weak and strong discharges are compared, and at fixed n_m, $\dot{M}(0)$ of C_8 and C_9 transitions are represented. Computations are added to examine the influence of different α-values on $\dot{M}(0)$ at fixed γ_r^P.
Comments on the agreement between experiment and computations are added for all plots. Logarithmic representations are chosen to allow an overview of the whole range of investigated conditions.

Figure 6.37 presents $\dot{M}(0)$ at $p_3 = 0.63$ mbar of C_8 and C_9 transitions at fixed n_m (weak rf excitation level), along with computations at fixed α using different assumptions for the intrinsic relaxation rate in the 2^3P-state.
The experimental $\dot{M}(0)$-values stem either from polarisation build-up experiments or from dedicated experiments to account for perturbations of 2^3S- and 2^3P-populations in presence of the pump laser. A good agreement between experimental $\dot{M}(0)$-values from both types of experiments is observed for the two investigated transitions C_8 and C_9, relative differences range between 0 and 6 %.

Comparing two different transitions at given n_m (here for the weak discharge), one observes higher $\dot{M}(0)$ on the C_9-line: C_9 pumps faster than C_8 as expected. Using equation (2.79) that defines the photon efficiency as $\eta = \frac{1}{2}\,\frac{\dot{M}(0) N_g V_C\, h\nu}{W_{abs}(0)}$, the ratio of $\dot{M}_{C9}$ / $\dot{M}_{C8}$ ($M = 0$) can be expressed by:

$$\frac{\dot{M}_{C9}}{\dot{M}_{C8}}(0) = \frac{\eta_{C9}}{\eta_{C8}}(0) \times \frac{W_{\text{abs}}^{C9}}{W_{\text{abs}}^{C8}}(0). \tag{6.8}$$

The first ratio on the right hand side is always > 1 as $\eta_{C9}(0) > \eta_{C8}(0)$ (cf. section 2.9). Furthermore, experimental data in figure 6.33 for instance illustrate that $T_p^{C9}(0) < T_p^{C8}(0)$. From $W_{\text{abs}} = (1 - T_p)\, W_{\text{inc}}$, it follows that $W_{\text{abs}}^{C9}(0) > W_{\text{abs}}^{C8}(0)$ at given W_{inc}, hence the second ratio on the right hand side of equation (6.8) is always > 1 as well. These considerations clearly demonstrate why $\dot{M}(C_9)$ is expected to exceed $\dot{M}(C_8)$ at given W_{inc} and $M = 0$.

In agreement with characteristics of photon efficiencies presented in section 2.9, compiled in table D.1, computations of $\dot{M}(0)$ in figure 6.37 confirm the qualitatively different expected behaviour of C_8 and C_9 in the two limiting cases of no and com-

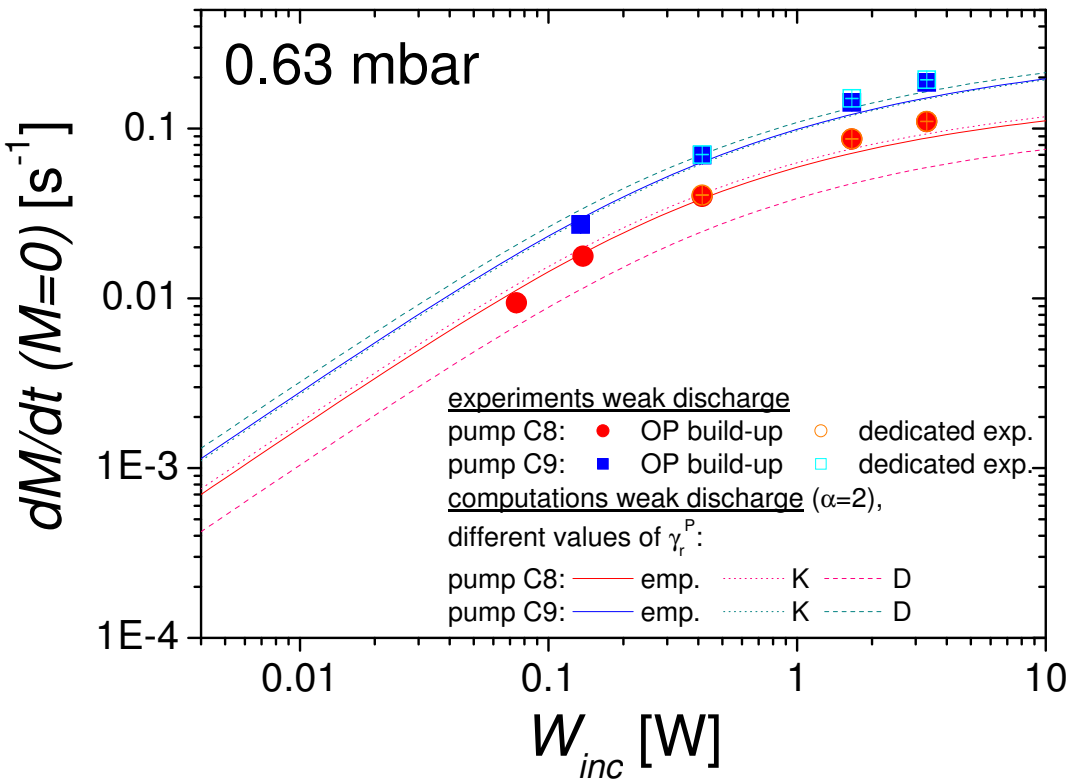

Figure 6.37: Experimental time derivative of polarisation at $M = 0$ and $p_3 = 0.63$ mbar: fixed n_{m} (weak discharge, parameters see caption of figure 6.32), two transitions: C_8 (circles) and C_9 (squares). Filled symbols: data from polarisation build-up experiments (cf. section 5.2); open symbols: data from dedicated experiments to account for perturbations of 2^3S- and 2^3P-populations in presence of the pump laser (cf. section 5.3). (Experimental errors are smaller than size of symbols.) Computations: Influence of $\gamma_{\mathrm{r}}^{\mathrm{P}}$ at fixed $\alpha = 2$. Solid lines: $1/\gamma_{\mathrm{r}}^{\mathrm{P}} = 4.86 \times 10^{-7}$ s, dotted lines: 'Kastler' OP regime (no redistribution in 2^3P, $1/\gamma_{\mathrm{r}}^{\mathrm{P}} = 1$ s), dashed lines: 'Dehmelt' OP regime (complete redistribution in 2^3P, $1/\gamma_{\mathrm{r}}^{\mathrm{P}} = 1 \times 10^{-20}$ s).

plete redistribution in 2^3P: For C_8: $\dot{M}(0)$(Kastler) > $\dot{M}(0)$(Dehmelt), and for C_9: $\dot{M}(0)$(Dehmelt) > $\dot{M}(0)$(Kastler).

Computed values of $\dot{M}(0)$ in figure 6.37 agree reasonably well with experimental data: In the intermediate range of incident laser powers, the agreement is very good for the empirically determined value of γ_r^P, at lower or higher values of W_{inc}, relative discrepancies between experiment and computations do not exceed 20 %.

Figure 6.38 presents experimental $\dot{M}(0)$ values ($p_3 = 0.63$ mbar) at fixed transition (C_8) and different n_m (two discharges). For the weak discharge, the same experimental $\dot{M}(0)$ data as in figure 6.37 are plotted.
At given transition, higher values of $\dot{M}(0)$ are found at higher n_m: As expected, strong discharges pump faster as $\dot{M}(0)$ scales with n_m (through the ME-exchange rate Γ_e) and M^S.

When comparing experimental $\dot{M}(0)$ to computations using different assumptions for the radial n_m-parameter α in figure 6.38, one overall conclusion over the whole power range is not possible, but different observations are made in the different ranges of W_{inc}. As a general tendency, it can be noted that at low incident pump laser power, using a lower value of α in the computations yields a better agreement with experimental $\dot{M}(0)$, at higher W_{inc}, higher values of α are better suitable. The extracted value of α between 2 and 2.5 from the radial n_m-distribution measurements using a beam profiler (cf. figure 6.12) yields the best agreement between experiment and computations in the intermediate power range, between 0.1 and 1 W approximately.

To finish this paragraph, the findings on $\dot{M}(0)$ at 0.63 mbar are now qualitatively checked at higher pressure (2.45 mbar).
In figure 6.39, experimental $\dot{M}(0)$-values at $p_3 = 2.45$ mbar are presented as function of incident pump laser power, as well as computations at fixed $1/\gamma_r^P = 1.25 \times 10^{-7}$ s and variable α between 0 and 2.
One overall observation in figure 6.39 is a linear increase of $\dot{M}(0)$ up to approximately 0.5 W of incident pump laser power. At higher W_{inc}, $\dot{M}(0)$ further increases but less than linear compared to the general trend from lower values of W_{inc}: Computations and experimental $\dot{M}(0)$ seem to bend down. This behaviour can be explained by optical saturation effects, that are also observed in low pressure, e.g. figure 6.38.
At fixed metastable density (weak discharge), a comparison of $\dot{M}(0)$ on both pump transitions yields: $\dot{M}(0)(C_9) > \dot{M}(0)(C_8)$ in agreement with observations at low pressure.

A comparison of the computations with experimental $\dot{M}(0)$-values for the weak discharge, pump C_8 and C_9, reveals a good agreement in the intermediate power range (from approximately 0.2 to 1 W) using the radial n_m-parameter from the experimental mappings (cf. figure 6.11). The agreement is especially good for pump

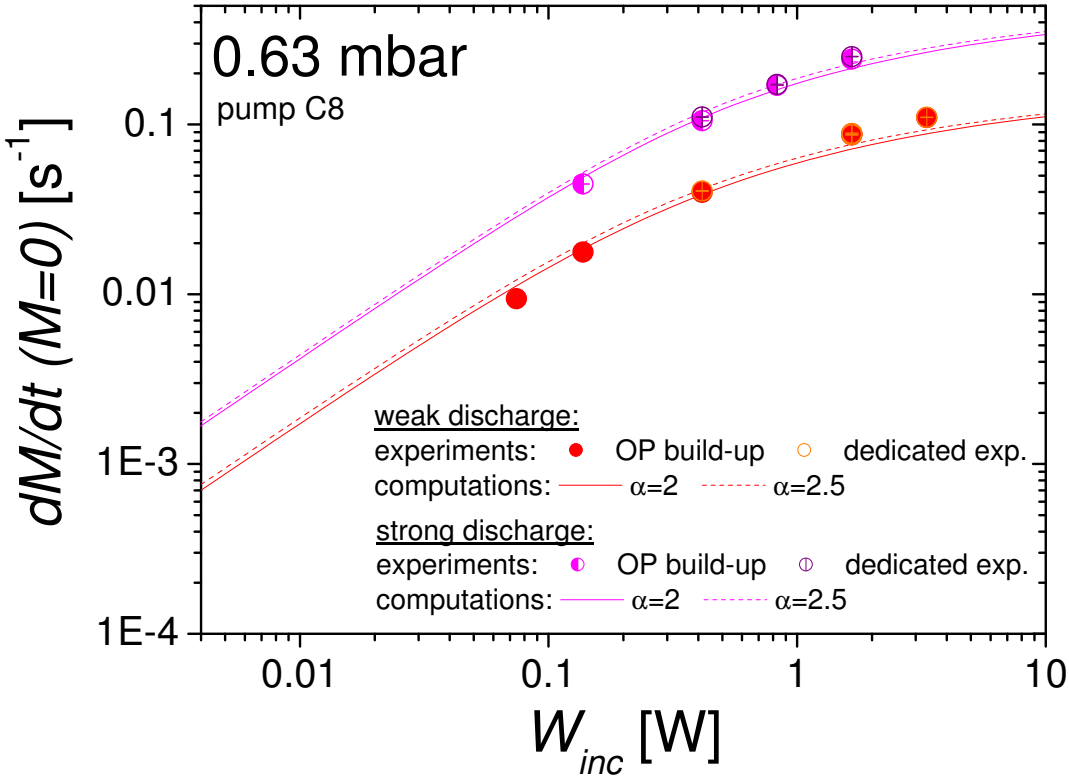

Figure 6.38: Experimental time derivative of polarisation at $M = 0$ and $p_3 = 0.63$ mbar: Two rf excitation levels (parameters of weak and strong discharges: see caption of figure 6.32), fixed transition C_8. Filled symbols: data from polarisation build-up experiments (cf. chapter 5.2) in weak discharge, half-filled symbols: data from same protocol in strong discharge; open symbols: data from dedicated experiments to account for perturbations of 2^3S- and 2^3P-populations in presence of the pump laser (cf. chapter 5.3). (Experimental errors are smaller than size of symbols.) Computations: Influence of α on $\dot{M}(0)$ at fixed $1/\gamma_{\mathrm{r}}^{\mathrm{P}} = 5 \times 10^{-7}$ s. Different assumptions of α: solid lines: $\alpha = 2$, dashed lines: $\alpha = 2.5$.

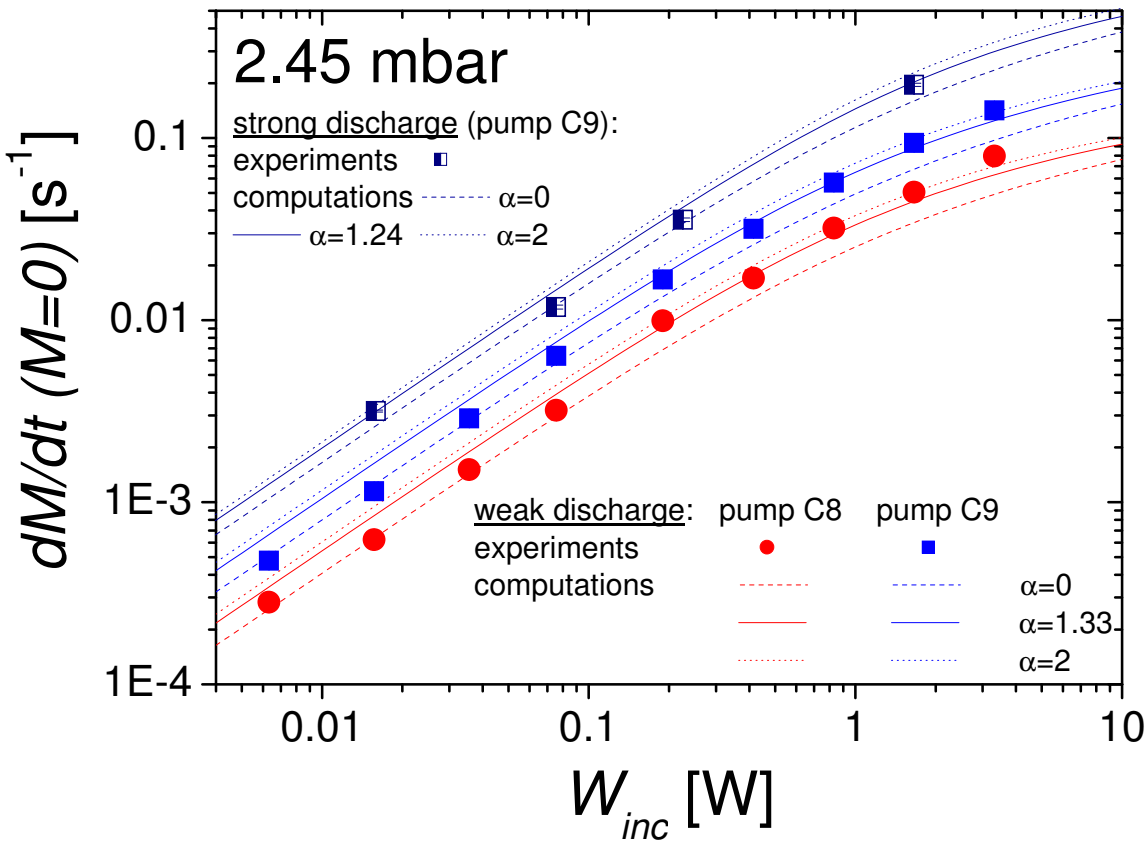

Figure 6.39: Experimental and computed time derivative of polarisation at $M = 0$ and $p_3 = 2.45$ mbar as function of incident pump laser power. Circles: pump on C_8 transition, squares: pump on C_9 transition. Filled symbols: weak discharge, half-filled symbols: strong discharge. (Experimental errors are smaller than size of symbols.) Fixed γ_r^P-value used in computations: $(1.25 \times 10^{-7}\,\mathrm{s})^{-1}$. Different assumptions of α: dashed lines: $\alpha = 0$, solid lines: $\alpha = 1.24$ (strong discharge) or $\alpha = 1.33$ (weak discharge), dotted lines: $\alpha = 2$. Parameters of weak and strong discharges: see caption of figure 6.35.

C_9, where the relative difference between experiment and computations amounts to 0-3 % in this power range. For pump C_8, relative discrepancies between 3 and 10 % are observed in this power range. At lower W_{inc}, the experimental $\dot{M}(0)$-values are about 25 % below the computed $\dot{M}(0)$ using the mapped α-value, and agree very well with computations based on a uniform n_{m}-distribution. At high W_{inc}, computations using the mapped α-value tend to predict lower $\dot{M}(0)$-values than experimentally measured (discrepancy between 10 and 30 %), using higher α in the computations would decrease the maximum relative difference to approximately 14 %.
For the strong discharge and pump C_9, a good overall agreement between experimental $\dot{M}(0)$ values and computations is observed using $\alpha = 1.24$, given by a linear fit of several α-values extracted from experimental radial n_{m}-mappings as function of $n_{\text{m}}/N_{\text{g}}$. At intermediate values of incident pump laser power, the relative scatter amounts to 15-20 %, and at $W_{\text{inc}} = 0.016$ W and 1.66 W, almost exact agreement is found between experiment and computations.

Direct quantitative comparisons of $\dot{M}(0)$ at different pressures are performed in the next paragraph where $\dot{M}(0)$ is presented as a function of $W_{\text{abs}}(0)$ for all three investigated values of He pressure at fixed transition C_8.

In conclusion, comparisons of experimental and computed values of pump transmission coefficients and time derivative of polarisation at $M = 0$ clearly demonstrate the importance of having information about the radial distribution of metastable atoms, since using the naive assumption of a radially uniform distribution in the computations ($\alpha = 0$) does not match experimental data in all investigated cases.
In general, the best agreement between experiment and computations is obtained in an intermediate range of incident pump laser power. At very low W_{inc}, experimental signal-to-noise-ratios become an issue, at higher W_{inc}, simplifications of the OP model might lead to higher relative differences.

Correlation between initial polarisation growth and absorbed laser power, both at $M = 0$

In the previous paragraph of this subsection, values of $\dot{M}(0)$ are investigated as function of incident pump laser power. In the following graph (figure 6.40), compiled experimental $\dot{M}(0)$-values **for C_8 pumping** for all systematically investigated pressure-values as well as corresponding computed quantities as function of *absorbed* laser power are presented. This is a more suitable representation for discussing $\dot{M}(0)$ results in terms of photon efficiency.

In a sealed cell where the total number of ^{3}He atoms is constant, we know from equation (2.79), using equation (2.83): $\eta \propto \frac{\dot{M}(0)}{W_{\mathrm{abs}}(0)}\, p_3$. Hence at given pressure, $\dot{M}(0)$ is proportional to $W_{\mathrm{abs}}(0)$, with η as proportionality factor. Furthermore, at given $W_{\mathrm{abs}}(0)$, $\dot{M}(0)$ scales as $\frac{\eta}{p_3}$.

These expectations are confirmed by data represented in figure 6.40: For each

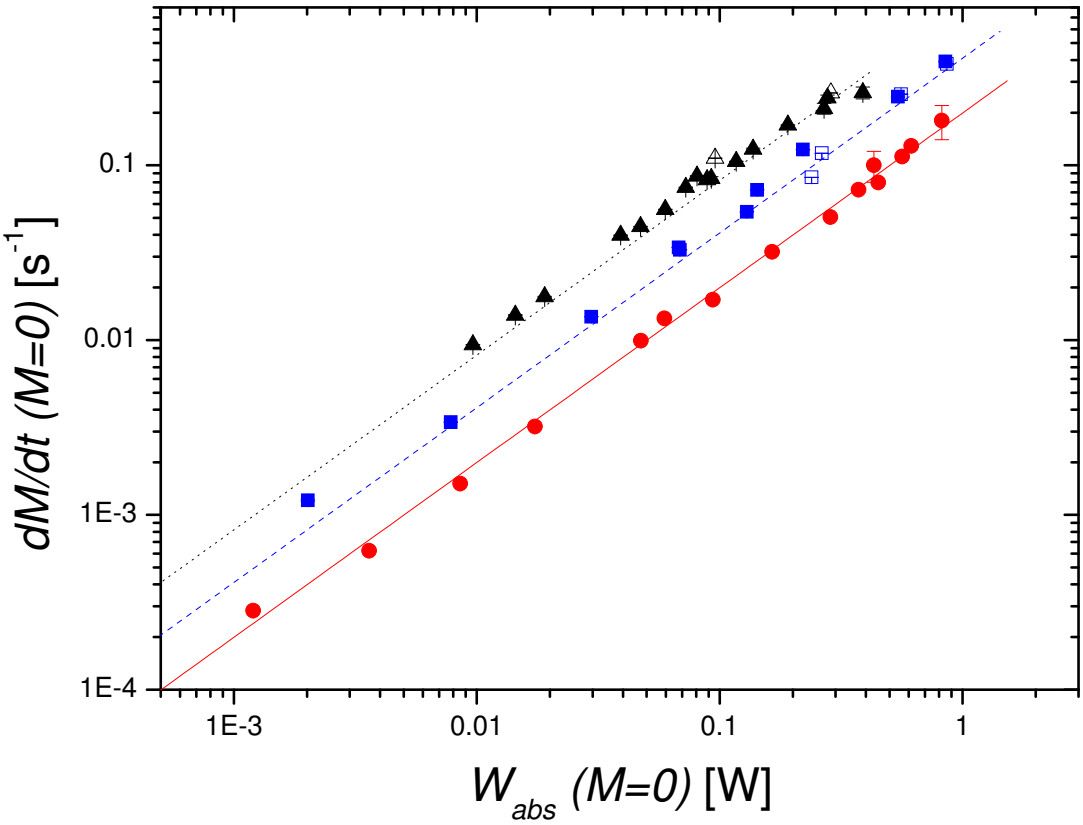

Figure 6.40: Experimental and computed values of $\dot{M}(0)$ (symbols and lines respectively) as function of absorbed laser power (comprising data of several different discharges), both on the C_8-pump-transition at $M = 0$ for three different pressure values: 0.63 mbar (triangles and dotted line), 1.19 mbar (squares and dashed line), and 2.45 mbar (circles and solid line). Filled symbols: probe C_8, open symbols: probe C_9. Whenever experimental error bars are invisible, they are smaller than the size of the symbols. Computations use empirically determined values of $\gamma_{\mathrm{r}}^{\mathrm{P}}$ (see subsection 6.3.2).

individual pressure, $\dot{M}$ increases linearly with absorbed laser power. Thus, higher absorption leads to faster pumping. At given $W_{\mathrm{abs}}(0)$ we observe: $\dot{M}(0$ @ 0.63 mbar$) > \dot{M}(0$ @ 1.19 mbar$) > \dot{M}(0$ @ 2.45 mbar$)$ as expected (measured values of η on the C_8 transition are provided in the next paragraph for all

three investigated pressure values.) For precise quantitative comparisons at different pressures, the fact that the inner volume of the high pressure cell (2.45 mbar) is about 8 % smaller than of the two other cells with low and intermediate pressures (0.63 and 1.19 mbar) due to slightly different inner dimensions of the first mentioned cell has to be taken into account.

In figure 6.40, only experiments where the pump transmission has been monitored during polarisation build-up and hence yield an extrapolated value of $T_p(M = 0)$ each are taken into account in order to determine the experimentally absorbed laser power at $M = 0$. Thus figure 6.40 first provides the opportunity to estimate $W_{\mathrm{abs}}(0)$ in cases where the pump transmission is not monitored. Second, this representation of data facilitates eliminating pathologic experiments that disobey the proportionality between $\dot{M}(0)$ and $W_{\mathrm{abs}}(0)$ that can be considered as intrinsic due to the definition of photon efficiency (in chapter 2.8.3).
Experimental $\dot{M}(0)$ values at 0.63 and 1.19 mbar in figure 6.40 mainly contain data where the probe laser is tuned to the C_8-transition, but some additional data with probe laser on C_9 as well. In the present context, the probe C_9-data is compatible with the probe C_8-data: there are cases with almost perfect agreement, others where $\dot{M}$(probe C_9) is slightly higher or lower than $\dot{M}$(probe C_8). However, these relative differences between extracted $\dot{M}$ values on both probe transitions are well comprised within the experimental scatter of probe C_8-data exclusively and can therefore not be imputed to different probe transitions here.
The lines in figure 6.40 are no fits of experimental data, but stand-alone computations. The computed results are in turn independent of the radial n_{m}-parameter α in this case provided that the same value of alpha is used to compute corresponding $\dot{M}(0)$- and $T_p(0)$-values.
The relative difference between experimental and computed $\dot{M}(0)$ is highest at low (0.63 mbar) and intermediate (1.19 mbar) pressures, where it ranges between 4.5 and 40 % (in one case), and 2 and 35 % respectively, with one exception at 1.19 mbar at very low W_{abs} where the relative discrepancy amounts to 48 %. In most of all cases at these two pressure-values, experimental $\dot{M}(0)$ are above computations.
The best agreement between experimental and computed $\dot{M}(0)$-values is obtained at the highest pressure of 2.45 mbar, where the relative difference amounts to values between 1 and 26 %. Slightly more experimental $\dot{M}(0)$-values are above than below the computations.

Photon efficiency of C_8 transition at $M = 0$

When comparing experimental with computed values of T_p and $\dot{M}$ for C_8 at $M = 0$ in the last two preceding paragraphs, the three parameters n_{m}, α and $\gamma_{\mathrm{r}}^{\mathrm{P}}$,

necessary for the computations, are difficult to precisely assess due to unknown influences on the plasma. n_m and α may possibly depend on the incident pump laser power. Since the pump laser creates electronic orientation in $2^3\mathrm{S}$ ($M^\mathrm{S} \neq 0$), Penning collisions are known to change and thus affect the metastable density n_m. As described in section 4.4, the determination of n_m is based on the measured probe absorption. This determined value of n_m is fully appropriate as parameter in the OP model for situations without pump laser, but less adequate in presence of the pump laser due to the fact that the probe path is different from the pump path and that the measured probe absorption yields averages over the Gaussian pump profile and the radial n_m-distribution.
For these reasons, photon efficiencies, inferred from *measured* polarisation growth and pump light transmission, that are proportional to $\dot{M}(0)$ / $W_\mathrm{abs}(0)$ (see equation (2.79)), are considered in the present paragraph, since possible influences of the pump laser on n_m and its radial distribution cancel out in the above mentioned ratio for the C_8 transition (when using C_9, that is not the case, since $\eta_{\mathrm{C}9}$ depends on actual populations in $2^3\mathrm{S}$, hence on local laser intensity and thus on the overlap between laser and metastable density profiles).
Only the dependence of computed data on the intrinsic relaxation rate in $2^3\mathrm{P}$ is remaining. However, in subsection 6.3.2, we make use of this fact in order to empirically determine this pressure dependent parameter $\gamma_\mathrm{r}^\mathrm{P}$ by comparisons of experimental data with computations varying $\gamma_\mathrm{r}^\mathrm{P}$.

In the following graphs, one for each ^{3}He-pressure value in figures 6.41 to 6.43, photon efficiencies at $M = 0$ are compiled for various experiments, all with pump laser tuned to the C_8-transition. On C_8, the photon efficiency is constant as function of polarisation as explained in chapter 2.9. From the various compiled values of $\eta_{\mathrm{C}8}(0)$, a weighted mean value for each pressure is determined (that is needed e.g. in section 6.3.3).

The photon efficiency values at $M = 0$ for all three different pressure values (figures 6.41, 6.42 and 6.43) are represented as function of incident pump laser power in a logarithmic scale in order to expand the power scale for reasons of readability. Different values of η at fixed incident pump laser power stem from different experiments and illustrate a possible, realistic scatter range. The shown photon efficiencies for each pressure contain experimental data of different discharges. As expected, no systematic dependence of η on n_m is observed.
The experimental values of η are determined from the measured values of $\dot{M}(0)$ and $T_p(0)$ using equation (2.79):

$$\eta = \frac{\dot{M}(0)}{W_\mathrm{abs}(0)} \frac{p_3[\mathrm{mbar}]\, V_c[\mathrm{cm}^3]}{T[\mathrm{K}]}\ 7.243 \times 10^{18}\ \frac{\mathrm{K}}{\mathrm{mbar\ cm}^3}\ 1.834 \times 10^{-19}\ \mathrm{Ws}.$$

The highest scatter of experimental photon efficiencies, especially at higher

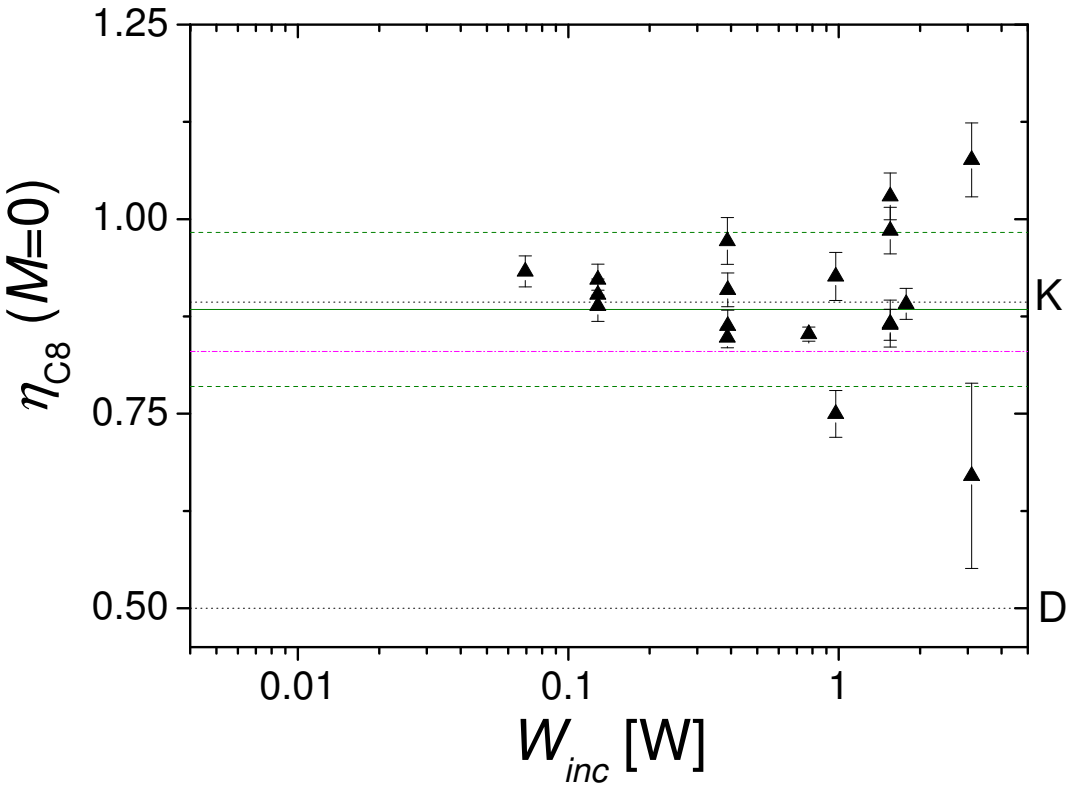

Figure 6.41: Photon efficiency of C_8 pump transition at $p_3 = 0.63$ mbar as function of incident pump laser power: Compilation of $\eta_{C8}(M = 0) = \eta_{C8}(M)$ of various experiments. (Black) Dotted lines: Analytical borders of photon efficiency on C_8: Dehmelt OP-regime: 0.5 (line 'D'), Kastler OP-regime: 0.8934 (line 'K'). (Green) Solid line: weighted mean value of experimental data points: 0.884. (Green) Dashed lines: weighted mean value ± standard deviation σ_η: 0.099. (Pink) Dash-dotted line: Computed η_{C8} for empirically determined intrinsic relaxation rate in 2^3P, see section 6.3.2.

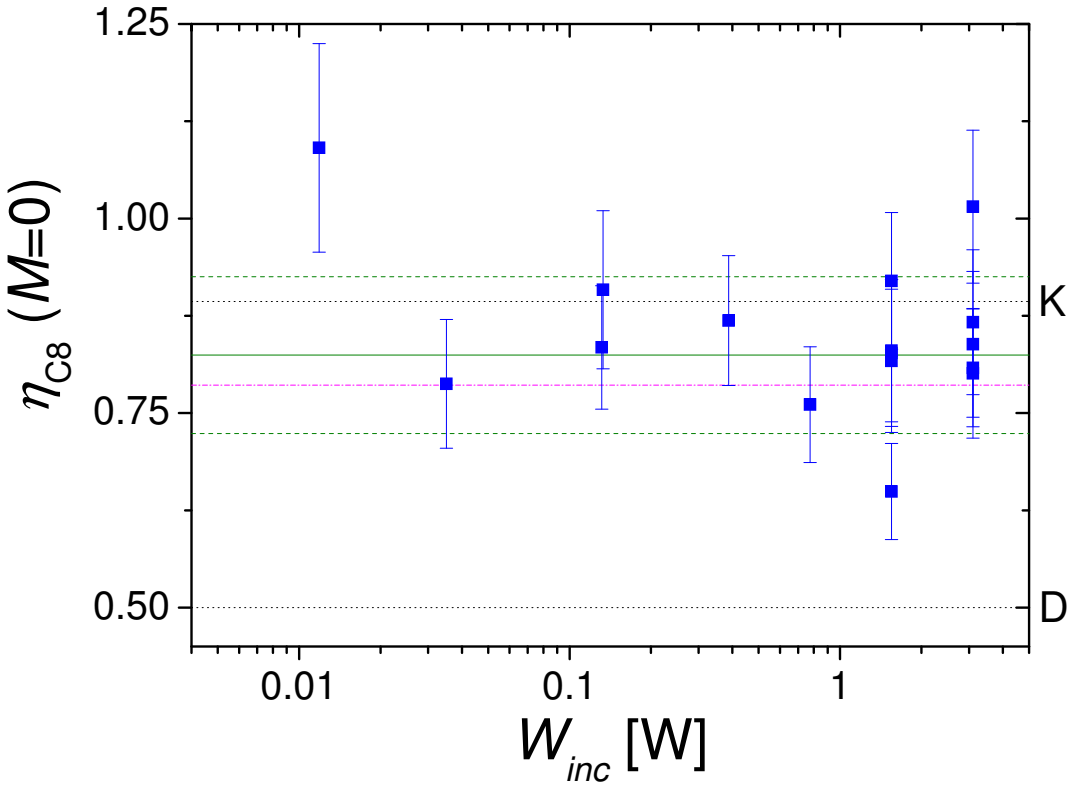

Figure 6.42: Photon efficiency of C_8 pump transition at $p_3 = 1.19$ mbar as function of incident pump laser power: Compilation of $\eta_{\,C8}(M = 0) = \eta_{\,C8}(M)$ of various experiments. (Green) Solid line: weighted mean value of experimental data points: 0.824. (Green) Dashed lines: weighted mean value $\pm$ standard deviation σ_η: 0.108. Other lines: see caption of figure 6.41. Errors will be reviewed in the final published version of data.

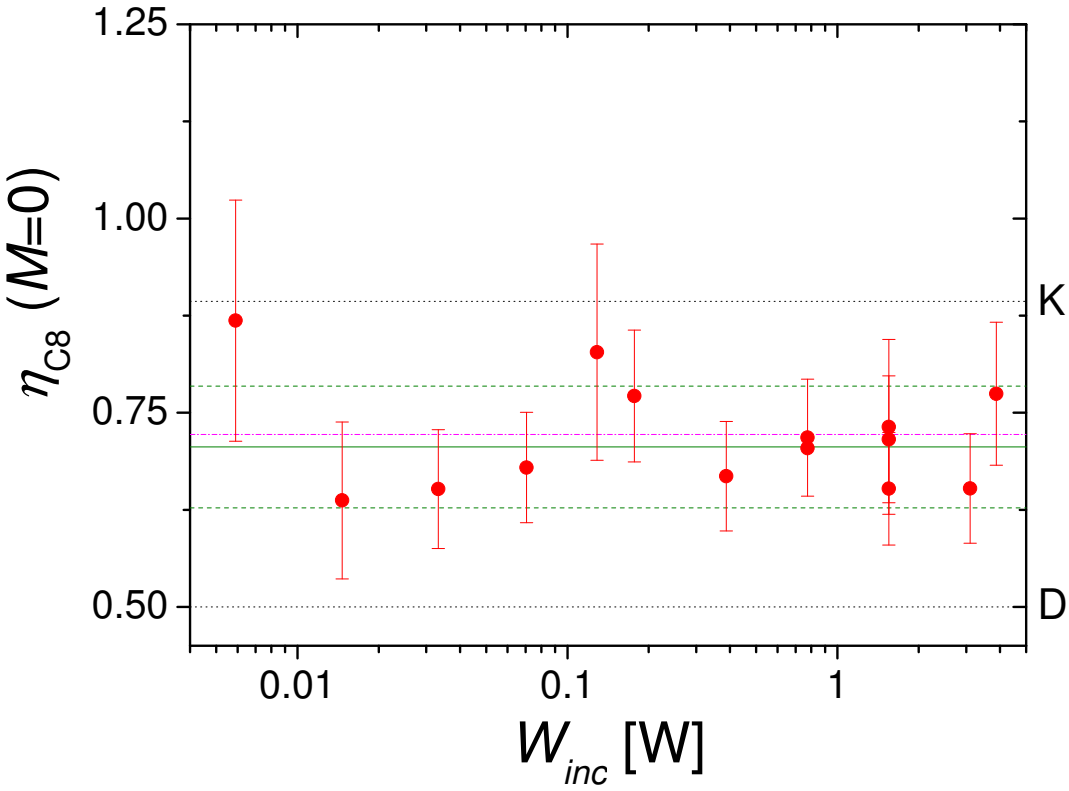

Figure 6.43: Photon efficiency of C_8 pump transition at $p_3 = 2.45$ mbar as function of incident pump laser power: Compilation of $\eta_{C8}(M = 0) = \eta_{C8}(M)$ of various experiments. (Green) Solid line: weighted mean value of experimental data points: 0.706. (Green) Dashed lines: weighted mean value $\pm$ standard deviation σ_η: 0.084. Other lines: see caption of figure 6.41. Errors will be reviewed in the final published version of data.

values of incident pump laser power is observed on the 0.63 mbar-data. There are two cases where, at given W_{inc}, η-values are incompatible within experimental error bars. At 1.19 mbar, less scatter is observed at fixed W_{inc} except one runaway point at very low incident pump laser power. The 2.45 mbar photon efficiency data has the least scatter. At all values of incident pump laser power, η-values of different experiments are compatible within error bars.
Furthermore, η-values of 2.45 mbar cover the whole incident power-range. Taking into account these overall observations, the decision was made to base the empirical determination of the intrinsic relaxation time in 2^3P (see section 6.3.2) mainly on these 2.45 mbar-data and scale the determined value with pressure for other values of p_3.

For each of these ^{3}He-pressure values, the error-weighted mean value $\overline{\eta}$ and its standard deviation σ_η are determined as follows from experimental values of photon efficiencies η_i and the corresponding experimental error of each individual data point $\Delta\eta_i$. With the weighting factor $\frac{1}{\Delta\eta_i^2}$ (chosen because individual data points are uncorrelated) one obtains:

$$\overline{\eta} = \frac{\sum_i(\eta_i/\Delta\eta_i^2)}{\sum_i(1/\Delta\eta_i^2)} \text{ and} \tag{6.9}$$

$$\sigma_\eta = \sqrt{\frac{1}{\sum_i(1/\Delta\eta_i^2)}}. \tag{6.10}$$

The results for all three investigated pressures are given in table 6.3.
The general tendency of $\overline{\eta}$-values at the three investigated values of pressure confirms

Table 6.3: Compilation of error-weighted mean values of η_{C8} and corresponding standard deviations for different ^{3}He-pressures

p_3 [mbar]	$\overline{\eta}$	σ_η
0.63	0.884	0.099
1.19	0.824	0.108
2.45	0.706	0.084

the expectations: the highest photon efficiency is found at 0.63 mbar, compatible with the 'Kastler'-limit, the lowest one at 2.45 mbar, starting to depart from the low-pressure-limit towards the 'Dehmelt'-regime, and the $\overline{\eta}$-value at 1.19 mbar is in between the other two weighted mean values as anticipated.

Due to imperfectly known overall scaling factors like the total number of atoms or the absolute power scale, it appears advantageous to consider *ratios* of photon efficiencies $\frac{\eta_{\mathrm{C9}}}{\eta_{\mathrm{C8}}}$ whenever precise quantitative information is essential as for instance when using photon efficiencies to determine intrinsic relaxation rates in 2^3P (see section 6.3.2). These global scaling factor are identical for both transitions and thus cancel out in the ratio.

The intention of the present subsection on comparisons between relaxation-free data and corresponding computations at $B = 1$ mT and $M = 0$ was to test and validate the model for MEOP kinetics. From all the above presented results we may conclude that the OP model is well appropriate to qualitatively predict all observed behaviours and therefore is an important tool to gain a deeper insight into all involved processes in optical pumping of gaseous ^{3}He. Due to necessary simplifications in the OP model (details see chapter 2), its ability to exact quantitative predictions is limited especially at higher laser power due to saturation effects. At very low laser power, limited experimental signal-to-noise-ratios are observed affecting the quality of comparisons to the OP model, that in the limit of linear absorption is robust and quantitatively reliable.

6.3.2 Empirical determination of the intrinsic relaxation rate in the 2^3P state

Another major result of the present work at $M = 0$ and $B = 1$ mT that is described in this subsection, is the determination of the pressure-dependent phenomenological relaxation rate in the 2^3P state of ^{3}He. This parameter is designated by $\gamma_{\mathrm{r}}^{\mathrm{P}}$ (cf. equation (2.35)). Two limiting cases can be distinguished: the case of low-pressure OP with $\gamma_{\mathrm{r}}^{\mathrm{P}} \ll \gamma$ (the radiative decay rate, equation (2.43)), where collisions between the B_j states are infrequent (no collisional redistribution, discussed by Kastler [Kas57], therefore named: OP type 'Kastler').
The opposite limiting case of high-pressure OP with $\gamma_{\mathrm{r}}^{\mathrm{P}} \gg \gamma$ is characterised by total collisional redistribution between the 18 B_j states (discussed by Dehmelt [Deh57], therefore named: OP type 'Dehmelt').
These two OP regimes are also discussed in early review articles and an original publication, where the high-pressure limiting case is also designated by 'Dehmelt-type pumping' [Coh66, Pin79] or 'depopulation pumping' [Hap72], and the low-pressure limiting case by 'Kastler-type pumping' [Pin79] or 'repopulation pumping' [Hap72].

In order to determine the relaxation rate of the 2^3P state empirically, experimental ratios of η_{C9}, photon efficiency on the C_9 transition, divided by η_{C8}, photon efficiency on the C_8 transition, both at zero nuclear polarisation $M = 0$, are represented as function of incident pump laser power in figure 6.44 and compared to computed ratios η_{C9}/η_{C8} by the model for MEOP kinetics using different values of γ_r^P as input parameter.
The determination of γ_r^P has been based on photon efficiencies at $M = 0$ for reasons explained in the following. Although a comparison of experimental results with computations using different values of γ_r^P as input parameter is also possible e.g. with $\dot{M}(0)$ or $T_p(0)$, we consider η better suitable for this purpose, as unknown influences of the pump on metastable densities and their radial distribution are eliminated in $\eta \propto \frac{\dot{M}(0)}{W_{\text{inc}}(1-T_p)}$. However, the absolute value of incident pump laser power - being the nominal value times a loss factor due to optical elements - has been measured (see chapter 3.2), but might not be known with a sufficient precision in order to infer γ_r^P reliably either from a comparison of experimental and computed absolute η_{C8}- or η_{C9}-values.
On account of this, the *ratio* of η_{C9}/η_{C8} is used to infer γ_r^P independently of the absolute value of W_{inc}, which cancels out in this ratio. (When plotting η_{C9}/η_{C8} as function of W_{inc}, the uncertainty on W_{inc} still influences the lateral x-position of the experimental points, but this fact constitutes a minor issue.)

The empirical determination of γ_r^P as illustrated in figure 6.44 is based on data acquired with the 2.45 mbar cell, because more data on C_8 *and* C_9 at different values of incident pump laser power are available, and in addition, the values of η at $M = 0$ of different experiments at 2.45 mbar (figure 6.43) have less scatter than data of both other cells.
Three computed possibilities of η_{C9}/η_{C8} versus W_{inc} using different values of $1/\gamma_r^P$ between 1 and 1.5×10^{-7} s are proposed in figure 6.44 for comparison with experimental data at 2.45 mbar. $1/\gamma_r^P = 1.5 \times 10^{-7}$ s clearly yields too low ratios of photon efficiencies over the whole range of incident pump laser powers. Experimental points at very low incident pump laser power seem to rather suggest a shorter intrinsic relaxation rate, possibly below $1/\gamma_r^P = 1 \times 10^{-7}$ s, but experimental uncertainties are high due to low SNR of the pump signal, both the directly transmitted and the demodulated signals (SNR of the probe signals and thus of M and dM/dt remains remarkable). The value of intrinsic relaxation rate in 2^3P that we consider to best fit experimental data at **2.45 mbar** is $\mathbf{1/\gamma_r^P = 1.25 \times 10^{-7}}$ **s**. The experimental ratios of η_{C9}/η_{C8} with good SNR above $W_{\text{inc}} = 0.07$ W coincide well with computed ratios using this value of γ_r^P.
In order to infer the values of intrinsic relaxation rate in 2^3P at *other* pressures, we apply a scaling with the inverse of cell filling pressure, i.e. of gas number density N_g, according to equation (6.11) given below: i.e. $\mathbf{1/\gamma_r^P = 2.57 \times 10^{-7}}$ **s** for the

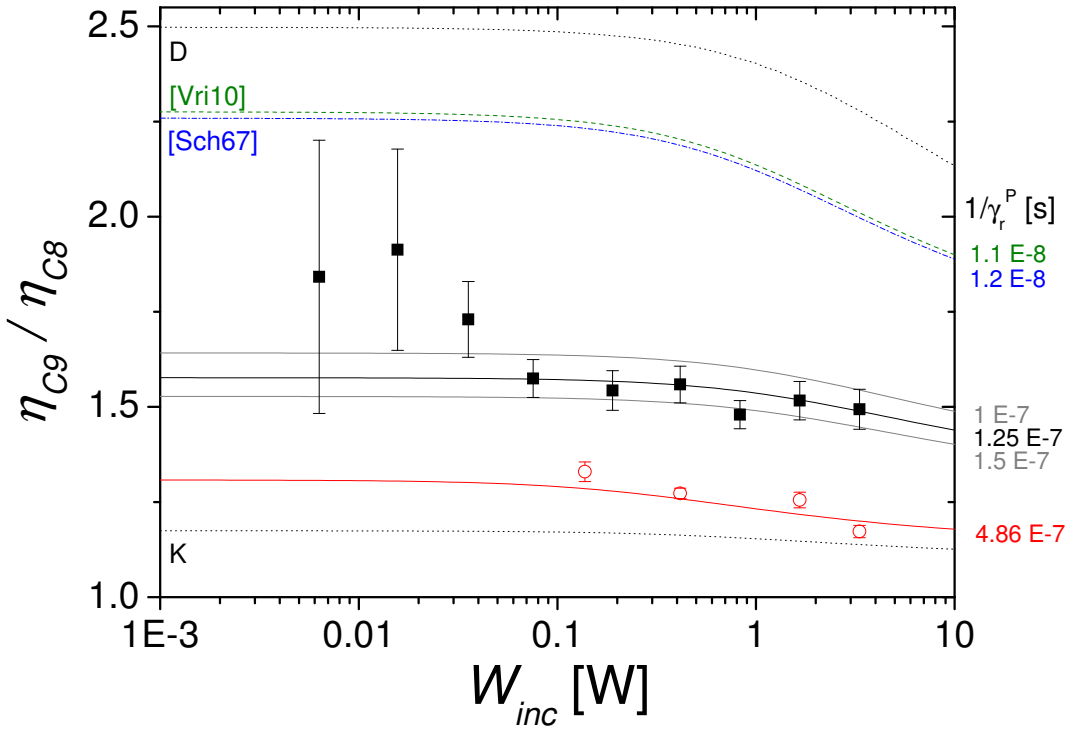

Figure 6.44: Empirical determination of intrinsic pressure-dependent relaxation rate in 2^3P by comparison of experimental and computed ratios of photon efficiencies η_{C9}/η_{C8} at $M = 0$ as function of incident pump laser power. Experimental data: Filled squares (black): $p_3 = 2.45$ mbar, open circles (red): $p_3 = 0.63$ mbar. Lines: Computations using different values of γ_r^P and the following parameters: $p_3 = 2.45$ mbar, $n_m^S(M = 0) = 1.7 \times 10^{16}$ atoms/m^3, $\alpha = 0$, no relaxation in 1^1S. From top to bottom: Dotted line: High-pressure limiting case: Dehmelt regime, $1/\gamma_r^P = 1 \times 10^{-20}$ s; (green) dashed line: $1/\gamma_r^P = 1.1 \times 10^{-8}$ s inferred from total cross section in [Vri10] at 2.45 mbar; (blue) dash-dotted line: $1/\gamma_r^P = 1.2 \times 10^{-8}$ s inferred from cross section in [Sch67] at 2.45 mbar; (grey, black and grey) solid lines: $1/\gamma_r^P = 1$, 1.25 and 1.5×10^{-7}s: most probable values of $1/\gamma_r^P$ at 2.45 mbar from this work; (red) solid line: $1/\gamma_r^P = 4.86 \times 10^{-7}$s: $1/\gamma_r^P$ at 0.63 mbar from this work (using the following parameters for the computations: $p_3 = 0.63$ mbar, $n_m^S(M = 0) = 1.1 \times 10^{16}$ atoms/m^3, $\alpha = 2.13$, no relaxation in 1^1S); dotted line: Low-pressure limiting case: Kastler regime, $1/\gamma_r^P = 1$s.

1.19 mbar cell and $\mathbf{1/\gamma_r^P = 4.86 \times 10^{-7}}$ **s** for the **0.63 mbar** cell.
Examples of experimental photon efficiency ratios at 0.63 mbar are added to figure 6.44. As expected, data points lie closer to the Kastler regime. They are consistent with the values computed for $1/\gamma_r^P = 4.86 \times 10^{-7}$ s.
When comparing the theoretical curve η_{C9}/η_{C8} of 0.63 mbar to all others computed for different values of γ_r^P at a *fixed* pressure of 2.45 mbar, one notices that at low pressure, the ratio of photon efficiencies starts to decrease at lower incident pump laser power (at W_{inc} around 0.03 W for 0.63 mbar computations) than at higher pressure (at W_{inc} approximately 0.3 W for 2.45 mbar computations). This observation can be explained as follows: At lower pressure, pump induced perturbations of populations of the different m_F sublevels in the 2^3S (and 2^3P) state(s) are more important than at higher pressure at fixed W_{inc}. Such perturbations (illustrated in figure 4.18), which cause a departure from a spin temperature distribution, increase with increasing pump laser power.
The photon efficiency on the single-component C_8 transition is *in*dependent of the actual sublevel populations in 2^3S as explained in detail in chapter 5.7. Therefore the value of η_{C8} is constant over the whole range of incident pump laser powers (at different absolute values depending on pressure: η_{C8} is smaller at higher pressure as expected).
On the multi-component transition C_9, the relative weighting of the m_F = -3/2 component compared to the m_F = -1/2 component (in the case of incident σ^+ light) changes with the 2^3S polarisation M^S and is thus dependent on the actual populations of the involved m_F sublevels. In figure 2.14, computed photon efficiencies are plotted as a function of M at very low fixed incident pump laser power in the spin temperature limit where $M^S = M$. Therefore this figure can be also used here for qualitative reasoning: The value of η_{C9} *de*creases with *in*creasing M^S (in both limiting cases of 'Kastler' and 'Dehmelt' OP regimes as well as in all intermediate cases). Here in figure 6.44 at $M = 0$, we do not have a spin temperature situation due to the intense pump laser light: M^S increases with W_{inc}. Altogether, the relative weighting of both components of the C_9 transition changes, and thus η_{C9} *de*creases, with *in*creasing W_{inc}. This behaviour is observed at all pressures (at higher absolute η_{C9} value at higher pressure as expected) and leads to a decrease of the ratio of photon efficiencies η_{C9}/η_{C8} at higher W_{inc}. The fact that at lower pressure, this observed decrease starts at lower values of incident pump laser power is due to the more important pump induced perturbations of the 2^3S (and 2^3P) sublevels at lower pressure.

To finish this subsection about intrinsic relaxation in the 2^3P state, previously published findings concerning this topic are presented and compared to our results.
In the first publication to be discussed here [Sch67], a ^{3}He gas cell was used containing atoms in the metastable 2^3S state, being pumped by a ^{4}He lamp in which the non-

resolved D_1- and D_2-lines excited to the 2^3P_0 level (C_9-transition in ^{3}He). By collisions with ground state 1^1S_0 atoms they can be transferred either to the 2^3P_1 or the 2^3P_2 levels (non-radiative transitions). The examined parameter was the scattered light by the ^{3}He absorption cell, and the ratio of the $2^3P_0 \rightarrow 2^3S_1$ (unseparated C_8- and C_9-transitions) to the $2^3P_{1,2} \rightarrow 2^3S_1$ (unseparated C_1- to C_7-transitions) intensities was measured. From these measurements, the cross-section for fine-structure mixing of different 2^3P_j levels ($j = 0, 1, 2$) i.e., collision-induced transitions out of the 2^3P_0 level, is determined at room temperature: $\sigma = (68 \pm 3) \times 10^{-20}\,\mathrm{m}^2$.
This cross-section can be transformed into a pressure-dependent value of $\gamma_\mathrm{r}^\mathrm{P}$ using:

$$\gamma_\mathrm{r}^\mathrm{P} = N_\mathrm{g}\,\sigma\,\langle v\rangle\,, \tag{6.11}$$

where $\langle v\rangle$ is the mean relative velocity according to [Dup71]:

$$\langle v\rangle = \sqrt{\frac{8}{\pi}}\sqrt{\frac{2\,k_B T}{M}}. \tag{6.12}$$

With the mass of a ^{3}He atom, M_3, and the Boltzmann constant k_B, both given at the beginning of this manuscript, $\langle v\rangle$ equals 2050 m/s at 300 K.
N_g in equation (6.11) designates the atom number density, i.e. the number of atoms per volume: $N_\mathrm{g} = N/V_c$, with N, the absolute total number of atoms and V_c, the volume of the cell. N_g can be determined using the ideal gas law:

$$p_3\,V_c = n\,R_m\,T \tag{6.13}$$
$$p_3\,V_c = n\,k_B\,N_A\,T \tag{6.14}$$
$$p_3\,V_c = N\,k_B\,T. \tag{6.15}$$

n is the amount of substance, i.e. the number of moles, $R_m = k_B\,N_A$ the universal molar gas constant, and $N_A = N/n$ the Avogadro constant (the values of all used constants are listed at the beginning of this manuscript).
With the help of equation (6.15), the total number of atoms N, or more suitable in our case, the atom number density N_g can be expressed as follows:

$$N = \frac{p_3\,V_c}{k_B\,T} \tag{6.16}$$
$$N_\mathrm{g} = \frac{N}{V_c} = \frac{p_3}{k_B\,T}. \tag{6.17}$$

At $T = 300$ K, the atom number density amounts to

$$N_\mathrm{g} = 2.42 \times 10^{22}\;\; p_3\,[\mathrm{mbar}]\;\; \frac{\mathrm{atoms}}{m^3}. \tag{6.18}$$

The resulting value of $1/\gamma_\mathrm{r}^\mathrm{P}$ inferred from the cross section of [Sch67] using equation (6.11) thus amounts to 1.2×10^{-8} s at 2.45 mbar (added to figure 6.44).

A comparison of $\gamma_{\mathrm{r}}^{\mathrm{P}}$ at given pressure reveals a disagreement between our result and the one of [Sch67]. The empirically determined value of $\gamma_{\mathrm{r}}^{\mathrm{P}}$ at 2.45 mbar in this work is a factor of 10 approximately below the corresponding value of [Sch67].
The computed ratio of photon efficiencies η_{C9}/η_{C8} using $\gamma_{\mathrm{r}}^{\mathrm{P}}$ of [Sch67] at $p_3 = 2.45$ mbar in figure 6.44 clearly does *not* match our experimental data of the same pressure and does not even attain the limit of experimental errors.
However, the parameter inferred by [Sch67] from measured wavelengths of reemitted photons from a ^{3}He absorption cell allows to draw conclusions about the change of F-level. It is possible that m_J is partially conserved in one single collision. Furthermore, the *nuclear* angular momentum quantum number m_I remains unchanged. The value of $\gamma_{\mathrm{r}}^{\mathrm{P}}$ inferred in the present work from comparisons of computed and experimental ratios of photon efficiencies constitutes a measure of *complete* angular momentum transfer. From these arguments, it is understandable that the empirically determined value of $\gamma_{\mathrm{r}}^{\mathrm{P}}$ of this work is smaller - e.g. when several collisions are needed for a total redistribution of m_F - than the one of [Sch67] based on emitted photons only.

A second publication addressing intrinsic relaxation in the 2^3P state is a theoretical work in which cross sections are calculated from potential energy curves [Vri10]. The calculated value for the total $2^3\mathrm{P}_{j=0\rightarrow j=1,2}$ mixing transfer cross section is $\sigma = 75 \times 10^{-20}$ m^2, in reasonable agreement with the measured cross section in ^{3}He [Sch67]. Indeed this also leads to a prediction for η_{C9}/η_{C8} that is excluded by our observations (cf. figure 6.44).

We thus believe that the choice of [Wol04] to characterise relaxation in the 2^3P state using values for $\gamma_{\mathrm{r}}^{\mathrm{P}}$ directly inferred from the cross section of [Sch67] is quantitatively not correct, and strongly overestimates the depolarising effects of collisions.

A third publication [Nac85] that broaches the subject of intrinsic relaxation rate in the 2^3P state - denoting it $\gamma_{dep} = \gamma_{\mathrm{r}}^{\mathrm{P}}$ according to the nomenclature used in the present work - compares different pumping components of the 1083 nm transition (C_1, C_3, C_5, C_8 and C_9) in the two limiting cases of no collisional redistribution in 2^3P ('Kastler' regime, assumed $\gamma_{\mathrm{r}}^{\mathrm{P}} \rightarrow 0$) and of full collisional mixing in 2^3P ('Dehmelt' regime, assumed $\gamma_{\mathrm{r}}^{\mathrm{P}} = 100\gamma$). The computations of steady state polarisation values with a former version of the model for MEOP kinetics as a function of incident laser intensity reveals interesting features: The sign of nuclear polarisation is inversed on C_1 and C_3 when passing from the 'Kastler'- to the 'Dehmelt'-OP regime, and collisions in 2^3P do not seem to affect the pumping efficiency on C_9. Actually, the latter mentioned finding is probably only due to a coincidence: In the considered range of M_{eq}-values in [Nac85], roughly between 0.4 and 0.6, the relative difference between photon efficiencies η_{C9} in the 'Kastler'- and the 'Dehmelt'-OP regimes

respectively does not exceed 5 %, and both are identical at $M = 0.5$, see figure 2.14. At lower M, η^{D}_{C9} is above η^{K}_{C9} by up to 15 %; at higher M, η^{K}_{C9} exceeds η^{D}_{C9} by up to more than 70 %.
Furthermore, [Nac85] contains an attempt to quantify $\gamma_{\mathrm{r}}^{\mathrm{P}}$ in one specific case at 0.4 mbar by comparing experimental M_{eq}-values obtained using a broadband-laser tuned close to the C_5-transition, adjusted to maximise M, and at laser intensities up to 400 mW, to theoretical computations. $\gamma_{\mathrm{r}}^{\mathrm{P}}$ constitutes an adjustable parameter in this case in the model for MEOP-kinetics in order to match experiment and computation: The extracted value of $\gamma_{\mathrm{r}}^{\mathrm{P}}$ amounts to $0.91\,\gamma$ (at 0.4 mbar).
Taking into account recent advances concerning aspects that limit MEOP performances though, this methodological approach would have to be revisited due to OP-enhanced relaxation effects that also have to be taken into account when trying to match experimental and theoretical steady state polarisation values. As the evidence of laser-enhanced relaxation was not established at that time, the whole difference between experimental and theoretical M_{eq}-values was attributed to the parameter $\gamma_{\mathrm{r}}^{\mathrm{P}}$. With the current state of knowledge, one would have to consider OP-enhanced relaxation effects as well as source of the discrepancy between experimental and theoretical steady state polarisation values. Here, we will not enter into details concerning possibilities to determine laser-enhanced relaxation rates quantitatively for the data of [Nac85], which in this case is not a straight forward procedure: C_5 is a multi-component transition so that the direct approach based on angular momentum balance for single-component transitions cannot be applied and furthermore, C_5 is very sensitive to detuning because of the C_3 component, that is only 1.78 GHz away (at $B = 0$) and pumps in the opposite sense compared to C_5 at higher $\gamma_{\mathrm{r}}^{\mathrm{P}}$-rates approaching the 'Dehmelt' regime [Nac85]. But based on the observation that obtainable steady state polarisation on the C_5 transition is higher at lower $\gamma_{\mathrm{r}}^{\mathrm{P}}$ in the 'Kastler' OP regime compared to the 'Dehmelt' regime [Nac85], we can estimate qualitatively, that the correct $\gamma_{\mathrm{r}}^{\mathrm{P}}$ value needed in order to match experimental and computed M_{eq}-values is below the one assumed in [Nac85], since part of the discrepancy between experiment and computations has to be attributed to OP-enhanced relaxation.

An earlier attempt to assess $\gamma_{\mathrm{r}}^{\mathrm{P}}$ from ratios of photon efficiencies between C_8 and C_9 at low OP intensity [Lar91] had provided the estimated value: $1/\gamma_{\mathrm{r}}^{\mathrm{P}} \approx 4 - 20 \times 10^{-7}$ s at 1.08 mbar. In spite of its inaccuracy, this result ruled out strong collisional mixing at this pressure, as confirmed by our findings.
For this reason, the values of $\gamma_{\mathrm{r}}^{\mathrm{P}}$ obtained in the present work by ratios of photon efficiencies, based on the balance of angular momentum approach, can be considered to be more reliable than the prior attempt in [Nac85].

However, concerning the comparison of experimental photon efficiency ratios and

corresponding parameters provided by the model of MEOP kinetics in the present work, the following remark has to be kept in mind: The phenomenological approach used to represent relaxation in 2^3P in the OP model, namely to suppose equal redistribution into all 18 sublevels of the 2^3P state described by a single time constant, is too coarse and oversimplifies the more complex collision mechanisms. Two aspects discussed by [Vri04], dealing with computations of j-changing and j-specific (= elastic) collisions in 2^3P as function of thermal energy in ^{4}He, suggest no total randomisation of 2^3P sublevels with a single time constant: First, the transition from 2^3P_0 to P_1 is forbidden, and the corresponding cross section is zero because one of the Clebsch-Gordan coefficients vanishes [Vri04]. Second, the cross section for transitions from P_1 to P_2 is twice as large as for transitions from P_0 to P_2 [Vri04].
According to the same publication, elastic (= j-specific) cross sections in 2^3P are 4-5 times larger than the j-changing cross sections mentioned above.

To conclude this subsection on the empirical determination of intrinsic relaxation rate in 2^3P, we would like to stress the fact that the main experimental results of the present work concerning OP-enhanced relaxation that are presented in the following two subsections 6.3.3 and 6.3.4 are *independent* of the extracted value of γ_r^P to be used as parameter in the model for MEOP kinetics as for single-component transitions like C_8, total relaxation rates during polarisation build-up can be directly inferred using the angular momentum budget approach. All characteristic features of laser-enhanced relaxation are derived from C_8 data. In figure 6.56, C_9 data - for which the MEOP model is needed to determine total relaxation rates in OP kinetics - are added to verify the general validity of our findings.

6.3.3 Results at M_{eq} ($B = 1$ mT) and evidence of laser-enhanced relaxation

In the present subsection, OP-results at steady state polarisation M_{eq} are presented, whereas in the two previous subsections the choice of presented results was focused on $M = 0$. The specific OP situation at M_{eq} is another interesting limiting case and hence deserves detailed investigation.
This subsection dealing with the limiting case of M_{eq} is organised in the following way: First, experimentally obtained steady state polarisation values as function of incident laser power at different ^{3}He-pressures and for different metastable densities and pumping transitions are compared to their computed counterparts. Second, our experimentally obtained M_{eq}-values are situated in a broader framework of other

experiments in similar and different OP-conditions before in the third part of this subsection, the balance of angular momentum in steady state conditions is examined in detail and conclusions are discussed.

Steady state polarisation M_{eq} as function of incident laser power W_{inc}

The obtained steady state polarisation in different conditions is one important parameter besides others like $\dot{M}$ or photon efficiency to characterise OP-performances. We present experimental low field examples ($B = 1$ mT) for different pump transitions at three ^{3}He-pressure values as function of incident pump laser power. Corresponding computations using measured decay rates as relaxation parameter are added in each graph for comparison.
Figure 6.45 shows M_{eq} at 0.63 mbar with the pump laser tuned to the C_8 transition.
At low incident laser power, steady state polarisation values in figure 6.45 increase with increasing W_{inc} up to approximately 0.75 W. Towards higher W_{inc}, higher power does *not* lead to higher steady state polarisation. This qualitative behaviour is observed for both discharges, independently of the metastable density; quantitatively, higher absolute M_{eq}-values are achieved at lower n_{m} (weak discharge).
Relative errors of experimental M_{eq}-values amount to approximately 0.5 %, errors of the exponential fit during a decay of polarisation in absence of the pump laser are a factor of 5 to 10 smaller.
Computed M_{eq}-values are above experimentally measured ones for both discharges. For the weak discharge, the relative difference between experiments and computations ranges between 8.5 and 21.5 %, for the strong discharge, this relative difference amounts to 13.5-21 %.
In order to match experimental steady state polarisation values by the computations, higher total relaxation rates Γ_{R} exceeding measured decay rates Γ_{D} in absence of OP have to be assumed as input parameter in the OP model. Labels in figure 6.45 indicate required values of Γ_{R} in the OP model in order to obtain by the computations the same (lower) M_{eq}-values as experimentally measured. For both discharges, required Γ_{R} rates are higher than measured Γ_{D} decay rates. Furthermore, in the "plateau"-region of M_{eq}, they are not constant at different W_{inc}-values.

In the next figure 6.46, similar results are given for 1.19 mbar-data and discussed subsequently.
Figure 6.46 containing experimental and computed steady sate polarisation values shows the same qualitative behaviour as observed for lower pressure using the same pump transition: computations performed for $\Gamma_{\mathrm{R}} = \Gamma_{\mathrm{D}}$ lie above experimental data, and experimental M_{eq}-values do not further increase with increasing pump laser power above approximately 0.75 W. The relative difference between measured and

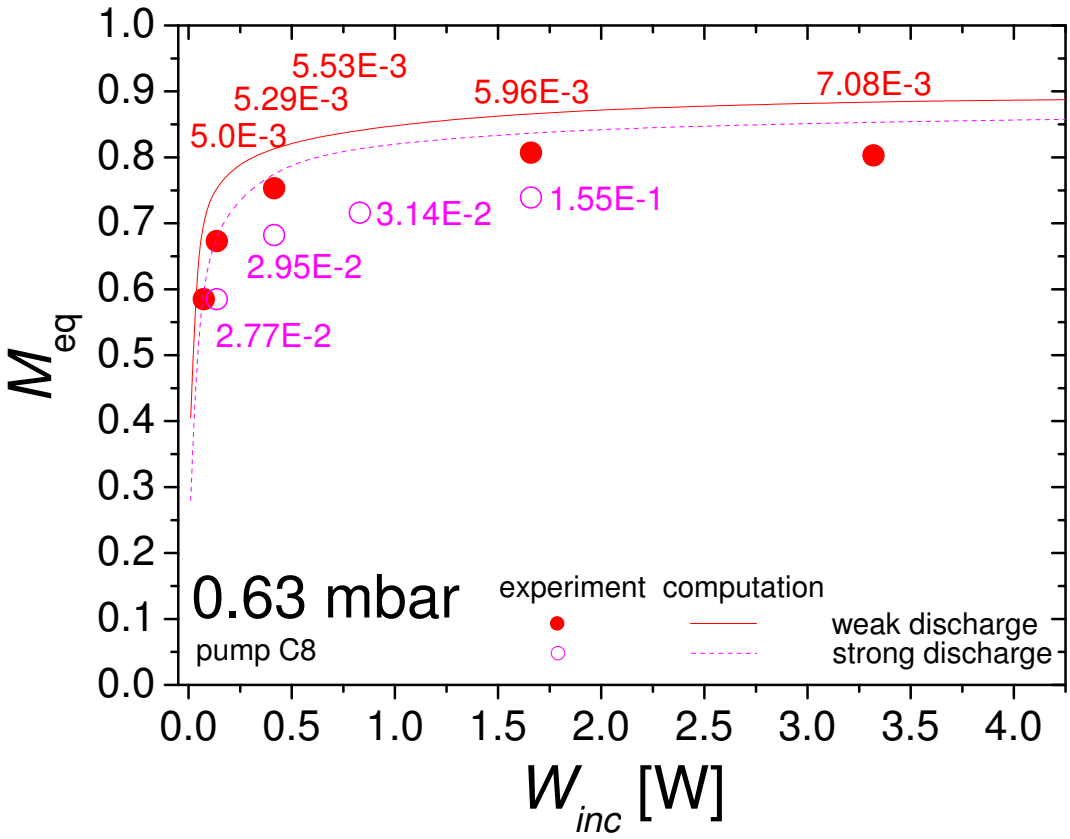

Figure 6.45: Steady state polarisation at $p_3 = 0.63$ mbar, pump and probe C_8 and $B = 1$ mT as function of incident pump laser power: Experiments (symbols) and computations (lines). Labels of data points indicate the total OP-enhanced relaxation rates Γ_R (in s^{-1}) that would be needed as input parameter in the OP model in order to obtain agreement between experimental and computed M_{eq}-values. Two different discharges are represented: weak discharge (filled symbols/solid line): $\Gamma_D = (350s)^{-1} = 2.86 \times 10^{-3}\,s^{-1}$, and strong discharge (open symbols/dashes line): $\Gamma_D = (70\,s)^{-1} = 1.42 \times 10^{-2}\,s^{-1}$. Other parameters of discharges: see caption of figure 6.32, radial n_m-parameter α used for computations: 2.1 (both discharges). Experimental errors are of the same order as the size of the symbols and therefore not plotted.

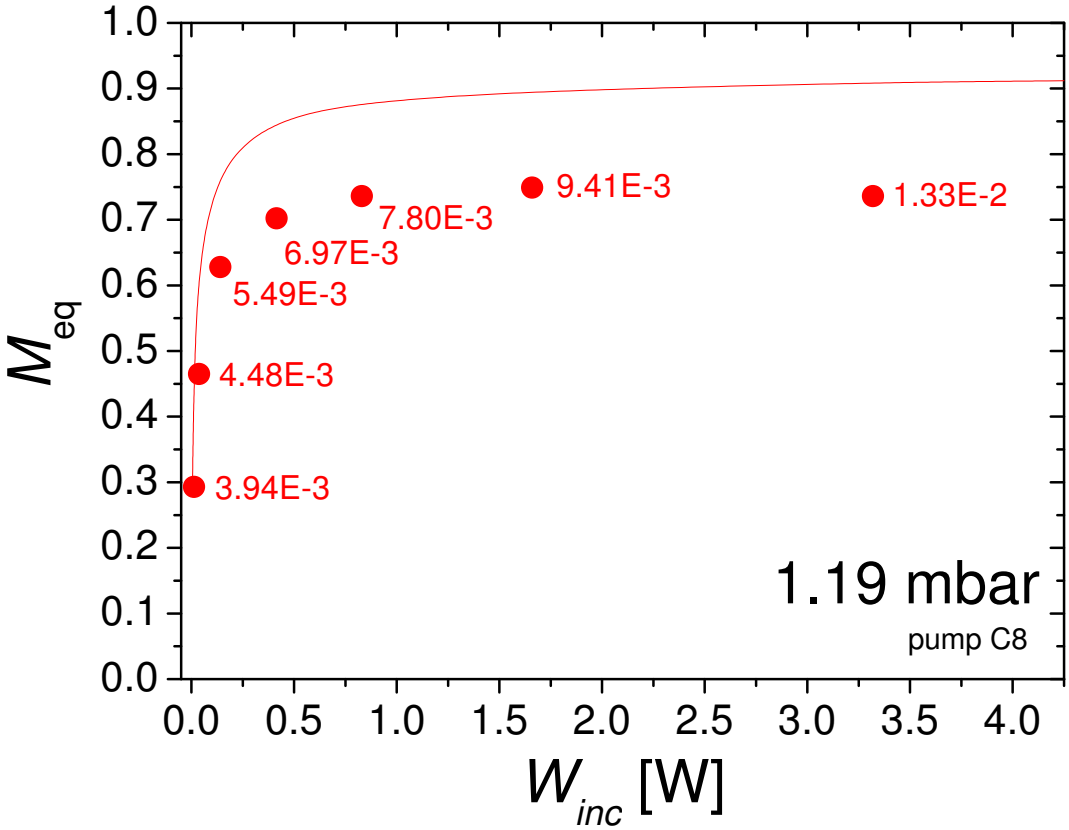

Figure 6.46: Steady state polarisation at $p_3 = 1.19$ mbar, pump and probe C_8 and $B = 1$ mT as function of incident pump laser power: Experiments (filled symbols) and computations (solid line). Labels of data points indicate the total OP-enhanced relaxation rates Γ_R (in s^{-1}) that would be needed as input parameter in the OP model in order to obtain agreement between experimental and computed M_{eq}-values. Parameters of the weak discharge: $\Gamma_D = (550\,s)^{-1} = 1.82 \times 10^{-3}\,s^{-1}$, $n_m^S(M = 0) = 1.6 \times 10^{16}$ atoms/m^3, $\alpha = 2$. $1/\gamma_r^P$ (1.19 mbar): 2.57×10^{-7} s. Experimental errors are of the same order as the size of the symbols and therefore not plotted.

computed M_{eq}-values ranges between 19.5 and 61 % at these OP conditions.
As in lower pressure, required Γ_{R} rates are higher than measured Γ_{D} decay rates, and they increase with W_{inc}. At the highest incident pump laser power of 3.32 W in this case, Γ_{R} exceeds Γ_{D} by almost one order in magnitude.

Figure 6.47 represents comparisons of experimental and computed steady state polarisation values for a different pump transition (C_9) and higher pressure (2.45 mbar).
All observations from previous examples at lower pressures are confirmed at $p_3 = 2.45$ mbar. At this pressure, the C_9 pump transition is known to yield higher M_{eq}-values than C_8. This is confirmed by our measurements and the reason for choosing C_9 here. The relative differences between computed and measured steady state polarisation values in these OP-conditions are higher than at lower pressures.
(In chapter 5.7, M_{eq}-values obtained by pumping on C_9 at lower n_{m} and identical pressure are presented in figure 5.17 exhibiting the same qualitative features).

Another common observation for all three pressure-values not commented so far is the following different behaviour between experiments and computations: While experimental M_{eq}-values are almost constant or even slightly decreasing towards higher W_{inc}, described by the expression "M_{eq}-plateau" above, computations keep slightly increasing at higher W_{inc}. This difference could tentatively be explained by the use of 100 % σ^+-polarised light in the computations whereas in experiments, this assumption is difficult to realise due to the non-perfect quality of the cell-windows, and a small fraction of σ^--light ($\lesssim 5$ ‰) is very probable. However, very poorly polarised light (9 % of σ^-) would be needed to account for such behaviour with a degree of σ^- polarisation varying with laser power and with chosen OP line. This is highly *im*probable.

The most important common observation for all three pressure values is the systematic discrepancy between experimental steady state polarisation values on the one hand and computed M_{eq}-values by the OP-model using measured decay rates Γ_{D} on the other hand.
This systematic discrepancy constitutes a strong evidence of laser-enhanced relaxation during polarisation build-up. Dependencies of Γ_{R} on relevant OP quantities will be discussed in detail in section 6.3.4.

Steady state polarisation M_{eq} and positioning with respect to other works

Before characterising laser-enhanced relaxation in more detail in the next paragraph, we first compile experimentally measured values of steady-state polarisation

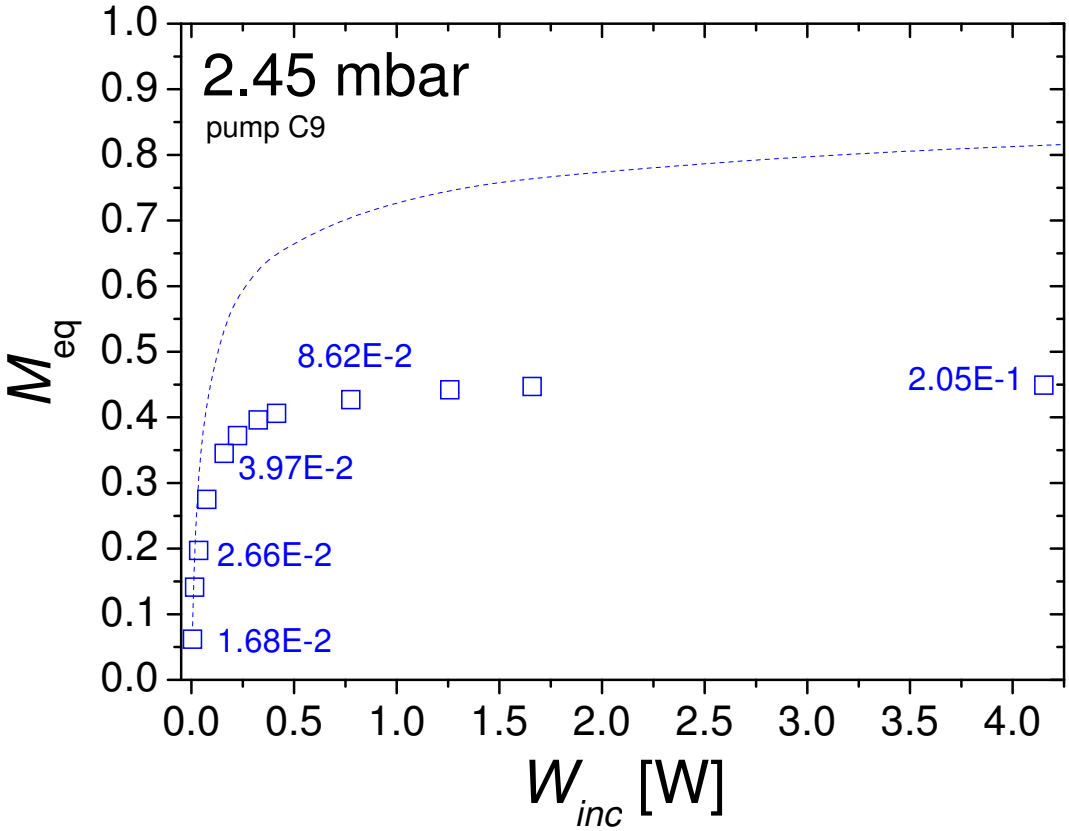

Figure 6.47: Steady state polarisation at $p_3 = 2.45$ mbar, pump C_9, probe C_8 and $B = 1$ mT as function of incident pump laser power: Experiments (open symbols) and computations (dashed line). Labels at selected data points indicate the total OP enhanced relaxation rates Γ_R (in s^{-1}) that would be needed as input parameter in the OP model in order to obtain agreement between experimental and computed M_{eq}-values. Strong discharge: $\Gamma_D = (77\,s)^{-1} = 1.30 \times 10^{-2}\,s^{-1}$. Other discharge parameters: see caption of figure 6.35, radial n_m-parameter α used for computations: 1.2. Experimental errors are of the same order as the size of the symbols and therefore not plotted.

from different groups performing MEOP of ^{3}He. In figure 6.48, M_{eq}-values are presented as function of pressure, mainly at low magnetic field (1-3 mT) with some additional points from the present work at $B = 30$ mT. Obtained results of steady state polarisation at higher B are not the main focus of this work and therefore not discussed here. They are presented for example in [Abb04] at 1.5 T, and in [Nik07] up to 2 T.

Almost all of the presented steady-state polarisation values in figure 6.48 are

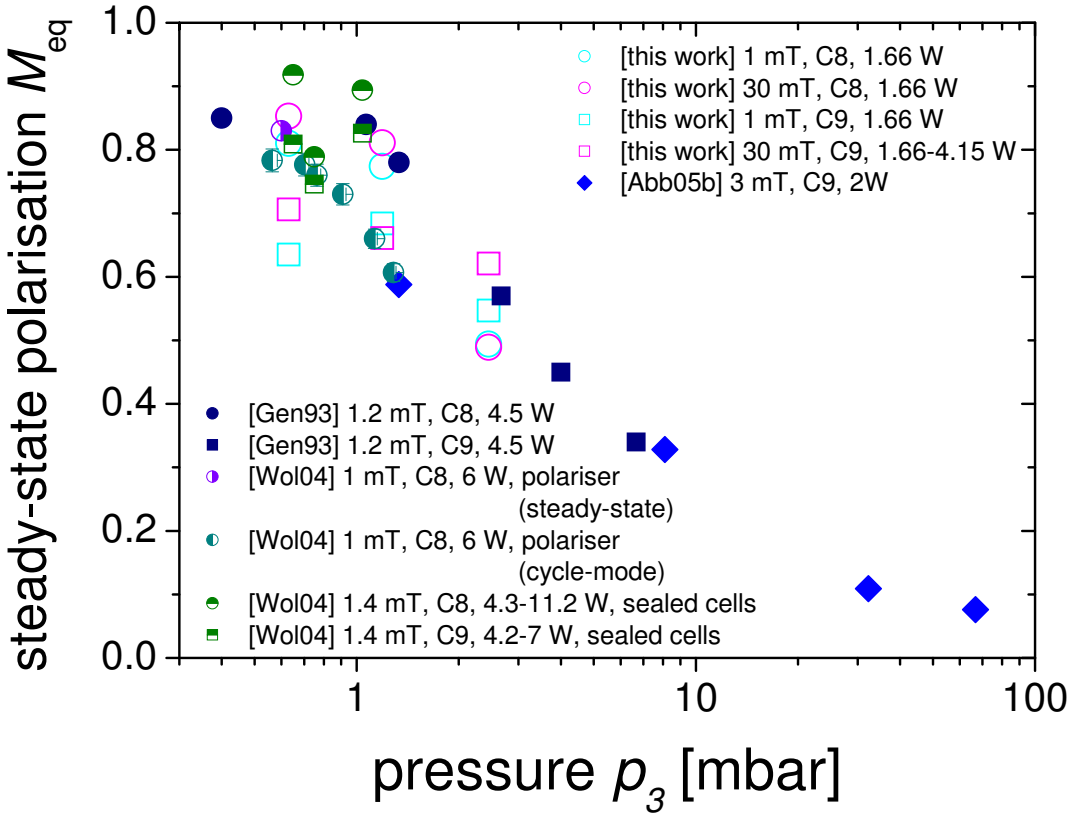

Figure 6.48: Experimental steady-state polarisation values M_{eq} as function of ^{3}He-pressure p_3 at magnetic fields between 1 and 30 mT, for different pumping transitions and incident pump laser powers (details and references: see legend, cell geometries are mentioned in the text).

obtained in sealed cells with different cell geometries: the quartz cells with uncoated cell windows used in this work have an inner diameter of 5.6 cm (0.63 mbar- and 1.13 mbar-cells) or 5.4 cm (2.45 mbar-cell) and an inner length of 29.4 or 29.1 cm respectively, and are presented in detail in chapter 3.1. Shorter cylindrical Pyrex cells with uncoated windows are used in [Abb05b] (inner length and diameter: both 4.6 cm) and in [Gen93] (inner diameter: 4.7 cm, length: 5.4 cm). In [Wol04], different

long cylindrical cells of outer diameter 5 cm are used. $p_3 = 0.65$ mbar: outer length 99 cm, each quartz window is anti-reflex-coated on both sides; $p_3 = 0.75$ mbar: outer length 80 cm, on both sides anti-reflex-coated quartz windows, remaining impurities visible in discharge spectrum; $p_3 = 1.04$ mbar: outer length 99 cm, uncoated Pyrex windows (Borofloat).
The only datasets with influences of cell configuration on M_{eq} are the vertically half-filled circles: These data stem from the open cell system of a polariser which can be unfavourable in terms of gas purity. One data-point at 0.6 mbar (open on left half) is obtained in steady-state conditions, the other points at different p_3-values (open on right half) are obtained in slow cycle-mode (time for one cycle: 40 s). This cycle-mode is described in detail in [Wol04], the only aspects that are important for our considerations are the following: During cycle-mode, the gas remains in an OP-cell for a predefined duration (no gas-flow during polarisation build-up), and is sucked out for compression before having reached M_{eq} in most cases in order to optimise production rates. The represented data of this type are mean values of the last three cells of the polariser with an inner diameter of 5.4 cm and an outer length of 240 cm, and are all approximately 5 % lower than the obtainable steady-state polarisation value (see comparison to the mentioned M_{eq}-value obtained in the same system).
The presented steady state polarisation values in figure 6.48 are measured by different methods: In [Abb05b] and this work, measurements of probe absorption in longitudinal configuration were used to precisely determine M_{eq}. Additionally, a calibrated NMR setup came into operation in [Abb05b].
In [Gen93] discharge polarimetry was employed, based on the principle of using a rotating quarterwave plate to determine the degree of circular polarisation of 668 nm-light emitted by the discharge described in [Pav70]. The degree of circular polarisation of the emitted light has been calibrated by means of NMR reported in [Lor93].
The data compiled in [Wol04] were also measured by discharge polarimetry based on the principle of [Pav70]. The pressure-dependent scaling factor between nuclear polarisation in the ground state and the degree of circular polarisation of the 668 nm-light emitted by the discharge has been parametrised based on a fit of experimental data given in [Lor93].
Calibration has been performed using a linear polariser and a quarterwave plate for 668 nm in order to obtain 100 % of circular polarisation of the emitted fluorescence light by the discharge. The fact that used optical elements in this calibration process are not ideal (especially when using a plastic quarterwave plate) has been taken into account in [Wol04] by estimating the degree of circular polarisation during calibration to 98 %.
Data measured by discharge polarimetry in the open system of the polariser (vertically half-filled circles) have once been compared to measurements of nuclear

^{3}He polarisation by neutron transmission at a reactor [Sch04], based on measurement principles described in [Sur97]. These comparison measurements that required transport of the polarised gas between the two sites (polariser and reactor) showed that both methods to infer nuclear polarisation of ^{3}He gas are compatible within experimental error bars. However, these comparison measurements revealed that relaxation (taking into account wall-relaxation of the glass cell and gradient-relaxation due to inhomogeneities in the magnetic transport field) was underestimated by 2-3 % (possibly additional polarisation losses during transport).
Such calibration measurements of discharge polarimetry against a second method to infer nuclear ^{3}He polarisation have not been performed on the data in sealed cells in [Wol04] (horizontally half-filled symbols). Furthermore, it is not explicitly mentioned in [Sch04] and [Wol04] that further corrections for various experimental imperfections as given by [Big92] were taken into account. In the experimental conditions of [Big92], the three main contributions to corrections, namely the imperfections in the optical components of the polarimeter, a finite solid angle in the detection of the 668 nm-line, and a non-zero magnetic field result in a 3 % *de*crease of the ratio of nuclear polarisation divided by the degree of circular polarisation of the emitted 668 nm-light.
These methodological differences in the compiled data of figure 6.48 have to be taken into account when drawing conclusions concerning the comparison of absolute M_{eq}-values.

A general observation in figure 6.48 is the following: obtainable steady-state polarisation values M_{eq} clearly decrease with increasing ^{3}He-pressure, which demonstrates that in low magnetic field, OP is less efficient at high pressure. One reason for this observation is the fact that the metastable density reaches a limit when p_3 increases due to the formation of molecules and due to Penning collisions [Nac02]. These processes limiting n_{m} are described in detail in subsections 6.1.1 and6.1.3.
Furthermore, figure 6.48 shows that at low pressure, below approximately 1.5 mbar, the C_8-transition yields higher M_{eq}-values, and at higher pressure, above approximately 2.5 mbar, higher M_{eq}-values can be reached by pumping on the C_9-transition as expected. In the intermediate pressure range between roughly 1.5 and 2.5 mbar, both transitions yield similar steady state polarisation values (no experimental data shown here).
A comparison of data at 1 and 30 mT from this work indicates that at least equivalent steady state polarisations within experimental error bars are obtained in both magnetic fields. In most cases, higher M_{eq}-values (up to 13 %) are reached at 30 mT. This aspect is not the main focus here though: the effect of magnetic field on OP performances is discussed in section 6.4.
In a more detailed comparison of steady state polarisation values from different works, we do not consider two data-sets from [Wol04]: polariser data in cycle mode

(half-filled circles, open on right half), as M_{eq} is not obtained, and data from sealed cells at $p_3 = 0.75$ mbar because of remaining impurities, both issues are described in more detail above.
For C_8-data at low pressure, up to approximately 1.5 mbar, [Gen93], this work and M_{eq}-polariser data from [Wol04] are in good agreement (less than 5 % of relative difference). M_{eq}-values on C_8 from sealed cells in [Wol04] are between 5 and 10 % above those of [Gen93] and our work in this low-pressure range ([Abb05b] does not contain results on C_8).
On the C_9-transition below 1.5 mbar, relative discrepancies of 10-25 % between data from [Abb05b], this work and [Wol04] are observed. These higher values of relative discrepancies on M_{eq}-values reached on C_9 compared to C_8 in the same pressure range, might be an indication of different degrees of the wrong circular polarisation component in the different optical setups. A small fraction of light with wrong polarisation component, as possibly introduced by birefringent cell windows for example, has a higher impact on C_9 compared to C_8.
At higher pressure, above 2.5 mbar, M_{eq}-values obtained on the C_9-transition from [Abb05b], [Gen93] and this work are in accordance within better than 5 % of relative difference where data at similar pressure values exist. Towards higher pressure-values, the work of [Gen93] contains C_9-data up to roughly 7 mbar, and [Abb05b] covers the whole range up to approximately 70 mbar. Data of both references complement each other quite well and constitute an almost continuous data-set.

In conclusion, the obtained experimental M_{eq}-values of the present work are consistent with other works, with [Gen93] and [Abb05b] in particular. Observed differences between different works are by far smaller than discrepancies that became manifest in comparisons between experimental and computed M_{eq}-values, in figures 6.45, 6.46 and 6.47 for example. Since M_{eq}-values of this work fit in with other works, the latter discrepancies, that amount up to 75 % in the given experimental conditions of this work at 2.45 mbar, *cannot* be imputed to specific experimental difficulties of our setup.
These discrepancies are an indication of a more general issue during polarisation build-up in presence of the pump laser in MEOP of ^{3}He, and are investigated in more detail in the next paragraph at M_{eq}, and as function of M in the following subsection 6.3.4.

Total relaxation rate Γ_{R} at steady-state polarisation

In the case of OP on the C_8 line, the angular momentum budget approach of section 5.7.2 relating the total relaxation rate Γ_{R} introduced in equation (2.77) to directly measured quantities provides a model-independent and parameter-free approach to evaluate Γ_{R} during polarisation build-up (using equation (2.81), results are presented in the next subsection 6.3.4) and at steady-state polarisation (using equation (2.82)). Selected results of inferred total relaxation rates at M_{eq} are presented in the following.

Data of total relaxation rates for OP on C_8 represented in the left graph of figure 6.49

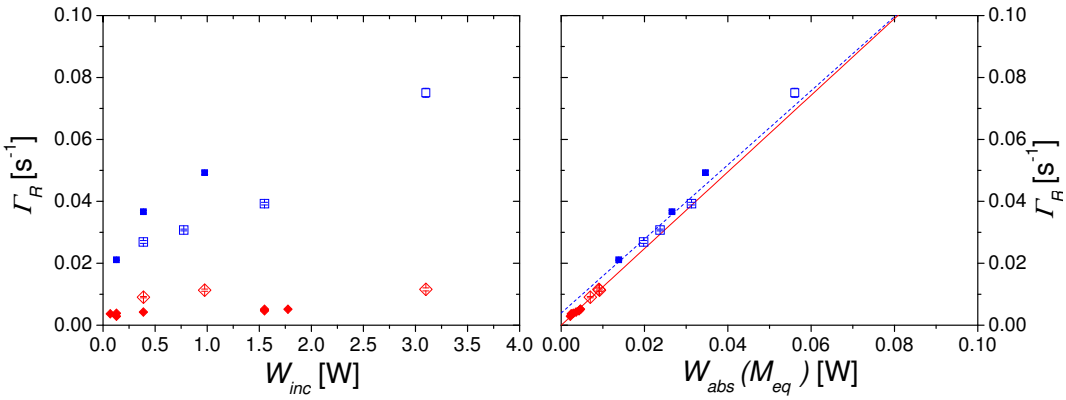

Figure 6.49: Total relaxation rate Γ_{R} at steady state polarisation M_{eq} at $p_3 = 0.63$ mbar, $B = 1$ mT and OP on C_8 as function of incident (left) and absorbed laser power (right). Open symbols: recently reanalysed data (including pump transmission coefficients at $M = 0$ and M_{eq} with corresponding errors, furthermore, uncertainties of W_{inc}, M_{eq} and $\dot{M}(M_{\mathrm{eq}})$), filled symbols: data from standard analysis. Plotted errors in this graph only take into account individual errors. (Red) diamonds: weak discharge: $n_{\mathrm{m}}^{\mathrm{S}}(M = 0) = 1.1 \times 10^{16}$ atoms/m^3, $\Gamma_{\mathrm{D}}^{w} = 0.003$ s^{-1}, solid (red) line: linear fit of weak discharge data, (blue) squares: strong discharge: $n_{\mathrm{m}}^{\mathrm{S}}(M = 0) = 3.3 \times 10^{16}$ atoms/m^3, $\Gamma_{\mathrm{D}}^{s} = 0.014$ s^{-1}, dashed (blue) line: linear fit of strong discharge data.

as function of incident pump laser power exceed measured decay rates in absence of OP by at least 45 %, except at very low W_{inc}. These directly inferred Γ_{R}-values do not yield any regular pattern.

However, when plotted as function of absorbed laser power, a regular structure emerges, Γ_{R}-data nicely 'collapse' and are observed to vary linearly with absorbed laser power in a given cell volume. Points recorded at a given discharge form groups, one below approximately 0.012 W of absorbed laser power here and one above this value of W_{abs}. Data of given discharge can be fitted by a linear function ($\Gamma_{\mathrm{R}} = \Gamma_{\mathrm{D}} + \kappa W_{\mathrm{abs}} = \Gamma_{\mathrm{D}} + \Gamma_{\mathrm{L}}$). These fit functions yield slightly different slopes for

different discharges, and especially different offsets (of the same order of magnitude as the respective measured decay rate). This behaviour can be clearly observed on the right graph of figure 6.49.
In most cases, the extracted offset by the linear fit is compatible with the experimentally measured decay rate Γ_{D}. When repeating linear fits on a given dataset with different fixed offset-values (e.g. 'initially extracted offset - error' and 'initially extracted offset + error'), the resulting slope only changes by approximately 0.5 to 2 %. The slope κ in these kind of graphs - representing the *increase* of total relaxation rates Γ_{R} as function of absorbed pump laser power - is thus a quite robust and reliable fit parameter.

Since a broad range of absorbed laser powers between 1×10^{-3} and 1 W is investigated in this work, we choose in the following to represent all results of relaxation rates using logarithmic scales on both axes, of abscissae and ordinates.

In figure 6.50, directly inferred total relaxation rates for OP on C_8 in weak discharges at all three investigated pressure-values are shown as function of incident and of absorbed laser power.
As it was the case in figure 6.49 for data obtained with different discharge intensities, the scatter of results from different cells here is reduced when rates are plotted versus absorbed pump laser power. Γ_{R}-values collapse and qualitatively show an unambiguous behaviour: Total relaxation rates are proportional to absorbed pump laser power in a given cell volume and exceed decay rates in most of the cases except at very low laser power. At $p_3 = 2.45$ mbar for example, the highest measured Γ_{R}-value of almost 0.1 s^{-1} exceeds the decay rate by a factor of approximately 80.
W_{abs} is thus a more adequate parameter as function of which relaxation rates are chosen to be plotted in the rest of this chapter.

When comparing Γ_{R}-values of different cells, their potentially different geometries have to be taken into account due the following arguments: The length of the cell has an influence on absorbed laser power, which is thus an extensive parameter. The diameter of the cell also possibly affects overall relaxation: e.g. at given pressure, fixed beam diameter and given cell length, absorbed laser power is constant in different cells, but effects of relaxation are possibly different depending on the overall number of atoms inside the cell (varying with cell volume) including atoms that do not interact with the laser beam.
In order to represent only intensive properties, i.e. scale invariant parameters, it appears therefore important to scale measured values of absorbed laser power with the cell volumes (i.e. to plot total relaxation rates as function of the *ratio* W_{abs} / V_{c}) in case Γ_{R}-values of cells with *different* volumes are compared.
This volume scaling will turn out to be important for the comparison to other exper-

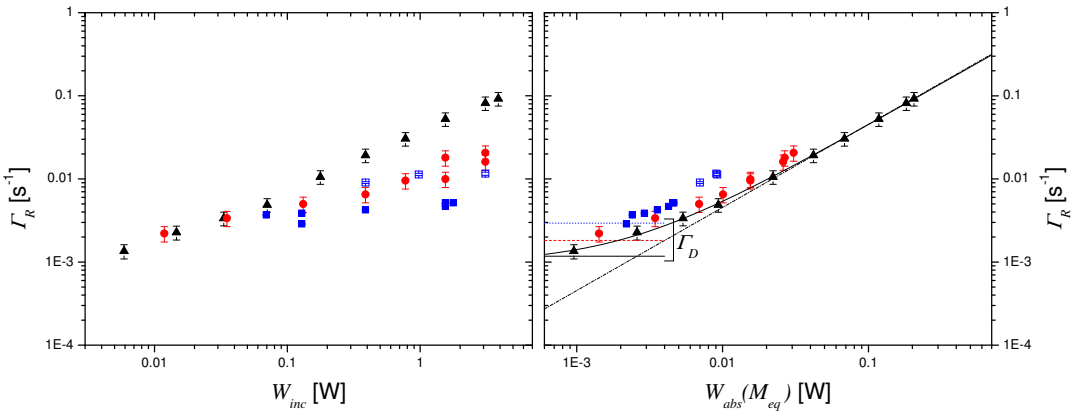

Figure 6.50: Total relaxation rate Γ_R at steady state polarisation M_eq, $B = 1$ mT and OP on C_8 for three different pressure values as function of W_inc (left) and W_abs (right). Only data of weak discharges are taken into account. (Blue) squares: 0.63 mbar, open/filled symbols and discharge parameters: see legend of figure 6.49; (red) circles: 1.19 mbar, $n_\mathrm{m}^\mathrm{S}(M = 0) = 1.56 \times 10^{16}$ atoms/m^3, $\Gamma_\mathrm{D}^w = 1.8 \times 10^{-3}$ s^{-1}; (black) triangles: 2.45 mbar, $n_\mathrm{m}^\mathrm{S}(M = 0) = 1.7 \times 10^{16}$ atoms/m^3, $\Gamma_\mathrm{D}^w = 1.2 \times 10^{-3}$ s^{-1}. In the right graph, the three short horizontal lines indicate these Γ_D-values: solid line: 2.45 mbar, dashed line: 1.19 mbar, dotted line: 0.63 mbar. The curved solid-line is a linear fit with offset through all 2.45 mbar-data points (details see text), the dash-dotted line ($y = x/2.2$) is a guide for the eye.

imental data obtained in cells of very different shapes and volumes (section 6.5.1). However, for this work, all 3 cells have almost identical dimensions (cf. table 3.1) and the scaling is not applied for simplicity, relaxation data are plotted as function of W_{abs}.

At low values of absorbed laser power, another characteristic behaviour of total relaxation rates can be observed in the left graph of figure 6.50 for all three pressure values: At low W_{abs}, Γ_{R}-values depart from the proportionality to W_{abs} in a given cell volume and seem to turn up towards a value close to the respective decay rate Γ_{D}. This behaviour is confirmed by the fit of Γ_{R}-values at 2.45 mbar: The chosen fit function is simply a linear function with slope and offset, similar to those represented in the right graph (with linear axes) of figure 6.49 for 0.63 mbar. In this linear representation it can easily been seen that linear fit functions are used. They appear to turn up towards an offset at low W_{abs} in logarithmic representation as chosen in figure 6.50. Of course, extracted offsets are different for data recorded in different discharge conditions as shown in figure 6.49.
A guide for the eye ($y = x/2.2$) using the extracted slope of the shown linear fit of 2.45 mbar-data in figure 6.50 will be kept in further figures throughout this chapter to situate and compare results of different graphs.

Additional OP-induced relaxation rate Γ_{L} at M_{eq}

In the next three graphs in figures 6.51, 6.52 and 6.53, differences between total relaxation rates Γ_{R}, inferred from directly measured quantities during polarisation build-up on the C_8-transition, and decay rates Γ_{D} are compiled for each pressure using the same guide for the eye everywhere in order to allow comparison between all data.

Plotting additional laser-induced relaxation rates Γ_{L} ($= \Gamma_{\mathrm{R}} - \Gamma_{\mathrm{D}}$ according to equation (5.20)) as function of absorbed pump laser power at fixed pressure and different metastable densities (figures 6.51, 6.52 and 6.53) improves the collapse of data already obtained in figure 6.49. In contrast to the observed behaviour of Γ_{R} at very low values of absorbed laser power that tend to turn up towards a value close to the respective Γ_{D}, Γ_{L} displays a linear dependency over the whole range of W_{abs}. Plotting Γ_{L} as function of absorbed pump laser power is thus an appropriate option to highlight and discuss the effect of laser-induced relaxation during polarisation build-up.

Comparing the extracted relaxation rates at the three different pressure values reveals that there is no clear pressure dependence. Although the common guide for the eye does not ideally fit data for all pressures, it describes reasonably well the general behaviour of Γ_{L}. The highest laser-induced relaxation rates are observed at

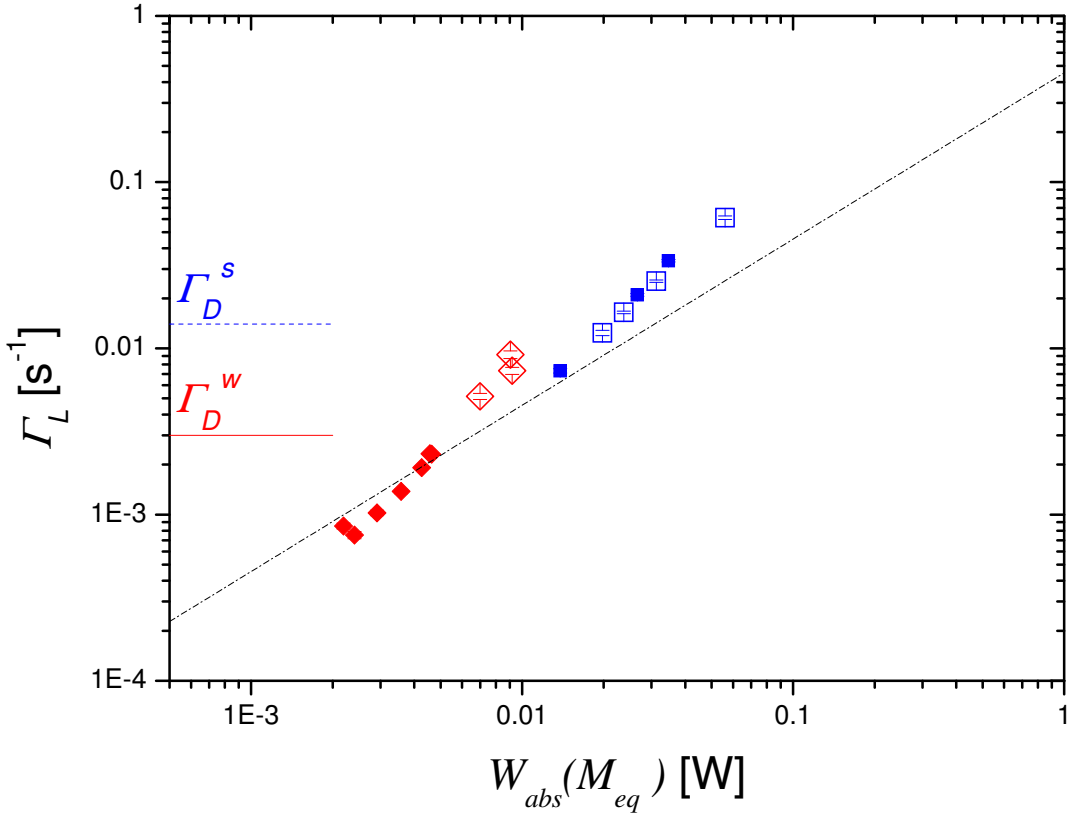

Figure 6.51: Difference between total relaxation rate Γ_R and decay rate Γ_D ($\Gamma_R - \Gamma_D = \Gamma_L$) at steady state polarisation M_{eq} at $p_3 = 0.63$ mbar, $B = 1$ mT and OP on C_8 as function of absorbed laser power. (Red) diamonds: weak discharge, (blue) squares: strong discharge, parameters see caption of figure 6.49. Open symbols: recent reanalysis of data (including pump transmission coefficients at $M = 0$ and M_{eq} with corresponding errors, furthermore, uncertainties of W_{inc}, M_{eq} and $\dot{M}(M_{eq})$); filled symbols: data from standard analysis. Plotted errors in this graph only take into account individual errors. Dash-dotted line: guide for the eye ($y = x/2.2$) from figure 6.50. Errors in x-direction on $W_{abs}(M_{eq})$ are observed to range between 0.5 and 3 % and are smaller than the symbol size in this logarithmic representation.

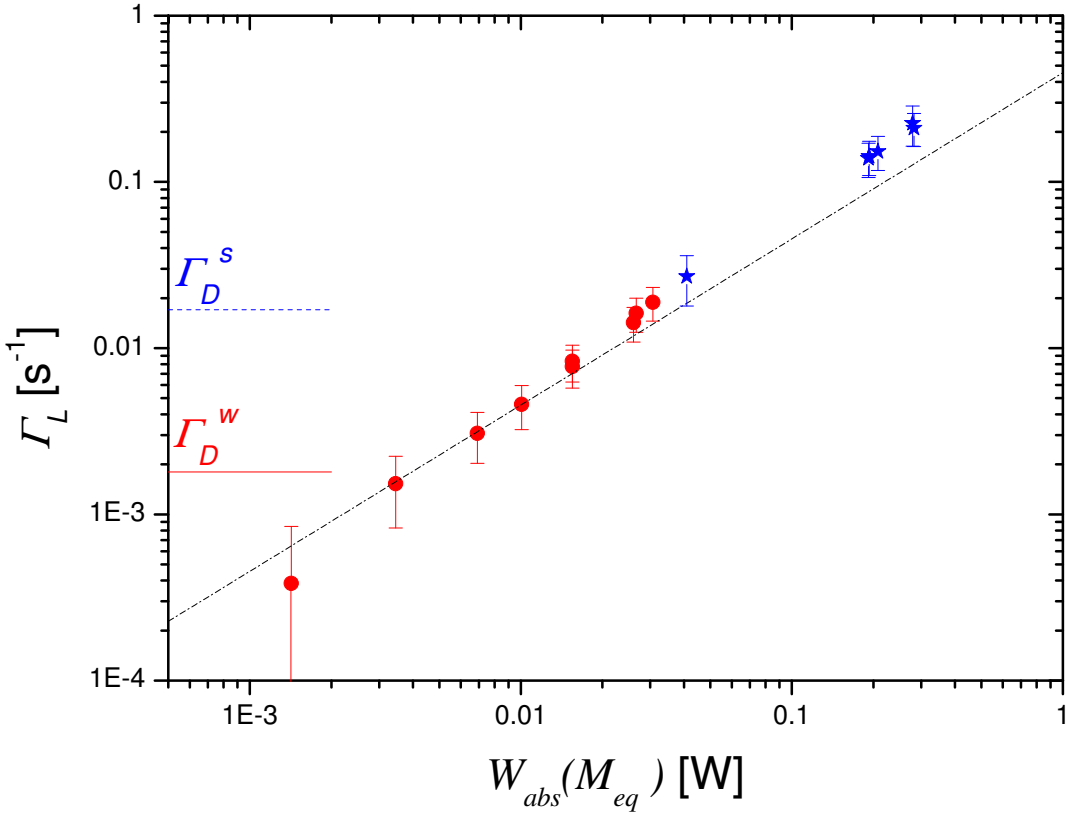

Figure 6.52: Difference between total relaxation rate Γ_R and decay rate Γ_D ($\Gamma_\mathrm{R} - \Gamma_\mathrm{D} = \Gamma_\mathrm{L}$) at steady state polarisation M_eq at $p_3 = 1.19$ mbar, $B = 1$ mT and OP on C_8 as function of absorbed laser power. (Red) circles: weak discharge (parameters see caption of figure 6.50), (blue) stars: strong discharge, $n_\mathrm{m}^\mathrm{S}(M = 0) = 5.7 \times 10^{16}$ atoms/m^3, $\Gamma_\mathrm{D}^s = 0.017$ s^{-1}. Dash-dotted line: guide for the eye ($y = x/2.2$) from figure 6.50. Errors in x-direction on $W_\mathrm{abs}(M_\mathrm{eq})$ are smaller than at 0.63 mbar due to higher SNR of the pump transmission coefficient at 1.19 mbar.

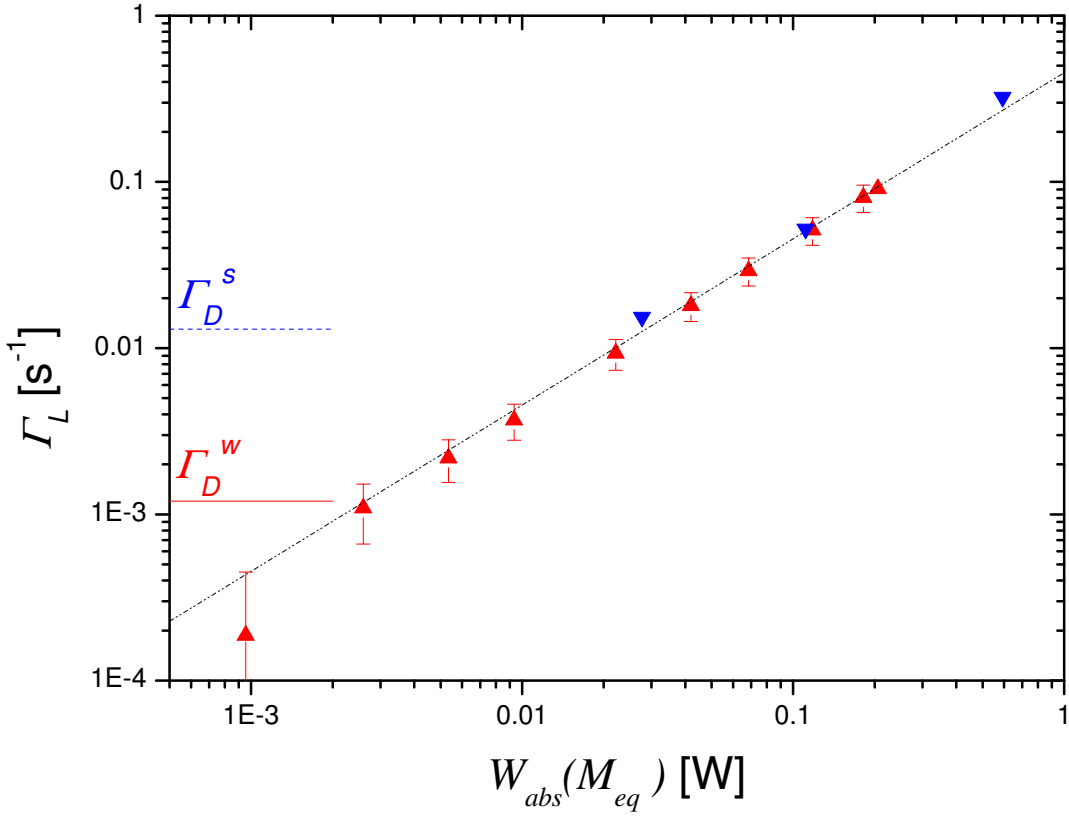

Figure 6.53: Difference between total relaxation rate Γ_R and decay rate Γ_D ($\Gamma_\mathrm{R} - \Gamma_\mathrm{D} = \Gamma_\mathrm{L}$) at steady state polarisation M_eq at $p_3 = 2.45$ mbar, $B = 1$ mT and OP on C_8 as function of absorbed laser power. (Red) triangles: weak discharge (parameters see caption of figure 6.50), (blue) downward triangles: strong discharge, $n_\mathrm{m}^\mathrm{S}(M = 0) = 4.15 \times 10^{16}$ atoms/m^3, $\Gamma_\mathrm{D}^s = 0.013$ s^{-1}. Dash-dotted line: guide for the eye ($y = x/2.2$) from figure 6.50. Errors in x-direction on $W_\mathrm{abs}(M_\mathrm{eq})$ are smaller than at 0.63 mbar due to higher SNR of the pump transmission coefficient at 2.45 mbar.

the highest investigated pressure value, coinciding with higher values of absorbed pump laser power with respect to low pressure. Measured decay rates in absence of OP for weak and strong discharge situations respectively are of the same order of magnitude for all investigated ^{3}He-pressures. Against this background, the following general tendency of maximum laser-induced relaxation rates Γ_{L} with respect to decay rates Γ_{D} for the three different pressure values appear plausible: At 0.63 mbar, maximum Γ_{L} exceeds Γ_{D} by a factor of 3 to 5, at 1.19 mbar, this factor amounts to roughly 10 to 13, and at 2.45 mbar, this excess factor ranges between 25 and 80, in accordance with pump absorption scaling.

All presented relaxation rates in this subsection 6.3.3 are steady state values, which means that M_{eq} as well as the lowest value of W_{abs} at the end of each polarisation build-up are reached. Hence, the presented Γ_{L}-values correspond only to the lowest point in W_{abs} within each complete build-up, but already exhibit a large influence on OP compared to measured decay rates in absence of OP. In order to investigate relaxation rates at higher absorbed pump laser power for given polarisation build-up experiments, entire OP kinetics are studied in the next subsection 6.3.4.

6.3.4 Results as function of M ($B = 1$ mT) and further characterisation of laser-induced relaxation

Before discussing extracted relaxation rates during entire polarisation build-up kinetics in different OP conditions, a comparison of independently analysed Γ_{L}-values at steady-state polarisation with the corresponding build-up experiments is presented in figure 6.54 for two examples at $p_3 = 0.63$ mbar.

In order to evaluate pros and cons of extracting relaxation rates during complete polarisation build-ups or only at steady-state polarisation M_{eq}, the main methodological differences should be clarified first (detailed independent descriptions of both methodological approaches are found in chapter 5.7).

The total relaxation rate Γ_R at steady state polarisation can be inferred from the expression: $\Gamma_R(M_{\mathrm{eq}}) = \left\langle \frac{\dot{M}(0)}{W_{\mathrm{nom}}\, A_0} \right\rangle \frac{W_{\mathrm{nom}}\, A_{\mathrm{eq}}}{M_{\mathrm{eq}}}$ (cf. equation (5.24)). The first term on the right hand side constitutes an error-weighted mean value at $M = 0$, proportional to the photon efficiency η, of several analysed experiments using C_8 as pumping transition at given pressure. This mean value has the advantage of containing individual errors (of $\dot{M}(0), W_{\mathrm{nom}}$ and A_0) only, the extracted value of $\Gamma_R(M_{\mathrm{eq}})$ itself does of course *not* depend on the choice of simplified or complete expression. For the routine analysis, the simplified expression is used throughout this work.

When the angular momentum approach for single-component transitions is applied

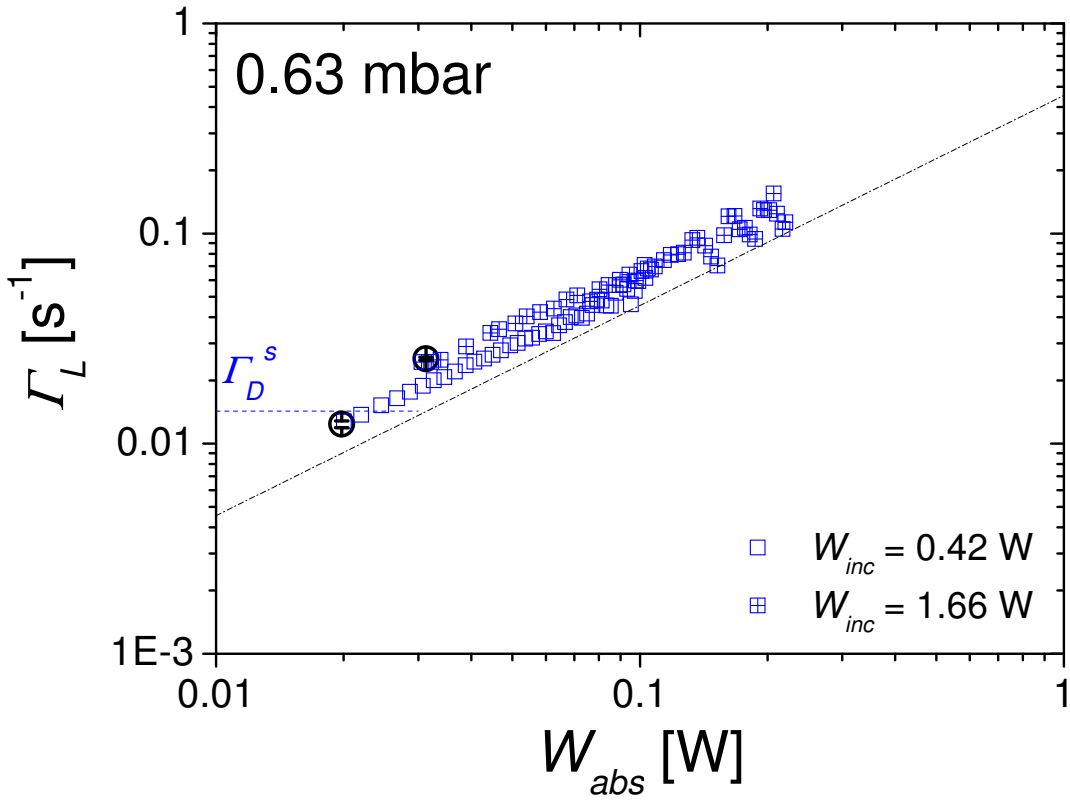

Figure 6.54: Comparison of Γ_L-values from polarisation build-up kinetics (open squares) and in steady state conditions (open circles) at $p_3 = 0.63$ mbar, $B = 1$ mT and OP on C_8 as function of absorbed laser power. Two kinetics at different incident pump laser powers (see legend) are shown, both recorded in strong discharge conditions: parameters see legend of figure 6.49. Dash-dotted line: guide for the eye ($y = x/2.2$) from figure 6.50.

to a complete recording of OP kinetics to directly infer total loss rates from the measured pump transmission coefficients and $\dot{M}(0)$ using equation (2.81) $\left(\Gamma_R(M) = \frac{\dot{M}(0)}{M}\,\frac{W_{\mathrm{abs}}(M)}{W_{\mathrm{abs}}(0)} - \frac{\dot{M}(M)}{M}\right)$, a time-dependent series of values for Γ_R, or the difference Γ_L after subtraction of measured decay rates Γ_{D}, is obtained that includes the value derived at M_{eq} as an end-point. Equation (2.81) only contains parameters of each individual experiment, both at $M = 0$ and as function of M.
In the first mentioned way of determining total relaxation rates at M_{eq} only, the mean value at $M = 0$ proportional to η tends to be more precise than the individual parameter used in each dynamic recording. In order to optimise the precision of relaxation rates during OP kinetics, it would also be possible to base the analysis on an error weighted mean value of several experiments at fixed pressure. From a practical point of view, less time is required to extract Γ_R at M_{eq} only. This merely yields information at the lowest value of absorbed pump laser power of a polarisation build-up, but higher accuracy can be obtained from signal averaging in steady-state. $\Gamma_R(M_{\mathrm{eq}})$-values might be more appropriate when an overview is required, e.g. in comparisons at different OP conditions as shown in the final discussion of laser-enhanced relaxation effects in section 6.5.
When the dynamic OP process is subject of the investigations, then the time- and thus polarisation-dependent series of values for Γ_R are more meaningful to describe their development during polarisation build-up, as well as to identify the maximum observable relaxation rate in given OP conditions at the highest value of absorbed pump laser power, right at the beginning of each polarisation build-up.

When comparing the two examples of time-dependent series of Γ_L-values presented in figure 6.54 with the independently extracted corresponding values at M_{eq}, the agreement at the end-points of the OP kinetics is satisfactory, slightly better at low incident pump laser power in this case. The relative discrepancy of approximately 3% in the case of higher incident pump laser power stems from the use of the individual $\dot{M}$ and T_p values at $M = 0$ in case the complete polarisation build-up is analysed instead of an error-weighted mean value proportional to η in case of the determination of $\Gamma_R(M_{\mathrm{eq}})$ as explained in the previous paragraph. The relative discrepancy observed in this case of a strong discharge at low pressure can be considered as an upper limit, as according to our experiences, T_p and $\dot{M}$ can be more accurately determined at higher pressure and weaker discharges.
In addition, figure 6.54 also shows that restricting the analysis to M_{eq} in all cases would impede us to assess the full influence of laser-enhanced polarisation effects that are of great importance during entire polarisation build-up dynamics.

In the following, the discussion of results concentrates on relaxation rates inferred from complete polarisation build-up dynamics. Figure 6.55 represents laser-induced

relaxation rates inferred from directly measured quantities only using the angular momentum approach for single-component transitions, for a selection of C_8-pumping experiments performed at various incident pump laser powers at all three values of ^{3}He-pressure.

Figure 6.55 shows that remarkably consistent sets of data are obtained when they

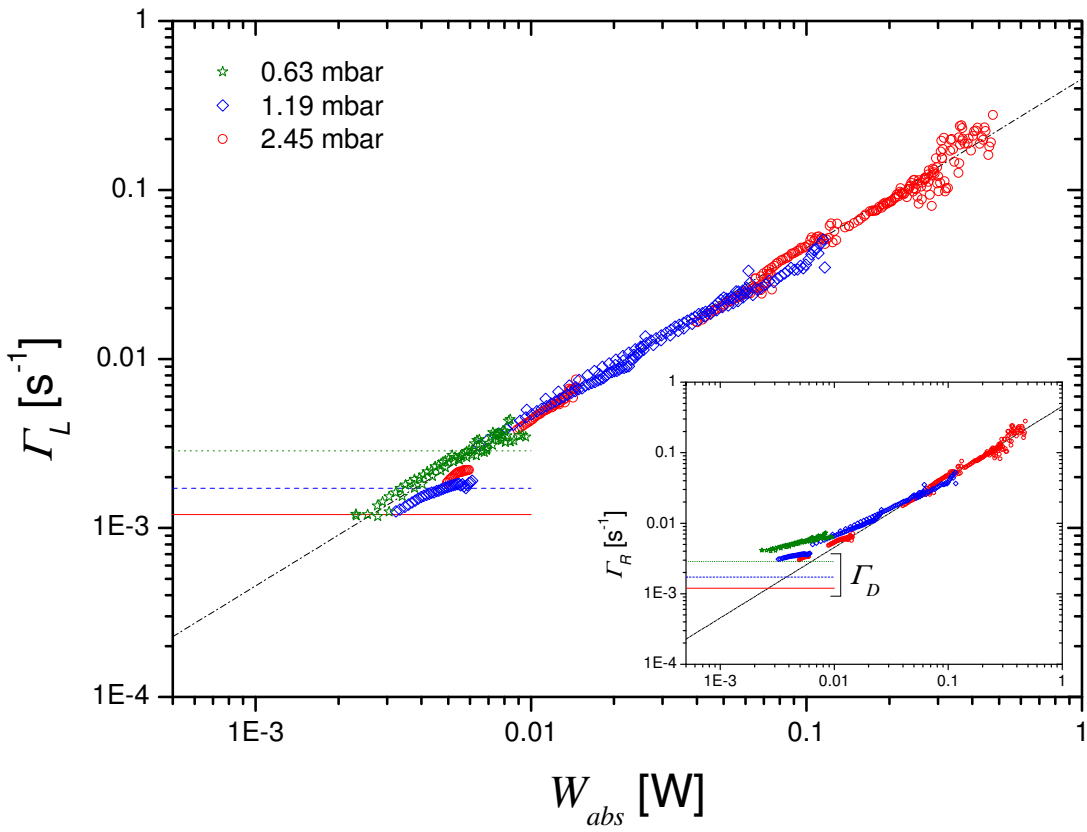

Figure 6.55: Examples of differences between experimental total polarisation loss rates Γ_R obtained from polarisation build-ups (using equation (2.81)) and decay rates Γ_D, measured during polarisation decays in absence of the pump laser ($\Gamma_R - \Gamma_D = \Gamma_L$), as function of absorbed OP power (C_8-pumping, $B = 1$ mT). The horizontal lines correspond to the measured Γ_D-values (all in weak discharges, parameters see caption of figures 6.49 and 6.50). Green stars and dotted line: 0.63 mbar; blue diamonds and dashed line: 1.19 mbar; red circles and solid line: 2.45 mbar. Dash-dotted line: guide for the eye ($y = x/2.2$) from figure 6.50. Inset (figure 17 from [Bat11]): Γ_R as function of W_{abs} (same data as in main graph).

are plotted as a function of the absorbed pump powers. The inset in the figure shows that at high absorbed pump powers, Γ_R data reveal a common behaviour and collapse to a line with Γ_R proportional to W_{abs} in a given cell volume. Under our

given experimental conditions, OP-enhanced relaxation rates reach values that are nearly a factor of 200 i.e., two orders of magnitude, above the respective decay rate Γ_D. At very low absorbed pump powers, Γ_R-data seem to split up into several groups, bending up from the common line at higher W_{abs} towards different values: Γ_R would indeed recover the respective Γ_D-values measured in each cell for the chosen weak rf discharge level.
This property of Γ_R at low W_{abs} disappears as expected when subtracting decay rates from total polarisation loss rates and plotting the differences $\Gamma_L = \Gamma_R - \Gamma_D$ as a function of absorbed pump power as in the main graph of figure 6.55. There is no noticeable pressure dependence in figure 6.55 over our investigated range of ^{3}He gas pressures and data show a consistent increase of Γ_L with the absorbed OP power. A closer look to the experimental data reveals minor systematic variations with pressure but relative changes in $\Gamma_L/(W_{abs}V_c)$ ratios at steady state polarisations, for instance, do not exceed 25 % as illustrated in figure 6.64.

Different values of W_{abs} in figure 6.55 are obtained by fixing the rf discharge level and varying the incident pump laser power. A second realised possibility to vary W_{abs}-values is to fix W_{inc} and to vary the rf discharge level and thus the metastable density. Hence, a given value of W_{abs} can be obtained by several combinations of W_{inc} and n_m, e.g. in a weak discharge at high W_{inc} and in intermediate or strong discharges at lower W_{inc}. Independently of the way a *given* value of absorbed pump power is obtained, the inferred OP-enhanced relaxation rates are *identical* (data not added in figure 6.55 for clearness). This has been checked at all three ^{3}He-pressures, and these verifications confirmed that OP-enhanced relaxation rates only depend on the overall value of absorbed pump power, and are independent of the combination of metastable density and incident pump laser power used to obtain this given value of W_{abs}.
A quantitative evaluation of the variation of the steady-state values of $\Gamma_L/(W_{abs}V_c)$ with 2^3S atom number density n_m^S is given in section 6.5.2, where selected results are provided in figure 6.64.

Laser-enhanced relaxation for C_9 OP

In order to provide a more complete view of results from our studies concerning OP-enhanced relaxation, further examples of relaxation rates obtained with the help of the model for MEOP-kinetics, also using multi-component transitions like C_9, are presented in the following and compared to directly obtained relaxation rates obtained by using the balance of angular momentum approach.
Figure 6.56 presents laser-induced relaxation rates obtained by the mentioned two different approaches at fixed pressure (p_3 = 2.45 mbar) and two different discharge

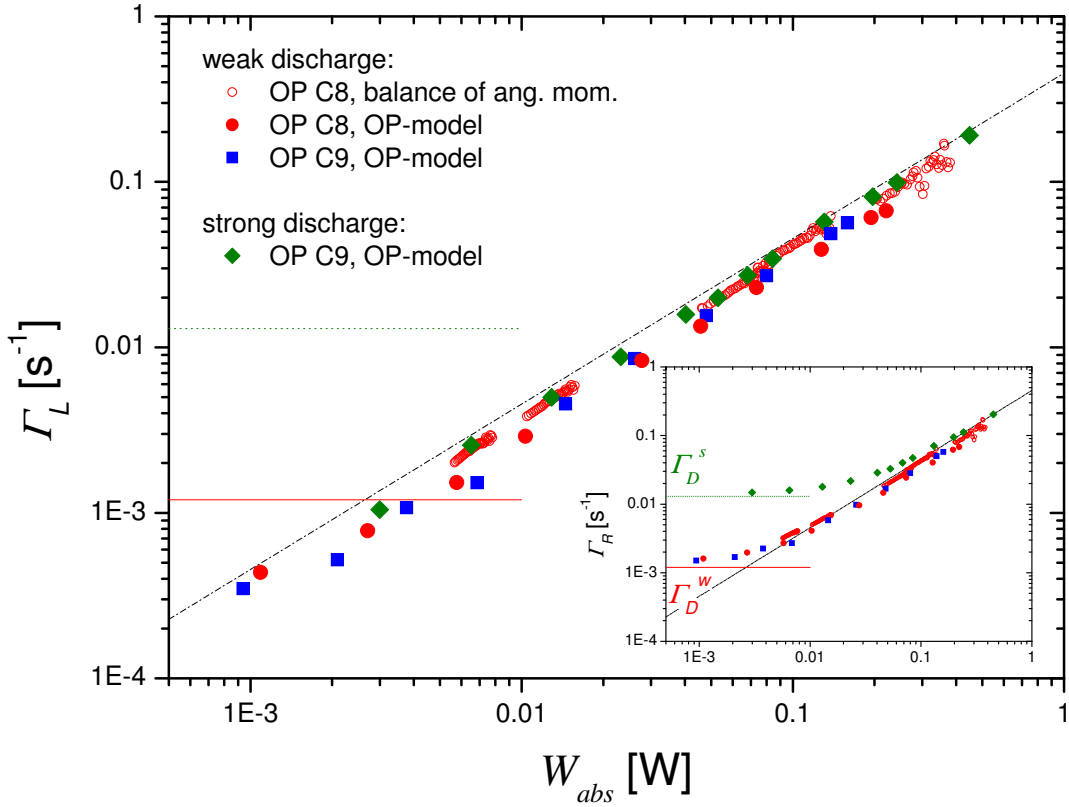

Figure 6.56: Differences between experimental total polarisation loss rates Γ_R and decay rates Γ_D ($\Gamma_R - \Gamma_D = \Gamma_L$) at $p_3 = 2.45$ mbar and $B = 1$ mT as function of absorbed OP power. Open red circles: OP on C_8, Γ_R directly inferred from balance of angular momentum. Filled symbols: Γ_R inferred using the model for MEOP-kinetics for OP on C_9 mainly, for two different rf discharge levels (blue squares: weak discharge and green diamonds: strong discharge), and on C_8 (red circles, weak discharge) for comparison with the direct approach, details see legend. The horizontal lines correspond to the measured Γ_D-values: red solid line: weak discharge: parameters see caption of figure 6.50, green dotted line: strong discharge: parameters see caption of figure 6.53. Dash-dotted line: guide for the eye ($y = x/2.2$) from figure 6.50. Inset: Γ_R as function of W_{abs} (same data as in main graph).

levels. The influence of decay rates is best discussed using the inset where the total OP-enhanced relaxation rate Γ_R is represented as a function of absorbed OP power. At low values of W_{abs}, Γ_R-rates obtained by using the model for MEOP-kinetics, for C_9-pumping at the strong discharge level and both transitions at the weak discharge level, also depart from the common line observed at higher values of W_{abs} and recover the respective Γ_D-values measured in absence of the pump laser at strong and weak discharge levels respectively. The same behaviour is observed for directly inferred total relaxation rates in the approach based on the balance of angular momentum, e.g. in figure 6.55 (inset). Here in the present figure, directly inferred Γ_R-values for C_8-pumping do not cover this range of very low absorbed pump powers.
Characteristics of OP-enhanced relaxation and comparisons of obtained values (with the help of both approaches for C_8-pumping and the model for MEOP-kinetics only for C_9-pumping) are best discussed using the main graph of figure 6.56 where $\Gamma_L = \Gamma_R - \Gamma_D$ is plotted to highlight the effect of laser-induced relaxation.

First, let us consider **C_8-data** (circles) only. The direct approach based on equation (2.81), containing only experimentally measured quantities, yields relaxation rates during complete build-up dynamics at five different values of incident pump laser power. The second approach based on the use of the model for MEOP-kinetics is mandatory for C_9-pumping as the photon efficiency η is not constant and changes with polarisation, and of course also applicable to OP on the C_8-transition. For simplicity, we only present results obtained using the MEOP model to infer Γ_L in experimental steady state conditions. This means that for C_8-pumping, a comparison of directly inferred Γ_L-rates at the end point of polarisation build-up kinetics with indirectly inferred Γ_L-values at M_{eq} of identical data sets is possible (not *all* data sets have been analysed in both ways). In the cases where both ways of analysis have been applied, the agreement between both approaches at M_{eq} is satisfactory given the approximations in the MEOP-model. The relative discrepancies between relaxation rates can probably in part be explained by differences between computed and measured η-values, and range between 10 and 30 %. However, these limited differences are negligible compared to a factor of approximately 10 to 100, depending on the discharge level, by which OP-induced relaxation rates exceed decay rates in absence of OP.

Second, in order to broaden the scope of this study, relaxation rates of multi-component **C_9-data** inferred with the help of the MEOP-model in the same **weak discharge** are discussed and compared to C_8-data. As expected, absorbed pump laser powers are different for C_8 and C_9 at given incident pump laser power (C_9 absorbs more than C_8 at $M = 0$, but less at high M), therefore, they do not have the same positions on the axis of abscissae. The values of Γ_L on the axis of ordinates however are of comparable size for both lines on the 2^3S_1 - 2^3P_0 transition and are consistently proportional to absorbed pump laser powers in a given cell volume.

As a third and last aspect concerning figure 6.56, the inferred laser-induced re-

laxation rates for **OP on C_9** at a **stronger rf discharge level** are reviewed. It could be reckoned with finding higher overall W_{abs}-values at this higher metastable density and comparable values of incident pump laser power, so that the range of abscissae can be expanded towards higher values of absorbed OP power. Extracted Γ_{L}-values fit in very well into the commonly observed proportional behaviour of OP-induced relaxation rates with respect to absorbed pump laser powers, also at higher values of W_{abs} in a given cell volume. The maximum observed Γ_{L}-rates still exceed Γ_{D}-rates by up to one order in magnitude.

To conclude this presentation of experimental results, either exploited independently or with the help of the model for MEOP-kinetics, it can be retained that laser-induced relaxation during polarisation build-up dynamics and in steady state constitutes a huge effect up to orders of magnitude higher than measured decay rates of polarisation in absence of OP. These high relaxation rates imply that deposited angular momentum by the pump laser cannot be entirely 'transformed' by the atomic system into stored angular momentum, i.e. polarised nuclei, thus limiting experimentally obtainable maximum nuclear polarisation values and also limiting OP performances in terms of production rates in gas polariser units for example.

6.4 Effects of magnetic field on OP performances

Effects of magnetic field on *plasma* are characterised in section 6.1, in the present section, we focus on *OP performances* in B up to 30 mT and discuss relevant measured OP quantities (M_{eq}, $\dot{M}$ and OP-induced relaxation rates during build-up Γ_{L}) in comparison to low field conditions.

In moderate magnetic fields between 0 and 30 mT, hf coupling and ME process are almost unaffected in the 2^3S-state. Higher excited states in the radiative cascade however are strongly decoupled above 10 mT [Pav70]. Therefore, angular momentum loss is reduced in the cascade, and subsequent reduced nuclear relaxation is expected to yield higher OP performances. This was our initial motivation to perform MEOP in $B = 1 - 30$ mT (cf. chapter 1). In the following, results are presented to check this expectation.

First, an overview of obtained steady state polarisation values at all 3 pressures on C_8 and C_9 transitions as function of metastable density at $M = 0$ is given in figure 6.57. Errors of M_{eq} and $n_{\mathrm{m}}^{\mathrm{S}}(0)$ (mean value of $n_{\mathrm{m}}(0)$ measured along the inclined probe beam path) are of the same order as the size of symbols.

When comparing the two transitions in figure 6.57, C_8 yields higher M_{eq} at low pres-

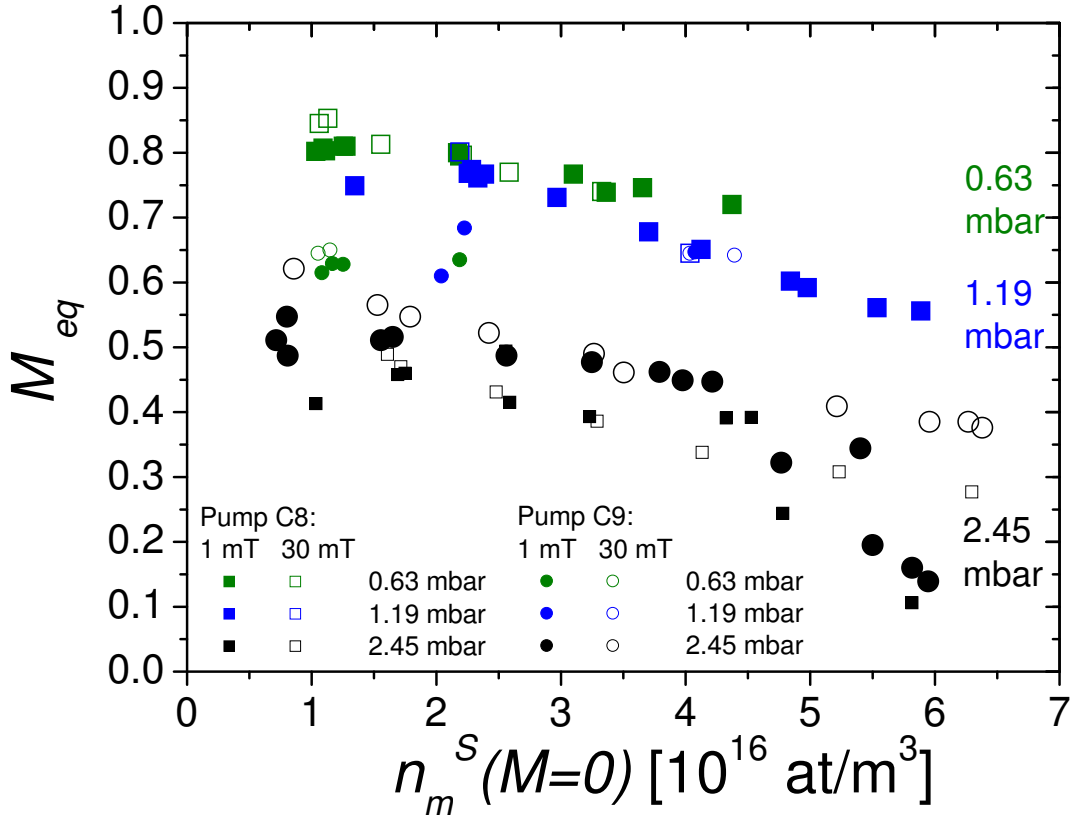

Figure 6.57: Steady state polarisation as function of metastable density $n_m^S(M=0)$ at fixed $W_{inc} = 1.66$ W at $B = 1$ mT (filled symbols) and $B = 30$ mT (open symbols). Squares: C_8 pump transition, circles: C_9 pump transition. Three values of ^{3}He pressure: Green symbols: 0.63 mbar, blue symbols: 1.19 mbar, black symbols: 2.45 mbar. For each pressure, data of the respective pumping line yielding highest M_{eq} values are represented by big symbols.

sure as expected, and at higher pressure, C_9 pumps best. At given electrode configuration, characteristic plasma parameters $n_m(0)$ and Γ_D usually change when increasing B from 1 to 30 mT, even when keeping the rf excitation voltage constant (by adjusting it to its initial value at 1 mT after having increased B to 30 mT). In most cases, higher $n_m(0)$ and shorter Γ_D are observed at 30 mT. As it is difficult to keep plasma parameters constant when increasing B at given rf excitation voltage, we chose here to plot M_{eq} as function of $n_m(0)$. M_{eq} values at 1 and 30 mT at identical $n_m(0)$ do not necessarily stem from the "same" discharge (= same excitation voltage).
At low metastable densities up to approximately 3×10^{16} atoms/m^3, the maximum obtainable M_{eq}-values at 30 mT are slightly higher than at 1 mT at all three investi-

gated pressures: 4-5 % at 0.63 and 1.19 mbar, 3-7 % at 2.45 mbar on C_8, and 6-12 % on C_9 at this highest investigated pressure. Thus on the C_9 line, similar M_{eq} values can be obtained at 2.45 mbar, 30 mT and 0.63 mbar, 1 mT.

At higher $n_m(0)$, no difference is observable between M_{eq} at 1 and 30 mT at lower pressure (0.63 and 1.19 mbar). At 2.45 mbar, there is also no significant difference observable in the intermediate $n_m(0)$ range (approximately between 3 and 4×10^{16} atoms/m^3), but in the higher $n_m(0)$ range, above roughly 4×10^{16} atoms/m^3, M_{eq}-values at 30 mT remain approximately at the same level, whereas at 1 mT, a break-in of M_{eq}-values in this high $n_m(0)$ range is observed. For C_8, M_{eq}(30 mT) exceeds M_{eq}(1 mT) by up to 30-50 % (20-37 % for C_9 respectively). Such increase of M_{eq} by a factor of up to 2 is only observed in some exceptional cases of very high $n_m(0)$ around 6×10^{16} atoms/m^3 and higher, where the decay time at 1 mT amounts to 1 s only, which is extremely unfavourable for build-up of polarisation. Obviously, this constitutes a different discharge regime that is not suitable to obtain high polarisations. At 30 mT, the decay time increases and is of order 80 s, higher obtained M_{eq} values are thus not surprising.

In the following, a more detailed investigation of 2.45 mbar data is presented, as most data were acquired at this pressure, and the effect of magnetic field on OP performances appears to be slightly higher than at lower pressure.

The time derivative of polarisation at $M = 0$ for C_8-pumping is examined next as a function of absorbed pump laser power in $B = 1$ and 30 mT. Figure 6.58 represents such data at 2.45 mbar for a weak rf discharge level with identical metastable densities at 1 and 30 mT.

This graph shows quantities that are of particular interest because the ratio of $\dot{M}(0)$ and $W_{abs}(0)$ is directly proportional to the photon efficiency at fixed pressure, cell-volume, temperature and transition frequency.

As expected at each magnetic field value separately, $\dot{M}(0)$ increases linearly with $W_{abs}(0)$. Furthermore, a comparison of both datasets and slopes reveals that the value of the photon efficiency on the C_8 transition remains unaffected and thus constant when increasing the magnetic field from 1 to 30 mT.

Another quantity that can be compared at different magnetic field values is OP-induced relaxation. Γ_L is directly inferred from C_8 data here using the balance of angular momentum approach at $p_3 = 2.45$ mbar at a weak rf discharge level. Differences between total relaxation rates Γ_R and decay rates Γ_D are shown in figure 6.59 as a function of absorbed pump laser power in steady state conditions at $B = 1$ and 30 mT, completed by three experiments at 30 mT where relaxation rates are inferred during complete polarisation build-ups.

Analysed experimental data in figure 6.59 indicate that there is no difference

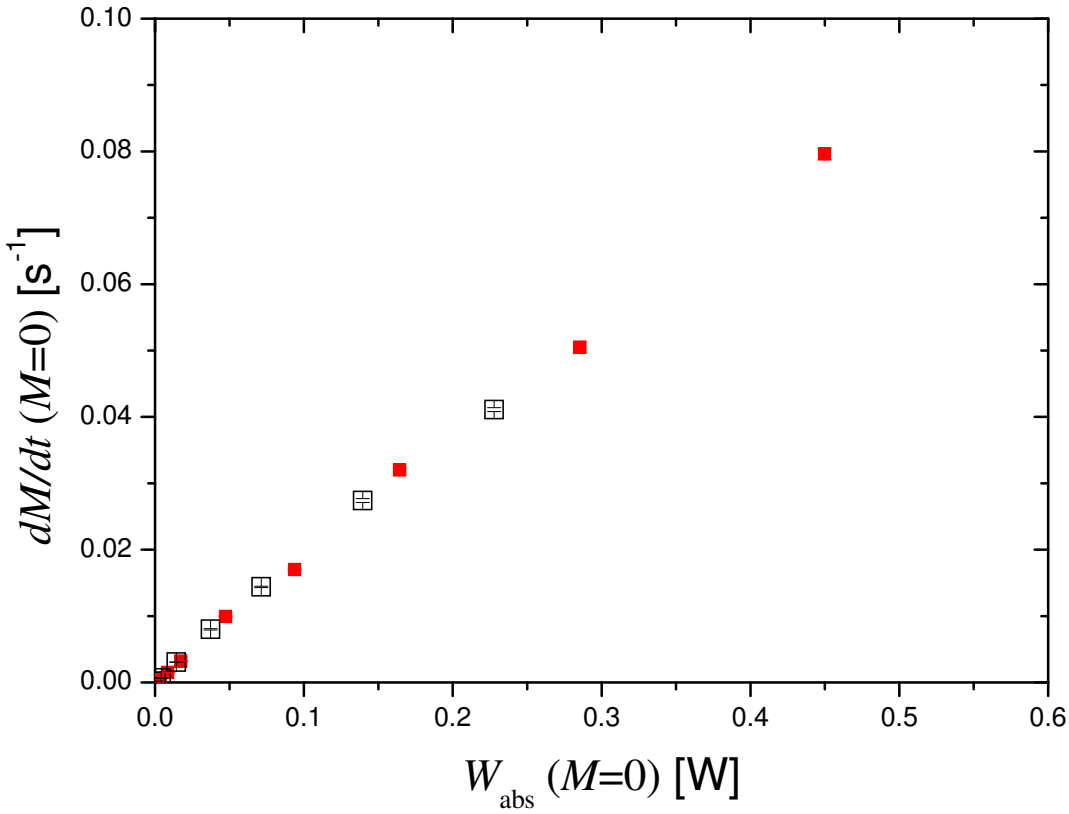

Figure 6.58: Time derivative of polarisation at $M = 0$ for C_8-pumping at 2.45 mbar as a function of absorbed pump laser power at $M = 0$, weak discharge (parameters: see caption of figure 6.60). Filled (red) squares: $B = 1$ mT, open (black) squares: $B = 30$ mT. Errors in y-direction ($\dot{M}(0)$) are plotted (barely visible in filled symbols); relative errors in x-direction on $W_{\text{abs}}(0)$ are observed to range between approximately 1 and 5 % at the lowest investigated pressure in this work of 0.65 mbar and are smaller at higher pressure due to better SNR and a more precisely determined pump transmission coefficient at $M = 0$.

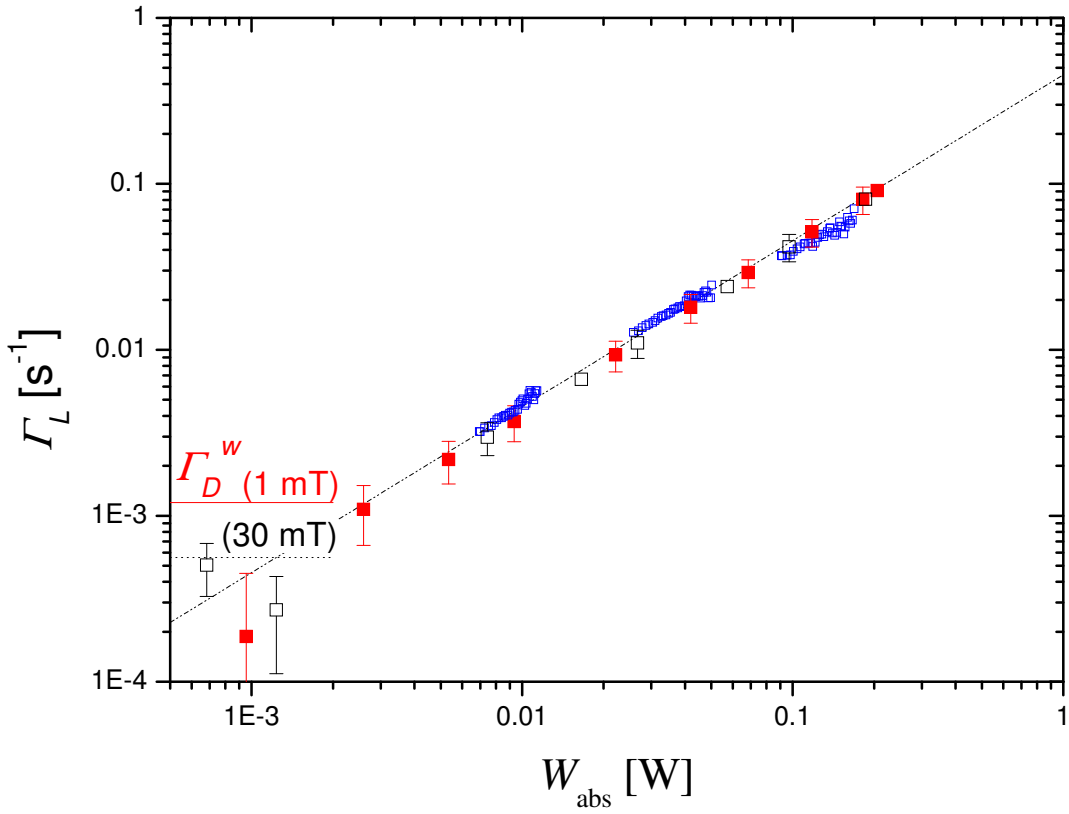

Figure 6.59: OP-induced relaxation rates for C_8-pumping as a function of absorbed pump laser power at 2.45 mbar, weak discharge (parameters: see caption of figure 6.60). Filled (red) squares: Γ_L at M_{eq} and $B = 1$ mT, open (black) squares: idem at $B = 30$ mT, open (blue) squares: Γ_L during 3 examples of complete OP build-up kinetics. The horizontal lines correspond to the measured Γ_D-values: red solid line: Γ_D (1 mT) $= 1.2 \times 10^{-3}$ s^{-1}, black dotted line: Γ_D (30 mT) $= 5.6 \times 10^{-4}$ s^{-1}. Dash-dotted line: guide for the eye ($y = x/2.2$) from figure 6.50.

between 1 and 30 mT. The same consistent behaviour is observed, independently of B.
Data at 1 and 30 mT complement one another quite well at different values of absorbed pump laser power. At 30 mT, relaxation rates inferred during complete kinetics and at steady state are in good agreement. An analysis of a complete polarisation build-up in terms of relaxation has the advantage of covering a range of W_{abs} values instead of a single value only.
The main features of OP-induced relaxation are confirmed at 30 mT: $\Gamma_{\mathrm{L}} = \Gamma_{\mathrm{R}} - \Gamma_{\mathrm{D}}$ is proportional to W_{abs} in a given cell volume and exceeding decay rates in absence of OP by up to a factor of 150 at 30 mT.
Although at higher B, it is possible to obtain smaller Γ_{D} rates, they are no longer relevant in terms of OP performances and obtainable nuclear polarisation at higher laser intensities.
It is thus plausible that in 30 mT, observed M_{eq} values are not much higher than in 1 mT, as Γ_{L} during build-up remains basically unchanged up to 30 mT compared to low magnetic field.

In figures 6.60 (2.45 mbar, weak discharge, same $n_{\mathrm{m}}(0)$ at 1 and 30 mT) and 6.61 (2.45 mbar, strong discharge: approximately same Γ_{D} at 1 and 30 mT), three quantities are represented as a function of absorbed pump laser power at M_{eq}: the fraction of absorbed pump laser intensity, steady state polarisation values on C_8 and C_9 and total relaxation rates Γ_{R} at the end of the polarisation build-up at M_{eq} (from section 6.3.4).
Figure 6.60 will be mainly used for discussing M_{eq} values (centre graph). The top graph with the fraction of absorbed pump laser power is added in order to avoid redundant representation as a function of incident pump laser power, the bottom graph (reused from figure 6.56) serves to establish a correlation between obtainable steady state polarisation values and laser-enhanced relaxation.
As expected at this pressure, C_9 yields higher M_{eq} than C_8. For a comparison between 1 and 30 mT, we consider different ranges of absorbed laser intensities: at low intensity, where Γ_{R} is of order Γ_{D}, the maximum obtainable M_{eq} is mainly determined by Γ_{D}. As at 30 mT, Γ_{D} is about a factor of 2 smaller than at 1 mT, it appears plausible that slightly higher steady state polarisation values are obtained at 30 mT. This situation changes towards higher absorbed laser intensities: approximately above 0.03 W where Γ_{D} no longer dominates, Γ_{L} being at least a factor of 10 higher (up to a factor of 60 in this example at highest measured W_{abs}), M_{eq} values on both investigated transitions are comparable at 1 and 30 mT.

At low absorbed intensities in figure 6.61, where Γ_{D} is the pertinent parameter, M_{eq} at 1 and 30 mT are approximately the same, as for this discharge, Γ_{D} rates are similar in both field values. As expected, we observe higher $n_{\mathrm{m}}(0)$ at 30 mT than at 1 mT. Therefore the absorbed fraction of laser intensity is higher at 30 mT. At the

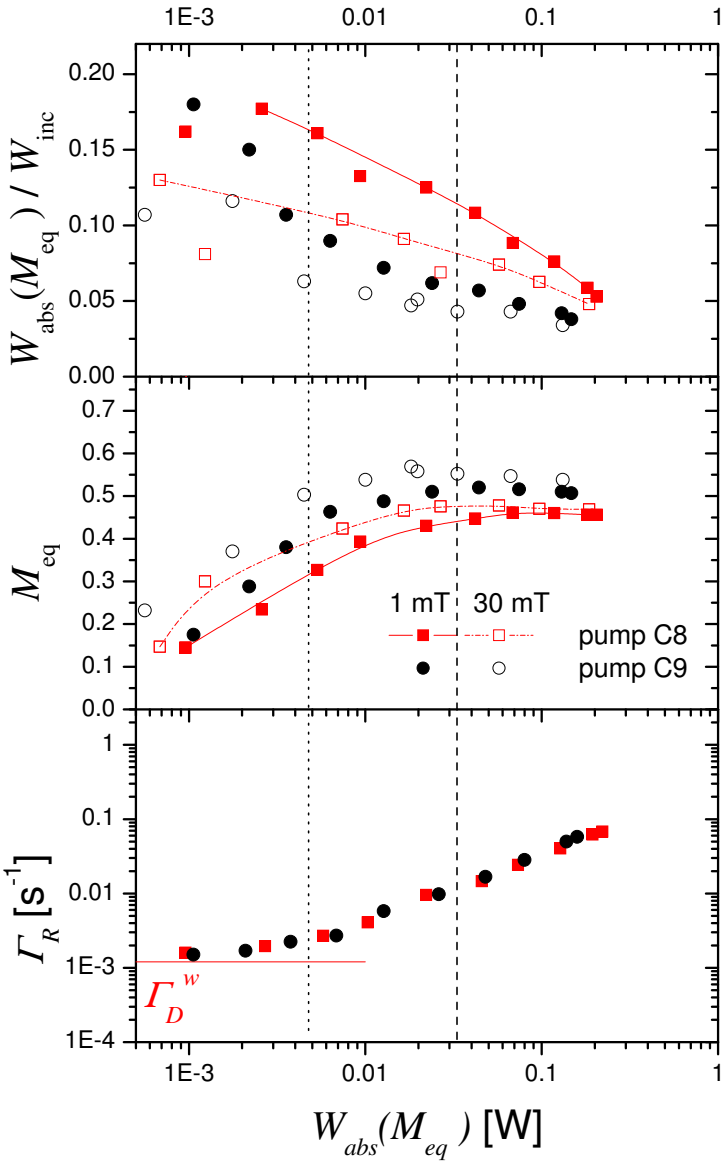

Figure 6.60: Comparison of 1 and 30 mT data at 2.45 mbar. Top: Fraction of absorbed pump laser power; middle: steady state polarisation and bottom: total relaxation rate at M_{eq} as function of absorbed pump laser power at M_{eq} (1 mT only, from figure 6.56). Filled symbols: 1 mT, open symbols: 30 mT. Red squares: C_8 pumping (straight (1 mT) and dash-dotted lines (30 mT) are just guides for the eye for better distinction between C_8 and C_9); black circles: C_9 pumping. Weak discharge: 1 mT: $n_{\mathrm{m}}^{\mathrm{S}}(M=0) = 1.7 \times 10^{16}$ atoms/m^3, $\Gamma_{\mathrm{D}} = (835\,\mathrm{s})^{-1}$; 30 mT: $n_{\mathrm{m}}^{\mathrm{S}}(M=0) = 1.7 \times 10^{16}$ atoms/m^3, $\Gamma_{\mathrm{D}} = (1786\,\mathrm{s})^{-1}$. Vertical lines: Corresponding $W_{\mathrm{abs}}(M_{\mathrm{eq}})$ values for which Γ_{R} equals approximately $2\,\Gamma_{\mathrm{D}}$ (1 mT): dotted line, and $10\,\Gamma_{\mathrm{D}}$ (1 mT): dashed line.

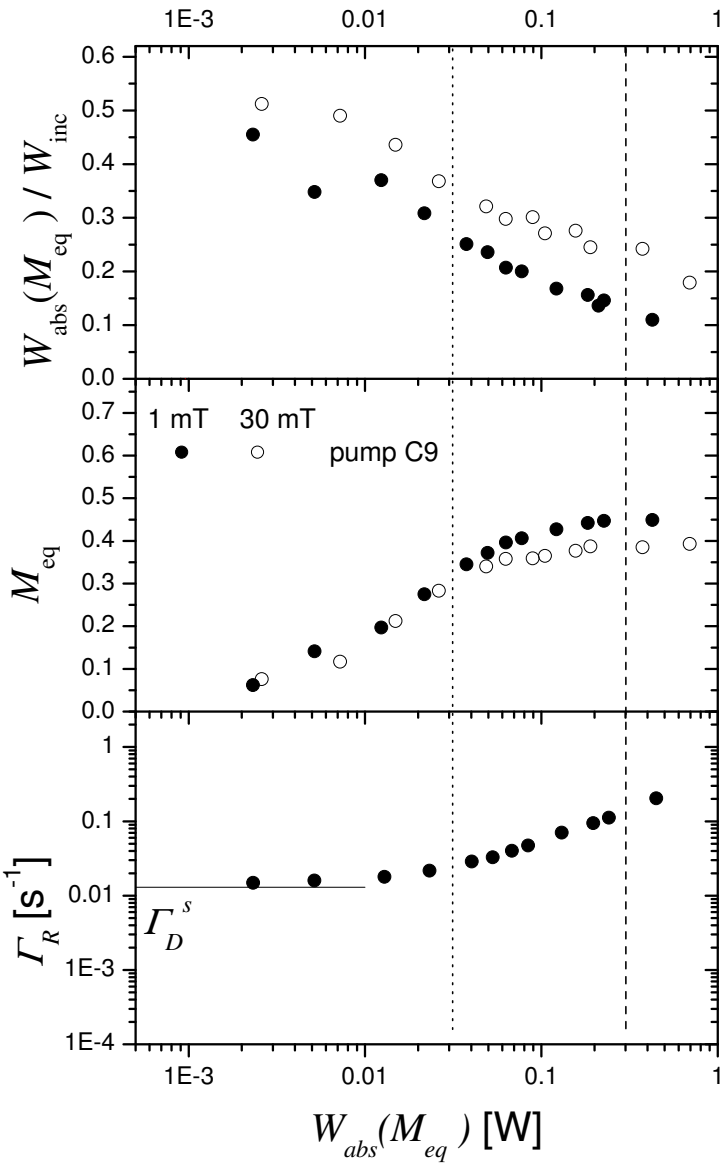

Figure 6.61: Comparison of 1 and 30 mT data for C_9 pumping at 2.45 mbar. Top: Fraction of absorbed pump laser power; middle: steady state polarisation and bottom: total relaxation rate at M_{eq} as function of absorbed pump laser power at M_{eq} (1 mT only, from figure 6.56). Filled circles: 1 mT, open circles: 30 mT. Strong discharge: 1 mT: $n_{\mathrm{m}}^{\mathrm{S}}(M = 0) = 4.2 \times 10^{16}$ atoms/m^3, $\Gamma_{\mathrm{D}} = (78\ \mathrm{s})^{-1}$; 30 mT: $n_{\mathrm{m}}^{\mathrm{S}}(M = 0) = 5.6 \times 10^{16}$ atoms/m^3, $\Gamma_{\mathrm{D}} = (90\ \mathrm{s})^{-1}$. Vertical lines: Corresponding $W_{\mathrm{abs}}(M_{\mathrm{eq}})$ values for which Γ_{R} equals approximately $2\,\Gamma_{\mathrm{D}}$ (1 mT): dotted line, and $10\,\Gamma_{\mathrm{D}}$ (1 mT): dashed line.

highest measured W_{abs} values for this strong discharge, Γ_{R} amounts to approximately $16\,\Gamma_{\mathrm{D}}$ (1 mT).
At higher absorbed intensities, when OP-induced relaxation becomes dominant, M_{eq} values are higher at 1 mT than at 30 mT. This observation suggests that laser-induced relaxation is higher at 30 mT in this case, which would be consistent with higher absorbed pump laser power ($\dot{M} = 0$ in the balance of angular momentum at M_{eq}). However, for the C_9 transition, great care should be taken to avoid false conclusions because in $B \neq 0$, the weighting of the two transition components may depend on laser frequency, and the photon efficiency in turn may depend on detuning. Such reasoning based on the balance of angular momentum is only incontestable for single component transitions like C_8.

In conclusion, OP performances remain comparable at 30 mT with respect to 1 mT, no pathologic features are observed. However, moderate magnetic field up to 30 mT does not yield spectacular improvement of OP. The presented results indicate that angular momentum loss in the radiative cascade and associated relaxation is *not* the dominant phenomenon setting limits to MEOP of ^{3}He.

6.5 Discussion of laser-enhanced relaxation effects

The good agreement between expected and measured polarisation growths rates at $M = 0$ (proportional to the absorbed power through the line-dependent photon efficiency) established in section 6.3.1 indicates that no significant loss of nuclear angular momentum occurs at null polarisation in presence of the strong pump laser light. Such a small loss can however not be fully excluded by the collected sets of experimental data and would lead to a slightly underestimation of the photon efficiency, hence to a small error in the inferred collisional mixing time $\tau_{\mathrm{P}} = 1/\gamma_{\mathrm{r}}^{\mathrm{P}}$.

In contrast, in sections 6.3.3, 6.3.4 and 6.4 (30 mT) clear evidence of OP-induced relaxation has been established and laser-induced relaxation rates in ^{3}He gas under MEOP could be assessed during polarisation build-up or at steady state polarisation using two different approaches: Γ_{L} values can be inferred from experimental data either directly (for single-component excitation) or indirectly (for multi-component excitation, using the model for MEOP kinetics). The main results of our work are that the measured laser-induced relaxation rates Γ_{L} are proportional to the amounts of absorbed pump light power per unit volume and

that they exceed the decay rates Γ_D measured in absence of OP by up to two orders in magnitude in our experimental conditions.

In the following, we compare our findings to the results obtained in other works (section 6.5.1). We then discuss two physical processes that potentially contribute to the additional polarisation losses observed in presence of OP: radiation trapping (section 6.5.2) and light-enhanced formation of 'poisonous' species in the plasma (section 6.5.3).

6.5.1 Comparison of Γ_L rates of different works

Comparison between our comprehensive results with preliminary evidence or reports of similar behaviours in MEOP studies performed at higher gas pressures and applied magnetic field strengths [Abb04, Abb05a] as well as with the results of on-going MEOP experiments in different experimental conditions [Kle08, Glo11, Col11] appears to be rewarding.
A compilation of inferred laser-induced relaxation rates is presented in figure 6.62. The additional relaxation rates $\Gamma_L = \Gamma_R - \Gamma_D$ are plotted as a function of W_{abs}/V_c according to the volume scaling arguments given in page 264 (influence of the length of the cell on the absorbed laser power and of the diameter of the cell on overall relaxation). It is worth mentioning that data of other works presented here do not stem from dedicated measurements and are therefore not ideal in different respects for the purpose of inferring total relaxation rates.

First we will restrict the discussion on low field MEOP data. This includes 4 sets of data, three from references [Abb05b, Kle08, Glo11] and one from our work. The data cover different ranges of absorbed pump laser powers with an overlapping interval at intermediate W_{abs} values. Laser-induced relaxation rates of [Abb05b] and [Kle08] agree qualitatively very well with results of this work and cover similar ranges of W_{abs}. Almost all Γ_R values are directly inferred using the balance of angular momentum approach for the single component transition C_8 except Γ_R values adapted from figure 6.21 of [Abb05b] for C_9 OP, that were inferred from the comparison of measured and computed M_{eq} data in a 32 mbar, 5 cm × 5 cm cylindrical cell (using the MEOP model as shown in figure 5.19 in section 5.7.1). At this pressure, MEOP is quite inefficient at low field ($M_{eq} = 0.11$ with 2 W OP on the C_9 line at 3 mT) where rather large decay rates are measured (here, $\Gamma_D = 13 \times 10^{-3}\ s^{-1}$), even for weak rf discharges. Still, OP-induced relaxation is observed and results are consistent with data from other works. Data of [Glo11] are particularly interesting since they extend the investigation range to approximately two orders of magnitude higher absorbed pump powers thanks to the high He pressure and the small bone-shaped

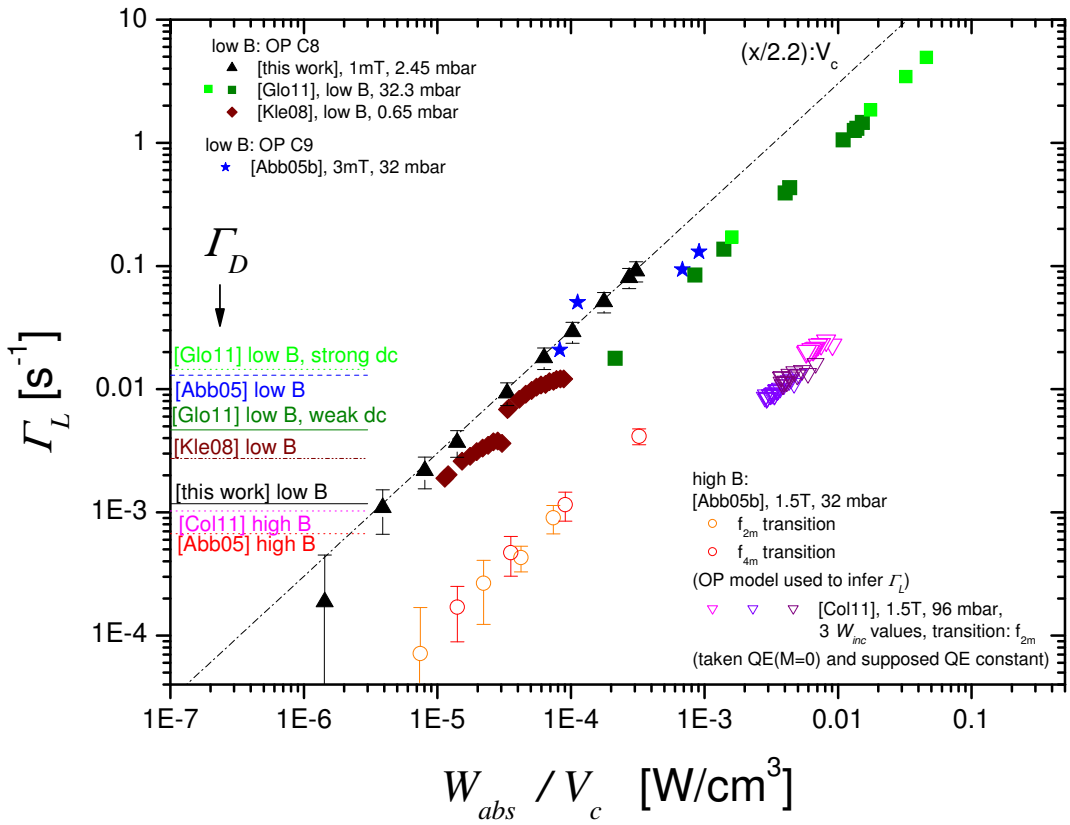

Figure 6.62: Comparison of OP-induced relaxation rates $\Gamma_L = \Gamma_R - \Gamma_D$ at steady state or during complete build-up kinetics as a function of absorbed pump laser power per cell volume. Results of different works in different conditions of pressure and magnetic field are compiled: details see legend. All low field data (filled symbols), except those from [Abb05b], are for C_8 pumping using the direct approach of angular momentum balance to infer relaxation rates. High field data (open symbols) are for f_2 and f_4 (multi-component) transitions which both necessitate the use of the model for MEOP kinetics or the assumption of approximations to infer Γ_R, details see text. Dash-dotted line: guide for the eye ($y = (x/2.2) : V_c$) from figure 6.50, with applied volume scaling.

cell volume specially adapted for creation of plasmas in high pressure/high field. The more W_{abs} per unit volume is increased, the more OP-induced relaxation is observed to increase as well. For the strong (weak) discharge, OP-induced relaxation rates are a factor of 360 (320) above decay rates. The obtained steady state polarisation value amounts to 0.09 only, similar to M_{eq} obtained in [Abb05b] in similar pressures. Lower observed M_{eq} values compared to [Kle08] and this work are consistent with high laser-induced relaxation rates of [Glo11]. (Experimental uncertainties on absorbed pump laser powers are higher in [Kle08] and [Glo11] than in [Abb05b] and this work.) Comparing all low field data, we observe the same overall qualitative behaviour. Applying natural volume scaling allows to reconcile all results, and thus satisfying quantitative agreement is obtained: Laser-induced relaxation rates scale with $W_{\mathrm{abs}}/V_{\mathrm{c}}$ in all works and are at least of the same order of magnitude as measured decay rates in absence of OP, and exceeding it to a considerable degree.

Second, high field data are included into the discussion. Background information about energy levels and pumping schemes (at 2T: f_2 and f_4 transitions for σ^+ and σ^- light) as well as absorption spectra for both light polarisations for four B-values between 0.45 and 2 T is provided e.g. in [Nik07]. High-field MEOP operates quite efficiently which constitutes a striking feature of this pumping scheme (for Γ_{R} data adapted from figure 6.21 of [Abb05b]: $M_{\mathrm{eq}} = 0.56$ with 0.5 W OP at 1.5 T in the same 5 cm $\times$ 5 cm cylindrical cell). Furthermore, decay rates are reduced (as expected in high B due to hf decoupling in the radiative cascade, here: $\Gamma_{\mathrm{D}} = 0.67 \times 10^{-3}\,\mathrm{s}^{-1}$). It also gives rise to a strong OP-light-induced relaxation of order Γ_{D} at least.
In contrast to the data of [Abb05b] that, like in low field, were inferred from the comparison of measured and computed M_{eq} data, [Col11] used the same direct approach to infer total relaxation rates during polarisation build-up as in our work, and also supposed the photon efficiency to be constant as function of M. This is true for single component transitions (like C8 in low field) but does not apply to the two most commonly used high B transitions f_2 and f_4 (consisting of two and four components respectively). This approximation assuming a constant value of η can cause a possible vertical shift of data points by a factor of 2 roughly, but this would not influence the observed qualitative behaviour, nor the interpretation of the results. The cylindrical cells used in [Abb05b] were not specially adapted for use in high field: in a plasma in these conditions, a high fraction of metastable atoms is located close to the cell walls. In such a cell geometry, it is impossible to generate more adapted plasmas and to further increase W_{abs} like in the bone shaped cells used in [Col11] with much smaller diameter.
Despite the two different methods of analysis, partly comprising approximations, both examples of high field relaxation rates at 1.5 T agree qualitatively very well with each other and are complementary concerning the covered range of absorbed pump laser powers.

In conclusion, the preliminary evidence of strong OP-light-enhanced relaxation found in [Abb05b] in completely different OP conditions than the ones in the present work, is confirmed by our results.
In high magnetic field, smaller laser-induced relaxation rates at given $W_{\mathrm{abs}}/V_{\mathrm{c}}$ are observed than in low B, which is consistent with high observed M_{eq} values at high pressure and high B (with respect to low M_{eq} and high Γ_{L} at high pressure and low B). The ratio $\Gamma_{\mathrm{L}}/W_{\mathrm{abs}}$ thus depends on magnetic field and is reduced for fields $\gg 30$ mT.
The compiled data of figure 6.62 show that OP-enhanced relaxation constitutes a universal effect over a considerable range of operating conditions (regarding gas pressure, magnetic field, size and shape of cell).

We now briefly discuss two physical processes that have not been taken into account in the OP model described in chapter 2. They both potentially contribute to the additional polarisation losses observed when OP is applied, but these contributions are currently difficult to quantitatively evaluate as explained below.

6.5.2 Radiation trapping

The OP model assumes that optical transitions are governed by the OP beam light only (equations (2.19) and (2.20)), and that all light that results from spontaneous emission from the 2^3P state escapes from the cell. Actually, a fraction of this secondary light might be absorbed before exiting the cell: this is the well-known radiation trapping phenomenon. An accurate description of the effect is technically difficult to model precisely, because it involves the way light is locally emitted at point $\vec{r}$ during 2^3P–2^3S transitions, after partial collisional redistribution among the 2^3P Zeeman sublevels, which determines the spectral, angular, and polarisation characteristics of this light. Furthermore, absorption probability at point $\vec{r}'$ of this light depends on the local populations a_i and b_j, that depend of course on local OP conditions but may also be affected by radiation trapping, and volume averaging over the cell must be performed. No attempt is made here to describe this complex process, but several simple remarks can still be made.

The reabsorbed light locally deposits angular momentum with a photon efficiency $\hat{\eta}(M, W_{\mathrm{inc}}, p_3)$ that depends in a very complex way on populations (hence on M and on W_{inc}) and on collisional redistribution (hence on p_3) for the reasons mentioned above. A reabsorption-induced loss can be generically written as

$$-M\Gamma_{\mathrm{RT}} \propto -\left[\hbar\hat{\eta}(M, W_{\mathrm{inc}}, p_3)W_{\mathrm{abs}}/\hbar\omega\right] \times n_{\mathrm{m}} \;/\; \left[\hbar N_{\mathrm{g}} V_{\mathrm{c}}/2\right] \tag{6.19}$$

(including e.g., implicit volume averages, cell shape factors). The first term in square brackets on the right hand side of the equation measures the deposited angular momentum (in units of $\hbar$) for full trapping, the n_{m} factor accounts for the (weak) absorption probability of the light, and the last term in square brackets is the total angular momentum of the nuclei in the cell. Equation (6.19) can be rewritten as

$$-M\Gamma_{\mathrm{RT}} \propto -2\hat{\eta}\,\frac{W_{\mathrm{abs}}}{N_{\mathrm{g}}V_{\mathrm{c}}\,\hbar\omega}\;\times\;n_{\mathrm{m}} \tag{6.20}$$

which shows that reabsorption-induced loss would provide a rate Γ_{RT} that apparently scales with the absorbed power per unit volume $W_{\mathrm{abs}}/V_{\mathrm{c}}$, with the 2^3S density n_{m} and with the inverse of the ground state density N_{g}, i.e. the inverse of gas pressure p_3, but only if the reabsorbed photon efficiency $\hat{\eta}$ did not depend on these quantities. This is certainly not quantitatively true, but one may argue that at high enough pressure, for full collisional redistribution (above several mbar), $\hat{\eta}$ may indeed become independent of p_3 hence Γ_{RT} may actually scale as $1/p_3$.

A quantitative evaluation of the radiation trapping effects is made in [Eck92], where analytical formulas are derived using two simplifications:
- spin-temperature distribution of populations in 2^3S is assumed, populations in 2^3P are neglected
- full collisional redistribution in 2^3P (Dehmelt OP regime) is assumed.

Equation (2) of [Eck92] is an angular momentum balance[4]. The reabsorption-induced amount of deposited angular momentum is written in equations (A.19) and (A.23) of [Eck92] as

$$\dot{L}_\rho = -\hbar\rho\frac{W_{\mathrm{abs}}}{\hbar\omega}f_k, \tag{6.21}$$

where the dimensionless reabsorption parameter ρ is given by:

$$\rho = k_i\frac{l_{\mathrm{eff}}}{2L_{\mathrm{cell}}}\ln\left(\frac{W_{\mathrm{inc}}(0)}{W_{\mathrm{inc}}(0)-W_{\mathrm{abs}}(0)}\right) \simeq k_i\frac{l_{\mathrm{eff}}}{2L_{\mathrm{cell}}}\frac{W_{\mathrm{abs}}(0)}{W_{\mathrm{inc}}(0)} = k_i\frac{l_{\mathrm{eff}}}{2L_{\mathrm{cell}}}\,(1-T_{\mathrm{p}}(0)), \tag{6.22}$$

with $W_{\mathrm{inc}}(0)$ and $W_{\mathrm{abs}}(0)$: incident and absorbed laser powers at $M=0$ (related by the light absorptance $1-T_{\mathrm{p}}(0)$) and $k_i = 7.23$ for C_8 and 5.7 for C_9. The effective length l_{eff} is equal to the radius R_{c} for a long cylindrical cell [Eck92]. In this weak absorption limit, the reabsorption parameter is proportional to the 2^3S density.
The M-dependent functions f_k of equations (A.19) for C_9 and (A.23) for C_8 as well as their ratios f_k/M to the nuclear polarisation are plotted in figure 6.63.

[4]In reference [Eck92], the efficiency (also noted η) used in equations (2) and (3) has a different meaning and is defined with respect to incident, not to absorbed, light.

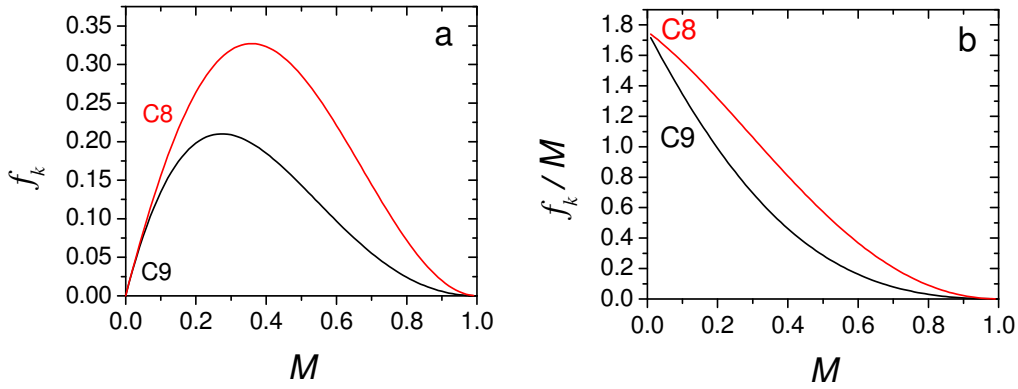

Figure 6.63: **a:** x-dependent functions f_k for C_8 and C_9 of [Eck92] are plotted as functions of M using the spin temperature parameter $x = (1+M)/(1-M)$.
b: Ratios of functions f_k divided by M.

This angular momentum loss is equivalent to an additional loss characterised by a rate Γ_{RT} given by:

$$-\hbar\rho\frac{W_{\mathrm{abs}}}{\hbar\omega}f_k = -\frac{\hbar}{2}N_{\mathrm{g}}V_{\mathrm{c}}\Gamma_{\mathrm{RT}}M, \tag{6.23}$$

hence

$$\Gamma_{\mathrm{RT}} = \frac{2\rho W_{\mathrm{abs}}}{N_{\mathrm{g}}V_{\mathrm{c}}\,\hbar\omega}\frac{f_k}{M} = 2k_i l_{\mathrm{eff}}\,\frac{(1-T_{\mathrm{p}})}{2L_{\mathrm{cell}}}\,\frac{W_{\mathrm{abs}}}{V_{\mathrm{c}}}\,\frac{1}{N_{\mathrm{g}}\,\hbar\omega}\,\frac{f_k}{M}. \tag{6.24}$$

The first factor l_{eff} is just the cell radius R_{c} (like many others, Eckert and co-workers worked with long cylinders [Eck92]), the second factor is the absorption per unit length (it scales with the 2^3S density), the third factor is the absorbed laser power per unit volume, the fourth factor is inversely proportional to the ground state density N_{g} (i.e. the gas pressure p_3), and the last factor is the numerical ratio f_k/M that decreases to 0 at high M (see figure 6.63).

The main features of the additional reabsorption-induced loss rate expected from the description of the impact of radiation trapping proposed in [Eck92], explicitly given by equation (6.24), can be summarised as follows:

- It should scale with absorbed laser power per unit volume $W_{\mathrm{abs}}/V_{\mathrm{c}}$
- It should scale as n_{m}/p_3.
- It should strongly decrease at high M through the f_k/M scaling (cf. figure 6.63).
- It leads to a very small quantitative impact of radiation trapping on steady state polarisation values M_{eq}, according to the numbers given in [Eck92].

The scaling of the additional reabsorption-induced loss rate Γ_{RT} with the absorbed laser power per unit volume predicted by equation (6.24) is confirmed by our results as well as by those of the other works compiled in section 6.5.1.

However, our results indicate that the expected scaling with n_{m}/p_3 is not observed.

- The OP-enhanced relaxation rates do not grow linearly with metastable number densities: within experimental errors as shown in section 6.3.4 identical values of Γ_{L} are measured at fixed absorbed power W_{abs} independently of the combination of rf excitation levels and incident pump laser powers used.
- The Γ_{L} data compiled in the 0.63 to 2.45 mbar gas pressure range fairly collapse when plotted versus the absorbed powers W_{abs} (figure 6.55).

Further evidence that our experimental observations are not consistent with the additional loss rates derived in [Eck92] for radiation trapping can be found in the detailed report presented in sections 6.3.3, 6.3.4 and 6.4. Selected results are provided in figure 6.64 for quantitative evaluation of the observed discrepancies at steady state polarisation, for instance.

Finally, the estimation of reabsorbed power performed in [Abb05b], where experimental conditions are different from those of the present work, also leads us to the conclusion that the discrepancies between measured and expected values of the steady state polarisation M_{eq} for high pressure (up to 67 mbar) and high magnetic field (1.5 T) MEOP in pure ^{3}He gas cannot be explained by the additional rates evaluated for radiation trapping in reference [Eck92].

6.5.3 OP-induced plasma 'poisoning' (e.g., by metastable He molecules)

Another process of potential importance in the context of OP-enhanced relaxation is the light-enhanced creation of a relaxing long-lived species Ξ through the 2^3P state. One could think for instance of metastable molecules He_2^*, that are formed in 3-body collisions involving two ground state atoms and one metastable helium atom (cf. section 6.1.1). The formation of He_2^* is about 100 times more efficient from 2^3P than from 2^3S due to different formation cross sections [Emm88].

A relaxation mechanism, similar to that investigated by Bonin and coworkers in [Bon88] to account for the depolarisation of ^{3}He in spin-polarised gaseous targets (through charge exchange during interactions with molecular ions $^3\mathrm{He}_2^+$), has been proposed in [Cou01] to explain relaxation by metastable helium molecules. $^3\mathrm{He}_2^*$

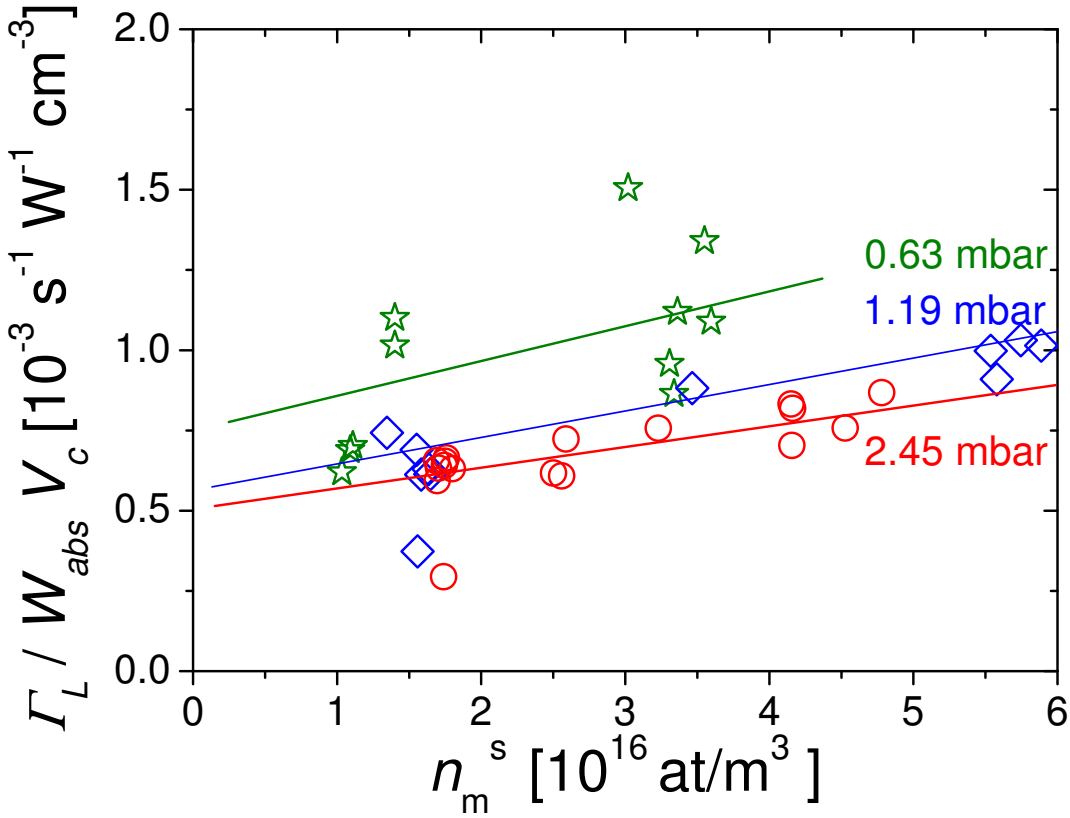

Figure 6.64: Variation of the steady-state values of $\Gamma_{\mathrm{L}}/(W_{\mathrm{abs}}V_{\mathrm{c}})$ (ratio of laser-induced polarisation loss rate Γ_{L} to measured absorbed light power W_{abs}, scaled to cell volume V_{c}) with 2^3S atom number density $n_{\mathrm{m}}^{\mathrm{S}}$. Experimental data are compiled for gas pressures p_3 =0.63 mbar (stars), 1.19 mbar (diamonds), and 2.45 mbar (circles). The solid lines are just guides for the eyes. The data are clearly *not* proportional to $n_{\mathrm{m}}^{\mathrm{S}}$ and, in spite of scatter, exhibit a mild increase with 2^3S atom density. They are observed to weakly decrease with gas pressure, which excludes both p_3^{-1} and p_3^{-2} scalings.

is a weakly bound dimer asymptotically corresponding to the association of one metastable atom and one ground state ^{3}He atom. In the proposed mechanism, during collisions between a $^3\mathrm{He}_2^*$ molecule and a spin-polarised ground state atom, an exchange of electronic excitation may occur so that the incoming spin-polarised atom remains bound and the outgoing ground state atom is unpolarised. Then, dissipation of nuclear angular momentum in the numerous rotational states of the molecule by spin-orbit coupling would provide an efficient relaxation channel. This potential relaxation process for the ^{3}He nuclear polarisation M would yield a light-sensitive polarisation loss rate Γ_Ξ proportional to number density of metastable molecules (or any other long-lived species Ξ with significant light-enhanced density and effective hyperfine coupling).

In [Cou01], metastable molecules could be detected in He plasmas and an increase of molecular density was demonstrated in presence of 1083 nm OP light: measurements performed at 40.4 mbar in a small radius cell have shown that a relative increase of molecular density by a factor of 5 at most could be obtained for the highest power density of the light available at 1083 nm, 220 W/cm^2, with an infrared laser tuned to the unresolved C_2-C_5 transitions.

In [Abb05b], an increase of additional OP-induced relaxation has been observed with increasing 2^3P density on the one hand (which could be interpreted as indication of a long lived relaxing species Ξ created through the 2^3P state) but on the other hand only a weak dependence of OP-induced relaxation on pressure has been observed. Thus no physical process could be clearly identified to cause laser-induced relaxation effects in these particular experimental conditions (high pressure MEOP in high magnetic field).

The proposed scenario does not directly involve the metastable atoms. For the ground state atoms, gas pressure may indirectly influence Γ_Ξ: In the worst-case scenario where dissipation of angular momentum is fast enough in the molecular state compared to the rate of exchange collisions between molecules and ground state atoms, Γ_Ξ is expected to be independent of p_3 [Bon88, Mil87]. However, when collisions become so frequent that only partial depolarisation occurs during the time elapsed on average between exchange collisions, a high pressure limit is reached where Γ_Ξ scales inversely with p_3 (due to the saturation of depolarisation in the molecular state) [Bon88]. In our low pressure cells, we expect to be in the worst case scenario with a p_3-independent relaxation rate at fixed density of Ξ.

Let us now examine what may determine the number density of relaxing long-lived species Ξ in our cells:

- The average 2^3P state density is equal to $n_\mathrm{P} = n_\mathrm{m} \sum_j b_j = W_\mathrm{abs}/(V_\mathrm{c}\, \hbar\omega\, \gamma)$ and the rate of formation of He_2^* through the above mentioned 3-body collisions is known to increase proportionally to $n_\mathrm{P} N_\mathrm{g}^2$.

- Gas pressure p_3 is expected to strongly favour high densities of Ξ due to the combined effects of the increased molecule formation (through the laser-assisted 3-body process mentioned above, characterised by a rate scaling as N_{g}^2) and of the slower decay (diffusion to cell walls is reduced, the diffusion coefficient scaling as $1/p_3$).

- The 2^3S number density n_{m} may influence the density of Ξ through ionising (Penning) collisions between one metastable molecule and one metastable atom: for this process, an increase in metastable density would lead to a decrease of Ξ density.

With a polarisation loss rate Γ_{Ξ} simply proportional to the density of Ξ, in order to account for our observations (see sections 6.3.3, 6.3.4 and 6.4) this density would need to actually scale as $W_{\mathrm{abs}}/V_{\mathrm{c}}$ with very little dependence on both metastable density n_{m} and gas pressure p_3. This is difficult to imagine given the complexity of competing processes involved in the plasma.

Furthermore, the laser-induced enhancement of molecular density has been measured to decrease at low pressure by Courtade and coworkers, as expected from a numerical study of the coupled rate equations for the formation and destruction of atomic and molecular metastable species: in 5-cm diameter cylinders, the enhancement factor does not exceed 2.4 (resp. 1.7) at 32 (resp. 8.6) mbar [Cou01]. This limited increase is consistent with the preliminary results of more systematic investigations undertaken at LKB (PhD work of B. Głowacz [Glo11]) and seems grossly insufficient to quantitatively explain the huge changes in loss rates observed in low field MEOP using the weak C_8 and C_9 lines.

Chapter 7

Conclusion and Outlook

In the present PhD work, a dedicated experimental setup for MEOP research in ^{3}He gas has been designed and constructed (chapter 3). Systematic measurements of OP performances and investigations of relaxation effects covered a pressure range of 0.63 to 2.45 mbar in magnetic fields between 1 and 30 mT.
The major outcome can be assigned to four different domains:

Methodological aspects

In this field, tools for diagnosis and measurement methods for use in OP experiments that allow to better characterise the system were developed and/or refined.

A light absorption technique to dynamically monitor two (sets) of 2^3S populations during polarisation build-up and decay and thus to measure ^{3}He nuclear polarisation was used. It involves weak probe beams at 1083 nm, that are either perpendicular or parallel to magnetic field and cell axis. In our experimental setup, a longitudinal probe scheme was implemented and systematically tested to fully evaluate potentials and systematic biases of this method (chapter 4). It could be shown that despite strong effects of OP light on absorption measurements, OP dynamics can be reliably studied over the whole range of experimental conditions. Comparisons to a transverse probe scheme implemented on the optical pumping cells of the on-site production unit at LKB were drawn [Tal11].

Most of the experiments were performed at fixed probe laser frequency, complemented by sweeps of the probe laser frequency in selected experimental situations: in order to investigate the velocity selective character of MEOP, measurements of apparent polarisation at $M = 0$ as a function of atomic velocity v_z were performed (see section 6.2.1).
Furthermore, probe laser frequency sweeps have been used to characterise the small frequency-dependent variations in the ratio of absorption signals (cf. sections 2.1 and 3.2) observed in the case of spatially overlapping σ^+ and σ^- circular polari-

sations (for the longitudinal scheme) when the probe is tuned to the C_9 line in ^{3}He gas (or to the D_0 line in isotopic gas mixtures). Similar observations have been made with the transverse probe scheme [Tal11]. Systematic investigations have been made for both probe schemes in a variety of experimental conditions, detailed results will be published when a comprehensive description can be given. However, these frequency-dependent variations can be eliminated by using two spatially separated beams for the absorption measurements which makes the optical technique robust against probe detuning and accurate at all polarisations.

In order to accurately separate optical signals from pump and probe lasers, as well as to allow a clear attribution of changes in optical signals to atomic response, a 2-step-modulation scheme has been used in this work (cf. section 3.3): slow amplitude modulation of the discharge at 70 Hz using moderate modulation depth not exceeding 30 % and fast modulation (4-5 kHz) either of the current of the probe laser diode near threshold or realised by mechanical chopping of the probe laser beam. Subsequent numerical demodulation of signals has been developed at LKB (see appendix E) and first used and validated for data reduction in this work. Accurate methods to extract relevant physical quantities from available experimental parameters have been established (cf. chapter 5).

The dedicated device to map the radial distribution of metastable atom density constitutes another instrumental implementation put into practice. Complemented by measurements using a commercial beam profiler, suitable methods for both devices to infer radial n_{m} mappings contributed to a comprehensive characterisation of a MEOP system. Results are presented in section 6.1.2.

These tools, methods and established principles developed for systematic MEOP studies in low magnetic field and low pressure in the present work are valuable in a larger context as well e.g., for MEOP at high field and high pressure, constituting different conditions for which they can be adapted. In parallel to this work, the group in Kraków pursued MEOP research in $B = 0.45 - 2$ T and 4.7 T at high pressure up to 500 mbar [Nik07, Suc07, Nik10, Doh11, Col11, Nik12]. Furthermore, the balance of angular momentum approach, recalled below in the paragraph on systematic OP measurements could be used to determine an optimum operating point of gas polarisers.

Investigation of plasma changes and OP performances in moderate magnetic field

Following the initial motivation to begin this work, expecting to potentially increase OP performances when higher excited states in the radiative cascade are strongly decoupled above 10 mT [Pav70] and thus angular momentum loss is reduced in the radiative cascade (cf. introduction, chapter 1), effects of moderate magnetic fields, up to $B = 30$ mT in this work, on plasma and OP performances were investigated. The results are presented in sections 6.1.1 and 6.4.
As expected from the reduced polarisation loss associated to hyperfine decoupling in the cascade, polarisation decay rates were reduced in 30 mT at fixed metastable density. But in spite of this, the obtained polarisations were not improved at high laser power. The origin of this apparent paradox could be clarified: At small incident pump laser powers, Γ_D, the measured decay rate of polarisation in absence of OP, basically determines the obtainable steady state polarisation. At higher incident pump laser powers however, Γ_D is not the pertinent parameter limiting M_{eq}. We found clear evidence of additional OP-induced relaxation effects.

Validation of OP model based on two velocity classes

The development of the improved model for MEOP kinetics based on two broad velocity classes by P.-J. Nacher (see chapter 2) was approximately finished at LKB at the beginning of this PhD work. Therefore part of this work was to validate it by comparisons to experimental data, which contributed to advancements concerning selected aspects in the OP model. Results are presented in sections 4.1, 4.3, 4.4.2, 6.1.2, 6.2 and 6.3.
In section 6.3.2 comparisons of experimental and computed ratios of photon efficiencies for C_8 and C_9 allowed to empirically determine the relaxation rate in the 2^3P state, $\gamma_{\mathrm{r}}^{\mathrm{P}}/p_3 \simeq 0.32\times10^7$ s^{-1}/mbar.
It could be shown that this new model actually provides a realistic description of all features of low field MEOP as well as robust quantitative results.

Systematic OP measurements and laser-enhanced relaxation

A large number of systematic OP measurements varying different parameters such as ^{3}He pressure, rf excitation level and thus metastable densities and decay rates, probe and pump transitions, and incident pump laser power were performed.
As reported in [Bat11], solid evidence of a new nuclear relaxation process could be established. Additional loss rates were introduced to account for the surprising exper-

imental fact that the achieved steady-state polarisations hardly increase when higher pump powers are used, in spite of higher pumping rates.

The methods developed for data reduction (cf. chapter 5) permitted to provide all relevant physical quantities at $M = 0$ and as a function of M.
The time derivative of polarisation, $\dot{M}$, as well as pump transmission coefficients T_p are of special interest since they allow to quantify photon efficiencies (cf. section 2.9, and results in sections 6.3.1 and 6.3.2).
The approach based on global angular momentum conservation (see section 5.7.2) emerged as very fruitful to quantify additional loss rates, in a straight forward procedure in the case of the single-component transition C_8 (cf. section 5.7.2) since the photon efficiency is constant and does not depend on polarisation or incident pump laser power. In other situations, the model for MEOP kinetics is needed to infer OP-induced loss rates e.g., for the multi-component transition C_9 (cf. section 5.7.1). The obtained results are robust and also suitable to illustrate characteristics of laser-enhanced relaxation (see for instance section 6.3.4).

The main observed features of additional loss rates Γ_L introduced to account for OP-enhanced relaxation effects are the following: They scale linearly with the ratio of absorbed laser power and cell volume, and exceed decay rates Γ_D by up to two orders in magnitude in the given experimental conditions of the present work (cf. sections 6.3.3 and 6.3.4).

Similar effects have been observed in other MEOP experiments as well:

1/ In similar low magnetic field and low pressure conditions, as data from [Kle08] that we reanalysed according to the established methods in this work indicate. The authors of [Gen93] recently provided MEOP raw data that will be processed in order to check whether OP-enhanced relaxation effects could have been observed already at that time. However, since these measurements were not performed for this purpose, this reanalysis will not be straightforward due to missing quantities like metastable densities and absorbed pump laser powers for instance. We will seek to reconstruct them with the help of the MEOP-model.

2/ In low magnetic field and high pressure conditions [Glo11] where due to the high obtainable values of W_{abs} / V_c, the observed increase of polarisation loss is even higher by a factor of 3 roughly than in the experimental conditions of our work (see discussion in section 6.5.1).

3/ In high magnetic field and high pressure [Abb05b, Col11]: Despite strong hf-decoupling, laser-enhanced relaxation can be observed as well, but seems to be less important than in low field situations: At given W_{abs}/V_c, Γ_L rates are lower by a factor of 25-40 approximately in the selected examples presented in section 6.5.1. This observed tendency is in accordance with much higher obtained M_{eq} values (compared to low B) in high pressure cells. Nevertheless, in such high B and high p_3 conditions, Γ_L rates still exceed measured decay rates Γ_D by roughly one order of magnitude.

The physical processes causing OP-enhanced relaxation effects remain to be elucidated. We provided two possible starting points in sections 6.5.2 and 6.5.3 for further considerations and investigations:

1/ Radiation trapping i.e., re-absorption of unpolarised 1083 nm fluorescence light, that will certainly have to be revisited in more detail in light of recent findings, and adequate dedicated experimental checks will have to be performed.

2/ Plasma 'poisoning' by light-enhanced creation of a relaxing long-lived species Ξ through the 2^3P state.

Concerning the second hypothesis, qualitative measurements of molecular densities in a pressure range of 1-400 mbar were carried out in parallel to this work [Glo11]. This extended pressure range possibly provides hints contributing to ultimately identify involved physical processes and/or potentially facilitates distinction of several conceivable effects. A tunable 465 nm probe laser [Tas10] was developed, corresponding to the transition from the lowest energy state $a^3\Sigma_u^+(v=0)$ to the $e^3\Pi_g(v=0)$ state of the He_2^* metastable molecule. Simultaneous optical measurements of molecular and atomic (2^3S) densities along with nuclear relaxation rates are performed in order to evaluate the potential contribution of He_2^* molecules to laser-enhanced polarisation losses. In presence of a 1083 nm pump laser, an increase of 465 nm light absorption is observed but so far mild in comparison with the spectacular enhancement of ^{3}He nuclear relaxation rates.

In low pressure conditions of the present work, the molecular density is presumably low anyhow, and it is questionable whether findings at higher pressure concerning molecular contribution to enhanced nuclear relaxation hold at lower pressure.

Another possible extension of experimental checks could be performed in isotopic mixtures in order to test whether similar effects of OP-enhanced relaxation are observed in these different conditions as well.

For the time being, no physical process can be clearly identified as origin of laser-induced relaxation. Both considered processes, radiation trapping and plasma poisoning, would result in additional laser-induced relaxation rates that scale with $W_{\mathrm{abs}}/V_{\mathrm{c}}$ as experimentally observed in our work. However, 1/ the expected amount of laser-induced polarisation losses for these processes is lower than observed, and 2/ the expected dependencies of the loss rates on metastable density and gas pressure for these processes (cf. sections 6.5.2 and 6.5.3) are not observed in our experiments. All these clues seem to rule out these processes as leading causes for the observed losses, but further investigations are needed.

For practical applications, the observed OP-enhanced relaxation effects also have a great impact on gas polarising systems. If this source of relaxation was eliminated, the "wasted" amount of angular momentum could be used to increase the gas flow per

unit time and thus lead to higher production rates while higher nuclear polarisations could be obtained.

In conclusion, identifying the physical processes leading to laser-enhanced relaxation and reducing or ultimately eliminating this source of relaxation would increase MEOP performances e.g., for use in fundamental physics experiments, and would also increase production rates of polarisers for use of polarised ^{3}He in applications such as lung MRI. As long as physical processes are not identified it is too early to cogitate about possibilities to overcome these limitations, but the introduction of buffer gases for instance to quench selected molecular or atomic states as presented in [Bon88, Bla04, Dim04] is conceivable.

All reported observations of this work as well as compiled results of other works provide useful clues in order to identify physical processes causing OP-enhanced relaxation effects and to ultimately overcome current limitations, but this question remains just as open as the physical origin of the recently discovered "excess" relaxation (described using the phenomenological parameter X) in spin exchange optical pumping of ^{3}He [Bab06, Che07, Lan10].

Appendix A

Tables and matrices for low magnetic field ($B < 0.162$ T): Transition frequencies and intensities for ^{3}He and ^{4}He, Zeeman shifts, hyperfine mixing parameters, vector and matrix operators

The 2^3S state mixing parameters θ_+ and θ_- (needed in section 2.2) are given by [Nac12]:

$$\tan\theta_\pm = \left[\sqrt{8 + (2b\beta \pm 1)^2} - (2b\beta \pm 1)\right] / 2\sqrt{2}, \tag{A.1}$$

in which $b{=}{-}g'_S\mu_B B/A_S$ is the reduced magnetic field (Equation A.7 of [Cou02], with g-factor g'_S and hyperfine coupling constant A_S, values given in Tables 6 and 8 of [Cou02]) and $\beta{=}1 - g_I/g'_S$ is very close to 1 (Table 6 of [Cou02]).

Table A.1: Table of optical transition intensities T_{ij} between metastable sublevels A_i and excited sublevels B_j of ^{3}He in null magnetic field ($B = 0$) for σ^+-polarised and π-polarised lights. Frequency shifts ϵ_{ij}/h (in GHz) are relative to the C_1 transition. Values of ϵ_{ij} and T_{ij} are the same for σ^+, σ^-, and σ polarisations in null field. [Nac12]

line,	$\sigma^\pm$ light			π light		
ϵ_{ij}/h	levels		T_{ij}	levels		T_{ij}
C_1,	A_6	B_{10}	.026745	A_6	B_9	.017830
0	A_5	B_9	.008915	A_5	B_8	.017830
C_2,	A_5	B_{12}	.374818	A_6	B_{12}	.187410
4.512				A_5	B_{11}	.187410
	A_4	B_6	1	A_4	B_5	.4
C_3,	A_3	B_5	0.6	A_3	B_4	.6
4.959	A_2	B_4	0.3	A_2	B_3	.6
	A_1	B_3	0.1	A_1	B_2	.4
C_4,	A_6	B_{16}	.973255	A_6	B_{15}	.648837
5.181	A_5	B_{15}	.324418	A_5	B_{14}	.648837
	A_3	B_{10}	.389302	A_4	B_{10}	.583953
C_5,	A_2	B_9	.519069	A_3	B_9	.064884
6.740	A_1	B_8	.389302	A_2	B_8	.064884
				A_1	B_7	.583953
C_6,	A_2	B_{12}	.072962	A_3	B_{12}	.145924
11.251	A_1	B_{11}	.218885	A_2	B_{11}	.145924
	A_3	B_{16}	.010698	A_4	B_{16}	.016047
C_7,	A_2	B_{15}	.014264	A_3	B_{15}	.001783
11.920	A_1	B_{14}	.010698	A_2	B_{14}	.001783
				A_1	B_{13}	.016047
C_8,	A_5	B_{17}	.291847	A_6	B_{17}	.145924
32.605				A_5	B_{18}	.145924
C_9,	A_2	B_{17}	.093705	A_3	B_{17}	.187410
39.344	A_1	B_{18}	.281115	A_2	B_{18}	.187410

Table A.2: Table of optical transition intensities $T_{ij}^{(4)}$ between metastable sublevels Y_i and excited sublevels Z_j of ^{4}He in null magnetic field ($B = 0$) for σ^+-polarised and π-polarised lights. Frequency shifts $\epsilon_{ij}^{(4)}/h$ (in GHz) are relative to the C_1 transition of ^{3}He. Values of $\epsilon_{ij}^{(4)}$ and $T_{ij}^{(4)}$ are the same for σ^+, σ^-, and σ polarisations in null field. [Nac12]

line	$\epsilon_{ij}^{(4)}/h$ GHz	$\sigma^\pm$ light			π light		
		levels		$T_{ij}^{(4)}$	levels		$T_{ij}^{(4)}$
D_2	38.534	Y_3	Z_5	1	Y_3	Z_4	1/2
		Y_2	Z_4	1/2	Y_2	Z_3	2/3
		Y_1	Z_3	1/6	Y_1	Z_2	1/2
D_1	40.825	Y_2	Z_8	1/2	Y_3	Z_8	1/2
		Y_1	Z_7	1/2	Y_1	Z_6	1/2
D_0	70.442	Y_1	Z_9	1/3	Y_2	Z_9	1/3

Table A.3: Values of the coefficients of the linear and quadratic terms in equations (2.2) and (2.3) for the commonly used optical transitions in low magnetic field. Linear terms are sufficient to provide a good accuracy up to a few mT, and second order terms extend this accuracy to several tens of mT: the highest relative difference between the quadratic approximation and the actual value is found for $T_{5,18}$ and amounts to 10^{-3} at B=0.05 T and to 2×10^{-2} at B=0.1 T [Nac12].
For convenience, we recall
equation (2.2): $\varepsilon_{ij}(B)/h = \varepsilon_{ij}(0)/h + C_\epsilon^{(1)}B + C_\epsilon^{(2)}B^2$ and
equation (2.3): $T_{ij}(B) = T_{ij}(0) + C_T^{(1)}B + C_T^{(2)}B^2$.

line	pol.	levels		$C_\epsilon^{(1)}$ GHz/T	$C_T^{(1)}$ T^{-1}	$C_\epsilon^{(2)}$ GHz/T^2	$C_T^{(2)}$ T^{-2}
C_8	σ_+	A_5	B_{17}	17.4	-0.883	-22.4	-0.935
C_8	σ_-	A_6	B_{18}	-17.4	0.883	-20.4	-1.104
C_8	π	A_5	B_{18}	19.9	0.589	-22.4	0.806
C_8	π	A_6	B_{17}	-19.9	-0.589	-20.3	1.004
C_9	σ_+	A_1	B_{18}	29.3	-0.280	4.40	0.08
C_9	σ_+	A_2	B_{17}	8.11	0.549	31.25	0.98
C_9	σ_-	A_3	B_{18}	-8.11	-0.549	29.21	1.14
C_9	σ_-	A_4	B_{17}	-29.3	0.280	4.45	0.08
C_9	π	A_2	B_{18}	10.6	-0.643	31.23	-0.93
C_9	π	A_3	B_{17}	-10.6	0.643	29.23	-1.13
D_0	σ_+	Y_1	Z_9	28	-0.316	4.41	0.07
D_0	σ_-	Y_3	Z_9	-28	0.316	4.45	0.07
D_0	π	Y_2	Z_9	0	0	4.43	-0.14

Table A.4: Table of transition frequencies ϵ_{ij}/h, reduced Zeeman shifts $Z_\pm$ (according to equations (4.25) and (4.26)) and optical transition intensities T_{ij} for the C_8 line in ^{3}He for typical values of magnetic field between $B = 0$ and 30 mT. σ^+ light: transition between metastable sublevel A_5 and excited sublevel B_{17}; σ^- light: transition between metastable sublevel A_6 and excited sublevel B_{18}.
For convenience, we recall
equation (4.25): $Z_+ = (\omega_{8+} - \omega_{80})/2\pi D$ and
equation (4.26): $Z_- = (\omega_{80} - \omega_{8-})/2\pi D$.

B mT	σ^+ light			σ^- light		
	ϵ_{ij}/h GHz	Z_+	T_{ij}	ϵ_{ij}/h GHz	Z_-	T_{ij}
0	32.605	0	.29185	32.605	0	.29185
1	32.622	.015	.29096	32.587	.015	.29273
5	32.691	.073	.28741	32.517	.074	.29623
10	32.777	.145	.28293	32.428	.149	.30056
15	32.861	.216	.27839	32.338	.224	.30484
20	32.945	.286	.27382	32.247	.301	.30906
25	33.027	.356	.26920	32.156	.378	.31322
30	33.108	.424	.26455	32.063	.456	.31732

Table A.5: Table of transition frequencies ϵ_{ij}/h, reduced Zeeman shifts Z_+ (according to equations (4.37) and (4.38)) and optical transition intensities T_{ij} for both components of the C_9 σ^+ line in ^{3}He for typical values of magnetic field between $B = 0$ and 30 mT.
For convenience, we recall
equation (4.37): $Z^+_{1,18} = (\omega_{1,18}(B) - \omega_{1,18}(0))/2\pi D$ and
equation (4.38): $Z^+_{2,17} = (\omega_{2,17}(B) - \omega_{2,17}(0))/2\pi D$.

B mT	A_1 to B_{18}			A_2 to B_{17}		
	ϵ_{ij}/h GHz	Z_+	T_{ij}	ϵ_{ij}/h GHz	Z_+	T_{ij}
0	39.344	0	.28111	39.344	0	.09370
1	39.373	.025	.28083	39.352	.007	.09425
5	39.491	.123	.27972	39.386	.035	.09648
10	39.637	.247	.27833	39.428	.071	.09930
15	39.784	.371	.27694	39.473	.108	.10217
20	39.931	.495	.27555	39.519	.147	.10509
25	40.079	.619	.27417	39.566	.187	.10804
30	40.226	.743	.27280	39.616	.229	.11104

Table A.6: Table of transition frequencies ϵ_{ij}/h, reduced Zeeman shifts Z_- and optical transition intensities T_{ij} for both components of the C_9 σ^- line in ^{3}He for typical values of magnetic field between $B = 0$ and 30 mT.

B mT	A_4 to B_{17}			A_3 to B_{18}		
	ϵ_{ij}/h GHz	Z_-	T_{ij}	ϵ_{ij}/h GHz	Z_-	T_{ij}
0	39.344	0	.28111	39.344	0	.09370
1	39.315	.025	.28139	39.336	.007	.09316
5	39.198	.123	.28252	39.304	.034	.09099
10	39.052	.246	.28392	39.266	.066	.08833
15	38.906	.369	.28533	39.229	.097	.08572
20	38.761	.492	.28674	39.194	.127	.08318
25	38.615	.614	.28816	39.160	.155	.08069
30	38.470	.736	.28958	39.127	.183	.07827

In the following, we provide the elements of the B-dependent vector operator L and of the matrix operators E^3 and F^3, needed in ME rate equations (e.g., section 2.4.2). They are taken from [Cou02], and in the given form valid up to $B = 0.162$ T, for which sublevels A_4 and A_5 cross. For more compact expressions, we use the following notations:

$$c_\pm = \cos^2\theta_\pm \quad \text{and} \quad s_\pm = \sin^2\theta_\pm, \tag{A.2}$$

with

$$c_\pm + s_\pm = 1, \tag{A.3}$$

and

$$L_\pm = c_\pm - s_\pm. \tag{A.4}$$

Table A.7: Matrix elements of operator L (for $B < 0.162$ T) [Cou02]

a_k	a_1	a_2	a_3	a_4	a_5	a_6
L_k	-1	L_-	L_+	1	$-L_-$	$-L_+$

Table A.8: Matrix elements of $2E^3_{ik}$ (for $B < 0.162$ T) [Cou02]. Squaring equation (A.3) yields: $(c_\pm + s_\pm)^2 = c_\pm^2 + 2c_\pm s_\pm + s_\pm^2 = 1$, hence the four diagonal elements $\neq 1$ can alternatively be expressed by: $1 - 2c_\pm s_\pm = c_\pm^2 + s_\pm^2$.

	a_1	a_2	a_3	a_4	a_5	a_6	$\leftarrow a_k$
a_1	1	c_-	0	0	s_-	0	
a_2	c_-	$c_-^2 + s_-^2$	$c_+ s_-$	0	$2c_- s_-$	$s_+ s_-$	
a_3	0	$c_+ s_-$	$c_+^2 + s_+^2$	s_+	$c_+ c_-$	$2c_+ s_+$	
a_4	0	0	s_+	1	0	c_+	
a_5	s_-	$2c_- s_-$	$c_+ c_-$	0	$c_-^2 + s_-^2$	$c_- s_+$	
a_6	0	$s_+ s_-$	$2c_+ s_+$	c_+	$c_- s_+$	$c_+^2 + s_+^2$	
$\uparrow a_i$							

Table A.9: Matrix elements of $2F^3_{ik}$ (for $B < 0.162$ T) [Cou02]

	a_1	a_2	a_3	a_4	a_5	a_6	$\leftarrow a_k$
a_1	-1	$-c_-$	0	0	$-s_-$	0	
a_2	c_-	$c_-^2 - s_-^2$	$-c_+s_-$	0	0	$-s_+s_-$	
a_3	0	c_+s_-	$c_+^2 - s_+^2$	$-s_+$	c_+c_-	0	
a_4	0	0	s_+	1	0	c_+	
a_5	s_-	0	$-c_+c_-$	0	$s_-^2 - c_-^2$	$-c_-s_+$	
a_6	0	s_+s_-	0	$-c_+$	c_-s_+	$s_+^2 - c_+^2$	
$\uparrow a_i$							

Appendix B

MEOP rate equations and angular momentum budget in the improved OP model

B.1 The improved OP model

For the ^{3}He gas confined in the cell, the quantum states of the atoms are statistically described by density matrices that depend on atomic positions and velocities. In MEOP the position-dependent parameters systematically include the local plasma characteristics and the OP light intensity. The distribution of metastable atoms is spatially inhomogeneous in the cell due to rf excitation pattern and atomic diffusion that lead to steady state density profiles that necessarily vanish at the walls. The incident light intensity has a radial variation because of the transverse profile of the OP beam (usually Gaussian) and may have a longitudinal dependence because of beam divergence (if any). As a result the resonant excitation experienced by the atoms inside the cell varies with position, in a rather complicated way due to the significant amount of light intensity absorbed by the gas. Furthermore in MEOP, at any position inside the cell, the time evolutions of the internal states depend on the atomic velocities since the Doppler shift of atomic resonance frequencies leads to a wide statistical distribution of optical transition rates.

The OP model developed at LKB to quantitatively describe the evolution of the system in a realistic but simple way, with as few free parameters as possible, relies on the following: 1/ the off-diagonal elements of the density matrices can be safely neglected; 2/ the nuclear polarisation of ground state (1^1S_0) atoms, M, is uniform over the cell (thanks to fast atomic diffusion and slow OP kinetics); 3/ the continuous distribution of diagonal elements for the density matrices for the metastable (2^3S) and excited (2^3P) atoms is replaced by two broad velocity classes of atoms for which the populations of 2^3S and 2^3P Zeeman sublevels satisfy specific rate equations (a single

optical transition rate is assigned to all atoms in each class); 4/ the transfers of atoms between velocity classes that are induced by the ME process and by the elastic collisions are both assumed to involve random changes in atomic velocities, but they provide very distinct contributions to these rate equations (for which the velocity dependence of collision kernels is overlooked); 5/ relaxation processes in metastable and excited states are described by uniform redistribution between Zeeman sublevels within each of the two velocity classes, with identical rates.

The major improvement introduced in the 2-class OP model, as compared to the initial one proposed by Nacher and Leduc in reference [Nac85], consists in assigning a small but *finite* optical transition rate to the atoms that do not belong to the velocity class most efficiently excited by the pump laser light. This modification, as explained in the main text, allows a better quantitative description of MEOP when powerful broadband light sources are used. It leads to a set of slightly more complicated rate equations for the atomic populations (described in this appendix) but preserves the ability of the model to capture the essentials of the strong velocity-dependence introduced by OP with a very limited number of physical parameters. In addition, in contrast with early work [Nac85] where the spatial variations of both incident light intensity and metastable number density were ignored, *local* rate equations are introduced for the populations of Zeeman sublevels in the metastable and excited states in the improved OP model to take the actual spatial inhomogeneity of MEOP dynamics into account.

B.2 Two-class partition and description of local OP rates

The statistical distribution of ^{3}He atoms in the 2^3S metastable state relevant for MEOP is characterised by their number density at position $\vec{r}$, noted $n_{\mathrm{m}}(\vec{r})$, and by the probability, noted $n_{\mathrm{m}}^{(v)}(\vec{r}, v_z)$, that the atom velocity has a projection along the direction z of propagation of the OP beam equal to v_z. The distribution of probability $n_{\mathrm{m}}^{(v)}(\vec{r}, v_z)$ satisfies:

$$n_{\mathrm{m}}(\vec{r}) = \int_{-\infty}^{+\infty} n_{\mathrm{m}}^{(v)}(\vec{r}, v_z) dv_z \tag{B.1}$$

and is assumed to be identical to the Maxwellian distribution of atomic velocities in the gas at thermal equilibrium (i.e., to be proportional to $\exp -v_z^2/\bar{v}^2$ where $\bar{v} = \sqrt{2k_B T/M_3}$ is the most probable atom velocity − see equation (2.8) and figure 2.5a in the main text).

Following reference [Cou02] the population of the metastable Zeeman sublevel A_i, equal to the diagonal elements of the density matrix $\rho_{\mathrm{S}}(\vec{r}, v_z)$ of ^{3}He atoms in the 2^3S state, is noted:

$$a_i^{(v)}(\vec{r}, v_z) = \langle \mathrm{A}_i \left| \rho_{\mathrm{S}}(\vec{r}, v_z) \right| \mathrm{A}_i \rangle \tag{B.2}$$

$$\text{with } \sum_{i=1}^{6} a_i^{(v)}(\vec{r}, v_z) = 1. \tag{B.3}$$

For the diagonal elements of the density matrices in the 2^3P state, the number density of ^{3}He atoms in excited Zeeman sublevel B_j with velocity projection v_z is chosen equal to $n_{\mathrm{m}}^{(v)}(\vec{r}, v_z) b_j^{(v)}(\vec{r}, v_z)$ so as to stick to the convenient notation introduced in references [Nac85] and [Cou02]. With this notation a closed set of rate equations can be written for MEOP using only one local statistical distribution[1], $n_{\mathrm{m}}^{(v)}(\vec{r}, v_z)$, where those for the excited atoms involve the quantities $b_j^{(v)}$ (still called "populations" for simplicity) that are actually *not* normalised populations:

$$\sum_{j=1}^{18} b_j^{(v)}(\vec{r}, v_z) \neq 1. \tag{B.4}$$

Thus, the statistical distribution of excited ^{3}He atoms in the 2^3P state is just characterised by the velocity distribution:

$$n_{\mathrm{P}}^{(v)}(\vec{r}, v_z) = n_{\mathrm{m}}^{(v)}(\vec{r}, v_z) \sum_{j=1}^{18} b_j^{(v)}(\vec{r}, v_z) \tag{B.5}$$

and the number density:

$$n_{\mathrm{P}}(\vec{r}) = \int_{-\infty}^{+\infty} n_{\mathrm{P}}^{(v)}(\vec{r}, v_z) dv_z = \int_{-\infty}^{+\infty} n_{\mathrm{m}}^{(v)}(\vec{r}, v_z) \sum_j b_j^{(v)}(\vec{r}, v_z) dv_z \tag{B.6}$$

where the populations $b_j^{(v)}(\vec{r}, v_z)$ are indeed fully determined by the 2^3S populations $a_i^{(v)}(\vec{r}, v_z)$ and statistical distribution $n_{\mathrm{m}}^{(v)}(\vec{r}, v_z)$.

In the improved OP model, the continuous distributions of number densities $n_{\mathrm{m}}^{(v)}(\vec{r}, v_z)$ and of populations $a_i^{(v)}(\vec{r}, v_z)$ (hence, of populations $b_j^{(v)}(\vec{r}, v_z)$) are replaced by **two sets of number densities and of populations**, used to characterise the two velocity classes, that are **both involved in OP.** These velocity classes are obtained from the coarse partition of the thermal Boltzmann distribution illustrated in figure 2.5a. These sets are noted $n_{\mathrm{m}}^*(\vec{r})$, $a_i^*(\vec{r})$ for the *strongly pumped* class of

[1] One could also introduce a number density velocity distribution of atoms in the 2^3P state $n_{\mathrm{P}}^{(v)}(\vec{r}, v_z)$ and the corresponding total number density $n_{\mathrm{P}}(\vec{r})$, together with normalised populations $\tilde{b}_j^{(v)}(\vec{r}, v_z)$, such that $n_{\mathrm{P}}^{(v)}\ \tilde{b}_j^{(v)} = n_{\mathrm{S}}^{(v)}\ b_j^{(v)}$. With such a choice of parameters, rate equations would be slightly less convenient to write and to solve numerically, containing one more parameter and one additional normalisation equation for $b_j^{(v)}$s. With our approach, a single number density velocity distribution function is used, and the actual number density velocity distribution in the 2^3P state is simply obtained as $n_{\mathrm{P}}^{(v)} = n_{\mathrm{S}}^{(v)} \times \sum_j b_j^{(v)}$.

metastable atoms and $b_j^*(\vec{r})$ for the coupled set of excited populations in the 2^3P state, and $n'_{\mathrm{m}}(\vec{r})$, $a'_i(\vec{r})$ and $b'_j(\vec{r})$ for the *weakly pumped* class, respectively.

As was the case in earlier work, the strongly pumped class (hatched part of the velocity distribution in figure 2.5a) is defined by a symmetric interval of atomic velocity projections around the null average value. Although the detuning δ_{L} between the average frequency of the pump laser and the targeted atomic transition is kept as small as possible in the experiments, it can never be exactly equal to zero in practice (especially when the C_9 line is used for OP at finite magnetic field strength). The actual laser profile is depicted in figure 2.5b and the atoms with velocity projections close to the $\bar{v}\delta_{\mathrm{L}}/D$ are indeed most efficiently excited by the pump light. However, since all experiments have been performed in a double-pass configuration (where the transmitted OP light beam is back-reflected into the gas cell) and ^{3}He atoms weakly absorb 1083 nm light, atoms with positive and negative velocity projections experience almost equal pumping rates and the description by a symmetrical velocity class is legitimate.

The velocity v_z^* that specifies the boundaries of the strongly pumped class is a free parameter in the model. The strongly (resp. weakly) pumped class consists of atoms in the central part (resp. the wings) of the Maxwellian velocity distribution that have velocity projections v_z such that $|v_z| < v_z^*$ (resp. $|v_z| > v_z^*$). The local 2^3S number densities n_{m}^* and n'_{m} are integrals of the statistical distribution $n_{\mathrm{m}}^{(v)}(\vec{r}, v_z)$ over the corresponding velocity intervals:

$$n_{\mathrm{m}}^*(\vec{r}) = \int_{-v_z^*}^{v_z^*} n_{\mathrm{m}}^{(v)}(\vec{r}, v_z) dv_z, \tag{B.7}$$

$$n'_{\mathrm{m}}(\vec{r}) = \int_{-\infty}^{-v_z^*} n_{\mathrm{m}}^{(v)}(\vec{r}, v_z) dv_z + \int_{v_z^*}^{+\infty} n_{\mathrm{m}}^{(v)}(\vec{r}, v_z) dv_z \tag{B.8}$$

that satisfy, everywhere in the OP cell:

$$n_{\mathrm{m}}(\vec{r}) = n_{\mathrm{m}}^*(\vec{r}) + n'_{\mathrm{m}}(\vec{r}). \tag{B.9}$$

A characteristic frequency offset Δ is associated to the maximum Doppler shift associated to the atoms in the strongly pumped class:

$$\Delta = D v_z^* / \bar{v}, \tag{B.10}$$

that best describes the part of the laser profile contributing most to OP of the ^{3}He atoms (see figure 2.5b).

As regards the distributions of populations, the choice made for both classes in the 2^3S state is:

$$\sum_{i=1}^{6} a_i^*(\vec{r}) = \sum_{i=1}^{6} a'_i(\vec{r}) = 1, \tag{B.11}$$

so that the local number density of 2^3S atoms in Zeeman sublevel A_i is equal to:

$$n^*_{\rm m}(\vec{r})a^*_i(\vec{r}) + n'_{\rm m}(\vec{r})a'_i(\vec{r}) \tag{B.12}$$

and the evolution in the 2^3P state is described by rate equations ruling the density distributions $n^*_{\rm m}b^*_j$ and $n'_{\rm m}b'_j$ for the 18 Zeeman sublevels of the excited state that are obtained from the corresponding 3-compartment binning of the continuous distributions.

B.3 Local rate equations for 2^3S and 2^3P populations

The *(quasi) stationary* local number densities $n^*_{\rm m}a^*_i$ and $n'_{\rm m}a'_i$ of all sublevels of the **2^3S state** are computed as solutions of **twin sets of local full rate equations** that involve **four terms** corresponding to OP (p), ME (e), velocity changing collisions (c), and relaxation (r) processes. For simplicity the dependence on position is not explicitly written in the equations, unless necessary. The full rate equations:

$$\left.\frac{d\,(n^*_{\rm m}a^*_i)}{dt}\right|_{\rm p} + \left.\frac{d\,(n^*_{\rm m}a^*_i)}{dt}\right|_{\rm e} + \left.\frac{d\,(n^*_{\rm m}a^*_i)}{dt}\right|_{\rm c} + \left.\frac{d\,(n^*_{\rm m}a^*_i)}{dt}\right|_{\rm r} = 0 \tag{B.13}$$

$$\left.\frac{d\,(n'_{\rm m}a'_i)}{dt}\right|_{\rm p} + \left.\frac{d\,(n'_{\rm m}a'_i)}{dt}\right|_{\rm e} + \left.\frac{d\,(n'_{\rm m}a'_i)}{dt}\right|_{\rm c} + \left.\frac{d\,(n'_{\rm m}a'_i)}{dt}\right|_{\rm r} = 0. \tag{B.14}$$

replace the generic full rate equation for populations in the 2^3S state (2.50) of the main text.

- The **OP terms** (p) are local both in space and momentum. They consist of contributions from spontaneous and stimulated emission by 2^3P atoms and from absorption by 2^3S atoms:

$$\left.\frac{d\,(n^*_{\rm m}a^*_i)}{dt}\right|_{\rm p} = \gamma \sum T_{ij}\; n^*_{\rm m}b^*_j + \sum \gamma^*_{ij}(n^*_{\rm m}b^*_j - n^*_{\rm m}a^*_i) \tag{B.15}$$

$$\left.\frac{d\,(n'_{\rm m}a'_i)}{dt}\right|_{\rm p} = \gamma \sum T_{ij}\; n'_{\rm m}b'_j + \sum \gamma'_{ij}(n'_{\rm m}b'_j - n'_{\rm m}a'_i), \tag{B.16}$$

where the radiative decay rate γ of the 2^3P state and the effective OP rates γ^*_{ij} and γ'_{ij} are those used in the main text (equations (2.43), (2.38), and (2.39), respectively).[2]

[2]Given the fast ME rate in the 2^3S state and the fast decay rate in the 2^3P state (both of order $10^7{\rm s}^{-1}$), and the diffusion coefficient of excited He atoms (D^*=550 cm^2/s in a gas at 1 torr, [Fit68]), the diffusion length is of order 0.15 mm. This is much shorter than the scale over which our experimental conditions significantly vary (e.g., the OP beam diameter), hence non-local contributions to the rate equations arising from atomic diffusion have been omitted in equations (B.13) and (B.14).

Equations (B.15) and (B.16) replace the generic OP rate equation (2.19) of the main text. The effective OP rates γ^*_{ij} and γ'_{ij} of the strongly and weakly pumped classes, respectively, depend on the local characteristics of the OP light (intensity, direction of propagation, spectral characteristics). They have been chosen equal to:

$$\gamma^*_{ij}(\vec{r}) = \frac{\int_{-v_z^*}^{v_z^*} \gamma^{(v)}_{ij}(\vec{r}, v_z) e^{-v_z^2/\bar{v}^2} dv_z}{\int_{-v_z^*}^{v_z^*} e^{-v_z^2/\bar{v}^2} dv_z} \tag{B.17}$$

$$\gamma'_{ij}(\vec{r}) = \frac{\int_{-\infty}^{-v_z^*} \gamma^{(v)}_{ij}(\vec{r}, v_z) e^{-v_z^2/\bar{v}^2} dv_z + \int_{v_z^*}^{+\infty} \gamma^{(v)}_{ij}(\vec{r}, v_z) e^{-v_z^2/\bar{v}^2} dv_z}{\int_{-\infty}^{-v_z^*} e^{-v_z^2/\bar{v}^2} dv_z + \int_{v_z^*}^{\infty} e^{-v_z^2/\bar{v}^2} dv_z} \tag{B.18}$$

in order to exactly describe the OP kinetics in the linear limit of weak pumping rates. The compact expressions appearing in equations (2.38) and (2.39), recalled below:

$$\gamma^*_{ij}(\vec{r}) = \bar{\gamma}_{ij}(\vec{r}) \frac{n_{\mathrm{m}}(\vec{r})}{n^*_{\mathrm{m}}(\vec{r})} \Sigma^* = \frac{\bar{\gamma}_{ij}(\vec{r}) \Sigma^*}{\mathrm{erf}(\Delta/D)} \tag{B.19}$$

$$\gamma'_{ij}(\vec{r}) = \bar{\gamma}_{ij}(\vec{r}) \frac{n_{\mathrm{m}}(\vec{r})}{n'_{\mathrm{m}}(\vec{r})} \Sigma' = \frac{\bar{\gamma}_{ij}(\vec{r}) \Sigma'}{1 - \mathrm{erf}(\Delta/D)}, \tag{B.20}$$

involve the average local optical transition rate $\overline{\gamma_{ij}}(\vec{r})$ (equation 2.40):

$$\overline{\gamma_{ij}}(\vec{r}) = \frac{\sqrt{\pi} \alpha f}{m_{\mathrm{e}} \omega D} \; T_{ij} \;\; I_{\mathrm{cell}}(\vec{r}), \tag{B.21}$$

associated to the broadband pump light (see section 2.3.2) and the dimensionless factors Σ^* and Σ' defined by integrals over the corresponding intervals of velocity projections:

$$\Sigma^* = \frac{D}{L\sqrt{\pi}} \int_{-v_z^*}^{v_z^*} \exp\left[-\left(\frac{\delta_{\mathrm{L}}}{L} - \frac{D}{L}\frac{v_z}{\bar{v}}\right)^2\right] \exp\left[-\left(\frac{v_z}{\bar{v}}\right)^2\right] \frac{dv_z}{\bar{v}} \tag{B.22}$$

$$\Sigma' = \frac{D}{L\sqrt{\pi}} \left\{ \int_{-\infty}^{-v_z^*} \exp\left[-\left(\frac{\delta_{\mathrm{L}}}{L} - \frac{D}{L}\frac{v_z}{\bar{v}}\right)^2\right] \exp\left[-\left(\frac{v_z}{\bar{v}}\right)^2\right] \frac{dv_z}{\bar{v}} + \int_{v_z^*}^{+\infty} \mathrm{idem} \right\}. \tag{B.23}$$

This leads to the following general expression of Σ^* for the strongly pumped class:

$$\Sigma^* = \frac{D}{2\sqrt{L^2 + D^2}} e^{-\delta_{\mathrm{L}}^2/\left(D^2+L^2\right)} \left\{ \mathrm{erf}\left[\frac{\sqrt{L^2+D^2}}{L}\left(\frac{v_z^*}{\bar{v}} + \frac{D\delta_{\mathrm{L}}}{D^2+L^2}\right)\right] + \mathrm{erf}\left[\frac{\sqrt{L^2+D^2}}{L}\left(\frac{v_z^*}{\bar{v}} - \frac{D\delta_{\mathrm{L}}}{D^2+L^2}\right)\right] \right\}, \tag{B.24}$$

from which Σ' is easily derived for the weakly pumped class, using:

$$\Sigma^* + \Sigma' = \frac{D}{\sqrt{D^2+L^2}} e^{-\delta_{\mathrm{L}}^2/\left(D^2+L^2\right)}. \tag{B.25}$$

When the laser is tuned to the atomic transition (δ_{L}=0), equations (B.24) and (B.25) reduce to the simpler form given in the main text (equations 2.41 and 2.42):

$$\Sigma^* = \frac{D}{\sqrt{L^2+D^2}} \operatorname{erf}\left(\frac{\sqrt{L^2+D^2}\Delta}{LD}\right) \tag{B.26}$$

$$\Sigma' = \frac{D}{\sqrt{L^2+D^2}} - \Sigma^*. \tag{B.27}$$

- The **ME terms** (e) describe the contribution of local exchanges with ground state atoms through collisions that strongly modify the velocities of colliding atoms in addition to modifying the internal variables (due to their small impact parameters, see main text). Thus, assuming fully uncorrelated velocities for incoming and outgoing atoms in ME collisions, these terms are simply written as:

$$\left.\frac{d\left(n_{\mathrm{m}}^* a_i^*\right)}{dt}\right|_{\mathrm{e}} = \gamma_{\mathrm{e}} n_{\mathrm{m}}^* \left[-a_i^* + \sum_{k=1}^{6}\left(E_{ik}^3 + MF_{ik}^3\right)\frac{n_{\mathrm{m}}^* a_k^* + n_{\mathrm{m}}' a_k'}{n_{\mathrm{m}}}\right] \tag{B.28}$$

$$\left.\frac{d\left(n_{\mathrm{m}}' a_i'\right)}{dt}\right|_{\mathrm{e}} = \gamma_{\mathrm{e}} n_{\mathrm{m}}' \left[-a_i' + \sum_{k=1}^{6}\left(E_{ik}^3 + MF_{ik}^3\right)\frac{n_{\mathrm{m}}^* a_k^* + n_{\mathrm{m}}' a_k'}{n_{\mathrm{m}}}\right]. \tag{B.29}$$

A common ME rate γ_{e} is used in both equations, in spite of a possible difference arising from the energy dependence of the ME cross-section (that leads, for instance, to the temperature-dependence of γ_{e} [Fit68]). Atoms in the strongly pumped class are indeed slower on average, hence may have a lower ME rate than atoms in the weakly pumped class. But, as was done in earlier work [Nac85], this difference is overlooked in the model for simplicity. Equations (B.28) and (B.29) replace the generic ME rate equation for 2^3S populations (2.21) of the main text. They involve the same matrix operators E^3 and F^3, whose field-dependent coefficients are listed in tables A.8 and A.9. It can be easily checked that they can be combined to obtain the generic ME rate equation (2.21), satisfied indeed by the local number density of 2^3S atoms in Zeeman sublevel A_i (B.12).

- The **velocity changing terms** (c) in equations (B.13) and (B.14) also arise from local interactions but involve elastic collisions (i.e., not affecting the internal variables, unlike ME collisions) leading to changes in velocities that are sufficient to exchange atoms between the two classes. No attempt is made to derive quantitative rates from collision kernels and the effects of these collisions on the populations of the 2^3S state are phenomenologically described using a single effective rate γ_{c} for all Zeeman sublevels:

$$\left.\frac{d\left(n_{\mathrm{m}}^* a_i^*\right)}{dt}\right|_{\mathrm{c}} = \gamma_{\mathrm{c}} n_{\mathrm{m}}^* \left[-a_i^* + \frac{n_{\mathrm{m}}^* a_i^* + n_{\mathrm{m}}' a_i'}{n_{\mathrm{m}}}\right] \tag{B.30}$$

$$\left.\frac{d\left(n_{\mathrm{m}}' a_i'\right)}{dt}\right|_{\mathrm{c}} = \gamma_{\mathrm{c}} n_{\mathrm{m}}' \left[-a_i' + \frac{n_{\mathrm{m}}^* a_i^* + n_{\mathrm{m}}' a_i'}{n_{\mathrm{m}}}\right]. \tag{B.31}$$

These couplings between velocity classes have been ignored in reference [Nac85] but they were indirectly taken into account through a deliberately increased width of the pumped OP class. Equations (B.30) and (B.31) duly conserve the local number density of atoms in any Zeeman sublevel A_i:

$$\left.\frac{d\left(n_{\mathrm{m}}^{*}a_{i}^{*}\right)}{dt}\right|_{\mathrm{c}}+\left.\frac{d\left(n_{\mathrm{m}}^{\prime}a_{i}^{\prime}\right)}{dt}\right|_{\mathrm{c}}=0 \tag{B.32}$$

- The **relaxation terms** (r) still phenomenologically describe the contribution of all other processes by a uniform redistribution within Zeeman sublevels, and a single relaxation rate $\gamma_{\mathrm{r}}^{\mathrm{S}}$ is introduced for both velocity classes:

$$\left.\frac{d\left(n_{\mathrm{m}}^{*}a_{i}^{*}\right)}{dt}\right|_{\mathrm{r}}=\gamma_{\mathrm{r}}^{\mathrm{S}}n_{\mathrm{m}}^{*}\left[\frac{1}{6}-a_{i}^{*}\right] \tag{B.33}$$

$$\left.\frac{d\left(n_{\mathrm{m}}^{\prime}a_{i}^{\prime}\right)}{dt}\right|_{\mathrm{r}}=\gamma_{\mathrm{r}}^{\mathrm{S}}n_{\mathrm{m}}^{\prime}\left[\frac{1}{6}-a_{i}^{\prime}\right]. \tag{B.34}$$

Equations (B.33) and (B.34) replace the generic rate equation for relaxation of 2^3S populations (2.36) of the main text.

The *(quasi) stationary* local number densities $n_{\mathrm{m}}^{*}b_{j}^{*}$ and $n_{\mathrm{m}}^{\prime}b_{j}^{\prime}$ for the eighteen Zeeman sublevels of the excited **2^3P state** are solutions of twin sets of full rate equations that contain only **two terms**, one for the OP process (p) and one for relaxation (r):

$$\left.\frac{d\left(n_{\mathrm{m}}^{*}b_{j}^{*}\right)}{dt}\right|_{\mathrm{p}}+\left.\frac{d\left(n_{\mathrm{m}}^{*}b_{j}^{*}\right)}{dt}\right|_{\mathrm{r}}=0 \tag{B.35}$$

$$\left.\frac{d\left(n_{\mathrm{m}}^{\prime}b_{j}^{\prime}\right)}{dt}\right|_{\mathrm{p}}+\left.\frac{d\left(n_{\mathrm{m}}^{\prime}b_{j}^{\prime}\right)}{dt}\right|_{\mathrm{r}}=0. \tag{B.36}$$

Equations (B.35) and (B.36) replace the generic full rate equation for populations in the 2^3P state (2.49) of the main text.

- The OP terms (p), local both in space and momentum, describe the outflow due to spontaneous light emission by 2^3P atoms and radiative decay to 2^3S (first term on right-hand side of equations B.37 and B.38) and the net balance between inflow due to light excitation of 2^3S atoms and outflow due to stimulated light emission

by 2^3P atoms (second term on right-hand side of equations B.37 and B.38):

$$\left.\frac{d\left(n_{\mathrm{m}}^{*}b_{j}^{*}\right)}{dt}\right|_{\mathrm{p}} = -\gamma\ n_{\mathrm{m}}^{*}b_{j}^{*} + \sum \gamma_{ij}^{*}(n_{\mathrm{m}}^{*}a_{i}^{*} - n_{\mathrm{m}}^{*}b_{j}^{*}) \tag{B.37}$$

$$\left.\frac{d\left(n_{\mathrm{m}}'b_{j}'\right)}{dt}\right|_{\mathrm{p}} = -\gamma\ n_{\mathrm{m}}'b_{j}' + \sum \gamma_{ij}'(n_{\mathrm{m}}'a_{i}' - n_{\mathrm{m}}'b_{j}') \tag{B.38}$$

Equations (B.37) and (B.38) replace the generic OP rate equation for 2^3P populations (2.20) of the main text.

- The relaxation terms (r) phenomenologically account for a uniform redistribution within Zeeman sublevels with a single relaxation rate $\gamma_{\mathrm{r}}^{\mathrm{P}}$ in the 2^3P state:

$$\left.\frac{d\left(n_{\mathrm{m}}^{*}b_{j}^{*}\right)}{dt}\right|_{\mathrm{r}} = \gamma_{\mathrm{r}}^{\mathrm{P}}n_{\mathrm{m}}^{*}\left[\left(\frac{1}{18}\sum\nolimits_{k=1}^{18} b_{k}^{*}\right) - b_{j}^{*}\right] \tag{B.39}$$

$$\left.\frac{d\left(n_{\mathrm{m}}'b_{j}'\right)}{dt}\right|_{\mathrm{r}} = \gamma_{\mathrm{r}}^{\mathrm{P}}n_{\mathrm{m}}'\left[\left(\frac{1}{18}\sum\nolimits_{k=1}^{18} b_{k}'\right) - b_{j}'\right]. \tag{B.40}$$

Equations (B.39) and (B.40) replace the generic rate equation for relaxation of 2^3P populations (2.35) of the main text. The rate $\gamma_{\mathrm{r}}^{\mathrm{P}}$ that describes the effect of additional processes coupling the populations of various 2^3P sublevel is expected to significantly differ from the rate $\gamma_{\mathrm{r}}^{\mathrm{S}}$ involved in the metastable state, where the orbital angular momentum (L=0) cannot be affected by collisions and where Zeeman populations may only be coupled by spin-exchange (i.e., through ME collisions). Indeed relaxation is usually rather slow in the 2^3S state and associated, for instance, to de-excitation of the metastable atoms (19.6 eV energy) and re-population in the plasma. Depending on pressure, cell dimension, gas purity, etc., relaxation rates $\gamma_{\mathrm{r}}^{\mathrm{S}}$ are typically of order 10^3 s^{-1} in the 2^3S state. These rates may depend on position in the cell (if diffusion to cell walls significantly contributes to de-excitation) or on velocity (if energy-dependent quenching collisions are involved, but this is usually overlooked for the sake of simplicity). In contrast, redistribution between Zeeman sublevels occurs in the 2^3P state at a significantly higher rate and J-changing collisions, for instance, are associated to mixing rates that increase proportionally to pressure and are of order 10^7 s^{-1}/mbar (see references and discussion in section 6.3.2). This can result in significant population transfers during the excited state lifetime $1/\gamma$. The J-dependence of the collisional mixing rates is ignored in the model and relaxation is phenomenologically described by a single relaxation rate $\gamma_{\mathrm{r}}^{\mathrm{P}}$ for all 2^3P atoms.

Transfer between velocity classes may occur in the 2^3P state and yield contributions to the rate equations (B.35) and (B.36) similar to those introduced in equations (B.30) and (B.31), but involving the $n_{\mathrm{m}}^{*}b_{j}^{*}$ and $n_{\mathrm{m}}'b_{j}'$ number densities and another

phenomenological collision rate. However collisions with impact parameters that are small enough to significantly change atomic velocities would plausibly strongly affect the internal states of atoms in the 2^3P state. Such collisions would hence induce collisional mixing and be described as relaxation terms for the populations. Their contribution is thus neglected in the model by simply assuming that:

$$\left.\frac{d\left(n_{\mathrm{m}}^{*}b_{j}^{*}\right)}{dt}\right|_{\mathrm{c}} \ll \left.\frac{d\left(n_{\mathrm{m}}^{*}b_{j}^{*}\right)}{dt}\right|_{\mathrm{r}} \quad \text{and} \quad \left.\frac{d\left(n_{\mathrm{m}}'b_{j}'\right)}{dt}\right|_{\mathrm{c}} \ll \left.\frac{d\left(n_{\mathrm{m}}'b_{j}'\right)}{dt}\right|_{\mathrm{r}}. \tag{B.41}$$

The plasma discharge also steadily populates the 2^3P state of atoms that decay emitting 1083 nm light. In the absence of pumping light, the number densities in the 2^3S and 2^3P states can be expected to scale with the lifetimes in theses states, which are typically four orders of magnitude longer in the 2^3S state. This populating effect of the plasma is usually neglected (but might be also introduced for the sake of completeness).

B.4 Rate equation for M, MEOP dynamics, and global angular momentum budget

Since ground state polarisation M is uniform in the OP cells (thanks to to little z-dependence of the OP light intensity in long cells and fast transverse diffusion in low pressure gas) in all situations of interest, the local contributions to the rate equation arising from ME can be integrated over the cell volume and combined with that of relaxation to obtain the global rate equation that describes the slow time evolution of M:

$$\frac{dM}{dt} = \left.\frac{dM}{dt}\right|_{\mathrm{r}} + \left.\frac{dM}{dt}\right|_{\mathrm{e}}. \tag{B.42}$$

This global rate equation, formally identical to the generic one (2.51) has already been given in the main text (equation 2.53): a single rate Γ_{g} phenomenologically accounts for relaxation processes directly affecting the nuclear polarisation of ground state atoms *in given OP conditions*:

$$\left.\frac{dM}{dt}\right|_{\mathrm{r}} = -\Gamma_{\mathrm{g}}M \tag{B.43}$$

and in the improved OP model, the ME term reads:

$$\begin{aligned}\left.\frac{dM}{dt}\right|_{\mathrm{e}} &= \gamma_{\mathrm{e}}\int_{\mathrm{cell}}\frac{d^3\vec{r}}{V_{\mathrm{c}}}\,\frac{n_{\mathrm{m}}(\vec{r})}{N_{\mathrm{g}}}\left(\sum_{k=1}^{6}L_k\frac{n_{\mathrm{m}}^{*}(\vec{r})a_k^{*}(\vec{r},M)+n_{\mathrm{m}}'(\vec{r})a_k'(\vec{r},M)}{n_{\mathrm{m}}(\vec{r})}-M\right)\\ &= \gamma_{\mathrm{e}}\int_{\mathrm{cell}}\frac{d^3\vec{r}}{V_{\mathrm{c}}}\,\frac{n_{\mathrm{m}}(\vec{r})}{N_{\mathrm{g}}}(M^{\mathrm{S}}(\vec{r},M)-M),\end{aligned} \tag{B.44}$$

where $n^*_{\rm m}(\vec{r})a^*_k(\vec{r},M)$ (resp. $n'_{\rm m}(\vec{r})a'_k(\vec{r},M)$) explicitly refers to the *M-dependent* quasi-stationary local number density $n^*_{\rm m}a^*_i$ (resp. $n'_{\rm m}a'_i$) of metastable atoms in the strongly (resp. weakly) pumped velocity class that satisfies the steady-state equation (B.13) (resp. B.14). Equation (B.44) involves, of course, the same vector operator L as the generic ME contribution to ground state evolution (2.22) described in the main text.

The last form of the ME contribution $dM/dt|_{\rm e}$ in equation (B.44) makes use of the expression (2.54) given in the main text for the local value of the 2^3S nuclear angular momentum in the improved OP model:

$$M^{\rm S}(\vec{r}) = \sum_{k=1}^{6} L_k \frac{n^*_{\rm m}(\vec{r})a^*_k(\vec{r}) + n'_{\rm m}a'_k(\vec{r})}{n_{\rm m}(\vec{r})}. \tag{B.45}$$

In the improved OP model, the generic expression (2.30) of the local value of the longitudinal component of the total angular momentum in the metastable state is similarly replaced by:

$$\langle F_z\rangle_{2^3{\rm S}}(\vec{r}) = \hbar \sum_{i=1} m_{\rm F}(i)\ \frac{n^*_{\rm m}(\vec{r})a^*_k(\vec{r}) + n'_{\rm m}(\vec{r})a'_k(\vec{r})}{n_{\rm m}(\vec{r})} \tag{B.46}$$

and the equation that describes the global conservation of angular momentum projections (instead of the generic condition (2.29) of the main text):

$$\int_{\rm cell} \frac{d^3\vec{r}}{V_{\rm c}}\ n_{\rm m}(\vec{r})\ \left.\frac{d\,\langle F_z\rangle_{2^3{\rm S}}(\vec{r})}{dt}\right|_{\rm e} + N_{\rm g}\ \left.\frac{d\,\langle I_z\rangle_{1^1{\rm S}_0}}{dt}\right|_{\rm e} = 0 \tag{B.47}$$

can be checked to be duly satisfied, using the built-in property (2.27) of the operators E^3, F^3, and L_k.

The rate equations of the improved OP model yield exactly the same results as the generic ones in the absence of OP. *In the presence of OP*, they lead to the following expression of the global angular momentum budget (instead of equation (2.73) in the main text):

$$\begin{aligned}\frac{dM}{dt} = &\int_{\rm cell} \frac{d^3\vec{r}}{V_{\rm c}}\ \frac{n_{\rm m}(\vec{r})}{N_{\rm g}}\ 2\ \frac{1}{\hbar}\left.\frac{d\,\langle F_z\rangle_{2^3{\rm S}}(\vec{r})}{dt}\right|_{\rm p} \\ &- \int_{\rm cell} \frac{d^3\vec{r}}{V_{\rm c}}\ \frac{n_{\rm m}(\vec{r})}{N_{\rm g}}\ 2\ \gamma^{\rm S}_{\rm r}\ \frac{\langle F_z\rangle_{2^3{\rm S}}(\vec{r})}{\hbar} + \left.\frac{dM}{dt}\right|_{\rm r}.\end{aligned} \tag{B.48}$$

Appendix C

Computation of the average pump light intensity inside the cell for the improved OP model

The local pump light intensity $I_{\text{cell}}(r)$ used in the OP model is computed from the incident light distribution $I_0(r)$ (Gaussian transverse profile) of the pump beam that propagates along the cell in our experimental double-pass configuration. We recall here that in this 1-D model, only the radial variation of the number density of 2^3S atoms is considered, and the rate k_a of light absorption by the gas is assumed to be uniform at fixed distance to the cell axis (radial coordinate r)[1]. This light absorption rate depends on $I_{\text{cell}}(r)$ through the light-induced redistribution of populations in 2^3S Zeeman sub-levels (a_i^* and a_i' for the strongly and weakly pumped velocity classes). Therefore a self-consistent numerical computation of $I_{\text{cell}}(r)$ and k_a is actually performed for each discrete radial position r, as described in section 2.7.3, using an iterative procedure that involves an analytical expression of the *average* pump light intensity in the cell at fixed absorption rate k_a. In this appendix, we explain how this average light intensity is obtained at any arbitrarily fixed distance r from the cell axis.

The first step of our derivation consists in determining the pump light intensity $I(z)$ in the double-pass configuration, taking into account the absorption by the gas along the light path as shown in figure C.1. Reflections on the cell windows are neglected, and with uniform absorption rate k_a, the local variation (dI_i/dz) of light intensity I_i for pass i $(i = 1,\ 2)$ per unit length along the z-direction satisfies:

$$\frac{dI_i}{dz} = -k_a\ I_i(z).$$

[1]For simplicity we omit in this appendix the implicit dependence on the radial coordinate r for the absorption rate k_a, as well as for the computed light intensities I_1, I_2, I_{T}, I. We only retain the explicit r-dependence for the incident light intensity I_0.

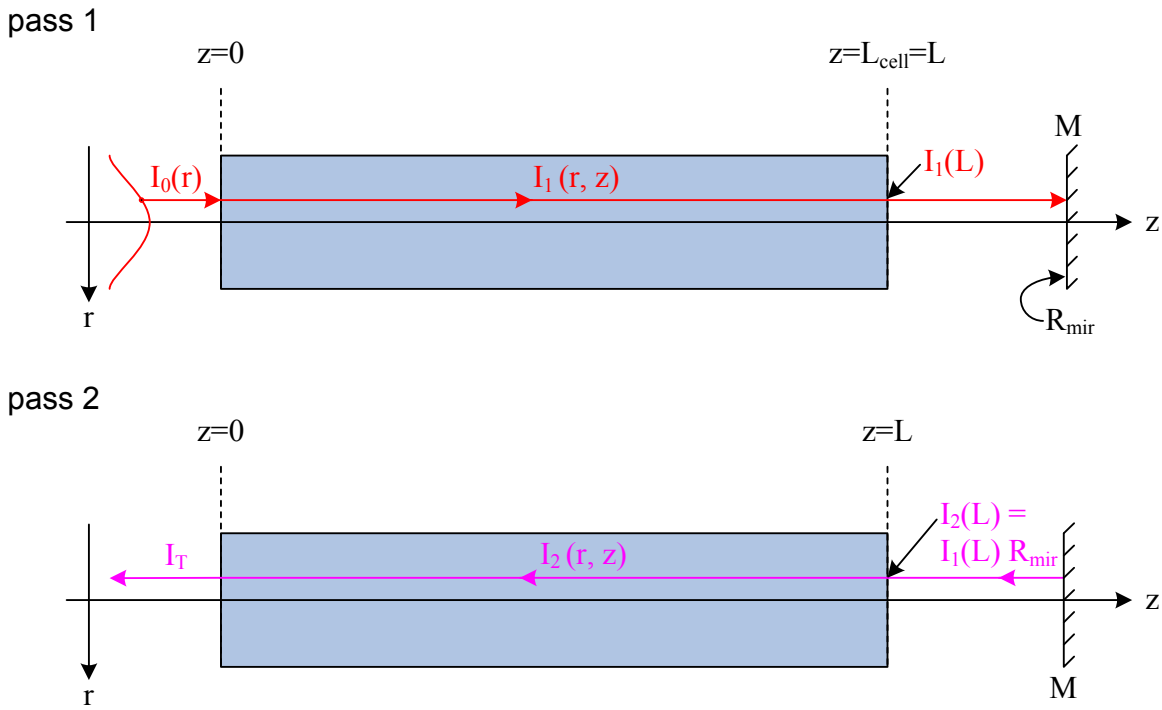

Figure C.1: Scheme illustrating the analytical derivation of the local pump light intensity $I(z) = I_1(z) + I_2(z)$ at fixed distance r from the cell axis, from the two contributions $I_1(z)$ (pass 1) and $I_2(z)$ (pass 2) of the propagating pump beam inside the cell (see text for details). The pump light intensity $I_{\text{cell}}(r)$ is then obtained as the average of $I(z)$ along z. I_0 is the (r-dependent) incident pump light intensity. I_{T} is the transmitted light intensity after the double-pass light path inside the cell of length $L = L_{\text{cell}}$. R_{mir} designates the reflectivity of the back-reflecting mirror M.

The intensity I_1 of the pump light propagating through the gas-filled cell on pass 1 is thus given by:

$$I_1(z) = I_0(r)\ \mathrm{e}^{-k_a z}. \tag{C.1}$$

The light beam exiting the cell with intensity:

$$I_1\ \mathrm{out} = I_1(L) = I_0(r)\ \mathrm{e}^{-k_a L} \tag{C.2}$$

is back reflected by the mirror and enters the cell again for pass 2 with intensity:

$$I_2\ \mathrm{in} = R_{\mathrm{mir}}\ I_0\ \mathrm{e}^{-k_a L} = I_2(L). \tag{C.3}$$

The intensity I_2 of the pump light propagating through the gas-filled cell on pass 2 is given by:

$$I_2(z) = I_2(L)\ \mathrm{e}^{-k_a (L-z)} \tag{C.4}$$

and the pump beam finally leaves the cell with transmitted intensity:

$$I_{\mathrm{T}} = I_2(z=0) = I_2(L)\ \mathrm{e}^{-k_a L}. \tag{C.5}$$

In figure C.2, the light intensities $I_1(z)$ and $I_2(z)$ are plotted for the limiting case of a perfect back-reflecting mirror ($R_{\mathrm{mir}} = 1$ in equations (C.3) and (C.6)), relevant for our experiment where a very high quality mirror (cf. section 3.2) has been used.

The local pump light intensity $I(z)$ is obtained as the sum of intensities for first (equation (C.1)) and second pass (equation (C.4)):

$$I(z) = I_1(z) + I_2(z) = I_0(r)\ \left[\mathrm{e}^{-k_a z} + R_{\mathrm{mir}}\ \mathrm{e}^{-k_a\ (2L-z)}\right]. \tag{C.6}$$

Its variation is also shown in figure C.2: for moderate absorption by the gas, the attenuations cumulated along the two passes combine so that the total light intensity experienced by the atoms inside the cell only weakly varies with longitudinal coordinate z.

In the second step of our derivation, the residual z-dependence is eliminated by taking the average value over the cell length. This yields the analytical link between the average pump light intensity $I_{\mathrm{cell}}(r)$:

$$I_{\mathrm{cell}}(r) = \frac{1}{L} \int_0^L I(z)\ dz, \tag{C.7}$$

and the absorption rate k_a.[2] Integration of equation (C.6) involves two simple definite integrals:

$$\int_0^L \mathrm{e}^{-k_a z}\ dz = \mathrm{e}^{-k_a\ L/2} \int_{-L/2}^{L/2} \mathrm{e}^{-k_a u}\ du = \mathrm{e}^{-k_a\ L/2}\ \frac{\sinh\left(k_a\ L/2\right)}{k_a/2} \tag{C.8a}$$

$$\int_0^L \mathrm{e}^{-k_a\ (2L-z)}\ dz = \mathrm{e}^{-k_a\ 3L/2} \int_{-L/2}^{L/2} \mathrm{e}^{-k_a u} du = \mathrm{e}^{-k_a\ 3L/2}\ \frac{\sinh\left(k_a\ L/2\right)}{k_a/2}. \tag{C.8b}$$

[2] In an approximate way that is significantly more accurate than just taking the value of $I(z)$ at the centre of the cell for I_{cell}, as done by Nacher and co-workers in the previous OP model.

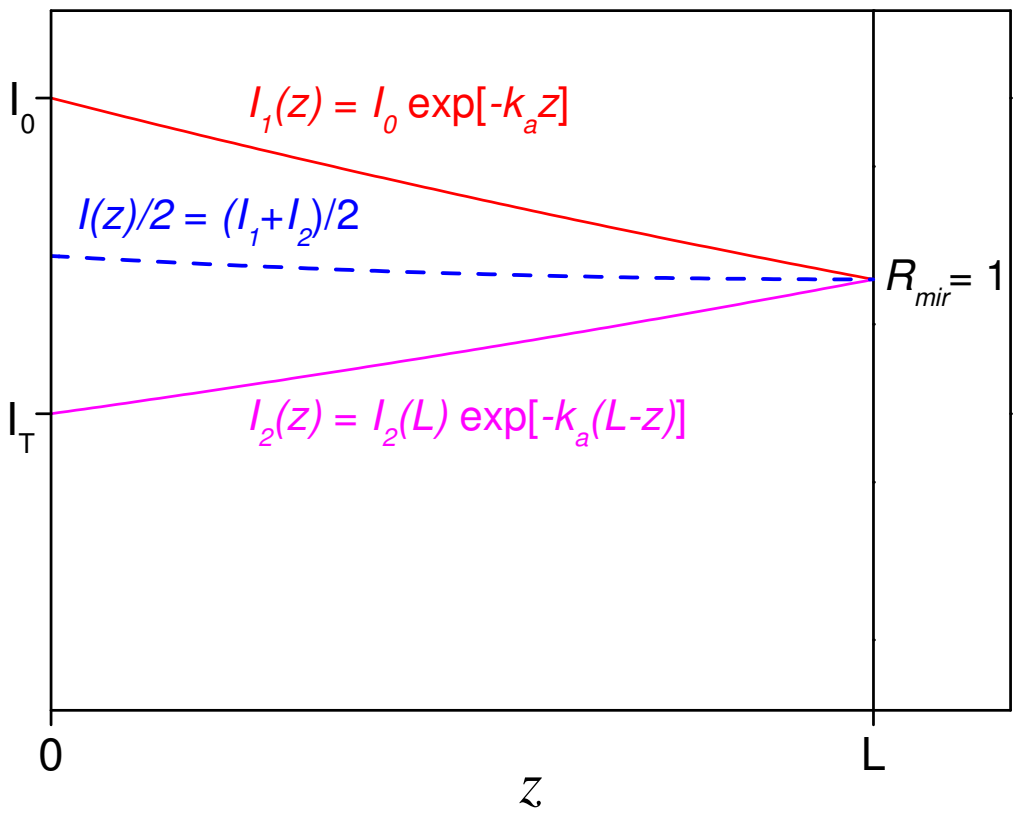

Figure C.2: Evolution of local pump light intensity $I(z)$ under the influence of progressive resonant absorption by the gas. The graph shows the light intensities for the first pass ($I_1(z)$, upper curve, solid red line) and for the second pass ($I_2(z)$, lower curve, solid magenta line) as a function of the longitudinal z-coordinate. The resulting local pump light intensity $I(z) = I_1(z) + I_2(z)$ is also shown, but scaled by a factor 0.5 to appear on the same graph (middle curve, dashed blue line). Constant light absorption rate (at fixed radial position r): $k_a = 0.1$. Reflectivity of the back-reflecting mirror: $R_{\mathrm{mir}} = 1$.

By combining equations (C.8a), (C.8b), (C.7), and (C.6), we obtain the explicit expression of the average pump light intensity $I_{\text{cell}}(r)$ needed for the numerical computations performed with the improved OP model:

$$I_{\text{cell}}(r) = I_0(r)\ \frac{\sinh\left(k_a\ L/2\right)}{k_a\ L/2}\left(\mathrm{e}^{-k_a\ L/2} + R_{\text{mir}}\ \mathrm{e}^{-k_a\ 3L/2}\right). \tag{C.9}$$

Appendix D

Computation of photon efficiencies of C_8 and C_9 lines at null polarisation and in zero magnetic field, for the limits of no and full collisional mixing in the 2^3P state (Kastler and Dehmelt OP regimes)

In this appendix, the values of the photon efficiency η are derived at zero magnetic field and null ^{3}He nuclear polarisation for the two lines of the $2^3\mathrm{S}-2^3\mathrm{P}$ transition that are mostly used in this work: C_8 and C_9. Photon efficiencies for a given line depend on the degree of collisional mixing in the 2^3P state because this mixing (i.e., the redistribution of excited atoms between the various Zeeman sublevels of this state) influences the net transfer of angular momentum as illustrated below. The degree of collisional mixing in the 2^3P state can be described by the pressure-dependent characteristic mixing time τ_P or by the corresponding relaxation rate $\gamma_{\mathrm{r}}^{\mathrm{P}} = 1/\tau_P$ for the 2^3P populations introduced in the OP model (section 2.5.1). The close correlation between the values of the photon efficiencies η_{C8} and η_{C9} (for the C_8 and C_9 lines, respectively) and that of the collisional mixing time is actually used in section 6.3.2 to infer empirical values of τ_P for the three ^{3}He gas pressures investigated in this work, through quantitative comparison between experimentally measured photon efficiencies and computed ones (section 2.9).

In order to give lower and upper bounds for η_{C8} and η_{C9}, two extreme cases are considered: the case of very short τ_P that is characterised by full collisional redistribution between the B_j sublevels (high pressure limit or so-called 'Dehmelt' OP regime) and the case of very long τ_P where transfers between the B_j sublevels are not frequent

at all and no collisional redistribution occurs (low pressure limit or so-called 'Kastler' OP regime). These asymptotic values are noted η^D_{C8} and η^D_{C9} (resp. η^K_{C8} and η^K_{C9}) for the Dehmelt (resp. Kastler) OP regime and they are obtained from the computed amount of angular momentum transferred, on average, to the ^{3}He atoms per induced OP cycle (cf. section 2.9).

In the Dehmelt OP regime, it is particularly simple to compute this net change in total angular momentum projection for the 2^3S atoms, $\overline{\Delta m_F}$ per absorbed photon, by statistical averaging over all combinations of $2^3\mathrm{S} - 2^3\mathrm{P} - 2^3\mathrm{S}$ radiative transfer channels where each channel consists in the following succession of individual steps: resonant $\mathrm{A}_i \rightarrow \mathrm{B}_j$ excitation by absorption of an incident photon, potential transfer to a different sublevel $\mathrm{B}_{j'}$ by collisional redistribution in the 2^3P state, and de-excitation into the metastable 2^3S state by spontaneous emission[1].

- C_8 corresponds to a single-component line with transition from the $2^3\mathrm{S}_1$, $F = 1/2$ state to the $2^3\mathrm{P}_0$ state, involving excitation from the A_5 ($F = 1/2, m_F = -1/2$) to the B_{18} ($2^3\mathrm{P}_0$, $m_F = +1/2$) sublevels in case of σ^+ light (excitation labelled "C_8 σ^+" in figure D.2). Due to the total collisional redistribution between the 18 B_j states and the subsequent *isotropic* reemission into *all* A_i states, the quantum number m'_F after the OP cycle is zero on average. The mean angular momentum transfer from $m_F = -1/2$ to $m'_F = 0$ amounts to $\overline{\Delta m_F}$ per photon, which yields:

$$\eta^{\mathbf{D}}_{\mathbf{C8}} = \frac{\mathbf{1}}{\mathbf{2}}.$$

- C_9 is a multi-component line with transition from the $2^3\mathrm{S}_1$, $F = 3/2$ state to the $2^3\mathrm{P}_0$ state, involving excitation from A_1 ($F = 3/2$, $m_F = -3/2$) to the B_{17} ($2^3\mathrm{P}_0$, $m_F = -1/2$) sublevels as well as excitation from the A_2 ($F = 3/2$, $m_F = -1/2$) to the B_{18} ($2^3\mathrm{P}_0$, $m_F = +1/2$) sublevels in case of σ^+ light, for instance. The relative weight of the two components of this line is $3/4 : 1/4$ due to the difference of optical transition rates associated to the difference in matrix elements $T_{ij}(B = 0)$ (see figure D.1).

Both line components have to be taken into account in order to compute η^D_{C9}. For each component, m'_F equals zero on average after the OP cycle (just as for the C_8 line described above). The mean angular momentum transfer from $m_F = -3/2$ to $m'_F = 0$ equals $\overline{\Delta m_F} = 3/2$, which has to be multiplied with the weighting factor of 3/4; similarly, the angular momentum transfer of the other component from $m_F = -1/2$ to $m_F = 0$ amounts to $\overline{\Delta m_F} = 1/2$ and must be weighted by a factor 1/4. The sum of both contributions yields for the photon efficiency of the C_9 line in the Dehmelt regime:

$$\eta^{\mathbf{D}}_{\mathbf{C9}} = \frac{\mathbf{5}}{\mathbf{4}}.$$

[1]Stimulated emission does *not* contribute to net change in angular momentum for the atoms.

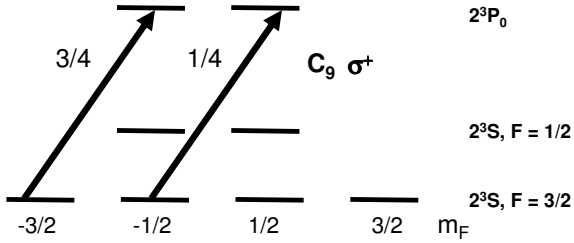

Figure D.1: Magnetic sublevels involved in σ^+ light excitation for the two-component C_9 line and relative weights of these two components at $M = 0$ and in $B = 0$.

In the Kastler OP regime, where there is no collisional redistribution in 2^3P, the net balance of angular momentum (in units of m_F) for the transfer between the initial and the final internal states can be determined using the branching ratios of the $2^3P_0 - 2^3S_1$ transition components, i.e. the probabilities of spontaneous re-emission of a 1083 nm photon for the allowed de-excitation channels (as sketched in figure D.2, for instance, for de-excitation from the $2^3P_0, m_F = +1/2$ sublevel).

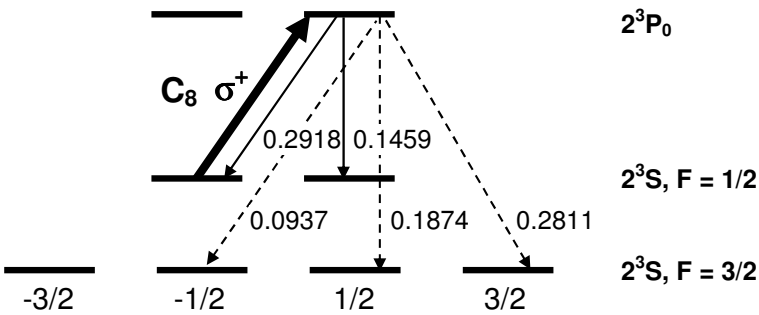

Figure D.2: C_8 OP cycle with no collisional redistribution in 2^3P. Solid lines: C_8 σ^+ excitation and reemission channels involving C_8 σ^+ and C_8 π components. Dashed lines: reemission channels *via* C_9 σ^+, π, and σ^- components. The numerical labels indicate the transition matrix elements in zero magnetic field ($B = 0$), listed in table A.1.

- For a C_8 OP cycle with σ^+ excitation, starting from the initial state $m_F = -1/2$ in the 2^3S level, there are two different possibilities for final states m'_F in the 2^3S level after the OP cycle depending on the polarisation of the emitted photon. This leads to two additive contributions to the photon efficiency:

1. $m_F = -1/2$ to $m'_F = 1/2$ (de-excitation *via* the π branch), yielding $\Delta m_F = 1$ with probability $P^1_{C8} = 0.1459 + 0.1874$ for re-emission of C_8 and C_9 light, respectively, see figure D.2:

2. $m_F = -1/2$ to $m'_F = 3/2$ (de-excitation *via* the σ^- branch of the C_9 line), yielding $\Delta m_F = 2$
   with probability $P^2_{C8} = 0.2811$.

The sum of the contributions of the de-excitation channels leading to these two final states m'_F leads to a photon efficiency for the C_8 line in the Kastler OP regime given by:

$$\eta^{\mathbf{K}}_{\mathbf{C8}} = \overline{\Delta m_F} = P^1_{C8} + 2 \times P^2_{C8} = \mathbf{0.8955}. \tag{D.1}$$

- For a C_9 OP cycle, the photon efficiency can be determined in a similar way for each of the two components of the C_9 line (using the transition probabilities given in figure D.2) but their contributions must be added taking into account their relative weights, determined by the corresponding optical excitation rates (i.e., by the values of the transition matrix elements T_{ij} since $M = 0$). There are now 4 additive contributions to the photon efficiency, since there are two possible final m'_F values for each transition component (originating from initial states $m_F = -3/2$ and $-1/2$ for σ^+ excitation, for instance):

1. $m_F = -3/2$ to $m'_F = -1/2$, yielding $\Delta m_F = 1$
   probability: $P^1_{C9} = 0.1459 + 0.1874$
2. $m_F = -3/2$ to $m'_F = 1/2$, yielding $\Delta m_F = 2$
   probability: $P^2_{C9} = 0.2918 + 0.0937$
3. $m_F = -1/2$ to $m'_F = 1/2$, yielding $\Delta m_F = 1$
   probability: $P^3_{C9} = 0.1459 + 0.1874$
4. $m_F = -1/2$ to $m'_F = 3/2$, yielding $\Delta m_F = 2$
   probability: $P^4_{C9} = 0.2811$

The first two contributions have to be weighted by 3/4 and the last two by 1/4. Thus, the photon efficiency for C_9 in the Kastler OP regime amounts to:

$$\eta^{\mathbf{K}}_{\mathbf{C9}} = \overline{\Delta m_F} = \frac{3}{4}[P^1_{C9} + 2 \times P^2_{C9}] + \frac{1}{4}[P^3_{C9} + 2 \times P^4_{C9}] = \mathbf{1.0521}. \tag{D.2}$$

In table D.1, the numerical values of the photon efficiencies for the C_8 and C_9 lines obtained at $M = 0$ in $B = 0$ with this detailed angular momentum budget approach are compiled for the two limiting cases of *no* or *full* collisional redistribution in 2^3P (Kastler and Dehmelt OP regimes, respectively). They are almost identical to those computed for $B = 1$ mT with the improved OP model (table 2.1), the small relative differences (on the order of 10^{-4} in the Kastler regime and 10^{-3} in the

Table D.1: Compilation of photon efficiency values at $M = 0$ in zero magnetic field for C_8 and C_9 lines in the two limiting cases of no or total collisional redistribution in 2^3P ('Kastler' or 'Dehmelt' OP regime).

η	C_8	C_9
Kastler	0.8955	1.0521
Dehmelt	0.5	1.25

Dehmelt regime) being due to the weak variation of transition matrix elements T_{ij} with magnetic field strength. This compilation of numerical values shows that the photon efficiency is always higher for the C_9 line than for C_8 line: the ratio of photon efficiencies varies from $\eta^K_{C9}/\eta^K_{C8} = 1.18$ in the case of no collisional redistribution in the 2^3P state to $\eta^D_{C9}/\eta^D_{C8} = 2.5$ in the case of full collisional redistribution within the Zeeman sublevels B_j. A higher photon efficiency η at $M = 0$ yields a higher initial rate of change of ^{3}He nuclear polarisation, $\dot{M}(0)$, for the C_9 line compared to the C_8 line at fixed absorbed power $W_{\text{abs}}(0)$. This is very well observed in the experiments, where the C_9 line systematically pumps faster than then the C_8 line (various examples are presented in chapter 6.3.1). The higher photon efficiency of the C_9 line is explained by the dominant contribution of the component that addresses the extremal $|m_F| = 3/2$ Zeeman sublevel: for incident σ^+ light, for instance, absorption of one photon in the $m_F = -3/2$ sublevel leads to the transfer of a larger average amount of angular momentum ($\Delta m_F = 2$) than the C_8 OP cycle addressing the $m_F = -1/2$ sublevel.

The photon efficiency values given in table D.1 can also be used to compare both limiting cases within the same transition separately. This comparison reveals that for the C_8 line, the photon efficiency η is higher in the Kastler than in the Dehmelt OP regime, whereas the opposite is true for the C_9 line. This can be understood by noting that collisional mixing in the 2^3P state is more favourable for C_9 in terms of net angular momentum gain (transfer to states with *higher* m_F quantum numbers in case of σ^+ excitation, for instance), whereas for C_8 collisional mixing in 2^3P results in a net loss of angular momentum (by transfer to state with *lower* m_F quantum number), as illustrated in figures D.1 and D.2.

Appendix E

Numerical demodulation of signals

E.1 Requirements and characteristic functionalities

In order to process acquired data retrospectively, a dedicated in-house Fortran-programme[1] designed to demodulate signals numerically, was used throughout this work. The main parts of the numerical demodulation are the generation of two internal sinusoidal reference signals (one phase-shifted by 90° compared to the other one) and the phase-sensitive detection.
The numerical demodulation of signals requires one additional channel of the data acquisition system to record the reference signal of the modulation source: a TTL-signal of the discharge generator in this work. Furthermore, a high enough sampling rate of the data acquisition system compared to the frequency of the reference signal has to be ensured. In this work, the sampling rate was approximately a factor of 15 higher than the reference frequency: the discharge was modulated at 70 Hz, and data was sampled at 1 kHz.
Demodulating acquired signals numerically afterwards has several advantages. First, the main advantage is that oscillation artefacts (see for instance figure E.1) observed when using a numerical lock-in amplifier, especially in the case of a low sampling rate compared to the reference frequency, are avoided. The same kind of artefacts were observed when using an earlier, simplified version of the programme to demodulate signals numerically. An example of these artefacts as well as their origin will be discussed in this appendix.
Second, the numerical demodulation of signals has the advantage that identical raw data can be processed afterwards with different parameters such as time constant or phase, so that an optimal choice of parameters is always fulfilled.
Third, from a practical point of view, it reduces the number of required lock-in

[1] developed by P.-J. Nacher

amplifiers; in this work, two lock-in amplifiers were needed for the demodulation of the current of both probe laser components instead of five in case the demodulation of the discharge on pump and probe laser signals could not have been done numerically. In contrast to a standard lock-in amplifier (analogue or numerical), the numerical demodulation of signals does *not* comprise an AC coupled amplifier on the signal input nor a low-pass filter on the signal output, but the features of these two stages of a standard lock-in amplifier are also implemented in the programme used to numerically demodulate signals in a particular manner.

In the following, the functionality of the main parts of the numerical demodulation of signals and the implementation of the above mentioned features are described in more detail. Furthermore, required input signals and input parameters as well as provided output signals are specified. In the end of this appendix, some examples of numerically demodulated data are given.

Using the recorded TTL-signal from the discharge generator, the programme used to numerically demodulate signals determines the period of this external reference signal on the first 1000 acquired points. It then generates two internal reference signals (sine and cosine) at the estimated frequency. Throughout the entire acquired period of time, the TTL signal is also treated as an incoming signal and passes the phase-sensitive detection in the same way as described below for regular input signals. This procedure to determine in-phase and quadrature components of the TTL-signal allows to detect phase changes by providing the actual phase at any time, and therefore, it constitutes a mechanism to always lock the input-signal to the reference.

The input signal as function of time, $V(t)$, can be represented as a sum of a constant offset V_0 and several sinusoidal waves with frequency ω and with different amplitudes V_x and V_y and phases (taken into account here by sine and cosine functions):

$$V(t) = V_0 + V_x \cos \omega t + V_y \sin \omega t. \tag{E.1}$$

The aim is to measure the amplitudes V_0, V_x and V_y. Therefore, the programme generates the following weighted mean values of n data points,

$$sumV = \alpha \sum_n e^{-\Gamma n \tau} \left(V_0 + V_x \cos \omega(t - n\tau) + V_y \sin \omega(t - n\tau)\right) \tag{E.2}$$

$$xV = \alpha \sum_n e^{-\Gamma n \tau} \left(V_0 \cos \omega(t - n\tau) + V_x \cos^2 \omega(t - n\tau) + V_y \sin \omega(t - n\tau) \cos \omega(t - n\tau)\right) \tag{E.3}$$

$$yV = \alpha \sum_n e^{-\Gamma n \tau} \left(V_0 \sin \omega(t - n\tau) + V_x \sin \omega(t - n\tau) \cos \omega(t - n\tau) + V_y \sin^2 \omega(t - n\tau)\right) \tag{E.4}$$

n being defined by the user's choice of the time constant $1/\Gamma$ (in the unit "number of sampled points") and the number of calculated output points per time constant.

τ represents the sampling period, α is a normalisation constant that is compensated in the following ($\frac{1}{\alpha}$ introduced by the inversed matrix A^{-1}). $\sum e^{-\Gamma n\tau}$ is a weighting term that is explained on page 334 in detail. Equation (E.2) is merely a multiplication of the signal with this weighting term, whereas equations (E.3) and (E.4) constitute the phase-sensitive detection stage of the numerical lock-in amplifier: Equation (E.3) is a multiplication of the signal and weighting term with the internal reference signal, in equation (E.4), the signal and weighting term are multiplied by the reference signal phase-shifted by 90°. This dual-phase lock-in technique allows to eliminate the phase dependency, since for every instant, the in-phase component as well as the quadrature component will be known.

In order to determine V_0 (the averaged, non-demodulated signal), V_x (the in-phase component) and V_y (the quadrature component), the system of equations (E.2)-(E.4) can be written in matrix form:

$$\begin{pmatrix} sumV \\ xV \\ yV \end{pmatrix} = A \begin{pmatrix} V_0 \\ V_x \\ V_y \end{pmatrix}, \tag{E.5}$$

with

$$A = \sum e^{-\Gamma n\tau} \begin{pmatrix} 1 & \cos\omega(t-n\tau) & \sin\omega(t-n\tau) \\ \cos\omega(t-n\tau) & \cos^2\omega(t-n\tau) & \sin\omega(t-n\tau)\cos\omega(t-n\tau) \\ \sin\omega(t-n\tau) & \sin\omega(t-n\tau)\cos\omega(t-n\tau) & \sin^2\omega(t-n\tau) \end{pmatrix}. \tag{E.6}$$

The matrix A is inverted numerically using the Gauss-Jordan algorithm, and hence, V_0, V_x and V_y can be deduced from:

$$\begin{pmatrix} V_0 \\ V_x \\ V_y \end{pmatrix} = A^{-1} \begin{pmatrix} sumV \\ xV \\ yV \end{pmatrix}. \tag{E.7}$$

Below, the differences between a standard lock-in amplifier (analogue or numerical) and the numerical demodulation of signals presented in this appendix are described, and the solutions that these differences demand for the numerical demodulation are explained.
The main basic principles of operation of standard lock-in amplifiers are summarised for example in [Sco94] and [Sig08].

One main difference consists in the absence of an AC coupled amplifier on the signal-input of the programme used to numerically demodulate signals. In a standard lock-in amplifier, an AC coupled amplifier is an adjustable-gain amplifier, that

matches the input signal more closely to the optimum input signal range of the phase-sensitive detection, and that filters out all DC-components of the signal (denoted V_0 here) in particular. Therefore, the output-components of the phase-sensitive detection in a lock-in amplifier are given by a sum of products of two sinusoidal signals each (similar to equations (E.3) and (E.4) without weighting term and without components including V_0). Each product of two sinusoidal signals can be represented by the sum of two new sinusoids, one at a frequency equal to the sum of both initial frequencies and the other one at the difference frequency. For the lock-in application, the two frequencies (of the reference and of the signal that should be measured) are identical. All signal components at other frequencies than the reference signal cancel out in the multiplier circuit of a lock-in amplifier with subsequent integration over a time much longer than the period of the functions due to the orthogonality of sinusoidal functions. Therefore, the output of these multiplications has components at the second harmonic (2ω) and at DC (difference frequency equals zero).
In the case of the numerical demodulation of signals, the DC-component V_0 is not filtered out by an AC coupled amplifier on the signal-input which leads to residual components at ω after multiplication with the reference signal (equations (E.3) and (E.4)). However, these components at ω, resulting from the DC-component V_0 of the signal, do not constitute any problem in the implemented demodulation procedure as they are eliminated after inverting the full 3×3 matrix as described above.

In an earlier version of the numerical demodulation of signals, that was based on a simplified approach (described starting page 337), the mean value of the signal was subtracted before multiplication by sine and cosine of the reference frequency for the phase sensitive detection. Subtracting the mean value of the signal constitutes the same approach as implemented in commercial lock-in amplifiers (capacitive coupling) and resolves the problem of DC components leading to components at ω after the phase sensitive detection in steady state conditions.

The method of inverting the full 3×3 matrix, used in the final version of the numerical demodulation of signals, constitutes a completely different approach in which the issue of components at ω is of no relevance.

The second main difference between a standard lock-in amplifier and the numerical demodulation of signals is that the first mentioned contains a low pass filter. In a lock-in amplifier, this low pass filter, whose time constant can be selected, filters out the 2nd harmonic-components of the output of the phase-sensitive detection and serves as integrator that removes high frequency components of the noise. Only the DC-component of the output of the phase-sensitive detection that is proportional to the amplitude of the measured input-signal remains as the desired output-signal (possibly amplified again) of the lock-in amplifier.
In the numerical demodulation of signals, these features of the low pass filter are provided by the introduction of the weighting term $\sum e^{-\Gamma n \tau}$ in equations (E.2)-(E.4),

where $1/\Gamma$ is the chosen time constant. The introduction of this weighting term has the effect that signal from far away in the past has a very small weighting and thus almost no contribution to the output-signal of the lock-in amplifier, whereas signal from recent time instants has a much more important weighting. The introduction of a weighting term in the time domain corresponds to a Lorentzian shape around the reference frequency with line width Γ in the frequency domain. Thus the weighting term used in the numerical demodulation of signals filters out all components at 2ω and also serves as integrator, the number of calculated output-points per time constant and the time constant itself being defined by the user.

In the following, a few practical aspects of the numerical demodulation of signals are evoked, namely the input-signals and input parameters as well as the output signals.
The programme used to numerically demodulate signals processes three input channels in parallel, in addition to one internal, auxiliary channel in which the TTL-signal is processed in order to determine the actual phase at any time. It is possible to implement more additional channels if needed.

The required input signals are given below:

- transmitted light powers of both probe components
- transmitted light power of the pump laser
- TTL signal of the discharge generator
- rejected pump light at the first polariser cube (see chapter 3.2)

The rejected pump light component is only averaged by the numerical lock-in amplifier and does not have to be demodulated since it does not pass the cell with the amplitude-modulated gas discharge. For the transmitted light power of the pump laser, the programme determines the offset at zero nuclear polarisation when the pump laser is still switched off (e.g. up to 1'30" in the standard polarisation build-up and decay protocol, see table 5.1), and subtracts the offset from the raw signal. The offsets of the probe laser components can be determined during acquisition periods in which the probe beam has been blocked (e.g. between 11'00" and 11'30" in the standard polarisation build-up and decay protocol). These offsets were considered in further non-automated steps of data processing.

The input parameters, that can be set by the user before starting data processing with the programme to numerically demodulate signals, are the following:

- time constant $1/\Gamma$ (in units "number of sampled points")
- sampling period τ
- number of calculated output points per time constant
- time instant up to which the offset of the transmitted pump component should be determined (pump off, M=0)
- phases for the probe σ^+ and probe σ^--components as well as for the pump
- time instant up to which the phase adjustment should be controlled prior to data processing

The last two input parameters only have to be set if besides the magnitude $R = \sqrt{V_x^2 + V_y^2}$ as output signal, a knowledge of the in-phase component is required as well. In this case, the phases for the three light powers i.e., the dephasing between each signal and the reference, are adjusted prior to actual data processing in such a way that the quadrature component is zero. To reduce computing time, this is checked on the first part of the acquired data file, the end of this control period being defined by the user. Throughout the remaining parts of the data file, the dephasing is controlled during data processing by demodulating the reference-signal.
In most cases of this work, determining the magnitudes of all demodulated signals turned out to be sufficient, but especially in experimental situations with low SNR, it can be advantageous in terms of noise to determine the in-phase component as well. This is explained in more detail by means of a processed example in part E.2 of this appendix.

After data processing, the programme used to numerically demodulate signals generates the following output signals:

- averaged transmitted light powers of both probe components
- demodulated probe signals (magnitude) divided by the averaged transmitted signals of both probe components
- averaged transmitted light power of the pump laser
- demodulated pump signal (magnitude) divided by the averaged transmitted pump signal
- averaged rejected pump light

The additional output signals in case the phases are adjusted for all three light components are mentioned below:

- in-phase probe components divided by the averaged transmitted signals of both probe components
- quadrature probe components divided by the averaged transmitted signals of both probe components
- in-phase pump component divided by the averaged transmitted pump signal
- quadrature pump component divided by the averaged transmitted pump signal

In both output files, the demodulated components (in-phase, quadrature or magnitude) are divided by the averaged transmitted light powers. The underlying reason is given in sections 4.2 and 5.1, explained in detail in [Cou01] and illustrated in one of the processed examples given in the next part of this appendix.

As a last comment concerning these practical aspects of the numerical demodulation of signals, it has to be mentioned that the provided output signals of the dedicated programme are peak amplitudes (A_{peak} in an oscillation like $S = S_0 + A_{peak}\cos(\omega t)$) whereas the used commercial, analogue lock-in amplifiers in this work provide root mean square amplitudes ($A_{rms} = \frac{A_{peak}}{\sqrt{2}} = 0.707\, A_{peak}$). This fact has to be taken into account when *comparing* output signals of these different devices for demodulation.

To conclude the description and characterisation of the numerical demodulation of signals, a few examples of processed data are shown in the following.

In the next paragraph, oscillation artefacts that occurred in earlier versions of the programme to numerically demodulate signals are illustrated, and it is described how this problem has been solved subsequently.
For long time constants compared to the period of the reference signal and a sampling rate that is high enough, matrix A (equation (E.6)) is quasi diagonal, and in this case, the off-diagonal matrix elements can be neglected. For this reason, a simplified approach to solve equation (E.7), only considering the diagonal matrix elements, was implemented in earlier versions of the programme to numerically demodulate signals. This simplified approach was able to provide proper results for experimental situations in which the signal changes were slow compared to the reference period and the sampling rate, e.g. during decay of nuclear polarisation in weak plasmas in absence of the pump laser. However, in experimental situations with fast signal changes compared to the reference period and the sampling rate, e.g. during polarisation build-up with sufficient incident laser power, this simplified approach turned out to be problematic.
In the left graph of figure E.1, raw data of the same example as described in detail in section 5.2 is processed with an earlier version of the programme to numerically demodulate signals using the above mentioned, simplified approach. The chosen time constant in the programme was 30 ms and the selected detail of the graph shows the demodulated signals (magnitude) of the σ^+- and σ^--probe components during the first 30 seconds of the polarisation build-up. A clear low-frequency beat signal of about 1 Hz is observed that occurs due to a coupling between the averaged, non-demodulated signal V_0, the in-phase component V_x and the quadrature component V_y (see equations (E.2) - (E.4)). This low-frequency beat signal can be considered as a sort of Moiré pattern between the acquisition frequency and the short observation interval (time constant of numerical demodulation: $\tau = 30$ ms) that is necessary in order to study dynamics of the fast build-up process. Thus, we do not dispose of many data points per observation interval.
The described coupling is correctly eliminated in newer versions of the programme to numerically demodulate signals that take into account all matrix elements of A (see equation (E.6)) and invert the complete matrix numerically in order to solve equation (E.7). Thus the beat signal disappears as shown in the right graph of figure E.1, in which exactly the same raw data as used for the left graph were processed using the *non*-simplified approach described in detail in this appendix.
Figure E.2 represents the averaged transmitted powers of both probe components in the same time interval. One the left, the transmitted probe signals are 'classically' averaged (i.e. building the mean-value of a certain number of points defined by the chosen time constant) by the simplified approach. On the right, the average transmitted probe signal is extracted from the matrix inversion as described in the beginning of this appendix in the non-simplified approach.
The averaged signals on the left (simplified approach) also clearly exhibit low-

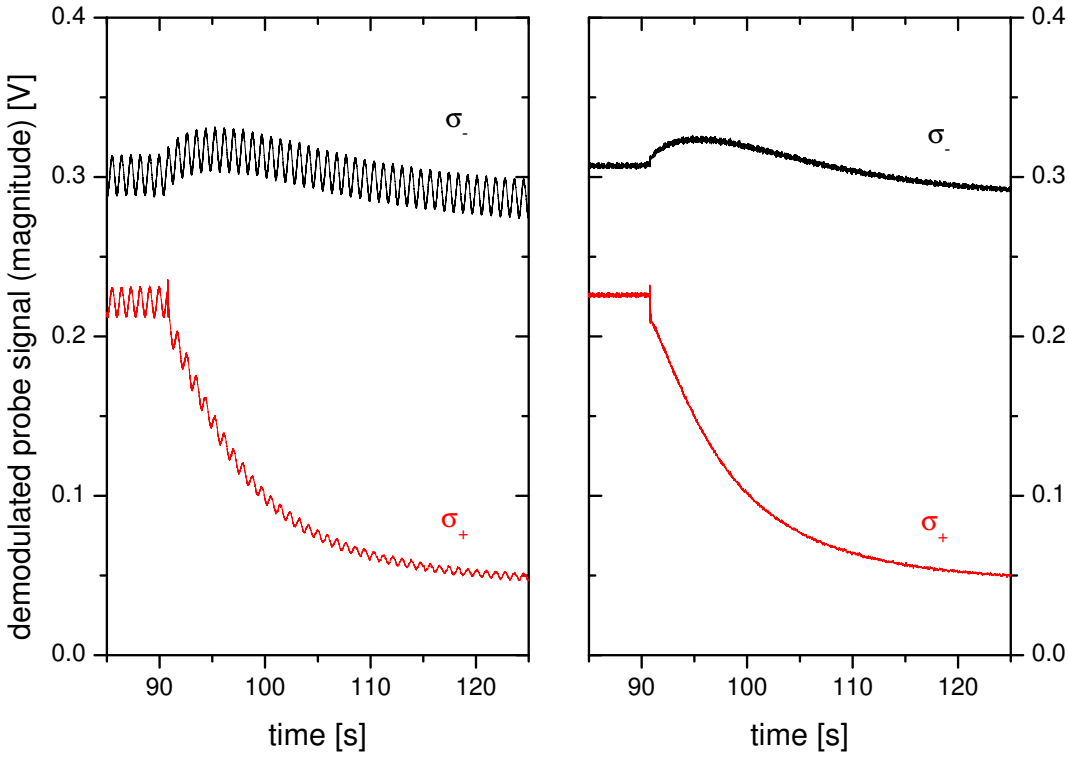

Figure E.1: Demodulated probe signals (magnitude) as function of time during polarisation build-up. Left: Numerical demodulation with a simplified approach neglecting off-diagonal matrix elements (see text) used to process the raw data: A clear low-frequency beat signal is observed. Right: Same raw data processed with the programme to numerically demodulate signals taking into account all matrix elements (see text): Correct elimination of coupling between averaged signal, in-phase and quadrature components, no beat signal. Common: Data acquisition frequency: 1 kHz, time constant of numerical demodulation: $\tau = 30$ ms (in both cases), ^{3}He pressure $p_3 = 0.63$ mbar, pump: C_8, $W_{\rm inc} = 0.42$ W, probe: C_8, $B = 1$ mT, $\Gamma_{\rm D} = (69\,{\rm s})^{-1}$, $n_{\rm m}^{\rm S}(M=0) = 3.34 \times 10^{16}$ atoms/m^3.

frequency Moiré patterns just as the demodulated signals. The non-simplified approach eliminates these oscillation artefacts correctly.

In figure E.3, probe absorption signals (= demodulated probe signals divided by

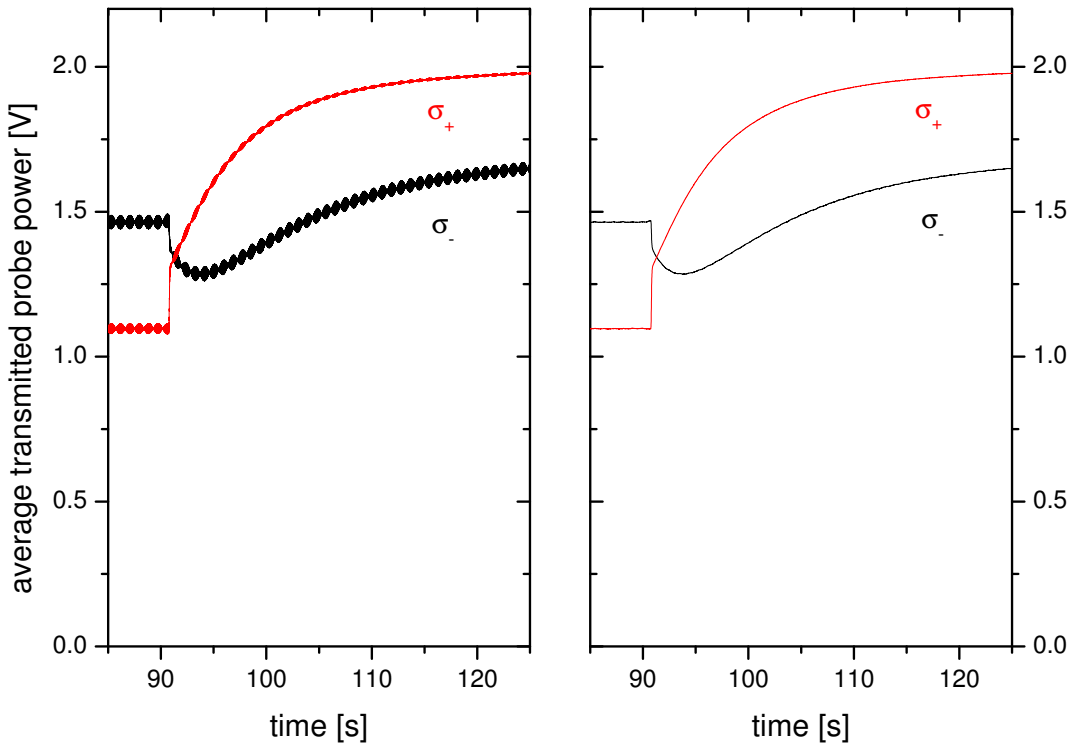

Figure E.2: Averaged transmitted probe powers during polarisation build-up. Left: 'Classically' averaged with a time constant of $\tau = 30$ ms by the simplified approach (see text). Right: Extracted by the non-simplified approach taking into account all matrix elements (see text). Experimental parameters: see figure E.1.

the averaged transmitted power), that are proportional to the absorbances -ln($T_s^{\pm}$) (cf. section 4.2), are represented as function of time, both using the simplified approach (on the left) and the non-simplified approach (on the right, this part is a detail of figure 5.3 (left)). As expected from figures E.1 and E.2, showing the quantities used to build the above mentioned ratio (= probe absorption signal), the simplified approach (left) yields clear low-frequency oscillation artefacts on the probe absorption signals that are already observable on both 'ingredients' of the ratio. The non-simplified approach (right) clearly solves this problem of Moiré patterns reliably.

Furthermore, comparing figure E.1 to figure E.3 shows a quantitative and slight qualitative difference between the demodulated signals and the demodulated signals *divided* by the averaged transmitted powers (= probe absorption signals proportional to absorbances -ln($T_s^{\pm}$)). This comparison demonstrates that dividing the demodu-

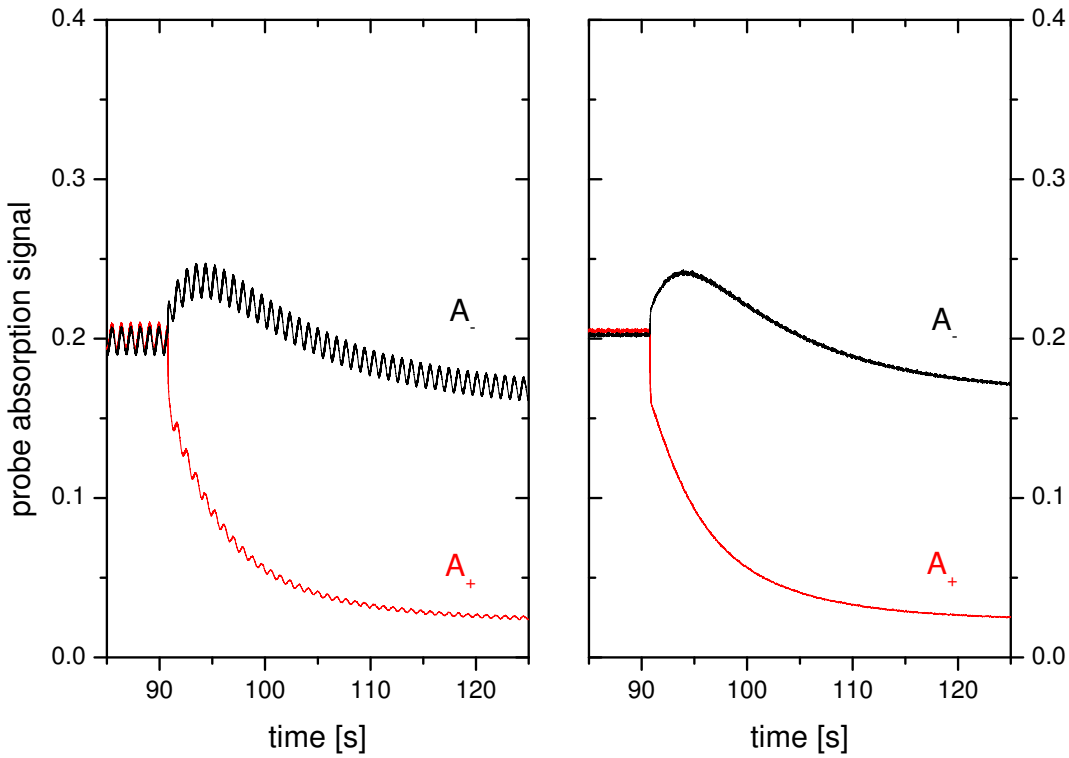

Figure E.3: Probe absorption signals proportional to absorbances $-\ln(T_s^{\pm})$ (magnitude (see page 336) divided by averaged transmitted power) as function of time during polarisation build-up. Left: simplified approach for numerical demodulation. Right: Non-simplified approach. Details and parameters: see figure E.1 and text.

lated probe signals by the averaged transmitted powers, that are not constant during the polarisation build-up process (see figure E.2), is necessary due to changes in the optical density of the gas and hence in the absorption of the probe laser components during the polarisation build-up process. Building this ratio as described is therefore essential in order to infer probe absorbances correctly.

To conclude this description of observed oscillation artefacts using a simplified approach to numerically demodulate signals, two characteristic properties of these oscillations are illustrated.
Figure E.4 shows the demodulated σ^+ probe signals of three different experiments during polarisation build-up: Line **a** is the same experiment (with 0.42 W of incident pump laser power) as discussed in the previous figures. The experiments represented by line **b** and line **c** respectively, were acquired at 0.83 W and 1.66 W of incident pump laser power respectively, keeping all other experimental parameters constant.
For improved legibility, lines **b** and **c** are not plotted in figure E.4 from $t = 70 - 90$ s. Both have the same amplitude of oscillations in this time interval at slightly different mean signal amplitudes (differences compared to line **a**: less than 3 %). All data are processed with a time constant τ of 30 ms. These different experiments were chosen in order to allow a comparison of the oscillation amplitudes at different signal amplitudes. Figure E.4 shows that the amplitude of the oscillations is higher when the signal amplitude is high ($t = 70 - 90$ s), and decreases when the signal amplitude decreases ($t > 90$ s). When comparing the three different experimental datasets with each other within this time interval of $t > 90$ s and moreover to line **a** between $t = 70 - 90$ s, it is clearly observable that the amplitude of the oscillations depends on the signal amplitude, line **a** with the highest signal amplitude having the highest oscillation amplitude, lines **b** and **c** exhibiting intermediate and small signal *and* oscillation amplitudes respectively.
A final remark concerning the shapes of the three different curves in the time interval of $t > 90$ s to conclude the discussion of figure E.4 (this is only a qualitative remark and no quantitative remark concerning probe absorbances since demodulated probe signals are represented here and *not* demodulated signals divided by transmitted signals): The curve of the experiment with the highest incident pump laser power, line **c**, decreases with the steepest slope starting at $t = 90$ s when the pump is released and then has the lowest signal amplitude, since nuclear polarisation in the system builds up very fast and thus, the gas gets more transparent for resonant laser light, and absorption is low. Line **a**, that represents the experiment with the lowest incident pump laser power, decreases more slowly and the signal amplitude remains at a higher level, since polarisation takes more time to build up and more laser light can still be absorbed at a given point in time. Line **b** with intermediate incident pump laser power constitutes an intermediate case.

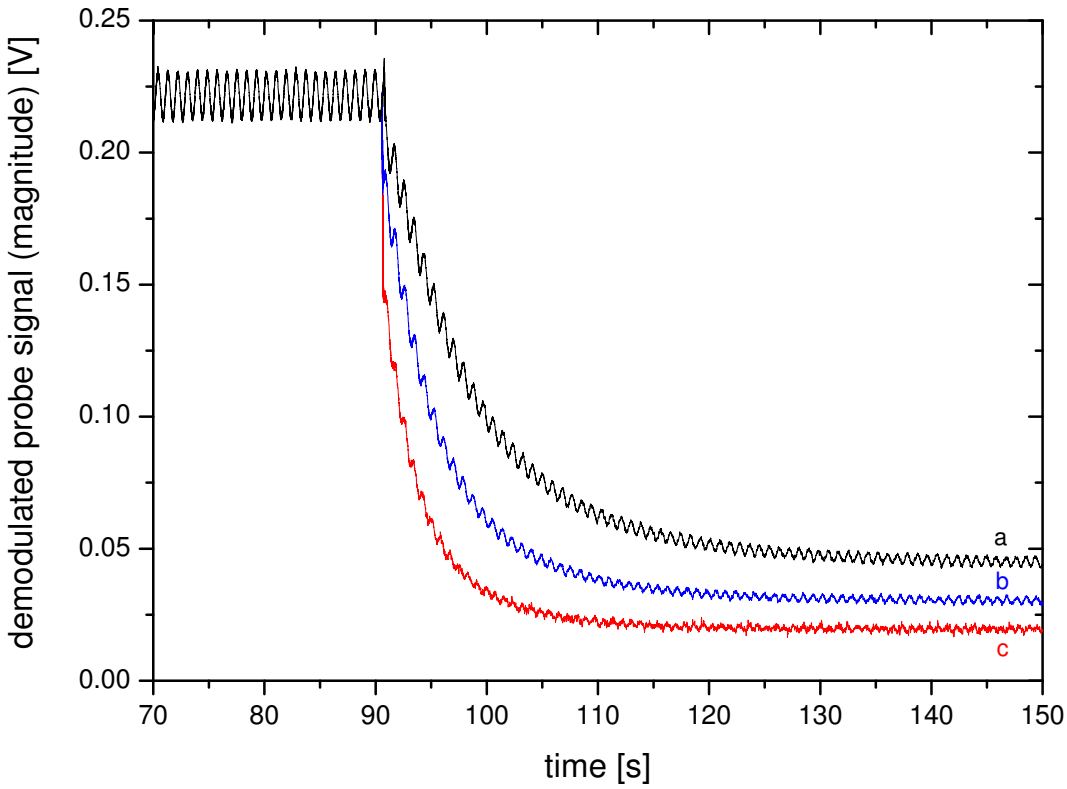

Figure E.4: Comparison of demodulated σ^+ probe signals (simplified approach) at different incident pump laser powers. Line **a**: Same experiment as discussed previously, $W_{\text{inc}} = 0.42$ W, further experimental parameters see caption of figure E.1, also valid for **b** and **c**. Line **b**: $W_{\text{inc}} = 0.83$ W. Line **c**: $W_{\text{inc}} = 1.66$ W. Time constant of numerical demodulation for all data: $\tau = 30$ ms. For a better legibility, lines **b** and **c** are not plotted from $t = 70 - 90$ s.

A second characteristic property of the observed oscillation artefacts when employing the simplified approach for numerical demodulation is illustrated in figure E.5.

Figure E.5 demonstrates that the frequency of the oscillation artefacts depends on

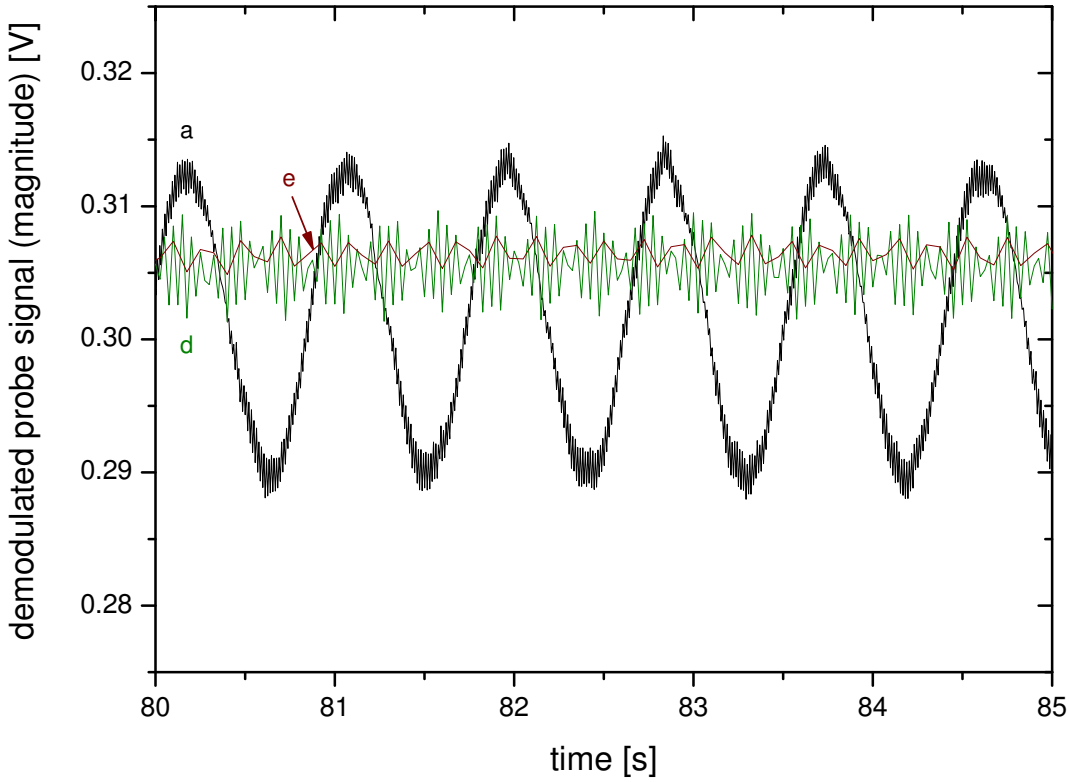

Figure E.5: Comparison of demodulated σ^- probe signals (simplified approach) processed with different time constants: Line **a**: $\tau = 30$ ms, line **d**: $\tau = 100$ ms and line **e**: $\tau = 300$ ms. Identical raw data in all cases: 'standard' example with $W_{\text{inc}} = 0.42$ W, further experimental parameters: see figure E.1.

the chosen time constant of the numerical demodulation compared to the acquisition frequency. Processing data with the shortest time constant in this comparison (30 ms) yields the lowest envelope frequency of the beat signal (line **a**). The longer the time constant at fixed acquisition frequency, the higher the envelope frequency of the beat signal (lines **d** and **e**). This observation can be explained by the fact that more data points are available within an observation interval using longer time constants for the demodulation. Hence at long time constants, the influence of the oscillation artefacts decreases. However, long time constants are inappropriate to study fast signal changes for build-up dynamics.

As a final comment concerning these oscillation artefacts, it is interesting to note that this issue does not pose a problem for *analogue* commercial lock-in amplifiers (in contrast to numerical ones) since acquisition is continuous. The dedicated Fortran-programme based on the *non*-simplified approach with the described full matrix inversion implemented is also capable to solve this issue of oscillation artefacts as pointed out in this section, which marks another advantage of the numerical demodulation of signals over standard numerical lock-in amplifiers.

The next example of processed data is a comparison of demodulated signals of the pump laser, the raw data being processed by a standard analogue lock-in amplifier (Ithaco model 3961 B) on the one hand, and by the programme to numerically demodulate signals on the other hand. For this comparison, the same example as previously used to illustrate oscillation artefacts was chosen; here focussed on the processing of the pump raw data.

In figure E.6, the pump absorption signal proportional to the pump absorbance -$\ln(T_p)$ (i.e., the in-phase component determined by the analogue lock-in amplifier divided by the averaged transmitted pump power) is plotted as function of the same quantity determined by the numerical demodulation of signals (the output signal of the analogue lock-in amplifier is multiplied by $\sqrt{2}$ to allow comparison with the numerically demodulated output signal by the dedicated programme, see comment on page 336).
The experimental slope slightly differs from the theoretically expected one (solid line with slope 1). This can be explained by the fact that in order to determine the pump absorption signal of the analogue lock-in amplifier, quantities from two different devices are used for the division: the in-phase component in Volts is determined by multiplying the output voltage of the analogue lock-in amplifier by the nominal sensitivity and dividing by the maximum voltage at full scale. This in-phase component in Volts is then divided by the averaged transmitted power in Volts recorded from the pump photodiode. It is possible that the gain factor of the analogue lock-in amplifier does not exactly correspond to the value indicated by the nominal sensitivity. This problem does not occur with the numerical demodulation since the same signal recorded from the pump photodiode is used for determining the in-phase component by demodulating it (without using any gain factors) and for determining the transmitted power by averaging it. Throughout this work, the pump signal was mainly demodulated numerically as this has the advantage of being able to post-process the data and to choose convenient parameters for demodulation afterwards.
Figure E.6 also shows that the typical signal-to-noise ratio of the demodulated pump laser signal is inferior to the typical SNR of the probe laser components. For a time constant of $\tau = 30$ ms, SNR of the pump absorption signal is approximately 5 in the

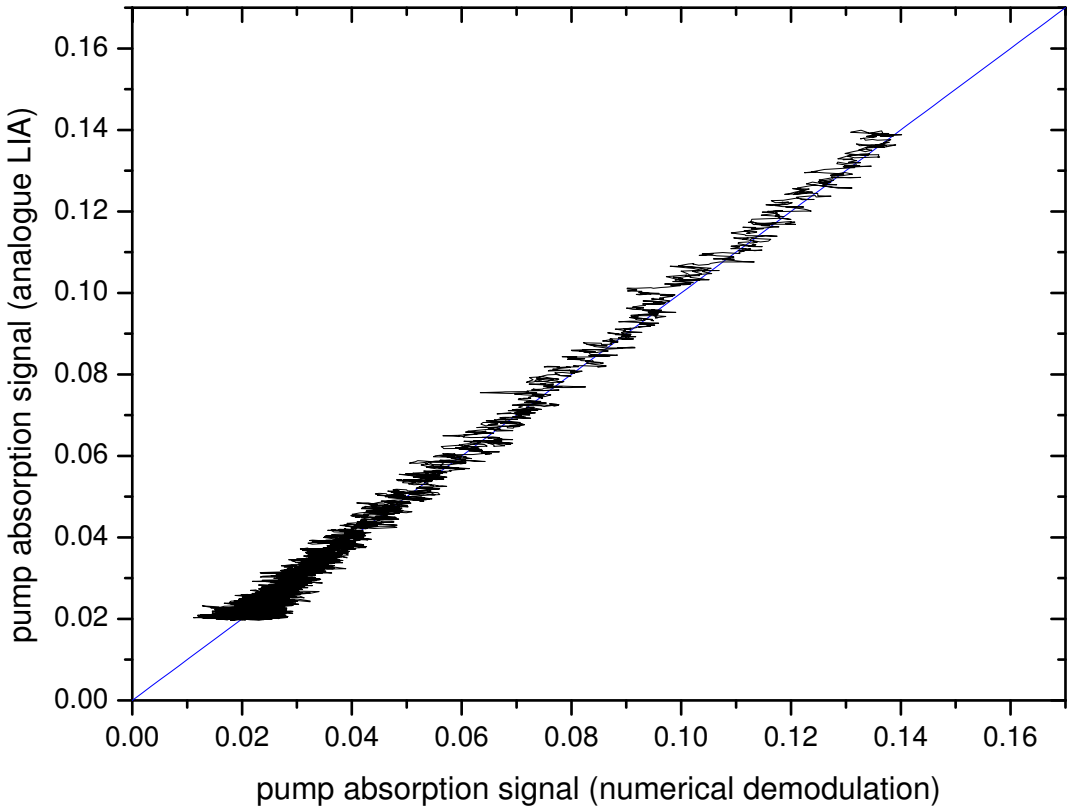

Figure E.6: Pump absorption signal proportional to pump absorbance i.e., in-phase component of the pump laser determined by an analogue lock-in amplifier (Ithaco model 3961 B), divided by the averaged transmitted pump power as function of the same quantity determined by the numerical demodulation of signals. Time constant of the numerical demodulation: $\tau = 30$ ms, identical for the analogue lock-in amplifier since its output-signal, acquired at 1 kHz, is averaged by the Fortran-programme with the same time constant τ. Pump transition: C_8, incident pump laser power $W_{\text{inc}} = 0.42$ W, $p_3 = 0.63$ mbar. (Blue) straight line: Theoretically expected relation: output of analogue lock-in amplifier = output of numerical demodulation. Discharge parameters and magnetic field: see caption of figure E.1.

shown example, whereas SNR of the probe absorption signal amounts to roughly 150. The same example processed at $\tau = 300$ ms leads to signal-to-noise ratios of 10 to 35 for the pump and more than 1000 for the probe.

E.2 Rician noise in the context of lock-in detection

To conclude this appendix, a more general issue in the context of lock-in detection - independent from the actual method to demodulate signals either by commercial (analogue or numerical) lock-in amplifiers or by the presented dedicated programme - is discussed in this subsection. For this purpose the demodulated in-phase component of a generated synthetic example with different noise levels is compared to the magnitude in order to illustrate the significance of Rician noise in this context.
The generated synthetic signal has the following properties: It is constant up to 1 second, and then decays exponentially within 9 seconds. In order to make it suitable as input-file for the programme to numerically demodulate signals, the signal has to be amplitude modulated, and a synthesised TTL signal has to be available. Three different input signals that fulfil these conditions were created: one without noise, and two more where random noise with two different noise amplitudes was added to the initial signal.
This example of demodulated synthetic data is used to discuss the question whether the determination of the magnitude is equivalent to the in-phase component in all cases or whether it can be preferable to use the in-phase component under certain conditions. The mainly used demodulated "standard" output signal in this work is the magnitude which has the advantage of being independent of the phase that therefore does not have to be adjusted before data processing. But as described above, it is also possible with the dedicated programme to numerically demodulate signals to adjust the phases of all three light powers on the input in order to obtain the in-phase component separately.
In figure E.7, the same quantity as shown above for real experimental data i.e., the magnitude or in-phase component divided by the averaged non-demodulated signal, is represented as function of time. The noise amplitude in the input file is 0.01. On the left of figure E.7, the input file has been processed with a time constant of $\tau = 300$ ms, on the right, with $\tau = 30$ ms. Two different time constants are chosen in order to illustrate the effect on the demodulated signals in terms of SNR. Each part of the figure contains two processed signals: The magnitudes of the noiseless and the noisy signals in the upper row, and the in-phase components of both signals in the lower row. For the processed signal without noise, magnitude and in-phase components are identical in all investigated cases. The data are represented in a semilogarithmic plot here, for easy verification that the decay is exponential. In-phase

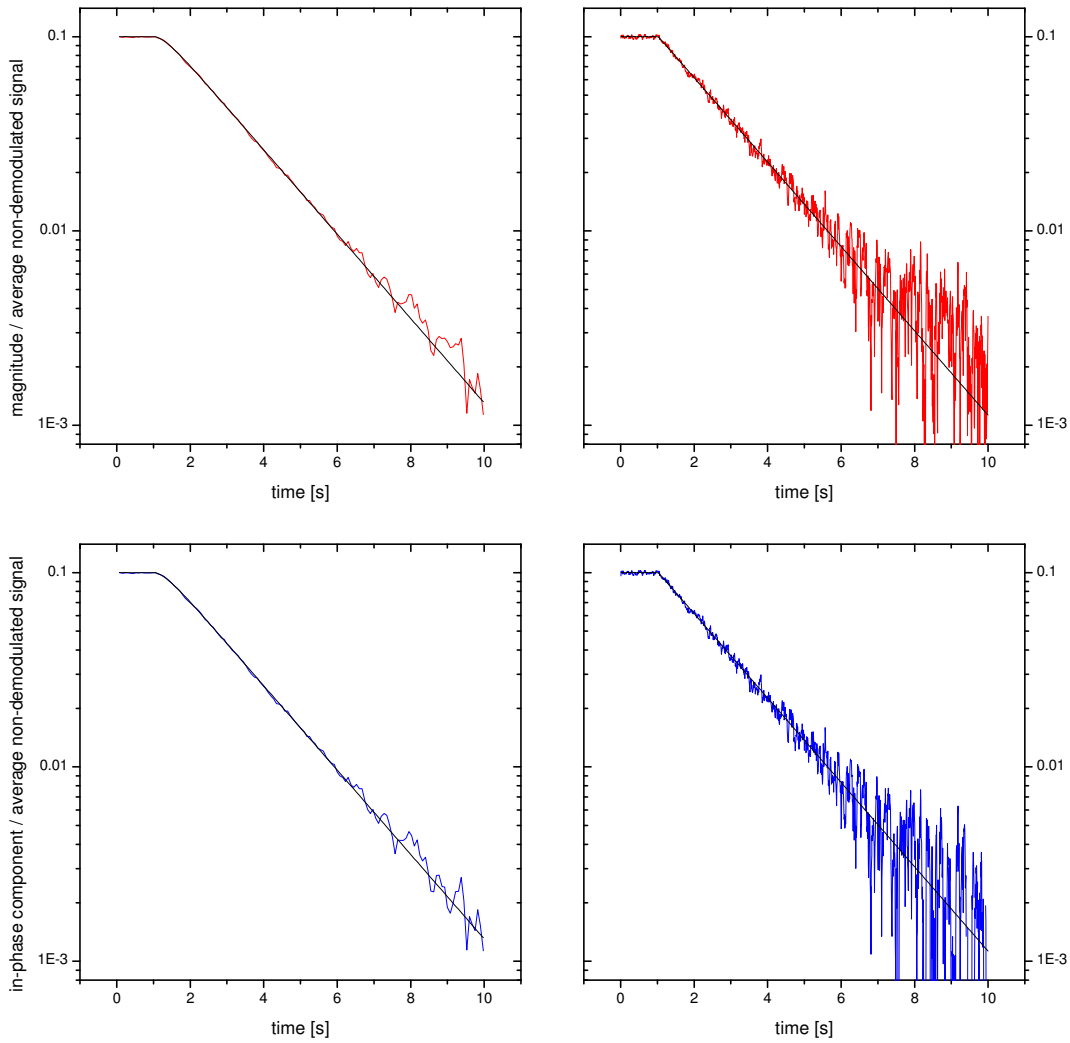

Figure E.7: Numerical demodulation of a synthetic input file with noise amplitude 0.01, details see text. Upper row: Magnitude divided by averaged non-demodulated signal of noiseless and noisy signal. Lower row: In-phase component divided by averaged non-demodulated signal of noiseless and noisy signal. Left: Time constant of numerical demodulation: $\tau = 300$ ms; right: $\tau = 30$ ms.

component and magnitude are almost equal, but differences are observable for $t > 8$ s (magnitude or in-phase component divided by the averaged non-demodulated signal ≤ 0.004 approximately).

These differences are more clearly observable in figure E.8, where the noise amplitude in the input file is ten times larger (0.1). Since negative data points disappear in a semilogarithmic plot and hence, all curves appear distorted, data are represented in a linear plot here, a verification that the decay is exponential is possible in figure E.7.

Comparing the magnitudes of the noisy and the noiseless signals in the upper row of figure E.8, especially for data processed at $\tau = 30$ ms (right), a clear offset of about 0.025 can be observed for $t > 5$ s. In this time interval ($t = 5 - 10$ s), the signal decreases at very low SNR. The noiseless signal approaches zero, whereas the magnitude of the noisy signal converges towards the non-zero mean of the rectified random noise. In this case, the noise is Rician distributed. Rician noise is no longer Gaussian at low SNR.

In the lower row of figure E.8, the in-phase components are represented. Even at a very low signal-to-noise ratio (on the right, $\tau = 30$ ms), the in-phase component of the noisy signal approaches zero correctly like the noiseless signal.

Figure E.9 shows the difference signals of magnitude (upper row) and in-phase component (lower row) as function of time. The difference signal is obtained by subtracting the noiseless from the noisy demodulated signal. For the magnitude in the upper row, the noise is clearly rectified in the time interval ($t = 5 - 10$ s) during which the signal is small, whereas for the in-phase component, the noise is basically symmetrically distributed around zero during the complete processed time period. Since the signal-to noise-ratio is lower for shorter time constants of the demodulation, the phenomenon can be better observed at $\tau = 30$ ms (on the right).

Rician noise is also known to corrupt magnetic resonance (MR) *magnitude* images for example, especially at low SNR (< 2 [Gud95], < 5 [Woo99]), because low signal amplitudes are biased due to the rectified noise. The noise characteristics of MR *phase* images are different from those of the magnitude images [Gud95]. The Rician distribution varies strongly with SNR: For high SNR > 5, it approximates a Gaussian distribution, whereas for low SNR tending to zero, it approaches a Rayleigh distribution, which is highly skewed. For MRI, many sophisticated correction schemes to denoise MR images have been developed (e.g. [Woo99]), for our applications, it is sufficient to use the demodulated in-phase component in critical cases.

In conclusion, since Rician noise influences small magnitude signals, in particular at low SNR, it is preferable to base the data analysis of demodulated signals on the in-phase component in these cases. Typical examples of SNR for the pump and the probe lasers are given above on page 344.

The consequences for the demodulation of pump and probe laser signals can be re-

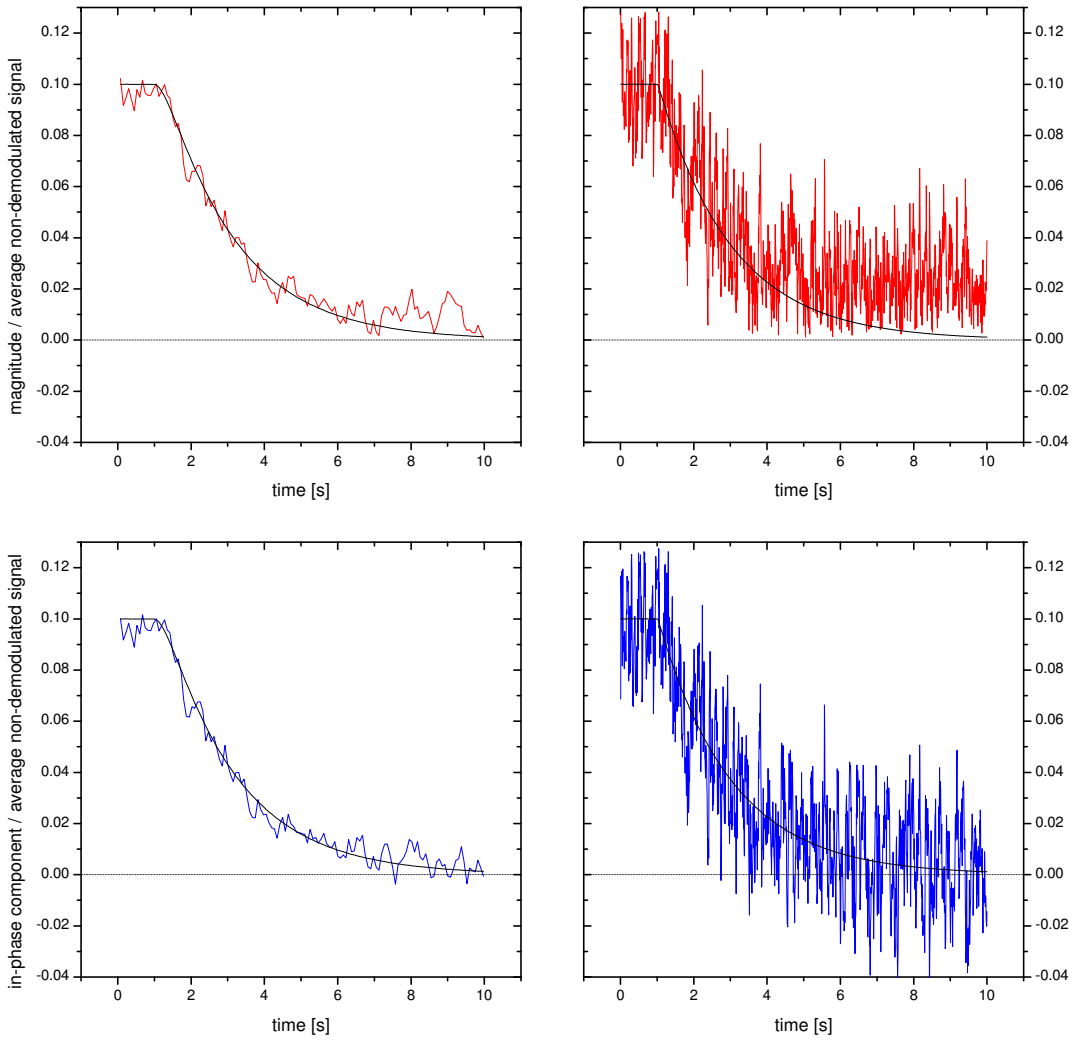

Figure E.8: Numerical demodulation of a synthetic input file with noise amplitude 0.1, details see text. Upper row: Magnitude divided by averaged non-demodulated signal of noiseless and noisy signal. Lower row: In-phase component divided by averaged non-demodulated signal of noiseless and noisy signal. Left: Time constant of numerical demodulation: $\tau = 300$ ms; right: $\tau = 30$ ms.

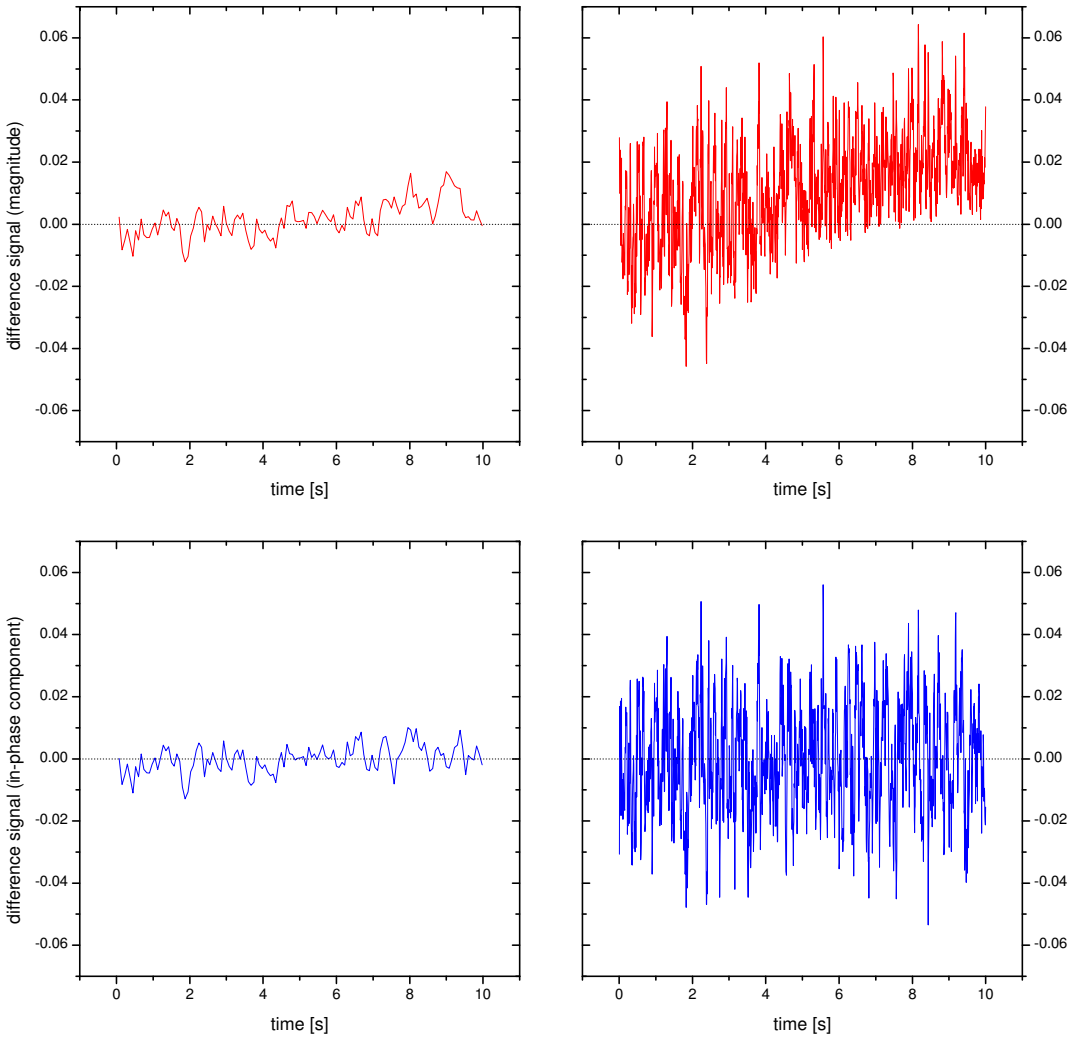

Figure E.9: Difference signals: Noisy minus noiseless demodulated synthetic data (noise amplitude: 0.1, details see text). Upper row: Difference of magnitudes versus time. Lower row: Difference of in-phase components versus time. Left: Time constant of numerical demodulation: $\tau = 300$ ms; right: $\tau = 30$ ms.

sumed as follows:
For the pump laser signal, SNR can become critical, especially at high incident pump powers and when the discharge is weak, since in this case, absorption is low. In such circumstances, it is advantageous to take the in-phase component to determine characteristic quantities as for example pump transmission coefficients at zero nuclear polarisation. This quantity is observed to increase by up to 5 % when the analysis is based on the magnitude instead of the in-phase component. (The experimental parameters of this example are the following: pump transition C_8, incident pump laser power $W_{\mathrm{inc}} = 3.32$ W, $\Gamma_{\mathrm{D}} = (356\,\mathrm{s})^{-1}$, weak discharge: $n_{\mathrm{m}}^{\mathrm{S}}(M = 0) = 1.09 \times 10^{16}$ atoms/m^3, $p_3 = 0.63$ mbar, $B = 1$ mT).
For the probe laser signal, a good to excellent SNR was obtained throughout this work, thus it appears correct to generally base the data analysis of demodulated signals on the magnitude, determined - as well as the in-phase component - by means of the Fortran programme to numerically demodulate signals described in this appendix.

Appendix F

Validation of methodological approach in analysis of polarisation build-up kinetics using synthetic data

In order to validate the methodological approach to extract $\dot{M}$ and T_b values described in section 5.5, an example of synthetic raw data (generated by the model of MEOP-kinetics, see chapter 2), that has been analysed by the dedicated Fortran-programme presented in section 5.5, is discussed in the following. Synthetic data is used for this purpose as the expected output parameters ($\frac{dM}{dt}$ and T_b) are perfectly known and can be compared to the actual parameters delivered by the programme.
First, the characteristics of the generated data are described, and the extracted $\dot{M}$ and T_b values with corresponding uncertainties for three different noise levels are discussed.
Second, variations of different parameters in the analysis and the resulting influences on $\frac{dM}{dt}$ and T_b are examined.

The synthetic data used for detailed testing of methods to analyse the polarisation build-up process are generated by the model for MEOP-kinetics (cf. chapter 2). All tests have also been performed on analytically generated data (non-exponential with time-dependent build-up characteristics), but as they do not illustrate any additional aspect, the presentation in the following is restricted to synthetic data generated by the MEOP-model, which in addition is more realistic concerning build-up dynamics.
The synthetic data is generated with reasonable input parameters: $p_3 = 0.63$ mbar, pump: C_8, $W_{\text{inc}} = 1$ W, pumping beam diameter: 1.6 cm (= waist), $B = 1$ mT, weak

discharge: $\Gamma_{\mathrm{D}} = (350\,\mathrm{s})^{-1}$, $n_{\mathrm{m}}^{\mathrm{S}}(0) = 1.1 \times 10^{16}$ atoms/m^3. Besides other parameters, the MEOP-model generates $\frac{dM}{dt}$ and T_b as function of M and yields the steady state polarisation value M_{eq}. From these parameters, $M(t)$ can be inferred in the following way: $\frac{dM}{dt} = \dot{M}$, with $\dot{M}$ being the polarisation growth values generated by the MEOP-model. Transposing this equation yields $dt = \frac{dM}{\dot{M}}$. By solving the integral $\int_{M=0}^{M_{\mathrm{eq}}} dt = \frac{1}{\dot{M}} dM$, $t(M)$ is obtained. Time as function of polarisation $t(M)$ is equivalent to polarisation as function of time $M(t)$ with non-equidistant time intervals which is no issue in this context.
After having obtained noiseless $M(t)$-data, two different noise levels are added: 1 % of generated random Gaussian noise with a standard deviation of 1, which is more than in most experimental situations, and 2 ‰ of generated random Gaussian noise, which is typical for experimental situations with about 1 Watt of incident laser power.

These three $M(t)$-datasets with different noise levels are then used as input in the dedicated programme to determine $\frac{dM}{dt}$ and T_b as function of M.
Figure F.1 shows $\dot{M}$ values on the left and T_b values on the right, both as function of polarisation for these three different noise levels. Furthermore, the continuous line indicates the values generated by the MEOP-model.
Basic observations on figure F.1 are the following: As expected, $\frac{dM}{dt}$ (left graph)

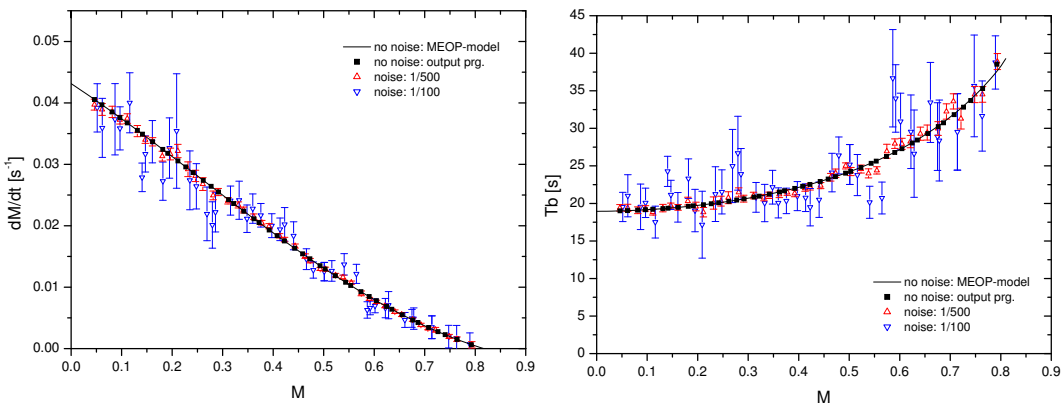

Figure F.1: Left: $\dot{M}$ as function of polarisation. Right: T_b as function of polarisation. Both graphs represent processed data by the dedicated programme for polarisation build-up analysis. As input, synthetic data generated by the model for MEOP-kinetics (parameters see text) was used with different noise levels: Triangle: Output of programme for noise level 2 ‰ of generated random Gaussian noise (with standard deviation = 1) on $M(t)$. Downward triangle: Output of programme for noise level 1% of generated random Gaussian noise on $M(t)$. Filled squares: Output of programme for noiseless data. Continuous line: Theoretical values of $\frac{dM}{dt}$ and T_b provided by the MEOP-model.

decreases (but not linearly) as the nuclear polarisation increases and equals zero when steady state polarisation M_{eq} is obtained. The right graph clearly shows that T_b is not a constant throughout the whole build-up process. As expected, T_b lengthens with increasing polarisation as the pumping process slows down at higher M. The gas gets more "transparent" for the laser light and absorbs less power than in the beginning of the non-linear build-up process.
In addition to these basic physical observations, figure F.1 shows that the output of the dedicated programme for noiseless data is identical to the theoretical values provided by the MEOP-model, both for $\frac{dM}{dt}$ and T_b. This observation on noiseless data demonstrates that the principle of the build-up analysis is valuable and that this principle is implemented correctly into the programme. The outputs $\frac{dM}{dt}$ and T_b feature reasonable sizes of error bars determined by the programme depending on the input noise level on $M(t)$.

The following series of paragraphs, treating variations of different parameters in the analysis and the resulting influences on $\frac{dM}{dt}$ and T_b, consists of four parts: The first part describes how $\frac{dM}{dt}(0)$ is extrapolated on noiseless and noisy data, for optical pumping on C_8 and on C_9, and for the case of an additional relaxation as it is observed in experimental data during build-up. In the second part, variations of the length of the fit interval in the programme for noisy C_8-data and their influence on the scatter of $\frac{dM}{dt}$-values as function of M and on the extrapolated $\frac{dM}{dt}(0)$-values are investigated. The third part deals with the influence, mainly on T_b, of different steady state polarisation values entered into the programme. The errors introduced by this fact are quantified and compared to statistical errors at different M. In the fourth part, a manual approach based on exponential fits directly on short intervals of the $M(t)$-curve to extract build-up times is compared to the results of the dedicated programme.

Extrapolation of $\dot{M}(M = 0)$

To begin with, the procedure of extrapolating $\frac{dM}{dt}(0)$ from one of the outputs of the dedicated programme, $\frac{dM}{dt}$ as function of M, is demonstrated. Figure F.2 represents $\dot{M}$ as function of polarisation for generated data by the MEOP-model (pumping on C_8, other parameters see above). Synthetic data points of two noise levels are included in this figure: On the left, the inputs of the dedicated programme are noiseless $M(t)$-curves, one without additional relaxation (filled symbols), the other one with additional, variable relaxation (open symbols), dependent on the absorbed laser power, as systematically observed in experimental data. On the right, noisy data with 1 % of generated random Gaussian noise (with standard deviation = 1) added to $M(t)$ was used, with and without additional relaxation. Only for an *exponential* build-up, as it has been observed e.g. in high-field optical

pumping of ^{3}He at low pressure [Nik12], all values of $\frac{dM}{dt}$ versus M are located on a straight line. But except for some particular cases, the polariation build-up process in general and especially for the investigated ranges of parameters in this work is a highly non-linear process as explained in subsection 5.5. Hence, $\frac{dM}{dt}$-values plotted versus M usually have different curvatures depending for example on the chosen pumping transition and on relaxation characteristics.

In order to extrapolate $\frac{dM}{dt}(M = 0)$ in each experiment, $\frac{dM}{dt}$ values as function of

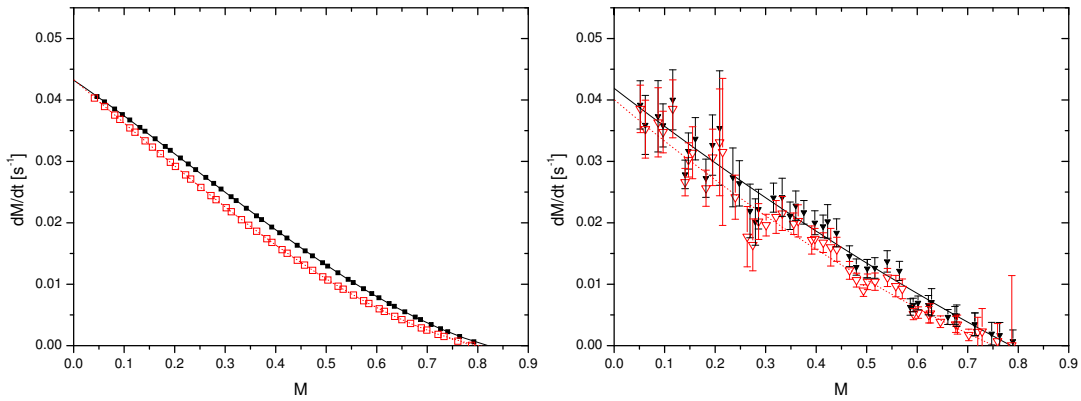

Figure F.2: $\dot{M}$ as function of M. Left: Noiseless generated C_8-data used as input of the dedicated programme: Filled symbols: No additional relaxation, open symbols: Generated data with variable, additional relaxation dependent on absorbed laser power. Right: Noisy data with 1 % of generated random Gaussian noise (with standard deviation = 1), with and without additional variable relaxation (open/filled symbols). Solid lines: Polynomial fits without error weighting to extrapolate $\dot{M}(M = 0)$ (details on extrapolation see text) on data without additional relaxation. Dotted lines: Polynomial fits on data with additional, variable relaxation.

M provided by the dedicated programme are used for polynomial curve fitting. On the left part of figure F.2, the noiseless data is best fitted by a 3rd order polynomial. $\dot{M}$ values obtained from data with additional, variable relaxation clearly feature a different curvature as function of M. Nevertheless, fitting by a 3rd order polynomial is appropriate in this case as well. On the right part of figure F.2, the noisy data with and without variable additional relaxation is fitted using 2nd order polynomials. Independent of the chosen fitting polynomials in different cases, $\frac{dM}{dt}(M = 0)$ is given by the intercept with the $\frac{dM}{dt}$-axis, i.e. by the constant parameter of the polynomial fit function.

Below in figure F.3, different possibilities of fitting polynomials (less appropriate ones as well) on the same noisy data with additional, variable relaxation as shown on the right of figure F.2 are presented and discussed. Furthermore,

the same quantity of a different example of random Gaussian noise (also with a standard deviation of 1) is added to the noiseless data with additional relaxation and processed in the same way in order to allow more generally valid conclusions concerning appropriate fit functions. These fitting possibilities on a different example of Gaussian noise added to $M(t)$ before data processing are presented in figure F.4.

All polynomial fits in this section are performed without error weighting unless explicitly indicated. Later in this appendix (starting on page 364), error-weighted polynomial fits are compared to non-error-weighted fits in the context of variations of the length of the fit interval in the dedicated programme. It was chosen to discuss the common characteristics and differences of polynomial fits *with* and *without* error weighting within the mentioned context below, because scatter and uncertainties of provided $\frac{dM}{dt}$-values as function of M are higher using short fit intervals in the programme.

At first glance, two of the fitting possibilities in figure F.3 can already be excluded:

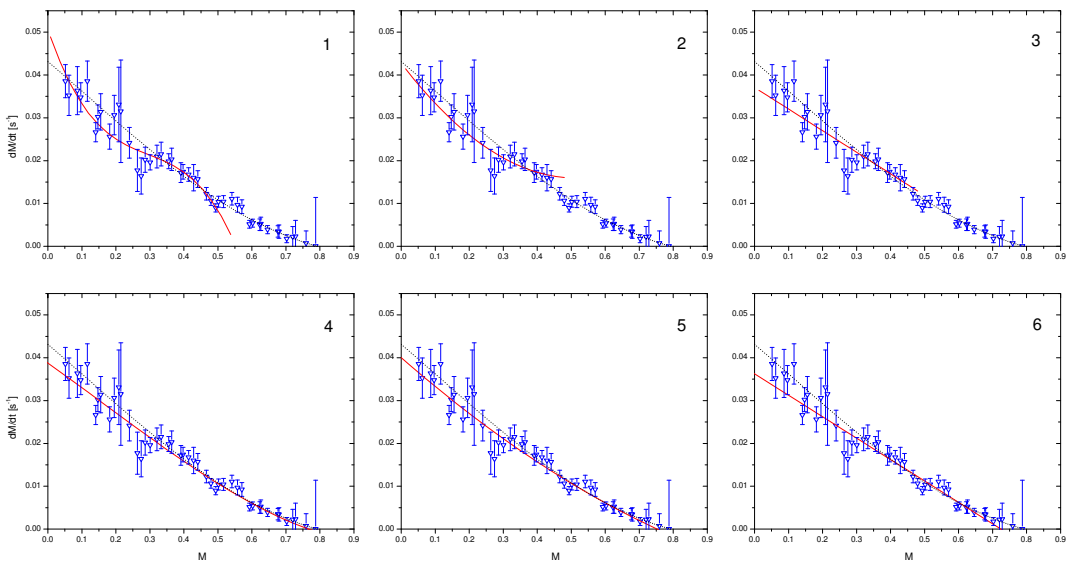

Figure F.3: Different fitting polynomials without error weighting on the same noisy data with additional, variable relaxation as shown on the right of figure F.2. All x-axes: M, all y-axes: $\frac{dM}{dt}$. Borders of fits in upper row (1-3): $M = 0$ up to $M = 0.5$ (approx. 60 % of M_{eq}), borders of fits in lower row (4-6): $M = 0$ up to M_{eq}. Left (1 and 4): 3rd order polynomial fits. Middle (2 and 5): 2nd order polynomial fits. Right (3 and 6): 1st order polynomial fits.

The 3rd and 2nd order polynomials up to 60 % of M_{eq} (fits 1 and 2) are clearly unsuitable to match the whole dataset. The linear fits up to 60 % of M_{eq} and over the whole range up to M_{eq} (fits 3 and 6) seem more adequate, but fit 6 is too low on

the dataset as a whole just as fit 3 would not suit the complete dataset. The best fit by eye is the 2nd order polynomial on the whole range. The 3rd order polynomial over the whole range better matches the curvature at high M, but is lower at small M and therefore less approriate based on a subjective, graphical impression only.
In order to objectify the goodness of the fits, for each fit, three parameters can be determined and compared to each other: the reduced χ^2, the squared correlation-coefficient of the (non-)linear regression R^2 and the ratio $r_{\dot{M}}$ of each extrapolated $\frac{dM}{dt}(0)$ divided by the corresponding value provided by the MEOP-model.
In table F.1, these three parameters are listed for the different fits shown in figure F.3 for noisy data with additional, variable relaxation. Objective criteria to decide which

Table F.1: Reduced χ^2, squared correlation-coefficient R^2 and ratio $r_{\dot{M}}$ of each extrapolated $\frac{dM}{dt}(0)$ divided by the by the corresponding value provided by the MEOP-model for all fits on $\frac{dM}{dt}$ as function of M shown in figure F.3. The first four columns indicate the number of the fit, the lower and upper borders of the fit M_l and M_u, and the order of the used polynomial for fitting.

fit #	M_l	M_u	order	χ^2	R^2	$r_{\dot{M}}$
1	0	0.5	3rd	1×10^{-5}	0.881	1.18(10)
2	0	0.5	2nd	9.75×10^{-6}	0.879	0.997(47)
3	0	0.5	1st	9.67×10^{-6}	0.875	0.86(3)
4	0	M_{eq}	3rd	6.38×10^{-6}	0.955	0.90(5)
5	0	M_{eq}	2nd	6.24×10^{-6}	0.955	0.93(5)
6	0	M_{eq}	1st	7.49×10^{-6}	0.945	0.83(1)

fit is best with the help of table F.1 are the following: χ^2 should be as small as possible, the correlation-coefficient R^2, which cannot exceed 1, ought to be as high as possible, and the ratio $r_{\dot{M}}$ of extrapolated and generated $\dot{M}(0)$ values should be as close as possible to 1.
The first observation concerning table F.1 is that the χ^2 values of the fits on the whole range of M up to M_{eq} (4, 5, 6) are smaller than the χ^2 values of the fits up to 60 % of M_{eq} (1, 2, 3). This can be explained by the fact that *reduced* χ^2 values are given here. Reduced χ^2 values are obtained from χ^2 divided by the difference of $N - P$, i.e. number of points minus number of parameters of the fit. As the number of points for the fits up to 60 % of M_{eq} is smaller, the reduced χ^2 values are thus higher than for the fits up to M_{eq} and cannot be directly compared without considering R^2 and $r_{\dot{M}}$ as well.
Within the fits up to $M = 0.5$, the first order polynomial exhibits the smallest χ^2, but also the smallest correlation-coefficient R^2, and the ratio $r_{\dot{M}}$ indicates a discrepancy of 14 % to $\frac{dM}{dt}(0)$ provided by the MEOP-model. The second order polynomial within

this subgroup of fits features the closest ratio $r_{\dot{M}}$ to 1, but is graphically clearly inappropriate to match the whole dataset just like the third order polynomial. The latter has the highest R^2 value in this subgroup, but at the same time the highest χ^2 and the highest discrepancy to $\frac{dM}{dt}(0)$ provided by the MEOP-model.
Within the subgroup of fits up to M_{eq}, the second order polynomial shows the smallest χ^2, the highest correlation-coefficient R^2 (the same as the third order polynomial), the closest ratio $r_{\dot{M}}$ to 1 and moreover is the best fit by eye.
These observations demonstrate that *all* objective parameters and the subjective, graphical impression have to be considered and combined in order to decide which fit is best. The "critical eye of a physicist" appears to be essential in order to avoid incorrect conclusions: e.g. considering the second order polynomial up to $M = 0.5$ (fit 2) as best fit in this case due to $r_{\dot{M}}$ very close to 1. A more appropriate strategy seems to be searching for cases in which the objective parameters confirm the subjective, graphical impression. This condition is fulfilled for fit 5 (second order polynomial on the whole range of M up to M_{eq}).

Below, in figure F.4 the different polynomials for fitting $\frac{dM}{dt}$ as function of M are presented on a *different* example of Gaussian noise added to the generated data before data-processing by the dedicated programme. Furthermore, the parameters χ^2, R^2 and $r_{\dot{M}}$ are given in table F.2. This different example of Gaussian noise is discussed in order to show that the conclusions drawn on the first example are generally valid.

Table F.2: Reduced χ^2, squared correlation-coefficient R^2 and ratio $r_{\dot{M}}$ of each extrapolated $\frac{dM}{dt}(0)$ divided by the corresponding value provided by the MEOP-model for all fits on $\frac{dM}{dt}$ as function of M shown in figure F.4. The first four columns indicate the number of the fit, the lower and upper borders of the fit M_l and M_u, and the order of the used polynomial for fitting.

fit #	M_l	M_u	order	χ^2	R^2	$r_{\dot{M}}$
I	0	0.5	3rd	7.31×10^{-6}	0.929	0.95(10)
II	0	0.5	2nd	8.18×10^{-6}	0.918	1.09(4)
III	0	0.5	1st	8.54×10^{-6}	0.911	0.95(2)
IV	0	M_{eq}	3rd	5.27×10^{-6}	0.968	1.02(5)
V	0	M_{eq}	2nd	5.19×10^{-6}	0.968	1.04(4)
VI	0	M_{eq}	1st	8.25×10^{-6}	0.948	0.85(2)

Within the subgroup of fits up to $M = 0.5$, the third order polynomial (fit I) has the smallest χ^2, the highest R^2 and the closest ratio $r_{\dot{M}}$ to 1 (the same as the first order polynomial: 0.95). However, the graphical impression of fit I is absolutely

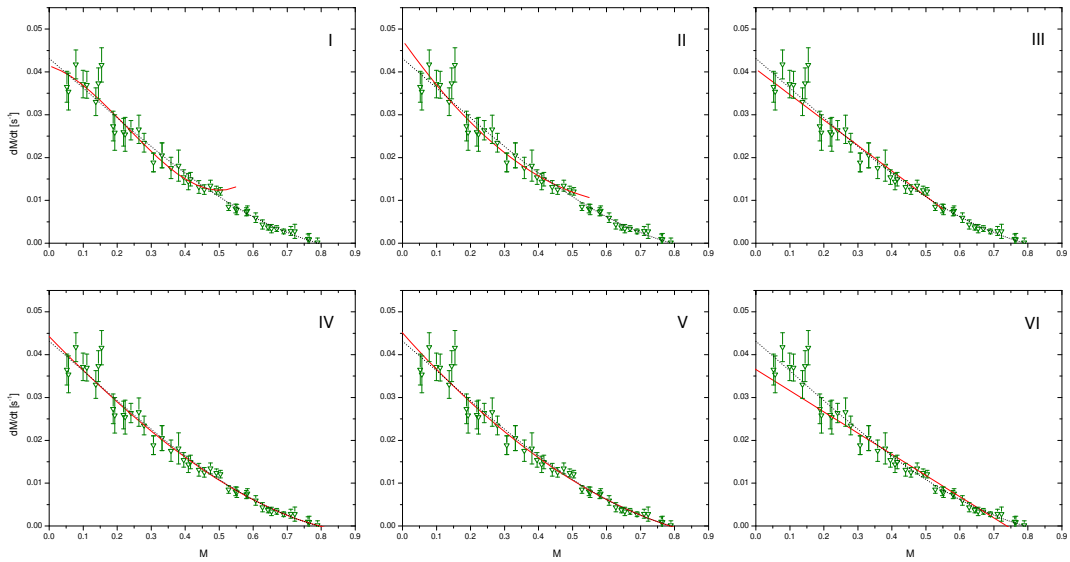

Figure F.4: Fitting polynomials without error weighting on a different example of noisy data with additional, variable relaxation. All x-axes: M, all y-axes: $\frac{dM}{dt}$. Borders of fits in upper row (I-III): $M = 0$ up to $M = 0.5$ (approx. 60 % of M_{eq}), borders of fits in lower row (IV-VI): $M = 0$ up to M_{eq}. Left (I and IV): 3rd order polynomial fits. Middle (II and V): 2nd order polynomial fits. Right (III and VI): 1st order polynomial fits.

inappropriate to match the entire dataset. Thus the conclusion drawn from the first example of Gaussian noise (figure F.3 and table F.1) remains valid: Only considering statistical parameters of the fit might be misleading in terms of locating the best fit to extrapolate $\frac{dM}{dt}(0)$.
Considering both objective, statistical parameters and the more subjective, graphical impression of each fit leads to more substantiated determinations of the best fit and the subsequent extrapolation of $\frac{dM}{dt}(M = 0)$. In the present case, fits IV and V (third and second order polynomials on the whole range of M) are graphically adequate to match the whole dataset. This impression coincides with the statistical parameters: Both fits show the same R^2 values, the second order polynomial exhibits a smaller χ^2 than the third order polynomial, but $r_{\dot{M}}$ of the third order polynomial is closer to 1. Choosing one of these two appropriate fits, the maximum discrepancy to $\dot{M}(0)$ provided by the MEOP-model is 4 %.

A last aspect in the discussion of extrapolating $\frac{dM}{dt}(0)$ concerns a different pumping transition: C_9. As already mentioned, the curvature of the $\frac{dM}{dt}$-curve plotted as function on M depends for example on the chosen pumping transition and on relaxation characteristics discussed above for C_8.
In figure F.5, $\frac{dM}{dt}$ values as function of M are represented for noiseless generated C_9-data (circles) without additional relaxation used as input of the dedicated programme. The parameters to generate OP-data with the help of the model are as follows: $p_3 = 0.63$ mbar, pump: C_9, $W_{\text{inc}} = 1$ W, pumping beam diameter: 1.6 cm (= waist), $B = 1$ mT, weak discharge: $\Gamma_{\text{D}} = (350\ \text{s})^{-1}$, $n_m(0) = 1.1 \times 10^{16}$ atoms/m^3. For the same parameters, but pumping on C_8, $\frac{dM}{dt}$ as function of M is taken from figure F.2 and added to this graph as well (squares).
The shape and curvature of $\frac{dM}{dt}$ versus M of C_9-data is clearly different from C_8-data. Nevertheless, in order to extrapolate $\frac{dM}{dt}(0)$ for C_9, a third order polynomial over the whole range of polarisation values from $M = 0$ up to M_{eq} is also well suited in this case. The extrapolated $\frac{dM}{dt}(0)$ value ($(0.04323 \pm 2 \times 10^{-5})$ s^{-1} for C_8 and $(0.07217 \pm 4 \times 10^{-5})$ s^{-1} for C_9 respectively) show less than 0.5 % of discrepancy compared to the theoretical values in both cases. The ratio of $\frac{dM}{dt}(0)$ values of C_9 divided by the value of C_8 equals 1.67 and is in very good agreement to the theoretical value (as expected for noiseless data).

Variation of the length of the fit interval and influence on $\dot{M}$

In the following second part, variations of the length of the fit interval in the programme are discussed for noisy C_8-data with 1 % of generated random Gaussian noise (with standard deviation = 1) and without additional relaxation. In particular, the influences on the scatter of $\frac{dM}{dt}$-values as function of M and on the extrapolated

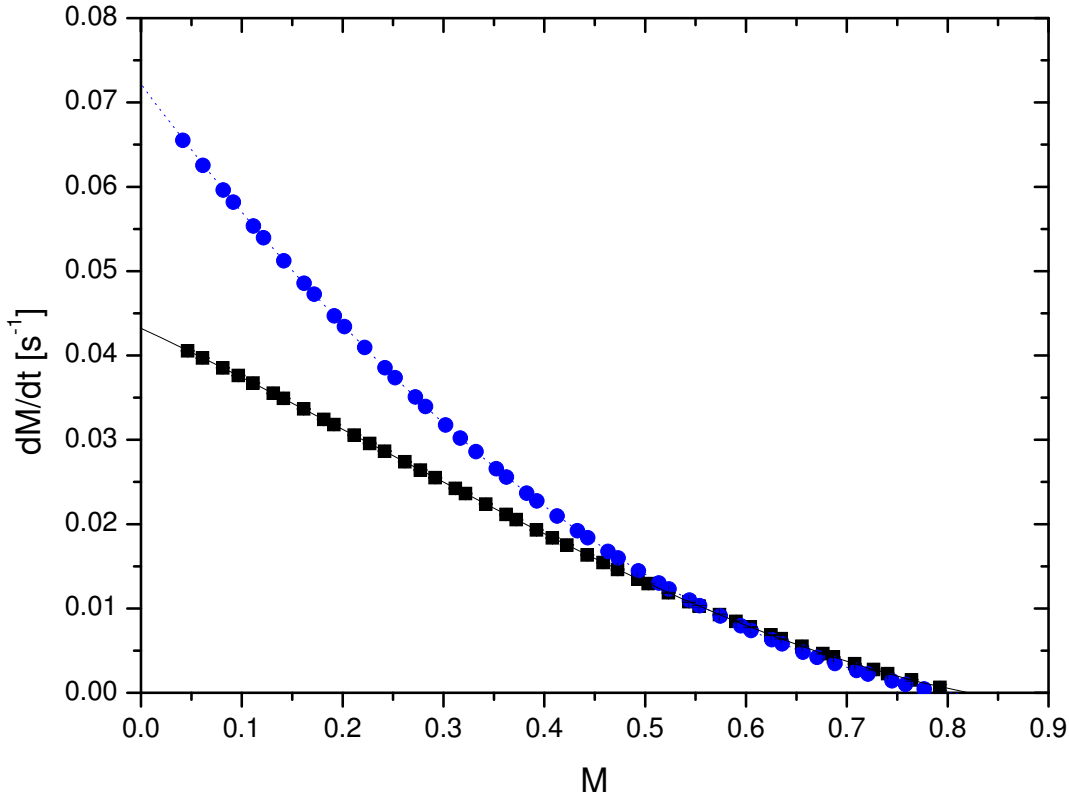

Figure F.5: Filled circles: $\frac{dM}{dt}$ as function of M for noiseless generated C_9-data (parameters see text) without additional relaxation used as input of the dedicated programme. Dotted line: Third order polynomial fit on whole range ($M = 0$ up to $M_{\text{eq}} = 0.795$) of C_9-data. Filled squares: $\frac{dM}{dt}$ as function of M for noiseless generated C_8-data. Solid line: Third order polynomial fit on whole range ($M = 0$ up to $M_{\text{eq}} = 0.817$) of C_8-data. (C_8-data and fit taken from figure F.2).

$\frac{dM}{dt}(0)$ value are investigated.
$\frac{1}{10}$ of the total variation span of polarisation (= 0.081 in absolute units of M in this case of synthetic data) constitutes the chosen standard length of the fit intervals in the dedicated programme. Furthermore, longer fit intervals ($\frac{1}{5}$ of the total variation span = 0.162 in absolute units of M) and shorter fit intervals ($\frac{1}{20}$ of the total variation span = 0.04 in absolute units of M) in the programme to determine $\dot{M}$ and T_b values as function of nuclear ground state polarisation are studied.
Using these three different outputs of the dedicated programme, $\frac{dM}{dt}(M = 0)$ is determined in each case by polynomial fits, and the results are then compared and discussed.
In figure F.6, $\frac{dM}{dt}$-values for the three cases evoked above are represented as function of M, as well as relative errors with respect to the noiseless $\dot{M}$ values given by the MEOP-model.
The graphs demonstrate the influence of the chosen length of fit intervals in the dedicated programme on $\dot{M}$ as function of M. The shorter the fit intervals, the more scatter of $\frac{dM}{dt}$ can be observed in the output of the programme. However, choosing shorter fit intervals in the programme produces more $\frac{dM}{dt}$-values close to $M = 0$, that are important especially for fast build-up dynamics to allow a precise extrapolation of $\frac{dM}{dt}(M = 0)$. The left graph in the lower row of figure F.6 clearly shows that for long fit intervals, the programme is unable to produce $\frac{dM}{dt}$-values between $M = 0$ and $M = 0.09$ due to the chosen length of the fit intervals.
For the extrapolation of $\frac{dM}{dt}(M = 0)$ in each of the three cases, all possibilities of polynomial fits have been evaluated following the above developed criteria. All fits have been performed without error weighting first. Only the best possibility for each case is represented by solid lines in the graphs of figure F.6: For standard and long fit intervals, second order polynomials over the whole M-range were most suitable, for short intervals, a first order polynomial over the whole range was the best choice. This observation can be generalised: In examples with noise, it is often better to limit the polynomial order and use a linear fit.
The extracted $\dot{M}(0)$ values are then compared to the theoretically predicted value at $M = 0$ by the MEOP-model ($\frac{dM}{dt}$ computed by the MEOP-model is plotted as function of M by a dotted line in each graph).
The influence of the chosen length of the fit intervals in the programme on the build-up times $T_b(M)$ is not discussed here. The effects resulting from variations of the length of the fit interval on T_b are very similar to the ones observed on $\frac{dM}{dt}(M)$.
In table F.3, the parameters of the fits without error weighting on $\frac{dM}{dt}$ as function of M are compiled. Table F.3 shows that the best statistical parameters χ^2 and R^2 as well as the closest extrapolated value to the theoretically predicted $\dot{M}(0)$ value are obtained using long fit intervals in the programme in this example. Choosing short fit intervals of course leads to a higher statistical error of the extrapolated $\frac{dM}{dt}(0)$, but the ratio $r_{\dot{M}}$ of the extrapolated value divided by the theoretical one is the same

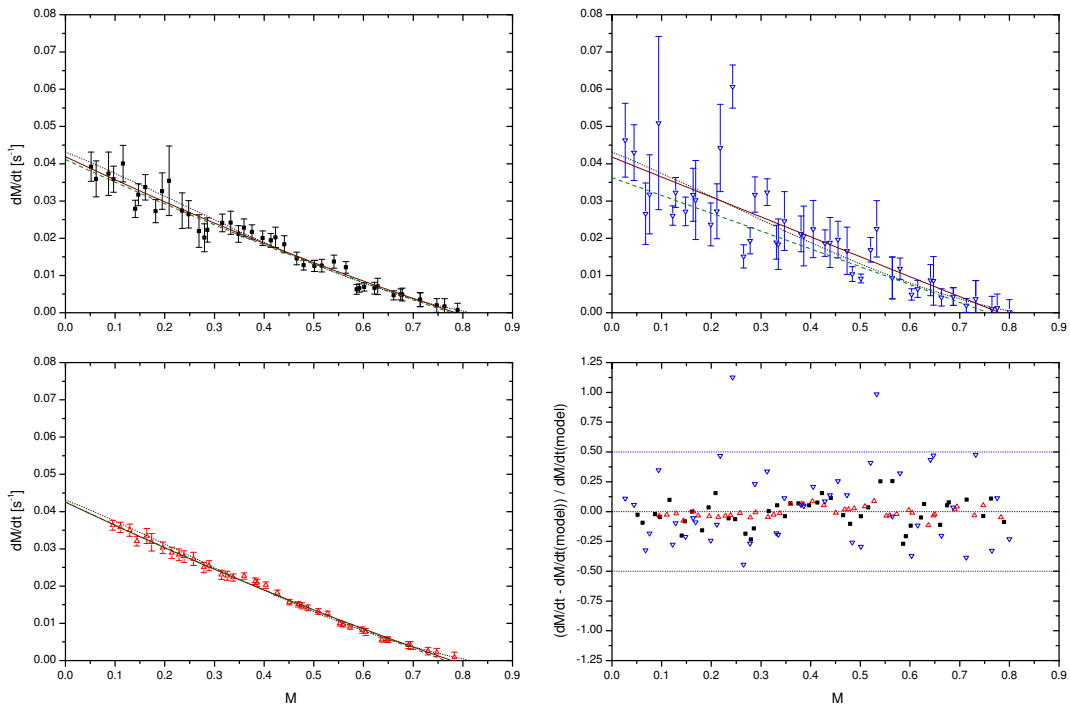

Figure F.6: $\dot{M}$ as function of M for noisy, synthetic data without additional relaxation: Left, upper row (filled squares): Standard length of fit interval ($\frac{1}{10}$ of the total variation span of polarisation) in the dedicated programme. Right, upper row (open downward triangles): Short fit intervals ($\frac{1}{20}$ of the total variation span) in the programme. Left, lower row (open triangles): Long fit intervals ($\frac{1}{5}$ of the total variation span) in the programme. The dotted lines in these three graphs represent noiseless $\frac{dM}{dt}$-values as function of M given by the MEOP-model. The solid lines show the best polynomial fit in each case for fits *without* error weighting (based on the criteria mentioned above). The dashed lines represent the fits *with* error weighting for the same polynomial orders and the same borders of the fits as used in the case without error weighting. Right, lower row: Relative errors with respect to noiseless $\dot{M}$ generated by the MEOP-model for all investigated lengths of fit intervals in the programme. Dotted lines in this graph: Zero- and 50 %-error-levels.

Table F.3: Extrapolation of $\frac{dM}{dt}(0)$ by polynomial fit (without error weighting) on $\dot{M}$ values as function of M provided by the dedicated programme for different lengths of the fit intervals (standard, short, long: details see text). The further columns (from left to right) indicate the lower and upper borders of the fit, the order of the used polynomial (= best choice) for fitting, the reduced χ^2-value, the squared correlation-coefficient R^2, $\frac{dM}{dt}(0)$ with statistical error of the fit (e.g. 0.0419(13) s^{-1} = (0.0419 ± 0.0013) s^{-1}) and the ratio $r_{\dot{M}}$ of each extrapolated $\frac{dM}{dt}(0)$ divided by the corresponding value (0.04313 s^{-1}) provided by the MEOP-model and its error resulting from $\dot{M}(0)$.

fit intervals	M_l	M_u	order	χ^2	R^2	$\frac{dM}{dt}(0)[s^{-1}]$	$r_{\dot{M}}$
standard	0	M_{eq}	2nd	5.51×10^{-6}	0.961	0.0419(13)	0.971(31)
short	0	M_{eq}	1st	5×10^{-5}	0.742	0.0418(22)	0.969(52)
long	0	M_{eq}	2nd	5.71×10^{-7}	0.995	0.04255(56)	0.987(13)

as for standard intervals.
These results do not automatically indicate that using long intervals in the programme is always the best choice. Long fit intervals (spanning $\frac{1}{5}$ of the change of M during polarisation build-up) are suitable for noisy or scarce data when optical pumping dynamics are close to being exponential. Standard intervals (spanning $\frac{1}{10}$ of the change of M during OP) turned out to be a good compromise between providing enough $\frac{dM}{dt}$-values in the beginning of the build-up and limiting the scatter on $\frac{dM}{dt}$ in order to extrapolate reasonably well $\dot{M}(0)$ in most of the cases. For build-ups with very good SNR, short intervals (spanning $\frac{1}{20}$ of the change of M during OP) might be best suitable.

On the other hand, for noisy data, it appears reasonable not to take too short fit intervals in the dedicated programme. This fact can be well illustrated when considering the fits *with* error weighting (dashed lines in figure F.6). The parameters of the fits with error weighting on $\frac{dM}{dt}$ as function of M are compiled in table F.4. When comparing the fits with and without error weighting in figure F.6, different observations depending on the chosen lengths of the fit intervals are made. For long intervals, there is no visible difference between the fit with and without error weighting, and for standard intervals, the difference is much smaller than the error bar of each $\frac{dM}{dt}$-value. The tendency of the error weighted fit, however, is more distant from the theoretical curve provided by the MEOP-model. This tendency is confirmed when comparing error-weighted with non-error-weighted polynomial fits for short fit intervals in the programme. In this case, where due to the relatively high noise, the polynomial order has to be limited to a linear fit, otherwise there are too many degrees of freedom to constrain the fit, the discrepancy between the polynomial fit

Table F.4: Extrapolation of $\frac{dM}{dt}(0)$ by polynomial fit (with error weighting) on $\dot{M}$ as function of M provided by the dedicated programme for different lengths of the fit intervals (standard, short, long: details see text). The further columns (from left to right) indicate the lower and upper borders of the fit, the order of the used polynomial for fitting (the same as without error weighting), the reduced χ^2-value, the squared correlation-coefficient R^2, $\frac{dM}{dt}(0)$ with statistical error of the fit and the ratio $r_{\dot{M}}$ of each extrapolated $\frac{dM}{dt}(0)$ divided by the corresponding value (0.04313 s^{-1}) provided by the MEOP-model and its error resulting from $\dot{M}(0)$.

fit intervals	M_l	M_u	order	χ^2	R^2	$\frac{dM}{dt}(0)[s^{-1}]$	$r_{\dot{M}}$
standard	0	M_{eq}	2nd	0.7887	0.961	0.0411(18)	0.954(44)
short	0	M_{eq}	1st	2.0824	0.772	0.0363(15)	0.841(40)
long	0	M_{eq}	2nd	0.6697	0.993	0.04259(97)	0.987(23)

and the theoretical curve of $\dot{M}$ values is much higher.
The discrepancies of the extrapolated $\frac{dM}{dt}(0)$ values by the fits with and without error weighting with respect to the provided value by the MEOP-model can be quantified using tables F.3 and F.4. For long fitting intervals in the programme, the differences between error-weighted fits and non-error-weighted fits are negligible. For standard intervals, the squared correlation coefficients R^2 are the same no matter whether the fits are performed with or without error weighting. The extracted $\dot{M}(0)$ values are compliant with each other within the errors. The discrepancies of the extrapolated $\frac{dM}{dt}$-values with respect to the theoretical value provided by the MEOP-model are also similar in both cases: without error weighting it amounts to 3% and with error weighting to almost 5%. Although the discrepancy is slightly higher for the error weighted fit, both fitting possibilities with or without error weighting yield reliable results of $\frac{dM}{dt}(0)$ even in case of a poor SNR as shown in this example of synthetic data. For a noisy dataset, it is not recommended to choose too short intervals in the dedicated programme. This can be substantiated by tables F.3 and F.4: Although the squared correlation coefficient R^2 is slightly closer to 1 for the error weighted fit in the case of short fit intervals in the dedicated programme, the discrepancy of the extrapolated $\frac{dM}{dt}(0)$-value to the theoretical one is much higher for the error-weighted fit, 16% compared to 3% for the fit without error weighting. However, the provided $\frac{dM}{dt}$-values by the programme using short intervals might still be useful in addition to the output of the programme for standard intervals. In cases where more $\frac{dM}{dt}$-values in the beginning of the build-up close to $M = 0$ are needed than the output of the programme using standard intervals produces, it is possible to add the first few $\frac{dM}{dt}$-points that the programme produces using short intervals and to perform the polynomial fit on the whole composed ensemble of $\frac{dM}{dt}(M)$. In the presented

example of figure F.6, it would be possible to take the first two $\frac{dM}{dt}$-values from the case of short fit intervals and add them to the case using standard intervals. As these two additional $\frac{dM}{dt}$-values are higher than $\dot{M}$ provided by the programme using standard intervals, a polynomial fit on this composed example yields a slightly higher extrapolation of $\dot{M}(0)$ which is closer to the theoretical $\frac{dM}{dt}(0)$ as the extrapolated value by a polynomial fit on the points provided by the output for standard intervals only.

In figure F.7, the ratios $r_{\dot{M}}$ (= extrapolated $\frac{dM}{dt}(0)$ divided by the theoretical one provided by the MEOP-model) for *all* polynomial fits performed without error weighting and for the best suitable polynomials with error weighting on standard, short and long fit intervals in the dedicated programme are represented.
The cases with and without error-weighting are already discussed based on tables F.3

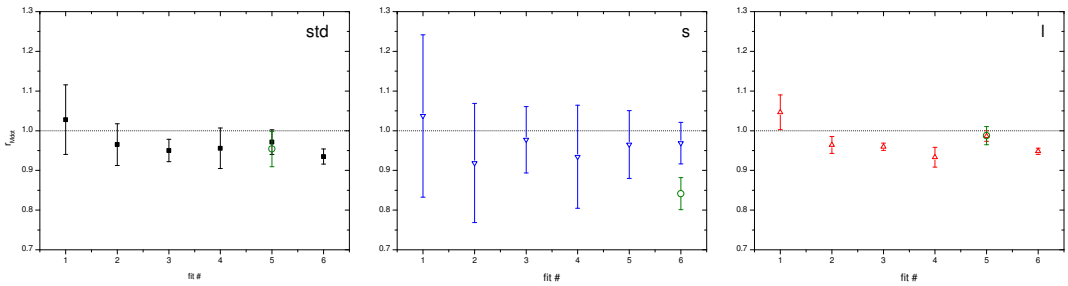

Figure F.7: Ratios $r_{\dot{M}}$ of extrapolated and theoretical $\dot{M}(0)$ values for standard intervals in the dedicated programme ("std": left graph), for short intervals ("s": central graph) and for long intervals ("l": right graph). The numbers of the fits on the axis of abscissae correspond to the numbers of the example presented in figure F.3: 1-3: fits up to 60% of M_{eq}, 4-6: fits on the whole range of data; for both fitting ranges: 3rd order polynomials (1 and 4), 2nd order polynomials (2 and 5) and 1st order polynomials (3 and 6). Non-error weighted fits are represented by filled squares for standard intervals, open downward triangles for short intervals and open triangles for long intervals. Error weighted fits are represented by open circles in all cases.

and F.4. For long and standard intervals, figure F.7 confirms that both $r_{\dot{M}}$-values from the fits with and without error weighting are compatible within the errors. That is not the case for short fit intervals in the programme, as both linear fits as function of M indicate in figure F.6.
Furthermore, the central graph of figure F.7 using short intervals shows that the errors of the determined $r_{\dot{M}}$-values are quite high and thus, for all different cases of fitting polynomials, $r_{\dot{M}}$ is compliant to 1, and hence no valuable conclusions can be drawn. This is another reason for avoiding too short fit intervals in the programme if possible when processing noisy experimental data.

On all three graphs for different lengths of fit intervals in the programme, checks of consistency concerning the determined $r_{\dot{M}}$-values confirm the graphical impression of the quality of a fit as function of M (not shown here, similar to figures F.3 and F.4): For the polynomial fits showing apparently satisfactory graphical agreement with experimental data including uncertainties, the corresponding $r_{\dot{M}}$-values feature the smallest discrepancies to 1 (fits 2, 4 and 5 for standard intervals, fits 3, 5 and 6 for short intervals, and fits 2 and 5 for long intervals).

For simplicity and historical reasons, the polynomial fits on the experimental $\dot{M}(0)$ values were performed without error weighting. As shown above for standard intervals in the programme (spanning 10 % of the total variation of M during build-up) on synthetic data of lower SNR than in most experimental situations, using polynomial fits without error weighting only has a small influence on the extracted $\dot{M}(0)$ values. The difference of the extracted $\frac{dM}{dt}(0)$-values using error-weighted or non-error-weighted polynomial fits is about 2 % only, much smaller than the error of each individual $\frac{dM}{dt}$-value as function of M: The mean value of the relative error of $\frac{dM}{dt}(M)$ amounts to 15 % ranging between 8 % (minimum) and 31 % (maximum).

Another more general remark seems to be useful at this point: The possibilities shown above, how to analyse quite noisy data and how nevertheless important characteristic parameters can be determined reliably, represent extreme cases and show how to get useful experimental information in case it is impossible to repeat a measurement or in case there are not enough experimental data available. Throughout this work, whenever experiments obviously had poor SNR or revealed unsolved experimental problems or any incoherences that were reflected by the experimental data, the corresponding experiment and all extracted characteristic parameters like $\dot{M}$ or T_b were discarded as it was possible to repeat measurements to obtain various large enough datasets of all necessary parameters.

Influence of the choice of M_{eq} in the dedicated programme on T_b

The next third part of this appendix, describing variations of different parameters in the polarisation build-up analysis, deals with variations of the steady state-polarisation value M_{eq} provided to the dedicated programme for build-up analysis. The influence on build-up times T_b as function of M are discussed as well as the relative errors $\frac{\Delta T_b}{T_b}$ caused by an inappropriate choice of M_{eq} compared to statistical errors. This influence of the choice of M_{eq} is investigated on the same synthetic C_8-data generated by the MEOP-model as used previously, without additional relaxation as well as with and without noise.
The necessity of varying the input parameter M_{eq} in the programme only arises

in cases where the steady state polarisation - which of course is not arbitrary but defined as the asymptotic polarisation value obtained at the end of the build-up process and depending on the chosen experimental parameters - cannot be precisely determined in the experimental data, e.g. at very low incident laser power when the polarisation build-up process is very slow and has not been recorded long enough, or at low signal-to-noise. The objective of varying the input-value of M_{eq} in the programme and of comparing the different extracted values of T_b afterwards, is to obtain an indication for the correct determination of M_{eq}.
Especially the T_b-values at higher polarisation close to M_{eq} are sensitive to the choice of the asymptote. For the investigated ranges of experimental parameters in this work, the model of MEOP kinetics predicts a regular, monotone variation of T_b without inflexion when passing $M = M_{\mathrm{eq}}$. The investigation of the influence on T_b thus allows to eliminate hypotheses of M_{eq} that are to be excluded.

In figure F.8, build-up time constants as function of M for different values of M_{eq} used in the programme for the noiseless case are represented (upper left graph). Furthermore, relative errors in comparison to statistical errors are plotted at different M-values as function of the used steady state polarisation in the programme.
Graph 1 of figure F.8 shows that, as expected, the choice of M_{eq} has an influence on build-up times mainly at high polarisation values approaching M_{eq}. At $M = 0.7$ ($\approx$ 85 % of M_{eq}) for example, varying M_{eq} in the programme up to $\pm$ 0.6 % from the theoretical value of 0.817 leads to discrepancies in T_b of 4-5 %. Moreover, graph 1 clearly indicates that the hypothetical M_{eq}-values of 0.812, 0.814, 0.818 and 0.822 (legend see figure caption) can be excluded due to the inflexions (negative for too small assumptions of M_{eq} or positive for too high assumptions respectively) of the build-up time constants as function of polarisation at high $M > 0.7$ approximately. Considering graph 1, it is possible to hesitate between three values of M_{eq}: 0.816, 0.817 and 0.815.
The relative errors on T_b resulting from a different choice of M_{eq} from the theoretically predicted value are represented in graphs 2, 3 and 4 of figure F.8 at three different polarisation values: $M = 0.046$ (closest value to $M = 0$, graph 2), $M \approx 0.74$ (approximately 90 % of M_{eq}, graph 3) and $M \approx 0.79$ (closest value to M_{eq}, graph 4). The relative errors of T_b for different values of M_{eq} entered into the programme with respect to T_b for 0.817 in graphs 2, 3 and 4 are given by $\frac{|T_b(M_{\mathrm{eq}})-T_b(0.817)|}{T_b(0.817)}$. The relative errors arising from the choice of M_{eq} in the programme are compared to the statistical errors of the determination by the dedicated programme of build-up times by linear fits on $\ln(M_{\mathrm{eq}} - M)$ as function of M.
Close to $M = 0$ (graph 2), statistical and relative errors are of comparable size. A variation of the used M_{eq}-value in the programme of $\pm$ 0.6 % (0.812 or 0.822 compared to the theoretical value of 0.817) leads to a maximum relative error of 0.65 % (0.3 % using $M_{\mathrm{eq}} = 0.815$, the furthermost M_{eq} with respect to the theoretical

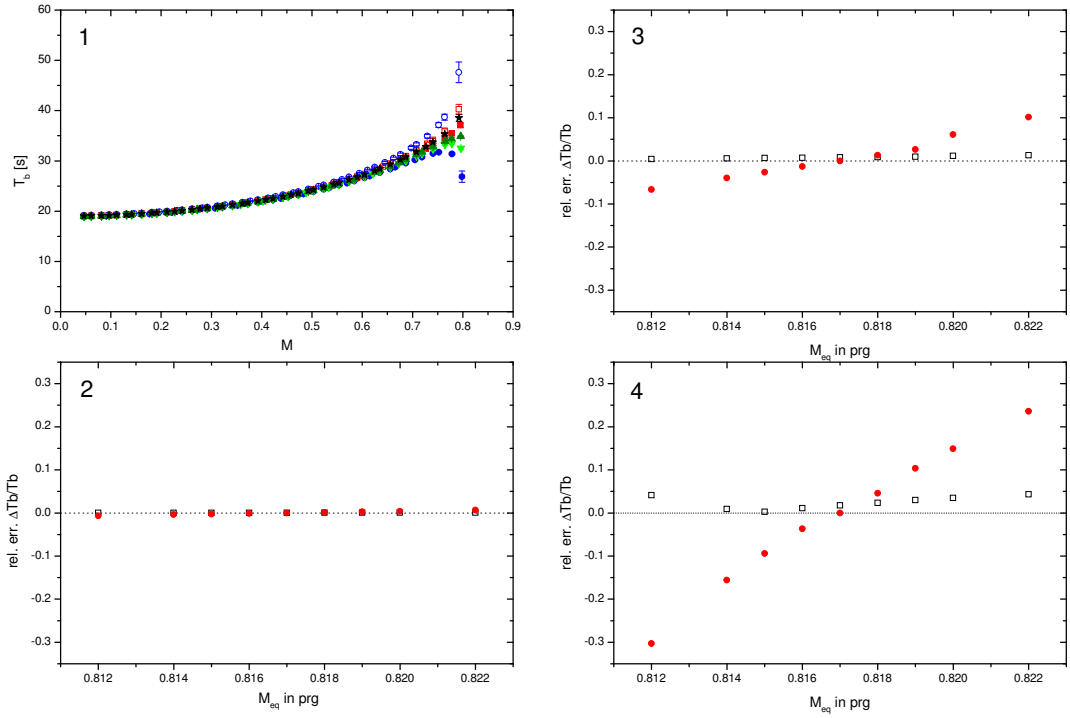

Figure F.8: Influence of the used M_{eq}-value in the dedicated programme on build-up time constants T_b. Graph 1: T_b as function of M during build-up for different values of M_{eq}: Filled stars: 0.817, filled squares: 0.816, filled triangles: 0.815, filled downward triangles: 0.814, filled circles: 0.812, open squares: 0.818, open circles: 0.822 (same symbols (open/filled) indicate the same difference from the theoretical steady state value of 0.817). Graphs 2, 3 and 4: Filled circles: Relative error $\frac{\Delta T_b}{T_b}$ as function of M_{eq} in programme, open squares: statistical error of determination of T_b. Graph 2: at $M = 0.046$ (closest value possible to $M = 0$), graph 3: at $M \approx 0.74$ (approximately 90 % of M_{eq}), graph 4: at $M \approx 0.79$ (closest value possible to M_{eq}).

value which is acceptable according to graph 1). At approximately 0.9 M_{eq} (graph 3), the same variation of M_{eq} of $\pm$ 0.6 % causes a relative error of 7 % (3 % using $M_{\mathrm{eq}} = 0.815$). The relative error caused by the inappropriate choice of M_{eq} is the dominant error, the statistical error of the determination of T_b is almost negligible. This is also the case close to M_{eq} (graph 4), where a maximum relative error of 30 % (10 % using $M_{\mathrm{eq}} = 0.815$) is observed.

For noisy data (graphs not shown here), the influence of the choice of M_{eq} on build-up times is qualitatively the same as represented in figure F.8 for noiseless data. Statistical errors of the determination of T_b are of course higher than for noiseless synthetic data, not exceeding 10 % (for the maximum noise level used in these tests: 1 % of generated random Gaussian noise added to the noiseless synthetic data before data processing). The relative errors on T_b for noisy data when varying the input parameter M_{eq} in the programme are comparable to the case of noiseless data. Thus for noisy data close to $M = 0$, the statistical error of T_b is higher than the relative error arising from an inappropriate choice of M_{eq} in the programme, which amounts to 0.7 % only. At approximately 0.9 M_{eq}, a variation of M_{eq} in the programme of $\pm$ 0.6 % leads to a maximum error in T_b of 8 % which is comparable to the noiseless case. Close to M_{eq}, varying the input parameter M_{eq} of up to $\pm$ 0.6 % yields a relative error of T_b of 28 %. Up to a variation of M_{eq} of $\pm$ 0.25 % (from $M_{\mathrm{eq}} = 0.815$ up to $M_{\mathrm{eq}} = 0.819$), the statistical error remains greater than or equal to the relative error due to the choice of the input parameter M_{eq} in the dedicated programme.

At the given degree of precision, the influence of the choice of M_{eq} on $\frac{dM}{dt}$ as function of M is infinitesimal. This observation supports the statement given on page 143, that - in contrast to T_b - $\dot{M}$ is a significant physical parameter as it is *in*dependent of the choice of M_{eq} as parameter in the analysis.

Comparison of two approaches to determine T_b

In the following fourth part of the current appendix about data processing and analysis of the build-up process, two ways to determine build-up times T_b are compared: First, linear fits on sliding intervals of $\ln(M_{\mathrm{eq}} - M)$ - the approach used for automatic determination by the dedicated programme - and second, a manual determination by exponential fits on short intervals of the build-up curve $M(t)$.
In addition to this comparison between two different methods described in detail below, it has been verified that when using manually exactly the same approach as implemented in the programme on noiseless and noisy data, the obtained T_b-values for different lengths of fit intervals are in perfect agreement with the provided T_b-values by the dedicated programme as expected.

In order to compare this method of linear fits on $\ln(M_{\text{eq}} - M)$ to determine T_b with the method of exponential fits on $M(t)$ (performed manually), noiseless C_8-data has been generated as well as noisy data with $\frac{1}{80}$ of the generated noise added to the noiseless data. This noise amplitude is higher than observed in typical OP measurements of this work. On the generated $M(t)$-curves with and without noise, build-up times have been determined at five different points of the polarisation build-up using the standard length of fit intervals ($\frac{1}{10}$ of the total variation of M), both in the programme and for the manual exponential fits. The central polarisation values of these five fitting intervals are: $M_c = 0.041$, $M_c = 0.241$, $M_c = 0.491$, $M_c = 0.75$ and $M_c = 0.776$. In the left graph of figure F.9, the ratios R_{pm} of the determined T_b-values by the dedicated programme divided by the corresponding manually determined build-up times are represented as function of M_c. In the right graph of figure F.9, four different ratios as function of M_c are represented: theoretical T_b divided by T_b determined by the programme (ratio R_{tp}) and theoretical T_b divided by manually determined T_b (ratio R_{tm}), both ratios with and without noise respectively.

The left graph of figure F.9 shows that R_{pm} is compliant to 1 within errors for all

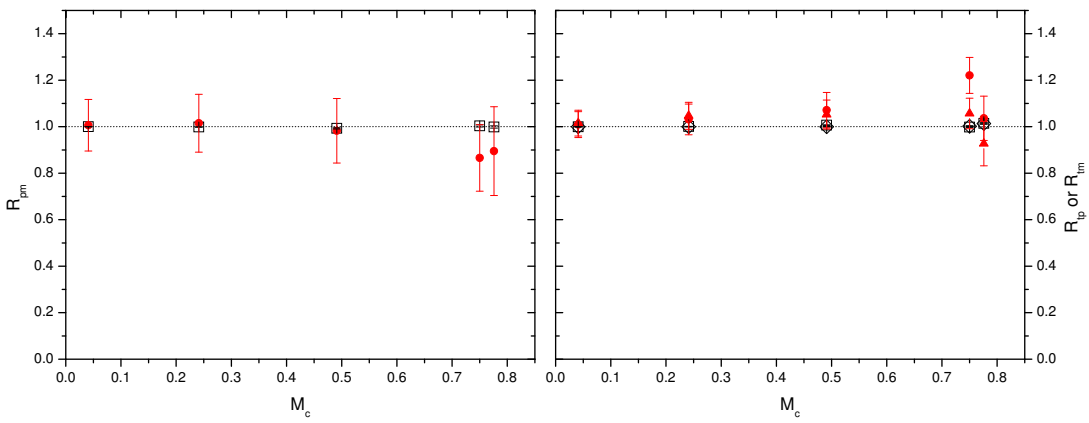

Figure F.9: Comparison of build-up times of synthetic data (characteristics see text) either determined by (manual) exponential fits on $M(t)$ or obtained from linear fits on $\ln(M_{\text{eq}} - M)$ by the dedicated programme. Left: ratio $R_{pm} = T_b$ (programme) / T_b (manual exponential fit), open squares: noiseless data, filled circles: noisy data. Right: ratio $R_{tp} = T_b$ (theoretical) / T_b (programme), ratio $R_{tm} = T_b$ (theoretical) / T_b (manual exponential fit). Open squares: R_{tp} noiseless data, open diamonds: R_{tm} noiseless data, filled circles: R_{tp} noisy data, filled triangles: R_{tm} noisy data.

investigated build-up intervals in the case of noiseless data. This observation remains valid in the case of noisy data (as errors are higher). However, at $M_c = 0.75$ and $M_c = 0.776$, the discrepancy between both methods is higher but does not exceed 15 %. In the case of noisy data at higher polarisation values, the programme per-

forming linear fits on $\ln(M_{\mathrm{eq}} - M)$ yields shorter T_b-values than manual exponential fits on $M(t)$.

This observation results from intrinsic features of the ln-function and does *not*

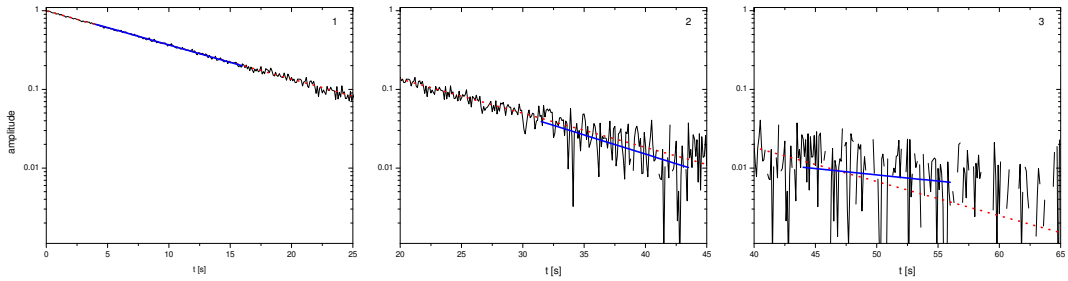

Figure F.10: Illustration to explain the observed behaviour of build-up times at high M (cf. figure F.9): Synthetic noiseless (dotted line) and noisy (solid line) exponential decays in three overlapping time intervals (zone 1 (on the left), zone 2 (in the centre) and zone 3 (on the right), details see text). In each zone, a linear fit of 10 s length is performed on noisy data and represented by straight, solid lines (exact fitting intervals and explanations see text).

represent a fault of the dedicated programme. The same behaviour is observable on manual linear fits on $\ln(M_{\mathrm{eq}} - M)$. With the help of figure F.10, intrinsic features of the ln-function applied to noisy data can be illustrated. This figure represents an analytically generated exponential decay from 1 to 0 within 100 s in logarithmic representation and is divided into three parts: Zone 1 - on the left - from t = 0-25 s, zone 2 - in the centre - from t = 20-45 s and zone 3 - on the right - from t = 40-60 s. In each part, the noiseless exponential decay (dotted line), the noisy exponential decay (with 1% of Gaussian noise with standard deviation of 1 added, solid line) and linear fits on 10 s-intervals of the noisy exponential decay (straight solid lines) are represented.

In zone 1, at the beginning of the exponential decay, applying the ln-function to the noisy data does not have an influence. The noise is distributed symmetrically around the noiseless curve and the slope of a linear fit on the noisy data from t = 5-15 s is almost identical with the slope of the noiseless curve: the ratio $R_{\frac{n}{no}}$ of the slope of the fit on the noisy curve divided by the slope of the noiseless curve amounts to 1.015 in zone 1.

Zone 2 corresponds to the part of the noisy exponential decay in which the two last M_c-values of figure F.9 are situated. On a $M(t)$-curve, this is the part where M-values are approaching the asymptotic value M_{eq} and the noise is of the same order as the difference to the asymptote. Before applying the ln-function to the generated exponential decay used here, the noise is symmetrically distributed around the noiseless curve. However, due to the non-linearity of the ln-function, the noise

appears distorted in zone 2 in logarithmic representation. The noise amplitude below the noiseless curve appears higher than above. When performing a linear fit from t = 32.5-42.5 s on the noisy exponential decay, the fit yields a steeper slope than the noiseless curve, $R_{\frac{n}{no}} = 1.122$. A steeper slope of the linear fit on $\ln(M_{\text{eq}} - M)$ corresponds to a shorter T_b-value. This discrepancy of more than 12 % is compatible with the observed difference of extracted build-up times of up to 15 % in the example shown in figure F.9.
Zone 3 corresponds to the part on a $M(t)$-curve, where M-values further approach the asymptotic value M_{eq}. Due to the noise, it is possible that there are values with $M > M_{\text{eq}}$, i.e., with a negative difference $M_{\text{eq}} - M$. Building the natural logarithm of a negative argument does not yield a *real* result, but contains an imaginary part as well, and is therefore cropped. In the last part of the exponential decay shown in zone 3 of figure F.10, these missing points are clearly observable, especially above $t = 55$ s. Due to this additional influence of cropped points which (over)compensates the distortion of noise, a linear fit from $t =$ 45-55 s on the noisy exponential decay yields a slope that is less steep than the noiseless data, leading to a ratio of $R_{\frac{n}{no}} = 0.365$ in this case.
In the investigated example of figure F.9, this last mentioned zone 3, where the approach of linear fits on $\ln(M_{\text{eq}} - M)$ to extract build-up times might yield too long T_b-values compared to exponential fits on $M(t)$, was not reached (only 2 out of more than 800 points exhibit a negative difference $M_{\text{eq}} - M$). However, if the noise was higher, these different behaviours of zones 2 and 3 would have been observed as well on the extracted build-up times.

In order to evaluate the quality of the extracted build-up times by the two introduced methods, the ratio R_{pm} is not sufficiently significant. The quality of an extracted T_b-value is defined here as the discrepancy to the theoretically expected T_b-value. Proceeding synthetic data generated by the MEOP-model has the advantage of knowing the theoretical T_b-value at each M_c. Therefore, the right graph of figure F.9 represents the following parameters as function of M_c, both for noiseless and noisy data respectively: the ratio R_{tp} of theoretical build-up times divided by the corresponding T_b-values provided by the programme, and the ratio R_{tm} of the theoretical T_b-values divided by the manually determined ones by exponential fits.
In general, it can be observed in this graph that all methods are equivalent to each other and compatible with theoretical predictions in the case of noiseless data: As expected, the different ratios for almost all M_c-values are compliant to 1.
Concerning extracted T_b-values of noisy data, the ratio R_{tm} is nearly constant, not exceeding 1.06, with increasing M_c up to 0.75, and then decreases to R_{tm}=0.93 at M_c=0.776. The ratio R_{tp} increases up to 1.22 at M_c=0.75. This observation is coherent with the left graph of figure F.9, as the programme yields shorter T_b-values at higher M_c than the manual determination. (These shorter T_b-values are caused by

the non-linearity of the ln-function and the resulting distortion of noise as described by figure F.10 and related explanations.) At high M_c=0.776, R_{tp} decreases to 1.04 featuring the same tendency as R_{tm}.
A closer look at the last two M_c-values of this graph reveals that at M_c=0.75, both methods yield T_b-values below the theoretical one, T_b extracted by exponential fit exhibits the smallest discrepancy to the theoretical T_b-value (which is 6 % above). At M_c=0.776 however, T_b determined by the programme is below, and T_b determined by exponential fit is above the theoretical T_b-value. In contrast to the previous M_c-value, T_b extracted by the programme using a linear fit on $\ln(M_{\mathrm{eq}} - M)$ exhibits the smallest discrepancy to the theoretical T_b-value (that is 4 % above) at $M_c = 0.776$.

To conclude this comparison of two different methods to extract build-up times - manual exponential fits on $M(t)$ versus linear fits on $\ln(M_{\mathrm{eq}} - M)$ performed by the dedicated programme, of course manually possible as well though - the following aspects should be retained: For noiseless data, both methods yield trustworthy T_b-values throughout the whole range of M_c-values during polarisation build-up. For noisy data, discrepancies with respect to the theoretically expected T_b-value occur with both methods: The discrepancies for the chosen noise-level in this example did not exceed 7 % up to 60 % of M_{eq}, and the highest observed discrepancies were of the order of 20 % at higher M_c. None of both methods was the best one in *all* cases. Therefore, if really T_b close to M_{eq} on noisy data has to be determined precisely, it is recommended to use both methods in order to estimate the maximum systematic error on T_b due to the choice of the method used to determine polarisation build-up times. For the routine analysis to characterise OP-dynamics, however, build-up times close to $M = 0$ are interesting and relevant, and in this range of polarisation values, the dedicated programme works reliably even on noisy data and has therefore been used for most of the build-up analyses in this work.

Appendix G

Influence of stimulated emission on scaling of M^a with incident pump laser power and pressure

In order to verify the expected scaling of apparent polarisation values M^a with the ratio of W_{inc}/p_3 theoretically, the model for MEOP kinetics is used to predict apparent polarisation values as function of actual polarisation in well defined conditions. In figure G.1, the model is used at constant n_{m} and constant reduced power of 1 W/torr and three different pressure-values: 0.5 torr, 1 torr and 2 torr. Furthermore, perturbations of populations like relaxation of metastable states as well as couplings between the two velocity classes (effectively and weakly pumped) are set to a negligible level.

Figure G.1 shows that in fixed conditions like constant n_m, constant reduced power and fixed intrinsic relaxation time in 2^3P (although this assumption is not perfectly realistic, see subsection 6.3.2), there are situations where apparent polarisation values scale perfectly with W_{inc}/p_3: In the Dehmelt-regime of complete collisional redistribution in 2^3P, all three M^a-curves are well superposed over the whole range of actual polarisations for both probe transitions C_8 and C_9. However, in the Kastler-regime of no collisional redistribution in 2^3P, especially for probe C_8, a departure from the expected scaling (up to 20 % between highest and lowest investigated pressure-values at $M = 0$) is still observed although all parameters are well controlled in the MEOP-model.

In order to understand this observed departure of M^a from the expected scaling with W_{inc}/p_3 at no collisional redistribution in 2^3P, further more detailed computations are performed: Important populations of 2^3S and 2^3P for the determination of nuclear polarisation are determined for different assumptions in order to investigate the influence of stimulated emission (SE) on apparent polarisation values. Stimulated

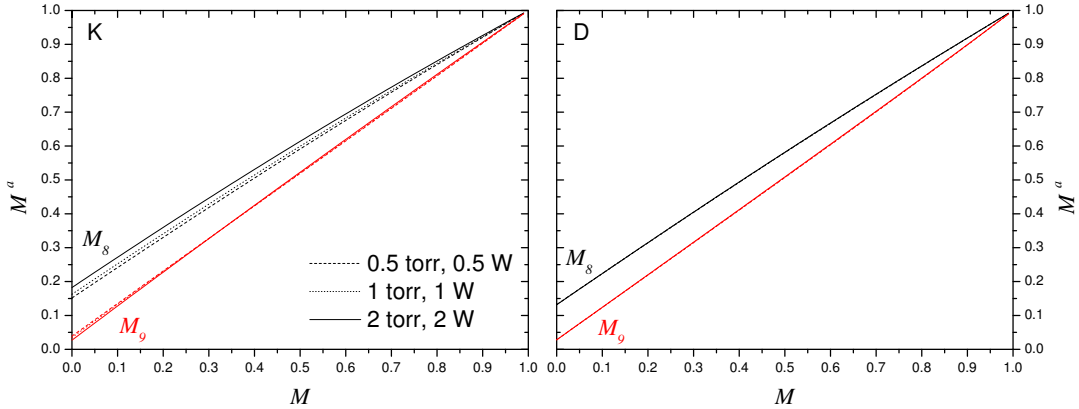

Figure G.1: Theoretical verification of scaling of apparent polarisation values with W_{inc}/p_3 in Kastler- and Dehmelt-regimes. Pump transition: C_8 with beam diameter $2a = 1.6$ cm, constant $n_m = 2.2 \times 10^{16}$ atoms/m^3, radial n_m-parameter $\alpha = 0$, three pressure values (see legend) with constant reduced incident power of 1 W/torr, probe transitions: C_8 (yielding higher M^a-values) and C_9 (lower M^a-values). Left: Kastler-regime (K) of no collisional redistribution in 2^3P: $\tau_P = 1$ s, right: Dehmelt-regime (D) of complete collisional redistribution in 2^3P: $\tau_P = 1 \times 10^{-20}$ s.

emission might be a possible explanation for the departure from the anticipated scaling as its effect on populations and thus on apparent polarisation is expected to depend on pressure.

Figure G.2 represents populations of 2^3S-sublevels A_5 (depopulated state due to OP on C_8, σ^+) and A_6 (overpopulated state) and of 2^3P-sublevel B_{17}, as well as apparent polarisation at $M = 0$ as function of reduced incident power for the case of no collisional redistribution in 2^3P, figure G.3 shows similar computations for the case of full collisional redistribution.

Figures G.2 and G.3 present populations for 0.5 and 2 torr including SE and the corresponding pressure-independent populations in the SE free case. Therefore, the radiative decay rate from 2^3P is deliberately increased in the model for MEOP-kinetics so that 2^3P-sublevels are empty and thus no stimulated emission into 2^3S is possible. In the left graphs of these two figures, the determination of apparent polarisation M^a for the SE free case is based on the ratio of these SE free populations a_6/a_5 (corresponding to C_8, using formulas valid in the spin temperature limit, cf. section 4.2.1).

The second determination of M^a (yielding the highest apparent polarisation values (in the Kastler-regime) represented by blue lines) is based on computed probe absorption rates that are proportional to the difference $(a_i - b_j)$, taking into account the non-negligible population b_{17} (pump transition C_8, σ^+: from A_5 to B_{17}).

The third represented determination of M^a in the left graphs of figures G.2 and G.3

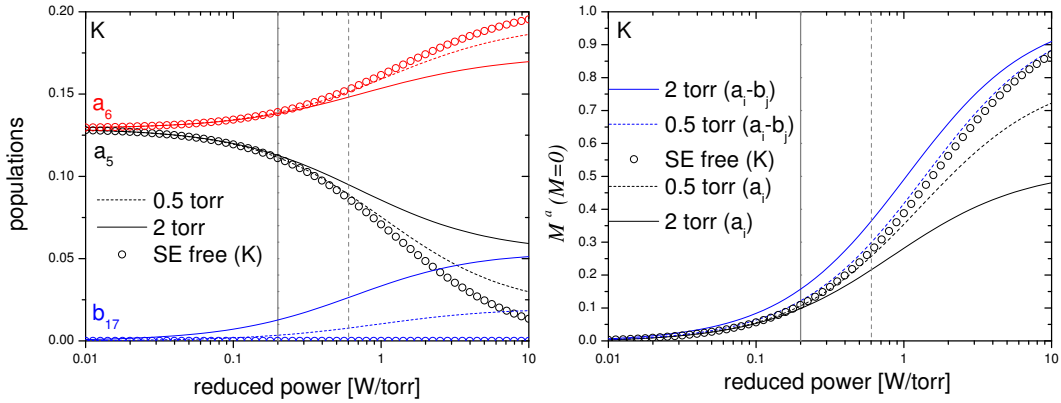

Figure G.2: Populations (of strongly pumped velocity class only) and apparent polarisation at $M = 0$ (probe C_8) as function of reduced incident power (pump C_8) for *no* collisional redistribution in 2^3P (Kastler-regime): on the right graph, two different pressure values are represented for each population a_5, a_6 and b_{17} (see legend) and the case of *no* stimulated emission (open circles, pressure independent). On the left graph, the determination of apparent polarisation is based on three different assumptions (details see text): from top to bottom: determination of M^a based on populations $a_i - b_j$ (2 pressure values), SE free case (independent of pressure), determination of M^a based on populations a_i (2 pressure values). Vertical lines: see comments in text.

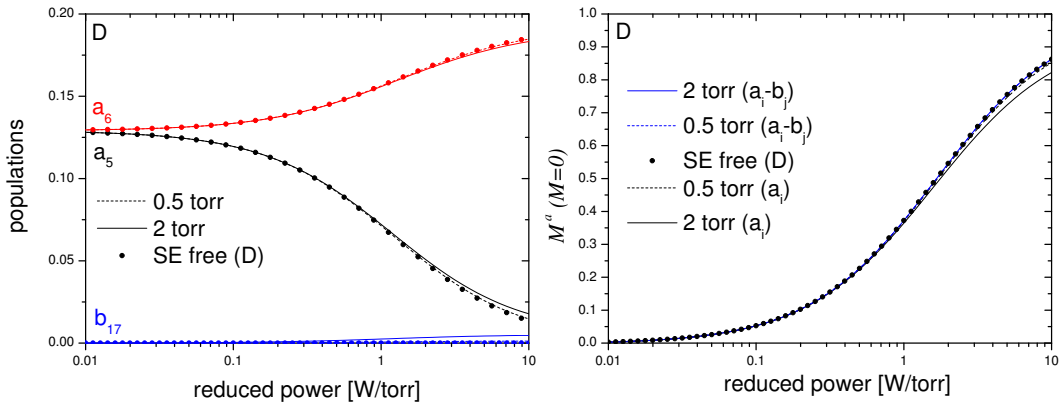

Figure G.3: Populations (of strongly pumped velocity class only) and apparent polarisation at $M = 0$ (probe C_8) as function of reduced incident power (pump C_8) for *full* collisional redistribution in 2^3P (Dehmelt-regime): The same cases of different pressure-values and assumptions to infer M^a including the SE free case as in figure G.2 are represented.

(yielding the lowest apparent polarisation values (in the Kastler-regime) represented by black lines) is based on the assumption that effects of SE are only inhibited on probe absorptions. This assumption can be realised by artificially stating that probe absorption rates are proportional to a_i (instead of $a_i - b_j$, neglecting populations in 2^3P) and using the same formulas to infer polarisation as for the two previously mentioned assumptions.

In the following, the case of no collisional redistribution in 2^3P (Kastler-regime), represented in figure G.2, is discussed first.
On the left graph, we observe that the populations of sublevels A_5 and A_6 are affected in a nicely scaling way up to 0.1-0.2 W/torr (solid vertical line) for the 2 torr cell, and up to 0.5-0.7 W/torr (dashed vertical line) at lower pressure. When these 'critical' reduced powers are reached, significant 2^3P populations have already developed.
Based on these observations, the behaviour of the orientations plotted on the left side can thus be understood: The spin temperature orientations that are computed from the ratio of populations a_i (black lines), nicely scale up to the same 'critical' reduced powers, and the impact of SE only occurs above.
The spin temperature orientation based on the second assumption to infer M^a from probe absorption rates proportional to $a_i - b_j$ (blue lines above SE free case), taking into account the non-negligible populations in 2^3P, has a much earlier departure from the scaling behaviour. Moreover, the pressure effect has the opposite sign: The increase of apparent polarisation results from the reduction of absorption of the less absorbed component due to SE. More precisely, the population a_5 is higher than expected due to SE from 2^3P. This results in less absorption of the σ^+ component (from A_5 to B_{17}) which entails a higher ratio of absorptions compared to the SE free case, so that M^a is higher at 2 torr than at 0.5 torr. The same explanation also applies to the left graph of figure G.1 where higher pressure also yields higher M^a-values.

In the case of full collisional mixing in 2^3P (Dehmelt-regime or depopulation OP), represented in figure G.3 for a pump laser still on C_8, the most striking point is that SE effects are very much reduced. This can be attributed to the much weaker population of the 2^3P sublevel B_{17}, approximately divided by 18 due to collisional redistribution among all 18 sublevels of 2^3P. Another effect of collisional redistribution is that sublevel B_{18} is also populated in the Dehmelt-regime, so that SE effects influence both probe absorption signals, and thus compensate in part. The right part of figure G.3 shows that the second assumption to infer M^a from probe absorption rates proportional to $a_i - b_j$ (blue lines superposed with SE free case) is perfectly suitable for the determination of nuclear polarisation in depopulation OP.

As a conclusion concerning the computations presented in the last paragraphs, it can be retained that the scaling of apparent polarisation roughly depends on the ratio

of W_{inc}/p_3 i.e., on the ratio of the optical pumping rate divided by the metastability exchange rate for given geometrical parameters. The departure from the 'naively' expected scaling can be attributed to effects of stimulated emission. Their impact depends on the degree of collisional mixing in 2^3P (Kastler-/Dehmelt-regime), which changes around 1 torr. Thus the 'critical' power limiting the validity of the scaling depends on the considered pressure.
When operating at low magnetic field and pressure values of order 1 torr as in all presented examples of the last paragraphs, the following three important rates in the OP process are set to similar values: metastability exchange rate, collisional mixing rate in 2^3P, and spontaneous emission in 2^3P. Their ratios and relative influences are very different at high magnetic field, or at very low or high pressure, and the behaviour of apparent polarisation as function of actual polarisation would be rather different.

Concerning a comparison of computed and experimentally observed scaling (cf. figure 6.31) of apparent polarisation with W_{inc}/p_3, the model for MEOP kinetics predicts the correct scale to explain effects of collisions leading to a departure of order 20-25 % from the expected scaling. However, computed relative differences e.g., of apparent polarisation values at $M = 0$ between highest and lowest investigated pressures, yield an opposite sign than experimental equivalents, but of correct order of magnitude. Other similar collisional effects might possibly be responsible to fully explain the experimentally observed departure of M^a-values from the scaling with W_{inc}/p_3.

Bibliography

[Abb04] M. Abboud, A. Sinatra, X. Maître, G. Tastevin, P.-J. Nacher; *High nuclear polarization of* ^{3}He *at low and high pressure by metastability exchange optical pumping at 1.5 tesla*; Europhys. Lett. **68**, 480 (2004). (Cited on pages 2, 5, 259 and 286.)

[Abb05a] M. Abboud, A. Sinatra, G. Tastevin, P.-J. Nacher, X. Maître; *Metastability Exchange Optical Pumping of Helium-3 at High Pressures and 1.5 T: Comparison of Two Optical Pumping Transitions*; Las. Phys. **15**, 475 (2005). (Cited on page 286.)

[Abb05b] M. Abboud; *Pompage optique de l'hélium-3 à forte pression dans un champ magnétique de 1.5 Tesla* (in French); Ph.D. thesis Université Paris VI (2005). available online at http://tel.archives-ouvertes.fr/tel-00011099 (Cited on pages VIII, 6, 49, 168, 173, 175, 176, 196, 259, 260, 262, 286, 287, 288, 289, 292, 294 and 299.)

[Adh06] B. Adhimoolam, I.D. Lindsay, C.J. Lee, P. Gross, K.J. Boller, M.E. Klein; *Spectral shaping of a 10 W diode laser*-Yb-*fiber amplifier system*; Rev. Sci. Instrum. **77**, 093101 (2006). (Cited on page 203.)

[And05] K.H. Andersen, R. Chung, V. Guillard, H. Humblot, D. Jullien, E. Lelièvre-Berna, A. Petoukhov, F. Tasset; *First results from Tyrex, the new polarized-*^{3}He *filling station at ILL*; Physica B **356**, 103 (2005). (Cited on page 2.)

[And59] L.W. Anderson, F.M. Pipkin, J.C. Baird; N^{14}–N^{15} *Hyperfine Anomaly*; Phys. Rev. **116**, 87 (1959). (Cited on page 38.)

[ASD11] NIST Atomic Spectra Database (ver. 4.1.0) (2011). available online at http://physics.nist.gov/asd (Cited on page XXII.)

[Bab03] E. Babcock, I. Nelson, S. Kadlecek, B. Driehuys, L.W. Anderson, F.W. Hersman, T.G. Walker; *Hybrid Spin-Exchange Optical Pumping of* ^{3}He; Phys. Rev. Lett. **91**, 123003 (2003). (Cited on page 6.)

[Bab06] E. Babcock, B. Chann, T.G. Walker, W.C. Chen, T.R. Gentile; *Limits to the Polarization for Spin-Exchange Optical Pumping of* ^{3}He; Phys. Rev. Lett. **96**, 083003 (2006). (Cited on pages 1 and 301.)

[Bar98a] A. Ben-Amar Baranga, S. Appelt, M.V. Romalis, C.J. Erickson, A.R. Young, G.D. Cates, W. Happer; *Polarization of* ^{3}He *by Spin Exchange with Optically Pumped* Rb *and* K *Vapors*; Phys. Rev. Lett. **80**, 2801 (1998). (Cited on page 6.)

[Bar74] R. Barbé, M. Leduc, F. Laloë; *Résonance magnétique en champ de radiofréquence inhomogène. 1re partie: Étude théorique* and *2e partie: Vérifications expérimentales; mesure du coefficient de self-diffusion de* ^{3}He; J. Physique **35**, 699 and 935 (1974). (Cited on page 63.)

[Bar77] R. Barbé; *Pompage optique de* ^{3}He *à basse température* (in French); Ph.D. thesis Université Paris VI (1977).
available online at http://tel.archives-ouvertes.fr/tel-00011827
(Cited on page 30.)

[Bat05] M. Batz, S. Baeßler, W. Heil, E.W. Otten, D. Rudersdorf, J. Schmiedeskamp, Y. Sobolev, M. Wolf; ^{3}He *Spin Filter for Neutrons*; J. Res. Natl. Inst. Stand. Technol. **110**, 293 (2005). (Cited on pages 1 and 2.)

[Bat11] M. Batz, P.-J. Nacher and G. Tastevin; *Fundamentals of metastability exchange optical pumping in helium*; J. Phys.: Conf. Ser. **294**, 012002 (2011).
available online at http://iopscience.iop.org/1742-6596/294/1/012002
(Cited on pages 9, 17, 18, 19, 23, 42, 43, 48, 157, 273 and 298.)

[Bat12] M. Batz, G. Tastevin, P.-J. Nacher, A. Deninger; *White noise modulation of laser frequency for enhanced efficiency of* ^{3}He *optical pumping at 1083 nm*; in preparation (2012). (Cited on page 203.)

[Bau08a] E. Baudin, M.E. Hayden, G. Tastevin, and P.J. Nacher; *Nonlinear NMR dynamics in hyperpolarized liquid* ^{3}He; C. R. Chim. **11**, 560 (2008).
available online at http://hal.archives-ouvertes.fr/hal-00180383
(Cited on page 1.)

[Bau08b] E. Baudin, M.E. Hayden, G. Tastevin, and P.J. Nacher; *NMR Time Reversal Experiments in Highly Polarised Liquid* ^{3}He-^{4}He *Mixtures*; J. Low Temp. Phys. **150**, 168 (2008).
available online at http://hal.archives-ouvertes.fr/hal-00177870
(Cited on page 1.)

[Bee03] E.J.R. van Beek, J. Schmiedeskamp, J.M. Wild, M.N.J. Paley, F. Filbir, S. Fichele, F. Knitz, G.H. Mills, N. Woodhouse, A. Swift, W. Heil, M. Wolf, E. Otten; *Hyperpolarized 3-helium MR imaging of the lungs: testing the concept of a central production facility*; Eur. Radiol. **13**, 2583 (2003). (Cited on page 2.)

[Bee04] E.J.R. van Beek, J.M. Wild, H.-U. Kauczor, W. Schreiber, J.P. Mugler, E.E. de Lange; *Functional MRI of the Lung Using Hyperpolarized 3-Helium Gas*; J. Magn. Reson. Imaging **20**, 540 (2004). (Cited on page 1.)

[Bee09] E.J.R. van Beek, A.M. Dahmen, T. Stavngaard, K.K. Gast, C.P. Heussel, F. Krummenauer, J. Schmiedeskamp, J.M. Wild, L.V. Søgaard, A.E. Morbach, L.M. Schreiber and H.-U. Kauczor; *Hyperpolarised* ^{3}He *MRI versus HRCT in COPD and normal volunteers: PHIL trial*; Eur. Respir. J. **34**, 1311 (2009). (Cited on page 1.)

[Ber03] J. Bermuth, P. Merle, C. Carasco, D. Baumann, R. Böhm, D. Bosnar, M. Ding, M.O. Distler, J. Friedrich, J.M. Friedrich, J. Golak, W. Glöckle, M. Hauger, W. Heil, P. Jennewein, J. Jourdan, H. Kamada, A. Klein, M. Kohl, B. Krusche, K.W. Krygier, H. Merkel, U. Müller, R. Neuhausen, A. Nogga, Ch. Normand, E. Otten, Th. Pospischil, M. Potokar, D. Rohe, H. Schmieden, J. Schmiedeskamp, M. Seimetz, I. Sick, S. Širca, R. Skibiński, G. Testa, Th. Walcher, G. Warren, M. Weis, H. Witała, H. Wöhrle, M. Zeier; *The neutron charge form factor and target analyzing powers from* $^3\overrightarrow{\mathrm{He}}(\vec{e}, e'n)$ *scattering*; Physics Letters B **564**, 199 (2003). (Cited on page 1.)

[Big92] N.P. Bigelow, P.J. Nacher, M. Leduc; *Accurate optical measurement of nuclear polarization in optically pumped* ^{3}He *gas*; J. Phys. II France **2**, 2159 (1992). (Cited on pages 75, 76 and 261.)

[Bla04] K.B. Blagoev, E. Dimova, G.M. Petrov; *Quenching of* ^{4}He$(2^1S;\ 2^1P)$ *and* ^{3}He$(2^1S;\ 2^1P)$ *states by collisions with* Ne$(^1S_0)$ *atoms*; J. Quant. Spectrosc. Radiat. Transfer **87**, 69 (2004). (Cited on page 301.)

[Blo85] D. Bloch, G. Trénec, M. Leduc; *Isotope shift of the* $2^3S_1 - 2^3P$ *transition in helium*; J. Phys. B: At. Mol. Phys. **18**, 1093 (1985). (Cited on pages 15 and 117.)

[Bon88] K.D. Bonin, T.G. Walker, and W. Happer; *Relaxation of gaseous spin-polarized* ^{3}He *targets due to ionizing radiation*; Phys. Rev. A **37**, 3270 (1988). (Cited on pages 292, 294 and 301.)

[Bou60] M.A. Bouchiat, T.R. Carver, C.M. Varnum; *Nuclear Polarization in* He^3 *Gas induced by Optical Pumping and Dipolar Exchange*; Phys. Rev. Lett. **5**, 373 (1960). (Cited on page 1.)

[Bro10] J.M. Brown, S.J. Smullin, T.W. Kornack, and M.V. Romalis; *New Limit on Lorentz- and CPT-Violating Neutron Spin Interactions*; Phys. Rev. Lett. **105**, 151604 (2010). (Cited on page 1.)

[Cat88a] G.D. Cates, S.R. Schaefer, W. Happer; *Relaxation of spins due to field inhomogeneities in gaseous samples at low magnetic fields and low pressures*; Phys. Rev. A **37**, 2877 (1988). (Cited on page 30.)

[Cat88b] G.D. Cates, D.J. White, T.-R. Chien, S.R. Schaefer, W. Happer; *Spin relaxation in gases due to inhomogeneous static and oscillating magnetic fields*; Phys. Rev. A **38**, 5092 (1988). (Cited on page 30.)

[Cha03] B. Chann, E. Babcock, L.W. Anderson, T.G. Walker, W.C. Chen, T.B. Smith, A.K. Thompson, T.R. Gentile; *Production of highly polarized* ^{3}He *using spectrally narrowed diode laser array bars*; J. Appl. Phys. **94**, 6908 (2003). (Cited on page 1.)

[Che07] W.C. Chen, T.R. Gentile, T.G. Walker and E. Babcock; *Spin-exchange optical pumping of* ^{3}He *with* $\mathrm{Rb-K}$ *mixtures and pure* K; Phys. Rev. A **75**, 013416 (2007). (Cited on pages 1 and 301.)

[Che97] S.V. Chernikov, J.R. Taylor, N.S. Platonov, V.P. Gapontsev, P.J. Nacher, G. Tastevin, M. Leduc, M.J. Barlow; *1083 nm ytterbium doped fibre amplifier for optical pumping of helium*; Electron. Lett. **33**, 787 (1997). (Cited on page 203.)

[Cho02] J. Choukeife, X. Maître, P.-J. Nacher and G. Tastevin; *On-site production of hyperpolarised helium-3 for lung MRI*; Magn. Res. Mat. in Phys., Biol. and Med., Suppl. 1 to Vol. **15**, 201 (2002). (Cited on page 2.)

[Cho03] J. Choukeife, X. Maître, P.J. Nacher and G. Tastevin; *On-site production of hyperpolarised helium-3 gas for lung MRI*; Abstracts ISSN 1524-6965, 1391 (2003). (Cited on page 2.)

[Cie07a] K. Cieślar, V. Stupar, E. Canet-Soulas, S. Gaillard, and Y. Crémillieux; *Alveolar Oxygen Partial Pressure and Oxygen Depletion Rate Mapping in Rats Using* ^{3}He *Ventilation Imaging*; Magn. Reson. Med. **57**, 423 (2007). (Cited on page 1.)

[Cie07b] K. Cieślar, H. Alsaid, V. Stupar, S. Gaillard, E. Canet-Soulas, R. Fissoune and Y. Crémillieux; *Measurement of nonlinear pO_2 decay in mouse lungs using* ^{3}He-*MRI*; NMR Biomed. **20**, 383 (2007). (Cited on page 1.)

[COD10] CODATA Internationally recommended values of the Fundamental Physical Constants (2010).
available online at http://physics.nist.gov/constants (Cited on page XXI.)

[Coh66] C. Cohen-Tannoudji, A. Kastler; *Optical pumping*; Progress in Optics **5**, 3 (1966). (Cited on page 246.)

[Col63] F.D. Colegrove, L.D. Schearer, G.K. Walters; *Polarization of* ^{3}He *Gas by Optical Pumping*; Phys. Rev. **132**, 2561 (1963). (Cited on pages 1, 4, 76 and 169.)

[Col11] G. Collier; *Metastability exchange optical pumping of helium-3 in situ*; Ph.D. thesis Uniwersytet Jagielloński Kraków (2011). (Cited on pages 286, 288, 297 and 299.)

[Cou01] E. Courtade; *Pompage optique de l'hélium dans des conditions non-standard* (in French); Ph.D. thesis Université Paris XI (2001).
available online at http://tel.archives-ouvertes.fr/tel-00001447
(Cited on pages 6, 58, 84, 123, 152, 168, 169, 172, 173, 292, 294, 295 and 336.)

[Cou02] E. Courtade, F. Marion, P.-J. Nacher, G. Tastevin, K. Kiersnowski, T. Dohnalik; *Magnetic field effects on the 1083 nm atomic line of helium – Optical pumping of helium and optical polarisation measurement in high magnetic field*; Eur. Phys. J. D **21**, 25 (2002). (Cited on pages XX, XXI, XXII, 5, 7, 8, 9, 11, 13, 15, 16, 18, 19, 20, 22, 37, 38, 44, 76, 77, 80, 84, 115, 117, 195, 196, 302, 308, 309, 311 and 312.)

[Dan71a] J.M. Daniels, R.S. Timsit, A.D. May, and V.L.S. Yuen; *A* ^{4}He *Discharge Light Source and Optical System for the Optical Pumping of* 2^3S_1 ^{3}He; Can. J. Phys. **49**, 517 (1971). (Cited on pages 4 and 169.)

[Dan71b] J.M. Daniels, R.S. Timsit; *The Expected Performance of an Optical Pumping Light Source, and the Kinetics of Optical Pumping of* 2^3S_1 ^{3}He; Can. J. Phys. **49**, 525 (1971). (Cited on pages 4, 77 and 169.)

[Dan71c] J.M. Daniels, R.S. Timsit; *The Determination of the Polarization of* ^{3}He *by Optical Methods*; Can. J. Phys. **49**, 539 (1971). (Cited on page 76.)

[Deh57] H.G. Dehmelt; *Slow Spin Relaxation of Optically Polarized Sodium Atoms*; Phys. Rev. **105**, 1487 (1957). (Cited on pages 51 and 246.)

[Den06] A. Deninger, W. Heil, E.W. Otten, M. Wolf, R.K. Kremer, and A. Simon; *Paramagnetic relaxation of spin polarized* ^{3}He *at coated glass walls*; Eur. Phys. J. D **38**, 439 (2006). (Cited on page 30.)

[Dim04] E. Dimova, G.M. Petrov, K.B. Blagoev; *Quenching of* ^{4}He *and* ^{3}He *excited states by collisions with* N_2; Vacuum **76**, 405 (2004). (Cited on page 301.)

[Dmi76] S.P. Dmitriev, R.A. Zhitnikov, and A.I. Okunevich; *Effect of Penning collisions between optically oriented* Rb *and* He *atoms on electron density in plasma*; Zh. Eksp. Teor. Fiz. **70**, 69 (1976) [Sov. Phys. JETP **43**, 35 (1976)]. (Cited on page 195.)

[Doh11] T. Dohnalik, A. Nikiel, T. Pałasz, M. Suchanek, G. Collier, M. Greńczuk, B. Głowacz, Z. Olejniczak; *Optimization of the pumping laser beam spatial profile in the MEOP experiment performed at elevated* ^{3}He *pressures*; Eur. Phys. J. Appl. Phys. **54**, 20802 (2011). (Cited on pages 186, 223 and 297.)

[Dra96] *Atomic, molecular, and optical physics handbook*; edited by G.W.F. Drake; AIP press (1996). (Cited on pages XXI and 29.)

[Dup71] J. Dupont-Roc, M. Leduc, and F. Laloë; *New Value for the Metastability Exchange Cross Section in Helium*; Phys. Rev. Lett. **27**, 467 (1971). (Cited on pages 30 and 250.)

[Dup73] J. Dupont-Roc, M. Leduc, and F. Laloë; *Contribution à l'étude du pompage optique par échange de métastabilité dans* ^{3}He; J. Physique **34**, 961 and 977 (1973). (Cited on pages 4, 42, 43 and 169.)

[Eck92] G. Eckert, W. Heil, M. Meyerhoff, E.W. Otten, R. Surkau, M. Werner, M. Leduc, P.J. Nacher and L.D. Schearer; *A dense polarized* ^{3}He *target based on compression of optically pumped gas*; Nucl. Instr. and Meth. A **320**, 53 (1992). (Cited on pages XI, 290, 291 and 292.)

[Elb90] M. Elbel, C. Larat, P.J. Nacher, M. Leduc; *Optical pumping of helium-3 with a frequency electromodulated laser*; J. Phys. France **51**, 39 (1990). (Cited on page 203.)

[Emm88] F. Emmert, H.H. Angermann, R. Dux and H. Langhoff; *Reaction kinetics of the* He*(2P) and the* He_2^**(a,v) states in high-density helium*; J. Phys. D: Appl. Phys. **21**, 667 (1988). (Cited on pages 171 and 292.)

[Fed96] P.O. Fedichev, M.W. Reynolds, U.M. Rahmanov, and G.V. Shlyapnikov; *Inelastic decay processes in a gas of spin-polarised triplet helium*; Phys. Rev. A **53**, 1447 (1996). (Cited on page 195.)

[Fit68] W.A. Fitzsimmons, N.F. Lane, and G.K. Walters; *Diffusion of* He *(2^3S_1) in Helium gas; 2^3S_1 – 1^1S_0 Interaction Potentials at Long Range*; Phys. Rev. **174**, 193 (1968). (Cited on pages 30, 171, 314 and 316.)

[Gem10a] C. Gemmel, W. Heil, S. Karpuk, K. Lenz, Ch. Ludwig, Yu. Sobolev, K. Tullney, M. Burghoff, W. Kilian, S. Knappe-Grüneberg, W. Müller, A. Schnabel, F. Seifert, L. Trahms, and St. Baeßler; *Ultra-sensitive magnetometry based on free precession of nuclear spins*; Eur. Phys. J. D **57**, 303 (2010). (Cited on page 1.)

[Gem10b] C. Gemmel, W. Heil, S. Karpuk, K. Lenz, Yu. Sobolev, K. Tullney, M. Burghoff, W. Kilian, S. Knappe-Grüneberg, W. Müller, A. Schnabel, F. Seifert, L. Trahms, and U. Schmidt; *Limit on Lorentz and CPT violation of the bound neutron using a free precession* ^{3}He / ^{129}Xe *comagnetometer*; Phys. Rev. D **82**, 111901(R) (2010). (Cited on page 1.)

[Gen93] T.R. Gentile, R.D. McKeown; *Spin-polarizing* ^{3}He *nuclei with an arc-lamp-pumped neodymium-doped lanthanum magnesium hexaluminate laser*; Phys. Rev. A **47**, 456 (1993). (Cited on pages 259, 260, 262 and 299.)

[Gen03] T.R. Gentile, M.E. Hayden, M.J. Barlow; *Comparison of metastability-exchange optical pumping sources*; J. Opt. Soc. Am. B **20**, 2068 (2003). (Cited on pages 2, 7, 9 and 203.)

[Gen05] T.R. Gentile, W.C. Chen, G.L. Jones, E. Babcock, T.G. Walker; *Polarized* ^{3}He *Spin Filters for Slow Neutron Physics*; J. Res. Natl. Inst. Stand. Technol. **110**, 299 (2005). (Cited on page 1.)

[Glo11] B. Głowacz; *Detection of metastable* He_2^* *molecules in helium plasma*; Ph.D. thesis Université Paris VI and Uniwersytet Jagielloński Kraków (2011). (Cited on pages 286, 288, 295, 299 and 300.)

[Gre64] R.C. Greenhow; *Optical Pumping in* He^3; Phys. Rev. **136**, A660 (1964). (Cited on pages 4, 76 and 169.)

[Gud95] H. Gudbjartsson, S. Patz; *The Rician Distribution of Noisy MRI Data*; Magn. Reson. Med. **34**, 910 (1995). (Cited on page 348.)

[Hap72] W. Happer; *Optical Pumping*; Rev. Mod. Phys. **44**, 169 (1972). (Cited on pages 1 and 246.)

[Has90] K.C. Hasson, G.D. Cates, K. Lerman, P. Bogorad, W. Happer; *Spin relaxation due to magnetic-field inhomogeneities: Quartic dependence and diffusion-constant measurements*; Phys. Rev. A **41**, 3672 (1990) - erratum in Phys. Rev. A **42**, 5766 (1990). (Cited on page 30.)

[Hay07] M.E. Hayden, E. Baudin, G. Tastevin, and P.J. Nacher; *NMR Time Reversal as a Probe of Incipient Turbulent Spin Dynamics*; Phys. Rev. Lett. **99**, 137602 (2007). (Cited on page 1.)

[Her00] N. Herschbach, P.J.J. Tol, W. Hogervorst, W. Vasen; *Suppression of Penning ionization by spin polarization of cold* He($2\,^3$S) *atoms*; Phys. Rev. A **61**, 050702(R) (2000). (Cited on page 195.)

[Hil72] J.C. Hill, L.L. Hatfield, N.D. Stockwell, and G.K. Walters; *Direct Demonstration of Spin-Angular-Momentum Conservation in the Reaction* He($2\,^3$S$_1$) + He($2\,^3$S$_1$) $\rightarrow$ He(1^1S$_0$) + He$^+$ + e^-; Phys. Rev. A **5**, 189 (1972). (Cited on page 194.)

[Hus05] D.S. Hussey, D.R. Rich, A.S. Belov, X. Tong, H. Yang, C. Bailey, C.D. Keith, J. Hartfield, G.D.R. Hall, T.C. Black, W.M. Snow, T.R. Gentile, W.C. Chen, G.L. Jones and E. Wildman; *Polarized* ^{3}He *gas compression system using metastability-exchange optical pumping*; Rev. Sci. Instr. **76**, 053503 (2005). (Cited on page 2.)

[Hut07] V. Hutanu, A. Rupp, J. Klenke, W. Heil and J. Schmiedeskamp; *Magnetization of* ^{3}He *spin filter cells*; J. Phys. D: Appl. Phys. **40**, 4405 (2007). (Cited on page 30.)

[Ich80] Y. Ichikawa, S. Teii; *Metastable atom density measurements in* He *and* Ne *positive column plasmas by an improved self-absorption method*; J. Phys. D: Appl. Phys. **13**, 1243 (1980). (Cited on pages 171 and 186.)

[Kas50] A. Kastler; *Quelques suggestions concernant la production optique et la détection optique d'une inégalité de population des niveaux de quantification spatiale des atomes. Application à l'expérience de Stern et Gerlach et à la résonance magnétique*; J. Phys. Radium **11**, 225 (1950). (Cited on page 1.)

[Kas57] A. Kastler; *Optical Methods of Atomic Orientation and of Magnetic Resonance*; J. Opt. Soc. Am. **47**, 460 (1957). (Cited on pages 51 and 246.)

[Kle08] J. Klemmer; *Untersuchungen zum optischen Pumpen von* ^{3}He *hinsichtlich der Entwicklung eines kompakten Polarisators* (in German); Diploma thesis Universität Mainz (2008). (Cited on pages 286, 288 and 299.)

[Kri09] J. Krimmer, M. Distler, W. Heil, S. Karpuk, D. Kiselev, Z. Salhi, E.W. Otten; *A highly polarized* ^{3}He *target for the electron beam at MAMI*; Nucl. Instr. and Meth. in Phys. Res. A **611**, 18 (2009). (Cited on page 1.)

[Kri11] J. Krimmer, P. Aguar Bartolomé, J. Ahrens, S. Altieri, H.J. Arends, W. Heil, S. Karpuk, E.W. Otten, P. Pedroni, Z. Salhi, A. Thomas; *A Polarized* ^{3}He *Target for the Photon Beam at MAMI*; Nucl. Instr. and Meth. in Phys. Res. A **648**, 35 (2011). (Cited on page 1.)

[Lal68] F. Laloë; *Étude d'une nouvelle méthode permettant d'orienter et d'aligner les divers niveaux excités de* ^{3}He; C. R. Acad. Sc. Paris **267**, 208 (1968). (Cited on page 76.)

[Lan10] B. Lancor, E. Babcock, R. Wyllie, and T.G. Walker; *Breakdown of Angular Momentum Selection Rules in High Pressure Optical Pumping Experiments*; Phys. Rev. Lett. **105**, 083003 (2010). (Cited on page 301.)

[Lan68] D.A. Landman; *Lifetimes and Alignment Depolarization Cross Sections of the (3p^{5}4p)* $^3D_3$ *and* $^1D_2'$ *Levels in Argon and the (1s2p)* ^3P *Term in Helium**; Phys. Rev. **173**, 33 (1968). (Cited on page 29.)

[Lar91] C. Larat; *Laser LNA de puissance; Application au pompage optique de l'hélium-3 et des mélanges hélium-3/hélium-4* (in French); Ph.D. thesis Université Paris VI (1991).
available online at http://tel.archives-ouvertes.fr/tel-00011879
(Cited on pages 5, 9 and 252.)

[Led00] M. Leduc, P.-J. Nacher, G. Tastevin and E. Courtade; *Kinetics of helium-3 laser optical pumping*; Hyperfine Interactions **127**, 443 (2000). (Cited on page 5.)

[Lef77] V. Lefèvre-Seguin and M. Leduc; *Metastability-exchange and depolarising collisions in xenon and krypton*; J. Phys. B: Atom. Molec. Phys. **10**, 2157 (1977). (Cited on page 1.)

[Lef82] V. Lefèvre-Seguin, P.J. Nacher, F. Laloë; *Relaxation nucléaire de* ^{3}He $\uparrow$ *dans un champ magnétique inhomogène*; J. Physique **43**, 737 (1982). (Cited on page 63.)

[Lef84] V. Lefèvre-Seguin; *Contribution à l'étude de* ^{3}He $\uparrow$ *gazeux. I. Relaxation à la surface de* H_2 *solide. II. Relaxation en volume: effets quantiques d'indiscernabilité*; Ph.D. thesis Université Paris VI (1984).
available online at http://tel.archives-ouvertes.fr/tel-00011847
(Cited on page 63.)

[Lel07] E. Lelièvre-Berna; *Mid-term report of the NMI3 neutron spin filter project*; Physica B **397**, 162 (2007).
(Cited on page 1.)

[Léo05] J. Léonard, A.P. Mosk, M. Waldhout, M. Leduc, M. van Rijnbach, D. Nehari and P. van der Straten; *Rotationally induced Penning ionization of ultracold photoassociated helium dimers*; Europhys. Lett. **70**, 190 (2005). (Cited on page 195.)

[Lor93] W. Lorenzon, T.R. Gentile, H. Gao, and R.D. McKeown; *NMR calibration of optical measurement of nuclear polarization in* ^{3}He; Phys. Rev. A **47**, 468 (1993). (Cited on pages 76 and 260.)

[Mar87] W.C. Martin; *Improved* ^{4}He I *1snl ionization energy, energy levels, and Lamb shifts for 1sns and 1snp terms*; Phys. Rev. A **36**, 3575 (1987). (Cited on page XXII.)

[McG08] K.P. McGee, R.D. Hubmayr, and R.L. Ehman; *MR Elastography of the Lung With Hyperpolarized* ^{3}He; Magn. Reson. Med. **59**, 14 (2008). (Cited on page 1.)

[Mil98] M.W. Millard, P.P. Yaney, B.N. Ganguly, and C.A. DeJoseph Jr; *Diode laser absorption measurements of metastable helium in glow discharges*; Plasma Sources Sci. Technol. **7**, 389 (1998). (Cited on pages 77, 112 and 186.)

[Mil87] R.G. Milner, R.D. McKeown and C.E. Woodward; *Study of spin relaxation by a charged particle beam in a polarized* ^{3}He *gas target*; Nucl. Instr. and Meth. in Phys. Res. A **257**, 286 (1987). (Cited on page 294.)

[Mue01] R.M. Mueller; *The* Yb *fiber laser for metastable* ^{3}He *optical pumping at Jülich*; Physica B **297**, 277 (2001). (Cited on pages 2 and 203.)

[Nac85] P.-J. Nacher, M. Leduc; *Optical pumping in* ^{3}He *with a laser*; J. Physique **46**, 2057 (1985). (Cited on pages 2, 4, 5, 8, 9, 11, 16, 18, 21, 23, 24, 27, 30, 33, 57, 58, 169, 251, 252, 311, 312, 316 and 317.)

[Nac99] P.-J. Nacher, G. Tastevin, X. Maitre, X. Dollat, B. Lemaire, J. Olejnik; *A peristaltic compressor for hyperpolarized helium*; Eur. Radiol. **9**, B18 (1999). (Cited on page 2.)

[Nac02] P.-J. Nacher, E. Courtade, M. Abboud, A. Sinatra, G. Tastevin, T. Dohnalik; *Optical pumping of helium-3 at high pressure and magnetic field*; Acta Phys. Pol. B **33**, 2225 (2002). (Cited on pages 5 and 261.)

[Nac12] P.-J. Nacher, G. Tastevin; *Metastability exchange optical pumping of helium-3: a general model*; in preparation (2012). (Cited on pages 5, 6, 15, 18, 24, 40, 48, 205, 302, 303, 304 and 305.)

[New93] N.R. Newbury, A.S. Barton, G.D. Cates, W. Happer, H. Middleton; *Gaseous* ^{3}He–^{3}He *magnetic dipolar spin relaxation*; Phys. Rev. A **48**, 4411 (1993). (Cited on page 30.)

[Nik07] A. Nikiel, T. Pałasz, M. Suchanek, M. Abboud, A. Sinatra, Z. Olejniczak, T. Dohnalik, G. Tastevin, P.-J. Nacher; *Metastability exchange optical pumping of* ^{3}He *at high pressure and high magnetic field for medical applications*; Eur. Phys. J. Special Topics **144**, 255 (2007). (Cited on pages 2, 176, 259, 288 and 297.)

[Nik10] A. Nikiel; *Polaryzacja* ^{3}He *w warunkach rozerwania sprzężenia struktury nadsubtelnej* (in Polish); Ph.D. thesis Uniwersytet Jagielloński Kraków (2010). (Cited on pages 117, 176, 186, 223 and 297.)

[Nik12] A. Nikiel, G. Collier, B. Głowacz, T. Pałasz, Z. Olejniczak, W. Węglarz, G. Tastevin, P.-J. Nacher, T. Dohnalik; *Metastability exchange optical pumping of* ^{3}He *gas up to hundreds of millibars at 4.7 T*; in preparation (2012). (Cited on pages 2, 117, 297 and 355.)

[Par09] S.R. Parnell, E. Babcock, K. Nünighoff, M.W.A. Skoda, S. Boag, S. Masalovich, W.C. Chen, R. Georgii, J.M. Wild, C.D. Frost; *Study of spin-exchange optically pumped* ^{3}He *cells with high polarisation and long lifetimes*; Nucl. Instr. and Meth. in Phys. Res. A **598**, 774 (2009). (Cited on page 1.)

[Pav70] M. Pavlović, F. Laloë; *Étude d'une nouvelle méthode permettant d'orienter, par pompage optique, des niveaux atomiques excités. Application à la mesure de la structure hyperfine de niveaux* ^1D *de* ^{3}He; J. Physique **31**, 173 (1970). (Cited on pages 2, 76, 260, 277 and 298.)

[Per01] F. Pereira Dos Santos, J. Léonard, Junmin Wang, C.J. Barrelet, F. Perales, E. Rasel, C.S. Unnikrishnan, M. Leduc, and C. Cohen-Tannoudji; *Bose-Einstein Condensation of Metastable Helium*; Phys. Rev. Lett. **86**, 3459 (2001). (Cited on page 195.)

[Pin74] M. Pinard, J. van der Linde; *Disorientation of* ^{3}He ^1D *States in* ^{3}He – ^{3}He *Collisions*; Can. J. Phys. **52**, 1615 (1974). (Cited on page 76.)

[Pin79] M. Pinard, C.G. Aminoff, and F. Laloë; *Velocity-selective optical pumping and Doppler-free spectroscopy*; Phys. Rev. A **19**, 2366 (1979). (Cited on page 246.)

[Ras99] E. Rasel, F. Pereira Dos Santos, F. Saviero Pavone, F. Perales, C.S. Unnikrishnan, and M: Leduc; *White light transverse cooling of a helium beam*; Eur. Phys. J. D **7**, 311 (1999). (Cited on page 203.)

[Ric02] D.R. Rich, T.R. Gentile, T.B. Smith, A.K. Thompson, G.L. Jones; *Spin exchange optical pumping at pressures near 1 bar for neutron spin filters*; Appl. Phys. Lett. **80**, 2210 (2002). (Cited on page 1.)

[Rob01] A. Robert, O. Sirjean, A. Browaeys, J. Poupard, S. Nowak, D. Boiron, C.I. Westbrook, A. Aspect; *A Bose-Einstein Condensate of Metastable Atoms*; Science **292**, 461 (2001). (Cited on page 195.)

[Sch65] L.D. Schearer, G.K. Walters; *Nuclear Spin-Lattice Relaxation in the Presence of Magnetic-Field Gradients*; Phys. Rev. **139**, 1398 (1965). (Cited on page 30.)

[Sch67] L.D. Schearer; *Collision-Induced Mixing in the 2^3P Levels of Helium*; Phys. Rev. **160**, 76 (1967). (Cited on pages 248, 249, 250 and 251.)

[Sch69a] L.D. Schearer; *Ion polarisation via Penning collisions with optically pumped metastable helium*; Phys. Rev. Lett. **22**, 629 (1969). (Cited on page 195.)

[Sch69b] L.D. Schearer; *Depolarization Cross Sections for the Metastable Noble Gases by Optical Pumping*; Phys. Rev. **188**, 505 (1969). (Cited on page 1.)

[Sch70] L.D. Schearer and L.A. Riseberg; *Spin conservation in ionizing collisions between* He*(2^3S_1) metastable atoms*; Phys. Lett. **33A**, 325 (1970). (Cited on page 194.)

[Sch04] J. Schmiedeskamp; *Weiterentwicklung einer Produktionsanlage und der Speicherungs- bzw. Transportkonzepte für hochpolarisiertes* ^{3}He (in German); Ph.D. thesis Universität Mainz (2004).
available online at
http://nbn-resolving.de/urn/resolver.pl?urn=urn:nbn:de:hebis:77-6860
(Cited on pages 2 and 261.)

[Sch06a] J. Schmiedeskamp, W. Heil, E.W. Otten, R.K. Kremer, A. Simon, and J. Zimmer; *Paramagnetic relaxation of spin polarized* ^{3}He *at bare glass surfaces*; Eur. Phys. J. D **38**, 427 (2006). (Cited on page 30.)

[Sch06b] J. Schmiedeskamp, H.-J. Elmers, W. Heil, E.W. Otten, Yu. Sobolev, W. Kilian, H. Rinneberg, T. Sander-Thömmes, F. Seifert, and J. Zimmer; *Relaxation of spin polarized* ^{3}He *by magnetized ferromagnetic contaminants*; Eur. Phys. J. D **38**, 445 (2006). (Cited on page 30.)

[Sco94] J.H. Scofield; *A Frequency-Domain Description of a Lock-in Amplifier*; American Journal of Physics **62**, 129 (1994). (Cited on page 333.)

[Shl94] G.V. Shlyapnikov, J.T.M. Walraven, U.M. Rahmanov, and M.W. Reynolds; *Decay Kinetics and Bose Condensation in a Gas of Spin-Polarized Triplet Helium*; Phys. Rev. Lett. **73**, 3247 (1994). (Cited on page 195.)

[Sig08] Signal Recovery, AMETEK Advanced Measurement Technology, Inc; *What is a lock-in amplifier?*; Technical Note TN 1000, V5.01/08UK (2008). available online at http://www.signalrecovery.com/literature/technical-notes.aspx (Cited on page 333.)

[Som92] T.J. Sommerer, M.J. Kushner; *Numerical investigation of the kinetics and chemistry of rf glow discharge plasmas sustained in* He, N_2, O_2, He / N_2 / O_2, He / CF_4 / O_2, *and* SiH_4 / NH_3 *using a Monte Carlo-fluid hybrid model*; J. Appl. Phys. **71**, 1654 (1992). (Cited on page 186.)

[Sta09] T. Stavngaard, L. Vejby Søgaard, M. Batz, L.M. Schreiber, A. Dirksen; *Progression of emphysema evaluated by MRI using hyperpolarized* ^{3}He *(HP* ^{3}He*) measurements in patients with alpha-1-antitrypsin (A1AT) deficiency compared with CT and lung function tests*; Acta Radiol. **50**, 1019 (2009). (Cited on page 1.)

[Sto96a] E. Stoltz, M. Meyerhoff, N. Bigelow, M. Leduc, P.-J. Nacher, G. Tastevin; *High nuclear polarization in* ^{3}He *and* ^{3}He – ^{4}He *gas mixtures by optical pumping with a laser diode*; Appl. Phys. B **63**, 629 (1996). (Cited on pages 7 and 9.)

[Sto96b] E. Stoltz, B. Villard M. Meyerhoff, P.-J. Nacher; *Polarization analysis of the light emitted by an optically pumped* ^{3}He *gas*; Appl. Phys. B **63**, 635 (1996). (Cited on page 76.)

[Suc05] K. Suchanek, K. Cieślar, Z. Olejniczak, T. Pałasz, M. Suchanek, T. Dohnalik; *Hyperpolarized* ^{3}He *gas production by metastability exchange optical pumping for magnetic resonance imaging*; Optica Applicata **XXXV**, 263 (2005). (Cited on page 2.)

[Suc07] K. Suchanek, M. Suchanek, A. Nikiel, T. Pałasz, M. Abboud, A. Sinatra, P.-J. Nacher, G. Tastevin, Z. Olejniczak, T. Dohnalik; *Optical measurement of* ^{3}He *nuclear polarization for metastable exchange optical pumping studies at high magnetic field*; Eur. Phys. J. Special Topics **144**, 67 (2007). (Cited on pages 77 and 297.)

[Sur97] R. Surkau, J. Becker, M. Ebert, T. Grossmann, W. Heil, D. Hofmann, H. Humblot, M. Leduc, E.W. Otten, D. Rohe, K. Siemensmeyer, M. Steiner, F. Tasset, N. Trautmann; *Realization of a broad band neutron spin filter with*

compressed, polarized ^{3}He *gas*; Nucl. Instr. and Meth. in Phys. Res. A **384**, 444 (1997). (Cited on page 261.)

[Tac05] K. Tachibana, Y. Kishimoto, and O. Sakai; *Measurement of metastable* He* *(2^3S_1) density in dielectric barrier discharges with two different configurations operating at around atmospheric pressure*; J. Appl. Phys. **97**, 123301 (2005). (Cited on page 15.)

[Tal11] C. Talbot, M. Batz, P.-J. Nacher, and G. Tastevin; *An accurate optical technique for measuring the nuclear polarisation of* ^{3}He *gas*; J. Phys.: Conf. Ser. **294**, 012008 (2011).
available online at http://iopscience.iop.org/1742-6596/294/1/012008
(Cited on pages 38, 41, 70, 78, 84, 213, 214, 296 and 297.)

[Tas87] G. Tastevin; *Hélium-trois polarisé: ondes de spin et liquéfaction du gaz* (in French); Ph.D. thesis Université Paris VI (1987).
available online at http://tel.archives-ouvertes.fr/tel-00011862
(Cited on page 173.)

[Tas04] G. Tastevin, S. Grot, E. Courtade, S. Bordais, P.-J. Nacher; *A broadband ytterbium-doped tunable fiber laser for* ^{3}He *optical pumping at 1083 nm*; Appl. Phys. B **78**, 145 (2004). (Cited on pages 2, 26 and 203.)

[Tas10] G. Tastevin, B. Głowacz, P.-J. Nacher; *Using a cw 465 nm Laser to Probe Metastable* He_2 *Molecules*; J. Low Temp. Phys. **158**, 339 (2010). (Cited on page 300.)

[Tim71] R.S. Timsit, J.M. Daniels; *The Polarizations Produced, and the Rates of Polarization, in the Optical Pumping of* 2^3S_1 ^{3}He; Can. J. Phys. **49**, 545 (1971). (Cited on page 77.)

[Tre92] P.Tremblay, J. Beaubien, A. Michaud, and E. Cauchon; *Enhancement of optical pumping efficiency by frequency-modulated lasers*; J. Opt. Soc. Am. B **9**, 1537 (1992). (Cited on page 203.)

[Vri04] D. Vrinceanu, S. Kotochigova, and H.R. Sadeghpour; *Pressure broadening and shift of* He*($2^3P_{0,1,2}$)*-He*(2^3S) lines*; Phys. Rev. A **69**, 022714 (2004). (Cited on pages 15, 56 and 253.)

[Vri10] D. Vrinceanu and H.R. Sadeghpour; *Spin polarization transfer in ground and metastable helium atom collisions*; New Journal of Physics **12**, 065039 (2010).(Cited on pages 248 and 251.)

[Wal97] T.G. Walker, W. Happer; *Spin-exchange optical pumping of noble-gas nuclei*; Rev. Mod. Phys. **69**, 629 (1997). (Cited on pages 1 and 6.)

[Wal96] C.D. Wallace, D.L. Bixler, D. Huang, A.H. Wagman, F.B. Dunning, and G.K. Walters; *Use of a diode laser to measure the polarization of an optically pumped ensemble of* He*(2*^{3}*S) atoms*; Rev. Sci. Instrum. **67**, 1684 (1996). (Cited on pages 77 and 112.)

[Wie66] W.L. Wiese, M.W. Smith, B.M. Glennon; *Atomic transition probabilities*; Nat. Stand. Ref. Data Ser. NBS **4**, US Government Printing Office, Washington DC (1966). (Cited on pages XXI and 29.)

[Wol04] M. Wolf; *Erzeugung höchster* $^3\overrightarrow{\mathrm{He}}$ *Kernspinpolarisation durch metastabiles optisches Pumpen* (in German); Ph.D. thesis Universität Mainz (2004). available online at
http://nbn-resolving.de/urn/resolver.pl?urn=urn:nbn:de:hebis:77-6554
(Cited on pages 2, 5, 57, 58, 168, 169, 170, 172, 173, 251, 259, 260, 261 and 262.)

[Woo99] J.C. Wood, K.M. Johnson; *Wavelet Packet Denoising of Magnetic Resonance Images: Importance of Rician Noise at Low SNR*; Magn. Reson. Med. **41**, 631 (1999). (Cited on page 348.)

[Xia10] T. Xia, S.W. Morgan, Y.-Y. Jau, and W. Happer; *Polarization and hyperfine transitions of metastable* ^{129}Xe *in discharge cells*; Phys. Rev. A **81**, 033419 (2010). (Cited on page 1.)

[Zha93] X. Zhao, P.A. Soletsky, W.H. Bryan, F.B. Dunning, and G.K. Walters; *Temperature dependence of* He*(2*^3P_J*) reactions: Collision-induced mixing and conversion to* He_2*(b* $^3\Pi_g$*) molecules*; Phys. Rev. A **48**, 4350 (1993). (Cited on page 171.)

[Zhi76] R.A. Zhitnikov, V.A. Kartoshkin, G.V. Klementiev, and L.V. Usacheva; *Metastability Exchange in a Mixture of* He-*3 and* He-*4 Isotopes*; Zhurnal Eksperimentalnoi I Teoreticheskoi Fiziki **71**, 1761 (1976).
(Cited on page 30.)

Metastability exchange optical pumping in ^{3}He gas up to 30 mT: Efficiency measurements and evidence of laser-induced nuclear relaxation

Abstract: Advances in metastability exchange optical pumping (MEOP) of ^{3}He at high laser powers, with its various applications, but also at high gas pressures p_3 and high magnetic field strengths B, have provided strong motivation for revisiting the understanding and for investigating the limitations of this powerful technique. For this purpose, we present systematic experimental and theoretical studies of efficiency and of relaxation mechanisms in $B \leq 30$ mT and $p_3 = 0.63 - 2.45$ mbar. ^{3}He nuclear polarisation is measured by light absorption in longitudinal configuration where weak light beams at 1083 nm parallel to magnetic field and cell axis with opposite circular polarisations are used to probe the distribution of populations in the metastable state. This method is systematically tested to evaluate potential systematic biases and is shown to be reliable for the study of OP dynamics despite the redistribution of populations by OP light. Nuclear polarisation loss associated to the emission of polarised light by the plasma discharge used for MEOP is found to decrease above 10 mT, as expected, due to hyperfine decoupling in highly excited states. However, this does not lead to improved MEOP efficiency at high laser power. We find clear evidence of additional laser-induced relaxation instead. The strong OP-enhanced polarisation losses, currently limiting MEOP performances, are quantitatively investigated using an angular momentum budget approach and a recently developed comprehensive model that describes the combined effects of OP, ME and relaxation, validated by comparison to experimental results.

Keywords: Helium-3, optical pumping, metastability exchange, nuclear polarisation, light absorption, hyperpolarised gas

Pompage optique par échange de métastabilité dans un gaz d'hélium-3 jusqu'à 30 mT: mesures d'efficacité et mise en évidence d'un processus de relaxation nucléaire induit par laser

Résumé: Les progrès en pompage optique (PO) par échange de métastabilité (EM) dans de l'hélium-3 gazeux à forte puissance laser, dont les applications sont variées, mais aussi à forte pression p_3 et fort champ magnétique B ont fortement motivé la reprise d'investigations pour comprendre les processus limitant cette technique puissante. Nous présentons une étude systématique, expérimentale et théorique, de l'efficacité du POEM et des mécanismes de relaxation à $B \leq 30$ mT et $p_3 = 0.63 - 2.45$ mbar. La polarisation nucléaire M de l'hélium-3 est mesurée par absorption en configuration longitudinale, en utilisant des faisceaux à 1083 nm de faible puissance, parallèles à B et à l'axe de la cellule, et de polarisations circulaires opposées pour sonder la distribution des populations dans l'état métastable. Nos tests détailés montrent que cette méthode est fiable pour l'étude de la dynamique du POEM malgré la redistribution des populations par la lumière de pompage. La perte de M associée à l'émission de lumière polarisée par la décharge qui crée le plasma nécessaire au POEM décroît au-dessus de 10 mT, comme attendu, à cause du découplage hyperfin dans les états très excités. Pourtant cela n'améliore pas l'efficacité du POEM à forte puissance laser. Par contre, nous avons mis en évidence une relaxation supplémentaire liée à la présence du laser pompe. Les pertes importantes de M renforcées par PO, qui limitent actuellement les performances du POEM, sont étudiées quantitativement avec une approche basée sur un bilan de moment angulaire et un modèle détaillé, récemment développé, qui décrit les effets combinés du PO, de l'EM et de la relaxation, validé par comparaison aux résultats expérimentaux.

Mots clés: Hélium-3, pompage optique, échange de métastabilité, polarisation nucléaire, absorption lumineuse, gaz hyperpolarisé

Metastabiles Optisches Pumpen in ^{3}He Gas bis 30 mT: Effizienzmessungen und Nachweis laser-induzierter Kernspinrelaxation

Zusammenfassung: Fortschritte im Bereich des Metastabilen Optischen Pumpens (MEOP) von ^{3}He bei hohen Laserleistungen, aber auch bei hohen Gasdrücken p_3 und hohen Magnetfeldern B, haben entscheidend dazu beigetragen, Untersuchungen limitierender Prozesse dieser leistungsfähigen Technik mit zahlreichen Anwendungen wiederaufzunehmen. Mit dieser Zielsetzung stellen wir eine systematische Studie (experimentell und theoretisch) über MEOP-Effizienz und Relaxationsmechanismen in $B \leq 30$ mT und bei $p_3 = 0.63 - 2.45$ mbar vor. Die Kernspinpolarisation von ^{3}He wird durch Absorption in longitudinaler Konfiguration gemessen mittels schwacher 1083 nm-Probelaserstrahlen, parallel zu B und zur Zellenachse, mit entgegengesetzten Zirkularpolarisationskomponenten, um die Verteilung der Besetzungszahlen im metastabilen Zustand zu messen. Detaillierte Tests zeigen, dass diese Methode trotz Umverteilung der Besetzungszahlen durch Pumplicht zuverlässig zur Untersuchung von MEOP-Dynamiken eingesetzt werden kann. Emission von polarisiertem Licht durch die Gasentladung führt zu Polarisationsverlusten, die oberhalb von 10 mT aufgrund der Hyperfeinentkopplung in höher angeregten Zuständen abnehmen. Dennoch erhöht dies nicht die MEOP-Effizienz bei hohen Laserleistungen. Stattdessen können wir bei vorhandenem Pumplaser zusätzliche Kernspinrelaxation nachweisen. Die beträchtlichen OP-verstärkten Polarisationsverluste, die gegenwärtig die MEOP-Effizienz limitieren, werden quantitativ untersucht mithilfe eines Drehimpulsbilanz-Ansatzes und eines kürzlich entwickelten umfassenden Modells, das die kombinierten Auswirkungen von OP, ME und Relaxation beschreibt und durch Vergleich mit experimentellen Ergebnissen validiert wird.

Schlagwörter: Helium-3, optisches Pumpen, metastabile Austauschstöße, Kernspinpolarisation, Lichtabsorption, hyperpolarisiertes Gas